

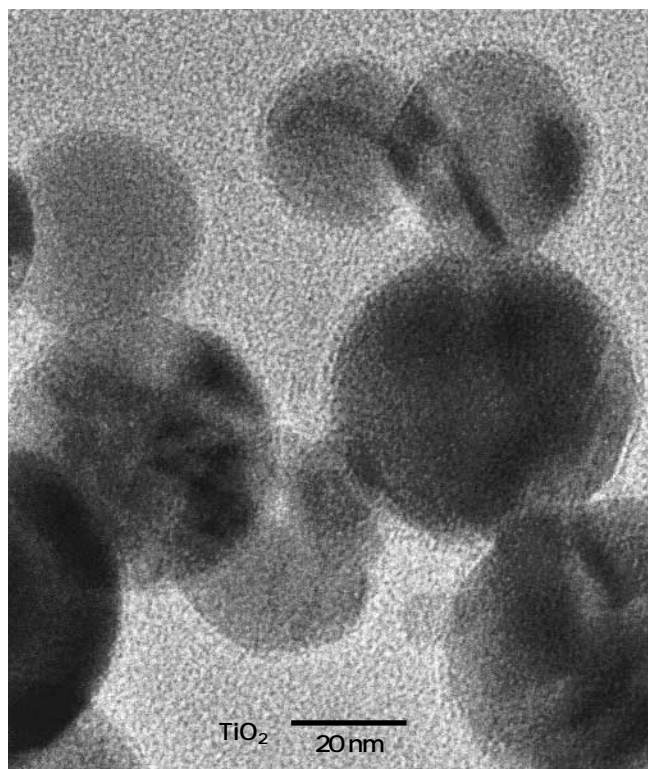
粉

KONA

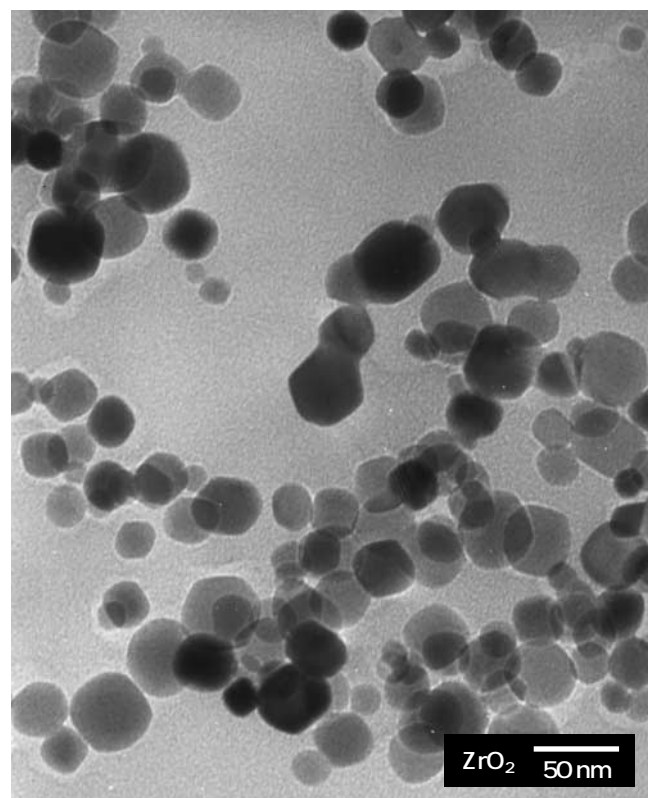
POWDER AND PARTICLE

No. 20 (2002)

Published by Hosokawa Powder Technology Foundation



Nanoparticles of zirconia and titania prepared
by Joule Quench Reactor



KONA

POWDER AND PARTICLE

KONA is a refereed scientific journal that publishes articles on powder and particle sciences and technology. KONA has been published annually since 1983 in Japan. KONA is distributed to researchers, members of the scientific community, universities and research libraries throughout the world.

About the Cover of Journal "KONA"

The Chinese character "粉" is pronounced "KONA" in Japanese, and means "Powder". The hand written "粉" is after the late Mr. Eiichi Hosokawa, founder of the Hosokawa Micron Corporation.



Hosokawa Micron Corporation and its R&D Center

Editorial Board

Y. Kousaka Editor in Chief
(Emeritus Professor of Osaka Prefecture Univ., JAPAN)

Asia / Oceania Editorial Board

Y. Tsuji Vice Chairman
(Osaka Univ., JAPAN)
Y. Morikawa (Emeritus Professor of Osaka Univ., JAPAN)
K. Miyanami (Emeritus Professor of Osaka Prefecture Univ., JAPAN)

H. Masuda (Kyoto Univ., JAPAN)
H. Emi (Kanazawa Univ., JAPAN)
K. Higashitani (Kyoto Univ., JAPAN)
K. Nogi (Osaka Univ., JAPAN)
Y. Fukumori (Kobe Gakuin Univ., JAPAN)
J. Hidaka (Doshisha Univ., JAPAN)
P. Arnold (Univ. of Wollongong, AUSTRALIA)
S.H. Kang (Yeungnam Univ., KOREA)
W. Tanthapanichakoon (Chulalongkorn Univ., THAILAND)

T. Yokoyama (Hosokawa Powder Technology Research Institute, JAPAN)

K. Yoshida (Hosokawa Micron Corp., JAPAN)

Secretariat

T. Kawamura (Hosokawa Powder Technology Foundation, JAPAN)

Europe / Africa Editorial Board

J. Schwedes Vice Chairman (Univ. Braunschweig, GERMANY)
K. Schönert (Technische Univ. Clausthal, GERMANY)
H. Schubert (TU Bergakademie Freiberg, GERMANY)
E. Forssberg (Univ. Lulea, SWEDEN)
H. Kalman (Ben Gurion Univ., ISRAEL)
J.F. Davidson (Univ. of Cambridge, UNITED KINGDOM)
J.F. Large (Univ. de Tech. de Compiègne, FRANCE)

Secretariat

P. van der Wel (Hosokawa Micron B.V. NETHERLANDS)
P. Krubeck (Hosokawa Micron GmbH, GERMANY)

Americas Editorial Board

D.W. Fuerstenau Chairman (Univ. of California, U.S.A.)
R. Flagan (California Institute of Technology, U.S.A.)
L. Augsburger (Univ. of Maryland School of Pharmacy, U.S.A.)
S.F. Thames (Univ. of Southern Mississippi, U.S.A.)
P.S. Santos (Univ. of São Paulo, BRAZIL)
B.M. Moudgil (Univ. of Florida., U.S.A.)
R. Hogg (Pennsylvania State Univ., U.S.A.)
D.J.W. Grant (Univ. of Minnesota., U.S.A.)

Secretariat

I. Pikus (Hosokawa Bepex Div., U.S.A.)
D.A. Scott (Hosokawa Micron Inter., U.S.A.)

Publication Office

Hosokawa Powder Technology Foundation (Japan) in Hosokawa Micron Corporation
No. 9, 1-chome, Shoudai Tajika, Hirakata-shi, Osaka 573-1132 Japan

Notes

○ Hosokawa Powder Technology Foundation has entrusted the editorial duty to the editorial board organized by the Council of Powder Technology, Japan.

(Complimentary Copy)

Printed in Japan

Obituary



On April, 29th. 2002, Professor Dr. Sunil de Silva died, totally unexpected and fast. Towards the end of a normal working day he felt some pain in his back and his stomach and they brought him by ambulance into a hospital. The physicians detected interior bleeding. These were so strong, that no help was possible. He died in an age of 59.

Sunil de Silva was borne in Colombo, Sri Lanka (at that time: Ceylon), on January 13th. 1943. He got his education up to university level in Colombo. After one year at Ceylon-University he went to the UK in Europe where he studied Chemical Engineering at the University of Loughborough. Already at that time he was aware of the effect that an education only in Ceylon would make him very much dependent upon his home-country. He stayed in Loughborough up to 1970 when he got his PhD with a thesis entitled "Transmission of Force through Particulate Systems with Restricted Geometries".

In 1970 Sunil moved on to the University of Karlsruhe in Germany, where he joined with Professor Kurt Leschonski as a scientific assistant within the Institute of Mechanical Process Engineering, headed by Professor Hans Rumpf. In 1972 he moved with Kurt Leschonski to the Technical University of Clausthal (Germany), where they founded a new Institute of Mechanical Process Engineering. Sunil stayed in Clausthal up to 1976. From 1976 to 1982 he worked in industry with Donaldson Europe in Belgium. His experiences in air classification, size analysis, jet mills and computer modelling of particulate flows, which he gained at the different places,

was an excellent basis to join Christian Michelsen Institute in Bergen, Norway, as a Post-Doctoral Fellow. In 1982 he was appointed as Head of Research in Powder Technology at Chr. Michelsen Institute.

In 1988 the management of the Chr. Michelsen Institute decided to close ist activities in Powder Technology. Sunil was appointed as an Adjunct Professor in Powder Technology in the faculty of Technology of Telemark University College in Porsgrunn and he was asked to move POSTEC to Porsgrunn. POSTEC (POWder Science and TEChnology) was a research programme which Sunil started in 1983 in Bergen together with his colleague and friend Gisle Enstad. Gisle Enstad and K. Manjunath moved with Sunil to Porsgrunn. Powder Science and Technology Research Ltd. (still: POSTEC) was founded with Sunil as the Managing Director. Very soon 25 companies got members of POSTEC. Sunil possessed the talent to motivate people and to convince them to work with POSTEC and to give them the necessary money. One of his mostly used sentence was "we don't have to convince people, we have to educate them". Thus, POSTEC got research money not only from companies but also from the European Community, from Scandinavian foundations as well as from the Norwegian Government.

In 1994 POSTEC was integrated as a Department within the foundation Telemark Technological R&D Centre (Tel-Tec) with Sunil as the Head of the Department. In 1995 he was appointed a full Professor in Powder Technology at Telemark University College. He retained his responsibility within Tel-Tec up to the end of 2002, when this responsibility was handed over to Gisle Enstad. Now, Sunil could devote all his time to the College, where he was Head of the Department, Pro-Dean and member of the College's Senate. He concentrated his activities more and more on questions of education, which following his ideas was not only teaching itself but more the formation and alteration of the existing teaching courses. He never followed existing rules without asking for their significance.

Sunil served on many international committees and working parties, he was member of several editorial boards. He gave a number of courses in many countries and he organised in Norway three well attended international conferences RelPowFlo I, II, III (Reliable Powder Flow). RelPowFlo IV should take place in Sri Lanka in winter 2003/2004. With that conference

Sunil wanted to retire. We all are very dispressed (sad) that it was not permitted to him to do so.

Sunil was a beloved and a requested partner in industry, in university, in committees and in private life. His places of activity in four European countries, but most of all his open, friendly, direct and honest nature was the reason for the enormous number of

friends he had around the world. Sunil was a “character” whom we cannot forget.

J. Schwedes
Vice Chairman of Europe/Africa Editorial Board
(Prof., Univ. of Braunschweig, Germany)

The Letter from the Editor



Yasuo Kousaka
Editor-in-Chief

The Fourth World Congress on Particle Technology (4WCPT) was successfully held in Sydney from July 21st to 25th, 2002. There were approximately 500 participants from 35 countries around the world and the number of papers including posters presented at the meeting was about 500. The number of participants was about 200 less than at the 3WCPT held in Brighton in 1998, whereas the number of papers increased by about 100. This meeting was partially supported by the Hosokawa Powder Technology Foundation. An informal KONA editorial board meeting was held on July 23rd during the 4WCPT to exchange ideas among the several editors from the Americas, Europe/Africa and Asia/Oceania Blocks. A forthcoming particle related meeting, the Second Asian Particle Technology Symposium (APT2003), will be held in Penang, Malaysia from December 17th to 19th, 2003.

The Hosokawa Powder Technology Foundation is now considering electronic publication of this journal. It is hoped that we will have the ability to download this issue from the Internet.

This year we lost another member of the KONA editorial board, chairman of the Europe/Africa Block, Professor S. de Silva in Postec-Research A/S, Norway. We all heartily lament his death and extend our sincere condolences.

In the past, issues of KONA have normally been published and distributed in February or March. However, the original KONA publication and distribution schedule was intended for the end of December. This year we have made an effort to advance the publication date, and I hope this issue will be in your hands in December of 2002.

Yasuo Kousaka



KONA

GENERAL INFORMATION

HISTORY OF THE JOURNAL

KONA journal has been published by the Council of Powder Technology, Japan. (CPT), from No.1 to No.12 issues, under the sponsorships of Hosokawa Micron Corporation (No.1 to No.9) and Hosokawa Powder Technology Foundation (No.10 to No.12).

The CPT has been established in 1969 as a non-profit organization to enhance the activities of research and development on powder science and technology in Japan under the sponsorship of Hosokawa Micron Corporation. In 1983, the CPT has decided to issue an international journal named "KONA", which publishes the excellent articles appeared in Japanese journals concerning powder science and technology, after translated into English, throughout the world. After the seventh volume issued in 1989, the CPT has changed its policy to internationalize the "KONA" from the 8th issue (1990) and on by incorporating the monographs originally written in English from the authors throughout the world. Immediately, the present editorial board including Asian, Americas' and European Blocks has been organized.

From the 13th issue and on, the Hosokawa Powder Technology Foundation has taken over the role of KONA publisher from the CPT in 1995 (No.13) and the Foundation has entrusted the editorial duty to the present KONA editorial board organized by the CPT without requesting any shift in our present editorial policies. This switching of publisher has been simply and only to make the aim and scope of the Foundation definite. Essentially no change has been observed in continuously editing and publishing this journal except in the designation on a part of the journal cover.

AIMS AND SCOPE OF THE JOURNAL

KONA Journal is to publish the papers in a broad field of powder science and technology, ranging from fundamental principles to practical applications. The papers discussing technological experiences and critical reviews of existing knowledge in specialized areas will be welcome.

These papers will be published only when they are judged, by the Editor, to be suitable for the progress of powder science and technology, and are approved by any of the three Editorial Committees. The paper submitted to the Editorial Secretariat should not have been previously published except the translated papers which would be selected by the Editorial Committees.

CATEGORY OF PAPERS

- Invited papers
Original research and review papers invited by the KONA Editorial Committees.
- Contributed papers
Original research and review papers submitted to the KONA Editorial Committees, and refereed by the Editors.
- Translated papers
Papers translated into English, which were previously published in other languages, selected by the KONA Editorial Committees with the permission of the authors and / or the copyright holder.

SUBMISSION OF PAPERS

Papers should be sent to each KONA Editorial Secretariat.

- Asia / Oceania Editorial Secretariat
T. Kawamura
Hosokawa Micron Corporation Micromeritics Laboratory 1-9,
Shoudai Tajika, Hirakata 573-1132 JAPAN
- Europe / Africa Editorial Secretariat
Dr. P. van der Wel or Mrs. P. Krubeck
Hosokawa Micron GmbH
Welsersstr. 9-11, 51149 Köln
P.O. Box 920262, 51152 Köln
GERMANY

- Americas Editorial Secretariat
Dr. I. Pikus or D.A. Scott
Hosokawa Micron International Inc.
10 Chatham Road, Summit, NJ 07901 USA

PUBLICATION SCHEDULE

KONA is published once a year.

SUBSCRIPTION

KONA is distributed free of charge to senior researchers at universities and laboratories as well as to institutions and libraries in the field throughout the world. The publisher is always glad to consider the addition of names of those who wish to obtain this journal regularly to the mailing list. Distribution of KONA is made by each Secretariat.

INSTRUCTIONS TO AUTHORS

- (1) Manuscript format
 - Two copies should be submitted to the Editorial Secretariat, in double-spaces typing on pages of uniform size.
 - Authorship is to give author's names, and the mailing address where the work has been carried out on the title page.
 - Abstract of 100-180 words should be given at the beginning of the paper.
 - Nomenclature should appear at the end of each paper. Symbols and units are listed in alphabetical order with their definitions and dimensions in SI units.
 - Literature references should be numbered and listed together at the end of paper, not in footnotes. Please give information as in the following examples:
 - 1) Carslaw, H.C. and J.C. Jaeger: "Conduction of Heat in Solids", 2nd ed., Clarendon Press, Oxford, England (1960).
 - 2) Howell, P.A.: US Patent, 3,334,603 (1963).
 - 3) Rushton, J.H., S. Nagata and D.L. Engle: AIChEJ., 10. 294 (1964).
 - 4) Seborg, D.E.: Ph.D. Dissertation, Princeton Univ., N.J., U.S.A. (1969).
 - Original figures with each single copy should be submitted, on separate sheets. Authors' names and figure numbers are marked in the corner.
 - Figure numbers and captions are listed on a separate sheet.
 - Place of figure insertion is to be indicated in the margin of the manuscript.
 - Tables should be typed on separated sheets.
 - Author's short biography and photograph should be attached.
 - Submit an IBM-readable floppy disk (3 $\frac{1}{2}$) with your unformatted text file in ASCII code. If you use either WORD or WORD PERFECT—as word processing system, please add the formatted text file.
- (2) Reprints
 - The authors shall receive 50 free reprints. Additional reprints will be furnished when ordered with return of galley proofs.
- (3) Publication policy
 - All papers submitted for publication become immediately the property of the CPT and remain so unless withdrawn by the author prior to acceptance for publication or unless released by the Editor. Papers are not to be reproduced or published in any form without the written permission of the CPT.

KONA Powder and Particle No. 20 (2002)

Contents

< **Review** >

* Motionless Mixers in Bulk Solids Treatments – A Review	<i>J. Gyenis</i>	9
* Gas-Phase Production of Nanoparticles	<i>A. Gutsch, M. Krämer, G. Michael, H. Mühlenweg, M. Pridöhl and G. Zimmermann</i>	24
* A Century of Research in Sedimentation and Thickening	<i>F. Concha and R. Bürger</i>	38
* Dry Powders for Pulmonary Delivery of Peptides and Proteins	<i>H. Okamoto, H. Todo, K. Iida and K. Danjo</i>	71
* Synthesis and Fabrication of Inorganic Porous Materials: From Nanometer to Millimeter Sizes	<i>M. Takahashi and M. Fuji</i>	84

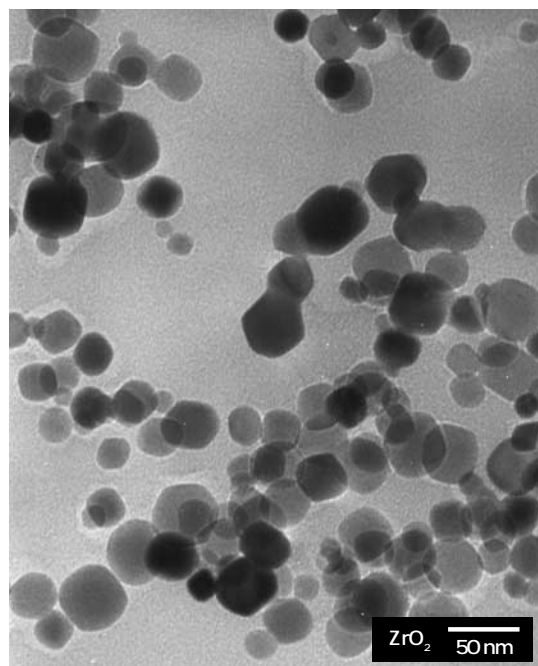
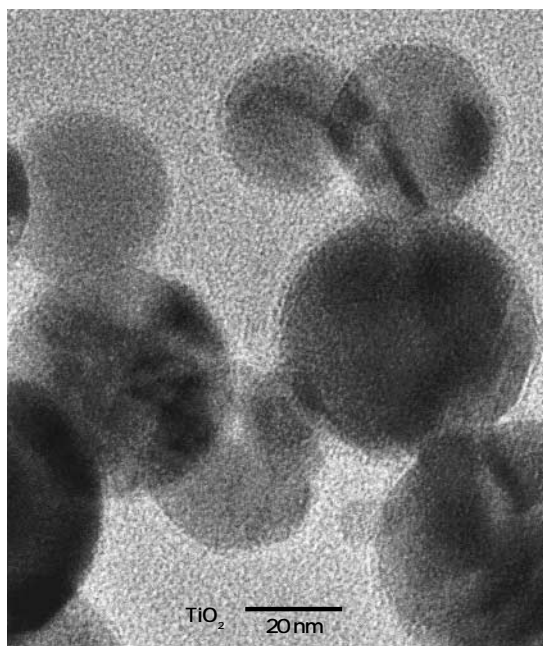
< **Original Research Paper** >

* The Feasibility of Ferro-alloy fines Recovery by using Centrifugal Separator Technology	<i>A.B. Nesbitt, S. Wanliss and F.W. Petersen</i>	98
* Stochastic Aspects of Granular Flow in Vibrated Beds	<i>R. Wildman and J.M. Huntley</i>	105
* Low-Frequency Vibration Effects on Coarse Particle Filtration	<i>R.J. Wakeman and P. Wu</i>	115
* Effects of Wall Inclinations and Wall Imperfections on Pressures during Granular Flow in Silos	<i>J. Tejchman</i>	125
* X-Ray Analysis of Fluidized Beds and Other Multiphase Systems	<i>J.G. Yates, D.J. Cheesman, P. Lettieri and D. Newton</i>	133
* Combination of SHS and Mechanochemical Synthesis for Nanopowder Technologies	<i>T. Grigorieva, M. Korchagin and N. Lyakhov</i>	144
* Performance and Cost-Effectiveness of Ferric and Aluminum Hydrous Metal Oxide Coating on Filter Media to Enhance Virus Removal	<i>T.M. Scott, R.C. Sabo, J. Lukasik, C. Boice, K. Shaw, L. Barroso-Giachetti, H. El-Shall, S.R. Farrah, C. Park, B. Moudgil and B. Koopman</i>	159
* Consolidation Behavior of Inhomogeneous Granular Beds of Ductile Particles using a Mixed Discrete-Continuum Approach	<i>S. Zheng and A.M. Cuitiño</i>	168
* Physical Properties of Supercritically-Processed and Micronised Powders for Respiratory Drug Delivery	<i>B.Y. Shekunov, J.C. Feeley, A.H.L. Chow, H.H.Y. Tong and P. York</i>	178
* Particle Shape Modification in Comminution	<i>E. Kaya, R. Hogg and S.R. Kumar</i>	188
* Primary Segregation Shear Cell for Size-Segregation Analysis of Binary Mixtures	<i>S.P. Duffy and V.M. Puri</i>	196
* A Load-Interactive Model for Predicting the Performance of Autogenous and Semi-Autogenous Mills	<i>H. Delboni Jr. and S. Morrell</i>	208

< **Translated Research Paper** >

- * Development of an Apparatus for Measuring Adhesive Force between Fine Particles *Y. Shimada, Y. Yonezawa, H. Sunada,..... 223*
R. Nonaka, K. Katou and H. Morishita
- * Continuous Synthesis of Monodispersed Alumina Particles by the Hydrolysis of Metal Alkoxide Using a Taylor Vortex *T. Ogihara and M. Nomura..... 231*
- * Production of Silica Particles by Electrostatic Atomization *Y. Mori and Y. Fukumoto 238*
- * Flocculation Mechanism of Suspended Particles Using the Hydrophilic/Hydrophobic Transition of a Thermosensitive Polymer *S. Sakohara, T. Kimura 246*
and K. Nishikawa
- * Development of Agglomerated Crystals of Ascorbic Acid by the Spherical Crystallization Technique for Direct Tableting, and Evaluation of Their Compactibilities *Y. Kawashima, M. Imai, H. Takeuchi, 251*
H. Yamamoto and K. Kamiya
- * Dispersion and Flocculation Behavior of Fine Metal Oxide Particles in Various Solvents *J. Shibata, K. Fujii, N. Murayama..... 263*
and H. Yamamoto

Explanation of the Cover Photographs
Nanoparticles of zirconia and titania prepared
by Joule Quench Reactor



The photographs show TEM images of zirconia (ZrO₂) and titania (TiO₂) particles produced using a nanoparticle generator, called “Joule Quench Reactor (JQR)”. JQR produces the nanoparticles by the chemical reaction of organic compounds including inorganic or metal components to generate core particles using plasma followed by rapid quenching. The ZrO₂ particles made by JQR have an average particle size calculated from BET specific surface area of 37 nm and a crystal size measured by X-ray diffraction method of 32 nm. The good agreement of these two means each particle consists of a single crystal, which is also presumed from the fact that the particles have polygonal shape. It is also remarkable that the ZrO₂ particles have higher whiteness than the conventional ones.

On the other hand, JQR also produces TiO₂ of anatase phase showing photocatalytic properties. The TiO₂ particles made by JQR have a BET equivalent particle size of 58 nm and a XRD crystal size of 38 nm. The particles have spherical shape and higher whiteness compared with the conventional TiO₂.

Motionless Mixers in Bulk Solids Treatments – A Review[†]

J. Gyenis

University of Kaposvar

*Research Institute of Chemical and Process Engineering**

Abstract

In this paper the general features, behavior and application possibilities of motionless mixers in mixing and treatments of bulk solids are overviewed, summarizing the results published during the last three decades. Working principles, mechanisms, performance, modeling and applications of these devices are described. Related topics, such as use in particle coating, pneumatic conveying, contacting, flow improvement, bulk volume reduction, and dust separation are also summarized.

1. Introduction

Motionless or static mixers are widely known and applied in process technologies for the mixing of liquids, especially for highly viscous materials, and to contact different phases to enhance heat and mass transfer. Producing dispersions in two- and multi-phase systems such as emulsions, suspensions, foams, etc., is also the common aim of using motionless mixers. Far less information is known on their behavior, capabilities and applications in bulk solids treatments. Although investigations started more than thirty years ago in this field, research and development is still under way even now. Recent studies and applications gave evidence on the beneficial features of such devices in powder technology for mixing and other treatments of bulk solids.

Motionless or static mixers are flow-modifying inserts, built into a tube, duct or vessel. These tools do not move themselves, but using the pressure difference or the kinetic and potential energy of the treated materials, create predetermined flow patterns and/or random movements, causing velocity differences and thus relative displacements of various parts of the moving material. In this way, motionless mixers can considerably improve the process to be carried out. In fluids, motionless mixers work efficiently both in turbulent and laminar regions. Splitting, shifting, shearing, rotating, accelerating, decelerating and

recombining of different parts of materials are common mechanisms in this respect, both in fluids and bulk solids.

Motionless mixers eliminate the need for mechanical stirrers and therefore have a number of benefits: No direct motive power, driving motor and electrical connections are necessary. The flow of materials (even particulate flow) through them may be induced either by gravity, pressure difference or by utilizing the existing potential or kinetic energy. The space requirement is small, allowing a compact design of equipment in bulk solids treatments. Installation is easy and quick, e.g. by simple replacement of a section of tube or by fixing inserts into a tube or vessel. Set-up and operating costs are much lower than those of mechanical mixers, while maintenance is practically superfluous. Motionless mixers are available in a number of different types, shapes and geometries, made from a great variety of materials. The mixer can therefore easily be matched to process requirements and to the features of the processed materials. Physical properties, e.g. flow behavior, particle size, mechanical strength, abrasive effects, safe prescriptions. e.g. for food and pharmaceutical industries, can be taken into account by the proper design of mixers. Applications in powder technology are equally feasible in gravity and pneumatic conveying tubes, in chutes, hoppers and silos, or even in rotating, vibrated or shaken containers.

The greatest advantages of motionless mixers in bulk solids treatment are: high performance, continuous operation, energy and manpower savings, minimum space requirement, low maintenance costs,

* Veszprem, Egyetem u. 2, Hungary

[†] Accepted: June 28, 2002

trouble-free operation, easy measurement and control, and improvement of product quality.

There are a number of different types of motionless mixers available from a number of manufacturers, most of them are applicable for bulk solids, too. The most widely known types are, e.g. Sulzer SMX and SMF mixers, Ross ISG and LPD mixers, Komax mixer, Kenics and FixMix mixers, etc. **Fig. 1** shows some examples of these devices.

The Sulzer SMX mixer (**Fig. 1a**) is a typical form of lamellar mixer, composed of narrow strips or lamellas placed side by side within a tube section. These strips decline from axial direction alternately by positive and negative angles, crossing the planes of each other, and thus constituting a 3-D series of X forms. During flow, the material is split into several streams or layers corresponding to the number of strips, shifted to opposite directions relative to each other. Flow cross-sections contract along its up-flow sides and expand at the down-flow sides. Thus, the material is forced laterally from the contracting to the neighboring expanding channels. One SMX element, i.e. one series of crossing strips, mixes principally in two dimensions along the plane of the X forms. Therefore, the next series of X forms is aligned at 90° to ensure three-dimensional mixing. Sulzer SMX is thus characterized by excellent cross-sectional (transversal) mixing and a high dispersing effect with a small space

requirement and a narrow residence time distribution. In multiphase flows no deposits and blockages occur, due to the high turbulence caused by the sharp edges and crossings. But, a drawback of this mixer also comes from this, because sharp edges and the sudden changes in flow directions increases pressure drop. In bulk solids flow, troubles can arise, especially for cohesive materials, for larger particles or broad size distributions.

Fig. 1b shows the Ross LPD mixer which consists of a series of slanted semi-elliptical plates positioned in a discriminatory manner in a tubular housing. When the material flows through this mixer, the input stream is split and diverted repeatedly in different directions along the cross-section of the tube, until a homogeneous mixture is achieved. This type of motionless mixer is generally used for the turbulent flow of low-viscosity liquids to enhance macro- and micro-mixing and/or to improve the heat transfer coefficient in heat exchangers. It is also feasible for particulate flows. But, since the flow at a given tube section is divided into two streams only, shear and material exchange takes place in one plane only between the two half-tube cross-sections, thus the mixing effect along a given length is weaker than in SMX mixers, especially for viscous materials or bulk solids. Naturally, the pressure drop is also less. For bulk solids, the maximal throughput in a Ross LPD

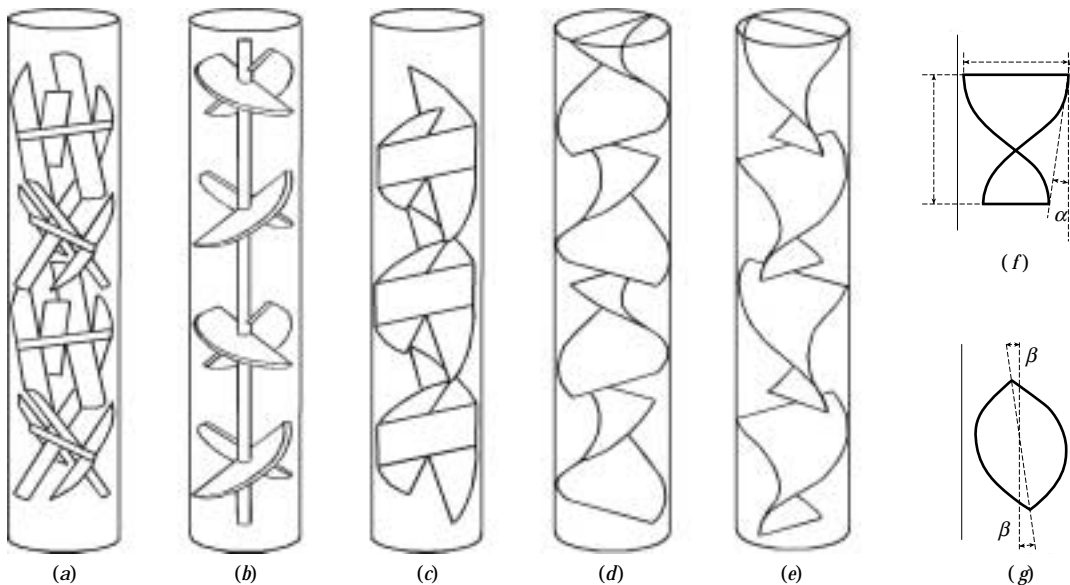


Fig. 1 Examples for motionless mixers also applicable for bulk solids
 (a) lamellar (Sulzer SMX) mixer, (b) Ross LPD mixer, (c) Komax mixer, (d) Kenics static mixer, (e) FixMix mixer, (f) α -taper and
 (g) β -skewness of a FixMix element

mixer is higher than in SMX, and the risk of plugging for cohesive powders or large particle sizes is considerably reduced. Another difference is that, due to the non-uniform axial velocity profile, the longitudinal mixing effect of the LPD mixer may be higher than that of the SMX mixer.

The Komax mixer (see **Fig. 1c**) consists of flat plates arranged essentially in axial direction in a tube, but at both ends of these plates they are hatched, rounded and bent in opposite directions. The neighboring mixer plates are arranged at 90° in radial direction, touching each other with the tips of the bent flaps. This mixer is also called a “Triple-Action Mixer”, because it provides (i) two-by-two division, (ii) cross-current mixing and (iii) back mixing of counter-rotating vortices. Each mixing element set in combination sweeps approximately two-thirds of the circumference of the pipe and directs the flow to the opposite side, providing very strong wall-to-wall radial transfer. Between the sets of generally four mixer elements, inter-set cavities provide space for intensive contacting of the sub-streams of material by strong momentum reversal and flow impingement. For multiphase flow, this mixer is resistant to fouling or clogging, because the flaps of the mixer elements are smoothly contoured with a large radius. Intersections between the element ends with the wall are all oblique angles, eliminating corners that can trap solid or fibrous materials and promote material accumulation. Momentum reversal and flow impingement provide a self-cleaning environment.

The Kenics static mixer shown in **Fig. 1d** possesses almost all the advantages of the Komax mixer. It consists of a long cylindrical pipe containing a number of helical elements twisted by 180° alternately in left-hand and right-hand directions, perpendicular to flow direction. The adjacent elements are set by 90° in radial direction, therefore the outlet edge of a given element and the inlet edge of the next one are perpendicular to each other. The smooth helical surface directs the flow of material towards the pipe wall and back to the center, due to secondary vortices induced by the spiral-form twist of the flow channels. Additional velocity reversal and flow division results from shearing of the material along the tube cross-section between the adjacent elements. The systematic division of streams and their recombination in another way enhance the mixing effect proportionally to 2^n , where n is the number of the applied mixer elements. For fluids or in multiphase flows, a relatively narrow residence time is ensured, in addition to excellent radial mixing. Due to the smooth and mildly bending

surfaces of the helices, the pressure drop along a Kenics mixer is very low, while it provides continuous and complete mixing and eliminates radial gradients in temperature, velocity and composition. For bulk solids, because of the non-uniform axial velocity profile, a certain degree of longitudinal mixing also takes place. Due to the smooth surfaces and relatively wide flow channels, the risk of plugging or blockage is very limited.

The FixMix motionless mixer shown in **Fig. 1e** is very similar to the Kenics static mixer, with the essential difference that the individual elements are slanted relative to the tube axis and are tapered along their length. It results in several benefits: the slightly increasing gap between the mixer element and the tube wall eliminates the corners or contact points between them. Therefore, there are no dead zones, and deposition or blockage cannot occur. On the other hand, the cross-section of the flow channels on the two sides of a mixer element changes continuously along its length: the cross-sectional area on one side expands while on the other side it contracts. Due to the tangential flow at the wall and the pressure difference between the two sides, an intensive cross-flow takes place between the neighboring flow channels. These features provide improved mixing efficiency, lower pressure drop with suitable cross-sectional turbulence, and more uniform radial and tangential velocity fields. The higher velocity and the turbulence close to the tube wall results in higher heat transfer coefficients and a cleaner surface. In addition to this self-cleaning effect, the lack of corners makes the cleaning easier for difficult materials. This mixer provides higher mixing efficiency per unit mixer length and reduces the risk of blockage in bulk solids treatment.

During the past three decades, quite a number of papers were published on the application of motionless mixers in this latter field, and it is worth surveying these results to initialize further studies and practical applications.

2. Motionless Mixers in Bulk Solids Mixing

The mixing of bulk solids is an important operation in many industries, such as in the chemical and pharmaceutical industries, mineral processing, food industry and for treatments of agricultural materials. Uniform composition in these processes is of primary importance, as well as to eliminate segregation. Besides mechanical mixers and silo blenders, motionless mixers represent a viable solution for this task,

especially if continuous operation is possible or necessary. The application to homogenize solids was already envisaged as early as in 1969 by Pattison [1].

A crucial condition of such an application is the trouble-free flow of the bulk solids to be treated. Therefore, motionless mixers can only be used for free-flowing particles, but cohesiveness to some extent is tolerable even in gravity flow of such materials.

In addition to the devices conventionally known as motionless mixers, any other tools inserted into a tube or vessel or the intentional changes of tube or chute cross-sections can modify the flow pattern of solids. Therefore, they may also be considered as some kind of motionless mixer. Various inserts in silos or hoppers, or cascade chute assemblies causing the multiple division and recombination or modification of bulk solids flows can also be ranked here.

2.1 Mixing Mechanisms of Motionless Mixers

Several workers investigated the mixing mechanisms of particulate solids in motionless mixers acting in transversal [2] and longitudinal directions [3]. Observing the interactions between the particles and mixer elements, four kinds of mixing actions were distinguished [3, 4]. Namely: (a) multiple division and recombination of the particle flow, (b) interaction of particles with other particles, with the surface of mixer elements and the tube wall, (c) changes in flow direction, and (d) differences in velocity profile. Three main mechanisms, namely diffusive, convective and shear mixing were attributed to these actions. *Shear*: certain particle regions are sheared during particle flow, creating velocity differences between the adjacent layers. *Convection*: multiple division and recombination of the particle flow, as it is split into sub-streams and diverted to different ducts or directions, and then unified with other sub-streams. *Dispersive or diffusive-type mixing*: stochastic movements with interchanges of different particles. A great deal of experience accumulated in the last decades indicates that these mixing mechanisms act more or less together in any type of motionless mixer, and therefore they are hardly separable from each other.

The majority of experimental studies carried out until now used helical mixer elements such as Kenics or FixMix-type devices. In a few works, other types of motionless mixers such as Sulzer (Koch) mixers and mixer grids composed of helices, rods or lamellas, were investigated.

For certain types of mixers, the mixing mechanisms influence the characteristic direction of mixing.

There is a general belief that motionless mixers perform mainly radial (transversal) mixing, and that axial (longitudinal) mixing is negligible. But, according to our experience, also seen from the results of other workers, this is not entirely valid even for viscous liquids or plastic materials, due to non-uniform axial velocity profiles. Depending on their shape, arrangement and operational conditions, and in addition to a high radial dispersion [2], motionless mixers may cause effective axial mixing [3, 4], too. This latter feature is of crucial importance in equalizing concentration variations in time and space in continuous particle flows caused either by segregation or by non-uniform feeding.

2.2 Mixing Kinetics and Performance

The performance of a bulk solids mixer is characterized by its throughput, i.e. the treatable mass per unit volume and time, and by the degree of homogeneity achieved. These features are in close relation with the mixing kinetics, i.e. with the rate of homogeneity improvement, characterizing how fast the concentration uniformity is getting better as a function of time or mixer length. The mixing kinetics determines the number of motionless mixers necessary to achieve a given degree of homogeneity or its equilibrium. The latter may be the result of two competing processes: mixing and segregation. In other words: whilst the mixing mechanism tells us *in what manner*, the mixing kinetics characterizes *by which rate* and *how far* the process is going on.

From a practical point of view, the performance of a mixer is the most important feature, if we disregard the actual mechanism of mixing. However, the mechanism gives an explanation of the mixing kinetics experienced, thus also serving as a starting point for further improvements. Therefore, almost all studies carried out in this field aimed at determining the rate of process [5-14], and only a few works dealt with the mechanism. The kinetics of the mixing and segregation processes competing with each other can be characterized by the equation [14]:

$$\frac{dM}{dt} = K_m(1 - M) \pm K_s\Phi \quad (1)$$

where M denotes the actual degree of mixedness, K_m and K_s are the kinetic constants of mixing and segregation, respectively, while Φ is the so-called segregation potential [14]. Although there are a number of various definitions for the degree of mixedness [15], the most simple and well applicable one was defined by Rose [16] as

$$M = 1 - \frac{s}{s_0} \quad (2)$$

where s and s_0 are the estimated standard deviations of the sample concentrations taken from the actual mixture and in a totally segregated state, respectively.

Among the earliest works carried out in this field, the mixing performance of the Kenics [2-4, 8] and Sulzer (Koch) motionless mixers [6, 7] was reported by the team of L. T. Fan. In some studies, the mixing of wheat, sorghum grains and flour was determined both in axial and radial directions. Among different experimental methods, the radioactive tracer technique was used to observe the rate of the process. The practical purpose of these investigations was to upgrade low-quality products by adding high-quality ones during continuous blending. Motionless mixers were proposed, e.g. to feed mills with a controlled quality of raw material. The kinetics of simultaneous mixing and segregation processes was investigated experimentally with free-flowing particles which differed in particle size or in particle density, or both. Under given conditions, comparison showed that differences both in particle size and density gave substantially faster mixing and segregation rates compared to systems where differences took place in either particle size or particle density alone [8].

The mixing of materials of different particle sizes, shapes and densities is generally accompanied by segregation. After quite a long mixing time, these concurrent processes result in a balanced degree of mixedness which is lower than it would be in a totally random distribution of the component particles. Depending on the initial positions of the components, equilibrium is approached gradually from below, or very often, after going through a maximum. In this latter case, the uniformity of a mixture decreases in the final period of the process, in spite of continued mixing action. Boss and his co-workers [10, 11] investigated the balanced degree of mixedness in systems of different particle sizes. Two types of motionless mixers were tested: (a) lamellar mixers composed of slanted metal strips crossing each other similarly to Sulzer SMX mixers, and (b) roof mixers consisting of grids of angle profiles arranged in horizontal rows at different cross-sections. Similarly to the works of Fan and his co-workers, these experiments showed significant segregation after certain passes through the motionless mixer. (In these experiments, increasing mixer lengths were simulated by repeated flows through a given length of mixer tube.)

2.3 Modeling and Simulations

To describe a process or equipment theoretically, or to predict the characteristic features and results of their applications under different conditions, mathematical modeling and simulation proved to be widely applied and useful tools. To investigate motionless mixers in solids mixing, various modeling principles and simulation methods were used till now. Chen et al. [4] adapted the concepts of an axially dispersed plug-flow model, commonly used at that time to describe the mixing of fluids in various unit operations. In their work, a quasi-continuous deterministic model was applied to describe the axial dispersion of particles in a gravity mixer tube containing motionless mixer elements. Residence time distributions were measured by the stimulus-response technique, and apparent Peclet numbers and axial dispersion coefficients were determined for three different kinds of solid particles, after different number of passes through the mixer tube.

Apparent Peclet numbers (Pe') and axial dispersion coefficients (K'_{ax}) have similar definitions here to those used in fluids to characterize the intensity of longitudinal mixing. Their values can be determined from the residence time distribution of tracer particles in the mixer tube determined by discrete sampling at the outlet at different times after they are introduced at the inlet in the form of a plug [17]. The second central moment μ_2 of the residence time distribution is as follows:

$$\mu_2 = \sum_i (\tau_i - \bar{\tau})^2 \cdot x_i \quad (3)$$

where τ_i is the residence time of tracer particles in the mixer tube taken off by the i -th sample, and x_i is the mass fraction of tracer particles in the i -th sample. The mean residence time of all tracer particles along the mixer tube corresponds to the first moment of the residence time distribution as:

$$\bar{\tau} = \sum_i \tau_i \cdot x_i \quad (4)$$

The apparent Peclet number is determined from the mean residence time $\bar{\tau}$ and the second central moment μ_2 of the residence time distribution, corrected by $\mu_{2,0}$, which is the second central moment obtained in a plain tube, i.e. without motionless mixer elements:

$$Pe' = \frac{2\bar{\tau}^2}{\mu_2 - \mu_{2,0}} \quad (5)$$

and the axial dispersion coefficient:

$$K'_{ax} = \frac{L_{mix}^2}{\bar{\tau} \cdot Pe'} \quad (6)$$

where L_{mix} is the length of the studied mixer section. The intensity of mixing, i.e. the achievable mixing effect of motionless mixer elements per unit length is the higher the lower Pe' is or the higher K'_{ax} is.

Chen et al. [4] pointed out that smaller particles had a higher apparent axial dispersion coefficient than the bigger ones. By increasing the linear velocity of solids through the motionless mixers, an almost exponential improvement was obtained in the axial dispersion coefficient. A similar technique and model was used by Gyenis et al. [17] to investigate the influence of different flow regimes, particle properties and length-to-diameter ratios of helical motionless mixers on the resultant axial dispersion coefficient.

In mixing processes, especially in particulate systems, stochastic behavior is a common feature which causes random variations both in flow characteristics and in the local concentrations of components. Such behavior in gravity mixer tubes containing motionless mixers was already recognized by the team of L. T. Fan [3, 7]. To interpret the experimental findings, a discrete stochastic model was applied [3, 7, 9, 18]. For this, prior knowledge of the one-step transition probabilities of the particles was necessary, which were determined experimentally. This model seemed to be suitable to predict concentration distributions after different passes through the mixers. However, on examining the results of experiments and those obtained by the stochastic model, two kinds of discrepancies can be recognized. One is that, in spite of identical particle properties, segregation and a spatially non-uniform mixing rate could be recognized [3]. Gyenis and Blicke proposed a possible theoretical explanation of this behavior [19]. It was assumed that spatially non-uniform transitions of particles between the adjacent layers were caused by the changing conditions during the non-steady-state flow. A correlation was proposed between the mixing rate and the energy dissipation caused by the interactions of the particles and the mixer elements.

The other discrepancy came from the fact that earlier stochastic models used only expected values to characterize the one-step transition probabilities, totally ignoring their possible random variation. This can be quite high if large-scale flow instabilities occur, especially in larger mixer volumes. Gyenis and Katai proposed [20] a new type of stochastic model to explain and describe the high random variations experienced in repeated experiments in an alterna-

tively revolving tumbler mixer, with and without motionless mixer grids. Some years later, this model was simplified for simulation purposes [21], and was then made more exact by Mihalyko and his co-worker [22], introducing the concept of a so-called double stochastic model.

DEM simulations based on a Lagrangian approach also helped to understand the features and working mechanisms of motionless mixers in particulate systems [23].

2.4 Application Studies for Bulk Solids Mixing

The mixing of free-flowing particle systems in gravity flow through motionless mixers was investigated by several workers [2-12]. Most of these studies resulted in suitable homogeneity after a few passes, but in some cases, depending on the physical properties of the components, considerable segregation also emerged. Herbig and Gottschalk [24] applied horizontal bars serving as motionless mixers built into a gravity mixer. It was found that assuring the smallest possible shear action is essential to suppress segregation.

A special, alternatively revolving bulk solids mixer equipped with motionless mixer elements shown in **Fig. 2** was studied by Gyenis and Arva [13, 14, 25, 26] and provides practically segregation-free mixing. This device consists of two cylindrical containers (1) and a mixer section between them containing horizontal mixer grids (2) composed of a number of

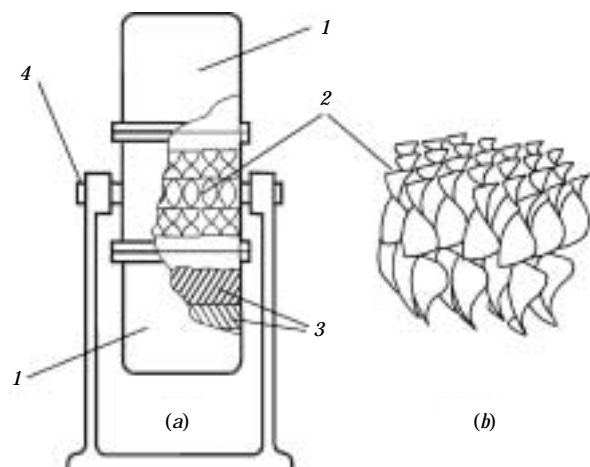


Fig. 2 Schematic diagram of the alternating revolving bulk solids mixer

(a) outline of the mixer, 1 - containers, 2 - grids composed of motionless mixer elements, 3 - components to be mixed, 4 - mount with rotating shaft, (b) helical motionless mixers arranged in grids

ordered FixMix elements. The material to be mixed (3) is filled into the lower container, then the mixer is rotated intermittently. In other words, the mixer body is turned through 180° in one direction, then stopped to allow the bulk solids that are meanwhile at the top enough time to flow down through the mixer elements. After this, the mixer is turned again through 180° but in the opposite direction. The whole procedure is then repeated till the required homogeneity is obtained. Because of the periodically reversing directions of particle flow and the changing direction of acceleration and deceleration of the particles, segregation can be almost totally avoided.

By this method, a considerable improvement of the mixing rate was achieved, resulting in a short mixing time and a high homogeneity at a reasonably low power consumption [27]. This was evidenced by examining the mixing kinetics of particle systems composed of materials with extremely different physical properties, listed in **Table 1**. The density ratios of the component particles were varied from 1.2 : 1 to 2.9 : 1, while the particle size ratios were changed from 1 : 2.7 to 1 : 110 as seen from **Table 2**. Kinetic curves, i.e. the variation of the degree of mixedness as a function of mixer turns are plotted in **Fig. 3**. It shows that this mixer provides rapid and segregation-free mixing. The degrees of mixedness were determined from the concentration variations of 65 spot samples taken after different numbers of mixer turns or mixing times by metal templates according to a regular pattern. A detailed description of this sam-

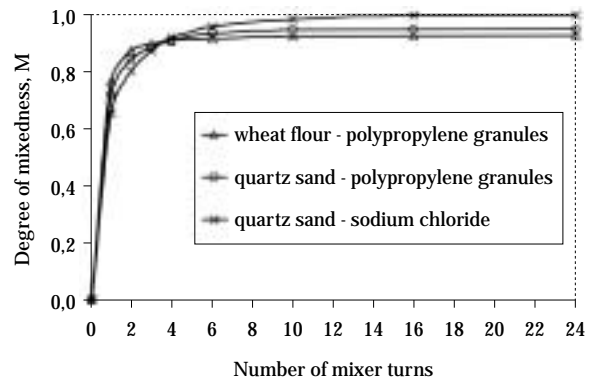


Fig. 3 Kinetic curves obtained by the mixer shown in **Figure 2** with extreme particle systems (particle sizes, densities, and their ratios are given in **Tables 1** and **2**)

pling method was given by Gyenis and Arva [13]. The mass of each sample was 20 g, and the compositions of samples were determined from 3×2.5 g material taken off from each sample, by dissolving the sodium chloride tracer particles and measuring the conductivity of the solution, or in other cases, by weighing the polypropylene tracer particles after mechanical separation of the samples.

Theoretical considerations gave an explanation of this segregation-free operation and of the high achievable equilibrium homogeneity [14].

Bauman [29] studied three different types of motionless mixers (Kenics, Komacs and Sulzer SMX) to mix particulate materials differing in mean particle size and size distribution, in bulk density and in mass ratio. It was concluded that the mass ratio of the components, as well as the shape and number of motionless mixers played a significant role in the achievable homogeneity. Kenics-type mixers proved to be the best when mass ratios were equal. But, when these differed significantly, Komacs and Sulzer SMX mixers gave much better results.

Motionless mixers are now increasingly applied in various process technologies to mix particulate solids. An interesting example for this is, e.g. the industrial standard of Tennessee [30], which mandates the use of Komax, Ross, Koch (Sulzer) or similar commonly accepted motionless mixers to manufacture hydraulic cement.

3. Bulk Solids Flow through Motionless Mixers

3.1 Gravity Flow Studies

The continuous flow of bulk solids in vertical tubes through Kenics-type motionless mixers was studied

Table 1 Particle sizes and densities of the constituents in mixes shown in **Fig. 3**.

Component	Mean particle size, mm	Density, kg/m ³
Quartz sand	0.17	2650
Sodium chloride	0.46	2160
Wheat flour	0.05	1510
Polypropylene granules	5.5	910

Table 2 Size and density ratios of the constituent particles in mixes shown in **Fig. 3**.

Component	Size ratio, —	Density ratio, —
Quartz sand - Sodium chloride	1 : 2.7	1.2 : 1
Quartz sand - Polypropylene	1 : 32.4	2.9 : 1
Wheat flour - Polypropylene	1 : 110	1.7 : 1

by Gyenis and his co-workers [12, 31, 32] under different conditions. These mixer tubes consisted of three sections: (1) a plain feeding tube at the top, (2) motionless mixers in the middle, and (3) another plain tube below the motionless mixers. The mass flow rate of solids was controlled by two means: (a) by adjusting the feeding rate at the inlet, or (b) by controlling the particle discharge at the bottom. Local particle velocities were measured by fiber-optical probes that captured light reflection signals. Average and local solids hold-ups were determined by weighing the material remaining in the tube after closing both ends, and by gamma-ray absorption during operation at different cross-sections, respectively. The axial mixing intensity was characterized by apparent Peclet numbers and dispersion coefficients calculated from residence time distributions of tracer particles. The details of experiments and the applied experimental devices were described in several papers of Gyenis and his co-workers [12, 31, 32].

Experiments [12, 31, 32] and DEM simulations [23] equally revealed that, depending on the feeding and discharging conditions, three characteristic flow regimes could be distinguished in such gravity mixer tubes, shown schematically by visualized simulation results in **Fig. 4**.

A first type of flow regime takes place, shown in **Fig. 4a**, if a solids flow withdrawn from the bottom, e.g. by a belt or screw conveyor, is less than the maximal possible throughput of the gravity mixer tube, determined by its diameter and the configuration of motionless mixers. Naturally, the inflow of particles at the tube inlet must be unlimited in this case, e.g. directly from a hopper. This 1st flow regime is characterized by dense flow, i.e. high solids hold-up in all the three tube sections.

By increasing the discharged flow rate in this 1st flow regime, the solids hold-up in the mixer tube decreases slightly, mainly due to the growing “gas bubbles” just below the lower surface of the motionless mixer elements. After reaching the maximal throughput, which is achieved by unlimited outflow, the solids hold-up suddenly drops to a well-determined value, resulting in a second flow regime shown in **Fig. 4b**. It is characterized by a dense sliding particle bed in the upper tube, accelerating particle flow along the mixer elements and almost free-falling particles in the lower plain tube section below the mixer section. The transition between the 1st and 2nd flow regimes can be well recognized from the snap-shots in **Fig. 4d**, obtained by DEM simulation, showing the actual situations at successive moments in time.

Another flow regime evolves when the solids flow rate is controlled at the inlet of the tube, with free outflow at the bottom. In this case, the flow rate of bulk solids fed into the tube must be lower than the maximal attainable throughput of the motionless mixers. This 3rd flow regime, shown in **Fig. 4c**, is characterized by almost free-falling particles in the upper and bottom plain tube sections with very low and progressively decreasing solids concentration. In the mixer section, however, a rapid sliding particle flow takes place along the surface of the mixer elements with a much higher solids hold-up compared to the upper and lower tube sections. When the solids flow rate in this flow regime is increased from zero to the maximal attainable capacity, the average solids volume fraction in the tube also increases from zero to a maximal value. Reaching this latter stage, the upper tube

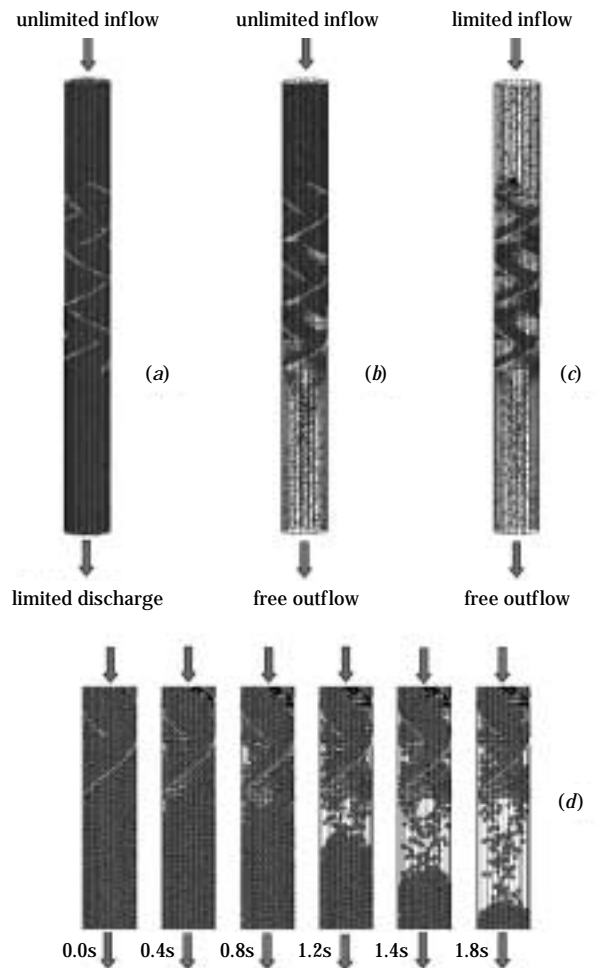


Fig. 4 Characteristic flow regimes in gravity mixer tubes with motionless mixers in the middle tube section (a) 1st flow regime, (b) 2nd flow regime, (c) 3rd flow regime, (d) transition between the 1st and 2nd flow regimes

section above the motionless mixers suddenly becomes choked with this sliding particle bed. This causes a rapid transformation from the 3rd to the 2nd flow regime.

Visual observations and experimental data revealed that in these flow regimes, a different and well-defined correlation exists between the solids hold-up in the mixer tube and the mass flow rate of particles taken off at the bottom or fed into the tube.

As seen from **Figs. 4a-d**, the particle concentration and thus solids volume fraction changes from place to place along the length of the tube. However, since the usual mixer tubes are composed of several sections (e.g. feeding, mixing and post-mixing sections) and, very frequently, free tube sections (inter-element distances) can be present between the individual mixer elements, it is reasonable to characterize operation conditions by the mean solids volume fraction averaged within the whole tube.

Plotting this mean solids volume fraction vs. the mass flow rate, important characteristics of the above-described flow regimes can be recognized, also indicating the conditions of transitions between them, as is shown in a general status diagram in **Fig. 5**.

The upper, slightly slanted curves of this diagram correspond to the changes in the 1st flow regime. Namely: by increasing the discharged mass flow rate at the tube bottom, the solids volume fraction averaged within the whole mixer tube also decreases slightly, mainly due to the increasing void fraction within the section containing motionless mixers. Decreasing the l/d ratio of the mixer elements also decreases the mean solids volume fraction, making

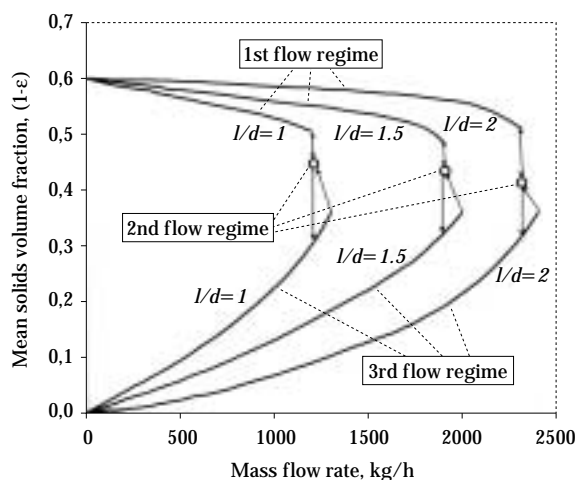


Fig. 5 General status diagram of flow regimes in gravity mixer tubes containing motionless mixers

these curves steeper.

Achieving the maximum throughput of the given mixer tube, the average solids volume fraction suddenly drops to a distinct point shown in **Fig. 5**, which characterizes the 2nd flow regime in the given system. It should be emphasized in this respect that local solids volume fractions in this flow regime changes from place to place, generally decreasing in downwards direction from the inlet of the mixer section, and especially in the plain tube below the mixer elements. However, the average solids volume fraction is a well-determined distinct value, belonging to the maximal possible mass flow rate of particles under this condition. This mass flow rate and average solids volume fraction depend on the diameter of tube, on the physical properties of material, e.g. particle size, density, shape, surface properties, particle-particle and particle-wall frictions, as well as on the geometrical and other properties of the motionless mixer elements, on the length ratios of feeding, mixing and post-mixing sections, on the distance between the mixer elements, etc. From **Fig. 5**, it is clearly seen that by decreasing the l/d ratio of the helical mixer elements, the maximal throughput of the tube belonging to the 2nd flow regime also decreases. The gap between the solids volume fraction at the end point of the 1st flow regime curves and at the 2nd flow regime mainly depends on the length of the plain tube below the mixing section and on the distances between the mixer elements: the gap diminishes if these plain tube sections are shorter.

In the 3rd flow regime, shown by the lower curves in **Fig. 5**, the mean solids volume fraction increases as the mass flow rate of solids fed into the tube inlet is increased. The higher the retaining effect of the mixer elements against the particulate flow, i.e. the lower their l/d ratio, the higher the mean solids volume fraction in the tube will be: i.e. the slope of the corresponding curves becomes steeper. After achieving the maximum throughput of the mixer tube from this side, the feeding section becomes choked and the mean solids volume fraction in the tube suddenly increases: i.e. the 3rd flow regime transforms to the 2nd flow regime. This transformation is reversible, but some hysteresis loop was experienced here. The gaps between the ends of the 3rd flow regime curves and the data point of the 2nd flow regime mainly depend on the length of the feeding section.

It should be noted that **Fig. 5** is a general diagram only and therefore does not give precise quantitative data on given particle systems or mixer tube configurations. It is a summary of our experiences and mea-

measurements carried out with different particle systems and mixer tubes under different conditions [12, 31, 32]. However, this is a quite realistic diagram regarding the scales of its axes and tendencies of its curves, since they are close to the results obtained for the gravity flow of quartz sand of 0.17 mm mean particle size in a gravity mixer tube of 1.6 m length and 0.05 m inner diameter, with about 0.6 m total length of helical mixer elements. Very similar curves were obtained by recent DEM simulations for polymer particles with 3 mm diameter and 1190 kg/m³ density [23], with the difference that the corresponding mass flow rates with similar mean solids fractions are somewhat lower compared to those of quartz sand.

Measurements [12] and DEM simulations [23] revealed a periodic variation of the local solids volume fractions along the motionless mixers in the middle tube section. As typical examples, **Figs. 6a,b,c** show the results obtained by the DEM simulation of particulate flow in a mixer tube of 0.05 m ID and 0.80 m length, composed of a feeding, a mixing and a post-mixing section of 0.20, 0.30 and 0.30 m length, respectively. The number of spherical model particles in the tube used for the DEM simulation was changed from 10,000 to 65,000, with 3.0 mm diameter and 1190 kg/m³ density. Other parameters such as stiffness, restitution coefficients, particle-particle and particle-wall frictions, and inlet velocity were described in detail by Szepvolgyi [23]. The mass flow rate controlled at the inlet or at the outlet of the tube to generate different flow regimes was varied between 300 and 1500 kg/h. From this diagram, it is seen that periodicity of local solids volume fractions took place in all the three flow regimes, due to the multiple interaction with the motionless mixers, which caused periodic deceleration and acceleration of the flow along the mixer lengths. These diagrams also show significant differences between the three flow regimes regarding the change of local solids volume fraction along the various sections of the mixer tube.

Experimental studies revealed that these flow regimes had a great influence on the mixing performance, too. **Fig. 7** shows some examples for residence time distributions of tracer particles measured during gravity flows through Kenics-type motionless mixers [12]. The model material for these experiments was quartz sand, the same as used for the solids volume fraction measurements, and a short plug of sodium chloride or polypropylene granules was used as the tracer. It was found that residence time distributions were somewhat broader in the 1st flow regime relative to the 2nd or 3rd flow regimes,

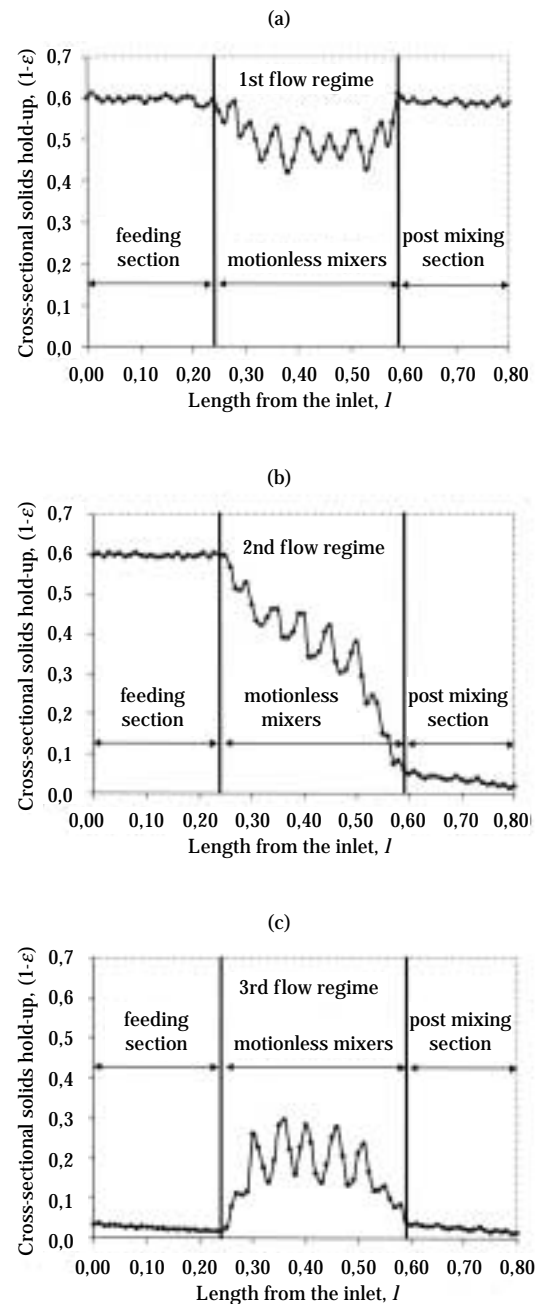


Fig. 6 Variation of the local cross-sectional solids volume fractions along the tube length in the three characteristic flow regimes
(a) 1st flow regime, (b) 2nd flow regime, (c) 3rd flow regime

especially for smaller length-to-diameter (l/d) ratios. However, due to the higher throughput and lower mean residence time, the apparent Peclet numbers and axial dispersion coefficients were more beneficial in the 2nd and 3rd flow regimes, mainly for higher l/d ratios. The best homogeneity values were obtained in the 2nd flow regime and, at higher mass flow rates in the 3rd flow regime, close to its transition point [12].

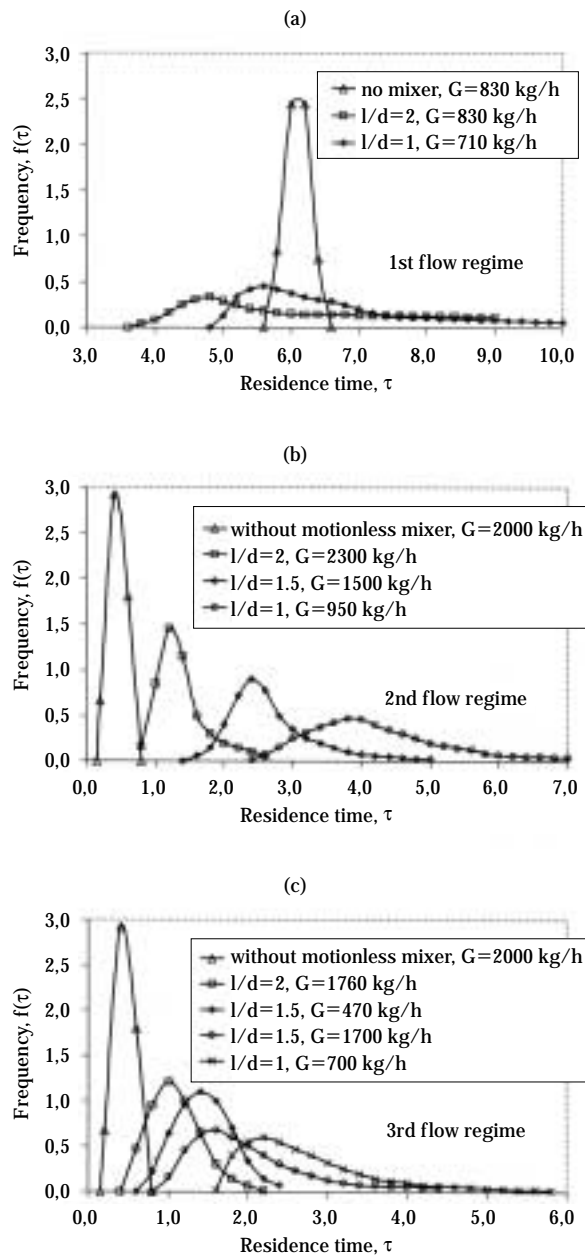


Fig. 7 Residence time distribution curves obtained with Kenics-type motionless mixers in different flow regimes
(a) 1st flow regime, (b) 2nd flow regime, (c) 3rd flow regime

3.2 Gas-solids two-phase flows

Experiments were carried out by Gyenis et al. [12] in a concurrent downward gas-solids two-phase flow in a test device where the flow rates of both phases could be controlled more or less independently. By increasing the gas flow rate, the mass flow rate and thus the solids hold-up could be enhanced considerably, which is generally beneficial to the performance

of in-line mixers and other operations by effective gas-solids contacting.

Motionless mixers can also be applied in counter-current gas-solids two-phase flow for more effective phase contacting. It is known that fluidized bed processes often use various types of inserts in the particle bed to improve the fluidization behavior [33]. Motionless mixers can replace the usual inserts, favorably influencing the minimum fluidization gas velocity, solids hold-up, and heat and mass transfer between the phases by enhancing the relative velocities and avoiding fluidization abnormalities.

4. Other Applications in Bulk Solids Handling

4.1 Improvement of Bulk Solids Flow and Reduction of Bulk Volumes

In handling bulk solids, motionless mixers are well suited to eliminate problems in the bulk solids flow, and to decrease the bulk density in storage and transport.

In silos, inserts are frequently used to enhance flow uniformity in space and/or time [34], avoiding pulsation and bridging, which may totally stop the flow. Concentric, inverted or double cones, slanted plates or rods are frequently used for this purpose. In this way, funnel flow can be transformed to mass flow, avoiding segregation during discharge. For this purpose, various forms of motionless mixers can also be used, but before their application, careful design work is necessary with preliminary investigation of material properties and its flow behavior through the motionless mixers to avoid potential troubles.

According to our experiences, motionless mixers in gravity tubes make the flow of fine powders more stable, even if they are cohesive to some extent, such as flour or ground coffee. It should be noticed, however, that this is true only for continuous or non-interrupted flows. If continuous discharge is stopped, troubles can arise in re-starting the flow. This difficulty can be avoided by applying quasi-motionless mixers, connected to each other elastically, joining them by springs, thus making the individual mixer elements mobile to a certain extent [35]. Stresses inside the bulk solids column cause some passive movements of the mixer elements, which is enough to start or to stabilize the flow, therefore avoiding choking.

In loading a container, silo, truck or railroad boxcar from a spout or hopper, the bulk volume of solids may expand. Therefore, during storage or transportation, a considerable part of the available space is occupied by air. However, if particulate materials are passed

through motionless mixers, the expansion of bulk volume can be reduced by 20-40 percent compared to loading via plain tube, as was proven by experiments with wheat grains [36]. When bulk solids, which were expanded already, are passed through motionless mixers, absolute reduction can also be achieved. By this method, as much as 4-10 percent more bulk solids can be stored or transported in a given volume of a container or ship. To this end, motionless mixer elements should be well designed to avoid attrition or breakage of the grains or particles.

4.2 Coating, Size Enlargement, Size Reduction

Motionless mixers are applicable not only to blend particulate solids, but also to contact different particles effectively with each other. In a suitably designed gravity mixer tube supplied continuously with two particulate solids differing in size, a coating of the bigger particles with the smaller ones can be realized if suitable binding material is also supplied. Gyenis et al. [37, 38] reported on a coating process of jelly bon-bons with crystalline sugar, applying motionless mixers. Similar equipment was used for coating ammonium nitrate fertilizer granules with limestone powder to avoid sticking during storage. Granulation or controlled agglomeration of particulate solids is also conceivable by this method, but a crucial point is to ensure proper conditions to avoid sticking of solids or deposition of the binding material onto the surface of the mixers. Disintegration or size reduction, as well as controlled attrition [39], can also take place during interaction between the particles and motionless mixers, especially at higher velocities ensured by gas-solids two-phase flows.

4.3 Applications in Pneumatic Conveying

As was mentioned above, concurrent gas-solids flow in vertical tubes containing motionless mixers increases the flow rate and solids hold-up, also enhancing the mixing process compared to simple gravity flows of particles [12]. Because of the retaining effect of motionless mixers, the velocity difference between the phases and also the residence time of the particles can be increased considerably, compared to a plain tube. Such conditions are favorable for heat and mass transfer processes or chemical reactions in gas-solids contactors, thus decreasing the necessary dimensions. This makes the realization of various operations during pneumatic conveying [39] conceivable. But for this, carefully planned pilot-scale experiments and caution in design are needed to avoid troubles, e.g. choking or damage of the parti-

cles.

Motionless mixers may be useful tools in pneumatic conveying lines, e.g. in horizontal tube sections. DEM simulation studies revealed that particles that tended to settle downwards could be re-dispersed into the gas stream again by suitably designed motionless mixer elements [23, 40]. This may reduce the saltation velocity, thus diminishing the required gas flow rate. By using motionless mixers, a given section of pneumatic conveying system can also serve as an effective gas-solids contactor, too, or to realize other types of solids treatments simultaneously with conveying. Caution and preliminary experiments mentioned above are also recommended here.

4.4 Heat Treatment of Particulate Solids

Heat transfer processes in particulate solids can be improved by motionless mixers built in a cooler or heater, due to the multiple transmissions of particles from the bulk material to the heating or cooling surface and back. In some cases, heat-transmitting tubes or lamellas themselves, arranged, e.g. in a hopper, can modify the flow pattern of the solids, similarly to motionless mixers.

Very often, heat treatment is carried out in rotary heater or kiln, as is frequently used in the cement industry or, in smaller dimensions, in food processing. Motionless mixers fixed inside a rotating unit, shown in **Fig. 8**, enhance the heat transfer between particles and a streaming gas, or between the particles and the heated surface, as was patented by Bucsky et al. [41]. It also ensures uniform temperature distribution throughout the cross-section of the particle bed, which is of crucial importance in the treatment of heat-sensitive materials. Such a device is also applicable for drying particulate solids.

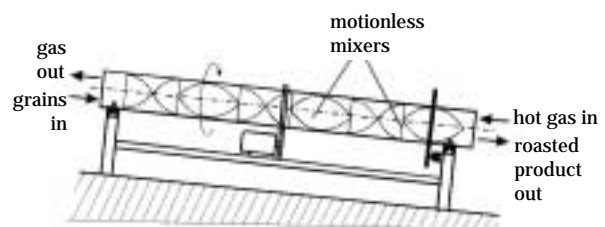


Fig. 8 Rotary heater with motionless mixers to roast agriculture materials

4.5 Drying

Godoi et al. [42] used a vertical tube equipped with helical motionless mixers with perforations on their surface for the continuous drying of agricultural grains. The particulate materials to be dried were fed continuously at the top, and slid or rolled down along the surface of the mixer elements. Heated gas streamed up along the flow channel between the mixer elements and through their perforations. Due to the interactions between the grains, the motionless mixers and the gas, an effective mass and heat transfer was achieved. The rotary equipment in Fig. 8 also can be used for such a purpose.

4.6 Dust Separation

Motionless mixers are applicable for the separation of particles from gases. The dust or volatile solids content of hot industrial gases often causes troubles in pipeline operation due to deposition onto the tube wall, especially at critical sections. Based on laboratory- and pilot-scale experiments, Ujhidy et al. [43] described a new gas purification method and equipment applying helical motionless mixers shown in Fig. 9. Solid particles are captured by a liquid film trickling down along the surface of mixer elements, totally avoiding plugging and thus extra maintenance of the gas pipeline system. Applying proper conditions, i.e. optimal superficial gas velocity and suitable motionless mixer geometry, the dry separation of solids is also feasible, especially above one hundred or several hundred microns particle size. This effect is due to the centrifuging and collision of particles with the motionless mixers.

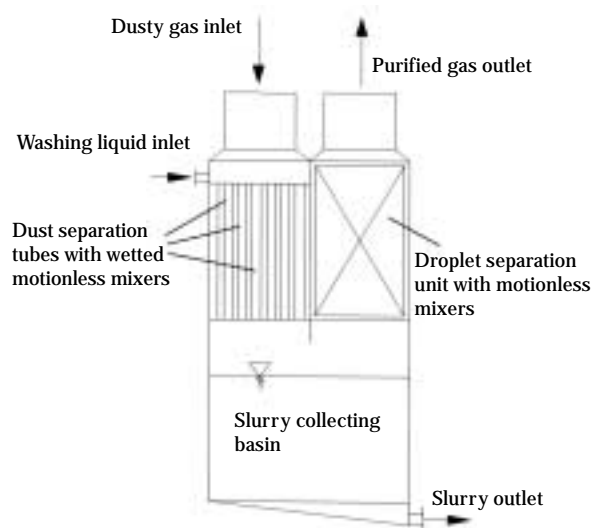


Fig. 9 Dust removal unit applying motionless mixers

Concluding Remarks

As was seen from this review, motionless mixers are useful tools for process improvements: not only for fluid treatments, but also in bulk solids technologies. In this latter field, the most detailed knowledge is available in bulk solids mixing, discussed in a great number of papers. Investigations started more than thirty years ago, elucidating the kinetics and mechanisms of this operation, mainly in gravity mixing tubes, but also in a special alternatively rotating bulk solids mixer. Modeling and simulations helped to understand experimental findings and to predict the behavior and results of such equipment.

Particulate flows in motionless mixer tubes show exiting phenomena which greatly influence the processes taking place in these devices. Other applications such as to improve the bulk solids flow in tubes, chutes and silos, or to reduce the bulk volume expansion led to significant results. In gas-solids two-phase flows, namely in pneumatic conveying and simultaneous treatment of bulk solids, their use offers new possibilities for realization and process improvement. Coating, size enlargement, size reduction and attrition, heat treatment, drying, wet dust removal and dry particle separation are also promising fields of applications.

Acknowledgement

The author wishes to acknowledge the support of the Hungarian Scientific Research Fund (OTKA T29313).

Nomenclature

d	diameter or width of motionless mixer element	m
K'_{ax}	axial dispersion coefficient, Eqn.6	m^2/s
K_m	kinetic constant of mixing	—
K_s	kinetic constant of segregation	—
L_{mix}	total length of the studied mixer section	m
L	length, measured from the inlet	m
l	length of one motionless mixer element	m
l/d	length-to-diameter ratio of a motionless mixer element	—
M	degree of mixedness, defined by Eqn.2 [15, 16]	—
s	estimated standard deviations of sample concentrations taken from a mixture	—
s_0	estimated standard deviations of sample concentrations taken in a totally segregated	—

	state	—
x_i	mass fraction of the tracer particles within the i -th sample taken at the outlet of the mixer tube	—
Pe'	apparent Peclet number, Eqn.5	—
μ_2	second central moment of the residence time distribution of the tracer particles, Eqn.3	s^2
τ_i	the residence time of tracer particles within the i -th sample	s
$\bar{\tau}$	the mean residence time of all tracer particles in the mixer tube, Eqn.4	s
Φ	segregation potential [14]	—

Bibliography

- 1) Pattison D, A.: Motionless Inline Mixers Stir Up Broad Interest, *Chem. Eng.*, May 19, 1969, 94-96.
- 2) Wang R, H.; Fan L, T.: Contact Number as an Index of Transverse Mixing in a Motionless Mixer, *Particulate Science and Technology*, 1, 1983, 269-280.
- 3) Chen S, J.; Fan L, T.; Watson C, A.: The Mixing of Solid Particles in a Motionless Mixer – A Stochastic Approach, *AIChE J.*, 18 (5), 1972, 984-989.
- 4) Chen S, J.; Fan L, T.; Watson C, A.: Mixing of Solid Particles in Motionless Mixer – Axial-Dispersed Plug-Flow Model, *Ind. Eng. Chem. Process Des. Develop.*, 12 (1), 1973, 42-47.
- 5) Fan L, T.; Chen S, J.; Eckhoff N, D.; Watson C, A.: Evaluation of a Motionless Mixer Using a Radioactive Tracer Technique, *Powder Technol.*, 4 (6), 1971, 345-350.
- 6) Lai F, S.; Fan L, T.: A Study on the Mixing of Flour in a Motionless Sulzer (Koch) Mixer Using a Radioactive Tracer, *Powder Technol.*, 13 (1), 1975, 73-83.
- 7) Wang R, H.; Fan L, T.: Axial Mixing of Grains in a Motionless Sulzer (Koch) Mixer, *Ind. Eng. Chem., Process Des. Dev.*, 15 (3), 1976, 381-388.
- 8) Fan L, T.; Gelves-Arocha H, H.; Walawender W, P.; Lai F, S.: A Mechanistic Kinetic Model of the Rate of Mixing Segregating Solid Particles, *Powder Technol.*, 12 (2), 1975, 139-156.
- 9) Lai F, S.; Fan L, T.: Application of a Discrete Mixing Model to the Study of Mixing of Multicomponent Solid Particles, *Ind. Eng. Chem. Process Des. Dev.*, 14 (4), 1975, 403-411.
- 10) Boss J.; Knapik A, T.; Wegrzyn M.: Segregation of Heterogeneous Grain System during Mixing in Static Mixers, *Bulk Solids Handling*, 6 (1), 1986, 145-149.
- 11) Boss J.; Wegrzyn M.: The Effect of the Tracer Particles Distribution on the Equilibrium Degree of Mixture, *Powder Handling and Processing*, 3 (3), 1991, 253-255.
- 12) Gyenis J.; Arva J.; Nemeth L.: Steady State Particle Flow in Mixer Tubes Equipped with Motionless Mixer Elements, *Industrial Mixing Technology: Chemical and Biological Applications*. Eds.: Gaden E. L; Tatterson G. B., *AIChE Symp. Ser. Vol. 90*, New York, 1994, 144-160.
- 13) Gyenis J.; Arva J.: Improvement of Mixing Rate of Solids by Motionless Mixer Grids in Alternately Revolving Mixers, *Powder Handling and Processing*, 1 (2), 1989, 165-171.
- 14) Gyenis J.: Segregation-Free Particle Mixing, *Handbook of Powder Technology*, Vol. 10 [Eds. A. Levy and H. Kalman]. Elsevier, Amsterdam-Tokyo, 2001, 631-645.
- 15) Fan L, T.; Wang R, H.: On Mixing Indices, *Powder Technol.*, 11, 1975, 27-32.
- 16) Rose H, H.: A Suggested Equation Relating to the Mixing of Powders and its Application to the Study of Performance Certain Types of Machines, *Trans. Instr. Chem. Engrs.*, 37 (2), 1959, 47-56.
- 17) Gyenis J.; Nemeth J.; Arva J.: Gravity Mixing of Solid Particle Systems in Steady State Static Mixer Tubes, *Swiss Chem.*, 13 (5), 1991, 51-55.
- 18) Wang R, H.; Fan L, T.: Stochastic Modeling of Segregation in a Motionless Mixer, *Chem. Eng. Sci.*, 32, 1977, 695-701.
- 19) Gyenis J.; Blickle T.: Simulation of Mixing During Non-Steady State Particle Flow in Static Mixer Tubes, *Acta Chimica Hungarica – Models in Chemistry*, 129 (5), 1992, 647-659.
- 20) Gyenis J.; Katai F.: Determination and Randomness in Mixing of Particulate Solids, *Chem. Eng. Sci.*, 45 (9), 1990, 2843-2855.
- 21) Gyenis J.; Diaz E.: Simulation of the Stochastic Behavior during Bulk Solids Mixing, *Proc. 5th World Congress of Chemical Engineers*, San Diego, CA, U.S.A. July 14-18, 1996, 321-326.
- 22) Mihalyko Cs.; Mihalyko E, O.: A Double Stochastic Model of the Mixing of Solid Particles, *Handbook of Powder Technology*, Vol. 10 [Eds. A. Levy and H. Kalman]. Elsevier, Amsterdam-Tokyo, 2001, 659-664.
- 23) Szepvolgyi J.: Lagrangian Modelling of Particulate Flows in Static Mixer Tubes, Ph.D. Theses, University of Veszprem, 1999. p. 119.
- 24) Herbig R.; Gottschalk I.: Mixing of Segregating Solid Particles in a Static Mixer, *J. Powder and Bulk Solids Technol.*, 10 (2), 1986, 7-12.
- 25) Gyenis J.; Arva J.: Mixing Mechanism of Solids in Alternately Revolving Mixers I. Change of the Local Concentrations and Concentration Profiles, *Powder Handling and Processing*, 1 (3), 1989, 247-254.
- 26) Gyenis J.; Arva J.: Mixing Mechanism of Solids in Alternately Revolving Mixers II. The Role of Convection and Diffusion Mechanisms, *Powder Handling and Processing*, 1 (4), 1989, 365-371.
- 27) Gyenis J.; Nemeth J.: Power Consumption of an Alternately Revolving Bulk Solids Mixer, *Hung. J. Ind. Chem.*, 19, 1991, 69-73.
- 28) Gyenis J.; Arva J.; Nemeth J.: Mixing and Demixing of Non Ideal Solid Particle Systems in Alternating Batch Mixer, *Hung. J. Ind. Chem.*, 19, 1991, 75-82.
- 29) Bauman I.: Solid-Solid Mixing with Static Mixers, *Chemical and Biochemical Engineering Quarterly*, 15 (4), 2001, 159-165.
- 30) Supplemental Specification of the Standard Specifica-

- tion for Road and Bridge Construction. State of Tennessee. Section 900. March 3, 1995. Sheet of 5 of 19.
- 31) Gyenis J.: Strömungseigenschaften von Schüttgütern im statischen Mischrohr, Chem.-Ing.-Tech. 64 (3), 1992, 306-307.
 - 32) Nemeth J.; Gyenis J.; Nemeth J.: Gravity and Gas-Solid Flow in Static Mixer Tubes, PARTEC 95, Preprints of 3rd European Symposium Storage and Flow of Particulate Solids (Janssen Centennial), 21-23 March 1995, Nürnberg, 459-467.
 - 33) Hilal N.; Ghannam M, T.; Anabtawi M, Z.: Effect of Bed Diameter, Distributor and Inserts on Minimum Fluidization Velocity, Chem. Eng. Technol., 24 (2), 2001, 161-165.
 - 34) Yang S, C.; Hsiao S, S.: The Simulation and Experimental Study of Granular Materials Discharged from a Silo with the Placement of Inserts, Powder Technology, 120 (3), 2001, 244-255.
 - 35) Bucsky Gy.; et al.: Method and Equipment for Mixing of Continuous Streams of Particulate Materials, Hung. Pat. No. 22/90, 1990. (in Hungarian)
 - 36) Chen S, J.; Fan L, T.; Chung D, S.; Watson C, A.: Effect of Handling Methods on Bulk Volume and Homogeneity of Solid Materials, J. Food Science, 36, 1971, 688-691.
 - 37) Gyenis J.; Farkas I.; Németh J.; Hollósi S.: Energy Saving Coating of Grains with Smaller Particles, Magyar Kemikusok Lapja, 44 (1), 1989, 16-21. (in Hungarian)
 - 38) Gyenis J.; Arva J.; Nemeth J.: Coating of Grains with Fine Particles, Preprints of 9th International Congress of Chemical Engineering, CHISA' 87, Prague, 30 August – 4 September, 1987, 1-10.
 - 39) Kalman H.: Personal communications.
 - 40) Gyenis J.; Ulbert Zs.; Szepvolgyi J.; Tsuji Y.: Discrete Particle Simulation of Flow Regimes in Bulk Solids Mixing and Conveying, Powder Technol., 104, 1999, 248-257.
 - 41) Bucsky Gy.; et al.: Method and Equipment for Continuous Gentle Heat Treatment of Heat Sensitive Particulate Materials, Hung. Pat. No. 209 661 A, 1995, 1-7. (in Hungarian)
 - 42) Godoi L, F. G.; Park K, J.; Alonso L, F. T.; Correira W, A, Jr.: Particle Flow in an Annular Static Mixer Dryer, Proc. 5th World Congress of Chemical Engineers, Vol. VI, 14-18 July 1996, San Diego, CA, U.S.A., 356-361.
 - 43) Ujhidy A.; Bucsky Gy.; Gyenis J.: Application of Motionless Mixers in Gas Purification – A Case Study, Proc. Joint Symposium (Korea/Hungary) on Energy and Environmental Technology for 21st Century, November 16, 2001, Taejon, Korea, 3-15.

Author's short biography



Janos Gyenis

Professor Janos Gyenis graduated in Chemical Engineering at the University of Veszprem, Hungary. He received Dr. Habil and Ph.D. degrees at the Technical University of Budapest, and a D.Sc. title at the Hungarian Academy of Sciences. At present, he is a full professor at the University of Kaposvar, Department of Engineering, and director of the Research Institute of Chemical and Process Engineering. Since 1971, he has been involved in a number of collaborative research works with leading laboratories and university departments in Europe, the United States and Asia. He is now working with the mixing and flow of particulate solids and the application of motionless mixers for various purposes. Up to now, he has published about 120 papers and he is co-inventor of 22 patents.

Gas-Phase Production of Nanoparticles[†]

A. Gutsch, M. Krämer, G. Michael,
H. Mühlenweg, M. Pridöhl and G. Zimmermann
Degussa AG
Project House Nanomaterials*

Abstract

Gas-phase synthesis is a well-known chemical manufacturing technique for an extensive variety of nano-sized particles. Since the potential of ultra-fine and especially nano-sized particles in high-performance applications has been identified, the scientific and commercial interest has increased immensely, disclosing this field as a most important technology of the future.

The paper will present the basics of the gas-phase synthesis and particle formation process including the relation between the principal process conditions and the product characteristics.

Moreover, several reactor technologies such as flame, hot-wall, plasma and laser reactors will be introduced and their specific advantages will be pointed out. Precise process control is crucial in order to meet stringent specifications regarding the particles' chemical composition and morphology.

In addition, the paper will deal with some special nanoscaled gas-phase products of high innovative potential and their functional contribution in various applications.

1. Introduction

Nanomaterials and ultra-thin functional coatings of nanoparticles will determine the utility of many products in the future: superhard materials and superfast computers, dirt-repellent surfaces and new cancer treatments, scratch-proof coatings and environmentally friendly fuel cells with highly effective catalysts. The market for products manufactured by nanotechnology is already registering double-digit growth rates and will amount to hundreds of billions US\$ by 2002.

Nanoparticles are at the core of this technology. These are particles ranging in size from 1 millionth to 100 millionths of a millimetre – more than 1,000 times smaller than the diameter of a hair. In this order of magnitude, it is not only the chemical composition but also the size and the shape of the particles that determine their properties. Optical, electric and magnetic properties, but also hardness, toughness or the melting point of nanomaterials differ substantially from the properties of the macroscopic solids.

Table 1 gives an overview of effects associated with decreasing particle size.

Table 1 General effects of decreasing particle size.

The smaller the particles, the ...
• higher the catalytic activity (Pt@Al ₂ O ₃)
• higher the mechanical reinforcement (carbon black in rubber)
• higher the electrical conductivity of ceramics (CeO ₂)
• lower the electrical conductivity of metals (Cu, Ni, Fe, Co, Cu alloys)
• initially increasing and later decreasing magnetic coercivity, finally superparamagnetic behaviour (Fe ₂ O ₃)
• higher the hardness and strength of metals and alloys
• higher the ductility, hardness and formability of ceramics; the lower the sintering and superplastic forming temperature of ceramics (TiO ₂)
• higher the blue-shift of optical spectra of quantum dots (quantum confinement of Si)
• higher the luminescence of semiconductors (Si, GaAs, ZnS:Mn ²⁺)

Degussa possesses many years of experience in the manufacture and marketing of extremely fine powders. Examples are the pyrogenic silica (AEROSIL®), titania, alumina and industrial carbon black. Fumed

* Rodenbacher Chaussee 4, 63457 Hanau, Germany

[†] Accepted: June 28, 2002

silica, for which Degussa is the world market leader, is used in particular as a reinforcing filler in silicone rubber and to control the rheology of coatings and colorants. Industrial carbon black, in which Degussa ranks second in the world, is used particularly in the tyre industry and as a pigment in printing inks, coatings and plastics.

In industrial products, primary nanoscale particles are normally not isolated but build up aggregates and agglomerates. In aggregates, the primary particles contact each other at surfaces or edges and – as a rule – they cannot be broken down further by shear forces applied in the application. Agglomerates are formed when aggregates and/or primary particles contact each other at points. If nanoparticles are dispersed in a liquid, the agglomerates are destroyed and the surface chemical groups of the aggregates interact with each other (see **Fig. 1**).

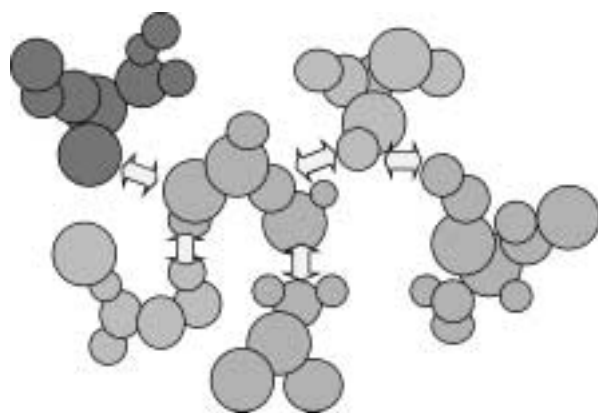


Fig. 1 Interaction of aggregates (schematically).

Table 2 Morphology control parameters and resultant effects in the application.

Parameter to control aggregate size	Application effects
residence time	
pressure	
loading	rheology
nature of precursor	optical effects
thermal treatment	reinforcement
densification	scratch resistance
surface chemistry	
structure modification	
dispersing energy	

In the case of fumed silica, this affinity is attributed to the hydrogen bridge linkages and results in a temporary, three-dimensional lattice structure becoming macroscopically “visible” in the form of thickening and thixotropy. To control the application behaviour often means to generate tailor-made aggregates with a tailor-made surface chemistry. In **Table 2**, some parameters during and “after” production are shown which have an influence on the aggregates and hereby also an influence on the application effects.

2. Project House Nanomaterials

2.1 Scope and structure

Degussa utilises the know-how from years of experience and the resultant market knowledge to develop the global, technology- and innovation-driven market for nanoscale materials.

This is done in the research groups of the business units Silica & Silanes and Advanced Fillers & Pigments, which are focusing on developing new or improved types of fumed silica, titania, alumina, carbon black and dispersions thereof.

The Project House Nanomaterials was created to develop new nanomaterials and also new gas phase processes. To this end, an interdisciplinary team with experienced people from different business units was formed. Chemists, materials scientists, process engineers and industrial management experts from the Project House Nanomaterials develop together with customers and universities innovative technologies and novel nanoscale materials such as special types of carbon black, zirconia, indium tin oxide, zinc oxide, ceria and superparamagnetic composite materials. Some examples are described in Chapter 5.

These new materials are manufactured in the gas phase at temperatures up to 10,000 K. The manufacturing process and conditions determine size and morphology of the particles and hence their application properties. Seven new pilot plants have been built comprising three flame reactors, two hot-wall reactors, a plasma reactor, and very new, a laser evaporation reactor. They are described in detail later on (see Chapter 4). One special feature of the Project House Nanomaterials is the close cooperation both with potential customers and with academia, the latter providing results from fundamental research. Some projects carried out together with the universities are described in the following section.

2.2 Cooperation with universities

The Project House Nanomaterials has nine cooper-

ation partners from eight universities (see Fig. 2). This tight cooperation is funded by the Deutsche Forschungsgemeinschaft, DFG (German Science Foundation).

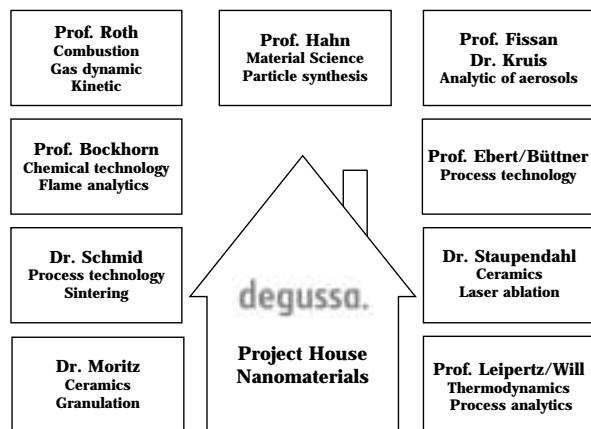


Fig. 2 Project partners from universities.

The universities provide state-of-the-art measuring technology and the results from their fundamental research in the fields of particle synthesis and processing, particle characterisation and simulation of particle formation. On the other hand, the universities are granted access to dedicated pilot reactors to test their equipment or to prove their results on larger, industrial-scale equipment. Following are some examples:

Prof. Bockhorn's aim is to model the formation of particles, especially of soot, in flames. To gather basic information on particle formation, he developed the RAYLIX method, which combines laser-induced incandescence (LII), Rayleigh scattering and extinction measurement, whereas the Rayleigh scattering and the LII-signal are detected in two dimensions. This set-up provides locally resolved information on soot volume fractions and on the size of the soot particles in flames [1].

Prof. Leipertz uses time-resolved laser-induced incandescence to monitor on-line the average particle size of just-formed soot particles. Both systems have been successfully transferred to monitor the carbon black formation in a plasma reactor. We also successfully adapted both systems to monitor the particle formation of carbon-free systems such as titania and zirconia in our laser evaporation reactor. This unique reactor is the result of the cooperation with Dr.

Staupendahl from the University of Jena. See Chapter 4.4. for details.

Prof. Ebert evaluates the feasibility of an adiabatic quench system in the low-pressure flame reactor to rapidly cool particle-gas mixtures by adiabatic expansion. This system also affects particle morphology.

Prof. Fissan further develops his SMPS (scanning mobility particle sizer) with respect to corrosion resistance against chlorine-containing atmospheres and operation of the SMPS connected to reactors, which are operated at reduced pressure.

Prof. Hahn is checking the scalability of his concept to synthesise non-aggregated oxidic nanoparticles using hot-wall reactor technology at reduced pressure. The experiments are done in a dedicated pilot reactor mainly producing SiO_2 .

Prof. Roth is proving the feasibility of the TEM-grid sampling system to take samples out of running reactors. The particles deposited by thermophoresis can be directly investigated by means of transmission electron microscopy (TEM). Thus particle size and morphology can be correlated with reactor settings and the particle formation can be monitored as a function of residence time and chemical conversion rate.

3. Gas-Phase Synthesis of Nanoparticles

Although a number of variations exist for gas-phase synthesis processes, they all have in common the fundamental aspects of particle formation mechanisms that occur once the product species is generated [2], [3], [4]. Product quality and application characteristics of nanoscaled particles depend strongly on the particle size distribution and on the morphology of the particles, i.e. the size and number of primary particles defining the degree of aggregation. In gas-phase reactors, the final characteristics of particulate products are determined by fluid mechanics and particle dynamics within a few milliseconds at the early stages of the synthesis process. Within this short time frame, three major formation mechanisms dominate the particle formation.

Chemical reaction of the precursor leads to the formation of product monomers (clusters) by nucleation or direct inception, and to the growth of particles by reaction of precursor molecules on the surface of newly formed particles; this is called surface growth [5], [6]. Coagulation is an intrinsic mechanism which inevitably occurs at high particle concentrations and therefore in all industrial aerosol processes. Particles dispersed in a fluid move randomly due to Brownian motion and collide with each other along their trajec-

tories. Assuming strong adhesive forces, characteristic for small particles, or chemical bonds, these collisions result in coagulation [7], [8]. Coalescence and fusion are sufficiently fast in the high-temperature zones of the reactor to effect a reduction in the level of aggregation or even the formation of spherical particles due to sintering processes [9], [10]. **Figure 3** shows the mechanisms' influence on particle formation, growth, and final morphology.

According to these particle formation mechanisms, the product quality can be influenced by a sensible selection of the process parameters. However, linking process parameters such as temperature, reactant state or reactor geometry to product characteristics requires a good understanding of the physico-chemical fundamentals of gas-phase synthesis. Measurements in gas-phase reactors are quite problematic as time scales are extremely small, temperatures very high and the gaseous atmosphere is often aggressive. Therefore, process simulation is a useful tool and can significantly improve the general understanding of particle formation and moreover can support product and process optimisation.

Numerous models based on the so-called particle population balance have been developed and applied to the simulation of particle formation and growth [11], [12]. A robust and time-efficient model is the simple monodisperse model developed by Kruis et al. [13], which has been coupled to fluid dynamics (CFD) successfully by Schild et al. [14]. While CFD-coupled simulations of the particle formation reveal specific reactor characteristics, the plain application of population balances, i.e. simulations reduced to time-temperature calculations for particle trajectories, is also very helpful in terms of increasing the basic understanding of the synthesis process.

As an example, the particle formation in a premixed flame reactor has been modelled by approximating the average time-temperature history of the particles' trajectories. The calculated particle size evolution was then compared to experimental data obtained by thermophoretic sampling on a TEM grid which enables direct measurements of particle sizes and morphology in the flame at various distances (residence times) from the burner mouth [15]. **Figure 4** presents the principle of the sampling device, sections of the TEM pictures taken and the corresponding average aggregates obtained from simulation. With increasing residence time, the expected advancing degree of aggregation can clearly be seen. Both results, from experiment and simulation, are in excellent conformity and validate the simulation technique.

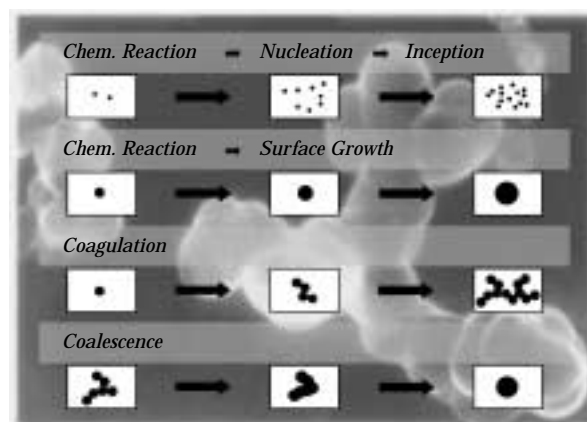


Fig. 3 Formation mechanisms relevant in gas-phase synthesis of particles.

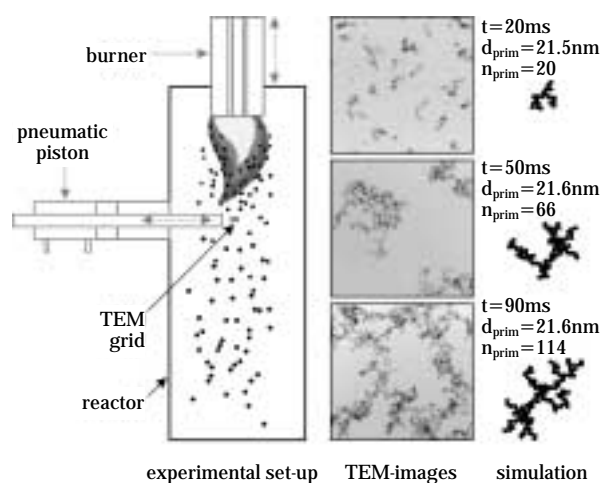


Fig. 4 Schematic of the TEM-grid sampling system mounted to a flame reactor, sampled TEM images, and corresponding simulation results.

4. Reactor Technologies

Researchers of the Project House Nanomaterials have improved existing processes and developed new technologies for the production of tailor-made nanoscaled materials.

4.1 Flame reactor

Flame reactors are one of the most common reactor designs for the production of high-purity nanoscale powders in large quantities [16-20]. The capability for full-production scale has been demonstrated for many metal oxides such as silica, titania, alumina and others. Powders, liquids and vapours can be used as precursors. The flame provides the energy to evaporate

the precursors and to drive the chemical reactions. Due to the high energy density in the flame, the precursor concentration can be quite high. In the flames, temperatures from 1000°C up to 2400°C can be realised. The residence time in the highest temperature region is very short and usually ranges between 10 and 100 ms. This region is crucial for the formation of the primary particles. After this zone only the size and the morphology of the aggregates can be influenced. With flame synthesis, primary particle sizes from a few nm up to 500 nm are accessible. The specific surface areas of these powders can go up to 400 m²/g and higher.

The shape of the flame can be influenced by using “premixed” or “diffusion” flames. In premixed flames the fuel and the air/oxygen are already mixed and the reaction takes place right at the burner mouth. These premixed flames are typically very short. In diffusion flames the fuel and the air/oxygen are fed separately to the burner mouth. The reactants have to diffuse together and combust in the diffusion zone [21].

The control of the three reactor parameters temperature profile, reactor residence time and reactant concentration is of great importance to generate tailor-made particles. Unfortunately, these parameters cannot be changed in flame reactors independently. Every adjustment of the feed flow causes a change in all three parameters.



Fig. 5 Low-Pressure Flame Reactor.



Fig. 6 Flame Reactor.

The Project House Nanomaterials runs two flame reactors (**Fig. 5, 6**). One of these flame reactors is especially designed for low pressures down to $p_{\min} = 20$ kPa. The control of the reactor pressure is interesting for two reasons:

1. Decreasing the pressure causes a dilution effect, which allows for the synthesis of less aggregated particles.
2. By controlling the pressure one can change the residence time independently from the flame temperature.

Fig. 7 shows the flow sheet of a flame reactor. Flame reactors consist usually of the burner, a flame tube, a particle collection unit (e.g. a bag filter) and an off-gas treatment unit (e.g. an alkaline scrubber).

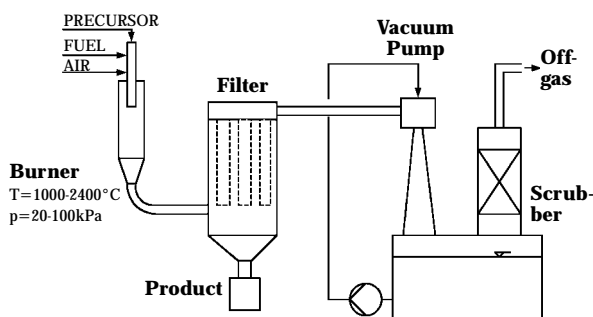


Fig. 7 Flow sheet of a flame reactor.

4.2 Hot-wall reactor

Hot-wall systems employ tubular furnace-heated reactors for initiating the synthesis reaction [20]. The construction is relatively simple and process parameters are moderate in comparison to other gas-phase reactors. Temperatures range below 1700°C, concentrations are variable, the gas composition is freely selectable and the system pressure is usually atmospheric but can also be used as a process parameter. The technique allows for precise process control and therefore allows for particle production with specific characteristics. Due to their high energy requirements, hot-wall systems have mainly been investigated on a lab scale. But there are also industrial applications. One important example is the production of Al-doped TiO₂ as a pigment. Precursors that are most often used for particle formation are metal chlorides and organometallic precursors. The mixing of the reactants and the carrier gas is, besides the above-mentioned process parameters, the most important instrument for controlling product characteristics. A variety of mixing arrangements has been investigated on a laboratory and industrial scale. Premixed systems, often used on a lab scale, are avoided in industrial applications as the reactant streams could react spontaneously before entering the reactor. The feeding location is also crucial. The reactants can be introduced concurrently at the reactor entrance or somewhat downstream, thus influencing the residence time within the reaction zone. Alternatively, the reactants can be fed separately at different locations, affecting the particle formation mechanisms and enabling even composites or coated particles.

To summarise, the hot-wall technology involves the following

Advantages:

- simplicity of design
- precise control of process parameters and flexibility with respect to gas composition and system pressure
- production of oxides, non-oxides, semiconductors and metals in the range from atomic to micrometre dimensions

Disadvantages:

- often requires volatile precursors with significant vapour pressure and stability below reaction temperature, often resulting in high precursor costs
- high degree of aggregation at high aerosol concentrations
- high energy requirement

Figure 8 presents the schematic set-up of a pilot-scale hot-wall reactor developed in cooperation with

the Department of Material Science of the Technical University of Darmstadt (Prof. Hahn) and operated at the Project House Nanomaterials. The hot zone is divided into three parts, allowing for specific temperature profiles, various precursor feeding locations and also for product sampling during particle formation.

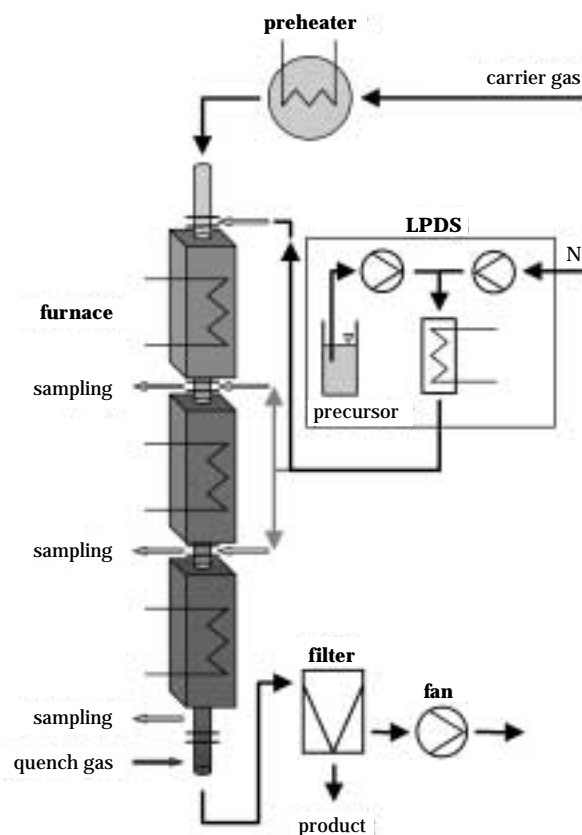


Fig. 8 Schematic of the pilot-scale hot-wall reactor operated by the Project House Nanomaterials.



Fig. 9 Photograph of the pilot-scale hot-wall reactor operated by the Project House Nanomaterials.

The carrier gas is preheated and the precursor is vaporised by a commercial liquid precursor delivery system (LPDS). Exiting the last furnace section, the aerosol stream is quenched and the powder is collected in a bag filter. So far, the pilot plant has been investigated intensely for the production of tailor-made silica particles and will be tested for mixed metal oxides in the near future (Fig. 9).

4.3 Plasma reactor

Thermal or hot plasmas are in or close to the local thermodynamic equilibrium, i.e. the temperature of heavy species in the plasma and the temperature of the electrons are mostly identical. Hot plasmas are characterised by a high electron density of 10^{21} – 10^{26} m^{-3} . These plasmas can be generated by gaseous discharge between electrodes, by microwaves, by laser or high-energy particle-beams or by electrodeless radio frequency (RF) discharge. An RF discharge can be maintained either by capacitive or by inductive coupling. The most widely used electrical methods for producing plasmas are high-intensity arcs and inductively coupled high-frequency discharge. An inductively coupled high-frequency discharge is maintained by a time-varying magnetic field operated at 3 MHz to 30 MHz [22].

Today, the plasma deposition of coatings and films by plasma spraying, thermal plasma chemical vapour deposition (TPCVD) and thermal plasma physical vapour deposition (TPPVD) is quite common. The production of nanoparticles by means of thermal plasma is a less evaluated field. One investigated example is the production of carbon black by means of high-intensity arc plasmas [23].

The electrodes necessary for arc discharge are typically made from thermally quite stable graphite. They are nevertheless eroded or evaporated within a short time, thus polluting the desired product. To avoid product contamination, plasma processes which do not use electrodes can be used, e.g. „cold“ microwave plasma or the thermal RF plasma. But the microwave plasma requires reduced pressure, thus strongly limiting production rate and particle temperature. Therefore we started to evaluate the nanoparticle synthesis by means of an inductively coupled plasma. Due to the missing electrodes, contamination in the product can be minimised.

Our high-frequency plasma reactor is operated at normal pressure with a frequency of 3–4 MHz, providing 40 kW of thermal power (efficiency 30–40%) and yielding locally up to 10 000 K. Particles are col-

lected by means of a cyclone or a filter, the waste gas can be washed with alkaline or acidic solutions. Up to 6 Nm^3/h of typical plasma gases such as nitrogen or argon as well as air can be used; solid, liquid or gaseous precursors can be fed up- or downstream of the plasma flame. The residence time in the hot zone is less than 1 s; cooling rates of 10^6 – 10^9 K/s are feasible. Depending on the gas composition the precursors are physically or chemically converted to nanoparticles. The reactor set-up and a picture thereof are given in Figures 10 and 11.

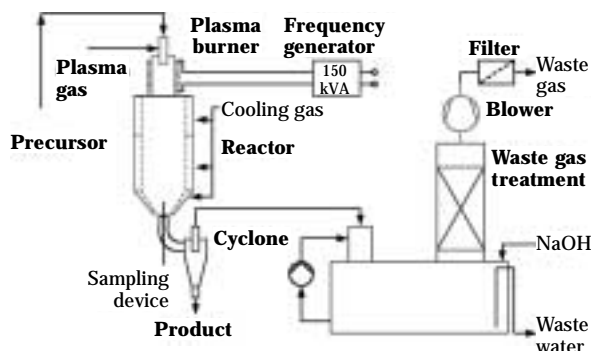


Fig. 10 Plasma reactor set-up.

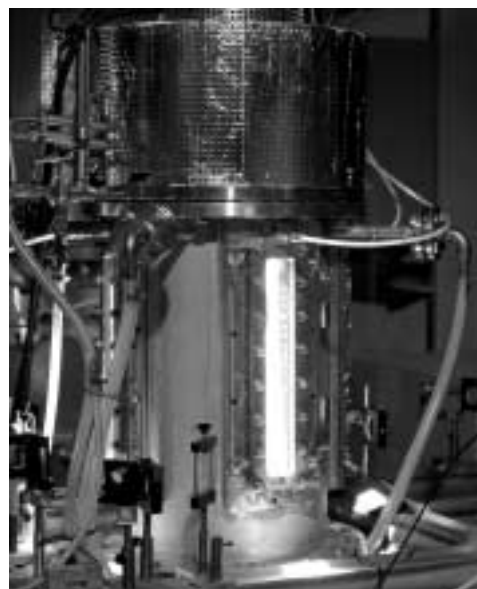


Fig. 11 Plasma reactor during operation.

4.4 Laser reactor

In cooperation with the German Science Foundation (DFG) and the University of Jena, the Project

House Nanomaterials has built a pilot-scale laser evaporation reactor (see **Fig. 12 a+b**). The reactor is a scale-up of the reactor from the University of Jena [24, 25] and features three CO₂ lasers of 2 kW laser power each at a wavelength of 10.59 μm, a reaction chamber and a product separation unit. **Figure 13** shows the schematic process flow diagram. The laser

beams are directed and focused into the reaction chamber, resulting in an intensity of 6 kW in a volume of only a few cubic millimetres. This high-intensity volume is located in the centre of the reaction chamber where the precursor, typically a coarse metal oxide powder, is fluidised. The gas-dispersed precursor powder is evaporated by the focused laser, and nanopowder is formed by condensation of the vapours. **Figure 14** is the view into the reactor during operation. The so-formed particles are separated from the gas stream by conventional filtration methods. **Figure 15** shows a TEM image of laser-synthesised particles.

The high-power intensity of the laser opens a wide field of solid precursor options having high vaporisation temperatures, e.g. ceramics and metal oxides, which are not suitable for the synthesis of nanoscaled powders by standard gas-phase processes. Due to the



a) Laser unit with reaction chamber to the right and filter to the left.



b) Reaction chamber.

Fig. 12

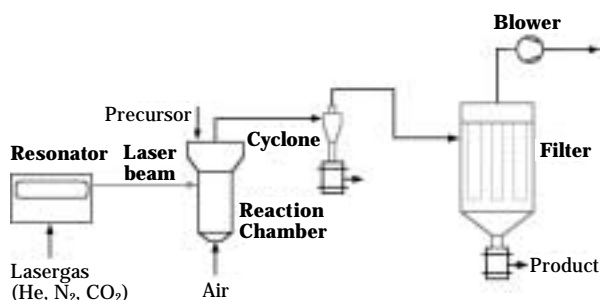


Fig. 13 Schematic process flow diagram of the laser reactor.



Fig. 14 Focus zone during operation.

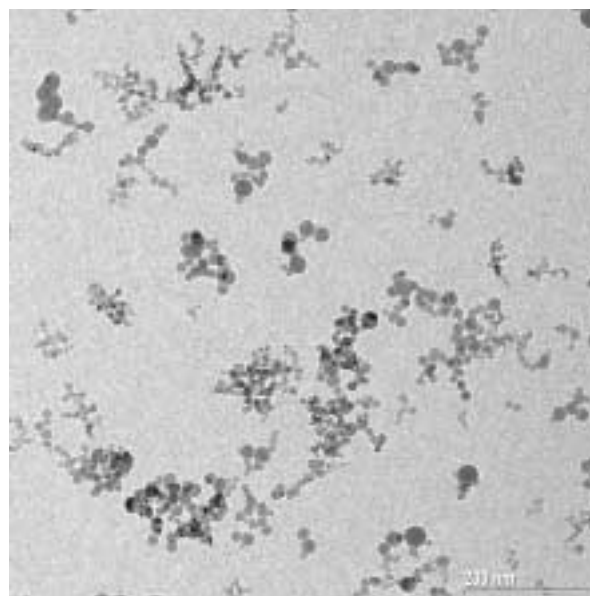


Fig. 15 TEM image of laser-synthesised particles.

high cooling rates, the morphologies of the laser-synthesised particles differ significantly from typical pyrogenic oxides, which opens new fields of potential applications.

5. Products – New Pyrogenic Oxides

5.1 Zirconia

The production of pyrogenic oxides by means of flame hydrolysis of metal chloride vapours is well known. Degussa has been using this approach successfully for decades producing, e.g. silica (AEROSIL®), alumina and titania. The synthesis of pyrogenic zirconia via the chloride route on a large scale is difficult and very costly. The chloride precursors make high demands on the materials of construction for the reactors, especially for the evaporation unit. Furthermore, the chloride in the product hinders its suitability toward several potential fields of applications. To reduce the chloride in the powder, a lot of effort has to be put into the process. One cannot use excessive temperatures for the deacidification because high temperature equals loss of specific surface area (BET). To overcome all these disadvantages, a new process was developed for the production of low-chloride (<500ppm) high-BET (>30m²/g) zirconia. In contrast to the existing chloride route, the new gas-phase process is based on metallorganic or non-chloride salt solutions.

The process uses a flame spray pyrolysis technique to yield nanoscaled high-purity (mixed) metal oxides. The precursor is sprayed into a flame reactor where the conversion into the oxide material takes place followed by the particle separation. Variations in the

time-temperature history of the particles in the combustion zone and the spraying parameters result in different product grades, e.g. specific surface area (BET). With this reactor set-up, various metal oxides and mixed metal oxide nanopowders are accessible. Zirconia and different yttrium-stabilised forms thereof (YSZ) but also indium tin oxide (ITO), alumina, etc. have been synthesised in the pilot-scale reactor. **Figure 16** shows a TEM image of ZrO₂ with a BET of 74 m²/g. In **Table 2** typical physico-chemical data of ZrO₂ and YSZ are listed. As the average primary particle size is in the 12-nm region, the sintering process starts at low temperatures (see also **Fig. 17**).

There are various applications for high-purity nanoscaled ZrO₂, e.g. dental, catalysts, ceramic membranes, thermal barrier coatings, gas sensors, optical connectors and polishing agents.

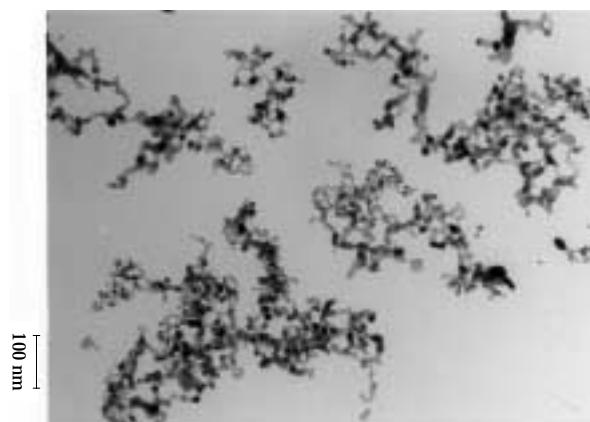


Fig. 16 TEM image of EP Zirconium Dioxide PH with a BET of 74 m²/g.

Table 3 Typical physico-chemical data of EP Zirconium Dioxide PH (ZrO₂) and stabilised EP Zirconium Dioxide 3-YSZ.

Properties	Units	ZrO ₂	YSZ
Specific surface area (BET)	m ² /g	45–75	45–75
Tapped density (approx. value)	g/l	100	100
Moisture	%	<=2.0	<=2.0
Ignition loss	%	<=3.0	<=3.0
pH-value	–	4.0 – 6.0	4.0 – 6.0
Y ₂ O ₃ content (based on ignited material)	%	–	5
HfO ₂ content (based on ignited material)	%	1.0–2.5	1.0–2.5
ZrO ₂ content (based on ignited material)	%	>=97.0	>=92.0
HCl content (based on ignited material)	%	<=0.05	<=0.05
Average primary particle size	nm	12	12

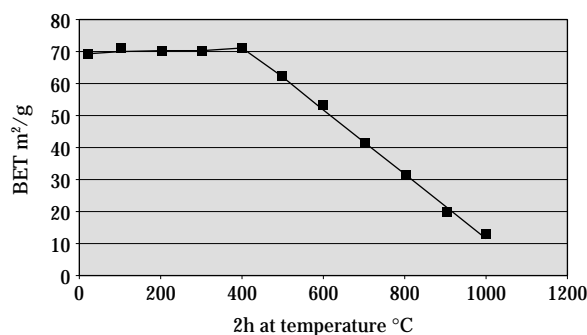


Fig. 17 Sintering behaviour of EP Zirconium Dioxide PH.

5.2 Indium tin oxide

For the production of transparent electrically conductive polymer composites, nanoscaled indium tin oxide (ITO) is being developed for use as a raw material. The ITO nanoparticles should be characterised by the following parameters:

- Colourless or slightly blue
- Specific resistance: $10^2 - 10^8 \Omega\text{cm}$
- Average primary particle size: $<20 \text{ nm}$
- Aggregate size: $<100 \text{ nm}$
- Good dispersibility
- Anisotropic self-organisation in the matrix

Such an ITO can be produced by spray pyrolysis (see **Figure 18**). It was demonstrated that the conductivity could be clearly improved by doping the ITO samples. Therefore the technical term DITO (doped indium tin oxide) is reasonable and may be applied. Under optimal circumstances it is possible to

reduce the specific resistance from $660 \Omega\text{cm}$ to $400 \Omega\text{cm}$ with DITO. Further post-treatment additionally reduces the resistance to $10 \Omega\text{cm}$, whilst BET surface area remains constant. The colour of the material can also be controlled by the addition of certain dopants.

5.3 Superparamagnetic nanocomposites

Superparamagnetic nanocomposites show the characteristic magnetic properties of paramagnetic as well as of ferromagnetic materials. Like paramagnets, these materials possess no permanently aligned structure of the elementary magnetic dipoles when no magnetic field is applied. Otherwise, the shape of the magnetisation curve looks like a ferromagnetic curve without hysteresis (see **Fig. 19**). Nanoscale magnetic particles display this superparamagnetic behaviour because the tiny magnetic domains are small enough to immediately become disordered due to entropy [26, 27].

A TEM image of a superparamagnetic material is shown in **Fig. 20**. Via flame synthesis, nanoscaled iron oxide particles were embedded in an amorphous silica matrix. The dark dots represent the iron oxide crystals. The TEM picture indicates that the magnetic domains of iron oxide are well distributed through the silica matrix and that they are smaller than 20 nm . These are important requirements to obtain single-domain and well-decoupled magnetic centres.

X-ray diffraction of the produced powders shows mainly the magnetic iron oxide phases magnetite and maghemite with a low content of non-magnetic hematite (**Fig. 21**). The specific surface area of the composite (BET) was varied from $114 \text{ m}^2/\text{g}$ to $214 \text{ m}^2/\text{g}$

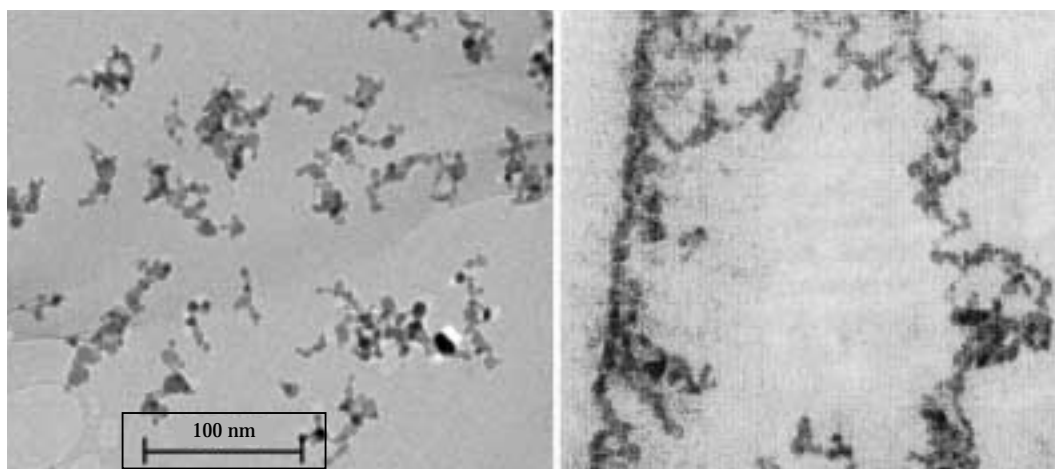


Fig. 18 TEM images of ITO (left: powder; right: in a polymer matrix).

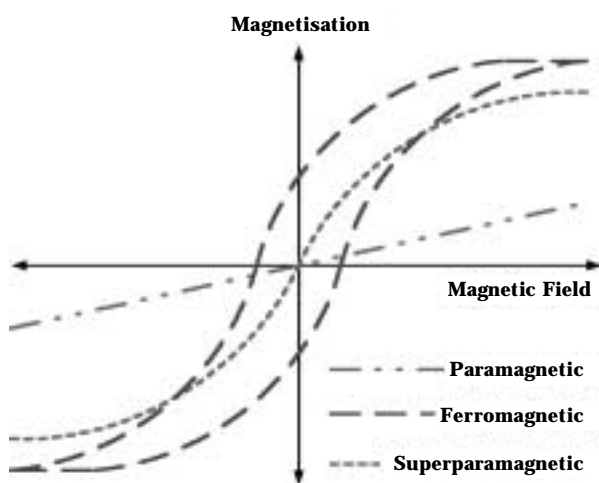


Fig. 19 Magnetisation curves of ferro-, para- and superparamagnetic materials.

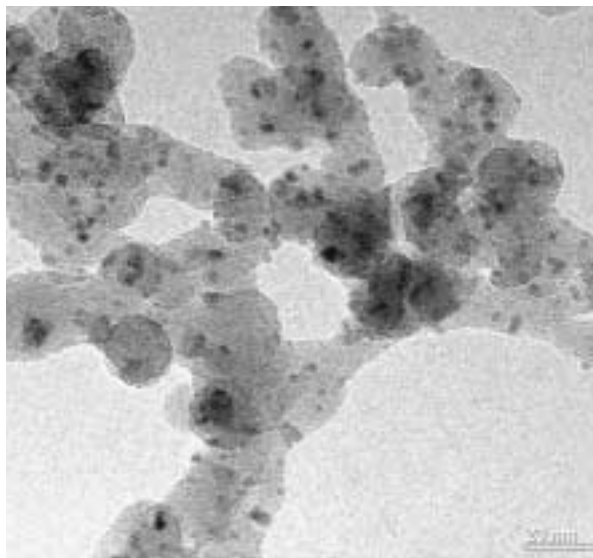


Fig. 20 TEM of iron oxide/ silica nanocomposite.

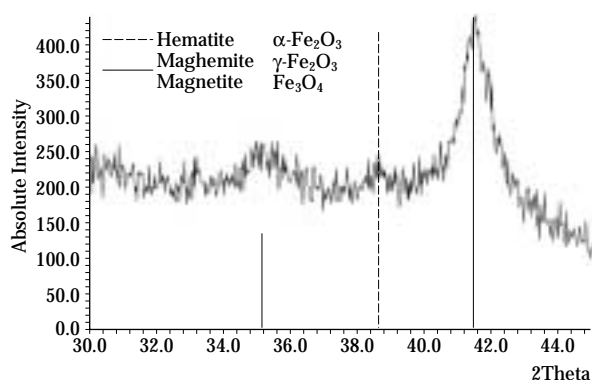


Fig. 21 XRD graph of iron oxide/ silica nanocomposite.

by adjusting process parameters. A SQUID magnetometer was used for magnetic characterisation. The particles display superparamagnetic behaviour above 50 K and the iron oxide domains are magnetically well decoupled. The so far highest saturation magnetisation achieved was 18 Am²/kg.

The advantage of the described superparamagnetic nanocomposites is their high chemical, mechanical and thermal stability, which is often well beyond that of traditional superparamagnetic materials with organic coatings.

6. Conclusion

Gas-phase synthesis is a well-known technique for the production of an extensive variety of nano-sized particles. The “original” commercial nanopowders generated by this method comprise the largest share of the market, e.g. as reinforcing fillers, for rheology control and as pigments. The growing need for multifunctional materials (scratch-resistant+transparent, transparent+conductive, etc.) drives the transition from *powders* to highly specialised *functional materials*.

Based on fundamental research, the detailed analysis of particle size and morphology together with a good understanding of the particle formation mechanisms, it is possible to design reactors and to precisely control the processes. Results thereof are technical innovations consisting of new synthesis routes and new forms of nanoparticles with custom-tailored characteristics which provide distinct performance advantages for specific applications.

The development of such technical innovations, however, comprises only the first step of the route to successful commercialisation of new nanoscale products. The real challenge lies in the discovery and development of markets and applications that can benefit from the technology. In practice, this requires a focused and dedicated marketing and applied technology effort, coupled with the willingness and ability to precisely fit your product to the needs of the customer. Degussa plans to implement such an approach in order to fully realise the commercial potential of their innovative nanomaterials and synthesis technologies resulting from their strategic research.

Acknowledgements

The authors want to thank the German Science Foundation (DFG) for the financial support and all university partners for the excellent cooperation.

Nomenclature

BET	specific surface area	(m ² /g)
CFD	computational fluid dynamics	
DFG	Deutsche Forschungsgemeinschaft (German Science Foundation)	
DITO	doped indium tin oxide	
d _{prim}	primary particle diameter	(nm)
ITO	indium tin oxide	
LII	laser-induced incandescence	
LPDS	liquid precursor delivery system	
n _{prim}	particle number	(-)
p _{min}	minimum pressure	(kPa)
RF	radio frequency	
SMPS	scanning mobility particle sizer	
SQUID	superconducting quantum interference device	
t	residence time	(ms)
T	Temperature	(°C)
TEM	transmission electron microscopy	
TPCVD	thermal plasma chemical vapour deposition	
TPPVD	thermal plasma physical vapour deposition	
XRD	x-ray diffraction	
YSZ	yttria-stabilised zirconia	

References

- [1] Geitlinger, H.; Streibel, T.; Suntz, R.; Bockhorn, H.: 27th Symposium (international) on Combustion/ The Combustion Institute, 1998, 1613-1621.
- [2] Ulrich, G. D.: Theory of Particle Formation and Growth in Oxide Synthesis Flames, *Combustion Science and Technology*, 4, 1971, 47.
- [3] Pratsinis, S. E.; Vemury, S.: Particle Formation in Gases – A Review, *Powder Technology*, 88, 1996, 267.
- [4] Kudas, T. T.; Hampden-Smith, M.: *Aerosol Processing of Materials*, Wiley-VCH, New York, 1999.
- [5] Schaefer, D. W.; Hurd, A. J.: Growth and Structure of Combustion Aerosols, *Aerosol Science and Technology*, 12, 1990, 876.
- [6] Pratsinis, S. E.; Spicer, P. T.: Competition between Gas Phase and Surface Oxidation of TiCl₄ during Synthesis of TiO₂ Particles, *Chemical Engineering Science*, 53, 1998, 1861.
- [7] Fuchs, N. A.: *The Mechanics of Aerosols*, Pergamon Press, Oxford, 1964.
- [8] Hinds, W. C.: *Aerosol Technology – Properties, Behavior and Measurement of Airborne Particles*, John Wiley & Sons, New York, 1999.
- [9] Koch, W.; Friedlander, S. K.: The Effect of Particle Coalescence on the Surface Area of a Coagulating Aerosol, *J. Colloid Interface Science*, 140, 1990, 419.
- [10] Johannessen, T.; Pratsinis, S. E.; Livbjerg, H.: Computational Fluid-Particle Dynamics for the Flame Synthesis of Alumina Particles, *Chemical Engineering Science*, 55, 2000, 177.
- [11] Ramkrishna, D.: *Population Balances – Theory and Applications to Particulate Systems in Engineering*, Academic Press, 2000.
- [12] Mühlenweg, H.; Gutsch, A.; Schild, A.; Pratsinis, S. E.: Process Simulation of Gas-to-Particle-Synthesis via Population Balances: Investigation of Three Models, *Chemical Engineering Science*, in press.
- [13] Kruijs, F. E.; Kusters, K. A.; Scarlett, B.; Pratsinis, S. E.: A Simple Model for the Evolution of the Characteristics of Aggregate Particles Undergoing Coagulation and Sintering, *Aerosol Science and Technology*, 19, 1993, 514.
- [14] Schild, A.; Gutsch, A.; Mühlenweg, H.; Pratsinis, S. E.: Simulation of Nanoparticle Production in Premixed Aerosol Flow Reactors by Interfacing Fluid Mechanics and Particle Dynamics, *J. Nanoparticle Research*, 1, 1999, 305.
- [15] Arabi-Katbi, O.I.; Pratsinis, S.E.; Morrison, P.W.; Megaridis, C.M.: Monitoring Flame Synthesis of TiO₂-Particles by in-situ FTIR Spectroscopy and Thermophoretic Sampling, *Combustion and Flame*, 124, 2001, 560.
- [16] Degussa, DE 762 723, 1942 (H. Klöpfer).
- [17] Degussa, Schriftenreihe Pigmente, Paper No. 11, Frankfurt 1992.
- [18] Degussa, Schriftenreihe Pigmente, Paper No. 56, Frankfurt 1990.
- [19] Ullmann's Encyclopedia of Industrial Chemistry, Vol. A23, 635ff.
- [20] Kudas, T. T.; Hampden-Smith, M.: *Aerosol Processing of Materials*, Wiley-VCH, New York, 1999.
- [21] Fristrom, R. M.: *Flame Structure and Processes*, Oxford University Press, 1995.
- [22] Boulos, I. B.; Fauchais, P.; Pfender, E.: *Thermal Plasmas, Fundamentals and Applications*, Plenum Press New York, Vol. 1, 1994, 1-19.
- [23] Fulcheri, L.; Probst, N.; Flamant, G.; Fabry, F.; Grivei, E.: 3rd Int. Conf. on Carbon Black, Mulhouse, 2000, 11-20.
- [24] Michel, G., Müller, E., Oestreich, Ch., Staupendahl, G., Henneberg, K.-H.: Ultrafine ZrO₂ Powder by Laser Evaporation: Preparation and Properties, *Materialwissenschaft und Werkstofftechnik*, 27, 1996, 345-349.
- [25] Michel, G., Staupendahl, G., Eberhardt, G., Vogelsberger, W.: Ultrafine ceramic powder by laser evaporation – Nanosized ceramic particles by laser evaporation and recondensation, *Fine Solid Particles*, Shaker Verlag Aachen, 1997, 127-135.
- [26] Cullity, B. D.: *Introduction to magnetic materials*, Adison-Wesley, 1972.
- [27] Kneller, E.: *Ferromagnetismus*, Springer Verlag, 1962.

Author's short biography



Andreas Gutsch

Dr. Gutsch studied chemical engineering in Karlsruhe, Germany, and began his career working as a free-lance consultant in the power engineering field. While he was doing his doctorate, he gained international experience at the University of Cincinnati, Ohio. In 1995, he joined former Degussa. Here he worked in the process engineering field, where he was appointed Chief of Section in 1998. He has been head of the Nanomaterials Project House since 2000. In April 2002 Dr. Gutsch has been appointed head of Creavis Technologies & Innovation. Dr. Gutsch belongs to a number of advisory committees at the German Research Union, acts as special adviser for the Land North Rhine-Westphalia, and is an appointed member of various scientific organisations.



Heike Mühlenweg

Heike Mühlenweg received her PhD-degree in Mechanical Process Engineering from the Technical University of Clausthal in 1995. The following year she accepted a scholarship from the German National Science Foundation (DFG) and spent eighteen month as a Post-Doc researcher at the Department of Mechanical and Aerospace Engineering, Arizona State University, USA. In 1998 she started at the Degussa AG. Following nine month of scientific work concerning population balances at the University of Cincinnati, USA, she worked as R&D engineer in Degussa's Department of Process Technology and Engineering. Her main topic was the simulation of particle synthesis in gas-phase reactors and the collaboration in preparation of the Project House Nanomaterials as a new strategic project for the development of advanced nano-scaled powders. In January 2000 she has been transferred to the starting Project House Nanomaterials and since she is responsible as R&D manager for the coordination of a joint venture project with nine leading German Universities funded by the DFG. Furthermore, based on her simulation know-how she developed and constructed a gas-phase reactor that is now operated for the generation of new nano-scaled powders.



Günther Michael

Dr. Michael studied chemistry at the University of Kaiserslautern where he received his PhD-degree on "Agostic complexes of chromium" in 1986. From 1987 on he has been working with the Aerosil Applied Technology Group of Degussa AG. He was also the quality supervisor for Aerosil. Since 2000 he is working with the Project House Nanomaterials as senior manager.



Markus Pridöhl

Dr. Pridöhl studied chemistry at the Technical University of Berlin where he received his PhD-degree on "Synthesis, ^{77}Se -NMR spectroscopy and HPLC analysis of Bis-organyl-sulfur-selen-chains" in 1995. In the same year he started with the former Cerdec AG in Frankfurt as a quality control manager. After a trainee assignment in the field of carbon black production and site management with Degussa AG in 1996 he worked as R&D manager with Degussa's Fillers and Pigments Division from 1998 on. In 2000 Dr. Pridöhl joined the Project House Nanomaterials as R&D manager.

Author's short biography



Guido Zimmermann

Guido Zimmermann got his chemical engineering degree from the university of applied science of Cologne in 1997. In the same year he started at the department „Process Technology and Engineering“ at DEGUSSA in a research group for developing ultra-fine particles as R&D engineer. Since 2000 he works for the Project House Nanomaterials as R&D manager and is responsible for the development and construction of novel types of gas-phase reactors and for the generation of new nanoscale powders.



Michael Krämer

Michael Krämer graduated in Chemical Engineering at the University of Karlsruhe, Germany, in 1999. He started his career at Degussa AG within the Process Technology and Engineering Department in the field of particle technology. Since 2000 he is working as R&D manager in Degussa's Project House Nanomaterials. Amongst his areas of expertise are the design and scale-up of gas-phase processes for the synthesis of new tailor-made nanoscaled powders.

A Century of Research in Sedimentation and Thickening[†]

Fernando Concha^{a,*} and Raimund Bürger^b

^a Department of Metallurgical Engineering,
University of Concepción

^b Institute of Applied Analysis and Numerical
Simulation, University of Stuttgart

Abstract

This paper provides a concise review of the contributions to research in sedimentation and thickening that were made during the 20th century, starting from the invention of the Dorr thickener in 1905. The different steps of progress that were made in understanding batch sedimentation and continuous thickening processes in mineral processing are reviewed. A major breakthrough was Kynch's kinematic sedimentation theory published in 1952. The authors' own contributions to sedimentation and thickening research are summarized, including the development of the appropriate mathematical framework for Kynch's theory and its extensions to continuous sedimentation and to polydisperse suspensions of spheres. An even more general model framework is provided by the phenomenological theory of sedimentation, which permits the description and simulation of the transient behavior of flocculent suspensions.

1. Introduction

The invention of the Dorr thickener in 1905 and its introduction in the mining concentrators of South Dakota can be regarded as the starting point of the modern era of thickening research. Therefore, the history of thickening can be associated with the beginning of the 20th century. Thus the beginning of the 21st century provides a good opportunity to review the steps of progress of those almost one hundred years of research and development of industrial thickeners. A second prominent reason for publishing this review just now is the 50th anniversary of the publication of Kynch's celebrated paper *A theory of sedimentation* in 1952, which can be considered as the origin of modern sedimentation and thickening research in numerous disciplines.

Thickening is not a modern undertaking and was certainly not discovered as a process in the Americas.

Whenever an ore was dressed to obtain a concentrate, two processes were used in an unseparable form: *crushing* and *washing*. There is evidence that in the IV Egyptian dynasty, some 2500 years BC, the ancient Egyptians dug for and washed gold. There is also evidence of gold washing in Sudan in the XII dynasty. Nevertheless, the earliest written reference for crushing and washing in Egypt is that of Agatharchides, a Greek geographer who lived 200 years before Christ. Ardaillon, author of the book *Les Mines du Laurion dans l'Antiquité*, described in 1897 the process used in the extensive installations for crushing and washing ores in Greece between the V to the III century BC. A.J. Wilson (1994) describes in his book *The Living Rock* mining of gold and copper in the Mediterranean from the fall of the Egyptian dynasties right to the Middle Ages and the Renaissance.

The development of mineral processing from unskilled labor to craftsmanship and eventually to an industry governed by scientific discipline is largely due to the Saxons in Germany and Cornishmen in England in the beginning of the 16th century. An international exchange of technology began between these two countries and continued for a long time. However, it was in Saxony where Agricola wrote his *De Re Metallica*, the first major contribution to the development and understanding of the mining indus-

^a Casilla 53-C, Correo 3, Concepción, Chile
Fax: +56-41-230759, E-mail: fconcha@udec.cl

^b Pfaffenwaldring 57, D-70569 Stuttgart, Germany
Fax: +49-711-6855599
E-mail: buerger@mathematik.uni-stuttgart.de

* Corresponding author

[†] Accepted: April 16, 2001

try, published in Latin in 1556, and shortly after translated to German and Italian.

Agricola's book describes several methods of washing gold, silver, tin and other metallic ores. He describes settling tanks used as classifiers, jigs and thickeners and settling ponds used as thickeners or clarifiers, see **Figures 1** and **2**. These devices operated in a batch or semi-continuous manner. A typical description is as follows: "To concentrate copper at the Neusohl mine in the Carpathians the ore is crushed and washed and passed through three consecutive washers-sifters. The fine particles are washed through a sieve in a tub full of water, where the undersize settles to the bottom of the tub. At a certain stage of filling of the tub

with sediment, the plug is drawn to let the water run away. Then the mud is removed with a shovel and taken to a second tub and then to a third tub where the whole process is repeated. The copper concentrate which has settled in the last tub is taken out and smelted."

It is evident from these references that, by using the washing and sifting processes, the ancient Egyptians and Greeks and the medieval Germans and Cornishmen knew the practical effect of the difference in specific gravity of the various components of an ore and used sedimentation in operations that can now be identified as classification, clarification and thickening. There is also evidence that in the early days no clear distinction was made between these three operations.

Agricola's book had a tremendous impact, not only in the mineral industry but also on society in general, and continued to be the leading textbook for miners and metallurgists outside the English speaking world for at least another three hundred years. Apart from its immense practical value as a manual, the greatest influence of *De Re Metallica* was in preparing the ground for the introduction of a system of mining education which, with various modifications to suit the local conditions, was later to be adopted internationally.

While in Russia the first mining school was opened in 1715 in Petrozavodsk, the most important mining academic institution, the *Freiberg Mining Academy*, was founded in Germany in 1765. Twenty years later the *Ecole des Mines* was established in Paris, but it did not become an important institution until several years later. Regardless of the intense and prolonged technological transfer that was established between Saxony and Cornwall, the British were backward in technical mining education and in the 19th century could virtually offer no facilities for the study of this discipline. The Royal School of Mines was founded in London in 1851 and the Camborn School of Mines, whose prospectus was presented in 1829, was not established until 1859. The irony is that by that time the school was properly established, the mining production of Cornwall was declining and emigration of miners was in full swing to North America, Australia, and later to South and Central Africa (Wilson 1994).

The discovery of gold in California in 1848 and in Nevada a few years later caught Americans ill-equipped to make the best of these resources. They worked with shovels and pans, digging out gravel from the stream-beds and washing it in much the same way as Egyptians had done five thousand years before them. The only professional mining engineers



Fig. 1 Settling tanks described by Agricola (1556).

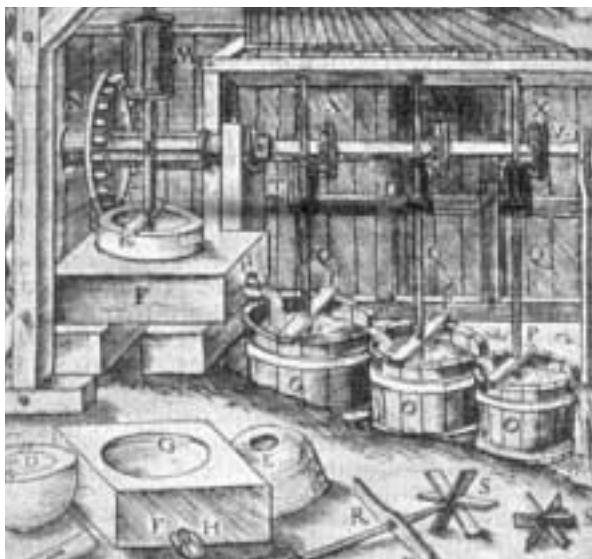


Fig. 2 Washing and settling according to Agricola (1556).

found in the North American continent until after the civil war were those which came from Freiberg or other European schools. The first American university to establish mining was the Columbia University in New York in 1864 (Wilson 1994).

It is the purpose of this review to describe the development of the science and technology of thickening during the 20th century, and to present the current accepted theory. This paper is therefore organized as follows: in Section 2, we present an overview of the most important contributions to thickening research that were made during the 20th century. This period can be subdivided into five phases: that of the invention of the Dorr thickener and initial research of thickener design (1900-1940, Sect. 2.1), that of the discovery of the operating variables in a continuous thickener (1940-1950, Sect. 2.2), the *Kynch Era*, during which the theory of sedimentation was developed (1950-1970, Sect. 2.3), the phase of the phenomenological theory (1970-1980, Sect. 2.4), and the current one of the mathematical theory (1980-present, Sect. 2.5). The year numbers are of course to a certain degree arbitrary and not meant in a precise sense. We shall discuss a few example of research work that either lagged behind or was far ahead of its surrounding current status of knowledge, and would therefore have merited to fall within a prior or subsequent phase than determined by the respective publication year. We will also mention a few instances in which historic achievements have turned out to be still important to contemporary research. In Sections 3 and 4, the authors' contribution to thickening research are summarized. In Section 3, results related to ideal suspensions, including the extension of Kynch's theory to continuous sedimentation and poly-disperse mixtures are presented, while Section 4 focuses on the recent phenomenological theory of sedimentation of flocculated suspensions. In Section 5, we comment some of the results of Sections 3 and 4, and discuss approaches by other current research groups. This paper closes with a concluding remark (Section 6).

2. Historical perspective

2.1 The invention of the Dorr thickener and thickener design (1900-1940)

Classification, clarification and thickening all involve the settling of one substance in solid particulate form through a second substance in liquid form, but the development of each one of these operations has followed different paths. While clarification deals with

very dilute suspensions, classification and thickening are forced to use more concentrated pulps. This is probably the reason for which clarification was the first of these operations amenable to a mathematical description. The work by Hazen in 1904 was the first analysis of factors affecting the settling of solid particles from dilute suspensions in water. It shows that detention time is not a factor in the design of settling tanks, but rather that the portion of solid removed was proportional to the surface area of the tank and to the settling properties of the solid matter, and inversely proportional to the flow through the tank. At the beginning, classification equipment mimicked clarification settling tanks, adding devices to discharge the settled sediment. Therefore, the first theories of mechanical classification were based on Hazen's theory of settling basins. The introduction of hydraulic classifiers led to theories of hindered settling in gravitational fields, and finally the introduction of the hydrocyclone moved away from gravity settling and used hindered settling in centrifugal fields as a mechanism.

The invention of the Dorr thickener in 1905 (Dorr, 1915) can be mentioned as the starting point of the modern thickening era. John V.N. Dorr, D.Sc., a chemist, cyanide mill owner and operator, consulting engineer and plant designer, tells (Dorr, 1936): "*The first mill I built and operated was turned into a profitable undertaking by my invention of the Dorr classifier in 1904 and, in remodeling another mill in the same district, the Dorr thickener was born in 1905. [...] Its recognition of the importance of mechanical control and continuous operation in fine solid-liquid mixtures and the size of its units have opened the way for advances in sewage and water purification and made wet chemical processes and industrial mineral processes possible.*"

The invention of the Dorr thickener made the continuous dewatering of a dilute pulp possible, whereby a regular discharge of a thick pulp of uniform density took place concurrently with overflow of clarified solution. Scraper blades or rakes, driven by a suitable mechanism, rotating slowly over the bottom of the tank, which usually slopes gently toward the center, move the material as fast as it settles without enough agitation to interfere with the settling.

It is well known that in many mineral processing operations, applications appear and are utilized far ahead of their scientific understanding. This is the case in thickening. The first reference on variables affecting sedimentation is due to Nichols (1908). Authors who studied the effects of solids and elec-

trolytes concentration, degree of flocculation, and temperature in the process also include Ashley (1909), Forbes (1912), Mishler (1912, 1918), Clark (1915), Ralston (1916), Free (1916), and the frequently cited work of Coe and Clevenger (1916).

Several of these studies introduced confusion in the comprehension of the settling process and Mishler (1912), an engineer and superintendent at the Tigre Mining Company in the Sonora desert in Mexico, was the first to show by experiments that the rate of settling of slimes is different for dilute than for concentrated suspensions. While the settling speed of dilute slimes is usually independent of the depth of the settling column, a different law governed extremely thick slimes, and sedimentation increases with the depth of the settling column. He devised a formula by means of which laboratory results could be used in continuous thickeners. These formulas represent macroscopic balances of water and solids in the thickener and can be written as

$$F = D, \quad (1)$$

$$FD_F = DD_D + O, \quad (2)$$

where F and D are the solid mass flow rates in the feed and the discharge respectively, O is the water mass flow rate in the overflow, and D_F and D_D are the dilutions of the feed and the underflow, respectively. The volume flow rate of water at the overflow $Q_O = O/\rho_f$, where ρ_f is the mass density of water, is given by

$$Q_O = F(D_F - D_D)/\rho_f. \quad (3)$$

Mishler (1912) assumed that the flow rate of water per unit area in a continuous thickener should be equal to the rate of formation of the column of water in a batch column, where a suspension with the same concentration as the thickener feed is allowed to settle. Since this rate of water formation is equal to the rate of descent of the water-suspension interface, Mishler equated this rate, Q_O/S , with the settling rate, which we denote by $\sigma_1(D_F)$. Then the cross-sectional area S of the thickener required to treat a feed rate of F is

$$S = \frac{F(D_F - D_D)}{\rho_f \sigma_1(D_F)}. \quad (4)$$

Clark (1915) carefully measured concentrations in a thickener with conical bottom, a configuration that clearly gives rise to at least a two-dimensional flow. Clark's note unfortunately is little more than half a page long but displays three diagrams of thickeners with the sample locations and the respective mixture

densities. The brevity of the note reflects that at the time of its writing the phenomena of settling were far from being understood, let alone in more than one space dimension. This also becomes apparent in Clark's introductory statement: "*Whatever interest they may possess lies in the fact that few determinations [the specific gravity of pulp] of this nature have been recorded, rather than in any unusual or unexpected conditions developed by the determinations themselves.*" Clark's measurements have received little attention as presented in his note, but it seems that they in part stimulated the well-known paper by Coe and Clevenger, which appeared in 1916, since Coe and Clevenger explicitly acknowledge Clark's experimental support.

Coe and Clevenger's paper was importance in two respects. On one hand, they were the first to recognize that the settling process of a flocculent suspension gives rise to four different and well-distinguished zones. From top to bottom, they determined a *clear water zone*, a zone in which the suspension is present at its *initial concentration*, a *transition zone* and a *compression zone*, see **Figure 3**. Coe and Clevenger reported settling experiments with a variety of materials showing this behaviour.

On the other hand, they were also the first to use the observed batch settling data in a laboratory column for the design of an industrial thickener. They argued that the *solids handling capacity*, today called *solids flux density*, has a maximum value in the thickener at a certain dilution D_k between the feed and discharge concentration. They developed, independently from Mishler, an equation similar to (4) but with the feed dilution D_F replaced by a limiting dilution D_k :

$$S = \frac{F(D_k - D_D)}{\rho_f |\sigma_1(D_k)|}, \quad (5)$$

where $\sigma_1(D_k)$ is the settling velocity of a pulp with the limiting dilution D_k . They recommend the determination of the limiting dilution by batch experiments for the desired underflow dilution D_D . Equation (5), with minor sophistications, continues to be the most reliable method of thickener design to date.

After the important contributions made in the development of thickening technology in the first two decades of the 20th century, the invention of the Dorr thickener and the development of thickener design procedures, the next two decades surely saw the expansion of this technology. Several authors made efforts to model the settling of suspensions by extending Stokes' equation or postulated empirical equations (Adamson and Glasson 1925, Robinson 1926,

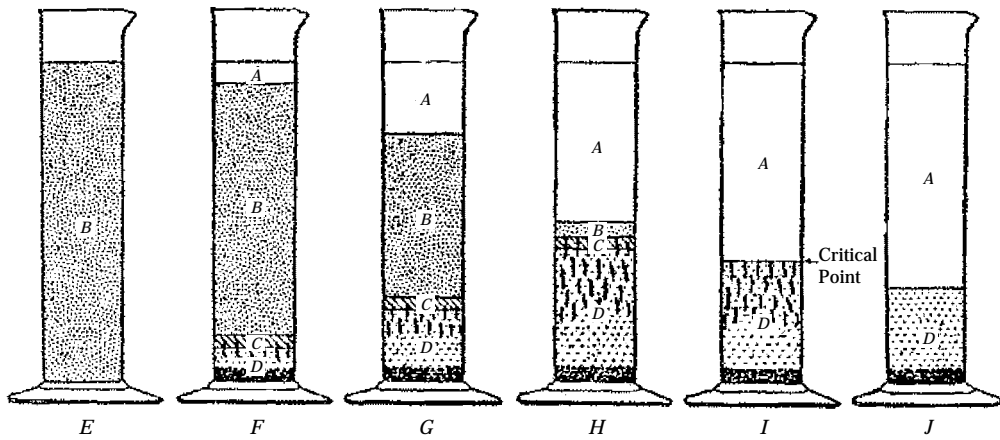


Fig. 3 Settling of a flocculent suspension as illustrated by Coe and Clevenger (1916), showing the clear water zone (A), the zone in which the suspension is at its initial concentration (B), the transition zone (C) and the compression zone (D).

Egolf and McCabe 1937, Ward and Kammermeyer 1940, Work and Kohler 1940), but no further important contributions were made until the forties. It is interesting to note that Robinson's paper was of minor influence for the development of sedimentation theory in the context of mineral processing, but that its approach seems to have been of great interest to investigators in the area of blood sedimentation half a century later (Puccini et al. 1977).

Stewart and Roberts (1933) give, in a review paper, a good idea of the state of the art of thickening in the twenties. They say: "*The basic theory is old but limitations and modifications are still but partially developed. Especially in the realm of flocculent suspensions is the underlying theory incomplete. Practical testing methods for determining the size of machines to be used are available, but the invention and development of new machines will no doubt be greatly stimulated by further investigation of the many interesting phenomena observed in practice and as fresh problems are uncovered.*"

2.2 The discovery of the operating variables in a continuous thickener (1940-1950)

The University of Illinois became very active in thickening research in the forties, shortly after Comings' paper *Thickening calcium carbonate slurries* had been published in 1940. It should be pointed out that this paper is the first to recognize the importance of local solids concentration and sediment composition for the thickening process, since it shows measurements of solids concentration profiles in a continuous thickener, while all previous treatments had been concerned with observations of the suspen-

sion-supernate and sediment-suspension interfaces, with the exception of Clark (1915).

At least nine B.Sc. theses were made under Comings' guidance, mainly on the effect of operating variables in continuous thickening. Examples of thesis subjects were: settling and continuous thickening of slurries; continuous thickening of calcium carbonate slurries; thickening of clay slurries and limiting rates of continuous thickening. These theses were summarized in an important paper by Comings, Pruiss and De Bord (1954).

The mechanism of continuous sedimentation was investigated in the laboratory in order to explain the behaviour of continuous thickeners. Comings et al. (1954) show four zones in a continuous thickener: the clarification zone at the top, the settling zone underneath, the upper compression zone further down and the rake action zone at the bottom. The most interesting conclusion, expressed for the first time, was that the concentration in the settling zone is nearly constant for a thickener at steady state, and that it depends on the rate at which the solids are fed into the thickener, and not on the concentration of the feed suspension. At low feed rate, the solids settled rapidly at a very low concentration, regardless of the feed concentration. When the feed rate was increased, the settling zone concentration increased and approached a definite value when the maximum settling capacity of the equipment was reached. If the feed rate was increased further, the settling zone stayed constant and the solids fed in excess of the settling handling capacity left the thickener by the overflow. It was verified that in most cases the feed suspension was diluted to an unknown concentration

on entering the thickener. Another finding was that, for the same feed rate, increasing or decreasing the sediment depth could adjust the underflow concentration.

It is worth mentioning that the paper by Comings et al. (1954) did not yet take into account Kynch's sedimentation theory published two years earlier (Kynch 1952), which is discussed below.

Another contribution of practical importance is the work of Roberts (1949), who advanced the empirical hypothesis that the rate at which water is eliminated from a pulp in compression is at all times proportional to that amount left, which can be eliminated upto infinite time:

$$D - D_{\infty} = (D_0 - D_{\infty}) \exp(-Kt), \quad (6)$$

where D_0 , D and D_{∞} are the dilutions at times zero and t and at infinite time, respectively. The equation has been used until today for the determination of the critical concentration.

2.3 Theory of sedimentation (1950-1970)

From the invention of the Dorr thickener to the establishment of the variables controlling the equipment, the only quantitative knowledge that was accomplished was Coe and Cleverger's (1916) design procedure. This method was solely based on a macroscopic balance of the solid and the fluid and on the observation of the different zones in the thickener. No underlying sedimentation theory existed.

The first attempts to formulate a theory of sedimentation in the sense of relating observed macroscopic sedimentation rates to microscopic properties of solid particles were made by Steinour in a series of papers that appeared in 1944 (Steinour 1944a-c). But it was Kynch, a mathematician at the University of Birmingham in Great Britain, who presented in 1952 his celebrated paper *A theory of sedimentation*. He proposed a kinematical theory of sedimentation based on the propagation of sedimentation waves in the suspension. The suspension is considered as a continuum and the sedimentation process is represented by the continuity equation of the solid phase:

$$\frac{\partial \phi}{\partial t} + \frac{\partial f_{bk}(\phi)}{\partial z} = 0, \quad 0 \leq z \leq L, \quad t > 0, \quad (7)$$

where ϕ is the local volume fraction of solids as a function of height z and time t , and

$$f_{bk}(\phi) = \phi v_s$$

is the *Kynch batch flux density function*, where v_s is the solids phase velocity. The basic assumption of

Kynch's theory is that the local solid-liquid relative velocity is a function of the solids volumetric concentration ϕ only, which for batch sedimentation in a closed column is equivalent to stating that $v_s = v_s(\phi)$. Equation (7) is considered together with the initial condition

$$\phi(z, 0) = \begin{cases} 0 & \text{for } z=L, \\ \phi_0 & \text{for } 0 < z < L, \\ \phi_{max} & \text{for } z=0, \end{cases} \quad (8)$$

where it is assumed that the function f_{bk} satisfies

$$f_{bk}(\phi) \begin{cases} = 0 & \text{for } \phi \leq 0 \text{ or } \phi \geq \phi_{max}, \\ < 0 & \text{for } 0 < \phi < \phi_{max}, \end{cases}$$

where ϕ_{max} is the maximum solids concentration. Kynch (1952) shows that knowledge of the function f_{bk} is sufficient to determine the sedimentation process, i.e. the solution $\phi = \phi(z, t)$, for a given initial concentration ϕ_0 , and that the solution can be constructed by the method of characteristics.

Kynch's paper had the greatest influence in the development of thickening thereafter. The period of twenty years after this paper may be referred to as the *Kynch Era*. When Comings moved from Illinois to Purdue, research on thickening continued there for another ten years. Although Comings soon moved on to Delaware, work continued at Purdue under the direction of P.T. Shannon. A Ph.D. thesis by Tory (1961) and M.Sc. theses by Stroupe (1962) and De Haas (1963) analyzed Kynch's theory and proved its validity by experiments with glass beads. Their results were published in a series of joint papers by these authors (Shannon et al. 1963, 1964, Tory and Shannon 1965, Shannon and Tory 1965, 1966).

Batch and continuous thickening was regarded as the process of propagating concentration changes upwards from the bottom of the settling vessel as a result of the downward movement of the solids. Equations were derived and experimental results for the batch settling of rigid spheres in water were found to be in excellent agreement with Kynch's theory. Experiments aiming at verifying the validity of Kynch's theory have repeatedly been conducted up to the present (Davis et al. 1991, Chang et al. 1997).

Kynch's paper also motivated industry to explore the possibilities of this new theory in thickener design. Again the Dorr Co. went a step further in their contribution to thickening by devising the Talmage and Fitch method of thickener design (Talmage and Fitch 1955). They affirmed that one settling plot contained all the information needed to design a thickener. Since the water-suspension interface slope (in a

z versus t diagram) gave the settling rate of the suspension, the slope at different times represented the settling velocity at different concentrations. They used this information in conjunction with the cited Mishler-Coe and Clevenger method to derive a formula for the unit area, that is, the thickener area required to produce a sediment of given concentration at a given solids handling rate. Talmage and Fitch's method is described in detail in our previous review article (Concha and Barrientos 1993) and in Chapter 11 of Bustos et al. (1999), so the resulting formulas and related diagrams are not explicitly stated here. Although Kynch's theory can not be regarded as an appropriate model for flocculent suspensions, thickener manufacturers still use and recommend Talmage and Fitch's method, which is based on this theory, for design calculations (Outukumpu Mintec 1997).

Yoshioka et al. (1957) and Hassett (1958, 1964, 1968) used the solid flux density function to interpret the operation of a continuous thickener and devise a method for thickener design (see Concha and Barrientos (1993) for details).

Experience by several authors, including Yoshioka et al. (1957), Hassett (1958, 1964, 1968), Shannon et al. (1963), Tory and Shannon (1965), Shannon and Tory (1965, 1966) and Scott (1968a,b), demonstrated that while Kynch's theory accurately predicts the sedimentation behaviour of suspensions of equally sized small rigid spherical particles, this is not the case for flocculent suspensions forming compressible sediments.

An interesting paper that seems to have been overlooked by the thickening literature is that of Behn (1957). This paper by its nature was ahead of its time and would have been well received in the seventies. Behn was the first writer to relate thickening compression with the consolidation process. Therefore he applies the following consolidation equation for the excess pore pressure p_e , that is, the pressure in the pores of the sediment in excess of the hydrostatic pressure:

$$\frac{\partial p_e}{\partial t} = \frac{k \Delta \rho h_c}{\rho_s} \frac{\partial^2 p_e}{\partial z^2}, \quad (9)$$

where k is the average sediment permeability, ρ_s is the solids density, $\Delta \rho$ is the solid-liquid density difference, and h_c is the initial height of the consolidating region. Unfortunately without explicitly mentioning the boundary conditions or presenting any detail of the derivation, Behn (1957) obtained the solution

$$D - D_\infty = (D_0 - D_\infty) \exp(-Kt), \quad K = \frac{k \Delta \rho}{h_c \rho_s}. \quad (10)$$

Equation (10) is identical to Roberts' equation (6) and gives some theoretical support to it, although Roberts' equation is essentially empirical (Fitch 1993).

Although Behn's paper is valuable in providing a concise review of the mathematical models of sedimentation that had been advanced until 1957 and in recognizing that the settling velocity formulas postulated in some of them in fact furnish the Kynch batch flux density function f_{bk} , it reflects at the same time that the implications of Kynch's theory had still not yet been well understood. This becomes apparent in Behn's conclusion that "*the Kynch theory does extend into the compression zone, although Kynch did not so indicate.*" It has already been pointed out that Kynch's theory does *not* apply to the compression zone. This becomes obvious by the fact that the compression zone is characterized by rising curved iso-concentration lines, which finally become horizontal, while in the framework of Kynch's theory concentration values always propagate along straight lines if cylindrical vessels are considered.

To describe the batch settling velocities of particles in a suspension several equations for $v_s = v_s(\phi)$ or $f_{bk}(\phi) = \phi v_s(\phi)$ were proposed, all of them extensions of the Stokes equation. The most frequently used was the two-parameter equation of Richardson and Zaki (1954):

$$f_{bk}(\phi) = u_\infty \phi (1 - \phi)^n, \quad n > 1, \quad (11)$$

where u_∞ is the settling velocity of a single particle in quiescent, unbounded fluid. This equation has the inconvenience that the settling velocity becomes zero at a solids concentration of $\phi = 1$, while experimentally this occurs at a maximum concentration ϕ_{max} between 0.6 and 0.7.

Michaels and Bolger (1962) proposed the following three-parameter alternative:

$$f_{bk}(\phi) = u_\infty \phi \left(1 - \frac{\phi}{\phi_{max}} \right)^n, \quad n > 1, \quad (12)$$

where the exponent $n = 4.65$ turned out to be suitable for rigid spheres.

For equally sized glass spheres, Shannon et al. (1963) determined the following equation by fitting a fourth-order polynomial to experimental measurements, see **Figure 4**:

$$f_{bk}(\phi) = \phi (-0.33843 + 1.37672\phi - 1.62275\phi^2 - 0.11264\phi^3 + 0.902253\phi^4) \times 10^{-2} \text{ m/s.}$$

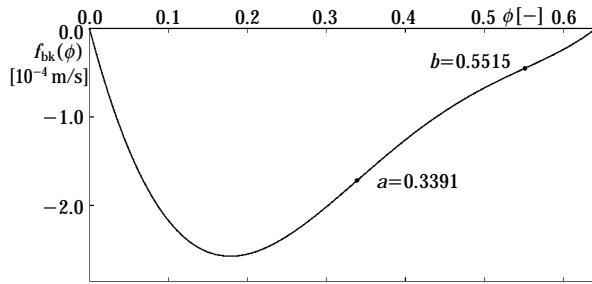


Fig. 4 Flux density function for glass beads with two inflection points *a* and *b*, after Shannon et al. (1963).

A paper that still belongs to the Kynch era, although it was published later, is the one by Petty (1975). He extended Kynch's theory from batch to continuous sedimentation. If q is defined as the volume flow rate of the mixture per unit area of the sedimentation vessel, Kynch's equation for continuous sedimentation can be written as

$$\frac{\partial \phi}{\partial t} + \frac{\partial}{\partial z}(q\phi + f_{bk}(\phi)) = 0. \quad (13)$$

Petty (1975) also discussed, for the first time, the proper boundary conditions at the bottom of the settling vessel, which is a non-trivial problem.

2.4 The phenomenological theory (1970-1980)

Although Behn (1957) was the first writer to apply consolidation theory for the settling of compressible slurries, it was Shirato and his co-workers (1970) who solved the consolidation problem taking into account the effect of sediment growth and compression due to deposition of solid particles from the hindered settling zone. The latter is, however, not explicitly modeled due to the use of material coordinates in the compressible sediment. The result were sediment concentration and excess pore pressure profiles.

If Behn's work had received greater attention, the development of a phenomenological theory would have started about fifteen years earlier. It took another five years for Adorján (1975, 1977) to present his ad-hoc theory of sediment compression, giving the first satisfactory method of thickener design, and for Smiles (1976a,b) to present his integral approach.

At about the same time, a group of researchers in Brazil made great efforts to give the phenomenological sedimentation theory a proper framework. Strong and important research on thickening, and in general in the field of flow through porous media, was going on in Brazil in the decade of the 1970s. At the Engi-

neering Graduate School of the Federal University of Rio de Janeiro, COPPE, several researchers and graduate students, among them Giulio Massarani, Affonso Silva Telles, Rubens Sampaio, I-Shih Liu, José Teixeira Freire, Liu Kay, João D'Avila and Satoshi Tobinaga, were involved in the application of a newly developed mathematical tool, the *Theory of Mixtures* of continuum mechanics, to particulate systems. Unfortunately these findings were rarely published in mainstream international journals, but are well documented in local publications and conference volumes, see for example D'Avila (1976, 1978), D'Avila and Sampaio (1977), D'Avila et al. (1978), Liu (1978) and Tobinaga and Freire (1980).

With strong ties with the Brazilian researchers, a group led by the first author of this review at the University of Concepción in Chile worked in the same direction. Findings were presented in the B.Sc. theses by O. Bascur (1976) and A. Barrientos (1978), at the XII International Mineral Processing Congress in São Paulo, Brazil in 1977 (Concha and Bascur 1977) and at the Engineering Foundation Conference on Particle Technology in New Hampshire, USA, in 1980.

Independently, Kos (1975) used the theory of mixtures to set up boundary value problems for batch and continuous sedimentation. Thacker and Lavelle (1977) used the same theory for incompressible suspensions.

2.5 Mathematical theory (1980-present)

At the end of the seventies and during the eighties several papers, for example Concha and Bustos (1985), Buscall and White (1987), Auzeais et al. (1988), Landman et al. (1988), Bascur (1989) and Davis and Russel (1989) show that the phenomenological model, based on the theory of mixtures, was well accepted by the international scientific community.

In spite of the fact that the theory of mixtures did a great job in unifying the sedimentation of dispersed and flocculated suspensions and, once appropriate constitutive equations were formulated, gave rise to a robust framework in which the sedimentation of any suspension could be simulated, the mathematical analysis of these models did not exists. Furthermore no adequate numerical method existed for solving the initial-boundary value problems for batch and continuous thickening.

While it is common that mathematics is needed in solving specific problems, many engineers regard the basic principles of mineral processing as purely physical and mathematical treatment as belonging only to a

later stage in the development of a theory. When finally mathematics get started, it could be precise, but setting up the theory is for them an extra-mathematical operation. Truesdell (1966) stated that the characteristics of a good theory are that the physical concepts themselves are made mathematical at the outset, and mathematics is used to formulate the theory and to obtain solutions.

At the beginning of the eighties, following Truesdell's ideas and convinced that the only way in establishing a rigorous theory of sedimentation consisted in the cooperation of engineers with mathematicians, the first author, together with María Cristina Bustos, then a staff member of the Department of Mathematics at the University of Concepción, and Wolfgang Wendland, professor of mathematics at the University of Darmstadt, started a fruitful cooperation on the topic of mathematical analysis of sedimentation models. After Wendland moved to the University of Stuttgart in Germany in 1986, first Matthias Kunik and then the second author joined this cooperation, which now also includes Elmer Tory, Professor Emeritus at Mount Allison University in Sackville, New Brunswick, Canada. The results of this cooperation, which has lasted for two decades now, are summarized in the following Sections 3 and 4.

3. Sedimentation of ideal suspensions

3.1 Kynch's sedimentation model and mathematical preliminaries

For batch sedimentation, equation (7) is solved together with the initial condition (8). Note that, due to the assumptions on f_{bk} , the initial condition (8) could be replaced by the initial condition

$$\phi(z, 0) = \phi_0(z) \quad \text{for } 0 \leq z \leq L,$$

combined with the boundary conditions

$$\phi(0, t) = \phi_{\max}, \quad \phi(L, t) = 0 \quad \text{for } 0 < t \leq T.$$

To construct the solution of the initial value problem (7), (8), the method of characteristics is employed. This method is based on the propagation of $\phi_0(z_0)$, the initial value prescribed at $z = z_0$, at constant speed $f'_{bk}(\phi_0(z_0))$ in a z versus t diagram. These lines might intersect, which makes solutions of equation (7) discontinuous in general. This is due to the nonlinearity of the flux density function f_{bk} . In fact, even for smooth initial data, a scalar conservation law with a nonlinear flux density function may produce discontinuous solutions, as the well-known example of

Burgers' equation illustrates, see Le Veque (1992). On the other hand, one particular theoretically and practically interesting initial-value problem for a scalar conservation law is the Riemann problem where an initial function

$$\phi_0(z) = \begin{cases} \phi_0^+ & \text{for } z > 0, \\ \phi_0^- & \text{for } z < 0 \end{cases} \quad (14)$$

consisting just of two constants is prescribed. Obviously, the initial-value problem (7), (8) consists of two adjacent Riemann problems producing two 'fans' of characteristics and discontinuities, which in this case start to interact after a finite time t_1 .

At discontinuities, equation (7) is not satisfied and is replaced by the Rankine-Hugoniot condition (Bustos and Concha 1988, Concha and Bustos 1991), which states that the local propagation velocity $\sigma(\phi^+, \phi^-)$ of a discontinuity between the solution values ϕ^+ above and ϕ^- below the discontinuity is given by

$$\sigma(\phi^+, \phi^-) = \frac{f_{bk}(\phi^+) - f_{bk}(\phi^-)}{\phi^+ - \phi^-}. \quad (15)$$

However, discontinuous solutions satisfying (7) at points of continuity and the Rankine-Hugoniot condition (15) at discontinuities are in general not unique. For this reason, an additional selection criterion, or entropy principle, is necessary to select the physically relevant discontinuous solution, the *entropy weak solution*.

One of these entropy criteria, which determine the unique entropy weak solution, is Oleinik's jump entropy condition requiring that

$$\frac{f_{bk}(\phi) - f_{bk}(\phi^-)}{\phi - \phi^-} \geq \sigma(\phi^+, \phi^-) \geq \frac{f_{bk}(\phi) - f_{bk}(\phi^+)}{\phi - \phi^+} \quad (16)$$

for all ϕ between ϕ^- and ϕ^+

is valid. This condition has an instructive geometrical interpretation: it is satisfied if and only if, in an f_{bk} versus ϕ plot, the chord joining the points $(\phi^+, f_{bk}(\phi^+))$ and $(\phi^-, f_{bk}(\phi^-))$ remains above the graph of f_{bk} for $\phi^+ < \phi^-$ and below the graph for $\phi^+ > \phi^-$, see **Figure 5**.

Discontinuities satisfying both (15) and (16) are called *shocks*. If, in addition,

$$f'_{bk}(\phi^-) = \sigma(\phi^+, \phi^-) \quad \text{or} \quad f'_{bk}(\phi^+) = \sigma(\phi^+, \phi^-) \quad (17)$$

is satisfied, the shock is called a *contact discontinuity*. In that case, the chord is tangent to the graph of f_{bk} in at least one of its endpoints.

A piecewise continuous function satisfying the conservation law (7) at points of continuity, the initial condition (8), and the Rankine-Hugoniot condition

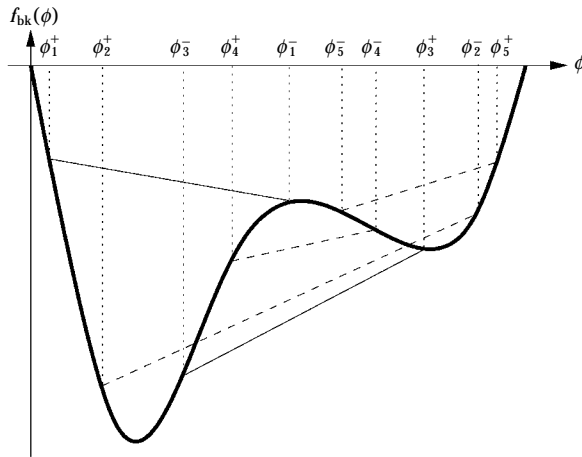


Fig. 5 Geometrical interpretation of Oleinik's jump entropy condition, applied to five jumps between $\phi^+ = \phi_i^+$ and $\phi^- = \phi_i^-$, $i=1, \dots, 5$. For $i=1, 3$ the condition is satisfied (solid chords), for $i=2, 4, 5$ it is violated (dashed chords).

(15) and Oleinik's jump entropy condition (16) at discontinuities is unique.

Consider equation (7) together with the Riemann data (14). If we assume (for simplicity) that $\phi_0^- < \phi_0^+$ and that $f''_{bk}(\phi) > 0$ for $\phi_0^- \leq \phi \leq \phi_0^+$, it is easy to see that no shock can be constructed between ϕ_0^- and ϕ_0^+ . In that case, the Riemann problem has a continuous solution

$$\phi(z, t) = \begin{cases} \phi_0^+ & \text{for } z > f'_{bk}(\phi_0^+)t, \\ (f'_{bk})^{-1}(z/t) & \text{for } f'_{bk}(\phi_0^-)t \leq z \leq f'_{bk}(\phi_0^+)t, \\ \phi_0^- & \text{for } z < f'_{bk}(\phi_0^-)t, \end{cases} \quad (18)$$

where $(f'_{bk})^{-1}$ is the inverse of f'_{bk} restricted to the interval $[\phi_0^-, \phi_0^+]$. This solution is called a *rarefaction wave* and is the entropy weak solution of the Riemann problem.

For details on entropy weak solutions of scalar conservation laws, we refer to the books by Le Veque (1992), Godlewski and Raviart (1991, 1996), Kröner (1997) or Dafermos (2000).

3.2 Solutions of the batch sedimentation problem

We now consider entropy weak solutions for the problem of equation (7) with the initial condition (8), where we set ϕ_0 *const.* corresponding to an initially homogeneous suspension and consider a flux density function f_{bk} with at most two inflection points. Using the method of characteristics and applying the theory developed by Ballou (1970), Cheng (1981, 1983) and Liu (1978), Bustos and Concha (1988) and Concha

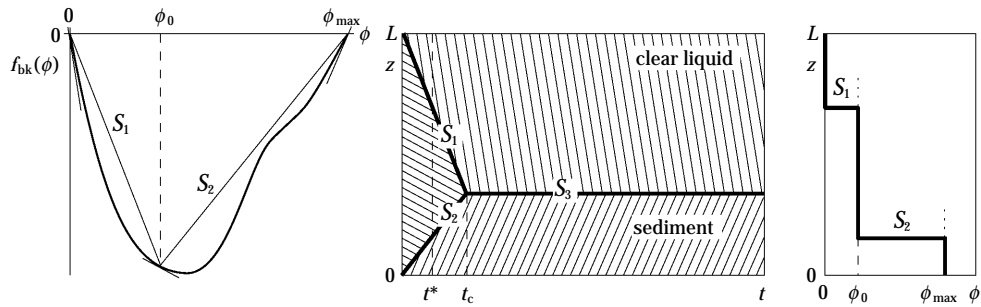
and Bustos (1991) construct entropy weak solutions of this problem in the class of piecewise continuous functions, in which zones of constant concentrations are separated by shocks, rarefaction waves or combinations of these. Therefore, it is necessary to solve the two Riemann problems given at $t=0, z=L$ and at $t=0, z=0$ and to treat the interaction of the two solutions at later times. For flux density functions with at most two inflection points, they obtain five qualitatively different entropy weak solutions or *modes of sedimentation*.

Their classification turned out to be not yet complete, since they had considered only functions with two inflection points similar to our **Figure 4**, and two inflection points can also be located in a different way, producing two additional modes of sedimentation. In these two new modes of sedimentation, the supernate-suspension interface is not a sharp shock but a rarefaction wave. The mathematically rigorous, detailed construction of the complete set of seven modes of sedimentation MS-1 to MS-7 is presented in Chapter 7 of Bustos et al. (1999). In this review, the construction of the seven different entropy solutions is outlined in **Figures 6** and **7**.

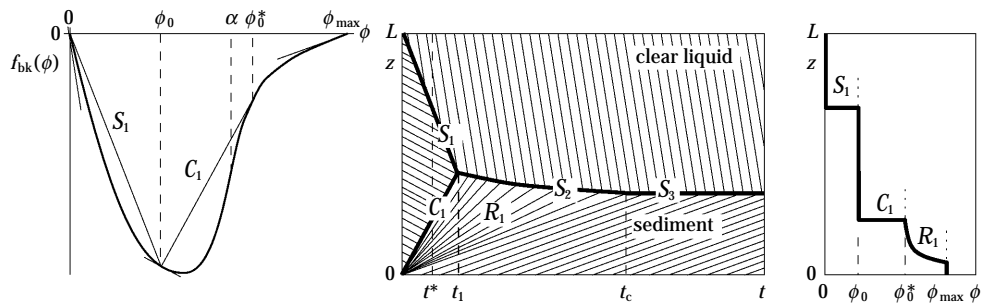
The solutions constructed by Bustos and Concha (1988) and Concha and Bustos (1991) were not new and had been published decades earlier by Straumann (1962) and Grassmann and Straumann (1963). However, at that time the mathematical concept of entropy solutions had not yet been developed, and Grassmann and Straumann (1963) had to introduce new physical arguments and insights in every case in order to obtain their solutions of the sedimentation process. Their paper certainly would have deserved greater attention, and should have been quoted by those who were active in thickening research in the 1960s, such as P.T. Shannon and his co-workers, but unfortunately was published in German.

The simplest case is that of a mode of sedimentation (MS) MS-1, in which the supernate-suspension and the suspension-sediment interfaces are both shocks, see **Figure 6 a**). These shocks meet at the critical time t_c to form a stationary clear water-sediment interface. In an MS-2, the rising shock is replaced, from top to bottom, by a contact discontinuity followed by a rarefaction wave, see **Figure 6 b**). In the flux plot, the contact discontinuity is represented by a chord joining the points $(\phi_0, f_{bk}(\phi_0))$ and $(\phi_0^*, f_{bk}(\phi_0^*))$ which is tangent to the graph of f_{bk} in the second point. If we take the same flux function and still increase ϕ_0 , this chord can no longer be drawn

a) MS-1:



b) MS-2:



c) MS-3:

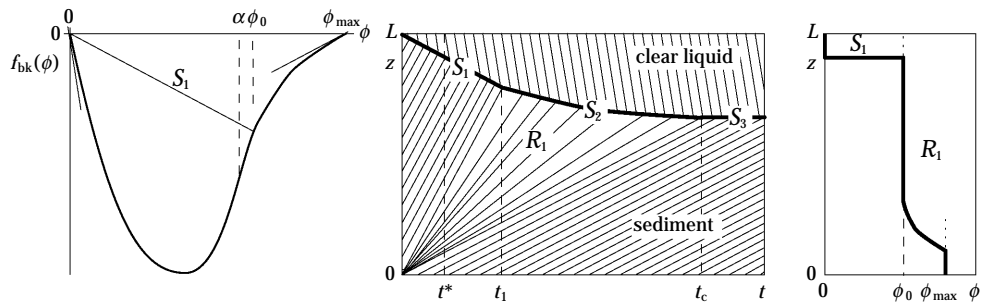


Fig. 6 Modes of sedimentation MS-1 to MS-3. From the left to the right, the flux plot, the settling plot showing characteristics and shock lines, and a representative concentration profile taken at time $t=t^*$ are shown for each mode. Chords in the flux plots and shocks in the settling plots having the same slopes are marked by the same symbols. Slopes of tangents to the flux plots occurring as slopes of characteristics in the settling plots are also indicated (Bürger and Tory, 2000).

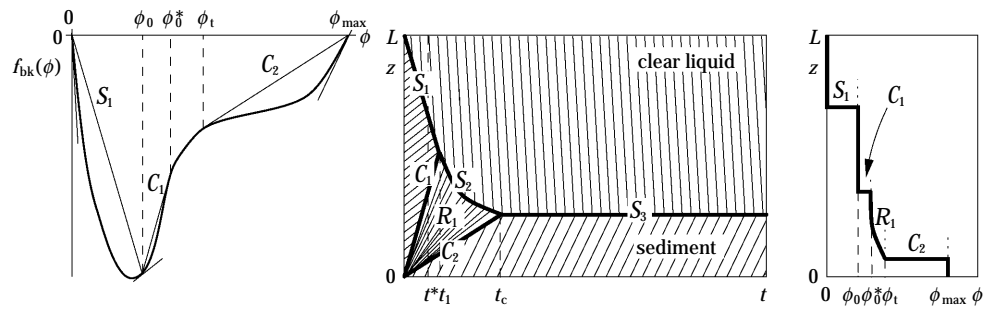
and the contact discontinuity becomes a line of continuity. This situation corresponds to an MS-3, see **Figure 6 c)**. Note that the modes of sedimentation MS-2 and MS-3 can occur only with a flux density function f_{bk} with exactly one inflection point (we recall that we always assume that $f'_{bk}(0) > 0$).

With a flux density function f_{bk} having exactly two inflection points, four additional modes of sedimentation are possible, which are collected in **Figure 7**. Clearly, an MS-1 is also possible with two inflection points. Bustos and Concha (1988) and Concha and Bustos (1991) obtained two of the four additional modes of sedimentation, namely the modes MS-4 and MS-5 shown in **Figure 7 a)** and **b)**. These modes are similar to an MS-2 and MS-3 respectively, but the second inflection point produces an additional contact

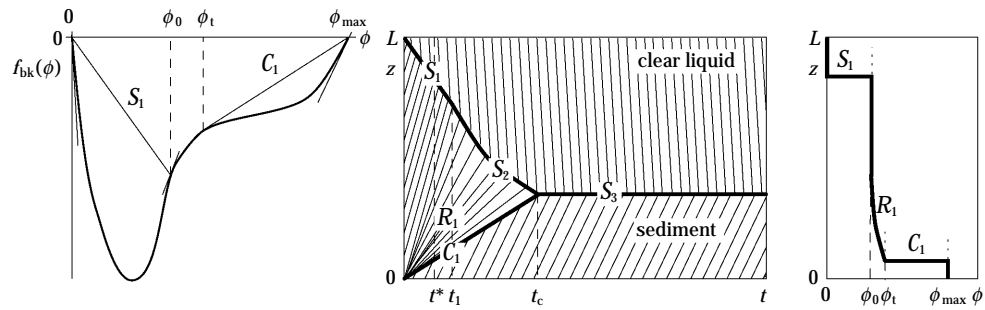
discontinuity, denoted by C_2 in **Figure 7 a)** and by C_1 in **Figure 7 b)**, which separates the lower rarefaction wave (R_1) from the rising sediment.

Of course, the shape of a given flux density function determines which modes of sedimentation are actually possible. In Chapter 7 of Bustos et al. (1999), a corresponding geometrical criterion to decide this is presented. It is quite obvious that flux density functions that are similar to that shown in **Figure 4** make an MS-4 or MS-5 possible. However, it is also possible to place the inflection points a and b in such a way that $f'_{bk}(a) < 0$, $f'_{bk}(b) < 0$, and that there exists a point $a < \tilde{\phi}_t < b$ such that the tangent to the graph of f_{bk} at $(\tilde{\phi}_t, f_{bk}(\tilde{\phi}_t))$ also goes through the point $(0, f_{bk}(0) = 0)$. This situation is shown in the flux plots of **Figure 7 c)** and **d)**. If the initial concentration ϕ_0 is then

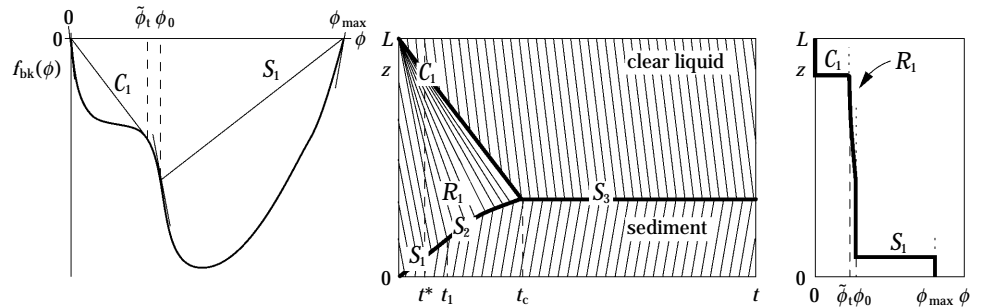
a) MS-4:



b) MS-5:



c) MS-6:



d) MS-7:

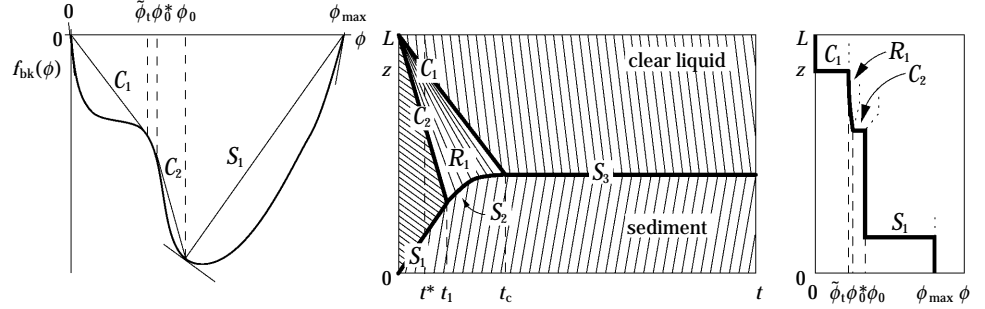


Fig. 7 Modes of sedimentation MS-4 to MS-7.

chosen between $\tilde{\phi}_t$ and the second inflection point b , a new mode of sedimentation, called MS-6, is produced, see **Figure 7 c)**: the supernate-suspension interface is no longer sharp, that is, a shock; rather, an upper rarefaction wave R_1 emerges from $z=L$ at $t=0$, which is separated from the supernate by a contact discontinuity and from the bulk suspension by a line of continuity. That line of continuity meets the rising sediment-suspension interface, the shock S_1 , at $t=t_1$.

After that a curved, convex shock S_2 forms, separating the rarefaction wave from the sediment. At the critical time $t=t_c$, the shock S_2 meets the upper end of the rarefaction wave, that is, the contact discontinuity C_1 , and the stationary shock S_3 forms, which denotes the sediment-supernate interface located at the sediment height z_c .

A similar construction applies if $\phi_0 > b$ is chosen such that there exists a point $\tilde{\phi}_t < \phi_0^* < b$ with $f'_{bk}(\phi_0^*) =$

$\sigma(\phi_0^*, \phi_0)$, see **Figure 7 d**). The resulting entropy weak solution is an MS-7, differing from an MS-6 in that the bulk suspension is separated from the upper rarefaction wave by a contact discontinuity instead of a line of continuity.

All modes of sedimentation terminate in a stationary sediment of the maximum concentration ϕ_{\max} and of height $z_c = \phi_0 L / \phi_{\max}$. This stationary state is attained at the critical time t_c .

3.3 Continuous sedimentation of ideal suspensions

Similar solutions of standardized initial-boundary value problems can be constructed by the method of characteristics for continuous sedimentation of ideal suspensions (Bustos et al. 1990b, Concha and Bustos 1992). These solutions satisfy the equation (13) wherever ϕ is discontinuous. At discontinuities between two solution values ϕ^- and ϕ^+ , the Rankine-Hugoniot condition

$$\sigma(\phi^+, \phi^-) = q(t) + \frac{f_{\text{bk}}(\phi^+) - f_{\text{bk}}(\phi^-)}{\phi^+ - \phi^-} \quad (19)$$

and Oleinik's jump entropy condition

$$\begin{aligned} q(t) + \frac{f_{\text{bk}}(\phi) - f_{\text{bk}}(\phi^-)}{\phi - \phi^-} &\geq \sigma(\phi^+, \phi^-) \\ &\geq q(t) + \frac{f_{\text{bk}}(\phi) - f_{\text{bk}}(\phi^+)}{\phi - \phi^+} \end{aligned} \quad (20)$$

for all ϕ between ϕ^- and ϕ^+

are satisfied. Conditions (19) and (20) are natural extensions of conditions (15) and (16) to the case of a flux density function with a convection term $q(t)\phi$ added to the Kynch batch flux density function $f_{\text{bk}}(\phi)$.

The standard initial function for continuous sedimentation, where $q(t)$ is a negative constant, is

$$\phi(z, 0) = \phi_0(z) = \begin{cases} \phi_L & \text{for } A < z \leq L, \\ \phi_{\max} & \text{for } 0 \leq z < A, \end{cases} \quad (21)$$

where $0 < A < L$ is the initial sediment height and ϕ_L is the concentration in the thickener to which the feed flux f_F is diluted. The value ϕ_L is obtained by solving the equation

$$q\phi_L + f_{\text{bk}}(\phi_L) = f_F. \quad (22)$$

In case Eq. (22) admits several solutions ϕ_L , the relevant one is selected by the physical argument that the feed suspension should always be diluted on entering the thickener, as shown by Comings et al. (1954), see Chapter 2 of Bustos et al. (1999).

It is assumed that the feed flux f_F and the volume

average flow velocity q are kept constant during the continuous sedimentation process. This suggests formulating the boundary conditions as

$$\phi(L, t) = \phi_L, \quad t > 0, \quad (23)$$

$$\phi(0, t) = \phi_{\max}, \quad t > 0. \quad (24)$$

However, the boundary conditions (23) and (24) can be imposed only in that special case where no characteristics carrying solution values intersect the boundary $z=L$ from below and $z=0$ from above, respectively. This case is exceptional, since the usual solution picture of the Riemann problem given by Eq. (13) and the initial datum (21) will be a centred wave, a so-called *Riemann fan*, emerging from $(z=A, t=0)$, consisting of characteristics and discontinuities, which after some finite time reach $z=L$ or $z=0$. If the entire Riemann fan cuts the boundary $z=L$, we say that the thickener *overflows*; if it cuts $z=0$, the thickener *empties*.

When such intersections with the boundaries occur, the boundary conditions (23) and (24) are no longer valid. The appropriate mathematical concept to maintain well-posedness of the initial-boundary value problem is that of set-valued *entropy boundary conditions*. This means that boundary conditions (23) and (24) are replaced by

$$\phi(L, t) \in \varepsilon_L(\phi_L; f), \quad t > 0, \quad (25)$$

$$\phi(0, t) \in \varepsilon_0(\phi_{\max}; f), \quad t > 0, \quad (26)$$

where $\varepsilon_L(\phi_L; f) \subset [0, \phi_{\max}]$ and $\varepsilon_0(\phi_{\max}; f) \subset [0, \phi_{\max}]$ are particular sets of admissible boundary values that can be constructed using the graph of the composite flux function f defined by

$$f(\phi) := q\phi + f_{\text{bk}}(\phi),$$

see Bustos and Concha (1992), Bustos et al. (1996), Bürger and Wendland (1998b) and Chapters 6 and 8 of Bustos et al. (1999) for details.

For a flux density function f_{bk} with exactly one inflection points (note that f_{bk} and f have the same inflection points), there exist three different *modes of continuous sedimentation* (Concha and Bustos 1992) depending on the structure of the Riemann fan. The solution is called a mode of continuous sedimentation MCS-1 if it consists of two constant states separated by a shock; an MCS-2 if it consists of two constant states separated by a contact discontinuity; and an MCS-3 if the solution is continuous and consists of two constant states separated by a rarefaction wave.

Note that we have to distinguish less modes of sedimentation in the continuous than in the batch case since we have to solve only *one* Riemann problem,

and no wave interactions occur at positive times. However, in each of these modes the thickener can either overflow, empty, or attain a *steady state*, i.e. approximates a stationary solution for $t \rightarrow \infty$, so that there are nine qualitatively different solution pictures.

For a detailed construction of the complete set of these solutions we refer to Chapter 8 of Bustos et al. (1999), and for a particularly concise overview to Concha and Bürger (1998). In this review, we present three examples from Chapter 8 of Bustos et al. (1999), see **Figure 8**, in which the left column shows two plots of the composite flux function f and the right one the corresponding settling plots. In **Figures 8** and **9**, $\varphi = \phi$ and $\varphi_\infty = \phi_{\max}$.

The construction method for exact entropy solutions of the problem of batch and continuous sedimentation of ideal suspensions with standardized initial and boundary data, and in particular the fact that the exact location and propagation speed of the sediment-suspension interface level are always known, have led Bustos et al. (1990b) to formulate a simple control model for continuous sedimentation. It is shown that steady states corresponding to an MCS-1 can always be recovered after a perturbation of the feed flux density $f_F = q\phi_L + f_{bk}(\phi_L)$ by solving two initial-boundary value problems at known times and with parameters q and ϕ_L that can be calculated a priori, see **Figure 9**.

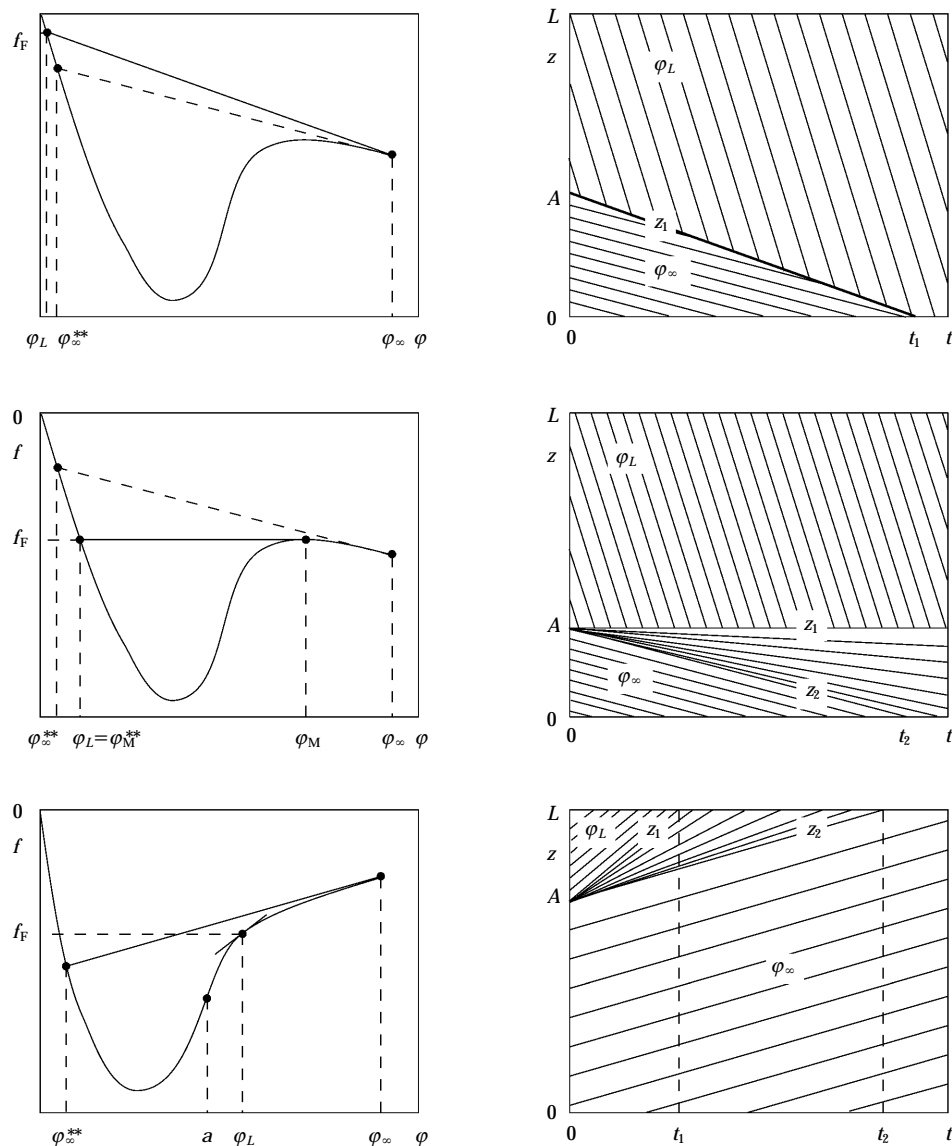


Fig. 8 Modes of continuous sedimentation (Bustos et al. 1999). Top: MCS-1 with emptying ICT; Middle: MCS-2 attaining a steady state; Bottom: MCS-3 causing the ICT to overflow.

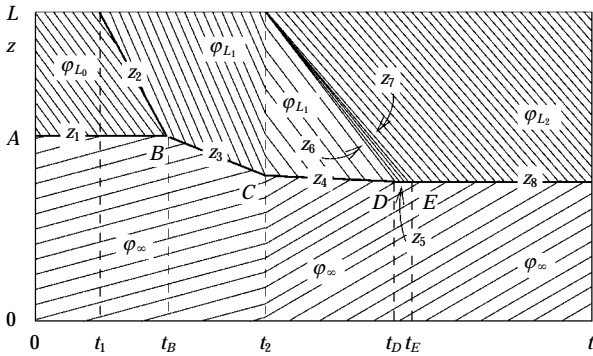


Fig. 9 Control of continuous sedimentation, after Bustos et al. (1990b) and Chapter 8 of Bustos et al. (1999).

3.4 Sedimentation of polydisperse suspensions of spheres

In this section we consider polydisperse mixtures, i.e. suspensions of rigid spheres with particles belonging to a finite number of species differing in size or density. For simplicity, the mathematical model is outlined here for the case of different sizes only; see Bürger et al. (2000a) for the general case.

If we denote by v_i and $\phi_i = \phi_i(z, t)$ the phase velocity and the local volumetric concentration of particle species i , respectively, the mass balances for the solids can be written as

$$\frac{\partial \phi_i}{\partial t} + \frac{\partial f_i}{\partial z} = 0, \quad i=1, \dots, N, \quad (27)$$

where

$$f_i = \phi_i v_i, \quad i=1, \dots, N.$$

These balances lead to a solvable system of N scalar equations if either the solid phase velocities v_i or the solid-fluid relative velocities $u_i = v_i - v_f$, where v_f denotes the fluid phase velocity, are given as functions of ϕ_1 to ϕ_N . The former approach is due to Batchelor (1982) and Batchelor and Wen (1982), while the latter has been advocated by Masliyah (1979). For sake of brevity, we present here only the model due to Masliyah, and refer to Concha et al. (1992), Bürger et al. (2000a) and Bürger et al. (2001c) for extensive treatments.

The settling of a polydisperse suspension in a column of height L can be described by a system of N conservation laws

$$\frac{\partial \Phi}{\partial t} + \frac{\partial \mathbf{f}(\Phi)}{\partial z} = 0, \quad 0 \leq z \leq L, \quad t > 0; \quad \mathbf{f}(\Phi) = (f_1(\Phi), \dots, f_N(\Phi))^T, \quad (28)$$

where $\Phi = (\phi_1, \dots, \phi_N)^T$ denotes the vector of concentration values, together with prescribed initial concentrations and the zero flux conditions

$$\begin{aligned} \phi_i(z, 0) &= \phi_i^0(z), \quad 0 \leq z \leq L, \quad 0 \leq \phi_1^0(z) + \dots + \phi_N^0(z) \leq \phi_{\max}; \\ \mathbf{f}|_{z=0} &= 0, \quad \mathbf{f}|_{z=L} = 0. \end{aligned}$$

It is well known that solutions of equation (28) are discontinuous in general. The propagation speed of a discontinuity in the concentration field ϕ_i is given by the Rankine-Hugoniot condition

$$\sigma_i(\Phi^+, \Phi^-) := \frac{f_i(\Phi^+) - f_i(\Phi^-)}{\phi_i^+ - \phi_i^-}, \quad i=1, \dots, N, \quad (29)$$

where Φ^+ , ϕ_i^+ , Φ^- and ϕ_i^- denote the limits of Φ and ϕ_i above and below the discontinuity, respectively. This condition can readily be derived from first principles by considering the flows to and from the interface.

For batch sedimentation in a closed column, the volume average velocity

$$q := (1 - \phi)v_f + \phi_1 v_1 + \dots + \phi_N v_N$$

vanishes, which can be seen easily by summing equation Eq. (27) over $i=1, \dots, N$ and by taking into account the continuity equation of the fluid,

$$\frac{\partial \phi}{\partial t} - \frac{\partial}{\partial z} ((1 - \phi)v_f) = 0, \quad (30)$$

and that $q=0$ at $z=0$. In terms of the relative velocities $u_i := v_i - v_f$, $i=1, \dots, N$, we can rewrite $q=0$ as

$$v_f = -(\phi_1 u_1 + \dots + \phi_N u_N).$$

Noting that

$$f_i = \phi_i(u_i + v_f),$$

we obtain

$$f_i = f_i(\Phi) = \phi_i(u_i - (\phi_1 u_1 + \dots + \phi_N u_N)).$$

Including in his analysis the momentum equations for each particle species and that of the fluid and using equilibrium considerations, Masliyah (1979) derived that the constitutive equation for the solid-fluid relative velocity u_i should be

$$u_i = \tilde{u}_{\infty i} V(\phi),$$

where $\tilde{u}_{\infty i}$ denotes the Stokes settling velocity of a single particle of species i with respect to a fluid of density

$$\rho(\phi) = \phi \rho_s + (1 - \phi) \rho_f,$$

i.e.,

$$\tilde{u}_{\infty i} = -\frac{2(\rho_s - \rho(\phi))g_i^2}{9\mu_f} = -\frac{2(1-\phi)\Delta\rho g_i^2}{9\mu_f}, \quad i=1, \dots, N, \quad (31)$$

and where $V(\phi)$ can be chosen as one of the hindered settling functions known in the monodisperse case, for example as the ubiquitous Richardson and Zaki (1954) formula $V(\phi) = V^{RZ}(\phi) = (1-\phi)^n$, with parameters $n > 1$, for $0 \leq \phi \leq \phi_{\max}$. With the parameters

$$\mu = -\frac{gd_1^2}{18\mu_f}, \quad \delta_i = \frac{d_i^2}{d_1^2}, \quad i=1, \dots, N,$$

we finally obtain

$$f_i(\Phi) = \mu(1-\phi)V(\phi) \left(\phi_i \sum_{j=1}^N \delta_j \phi_j - \delta_i \phi_i \right). \quad (32)$$

The mathematical theory of systems of conserva-

tion laws is significantly more complicated, and much less developed, than that of scalar equations. For initial-boundary value problems of nonlinear coupled systems such as that given by (28), supplemented with the flux density function (32), no general existence and uniqueness result is available. In fact, the analysis of these polydisperse sedimentation equations is just starting. It is, however, possible to obtain numerical solutions of these equations by the application of modern shock-capturing finite difference schemes for systems of conservation laws.

We present here a numerical example from Bürger et al. (2000a). Consider the experiment performed by Schneider et al. (1985) with glass beads of the same density $\rho_s = 2790 \text{ kg/m}^3$ and of the diameters $d_1 = 0.496 \text{ mm}$ and $d_2 = 0.125 \text{ mm}$ in a settling column of height $L = 0.3 \text{ m}$. The fluid density and viscosity are $\rho_f = 1208 \text{ kg/m}^3$ and $\mu_f = 0.02416 \text{ kgm}^{-1}\text{s}^{-1}$, respectively. The initial concentrations are $\phi_1^0 = 0.2$ and $\phi_2^0 = 0.05$, and the simulated time here is $T = 1200 \text{ s}$. Following Schneider et al. (1985), we employ Richardson

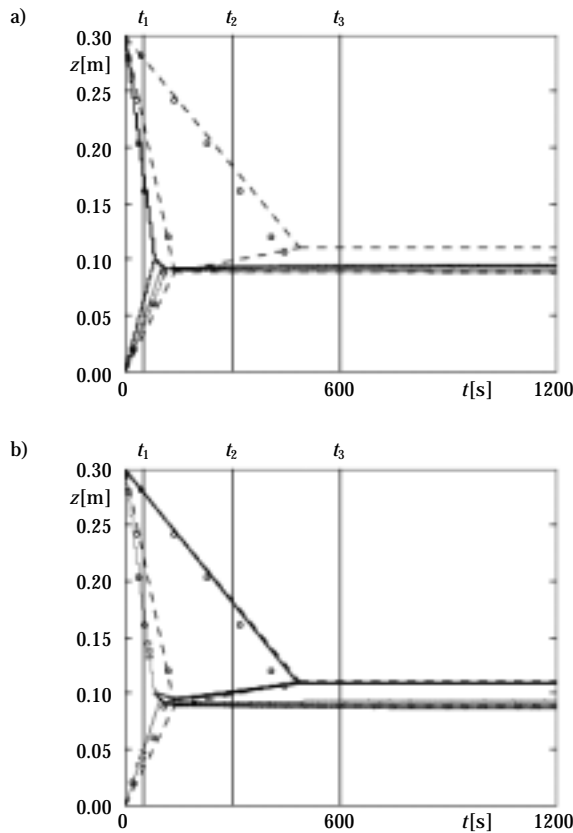


Fig. 10 Settling of a bidisperse suspension of heavy particles of two different sizes: iso-concentration lines (a) of the larger particles and (b) of the smaller particles, corresponding to the values of ϕ_i 0.02, 0.04, 0.06, 0.08, 0.1, 0.15, 0.25, 0.3, 0.4, 0.5 and 0.6. The circles and the dashed lines correspond to experimental measurements of interface locations and shock lines, respectively, obtained by Schneider et al. (1985). Concentration profiles taken at the times t_1 , t_2 and t_3 are given in **Figure 11**.

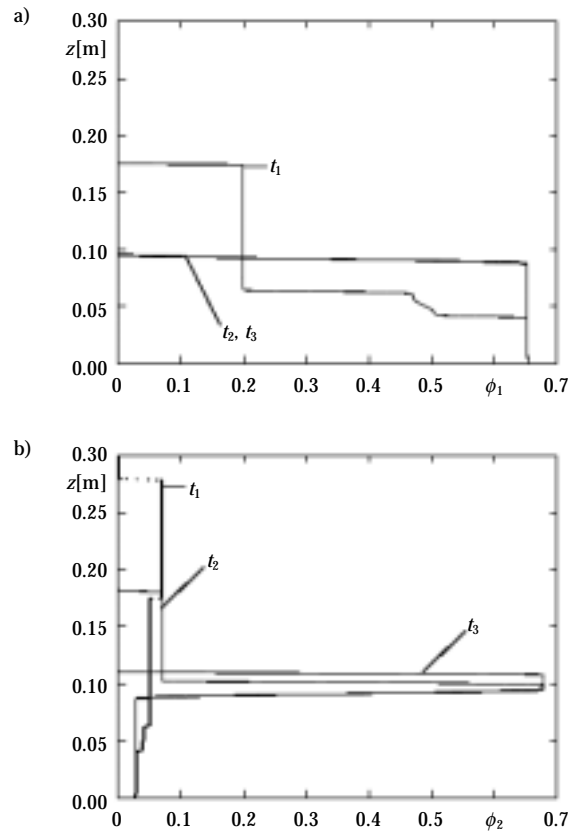


Fig. 11 Settling of a bidisperse suspension of heavy particles of two different sizes: concentration profiles (a) of the larger particles and (b) of the smaller particles (index 2) at $t_1 = 51.9 \text{ s}$, $t_2 = 299.8 \text{ s}$ and $t_3 = 599.7 \text{ s}$.

and Zaki's flux density function with $n=2.7$, which is cut at $\phi_{\max}=0.68$, see Concha et al. (1992).

Figure 10 displays the simulated iso-concentration lines for each species, together with the experimental measurements of interface locations and computed shock lines made by Schneider and co-authors, while **Figure 11** shows concentration profiles of both species at three selected times.

4. Phenomenological theory of thickening

4.1 The Theory of Mixtures

The *Theory of Mixtures* (Bowen 1976) states that a mixture of continuous media with components α may be described by the following quantities: the apparent component density $\bar{\rho}_\alpha$, the component velocity \mathbf{v}_α , the component stress tensor \mathbf{T}_α , the component body force, and the interaction force between components \mathbf{m}_α . These quantities constitute a *dynamic process* if, in regions where the field variables are continuous, they obey the following *field equations*:

$$\frac{\partial \bar{\rho}_\alpha}{\partial t} + \nabla \cdot (\bar{\rho}_\alpha \mathbf{v}_\alpha) = 0, \quad (33)$$

$$\bar{\rho}_\alpha \left(\frac{\partial \mathbf{v}_\alpha}{\partial t} + \nabla \mathbf{v}_\alpha \cdot \mathbf{v}_\alpha \right) = \nabla \cdot \mathbf{T}_\alpha + \bar{\rho}_\alpha \mathbf{b} + \mathbf{m}_\alpha. \quad (34)$$

In regions with discontinuities, the field equations must be replaced by the following *jump conditions*:

$$[\bar{\rho}_\alpha \mathbf{v}_\alpha \cdot \mathbf{e}_I] = [\bar{\rho}_\alpha \mathbf{v}_I \cdot \mathbf{e}_I], \quad (35)$$

$$[\bar{\rho}_\alpha \mathbf{v}_\alpha \mathbf{v}_\alpha \cdot \mathbf{e}_I] = [\bar{\rho}_\alpha \mathbf{v}_\alpha \mathbf{v}_I \cdot \mathbf{e}_I] + [\mathbf{T}_\alpha \cdot \mathbf{e}_I], \quad (36)$$

where \mathbf{e}_I is the normal vector of a jump discontinuity and $[\cdot]$ (bold square brackets) denotes the jump of a quantity across a discontinuity. The jump balances (35) and (36) can be derived from the appropriate integral or macroscopic mass and momentum balances (33) and (34) and do not involve nor provide supplementary information. More details can be found in Chapter 1 of Bustos et al. (1999).

4.2 Solid-fluid particulate systems

A *particulate system*, consisting of a finely divided solid in a fluid, can be regarded as a mixture of continuous media if the following assumptions are met (Concha et al. 1996):

1. The solid particles are small with respect to the containing vessel, and have the same density, size and shape.
2. Particles and fluid are incompressible.
3. There is no mass transfer between the solid and the fluid.

4. Gravity is the only body force.

For such a system, we let $\alpha=s$ denote the solid component and $\alpha=f$ the fluid component. Equations (33) and (34) then produce the following balance equations: the solid mass balance

$$\frac{\partial \phi}{\partial t} + \nabla \cdot (\phi \mathbf{v}_s) = 0, \quad (37)$$

the fluid mass balance

$$\frac{\partial \phi}{\partial t} - \nabla \cdot ((1-\phi) \mathbf{v}_f) = 0, \quad (38)$$

the solid linear momentum balance

$$\rho_s \phi \left(\frac{\partial \mathbf{v}_s}{\partial t} + \nabla \mathbf{v}_s \cdot \mathbf{v}_s \right) = \nabla \cdot \mathbf{T}_s + \rho_s \phi \mathbf{b} + \mathbf{m} \quad (39)$$

and the fluid linear momentum balance

$$\rho_f (1-\phi) \left(\frac{\partial \mathbf{v}_f}{\partial t} + \nabla \mathbf{v}_f \cdot \mathbf{v}_f \right) = \nabla \cdot \mathbf{T}_f + \rho_f (1-\phi) \mathbf{b} - \mathbf{m}. \quad (40)$$

Here ϕ denotes the local volume solid concentration, t time, \mathbf{v}_s and \mathbf{v}_f the respective solid and fluid phase velocity, ρ_s and ρ_f the respective solid and fluid mass densities, \mathbf{T}_s and \mathbf{T}_f the corresponding Cauchy stress tensors, \mathbf{b} the body force and \mathbf{m} the solid-fluid interaction force per unit volume.

In the cases of practical interest, the acceleration terms are small and can be neglected; the solid-fluid interaction force \mathbf{m} can be decomposed into a static term \mathbf{m}_b and a dynamic term \mathbf{m}_d ; and both stresses can be written as a pressure term and a viscous extra stress. For sake of simplicity, we limit the treatment here to one space dimension, in which the viscous extra stress tensors are unimportant, and introduce the constitutive assumption

5. Particles and fluid are contained in an impervious vessel with frictionless walls, in which all variables are constant across any cross-sectional areas.

The viscosity terms of the extra stress tensors play, however, a decisive role for the stability of the resulting model equations in two or three space dimensions (Bürger and Kunik 2001, Bürger et al. 2001d), see also the discussion in Section 5 of this review. Details on the justification of these assumptions and on the following deduction can be found in Concha et al. (1996) and Bürger and Concha (1998) for one space dimensions and in Bürger et al. (2000e) for several space dimensions.

Inserting the present assumptions into the linear momentum balances (39) and (40), we obtain

$$\frac{\partial p_f}{\partial z} = \rho_f(1-\phi)g - m_b - m_d, \quad (41)$$

$$\frac{\partial p_s}{\partial z} = \rho_s \phi g + m_b + m_d. \quad (42)$$

The quantities p_s and p_f are theoretical variables which we now express in terms of measurable variables, namely the pore pressure p and the effective solid stress σ_e . Assuming that the local surface porosity of every cross section of the network formed by the solid flocs equals the volume porosity, we can express p_f and p_s in terms of p and σ_e via the formulas

$$\begin{aligned} p_f &= (1-\phi)p = (1-\phi)[p_e + \rho_f g(H-z)], \\ p_s &= \phi[p_e + \rho_f g(H-z)] + \sigma_e(\phi), \end{aligned}$$

where p_e is again the excess pore pressure, that is, the pore pressure minus the hydrostatic pressure,

$$p_e = p - \rho_f g(H-z). \quad (43)$$

It can be shown (Concha et al. 1996) that the hydrostatic interaction force is proportional to the pore pressure and the concentration gradient:

$$m_b = p \frac{\partial \phi}{\partial z}, \quad (44)$$

and the hydrodynamic interaction force may be modeled by a Stokes-like (or Darcy-like) equation as a linear function of the solid-fluid relative velocity:

$$m_d = -\alpha(z, t)(v_s - v_f), \quad (45)$$

where $\alpha(z, t)$ is the resistance coefficient of the suspension or the sediment.

Collecting all these results, and introducing them into equations (41) and (42), reduces Eqns. (37)-(40) to

$$\frac{\partial \phi}{\partial t} + \frac{\partial(\phi v_s)}{\partial z} = 0, \quad (46)$$

$$\frac{\partial \phi}{\partial t} - \frac{\partial(1-\phi)v_f}{\partial z} = 0, \quad (47)$$

$$\frac{\partial \sigma_e}{\partial z} = \Delta \rho g \phi - \frac{\alpha(\phi)}{1-\phi}(v_s - v_f), \quad (48)$$

$$\frac{\partial p_e}{\partial z} + \frac{\partial \sigma_e}{\partial z} = -\Delta \rho g \phi. \quad (49)$$

At discontinuities, equations (46)-(49) have to be replaced by the appropriate jump conditions.

Three important steps have to be taken to transform Equations (46) to (49) into a usable mathematical model. First, observe that we consider six scalar

variables, but have only four scalar equations available to specify them. Thus two quantities should be specified by constitutive equations. We therefore assume that the resistance coefficient α and the effective solid stress function σ_e are given as constitutive functions of the types $\alpha = \alpha(\phi)$ and $\sigma_e = \sigma_e(\phi)$.

Second, we observe that the volume average velocity of the mixture,

$$q := \phi v_s + (1-\phi)v_f = v_s - (1-\phi)(v_s - v_f) \quad (50)$$

satisfies the simple equation

$$\frac{\partial q}{\partial z} = 0 \quad (51)$$

obtained from summing Equations (46) and (47). It is useful to replace Eq. (47) by (51).

Finally, we express the solid-fluid relative velocity $v_s - v_f$ from (50) in the form

$$v_s - v_f = \frac{1}{1-\phi}(v_s - q). \quad (52)$$

Substituting (52) into (48) and (49), we can now define a *Dynamic Process for a Particulate System* as a set of four unknown field variables: the volumetric solids concentration ϕ , the excess pore pressure p_e , the volume average velocity q and the solids volume flux

$$f := \phi v_s, \quad (53)$$

if in any regions of continuity, these four variables satisfy the four scalar field equations

$$\frac{\partial \phi}{\partial t} + \frac{\partial f}{\partial z} = 0, \quad (54)$$

$$\frac{\partial q}{\partial z} = 0, \quad (55)$$

$$\frac{\partial \sigma_e(\phi)}{\partial z} = -\Delta \rho g \phi - \frac{\alpha(\phi)}{\phi(1-\phi)^2}(f - \phi q), \quad (56)$$

$$\frac{\partial p_e}{\partial z} + \frac{\partial \sigma_e}{\partial z} = -\Delta \rho g \phi, \quad (57)$$

where σ_e and α are given as functions of ϕ . At discontinuities Equations (54)-(57) have to be replaced by the appropriate jump conditions.

4.3 Kinematical sedimentation process

An *ideal suspension* can be defined as a suspension of equally sized rigid spherical particles, such as glass beads, for which the effective solid stress is constant, i.e.

$$\frac{\partial \sigma_e}{\partial z} = 0. \quad (58)$$

Introducing (58) into (56), we obtain

$$f = q\phi - \frac{\Delta \rho g \phi (1 - \phi)}{\alpha(\phi)}.$$

Defining the Kynch batch flux density function $f_{bk} = f_{bk}(\phi)$ by

$$f_{bk}(\phi) = -\frac{\Delta \rho g \phi^2 (1 - \phi)^2}{\alpha(\phi)}, \quad (59)$$

we can rewrite f in the form

$$f = f(\phi, t) = \phi q + f_{bk}(\phi),$$

and Eq. (54) turns into the equation (13) of a continuous sedimentation process of an ideal suspension.

4.4 Dynamic sedimentation processes

In applying the phenomenological model of a particulate system to the sedimentation of a flocculent suspension forming compressible sediments, the following two assumptions are made:

6. The suspension is entirely flocculated at the beginning of the sedimentation process.
7. The solid and the liquid can perform a one-dimensional simple compression motion only.

For flocculent suspensions we consider again the equations (54)-(57) defining a Dynamic Process for a Particulate System, together with two constitutive equations for the resistance coefficient $\alpha = \alpha(\phi)$ (or, equivalently, for the Kynch batch flux density function $f_{bk} = f_{bk}(\phi)$), and for the effective solid stress $\sigma_e = \sigma_e(\phi)$.

Isolating f from Eq. (56) and using the definition of q yields

$$f = q\phi - \frac{\Delta \rho g \phi^2 (1 - \phi)^2}{\alpha(\phi)} \left(1 + \frac{\sigma'_e(\phi)}{\Delta \rho g \phi} \frac{\partial \phi}{\partial z} \right).$$

In view of Eq. (59), this can be rewritten as

$$f = q\phi + f_{bk}(\phi) \left(1 + \frac{\sigma'_e(\phi)}{\Delta \rho g \phi} \frac{\partial \phi}{\partial z} \right), \quad (60)$$

hence the solids mass balance equation can be written as

$$\frac{\partial \phi}{\partial t} + \frac{\partial}{\partial z} (q(t)\phi + f_{bk}(\phi)) = \frac{\partial}{\partial z} \left(-\frac{f_{bk}(\phi)\sigma'_e(\phi)}{\Delta \rho g \phi} \frac{\partial \phi}{\partial z} \right). \quad (61)$$

Observe that f is now a function of $\phi(z, t)$, $(\partial \phi / \partial z)(z, t)$ and t . However, for the definition of boundary conditions, it is more convenient to simply refer to $f = f(z, t)$.

Defining the diffusion coefficient

$$a(\phi) := -\frac{f_{bk}(\phi)\sigma'_e(\phi)}{\Delta \rho g \phi}$$

and its primitive

$$A(\phi) := \int_0^\phi a(s) ds,$$

we can rewrite Eq. (61) in the form

$$\frac{\partial \phi}{\partial t} + \frac{\partial}{\partial z} (q(t)\phi + f_{bk}(\phi)) = \frac{\partial^2 A(\phi)}{\partial z^2}. \quad (62)$$

We assume here that the effective solid stress is given as a function of the volumetric solids concentration ϕ satisfying

$$\sigma_e(\phi) \begin{cases} = \text{const.} & \text{for } \phi \leq \phi_c, \\ > 0 & \text{for } \phi > \phi_c, \end{cases} \quad \sigma'_e(\phi) \begin{cases} = 0 & \text{for } \phi \leq \phi_c, \\ > 0 & \text{for } \phi > \phi_c, \end{cases}$$

where ϕ_c is the critical concentration or gel point at which the solid flocs begin to touch each other. A common constitutive equation is the power law (Tiller and Leu 1980, Landman and White 1994)

$$\sigma_e(\phi) = \begin{cases} 0 & \text{for } \phi \leq \phi_c, \\ \sigma_0 [(\phi/\phi_c)^n - 1] & \text{for } \phi > \phi_c, \end{cases} \quad n > 1, \sigma_0 > 0. \quad (63)$$

Due to the constitutive assumptions concerning the functions f_{bk} and σ_e , we see that

$$a(\phi) \begin{cases} = 0 & \text{for } 0 \leq \phi \leq \phi_c \text{ and } \phi = \phi_{\max}, \\ > 0 & \text{for } \phi_c < \phi < \phi_{\max}. \end{cases} \quad (64)$$

Consequently, Eq. (61), or equivalently Eq. (62) is of the first-order *hyperbolic* type for $\phi \leq \phi_c$ and $\phi = \phi_{\max}$ and of the second-order *parabolic* type for $\phi_c < \phi < \phi_{\max}$. Summarizing, we say that (62) is a *quasilinear strongly degenerate parabolic equation*, where the attribute *strongly* states that the degeneration from parabolic to hyperbolic type not only takes place at isolated values, but on the whole interval $[0, \phi_c]$ of concentration values.

4.5 Initial and boundary conditions

In one space dimension, we see that the volume average velocity of the mixture is given by boundary conditions, and we are left with the quasilinear strongly degenerate parabolic equation (62) for $(z, t) \in (0, L) \times (0, T)$, together with the equation (57).

Obviously, only Eq. (62) has actually to be solved, since by Eq. (57) the excess pore pressure can always be calculated from the concentration distribution. It is therefore sufficient to consider initial-boundary value problem of Eq. (62) only.

For batch sedimentation of a flocculated suspen-

sion of initial concentration ϕ_0 in a closed column we consider the initial-boundary value problem of Eq. (62) with $q = 0$ on Q_T and the initial and boundary conditions $f(0, t) = f(L, t) = 0$, that is

$$\phi(z, 0) = \phi_0(z), \quad z \in [0, L], \quad (65a)$$

$$\left(f_{\text{bk}}(\phi) - \frac{\partial A(\phi)}{\partial z} \right)(L, t) = 0, \quad t \in [0, T], \quad (65b)$$

$$\left(f_{\text{bk}}(\phi) - \frac{\partial A(\phi)}{\partial z} \right)(0, t) = 0, \quad t \in [0, T]. \quad (65c)$$

For continuous sedimentation we assume that the solids flux at $z=0$, $f(0, t)$ reduces to its convective part $q(t)\phi(0, t)$, and that the concentration does not change when the concentrated sediment leaves the thickener. This implies the equation

$$f(0, t) \left(q(t)\phi + f_{\text{bk}}(\phi) - \frac{\partial A(\phi)}{\partial z} \right)(0, t) = q(t)\phi(0, t),$$

from which we deduce that boundary condition (65c) is valid also in the continuous case. At $z=L$, we prescribe in the continuous case a solids feed flux $f_F(t)$, i.e. $f(L, t) = f_F(t)$, which leads to the following boundary condition replacing (65b):

$$\left(f_{\text{bk}}(\phi) + q(t)\phi - \frac{\partial A(\phi)}{\partial z} \right)(L, t) = f_F(t), \quad t \in [0, T]. \quad (66)$$

4.6 Mathematical analysis of the initial-boundary value problems

It is well known that, due to both the type degeneracy and to the nonlinearity of the function f_{bk} , solutions of (62) are discontinuous and have to be defined as entropy solutions. The basic ingredient of the appropriate solution concept of entropy weak solutions is an entropy inequality, which can be formulated by suitably modifying the well-known results of the pioneering papers by Kruřkov (1970) and Vol'pert (1967) for first-order partial differential equations and by Vol'pert and Hudjaev (1969) for second-order partial differential equations.

By the vanishing viscosity method using a mollifier technique, Bůrger et al. (2000c) showed that an entropy solution of the initial-boundary value problem (62), (65) exists, even if the function $a = a(\phi)$ has a jump at $\phi = \phi_c$, which in turn is a consequence of the fact that the vast majority of effective solid stress functions $\sigma_e = \sigma_e(\phi)$ suggested in the literature have discontinuous derivatives σ'_e at $\phi = \phi_c$. In that case, the integrated diffusion coefficient $A(\phi)$ will only be continuous, but not differentiable at $\phi = \phi_c$.

The existence proof for this case is a fairly straight-

forward extension of the previous proof presented by Bůrger and Wendland (1998a). However, to show uniqueness of entropy solutions for a discontinuous diffusion function, new arguments have to be invoked. In fact, the uniqueness proof by Bůrger and Wendland (1998a) is based on a particular jump condition derived by Wu and Yin (1989), which is valid only for Lipschitz continuous diffusion functions $a(\phi)$ and is limited to one space dimension. Fortunately, a recent result by Carrillo (1999) made it possible to avoid these limitations. He utilized a technique known as "doubling of the variables", introduced by Kruřkov (1970) as a tool for proving the L^1 contraction principle for entropy solutions of scalar conservation laws, in order to establish the uniqueness result. Most notably, Carrillo's approach is *not* based on jump conditions and only presupposes that $A(\phi)$ is Lipschitz continuous, i.e. $a(\phi)$ may have discontinuities. Carrillo's results were employed by Bůrger et al. (2000c) to show uniqueness of entropy solutions of the initial-boundary value problem (62), (65).

4.7 Numerical methods for sedimentation-consolidation processes

A numerical scheme that approximates entropy solutions of the initial-boundary value problem (62), (65) (or one of its variants) should have the built-in property to reproduce discontinuities of the entropy solutions, most notably the suspension/sediment interface where the equation changes type, appropriately without the necessity to track them explicitly, i.e. the scheme should possess the shock capturing property. Moreover, an obvious requirement is that the scheme should approximate (converge to) the correct (entropy) solution of the problem it is trying to solve. This clearly rules out classical schemes based on naive finite differencing for strictly parabolic equations, which otherwise work well for smooth solutions, see Evje and Karlsen (2000).

In this section we present an example of a working finite difference scheme having all these desired properties, and which is moreover easy to implement. This scheme is presented for the application to batch or continuous sedimentation. There also exist variants of the scheme for the simulation of batch centrifugation of a flocculated suspension (Bůrger and Concha 2001) or of pressure filtration (Bůrger et al. 2001b). For alternative schemes, in particular schemes that are based on operator splitting and front tracking, that are equally suitable for the sedimentation-consolidation model we refer to Bůrger et al. (2000d) and the references cited therein.

The scheme considered here can be referred to as generalized upwind scheme with extrapolation. We consider a rectangular grid on Q_T with mesh sizes $\Delta z=L/J$, $\Delta t=T/N$ and let $\phi_j^n \approx (j\Delta z, n\Delta t)$. The calculation starts by setting

$$\phi_j^0 = \phi_0(j\Delta z), \quad j=0, \dots, J.$$

The partial differential equation to be solved, Eq. (62), is approximated by the explicit scheme

$$\begin{aligned} & \frac{\phi_j^{n+1} - \phi_j^n}{\Delta t} + q(n\Delta t) \frac{\phi_{j+1}^L - \phi_j^R}{\Delta z} + \frac{f_{bk}^{EO}(\phi_j^R, \phi_{j+1}^L) - f_{bk}^{EO}(\phi_{j-1}^R, \phi_j^L)}{\Delta z} \\ & = \frac{A(\phi_{j+1}^n) - 2A(\phi_j^n) + A(\phi_{j-1}^n)}{\Delta z^2}, \quad j=1, \dots, J-1. \end{aligned} \quad (67)$$

The boundary condition at $z=0$ is inserted into Eq. (67) for $j=0$:

$$\frac{\phi_0^{n+1} - \phi_0^n}{\Delta t} + q(n\Delta t) \frac{\phi_1^n - \phi_0^n}{\Delta z} + \frac{f_{bk}^{EO}(\phi_0^n, \phi_1^n)}{\Delta z} = \frac{A(\phi_1^n) - A(\phi_0^n)}{\Delta z^2}.$$

For boundary condition (65b), we obtain for $j=J\phi_j^n = \phi_1(n\Delta t)$, while boundary condition (65c) turns the interior scheme (67) into the boundary formula

$$\begin{aligned} & \frac{\phi_j^{n+1} - \phi_j^n}{\Delta t} + q(n\Delta t) \frac{\Psi(n\Delta t) - \phi_j^n}{\Delta z} \\ & + \frac{f_{bk}^{EO}(\phi_j^R, \phi_{j+1}^L) - f_{bk}^{EO}(\phi_{j-1}^R, \phi_j^n)}{\Delta z} = \frac{A(\phi_{j-1}^n) - A(\phi_j^n)}{\Delta z^2}. \end{aligned}$$

The numerical flux function of the generalized upwind or Engquist-Osher method (Engquist and Osher, 1981) is given by

$$f_{bk}^{EO}(u, v) = f_{bk}(0) + \int_0^u \min\{f_{bk}'(s), 0\} ds + \int_0^v \max\{f_{bk}'(s), 0\} ds.$$

The quantities ϕ_j^L and ϕ_j^R are given by extrapolation:

$$\phi_j^L := \phi_j^n - \frac{\Delta z}{2} s_j^n, \quad \phi_j^R := \phi_j^n + \frac{\Delta z}{2} s_j^n,$$

which makes the scheme second order accurate in space. The slopes are given by $s_0^n = s_1^n = s_{J-1}^n = s_J^n = 0$ and are otherwise calculated using a limiter function, e.g.

$$s_j^n = \frac{1}{\Delta z} \text{MM}\left(\theta(\phi_j^n - \phi_{j-1}^n), \frac{\phi_{j+1}^n - \phi_{j-1}^n}{2}, \theta(\phi_{j+1}^n - \phi_j^n)\right),$$

$$\theta \in [0, 2], \quad j=2, \dots, J-2$$

using the so-called minmod limiter function

$$\text{MM}(a, b, c) = \begin{cases} \min\{a, b, c\} & \text{if } a, b, c > 0, \\ \max\{a, b, c\} & \text{if } a, b, c < 0, \\ 0 & \text{otherwise,} \end{cases}$$

in order to ensure that the total variation of the

numerical solution is bounded. The scheme converges to the entropy solution if the following stability condition is satisfied:

$$\left(\max_{t \in [0, T]} |q(t)| + \max_{\phi \in [0, \phi_{\max}]} |f_{bk}'(\phi)| \right) \frac{\Delta t}{\Delta z} + \max_{\phi \in [0, \phi_{\max}]} |a(\phi)| \frac{2\Delta t}{\Delta z^2} \leq 1.$$

The Engquist-Osher method has also been used by other authors for the simulation of sedimentation processes, see e.g. Amberg and Dahlkild (1987).

4.8 Numerical examples

4.8.1 Simulation of batch sedimentation

As a first example of the use of the numerical technique, we present in the sequel four different simulations of batch sedimentation in which published settling experiments were utilized to compare the numerically predicted settling behaviour with the respective experimental findings. In every case, the required model functions σ_e and f_{bk} had to be determined or constructed from the published experimental information. We refer to Bürger et al. (2000b) and Garrido et al. (2000) for details.

The simulation of a settling experiment by Holdich and Butt (1997), as presented by Bürger and Karlsen (2001b), shall be discussed here in detail (**Figures 12 and 13**). For simulations of experiments performed by Shirato et al. (1970), Shih et al. (1986) and Bergström (1992), we present here only the numerical results (**Figures 14, 15 and 16**), and refer to the paper by Garrido et al. (2000) for details.

Holdich and Butt (1997) performed sedimentation experiments with a suspension of talc in tap water ($\Delta\rho=1690 \text{ kg/m}^3$) and obtained settling plots from conductivity measurements. From the published experimental data, Garrido et al. (2000) obtained the following constitutive functions:

$$f_{bk}(\phi) = \begin{cases} v_\infty (a_2 \phi^2 + a_1 \phi) & \text{for } \phi \leq \phi_M := \frac{3b_1 - b_2}{2b_2}, \\ v_\infty \frac{(1-\phi)^3}{b_1 - b_2 \phi} & \text{for } \phi_M < \phi < \phi_{\max} := b_1/b_2, \end{cases}$$

$$\sigma_e(\phi) = \begin{cases} 0 & \text{for } \phi \leq \phi_c := 0.04, \\ 2.14 \times 10^7 \phi^7 \text{ Pa} & \text{for } \phi > \phi_c, \end{cases}$$

where the constants have the values $v_\infty = -4.4 \times 10^{-6} \text{ m/s}$, $a_1 = 3.0693$, $a_2 = -28.5004$, $b_1 = 12$ and $b_2 = 32.5$. The remaining parameters are $L = 0.331 \text{ m}$ and $\Delta z = L/300$. We considered three different initial concentrations, $\phi_0 = 0.052, 0.072$ and 0.112 . **Figures 12 and 13** show the corresponding numerical simulations. Observe that essentially due to the presence of the diffusion term, the settling process can be simulated

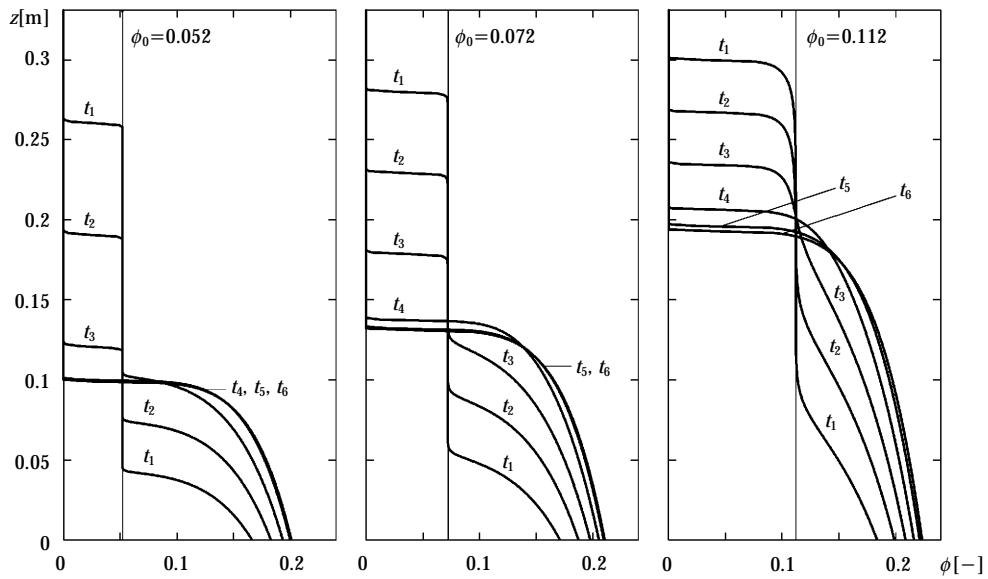


Fig. 12 Simulation of batch sedimentation of a talc suspension in a column (Bürger and Karlsen 2001, Garrido et al. 2000, Holdich and Butt 1997): concentration profiles at different times for three different initial concentrations.

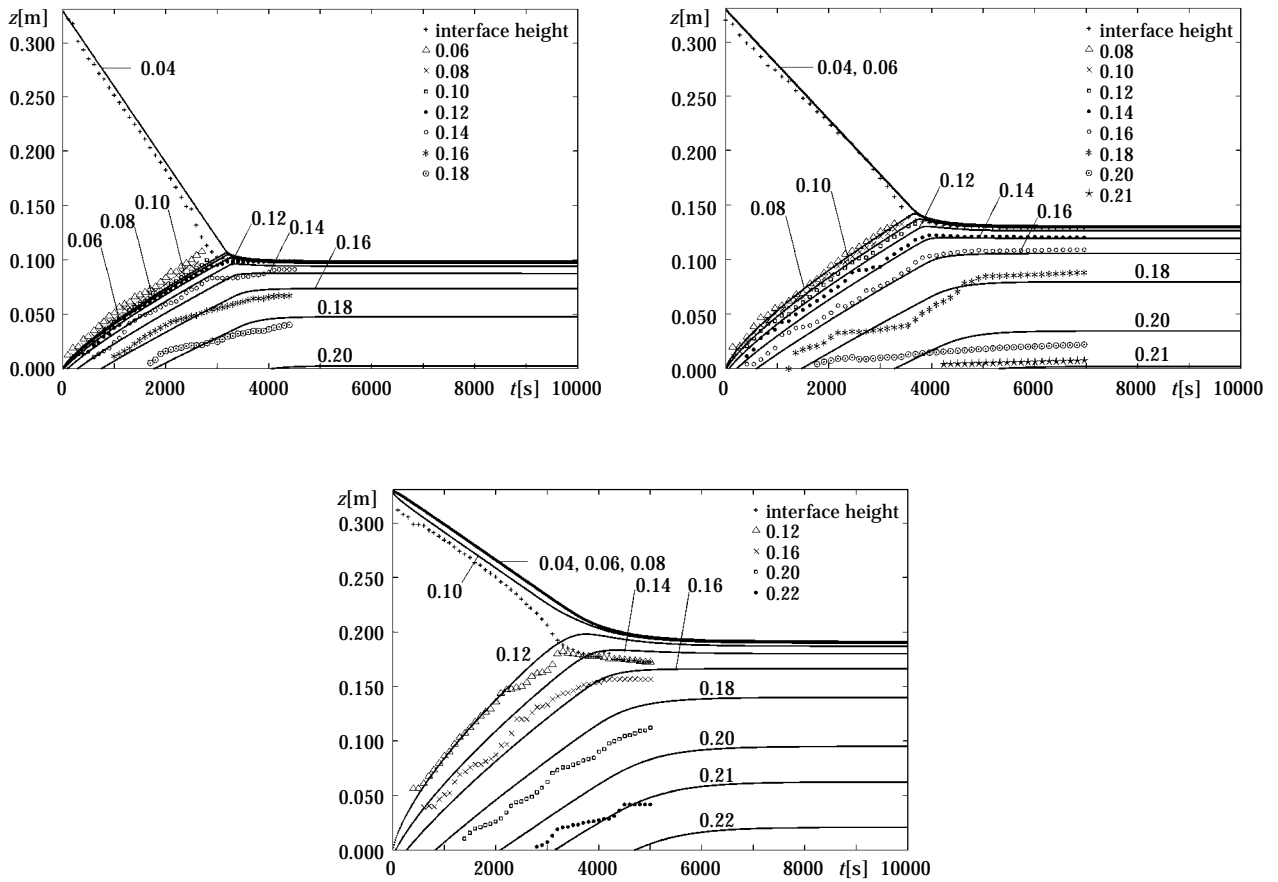


Fig. 13 Simulation of batch sedimentation of a talc suspension in a column, after Bürger and Karlsen (2001): settling plots for three different initial concentrations (0.052, top left, 0.072, top right, and 0.112, bottom). The symbols denote the measured iso-concentration lines.

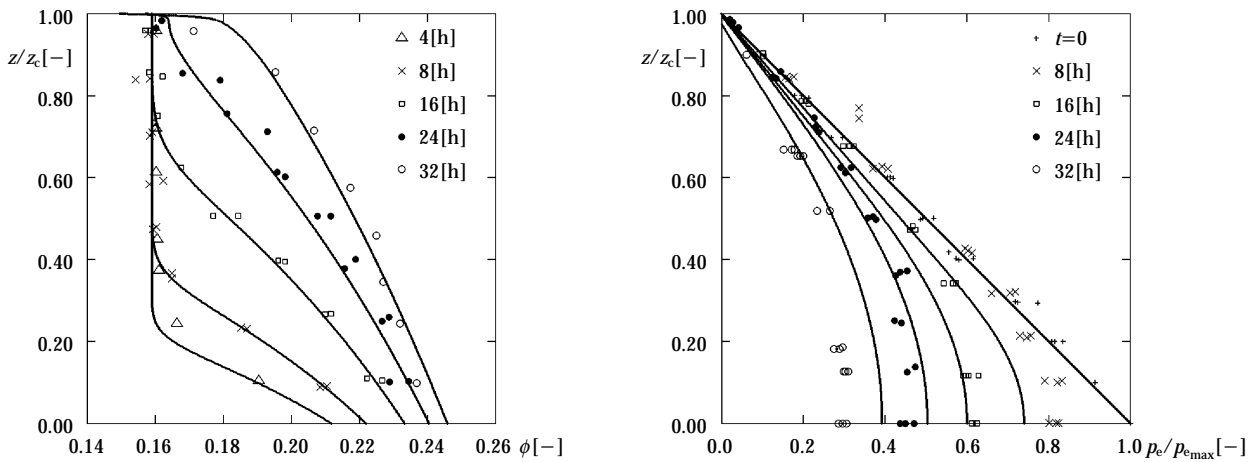


Fig. 14 Simulation of the experiment by Shirato et al.: comparison of simulated with measured concentration (left) and excess pore pressure profiles (right); after Garrido et al. (2000).

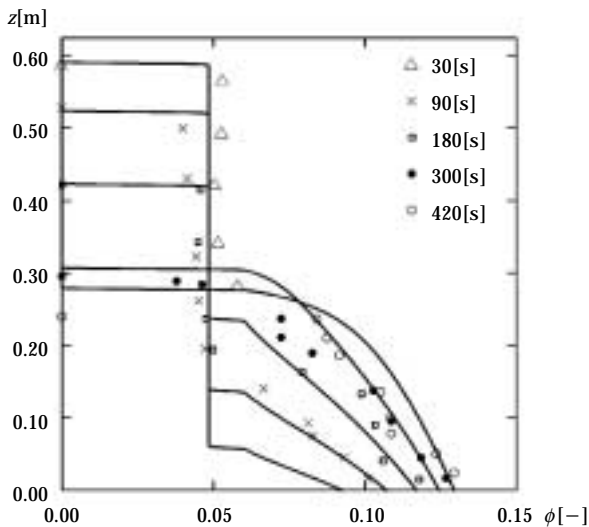


Fig. 15 Comparison of concentration profiles measured by Shih et al. (1986) with numerical simulation of the settling experiment, after Garrido et al. (2000).

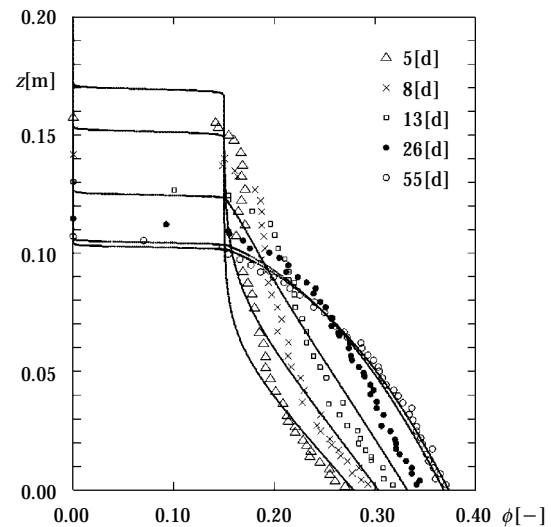


Fig. 16 Comparison of concentration profiles measured by Bergström (1992) with numerical simulation of the settling experiment, after Garrido et al. (2000).

by the numerical algorithm although the flux density function has a singularity at $\phi_{\infty}=0.3692$.

The simulations of these four experimental cases illustrate that the phenomenological model is able to predict the most important features normally observed during batch settling of initially unnetworked suspensions in a column, which are the following:

- Before sedimentation begins, the suspension is homogenized by stirring to obtain a homogeneous concentration. When sedimentation starts, all the solid flocs have the same settling velocity

so that they form a sharp water-suspension interface in the upper portion of the column. This stage is called *hindered settling*.

- Particles at the bottom of the column rapidly occupy the entire surface available. Immediately, new flocs start to accumulate over the deposited sediment pressing over them and, in that way, squeezing out some of its retained water. From that point on the sediment is under *compression* or *consolidation*. The sediment surface, that is the suspension-sediment interface, moves upward as new particles incorporate into the sediment.

- In the case of suspensions with $\phi \leq \phi_c$, at each point in the column under the supernate-suspension interface the concentration either stays constant or increases.
- Utilizing X-ray, γ -ray or conductivity measurement instruments, one can generate data from which it is possible to track determined concentration values as they move upward in the column. For dilute concentrations, that is in regions where $\phi \leq \phi_c$, these iso-concentration curves form straight lines which in cylindrical vessels are identical to the *characteristics* of the scalar convection law (7). In the compression zone, that is in the sediment, the iso-concentration lines for concentrations greater than the critical emerge from the bottom $z=0$ at positive slope, and become horizontal as the consolidation process proceeds. Experiments in which this behaviour is particularly well visible have been reported by Scott (1968a), Been and Sills (1981) and Tiller et al. (1990).
- At a given instant and a certain height in the column, the water-suspension and the suspension-sediment interfaces meet, leaving an area of approximately triangular shape to their left in a settling plot, in which the concentration equals the constant initial concentration ϕ_0 . The coordinates of this event are the *critical time* t_c and the *critical height* z_c , forming the critical point at which simultaneous hindered settling and consolidation end and only consolidation perdures. The new suspension-sediment interface moves downward at a diminishing (in absolute value) speed.
- After a sufficiently large finite time, consolidation ends and a constant concentration gradient is established from the critical concentration at the top to a greater concentration at the bottom. Consequently, the entire sedimentation-consolidation process terminates after a finite time. In spite of the fact that this observation has been made by a series of numerical experiments, it is still to be shown that it is an inherent property of the mathematical model.

4.8.2 Continuous thickening of flocculated suspensions

The second example presents a simulation of the dynamic behaviour of a flocculated suspension an Ideal Continuous Thickener from Bürger et al. (2000d). The numerical algorithm employed for this simulation is not based on the one presented in Section 4.7, but rather on an equally suited three-step operator splitting method, see Bürger et al. (2000d)

and Chapter 9 of Bustos et al. (1999) for details.

We use a Kynch batch flux density function of the well known Richardson and Zaki type (1954),

$$f_{bk}(\phi) = -6.05 \times 10^{-4} \phi (1 - \phi)^{12.59} \text{ m/s,}$$

and the effective solid stress function

$$\sigma_e(\phi) \begin{cases} 0 & \text{for } \phi \leq \phi_c = 0.23, \\ 5.35 \times \exp(17.9\phi) \text{ Pa,} & \text{for } \phi > \phi_c \end{cases}$$

determined by Becker (1982) based on experimental measurements on Chilean copper ore tailings. Note that this choice of the function $\sigma_e(\phi)$ leads to a diffusion function $a(\phi)$ that is discontinuous. Furthermore, we use the parameters $\Delta\rho = \rho_s - \rho_f = 1500 \text{ kg/m}^3$ and $g = 9.81 \text{ m/s}^2$.

We consider continuous sedimentation with piecewise constant average flow velocity $q(t)$ and feed flux $f_F(t)$. We start with a steady state, that is, a stationary concentration profile, and then attain two new steady states by manipulating f_F and q appropriately. Steady states are obtained as stationary solutions of equation (62). It is assumed that a desired discharge concentration ϕ_D is prescribed. Then the discharge flux is $f_D = q\phi_D$. The requirement that at steady state the discharge flux must equal the feed flux, $f_D = f_F$, leads to an equation from which the concentration value ϕ_L at $z=L$ can be computed:

$$q\phi_L + f_{bk}(\phi_L) = q\phi_D. \quad (68)$$

The sediment concentration profile is then calculated from

$$\frac{d\phi}{dz} = \frac{q\phi(z) + f_{bk}(\phi(z)) - q\phi_D}{a(\phi(z))}, \quad z > 0, \quad \phi(0) = \phi_D. \quad (69)$$

The boundary value problem (69) is solved until the critical concentration is reached at a certain height z_c denoting the sediment level. Above this level, the concentration assumes the constant value ϕ_L calculated from (68). The choice of ϕ_D is subject to the requirement that the concentration increases downwards. See Bürger et al. (1999) and Bürger and Concha (1998) for details. Consider the three steady states with parameters given in **Table 1**. We now prescribe the steady state $\phi_1(z)$ as the initial concentration pro-

Table 1 Parameters of the steady states considered in **Figure 17**.

i	$q^i [10^{-4} \text{ m/s}]$	ϕ_D^i	ϕ_L^i	$f_F^i [10^{-4} \text{ m/s}]$	$z_c [m]$
1	-0.10	0.41	0.0072993552	-0.041	3.10
2	-0.15	0.38	0.0104589127	-0.057	1.77
3	-0.05	0.42	0.0036012260	-0.021	2.49

file. After operating the ICT at this steady state for some time, we then change successively to the steady states $\phi_2(z)$ and $\phi_3(z)$. The changes in $\phi_L(t)$ and $q(t)$ will be described in detail now.

The ICT is operated at the steady state $\phi_1(z)$ for $0 < t \leq t_2 = 50000$ s. At $t = t_2$, we change the volume average velocity q to the next smaller value q^2 . However, the value of the feed flux density should remain constant during this operation, therefore the boundary concentration value ϕ_L^1 has to be changed to a new value ϕ_L^{12} , which is calculated from the feed flux conti-

nuity condition

$$q^2 \phi_L^{12} + f_{bk}(\phi_L^{12}) = f_F^1,$$

yielding $\phi_L^{12} = 0.0076397602$. The change from ϕ_L^1 to ϕ_L^{12} should be performed at such a time that the new value ϕ_L^{12} is present above the sediment level at $t = t_2$. The change propagates as a rarefaction wave into the vessel. This rarefaction wave is marked by R_1 in **Figure 17 b)**. We assume that the relevant speed is

$$\sigma_2 = q^1 + f'_{bk}(\phi_L^1) = -5.0607 \times 10^{-4} \text{ m/s},$$

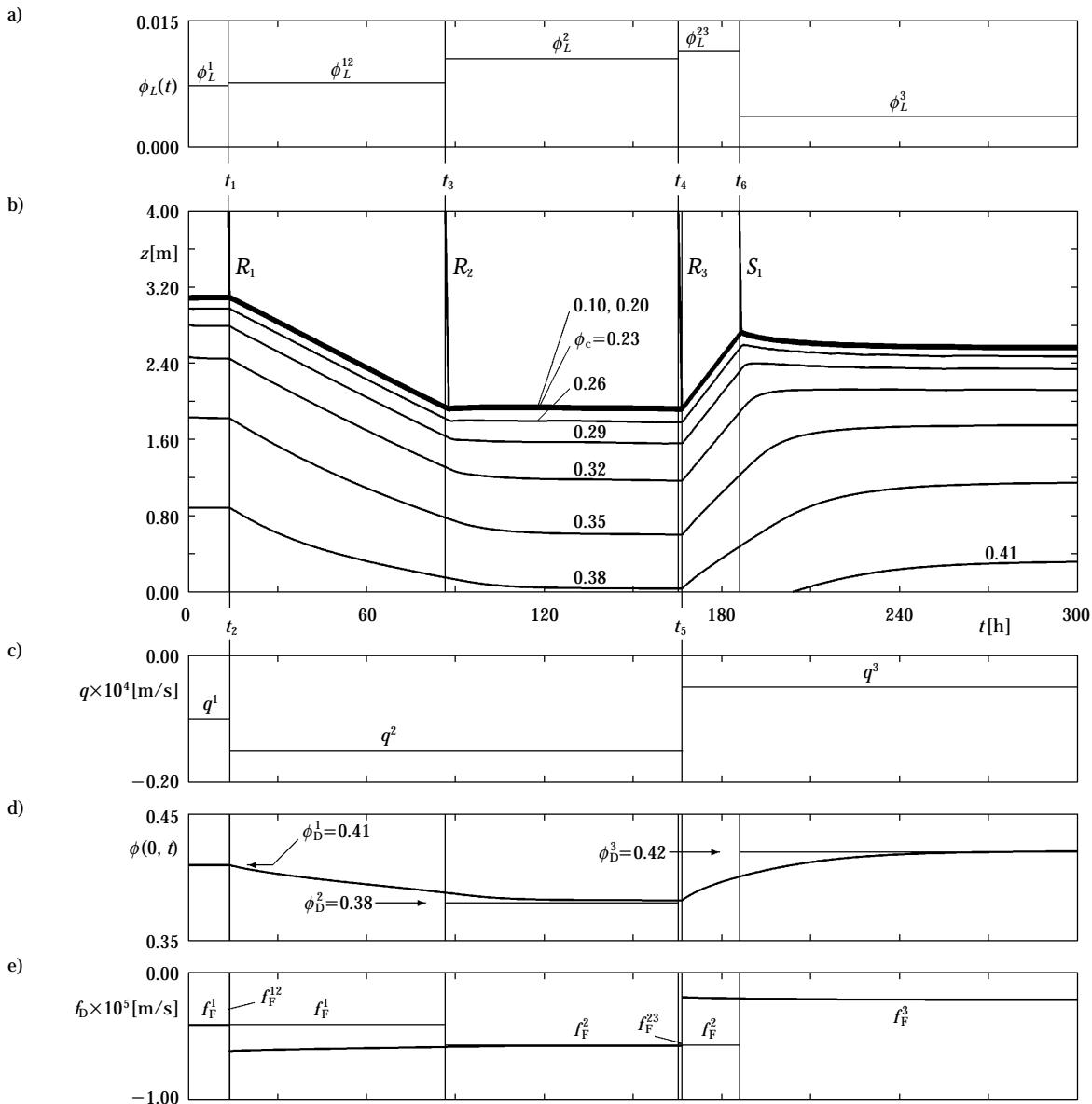


Fig. 17 Simulation of transitions between three steady states in an ICT: a) prescribed values of ϕ_L , b) settling plot (the iso-concentration lines correspond to the annotated values), c) prescribed values of $q(t)$, d) the numerically calculated discharge concentration, together with the discharge concentrations of the target steady states, e) the numerically computed solids discharge flux, compared with prescribed values of the feed flux.

therefore the change from ϕ_L^1 to ϕ_L^{12} is performed at

$$t_1 = t_2 + \frac{L - z_c^1}{\sigma_2} = 48222 \text{ s} \approx 13.4 \text{ h.}$$

It should be noted that the feed flux does not remain precisely constant; it is different from f_F^1 in the small time interval $[t_1, t_2]$, during which we have

$$\begin{aligned} f_F &= f_F^{12} = q^1 \phi_L^{12} + f_{bk}(\phi_L^{12}) = f_F^1 + (q^1 - q^2) \phi_L^{12} \\ &= -0.04138 \times 10^{-4} \text{ m/s.} \end{aligned}$$

From **Figure 17 e)** it becomes apparent that for $t > t_2$, the actual solids discharge flux density $f_D(t) = q^2 \phi(0, t)$ is larger than the feed flux f_F prescribed. This leads to a slow emptying of the vessel and the sediment level falls at almost constant speed. It may therefore be estimated that it will have fallen to the height z_c^2 of the next target steady state by $t = 316560 \text{ s} \approx 87.9 \text{ h}$. At that time, the concentration value ϕ_L^2 corresponding to the new feed flux density f_F^2 should have propagated to the sediment level. Again, this change propagates downwards as a rarefaction wave (marked by R_2 in **Figure 17 b)**). The relevant propagation velocity may be taken as

$$\sigma_4 = q^2 + f'_{bk}(\phi_L^2) = -4.7746 \times 10^{-4} \text{ m/s,}$$

hence we change ϕ_L again from ϕ_L^{12} to ϕ_L^2 at

$$t_3 = 316560 \text{ s} + \frac{L - z_c^2}{\sigma_4} = 311854 \text{ s} \approx 86.6 \text{ h.}$$

For $t > t_3$, both the value of q and the feed flux f_F correspond to the steady state $\phi_2(z)$ given in **Table 1**. Although this value is not prescribed explicitly, we observe in **Figures 17 d)** and **e)** that both the discharge flux and the discharge concentration converge to the appropriate values pertaining to the target steady state $\phi_2(z)$. At $t_5 = 600000 \text{ s} \approx 166.7 \text{ h}$ we wish to change to the next steady state by changing q from q^2 to q^3 . The feed flux above the sediment is assumed to remain constant. Therefore ϕ_L^2 is changed to the value $\phi_L^{23} = 0.0113417003$ which is calculated from

$$q^3 \phi_L^{23} + f_{bk}(\phi_L^{23}) = f_F^2.$$

Again, the change from ϕ_L^2 to ϕ_L^{23} propagates as a rarefaction wave into the vessel (marked by R_3 in **Fig. 17 b)**). The value ϕ_L^{23} propagates at speed

$$\sigma_6 = q^2 + f'_{bk}(\phi_L^{23}) = -4.6338 \times 10^{-4} \text{ m/s,}$$

hence the change is performed at

$$t_4 = t_5 + \frac{L - z_c^2}{\sigma_6} = 595182 \text{ s} \approx 165.3 \text{ h.}$$

Similar to the change from ϕ_L^1 to ϕ_L^{12} , the feed flux

assumes a value in the time interval $[t_4, t_5]$ which is slightly different from f_F^2 ; namely, there we have

$$\begin{aligned} f_F &= f_F^{23} = q^2 \phi_L^{23} + f_{bk}(\phi_L^{23}) = f_F^2 + (q^3 - q^2) \phi_L^{23} \\ &= -0.0559 \times 10^{-4} \text{ m/s.} \end{aligned}$$

After $t = t_5$, the feed flux exceeds the discharge flux in absolute value, as can be conceived from **Fig. 17 e)**. This causes a rise of the sediment level, again taking place at apparently constant speed, and it will have attained the last desired level z_c^3 when $t = 672240 \text{ s} \approx 186.7 \text{ h}$. At that time, the last value of the feed flux f_F^3 should be valid above the sediment level. In contrast to the previous changes of ϕ_L , the change from ϕ_L^{23} to ϕ_L^3 propagates as a shock (marked by S_1 in **Fig. 17 b)**) with the speed

$$\sigma_7 = q^3 + \frac{f_{bk}(\phi_L^{23}) - f_{bk}(\phi_L^3)}{\phi_L^{23} - \phi_L^3} = -5.1391 \times 10^{-4} \text{ m/s.}$$

This discontinuity reaches the sediment level at the desired time if the change from ϕ_L^{23} to ϕ_L^3 is done at

$$t_7 = 672240 \text{ s} + \frac{L - z_c^3}{\sigma_7} = 669301 \text{ s} \approx 185.9 \text{ h.}$$

After $t = t_7$, no more changes are made. **Figures 17 b), d)** and **e)** indicate convergence to the third steady state. The simulation is terminated after a simulated time of $T = 300 \text{ h} = 1080000 \text{ s}$.

5. Discussion

We now comment some of our results that are outlined in Sections 3 and 4, and put them in the appropriate perspective of current research efforts, both our own and those of other groups. We begin with a remark related to the way Petty (1975) extended Kynch's theory to continuous sedimentation by modeling feed and discharge by boundary conditions. This description was the starting point for the treatment presented in Section 3.3 and gave rise to the investigation of conservation laws with boundary conditions. However, this model still has severe shortcomings, among them the neglected clarification zone, that is the zone above the feed level to which solids may pass in the case of overflow, and the violation of conservation of mass principles due to the choice of boundary conditions, since entropy boundary conditions lead to *mathematical* well-posedness, but may be *physically* incorrect. More appropriate models for continuous sedimentation within Kynch's theory were studied by Diehl in a recent series of papers (Diehl 1995, 1996, 1997, 2000, 2001), in which he analyses a model of continuous sedimentation in a

so-called settler-clarifier, in which the feed, discharge and overflow mechanisms are merely expressed by discontinuities of the flux-density function at the bottom, at the (intermediate) feed level and at the top of the vessel, and an additional singular source term at the feed level. Conservation of mass yields jump conditions valid across these discontinuities. The apparent advantages of this elegant model consist in the completeness of the treatment (since the overflow zone above the feed level, $z=L$, has so far not been considered in our work) and in the avoidance of boundary conditions, such that only initial conditions need to be considered. Although exact solutions can be constructed for all practically relevant cases, a global existence and uniqueness result is not yet available, so we do not yet wish to elaborate on this sedimentation model here, but recommend studying Diehl's original papers.

We now discuss some issues related to the phenomenological theory of sedimentation. It should be mentioned that the postulate of a constitutive equation of the type $\sigma_e = \sigma_e(\phi)$ follows widespread usage in the engineering literature, see Bustos et al. (1999) and the references cited therein and recent handbooks on solid-liquid separation such as Rushton et al. (2000), Wakeman and Tarleton (1999) and Concha (2001). One should, however, bear in mind that this relationship is a strong (albeit in many cases useful) simplification, and that different approaches for σ_e , although altering the nature of the resulting model equation, could possibly describe better observed consolidation behaviour. In fact, several researchers recently proposed alternate equations for the effective solid stress function. Some of them suggest expressing σ_e as an integral (with respect to height) of a new concentration-dependent phenomenological function (Dreher 1997, Toorman and Huysenstruyt 1997, Toorman 1999). It can be easily seen that in the present model framework this will lead again to a first-order equation, i.e. one essentially falls back to the equation (7) of Kynch's kinematic sedimentation theory, with all its well-known shortcomings. A different, and to our view potentially more promising approach was advanced by Zheng and Bagley (1998, 1999), who proposed an effective stress equation (Eq. 18 of Zheng, 1998) that depends on both the value of the local solids concentration and its rate of change. Thereby the necessity to refer to a critical concentration is removed. However the appropriate mathematical framework, in which the resulting mathematical model should be studied, still remains to be explored.

Another natural question arising from the presenta-

tion of Section 4 is whether the phenomenological model extends to several space dimensions and if so, under which extensions. The constitutive assumptions introduced in Section 4 remain valid if the one-dimensionality of the motion is no longer imposed, that is, if a truly multidimensional framework is considered. It is then straightforward to derive the following field equations, which replace (54)-(57):

$$\frac{\partial \phi}{\partial t} + \nabla \cdot (\phi \mathbf{q} + f_{bk}(\phi) \mathbf{k}) = \nabla \cdot (a(\phi) \nabla \phi), \quad (70)$$

$$\nabla \cdot \mathbf{q} = 0, \quad (71)$$

$$\nabla p_e = -\Delta \rho g \phi \mathbf{k} - \nabla \sigma_e(\phi). \quad (72)$$

In two or three space dimensions, the unknown flow variables are the concentration ϕ , the volume average flow velocity field \mathbf{q} and the excess pore pressure p_e . The latter can be calculated a posteriori from the concentration distribution. In one space dimension, however, $q = q(t)$ is determined by a boundary condition, and only solving the scalar equation (62) for ϕ requires computational effort.

Schneider (1982, 1985) was the first to observe a remarkable property of equations (70)-(72): taking the curl of equation (72) reveals that ϕ depends only on the vertical space coordinate and on time wherever it is continuous. The same will then be true for the vertical component of \mathbf{q} . Under specific assumptions on the geometry of the vessel considered, the velocity field \mathbf{q} can be determined from suitable boundary conditions. However, since equation (72) does not depend on \mathbf{q} , equations (70)-(71) are in most circumstances not sufficient to determine that quantity, and in any case the resulting mathematical model is not well posed and seems to be of little practical use (Bürger and Kunik 2001).

The independence of equation (72) from \mathbf{q} is, of course, a result of the simplifications performed based on the dimensional analysis. As mentioned before, the more general phenomenological sedimentation-consolidation theory, in the sense that not only several space dimensions but also viscous stresses are considered, and that fewer terms are neglected, is developed by Bürger, Wendland and Concha (2000e). That analysis leads to a set of equations that are similar to (70)-(72), but in which the analogue of equation (72) contains additional viscous and advective acceleration terms. That equation, together with (71), represents a nonlinear version of the well-known Navier-Stokes equations for an incompressible fluid, to which (in the proper sense) they reduce in the case of a pure fluid ($\phi = 0$). The model equations derived

by Bürger et al. (2000e) (see also Bürger 2000) are sufficient for the computation of ϕ , \mathbf{q} and p_e . However, some new source terms describing the interaction between the evolution of the concentration distribution, or kinematic waves, and the average flow field appear. In one space dimension, these terms affect only the excess pore pressure distribution, so that the interaction they describe becomes effective only in a truly two- or three-dimensional setup. Schneider (1985) pointed out that this interaction makes the two- or three-dimensional treatment qualitatively different from what is known in one space dimension.

The significance of these terms and their actual magnitude has not yet been analysed. Moreover, if the viscous stress tensors are not neglected, additional difficulties arise from the necessity to relate the solid and fluid phase viscosities, which are theoretical variables, to the effective viscosity of the mixture, which can be measured experimentally. Obviously additional steps of progress in the theoretical understanding of the phenomenological framework have to be made before a definite multidimensional model for sedimentation with compression can be advocated. Having said this, some recent results by Bürger et al. (2001d) are available.

Finally, we mention that the phenomenological framework has led to a variety of similar mathematical models of spatially one-dimensional solid-liquid separation processes of flocculent suspensions such as centrifugation (Bürger and Concha 2001, Bürger and Karlsen 2001a) pressure filtration (Bürger et al. 2001b, Garrido et al. 2001) of flocculated suspensions, and can be regarded as the foundation of a robust and unified theory of solid-liquid separation of flocculated suspensions (Bürger et al. 2001a, Garrido et al. 2002).

6. Concluding remark

This paper has outlined the development of research in sedimentation and thickening during the last century from the invention of the Dorr thickener in 1905 onwards. The development that took place in the first half of that period was perhaps best characterized in the introduction of Roberts' paper (1949): "*Prior to 1916, thickening was an art, and any accurate decision as to what size of machine to install to handle a given tonnage of a specific ore must have been one of those intuitive conclusions, based on both intimate and extensive acquaintance with thickeners and ore pulps. Then in 1916 "knowledge of acquaintance," became "knowledge about" with the publication of the Coe and Clevenger paper. The unit operation of thicken-*

ing had graduated to the status of an engineering science." He concludes that "*Thickening has long held the status of an engineering science but it is still long way from being an exact science. On the other hand there is considerable "art" involved in deciding certain points; namely, what safety factor to specify to take care of possible changes in feed characteristics; whether to use the compression depth indicated or to increase the area to get a lower compression depth; how to prophesy island formation; what to do about island formation if it does occur, and so on. Careful, planned observation and reporting on part of operators is needed before some of these items can be reduced to the engineering science status."*

Roberts' statements show that the title of his paper, *Thickening – Art or Science?*, must be understood as a serious question thrown up from the status of knowledge of 1949. He could not foresee that only three years later, Kynch's paper would definitely turn sedimentation and thickening not only into an engineering science, but eventually also into a topic of profound and still very active research in a variety of disciplines, such as chemistry, biology medicine and, most notably from the authors' viewpoint, mechanics and mathematics.

Acknowledgements

The preparation of this work was made possible through Fondef Project D97-I2042 at the University of Concepción and through the Sonderforschungsbereich 404 at the University of Stuttgart.

References

- Adams, W.H. Jr. and Glasson, P.S. (1925) MIT Thesis, cited by Robinson (1926).
- Adorján, L.A. (1975) 'A theory of sediment compression', XI International Mineral Processing Congress, Cagliari, Italy, Paper 11:1-22.
- Adorján, L.A. (1977) Determination of thickener dimensions from sediment compression and permeability test results, *Trans. Inst. Min. Met* **85**, C157-C163.
- Agricola, G. (1556) *De Re Metallica*. Translated from Latin by H.C. Hoover, Dover Publications, Inc., New York 1950.
- Amberg, G. and Dahlkild, A.A. (1987) Sediment transport during unsteady settling in an inclined channel, *J. Fluid Mech.* **185**, 415-436.
- Ashley, H.H. (1909) Theory of the settlement of slimes, *Min. Scient. Press*, 831-832, June 12.
- Ardaillon, E. (1897) *Les Mines du Laurion dans l'Antiquité*. Paris.
- Auzerais, F.M., Jackson, R. and Russel, W.B. (1988) The res-

- olution of shocks and the effects of compressible sediments in transient settling, *J. Fluid Mech.* **195**, 437-462.
- Ballou, D.P. (1970) Solutions to non-linear hyperbolic Cauchy problems without convexity conditions, *Trans. Amer. Math. Soc.* **152**, 441-460.
- Barrientos, A. (1978) *Modelo Fenomenológico de la sedimentación: obtención de parámetros y aplicación*, M.Sc. Thesis, University of Concepción, Chile.
- Bascur, O. (1976) *Modelo fenomenológico de suspensiones en sedimentación*, B.Sc. Thesis, University of Concepción, Chile.
- Bascur, O. (1989) A unified solid-liquid separation framework. Presented at the *First Regional Meeting of the American Filtration Society*, Houston, Texas, Oct. 30-Nov. 1, 1989, 11 pp.
- Batchelor, G.K. (1982) Sedimentation in a dilute polydisperse system of interacting spheres. Part 1. General theory, *J. Fluid Mech.* **119**, 379-408.
- Batchelor, G.K. and Wen. C.S. (1982) Sedimentation in a dilute polydisperse system of interacting spheres. Part 2. Numerical results, *J. Fluid Mech.* **124**, 495-528.
- Becker, R. (1982) *Espesamiento continuo, diseño y simulación de espesadores*, M.Sc. Thesis, University of Concepción, Chile.
- Been, K. and Silts, G.C. (1981) Self-weight consolidation of soft soils: An experimental and theoretical study, *Geotechnique* **31**, 519-535.
- Behn, V.C. (1957) Settling behavior of waste suspensions, *J. San. Engrg. Div. ASCE* **83** No. SA 5, 1423-1-1423-20.
- Bergström, L. (1992) Sedimentation of flocculated alumina suspensions: γ -ray measurements and comparison with model predictions, *J. Chem. Soc. Farad. Trans.* **88**, 3201-3211.
- Bowen, R. (1976) Theory of mixtures. In: Eringen, A.C. (Ed.), *Continuum Physics Vol. 3*, Academic Press, New York, pp. 1-127.
- Bürger, R. (1996) *Ein Anfangs-Randwertproblem einer quasi-linearen parabolischen entarteten Gleichung in der Theorie der Sedimentation mit Kompression*, Doctoral Thesis, University of Stuttgart, Germany.
- Bürger, R. (2000) Phenomenological foundation and mathematical theory of sedimentation-consolidation processes, *Chem. Eng. J.* **80**, 177-188.
- Bürger, R., Bustos, M.C. and Concha, F. (1999) Settling velocities of particulate systems: Phenomenological theory of sedimentation: 9. Numerical simulation of the transient behaviour of flocculated suspensions in an ideal batch or continuous thickener. *Int. J. Mineral Process.* **55**, 267-282.
- Bürger, R. and Concha, F. (1998) Mathematical model and numerical simulation of the settling of flocculated suspensions, *Int. J. Multiphase Flow* **24**, 1005-1023.
- Bürger, R. and Concha, F. (2001) Settling velocities of particulate systems: 12. Batch centrifugation of flocculated suspensions, *Int. J. Mineral Process.*, **63**, 115-145.
- Bürger, R., Concha, F., Fjelde, K.-K. and Karlsen, K.H. (2000a) Numerical simulation of the settling of polydisperse suspensions of spheres. *Powder Technol.* **113**, 30-54.
- Bürger, R., Concha, F. and Garrido, P. (2001a) A unified mathematical model of thickening, filtration and centrifugation of flocculated suspensions. In: da Luz, A.B., Soares, P.S.M., Torem, M.L. and Trindade, R.B.E. (eds.), *Proceedings of the VI Southern Hemisphere Meeting on Mineral Technology, Rio de Janeiro, Brazil, 2001*, vol. 1, CETEM/MCT, Rio de Janeiro, 123-129.
- Bürger, R., Concha, F. and Karlsen, K.H. (2001b) Phenomenological model of filtration processes: 1. Cake formation and expression. *Chem. Eng. Sci.* **56**, 4537-4553.
- Bürger, R., Concha, F. and Tiller, F.M. (2000b) Applications of the phenomenological theory to several published experimental cases of sedimentation processes, *Chem. Eng. J.* **80**, 105-117.
- Bürger, R., Evje, S. and Karlsen, K.H. (2000c) On strongly degenerate convection-diffusion problems modeling sedimentation-consolidation processes, *J. Math. Anal. Appl.* **247**, 517-556.
- Bürger, R., Evje, S., Karlsen, K.H. and Lie, K.-A. (2000d) Numerical methods for the simulation of the settling of flocculated suspensions, *Chem. Eng. J.* **80**, 91-104.
- Bürger, R., Fjelde, K.-K., Höfler, K. and Karlsen, K.H. (2001c) Central difference solutions of the kinematic model of settling of polydisperse suspensions and three-dimensional particle-scale simulations, *J. Eng. Math.* **41**, 167-187.
- Bürger, R. and Karlsen, K.H. (2001a) A strongly degenerate convection-diffusion problem modeling centrifugation of flocculated suspensions. In: Freistühler, H. and Warnecke, G. (eds.), *Hyperbolic Problems: Theory, Numerics, Applications*. Birkhäuser Verlag, Basel, 207-216.
- Bürger, R. and Karlsen, K.H. (2001b) On some upwind schemes for the phenomenological sedimentation-consolidation model, *J. Eng. Math.* **41**, 145-166.
- Bürger, R. and Kunik, M. (2001) A critical look at the kinematic-wave theory for sedimentation-consolidation processes in closed vessels, *Math. Meth. Appl. Sci.* **24**, 1257-1273.
- Bürger, R., Liu, C. and Wendland W.L. (2001d) Existence and stability for mathematical models of sedimentation-consolidation processes in several space dimensions. *J. Math. Anal. Appl.* **264**, 288-310.
- Bürger, R. and Tory, E.M. (2000) On upper rarefaction waves in batch settling. *Powder Technol.* **108**, 74-87.
- Bürger, R. and Wendland, W.L. (1998a) Existence, uniqueness and stability of generalized solutions of an initial-boundary value problem for a degenerating quasilinear parabolic equation. *J. Math. Anal. Appl.* **218**, 207-239.
- Bürger, R. and Wendland, W.L. (1998b) Entropy boundary and jump conditions in the theory of sedimentation with compression. *Math. Meth. Appl. Sci.* **21**, 865-882.
- Bürger, R., Wendland, W.L. and Concha, F. (2000e) Model equations for gravitational sedimentation-consolidation processes, *Z. Angew. Math. Mech.* **80**, 79-92.
- Buscall, R. and White, L.R. (1987) The consolidation of concentrated suspensions, Part 1. The theory of sedimenta-

- tion, *J. Chem. Soc. Faraday Trans. 1* **83**, 873-891.
- Bustos, M.C. and Concha, F. (1988) On the construction of global weak solutions in the Kynch theory of sedimentation, *Math. Meth. Appl. Sci.* **10**, 245-264.
- Bustos, M.C. and Concha, F. (1992) Boundary conditions for the continuous sedimentation of ideal suspensions, *AIChE J.* **38**, No. 7, 1135-1138.
- Bustos, M.C., Concha, F., Bürger, R. and Tory, E.M. (1999) *Sedimentation and Thickening: Phenomenological Foundation and Mathematical Theory*, Kluwer Academic Publishers, Dordrecht, The Netherlands.
- Bustos, M.C., Concha, F. and Wendland, W.L. (1990a) Global weak solutions to the problem of continuous sedimentation of an ideal Suspension, *Math. Meth. Appl. Sci.* **13**, 1-22.
- Bustos, M.C., Paiva, F. and Wendland, W.L. (1990b) Control of continuous sedimentation of ideal suspensions as an initial and boundary value problem, *Math. Meth. Appl. Sci.* **12**, 533-548.
- Bustos, M.C., Paiva, F. and Wendland, W.L. (1996) Entropy boundary conditions in the theory of sedimentation of ideal suspensions, *Math. Meth. Appl. Sci.* **19**, 679-697.
- Carrillo, J. (1999) Entropy solutions for nonlinear degenerate problems, *Arch. Rat. Mech. Anal.* **147**, 269-361.
- Chang, D., Lee, T., Jang, Y., Kim, M. and Lee, S. (1997) Non-colloidal sedimentation compared with Kynch theory, *Powder Technol.* **92**, 81-87.
- Cheng, K.S. (1981) Asymptotic behaviour of solutions of a conservation law without convexity conditions, *J. Diff. Eqns.* **40**, 343-376.
- Cheng, K.S. (1983) Constructing solutions of a single conservation law, *J. Diff. Eqns.* **49**, 344-358.
- Clark, A. (1915) A note on the settling of slimes, *Eng. Min. J.* **99**, 412.
- Coe, H.S. and Clevenger, G.H. (1916) Methods for determining the capacity of slimesettling tanks, *Trans. AIME* **55**, 356-385.
- Comings, E.W. (1940) Thickening calcium carbonate slurries, *Ind. Eng. Chem.* **32**, 663-640.
- Comings, E.W., Pruijs, C.E. and De Bord, C. (1954) Continuous settling and thickening, *Ind. Eng. Chem.* **46**, 1164-1172.
- Concha, F. (2001) *Manual de Filtración & Separación*, Centro de Tecnología Mineral, Universidad de Concepción/Fundación Chile, Concepción, Chile.
- Concha, F. and Barrientos, A. (1993) A critical review of thickener design methods, *KONA* **11**, 79-104.
- Concha, F. and Bascur, O. (1977) Phenomenological model of sedimentation. Proceedings of the *12th International Mineral Processing Congress (XII IMPC)*, São Paulo, Brazil, **4**, 29-46.
- Concha, F. and Bürger, R. (1998) Wave propagation phenomena in the theory of sedimentation. In: Toro, E.F. and Clarke, J.F. (Eds.), *Numerical Methods for Wave Propagation*, Kluwer Academic Publishers, Dordrecht, The Netherlands, pp. 173-196.
- Concha, F. and Bustos, M.C. (1985) Theory of sedimentation of flocculated fine particles. In: Moudgil, B.M. and Somasundaran, P. (Eds.), *Proceedings of the Engineering Foundation Conference on Flocculation, Sedimentation and Consolidation*, Sea Island, GA, AIChE, New York, pp. 275-284.
- Concha, F. and Bustos, M.C. (1991) Settling velocities of particulate systems: 6. Kynch sedimentation processes: Batch settling, *Int. J. Mineral Process.* **32**, 193-212.
- Concha, F. and Bustos, M.C. (1992) Settling velocities of particulate systems: 7. Kynch sedimentation processes: Continuous thickening, *Int. J. Mineral Process.* **34**, 33-51.
- Concha, F., Bustos, M.C. and Barrientos, A. (1996) Phenomenological theory of sedimentation. In: Tory, E.M. (Ed.), *Sedimentation of Small Particles in a Viscous Fluid*, Computational Mechanics Publications, Southampton, UK, pp. 51-96.
- Concha, F., Lee, C.H. and Austin, L.G. (1992) Settling velocities of particulate systems: 8. Batch sedimentation of polydispersed suspensions of spheres, *Int. J. Mineral Process.* **35**, 159-175.
- Dafermos, C.M. (2000) *Hyperbolic Conservation Laws in Continuum Physics*, Springer Verlag, Berlin.
- D'Avila, J.S. (1976) Uma análise da teoria de Kynch para sedimentação, *Revista Brasileira de Tecnologia* **7**, 447-453.
- D'Avila, J.S. (1978) *Um modelo matemático para a sedimentação*, Doctoral Thesis, Federal University of Rio de Janeiro.
- D'Avila, J.S., Concha, F. and Telles, A.S. (1978) Um modelo fenomenológico para sedimentação bidimensional contínua, Anais VI Encontro de Escoamento em Meios Porosos, Rio Claro, Brasil, 11-13 outubro 1978, **II**, pp. III-1-1—III-1-19.
- D'Avila, J.S. and Sampaio, R. (1977) Equações de estado para a pressão no sólido, *Revista Brasileira de Tecnologia* **8**, 177-191.
- Davis, K.E. and Russel, W.B. (1989) An asymptotic description of transient settling and ultrafiltration of colloidal dispersions, *Phys. Fluids A* **1**, 82-100.
- Davis, K.E., Russel, W.B. and Glantschnig, W.J. (1991) Settling suspensions of colloidal silica: observations and X-ray measurements, *J. Chem. Soc. Faraday Trans.* **87**, 411-424.
- De Haas, R.D. (1963) *Calculation of the Complete Batch Settling Behavior for Rigid Spheres in a Newtonian Liquid*, M.Sc. Thesis, Purdue University, West Lafayette, IN, USA.
- Diehl, S. (1995) On scalar conservation laws with point source and discontinuous flux function, *SIAM J. Math. Anal.* **26**, 1425-1451.
- Diehl, S. (1996) A conservation law with point source and discontinuous flux function modelling continuous sedimentation, *SIAM J. Appl. Math.* **56**, 388-419.
- Diehl, S. (1997) Dynamic and steady-state behaviour of continuous sedimentation, *SIAM J. Appl. Math.* **57**, 991-1018.
- Diehl, S. (2000) On boundary conditions and solutions for ideal clarifier-thickener units, *Chem. Eng. J.* **80**, 119-

- 133.
- Diehl, S. (2001) Operating charts for continuous sedimentation I: Control of steady states, *J. Eng. Math.* **41**, 117-144.
- Dorr, J.V.N. (1915) The use of hydrometallurgical apparatus in chemical engineering, *J. Ind. Eng. Chem.* **7**, 119-130.
- Dorr, J.V.N. (1936) *Cyanidation and Concentration of Gold and Silver Ores*. McGraw-Hill Book Co. Inc., New York.
- Dreher, T. (1997) Non-intrusive measurement of particle concentration and experimental characterization of sedimentation. Preprint 97/34, Sonderforschungsbereich 404, University of Stuttgart, Germany.
- Egolf, C.B. and McCabe, W.L. (1937) Rate of sedimentation of flocculated particles, *Trans. Amer. Instn. Chem. Engrs.* **33**, 620-640.
- Engquist, B. and Osher, S. (1981) One-sided difference approximations for nonlinear conservation laws, *Math. Comp.* **36**, 321-351.
- Evje, S. and Karlsen, K.H. (2000) Monotone difference approximation of BV solutions to degenerate convection-diffusion equations, *SIAM J. Numer. Anal.* **37**, 1838-1860.
- Fitch, E.B. (1993) Thickening theories – an analysis, *AIChE J.* **39**, 27-36.
- Forbes, D.L.H. (1912) The settling of mill slimes, *Eng. Min. J.* **93**, 411-415.
- Free, E.E. (1916) Rate of slimes settling, *Eng. Min. J.* **101**, 681-686.
- Garrido, P., Bürger, R., and Concha, F. (2000) Settling velocities of particulate systems: 11. Comparison of the phenomenological sedimentation-consolidation model with published experimental results, *Int. J. Mineral Process.* **60**, 213-227.
- Garrido, P., Concha, F. and Bürger, R. (2001) Application of the unified model of solid-liquid separation of flocculated suspensions to experimental results. In: da Luz, A.B., Soares, P.S.M., Torem, M.L. and Trindade, R.B.E. (eds.), *Proceedings of the VI Southern Hemisphere Meeting on Mineral Technology, Rio de Janeiro, Brazil, 2001*, vol. 1, CETEM/MCT, Rio de Janeiro, 117-122.
- Garrido, P., Concha, F. and Bürger, R. (2002) Settling velocities of particulate systems: 14. Unified model of sedimentation, centrifugation and filtration of flocculated suspensions. *Int. J. Mineral Process.*, to appear.
- Godlewski, E. and Raviart, P.-A. (1991) *Hyperbolic Systems of Conservation Laws*, Mathématiques et Applications, Ellipses, Paris, France.
- Godlewski, E. and Raviart, P.-A. (1996) *Numerical Approximation of Hyperbolic Systems of Conservation Laws*, Springer Verlag, New York, Berlin, Heidelberg.
- Grassmann, P. und Straumann, R. (1963) Entstehen und Wandern von Unstetigkeiten der Feststoffkonzentration in Suspensionen, *Chem.-Ing.-Techn.* **35**, 477-482.
- Hassett, N.J. (1958) Design and operation of continuous thickeners, *Ind. Chemist* **34**, 116-120, 169-172, 489-494.
- Hassett, N.J. (1964) Mechanism of thickening and thickener design, *Trans. Inst. Min. Met.* **74**, 627-656.
- Hassett, N.J. (1968) Thickening in theory and practice, *Min. Sci. Engrg.* **1**, 24-40.
- Hazen, A. (1904) On sedimentation, *Trans. ASCE* **53**, 45-71.
- Holdich, R.G. and Butt, G. (1997) Experimental and numerical analysis of a sedimentation forming compressible compacts, *Separ. Sci. Technol.* **32**, 2149-2171.
- Kos, P. (1977) Fundamentals of gravity thickening, *Chem. Eng. Prog.* **73**, 99-105.
- Kröner, D. (1997) *Numerical Schemes for Conservation Laws*, Wiley-Teubner, Chichester & Stuttgart.
- Kružkov, S.N. (1970) First order quasilinear equations in several independent variables, *Math. USSR Sb.* **10**, No. 2, 217-243.
- Kynch, G.J. (1952) A theory of sedimentation, *Trans. Faraday Soc.* **48**, 166-176.
- Landman, K.A. and White, L.R. (1994) Solid/liquid separation of flocculated suspensions, *Adv. Colloid Interf. Sci.* **51**, 175-246.
- Landman, K.A., White, L.R. and Buscall, R. (1988) The continuous-flow gravity thickener: steady state behavior, *AIChE J.* **34**, 239-252.
- Liu, I. (1978) On chemical potential and incompressible porous media, Preprint *Memórias de Matemática 108*, Instituto de Matemática, UFRJ, Rio de Janeiro, Brazil.
- Liu, T.P. (1978) Invariants and asymptotic behavior of solutions of a conservation law, *Proc. Amer. Math. Soc.* **71**, 227-231.
- Masliyah, J.H. (1979) Hindered settling in a multiple-species particle system, *Chem. Eng. Sci.* **34**, 1166-1168.
- Michaels, A.S. and Bolger, J.C. (1962) Settling rates and sediment volumes of flocculated Kaolin suspensions, *Ind. Eng. Chem. Fund.* **1**, 24-33.
- Mishler, R.T. (1912) Settling slimes at the Tigre Mill, *Eng. Min. J.* **94**, 643-646.
- Mishler, R.T. (1918) Methods for determining the capacity of slime-settling tanks, *Trans. AIME* **58**, 102-125.
- Outokumpu Mintec (1997) Supaflo Thickeners & Clarifiers, brochure distributed at the *XX International Mineral Processing Congress*, Aachen, Germany, September 1997.
- Petty, C.A. (1975) Continuous sedimentation of a suspension with a nonconvex flux law, *Chem. Eng. Sci.* **30**, 1451-1458.
- Puccini, C., Stasiw, D.M. and Cerny, L.C. (1977) The erythrocyte sedimentation curve: a semi-empirical approach, *Biorheology* **14**, 43-49.
- Ralston, O.C. (1916) The control of ore slimes – II, *Eng. Min. J.* **101**, 890-894.
- Richardson, J.F. and Zaki, W.N. (1954) Sedimentation and fluidization: Part I. *Trans. Instn. Chem. Engrs. (London)* **32**, 35-53.
- Roberts, E.J. (1949) Thickening – art or science? *Mining Eng.* **1**, 61-64.
- Robinson, C.S. (1926) Some factors influencing sedimentation, *Ind. Eng. Chem.* **18**, 869-871.
- Rushton, A., Ward, A.S., and Holdich, R.G. (2000) *Solid-liquid Filtration and Separation Technology*, Second Edition, Wiley-VCH, Weinheim, Germany.
- Schneider, W. (1982) Kinematic-wave theory of sedimentation beneath inclined walls, *J. Fluid Mech.* **120**, 323-346.

- Schneider, W. (1985) Kinematic wave description of sedimentation and centrifugation processes. In: Meier, G.E.A. and Obermaier, F. (Eds.), *Flow of Real Fluids*, Lecture Notes in Physics, Springer-Verlag, Berlin, pp. 326-337.
- Schneider, W., Anestis, G. and Schaflinger, U. (1985) Sediment composition due to settling of particles of different sizes, *Int. J. Multiphase Flow* **11**, 419-423.
- Scott, K.J. (1968a) Theory of thickening: factors affecting settling rate of solids in flocculated pulps, *Trans. Inst. Min. Met.* **77**, C85-C97.
- Scott, K.J. (1968b) Experimental study of continuous thickening of a flocculated silica slurry, *Ind. Engrg. Fund.* **7**, 582-595.
- Shannon, P.T., Dehaas, R.D., Stroupe, E.P. and Tory, E.M. (1964) Batch and continuous thickening, *Ind. Eng. Chem. Fund.* **3**, 250-260.
- Shannon, P.T., Stroupe, E.P. and Tory, E.M. (1963) Batch and continuous thickening, *Ind. Eng. Chem. Fund.* **2**, 203-211.
- Shannon, P.T. and Tory, E.M. (1965) Settling of slurries, *Ind. Eng. Chem.* **57**, 18-25.
- Shannon, P.T. and Tory, E.M. (1966) The analysis of continuous thickening, *SME Trans.* **235**, 375-382.
- Shih, Y.T., Gidaspow, D. and Wasan, D.T. (1986) Sedimentation of fine particles in nonaqueous media: Part I – Experimental, Part II – Modeling, *Colloids and Surfaces* **21**, 393-429.
- Shirato, M., Kato, H., Kobayashi, K. and Sakazaki, H. (1970) Analysis of settling of thick slurries due to consolidation, *J. Chem. Eng. Japan* **3**, 98-104.
- Smiles, D.E. (1976a) Sedimentation: integral behaviour, *Chem. Eng. Sci.* **31**, 273-275.
- Smiles, D.E. (1976b) Sedimentation and filtration equilibria, *Sep. Sci.* **11**, 1-16.
- Steinour, H.H. (1944a) Rate of sedimentation. Nonflocculated suspensions of uniform spheres. *Ind. Eng. Chem.* **36**, 618-624.
- Steinour, H.H. (1944b) Rate of sedimentation. Suspensions of uniform-size angular particles. *Ind. Eng. Chem.* **36**, 840-847.
- Steinour, H.H. (1944c) Rate of sedimentation. Concentrated flocculated suspensions of powders. *Ind. Eng. Chem.* **36**, 901-907.
- Stewart, R.F. and Roberts, E.J. (1933) The sedimentation of fine particles in liquids, *Trans. Instn. Chem. Engrs.* **11**, 124-141.
- Straumann, R. (1962) *Über den Einfluß der Sedimentation auf die Filtration*. Doctoral Thesis ETH Prom. Nr. 3187, Swiss Federal Polytechnical Institute (ETH), Zurich.
- Stroupe, E. (1962) *Batch Sedimentation of Rigid Spheres in a Newtonian Liquid*, M.Sc. Thesis, Purdue University, West Lafayette, IN, USA.
- Talmage, W.P. and Fitch, E.B. (1955) Determining thickener unit areas, *Ind. Eng. Chem.* **47**, 38-41.
- Thacker, W.C. and Lavelle, J.W. (1977) Two-phase flow analysis of hindered settling, *Phys. Fluids* **20**, 1577-1579.
- Tiller, F.M., Hsyung, N.B., Shen, Y.L. and Chen, W. (1990) CATSCAN analysis of sedimentation and constant pressure filtration. Proceedings of the *V World Congress on Filtration*, Société Française de Filtration, Nice, France, **2**, pp. 80-85.
- Tiller, F.M. and Leu, W.F. (1980) Basic data fitting in filtration, *J. Chin. Inst. Chem. Engrs.* **11**, 61-70.
- Tobinaga, S. and Freire, J.T. (1980) Escoamento de agua em solos não-saturados: Uma descrição pela teoria de misturas. *Revista Brasileira de Tecnologia* **11**, 105-115.
- Toorman, E.A. (1999) Sedimentation and self-weight consolidation: constitutive equations and numerical modeling, *Géotechnique* **49**, 709-726.
- Toorman, E.A. and Huysenstruyt, H. (1997) Towards a new constitutive equation for effective stress in self-weight consolidation. In: Burt, N., Parker, R. and Watts, J. (Eds.), *Cohesive Sediments*, Wiley, Chichester, UK, pp. 121-132.
- Tory, E.M. (1961) *Batch and Continuous Thickening of Slurries*, PhD Thesis, Purdue University, West Lafayette, USA.
- Tory, E.M. and Shannon, P.T. (1965) Reappraisal of the concept of settling in compression, *Ind. Engrg. Chem. Fund.* **4**, 194-204.
- Truesdell, C. (1966) Method and taste in Natural Philosophy. In: Truesdell, C., *Six Lectures on Modern Natural Philosophy*, Springer-Verlag, Berlin.
- Truesdell, C. and Noll, W. (1965) The nonlinear field theories of mechanics. In: Flügge, S. (ed.), *Handbuch der Physik*, Vol. III/3, Springer-Verlag, Berlin.
- Ungarish, M. (1993) *Hydrodynamics of Suspensions*, Springer-Verlag, Berlin.
- Vol'pert, A.I. (1967) The spaces BV and quasilinear equations, *Math. USSR Sb.* **2**, No. 2, 225-267.
- Vol'pert, A.I. and Hudjaev, S.I. (1969) Cauchy's problem for degenerate second order quasilinear parabolic equations, *Math. USSR Sb.* **7**, No. 3, 365-387.
- Wakeman, R.J. and Tarleton, E.S. (1999) *Filtration: Equipment Selection, Modelling and Process Simulation*, Elsevier Science, Oxford, UK.
- Ward, H.T. and Kammermeyer, K. (1940) Sedimentation in the laboratory: Design data from laboratory experimentation, *Ind. Eng. Chem.* **32**, 622-626.
- Wilson, A.J. (1994) *The Living Rock*, Woodhead Publishing Limited, England.
- Work, L.T. and Kohler, A.S. (1940) Sedimentation of suspensions, *Ind. Eng. Chem.* **32**, 1329-1334.
- Wu, Z. and Yin, J. (1989) Some properties of functions in BV_x and their applications to the uniqueness of solutions for degenerate quasilinear parabolic equations, *North-east. Math. J.* **5**, 395-422.
- Yoshioka, N., Hotta, Y., Tanaka, S., Naito, S. and Tsugami, S. (1957) Continuous thickening of homogeneous flocculated slurries, *Chem. Eng. Japan* **21**, 66-75.
- Zheng, Y. and Bagley, D.M. (1998) Numerical simulation of batch settling process, *J. Environ. Eng.* **124**, 953-958.
- Zheng, Y. and Bagley, D.M. (1999) Dynamic model for zone settling and compression in gravity thickeners, *J. Environ. Eng.* **125**, 1007-1013.

Author's short biography



Fernando Concha Arcil

Fernando Concha Arcil, obtained a Bachelor degree in Chemical Engineering at the University of Concepcion in Chile in 1962 and a Ph.D. in Metallurgical Engineering from the University of Minnesota in 1968. He is professor at the department of Metallurgical Engineering, University of Concepción. His main research topic is the application of transport phenomena to the field of Mineral Processing. He has published four books: *Modern Rational Mechanics*, *Design and Simulation of Grinding-Classification Circuits and Filtration and Separation*, all in Spanish and *Sedimentation and Thickening: Phenomenological Foundation and Mathematical Theory*, in English and more than 90 technical papers in international journals. For his work in sedimentation with applications to hydrocyclones and thickeners he obtained the Antoine Gaudin Award-1998, presented by the American Society for Mining Metallurgy and Exploration, SME.



Raimund Bürger

Raimund Bürger is a scientific assistant at the Institute of Applied Analysis and Numerical Simulation of the University of Stuttgart, Germany. He has specialized in the formulation, analysis and numerics of mathematical models of solid-liquid separation processes. This includes in particular the mathematical analysis of the nonlinear partial differential equations involved, which frequently exhibit non-standard properties such as type degeneracy and discontinuous coefficients. He studied Mathematics at the Technische Universität Darmstadt in Germany and received his diploma degree in 1993. From 1995 to 2001 he held a position as research fellow within the Collaborative Research Center (Sonderforschungsbereich) 404 "Multifield Problems in Continuum Mechanics" at the University of Stuttgart. He obtained his doctoral degree in Applied Mathematics in 1996 under guidance of Professor Wolfgang L. Wendland and finished his habilitation in 2002. In 1997 he was awarded a scholarship by Fundación Andes, Chile, which he used for a post-doctoral research visit to Fernando Concha's group at the Department of Metallurgical Engineering of the University of Concepción during the period from July 1997 to August 1998. Raimund Bürger is co-author of the monograph *Sedimentation and Thickening*, more than 30 articles in refereed journals and 15 contributions to proceedings volumes. He is married, has a little son, and lives in Stuttgart, Germany.

Dry Powders for Pulmonary Delivery of Peptides and Proteins[†]

Hirokazu Okamoto*, Hiroaki Todo, Kotaro Iida,
and Kazumi Danjo

Faculty of Pharmacy, Meijo University**

Abstract

Because proteins and peptides are poorly absorbed through the gastrointestinal tract, the lungs are a promising organ for administering these substances because of their large inner surface area, thin epithelium, and relatively low protease activity. Pulmonary absorption rate constants are inversely related to molecular weights. Adding an absorption enhancer is a promising method to increase systemic bioavailability of inhaled peptides and proteins. The local lung toxicity of soluble powder seems to be minimal. Spray drying is a useful and widely applied technique to prepare powders for inhalation, and supercritical fluids have recently been used for producing such powders. Selecting operating conditions and adding proper additives such as sugars yields hollow porous particles, which are easily dispersed and avoid phagocytic clearance in the lungs, with maximized chemical and physical stability.

1. Introduction

Recent advances in biotechnology have made it possible to use macromolecules such as peptides and proteins as therapeutic agents. At this time intravenous, intramuscular, and subcutaneous injections are the practical routes for administering such macromolecules. One would expect peroral administration to be the most convenient for patients, but the peroral bioavailability of macromolecules is extremely low due to their large molecular size and high susceptibility to enzymes in the gastrointestinal tract. Meanwhile, it has been suggested that the lungs are useful for administering macromolecules, which are poorly absorbed from the intestines.

So far, inhalation therapy has been used with low-molecular-weight drugs to treat local lung diseases such as asthma and infections. Recombinant human deoxyribonuclease (rhDNase) is the first protein approved for inhalation therapy (1). Patients with cystic fibrosis are given 2.5 ml of a 1 mg/ml solution of rhDNase by nebulization (2).

In the area of systemic therapy, insulin is the pep-

tide that is expected to be the first approved for inhalation therapy. Exubera[®] is a rapid-acting dry powder insulin being developed through a collaboration between Pfizer Inc. and Aventis Pharma. The six-month Phase III studies involving 328 patients with type 1 diabetes and 309 patients with type 2 diabetes were completed in 2002 (3, 4). The AERx[®] Pulmonary Drug Delivery System is a broadly applicable technology platform that converts large or small molecules into fine-particle aerosols. AERx[®]iDMS (insulin Diabetes Management System) was developed through a collaboration between Novo Nordisk and Aradigm Co. A 12-week-long Phase II study including 107 non-smoking patients with type 2 diabetes has been completed (5).

The three main delivery systems used for aerosol inhalation in humans are pressurized metered-dose inhalers (MDI), nebulizers, and dry powder inhalers (DPI) (6). DPIs appear to be the most promising of these for future use because the device is small and relatively inexpensive, no propellants are used, and breath actuation can be used successfully by many patients with poor MDI technique (6, 7).

This review will focus on the dry powder peptides and proteins for inhalation. The success of inhalation therapy with dry powders is determined by the active ingredient's biological aspects, by the physicochemical aspects of formulation, and by inhaler performance (**Fig. 1**). Here we briefly review some of the

* Corresponding author.

Phone: 81-52-832-1781 (ext. 359); Fax: 81-52-834-8090;

E-mail: okamoto@ccmfs.meijo-u.ac.jp

** 150 Yagotoyama Tempaku-ku, Nagoya 468-8503, Japan

[†] Accepted: July 31, 2002

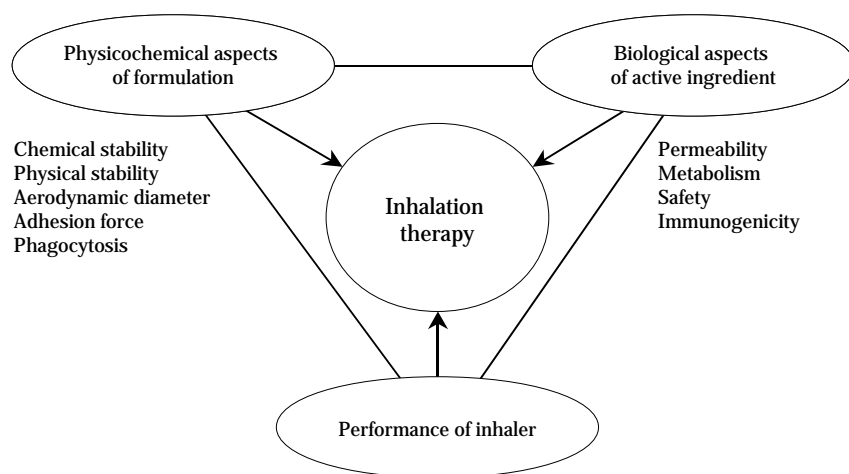


Fig. 1 Factors determining successful inhalation therapy with dry powders.

biological and physicochemical aspects of inhalation therapy with dry powder peptides and proteins. Extensive reviews on inhalers are available elsewhere (8, 9).

2. Biological aspects of the pulmonary absorption of peptides and proteins

This section summarizes the histological features of the lungs, drug permeability through the lung epithelium, the metabolism of proteins and peptides in lung tissue, and the safety of peptides and proteins administered through the lungs. It also reviews how chemicals and enzyme inhibitors enhance the pulmonary absorption of peptides and proteins.

2.1 Histological features of the lungs

The respiratory tract can be divided into upper airways (the nose, mouth, larynx, and pharynx) and lower airways (from the trachea to the alveoli) (10). The average weight of human lungs is 0.6 kg. Because the lungs receive the entire cardiac output, their blood flow is as high as 5,700 ml/min, more than five times that of the portal system (1,125 ml/min), including the stomach and the small and large intestines (11).

Airway diameter decreases and surface area increases according to the successive branching of the airways. The cross sectional area of the trachea is about 2.5 cm², while that of the respiratory zone is much wider (10). The total cross sectional area of the alveoli is about 10⁴ cm². The total surface area of the airway tubes also increases and that of alveoli is more than 100 m² as large as that of the small intestine.

The epithelial layer of the trachea is composed mainly of columnar ciliated cells. The thickness from the airway surface to blood vessels is on the order of 30 to 40 μm (12). Particulates deposited in the upper airways are rapidly carried away by mucociliary transport, resulting in a short of residence time (13).

The alveolar surface is populated by two major epithelial cell types: the terminally differentiated type I cell and its progenitor type II cell (14). The alveolar epithelium is quite thin. In the alveoli drugs have to travel only 0.5 to 1.0 μm to enter the blood stream. Total fluid volume in the human lungs is approximately 10 ml (15). Lung pH at the site of drug absorption has been estimated at about 6.6 using pulmonary absorption data for several weak electrolytes in rats (16). The alveolar surface is lined by a surface-active material called the lung surfactant, which is a mixture of lipids, proteins, and carbohydrates (17). Phospholipids account for 75-80% of the total weight, and dipalmitoyl phosphatidylcholine accounts for nearly half of that. The lung surfactant reduces alveolar surface activity and stabilizes alveolar structure.

Lavage of a normal adult lung yields a cell count that is 93% macrophages, 7% lymphocytes, and less than 1% neutrophils, eosinophils, or basophils (18). Alveolar macrophages interact with microorganisms or particulates, act as effector and accessory cells in inflammatory and immune reactions, and protect alveolar structures to form a protease attack (18).

2.2 Drug absorption through the lungs

The pulmonary absorption of small molecules basically obeys pH-partition theory, i.e., drugs are likely absorbed by diffusion across a lipid membrane (19,

20). In vivo rat lung absorption data for saccharides of various molecular weights (122 to 75,000) showed that the absorption rate constants were inversely related to molecular weight and directly related to the diffusion coefficients of the compounds (21). The transport of dextrans (4 to 150 kDa) across cultured rat alveolar epithelial cell monolayers suggested that macromolecules with radii under 5 μm traverse the alveolar epithelial barrier via paracellular pathways, while macromolecules with radii of 6 μm or larger cross the barrier via other pathways such as pinocytosis (22). The penetration of hydrophilic compounds through excised rabbit trachea sacs also inversely correlates to molecular weight (23). When several hydrophilic and lipophilic drugs were administered through rat trachea as aerosols, the absorption rates were roughly twice as rapid as when administered by the intratracheal injection of drug solutions. These results suggest that drug absorption is more rapid in the alveolar region than in the tracheobronchial region of the lungs (24). The distal or deep lung is the optimal site for the high absorption of proteins. Inhaler systems should be designed to maximize deposition in this region (12).

It is known that peptides or proteins could be absorbed through the lungs (25, 26). The pulmonary bioavailability of peptides can be easily evaluated with small animals by the method proposed by Enna and Schanker (21). The pulmonary bioavailability of insulin administered as a pH 7.0 solution was 13 to 14% better than subcutaneous administration in rats (27).

2.3 Metabolism in the lungs

In general, the metabolic activity of the lungs is much lower than that of the intestinal wall and liver. In the lungs there is no first-pass conjugation of salbutamol, which undergoes extensive first-pass conjugation in the intestinal wall and liver. The systemic bioavailability of orally administered budesonide is 11%, whereas that when inhaled is 73%. Fluticasone propionate's hepatic first-pass metabolism is 99%, but it is zero in the lungs (28).

However, it is known that peptides such as insulin are subjected to enzymatic degradation in the lungs (29-31). The degradation of insulin in lung cytosol from diabetic rats was significantly less than in that from normal rats (30). An experiment with synthesized model peptides suggested that the lung has the ability to metabolize peptides through pathways not observed in the rat intestine. However, avoiding the hepatic first-pass effect through the pulmonary route

would eliminate the disadvantage of pulmonary metabolism (32). Type II cells have higher metabolic activity than type I cells. The degradation rate constant of luteinizing hormone releasing hormone (LHRH) in type II cells was higher than that of type I cells but lower than that of nasal and rectal epithelial membranes. The transformation of type II cells into type I cells resulted in a more than 10-fold decrease in LHRH proteolytic activities (14).

2.4 Safety of inhaled proteins

Researchers have investigated the systemic toxicity of therapeutic peptides and proteins following subcutaneous administration. When discussing the safety aspect of inhaled proteins, interest focuses on local toxicity to the lungs and on adverse immune reactions. Assaying bronchoalveolar lavage is useful in screening lung injuries from inhaled substances (33). An increase in the extracellular activity of lactate dehydrogenase (LDH), a cytosol enzyme, indicates cell lysis or cell membrane damage. An increase in the number of phagocytic cells suggests an inflammation reaction in the lungs. When a suspension of superfine silica was intratracheally instilled in rats, the LDH activity and number of cells recovered in the lavage increased at 4 hr and reached a maximum at 24 hr. The LDH activity and number of cells declined thereafter for a week, then gradually increased over the succeeding two months (34, 35).

However, the local lung toxicity of soluble powder seems to be minimal. When insulin dry powder formulated with mannitol was intratracheally administered in rats, the LDH level (36) and number of cells (unpublished data) in the lavage did not increase over 24 hr. Clinical studies for inhaled DNase, insulin, interferon α , interferon γ , leuprolide acetate, and α -1-antitrypsin showed virtually no adverse lung reactions (12).

2.5 Additives for improving bioavailability of inhaled peptides and proteins

One of the reasons of the low bioavailability of large molecules relates to low diffusivity through the epithelial barrier. To overcome this, several chemicals and enzyme inhibitors were examined as pulmonary absorption enhancers. In the 1990s there were many reports on the enhancement of the pulmonary absorption of peptides and proteins. These reports examined bile acids, surfactants, fatty acids, citric acid, and protease inhibitors (**Tables 1 and 2**).

Glycocholate and bacitracin had higher enhancing activity for the pulmonary absorption of peptide so-

Table 1 Effect of absorption enhancers on pulmonary absorption of peptides and proteins

Peptide/Protein	Enhancer	DF ^a	ER ^b	Ref.
insulin	50 mM glycocholate	SL	5.1	27, 37
insulin	10 mM glycocholate	SL	4.2	38
eel calcitonin	10 mM glycocholate	SL	4.0	38
eel calcitonin	20 mM glycocholate	SL	3.1	39
TSH	50 mM glycocholate	SL	6.3	37
FSH	50 mM glycocholate	SL	5.9	37
HCG	50 mM glycocholate	SL	20	37
salmon calcitonin	250 µg/dose taurocholic acid	SL	1.4	40
salmon calcitonin	250 µg/dose taurocholic acid	DP	1.9	40
insulin	1% Span 85	SL	3.1	27
insulin	1% Span 85	SL	7.2	36
insulin	160 µg/dose Span 85	DP	0.7	36
insulin	10 mM MM ^c	SL	2.5	38
eel calcitonin	10 mM MM	SL	4.0	38
salmon calcitonin	250 µg/dose dimethyl-β-cyclodextrin	SL	2.4	40
salmon calcitonin	250 µg/dose dimethyl-β-cyclodextrin	DP	2.1	40
salmon calcitonin	250 µg/dose lecithin	SL	1.5	40
salmon calcitonin	250 µg/dose lecithin	DP	1.8	40
salmon calcitonin	250 µg/dose octyl-β-glucoside	SL	1.4	40
salmon calcitonin	250 µg/dose octyl-β-glucoside	DP	1.6	40
insulin	5 mM LM ^d	SL	7.1	38
eel calcitonin	5 mM LM	SL	5.7	38
salmon calcitonin	0.5% palmitoleic acid	SL	2.5	41
salmon calcitonin	0.5% linoleic acid	SL	2.4	41
salmon calcitonin	0.5% oleic acid	SL	2.2	41
salmon calcitonin	250 µg/dose oleic acid	SL	1.6	40
salmon calcitonin	250 µg/dose oleic acid	DP	2.8	40
insulin	100 mM EDTA	SL	0.6	27
eel calcitonin	10 mM EDTA	SL	1.8	38
insulin	100 mM salicylate	SL	0.5	27
insulin	citrate (pH5.0)	SL	3.4	36
insulin	citrate (pH3.0)	SL	4.5	36
insulin	36 µg/dose citric acid	DP	2.1	36
insulin	citrate (pH 3.0)	SL	3.2	37
insulin	0.5 mg/dose citrate	DP	2.7	37
TSH	citrate (pH 3.0)	SL	3.2	37
FSH	citrate (pH 3.0)	SL	3.9	37
HCG	citrate (pH 3.0)	SL	26	37
salmon calcitonin	250 µg/dose citric acid	SL	1.5	40
salmon calcitonin	250 µg/dose citric acid	DP	2.2	40

^a Dosage form. SL=solution and DP=dry powder.

^b Enhancement ratio. Ratio of AUC or biological response between a dosage form with absorption enhancer and that without absorption enhancer.

^c Mixed micelles of linoleic acid and HCO60 at a molar ratio of 30:4 in phosphate buffered saline.

^d *N*-Lauryl-β-D-maltopyranoside.

lutions. Yamamoto et al. intravenously injected Evans Blue and examined the leakage of Evans Blue in the lung. Although increasing calcitonin activity, 5 mM *N*-Lauryl-β-D-maltopyranoside increased Evans Blue leakage, suggesting lung toxicity. On the other hand, 1 mM *N*-Lauryl-β-D-maltopyranoside, 10 mM glycocholate, and 10 mM mixed micelles of linoleic acid

and HCO60 were safe and effective enhancers (42). Citrate is a potent pulmonary absorption enhancer for peptides formulated as dry powders. When insulin dry powder containing 0.036 mg/dose of citric acid was administered to rat lungs, bronchoalveolar lavage was as low as that for saline administration, suggesting that citric acid is a safe additive (36). Adding an

Table 2 Effect of enzyme inhibitors on pulmonary absorption of peptides and proteins

Peptide/Protein	Enzyme inhibitor	DF ^a	ER ^b	Ref.
insulin	1 mM bacitracin	SL	0.9	27
insulin	20 mM bacitracin	SL	6.8	38
eel calcitonin	20 mM bacitracin	SL	19	39
salmon calcitonin	0.2 mM bacitracin	SL	2.2	41
insulin	10 mM bacitracin	SL	7.0	36
insulin	420 µg/dose bacitracin	DP	1.0	36
insulin	13 mM nafamostat	SL	2.1	27
eel calcitonin	20 mM nafamostat	SL	3.9	39
insulin	10 mM surfactin	SL	6.1	27
insulin	10 mg/mL aprotinin	SL	2.0	38
insulin	10 mg/mL STI	SL	2.5	38
salmon calcitonin	0.2 mM chymostatin	SL	2.1	41

^a Dosage form. SL=solution and DP=dry powder.

^b Enhancement ratio. Ratio of AUC or biological response between a dosage form with absorption enhancer and that without absorption enhancer.

absorption enhancer is a promising method for increasing the systemic bioavailability of inhaled peptides and proteins, but long-term safety should be examined for application to humans.

It should be noted that the effect of absorption enhancers depends on their formulation. Bacitracin and Span 85 increased pulmonary insulin absorption from solutions in rats, but were not effective when formulated as dry powders with insulin (36).

In research on protease inhibitors, a relatively favorable correlation was observed between the calcitonin absorption-enhancing activity and membrane enzyme inhibition activity of 18 protease inhibitors (41).

3. Physical aspects of dry powder peptides and proteins

Spray drying is a useful and widely applied technique to prepare powders for inhalation. Supercritical fluids have recently been applied for producing powders for inhalation. In this section, we briefly review these techniques, stability of the produced dry powder peptides and proteins, and aerodynamic diameter being one of the most critical factors to determine the success of inhalation therapy.

3.1 Spray dry for preparation of dry powder peptides and proteins

Spray drying is a useful and widely applied technique for one-step preparation of powders for inhalation with a drug solution or suspension. The independent variables of spray drying processes are liquid feed rate, atomizing air flow rate, drying air

flow rate, and inlet air temperature. Outlet temperature linearly depends on each of these variables (43), suggesting that it can be estimated if the regression lines between outlet temperature and the independent variables are available for a spray drier. The inlet temperature is usually several tens of degrees higher than the outlet temperature. Determining the temperature variation within a drying chamber revealed that the temperature at 5 cm below the nozzle was much closer to the outlet temperature than the inlet temperature, and that the temperature at 17 cm below the nozzle, midway between the nozzle and outlet, was approximately the same as the outlet temperature (43). This means that during spray drying, droplets in the drying chamber were exposed to the temperature swayed by the outlet temperature.

It is likely that proteins are susceptible to degradation upon spray drying due to the relatively high temperatures (44). **Table 3** summarizes the effect of inlet and outlet temperatures on spray-dried peptides and proteins. Spray drying of a 5 mg/ml aqueous insulin solution caused minor degradation of insulin at outlet temperatures below 120°C. However, degradation of high-molecular-weight proteins, A-21 desamido insulin, and other insulin-related compounds increased with outlet temperature above 120°C (47). β -galactosidase activity is susceptible to spray drying temperature, and only half of its activity remained after spray drying without additives at an outlet temperature of 50°C. When 6% β -galactosidase was spray-dried with 5% mannitol, no activity was lost at outlet temperatures below 50°C, but it decreased above 50°C. Replacing mannitol with trehalose stabilized the spray-dried β -galactosidase, and its activity was maintained at

Table 3 Effect of inlet and outlet temperatures on spray-dried peptides and proteins

Peptide/Protein	Temperature (°C)		Activity (%)	Degradation (%)	Moisture (%)	D ^a (μm)	Ref.
	Inlet	Outlet					
β-galactosidase		50	100				45
		70	80				
		90	30				
oxyhemoglobin	50			2.0			46
	80			2.9			
	120			5.0			
rhDNase	91	53			8.3	2.0	43
	120	72			7.6	2.2	
	150	90			6.1	2.3	
insulin	100	50		0.36 ^b	5.1	3.2 ^b	47
	100	74		0.44	3.1	3.1	
	160	100		0.49	3.1	2.2	
	220	120		0.77	3.3	2.1	
	220	150		3.32	1.9	4.2	

^a Geometric or aerodynamic diameter.

^b High-molecular-weight protein.

100% at an outlet temperature of 100°C (45).

Surface denaturation at the air-liquid interface of sprayed droplets may play a significant role in protein degradation. Spray drying of mannitol-formulated human growth hormone (hGH) at room temperature resulted in increased protein degradation by increasing the atomizing air rate, which suggested degradation at the air-liquid interface during spray drying (48). Adding polysorbate-20 into the liquid feed significantly reduced the formation of insoluble hGH aggregates, and adding divalent metal zinc ions effectively suppressed the formation of soluble hGH aggregates (49).

3.2 Application of supercritical fluids to preparation of dry powder proteins

Fluids at temperatures and pressures above critical values are called supercritical fluids (SCFs). SCF densities of similar to those of liquids, while their viscosities and diffusivities are in the range of gases (50). The application of SCFs to particle design has recently emerged as a promising techniques for producing powders for inhalation. Carbon dioxide is the most widely used supercritical solvent because it is cheap and nontoxic, and because of its easily accessible critical parameters (T_c=31.1°C and P_c=73.8 bar) (50).

When a substrate has a reasonable solubility in a SCF, dry powders are obtained by depressurizing the SCF solution through an adequate nozzle. This process is called the rapid expansion of supercritical solutions (RESS). However, the solubility of many peptides and proteins in SCFs is relatively low. When

a SCF is a poor solvent for the substrate, it can be used as an anti-solvent to precipitate the substrate dissolved in a good solvent (51).

Dimethylsulfoxide (DMSO) is a good solvent for lysozyme. When CO₂ is put into lysozyme dissolved in DMSO, and the CO₂ mole fraction reaches a critical value, the solution becomes saturated and causes the catastrophic precipitation of lysozyme (52). This process is called the gas-antisolvent (GAS) precipitation process.

Other techniques to produce powders with SCFs as anti-solvents are the aerosol solvent extraction system (ASES) (53, 54), precipitation with a compressed fluid antisolvent (PCA) (55, 56), the supercritical antisolvent technique (SAS) (57-60), and solution enhanced dispersion by supercritical fluids (SEDS) (61, 62). These techniques introduce protein solutions through a nozzle at a relatively low flow rate into the flow of a SCF in a vessel. The SCF removes the solvent of the protein solution and precipitates the protein in the vessel.

Yeo et al. applied the SAS technique to a 5 mg/ml insulin solution in DMSO. The slow CO₂ injection rate favored the growth of larger particles (57). A significant increase in β-sheet content and a corresponding decrease in α-helix content were observed for the precipitated insulin relative to a commercial powder. However, the precipitated insulin solution in 0.01 M HCl yielded a solution structure similar to that of the dissolved commercial powder (58). Intravenous administration to rats revealed that the processed insulin maintained its biological activity (57). The increase in β-sheet content and the concomitant de-

crease in α -helix content, which were reversible upon reconstitution, were also observed in lysozyme and trypsin precipitated by the SAS technique (60).

When the solubility of the solvent (for instance, water) in the SCF (for instance, CO_2) is very low, a modifier (for instance, ethanol) is employed in the system. Powders of lysozyme, albumin, insulin, and recombinant human deoxyribonuclease (rhDNase) were prepared by the ASES process. An aqueous solution of a protein was put into a precipitation chamber through the inside tube of a coaxial nozzle. Supercritical CO_2 modified by ethanol was fed through the outside tube of the coaxial nozzle. The mole fraction of ethanol in CO_2 was 0.2 and the volumetric flow rate ratio of the aqueous solution to CO_2 was 0.4/12. The ASES process at 35 or 45°C and at 80 to 90 bar produced lysozyme powder without activity loss. Some aggregation was observed for insulin and albumin powders. rhDNase was substantially denatured during the processing (63).

A new supercritical CO_2 -assisted aerosolization coupled with bubble drying was recently reported (64). This process involves mixing a stream of drug solution and a SCF stream inside a low dead-volume tee. The emulsion is allowed to expand out of a capillary restrictor, resulting in the aerosolization of the drug solution.

3.3 Stability of peptides and proteins

A crystalline solid of small molecule drugs is generally less prone to chemical decomposition than the amorphous form. In some cases, however, the crystalline state may not be more stable for protein and peptide formulations (65). The primary degradation pathways of biosynthetic human insulin involve deamidation at the Asn^{A21} site and covalent dimer formation. When storing at 25°C and 40°C at relative humidities between 0 and 75%, amorphous insulin was far more stable than crystalline insulin under all conditions (66).

The hydration state of proteins affects their solid-state stability. The aggregation of humanized monoclonal antibodies and rhDNase in mannitol-formulated spray-dried powders increased as storage humidity rose (67). Deamidation at the Asn^{A21} site of crystalline insulin increased sharply as moisture content increased, while that of amorphous insulin was almost independent of moisture (66).

It is known that the chemical stability of proteins in the solid state is enhanced by the presence of certain amorphous sugars. Two hypotheses have been proposed for the mechanism of protein stabilization by an

amorphous sugar (68). The water substitution hypothesis supposes that sugar molecules form hydrogen bonds with dried proteins in place of water molecules to maintain higher-order protein structure. The glassy state theory supposes that the high viscosity of an amorphous sugar prevents proteins from degrading physically or chemically by retarding molecular movement. **Table 4** summarizes the effect of sugars on spray-dried peptides and proteins.

Izutsu et al. examined the stabilizing effect of mannitol during the freeze-drying of L-lactate dehydrogenase, β -galactosidase, and L-asparaginase. The activities of the freeze-dried enzymes depended on the content of amorphous mannitol in the cake. The stabilizing effect of mannitol decreased as mannitol crystallinity increased, suggesting that amorphous mannitol protected proteins against degradation (72).

The physical state of sugars used as an excipient for protein powder plays a role not only in maintaining protein stability but also in providing suitable aerosol performance. When recombinant humanized anti-IgE monoclonal antibodies (rhuMAbE25) were spray-dried with 10, 20, and 30% mannitol, the spray-dried powders with 10 and 20% mannitol remained amorphous during storage, while the powder with 30% mannitol crystallized. The fine-particle fraction (FPF) for the powder with 10 and 20% mannitol was maintained at 30-40% during storage for 36 weeks at 30°C. However, the fraction of the powder with 30% mannitol exhibited a dramatic decrease upon storage due to mannitol crystallization and an increase in particle size (44).

Moisture mediates the crystal growth of sugars in dry protein powders. Spray drying rhDNase with lactose produced spherical powders with noncrystalline substances. However, α -lactose monohydrate crystals were identified in the powders stored at high humidities (73).

3.4 Mass median aerodynamic diameter

Particle size and its distribution affect particle retention in the lungs (70, 74). Particles larger than 20 μm likely fail to go beyond the terminal bronchioles. Those larger than 6 μm fail to reach the alveolar ducts. The optimum particle size to reach and be deposited in the alveolar region seems to be 1 to 5 μm (70, 71, 74, 75). Submicrometer-size particles are exhaled, deposited, or both by random Brownian motion in distal regions. It should be noted that the particle size referred to in this context is not geometric diameter but aerodynamic diameter.

The theoretical aerodynamic diameter, d_{aer} , of indi-

Table 4 Effect of sugars on spray-dried peptides and proteins

Peptide/Protein	Sugar ^a	Activity (%)	Degradation (%)	FPF (%)	Moisture (%)	D ^b (μm)	Ref.
β-galactosidase	none ^c	42			4.5	3.9	45
	10% mannitol	81			1.5	4.3	
	10% sucrose	102			2.8	4.3	
	10% trehalose	109			4.0	4.0	
catalase	none	197 ^d				5.8	69
	50% lactose	153				6.4	
	50% mannitol	107				4.4	
insulin	none	18 ^d				2.9	69
	50% lactose	24				3.9	
	67% mannitol	18				5.0	
oxyhemoglobin	none ^e		50				46
	0.01M sucrose		40				
	0.10M sucrose		10				
	0.20M sucrose		2				
Albumin/DPPC (20/60)	20% sucrose			53		4.8 ^c	70
	20% mannitol			11.3		10.4	
Albumin/DPPC (20/60)	20% lactose ^b			38		1.2	71
	20% trehalose			34		1.1	
	20% mannitol			11		1.5	
rhDNase	none			46		3.4	63
	50% mannitol			14		6.1	
	20% trehalose			29		2.9	
	40% trehalose			36		2.6	
	60% trehalose			20		3.2	
	40% sucrose			27		2.8	
anti-IgE MAb	none			27		3.3	63
	10% mannitol			25		3.8	
	20% mannitol			29		4.0	
	40% trehalose			31		3.3	
rhuMAbE25	none			27	2.23 ^f		44
	10% mannitol			35	1.31		
	20% mannitol			28	0.86		
	30% mannitol			27	1.00		
	40% mannitol			8.5	1.11		

^a Percentage stands for the sugar content in dry powder except for β-galactosidase and oxyhemoglobin.

^b Geometric or aerodynamic diameter.

^c Concentration in feed solution. β-Galactosidase concentration was 6%.

^d Activity relative to that of raw material.

^e Concentration in feed solution. Oxyhemoglobin concentration was 10%.

^f Pseudo first-order degradation rate constant at 30°C.

vidual particles is calculated according to the following definition (76):

$$d_{\text{aer}} = (\rho/F)^{0.5}d \quad (1)$$

Where:

d is mass median particle diameter as measured by light microscopy,

ρ is particle density, and

F is the dynamic shape correction factor.

The F values for spheres and cubes are 1.00 and 1.08, respectively (76). The tap density could be an estimate of the particle density, ρ, although it remains an approximately 20% systemic underestimate of ρ (15).

The experimental mass median aerodynamic diameter (MMAD) of the particles is obtained as follows with an Andersen cascade impactor (70, 71). The cumulative mass of powder less than the stated size of each stage of the impactor is calculated and plotted on a log probability scale, as the percent of total mass recovered in the impactor against the effective cut-off diameter. The MMAD of the particles is defined from this graph as the particle size at which the line crosses the 50% mark. The geometric standard deviation (GSD) is calculated as $GSD = (X/Y)^{0.5}$, where X and Y are the particle sizes at which the line crosses the 84.13% mark and the 15.87% mark, respectively.

Fine particle fraction (FPF) is defined as the mass

fraction of particles smaller than a certain aerodynamic diameter (for instance, 5 μm). The twin impinger is often used to estimate FPF values and is valuable for the routine quality assessment of aerosols during product development, stability testing, and for quality assurance and comparison of products (77). The particles captured in stage 2 are considered to be the FPF. The aerodynamic cutoff diameter between stages 1 and 2 of the twin impinger with an air stream of 60 l/h is 6.4 μm (78). The cutoff size of the impinger stage can easily be changed because it is inversely proportional to the square root of the air flow (79).

3.5 Hollow porous particles

Equation 1 predicts that a large and light particle may have the same aerodynamic diameter as a small and heavy particle. Edwards et al. showed in 1997 that the FPF for large porous particles was much higher than that for small nonporous particles, even though the aerodynamic diameters were nearly identical. Large porous particles also increased systemic bioavailability of insulin in rats (80). The advantage of large porous particles can be attributed to the smaller surface-to-volume ratio for the porous particles, which results in less particle aggregation.

Another benefit to the use of large particles is that they can avoid phagocytic clearance from the lungs. Radiolabeled polystyrene microspheres of 3, 9, and 15 μm in diameter administered into rat lungs were cleared with biphasic patterns. The half lives for the late phases of the 3 and 9 μm microspheres were 69 and 580 days, respectively, while that for the 15 μm microsphere was found not measurable during the 106-day study (81).

Spray drying produced hollow porous powders consisting of albumin, DPPC, and lactose. The solution feed rate and pressure of the compressed air had little impact on powder properties. Increasing the inlet temperature tended to make the powders heavier (15). The lower the bulk powder tap density, the higher the FPF. Removing albumin or DPPC from the composition led to denser and smaller particles. Replacing lactose with mannitol resulted in a poor FPF value. The FPF was maximized at albumin/DPPC/lactose=10/60/30 (71).

Large porous particles composed of albuterol sulfate (4%), a short-acting bronchodilator, and human serum albumin (18%), lactose (18%), and DPPC (60%) were prepared by spray drying. Inhalation of the albuterol particles obtained produced a significant inhibition of carbachol-induced bronchoconstriction

for at least 16 hr in guinea pigs, while small nonporous albuterol particles were effective for up to 5 hr. It is possible that the long-lasting action observed in the large porous particles was at least partly due to the slower clearance by phagocytosis (82).

PulmoSphere™ particles are hollow porous particles with geometric diameters between 3 and 5 μm and tap densities of about 0.1 g/cm^3 prepared by a spray-drying method. A submicrometer fluorocarbon-in-water emulsion stabilized by a monolayer of phospholipid at the fluorocarbon-water interface is combined with a second aqueous phase containing the drug and any wall-forming excipients desired. Spray drying the aqueous dispersion produces hollow porous powders. The fluorocarbon serves as a blowing agent or inflation agent during the spray-drying step (83). Deposition of PulmoSphere™ particles of albuterol sulfate in the human respiratory tract delivered by pMDI was double the deposition of a conventional micronized drug pMDI formulation (84).

The spray freeze-drying technique has been proposed as a method to produce light and porous protein particles (63). A protein solution with excipient is sprayed in liquid N_2 . After spraying, the whole content of the liquid N_2 was lyophilized to harvest powders. This technique produced powders of DNase and anti-IgE MAb with a high FPF up to 70% (63).

When the GAS process with supercritical carbon dioxide is used to produce protein powders, the operating temperature or rate of CO_2 addition had a minor effect on the morphology and size of the powders. Large porous particles were obtained at a high concentration of proteins, while agglomeration of the precipitated particles occurs at dilute concentrations (52). ASES processing at higher temperatures with higher concentrations of the protein reduced the agglomeration of primary particles due to a higher degree of supersaturation and a higher nucleation rate (85).

4. Conclusion

Although pulmonary absorption of peptides and proteins is much better than that through the gastrointestinal tract, the bioavailability of inhaled peptides and proteins is still below that administered intravenously or subcutaneously. The success of inhalation therapy with dry powders is determined by the biological aspects of active ingredients, the physicochemical aspects of formulation, and inhaler performance. The bioavailability of inhaled peptides and proteins will be improved by considering these

factors. The application of hollow porous particles has opened a new avenue for inhalation therapy in humans. We now expect groundbreaking success in increasing permeability, reducing metabolic degradation, maximizing the FPF, and in other areas that will make inhalation therapy with peptides and proteins more effective and economical.

References

- 1) Cipolla, D. C., Clark, A. R., Chan, H. K., Gonda, I. and Shire, S. J. "Assessment of aerosol delivery system for recombinant human deoxyribonuclease," *STP Pharma Sciences* **4**, 50-60 (1994).
- 2) Chan, H. K., Clark, A., Gonda, I., Mumenthaler, M. and Hsu, C. "Spray dried powders and powder blends of recombinant human deoxyribonuclease (rhDNase) for aerosol delivery," *Pharm Res* **14**, 431-437 (1997).
- 3) Pfizer Inc. Press Release, June 15, 2002. "Study shows Exubera[®] (inhaled insulin) provides glycemic control equal to insulin injections in patients with type 1 diabetes," <http://www.pfizer.com/pfizerinc/about/press/exubera0615.html>
- 4) Pfizer Inc. Press Release, June 15, 2002. "Exubera[®] (inhaled insulin) provides better glycemic control than oral therapy for patients with type 2 diabetes, new data show," <http://www.pfizer.com/pfizerinc/about/press/exubera0615b.html>
- 5) Aradigm Co. News Release, June 17, 2002. "New data show first electronic inhalation insulin system comparable to multiple injections in controlling glucose," <http://www.aradigm.com/>
- 6) Timsina, M. P., Martin, G. P., Marriott, C., Ganderton, D. and Yianneskis, M. "Drug delivery to the respiratory tract using dry powder inhalers," *Int J Pharmaceut* **101**, 1-13 (1994).
- 7) Newman, S. P., Hollingworth, A. and Clark, R. "Effect of different modes of inhalation on drug delivery from a dry powder inhaler," *Int J Pharmaceut* **102**, 127-132 (1994).
- 8) Dunbar, C. A., Hickey, A. J. and Holzner, P. "Dispersion and characterization of pharmaceutical dry powder aerosols," *Kona* **16**, 7-45 (1998).
- 9) Chew, N. Y. K. and Chan, H. K. "Pharmaceutical dry powder aerosol delivery," *Kona* **19**, 46-56 (2001).
- 10) Suarez, S. and Hickey, A. J. "Drug properties affecting aerosol behavior," *Respiratory Care* **45**, 652-666 (2000).
- 11) Benowitz, N., Forsyth, R. P., Melmon, K. L. and Rowland, M. "Lidocaine disposition kinetics in monkey and man I. Prediction by a perfusion model," *Clin Pharmacol Ther* **16**, 87-98 (1974).
- 12) Wolff, R. K. "Safety of inhaled proteins for therapeutic use," *Journal of Aerosol Medicine* **11**, 197-219 (1998).
- 13) McConville, J. T., Patel, N., Ditchburn, N., Tobbyn, M. J., Staniforth, J. N. and Woodcock, P. "Use of a novel modified TSI for the evaluation of controlled-release aerosol formulations," *I. Drug Dev Ind Pharm* **26**, 1191-1198 (2001).
- 14) Ang, X. D., Ma, J. K. A., Malanga, C. J. and Rojanasakul, Y. "Characterization of proteolytic activities of pulmonary alveolar epithelium," *Int J Pharmaceut* **195**, 93-101 (2000).
- 15) Vanbever, R., Mintzes, J. D., Wang, J., Nice, J., Chen, D. H., Batycky, R., Langer, R. and Edwards, D. A. "Formulation and physical characterization of large porous particles for inhalation," *Pharm Res* **16**, 1735-1742 (1999).
- 16) Schanker, L. S. and Less, M. J. "Lung pH and pulmonary absorption of nonvolatile drugs in the rat," *Drug Metabol Dispos* **5**, 174-178 (1977).
- 17) Fisher, A. B. and Chander, A. "Introduction: Lung surfactant – phospholipids and apoproteins," *Exp Lung Res* **6**, 171-174 (1984).
- 18) Hunninghake, G. W., Gadek, J. E., Kawanami, O., Ferrans, V. J. and Crystal, R. G. "Inflammatory and immune processes in the human lung in health and disease: evaluation by bronchoalveolar lavage," *Am J Pathol* **97**, 149-206 (1979).
- 19) Lanman, R. C., Gillilan, R. M. and Schanker, L. S. "Absorption of cardiac glycosides from the rat respiratory tract," *J Pharmacol Exp Ther* **187**, 105-111 (1973).
- 20) Enna, S. J. and Schanker, L. S. "Absorption of drugs from the rat lung," *Am J Physiol* **223**, 1227-1231 (1972).
- 21) Enna, S. J. and Schanker, L. S. "Absorption of saccharides and urea from the rat lung," *Am J Physiol* **222**, 409-414 (1972).
- 22) Matsukawa, Y., Lee, V. H. L., Crandall, E. D. and Kim, K. J. "Size-dependent dextran transport across rat alveolar epithelial cell monolayers," *J Pharm Sci* **86**, 305-309 (1997).
- 23) Morimoto, K., Uehara, Y., Iwanaga, K. and Kakemi, M. "Tracheal barrier and the permeability of hydrophilic drugs and dipeptides," *Biol Pharm Bull* **22**, 510-514 (1999).
- 24) Brown, R. A. J. and Schanker, L. S. "Absorption of aerosolized drugs from the rat lung," *Drug Metab Dispos Biol Fate Chem* **11**, 355-360 (1983).
- 25) Yoshida, H., Okumura, K., Hori, R., Anmo, T. and Yamaguchi, H. "Absorption of insulin delivered to rabbit trachea using aerosol dosage form," *J Pharm Sci* **68**, 670-671 (1979).
- 26) Patton, J. S., Trincherro, P. and Platz, R. M. "Bioavailability of pulmonary delivered peptide and proteins: α -interferon, calcitonins and parathyroid hormones," *J Controlled Release* **28**, 79-85 (1994).
- 27) Okumura, K., Iwakawa, S., Yoshida, T., Seki, T. and Komada, F. "Intratracheal delivery of insulin Absorption from solution and aerosol by rat lung," *Int J Pharmaceut* **88**, 63-73 (1992).
- 28) Lipworth, B. J. "Pharmacokinetics of inhaled drugs," *Br J Clin Pharmacol* **42**, 697-705 (1996).
- 29) Lie, F. Y., Kildsig, D. O. and Mitra, A. K. "Pulmonary biotransformation of insulin in rat and rabbit," *Life Science* **51**, 1683-1689 (1992).
- 30) Shen, Z., Zhang, Q., Wei, S. and Nagai, T. "Proteolytic

- enzymes as a limitation for pulmonary absorption of insulin: in vitro and in vivo investigations," *Int J Pharmaceut* **192**, 115-121 (1999).
- 31) Hsu, M. C. P. and Bai, J. P. F. "Investigation into the presence of insulin-degrading enzyme in cultured type II alveolar cells and the effects of enzyme inhibitors on pulmonary bioavailability of insulin in rats," *J Pharm Pharmacol* **50**, 507-514 (1998).
 - 32) Hoover, J. L., Rush, B. D., Wilkinson, K. F., Day, J. S., Burton, P. S., Vidmar, T. J. and Ruwart, M. J. "Peptides are better absorbed from the lung than the gut in the rat," *Pharm Res* **9**, 1103-1106 (1992).
 - 33) Henderson, R. F. "Use of bronchoalveolar lavage to detect lung damage," *Environ Health Perspect* **56**, 115-129 (1984).
 - 34) Morgan, A., Moores, S. R., Holmes, A., Evans, J. C., Evans, N. H. and Black, A. "The effect of quartz, administered by intratracheal instillation, on the rat lung. I. The cellular response," *Environ Res* **22**, 1-12 (1980).
 - 35) Moores, S. R., Black, A., Evans, J. C., Evans, N., Holmes, A. and Morgan, A. "The effect of quartz, administered by intratracheal instillation, on the rat lung. II. The short-term biochemical response," *Environ Res* **24**, 275-285 (1981).
 - 36) Todo, H., Okamoto, H., Iida, K. and Danjo, K. "Effect of additives on insulin absorption from intratracheally administered dry powders in rats," *Int J Pharmaceut* **220**, 101-110 (2001).
 - 37) Komada, F., Iwakawa, S., Yamamoto, N., Sakakibara, H. and Okumura, K. "Intratracheal delivery of peptide and protein agents: Absorption from solution and dry powder by rat lung," *J Pharm Sci* **83**, 863-867 (1994).
 - 38) Yamamoto, A., Umemori, S. and Muranishi, S. "Absorption enhancement of intrapulmonary administered insulin by various absorption enhancers and protease inhibitors in rats," *J Pharm Pharmacol* **46**, 14-18 (1993).
 - 39) Morita, T., Yamamoto, A., Takakura, Y., Hashida, M. and Sezaki, H. "Improvement of the pulmonary absorption of (Asu1,7)-eel calcitonin by various protease inhibitors in rats," *Pharm Res* **11**, 909-913 (1994).
 - 40) Kobayashi, S., Kondo, S. and Juni, K. "Pulmonary delivery of salmon calcitonin dry powders containing absorption enhancers in rats," *Pharm Res* **13**, 80-83 (1996).
 - 41) Kobayashi, S., Kondo, S. and Juni, K. "Study on pulmonary delivery of salmon calcitonin in rats: Effects of protease inhibitors and absorption enhancers," *Pharm Res* **11**, 1239-1243 (1994).
 - 42) Yamamoto, A., Okumura, S., Fukuda, Y., Fukui, M., Takahashi, K. and Muranishi, S. "Improvement of the Pulmonary Absorption of (Asu1,7)-eel Calcitonin by Various Absorption Enhancers and Their Pulmonary Toxicity in Rats," *J Pharm Sci* **86**, 1144-1147 (1997).
 - 43) Maa, Y. F., Costantino, H. R., Nguyen, P. A. T. and Hsu, S. S. "The effect of operating and formulation variables on the morphology of spray-dried protein particles," *Pharmaceut Dev Technol* **2**, 213-223 (1997).
 - 44) Costantino, H. R., Andya, J. D., Nguyen, P. A., Dasovich, N., Sweeney, T. D., Shire, S. J., Hsu, C. C. and Maa, Y. F. "Effect of mannitol crystallization on the stability and aerosol performance of a spray-dried pharmaceutical protein, recombinant humanized anti-IgE monoclonal antibody," *J Pharm Sci* **87**, 1406-1411 (1998).
 - 45) Broadhead, J., Rouan, S. K. and Rhodes, C. T. "The effect of process and formulation variables on the properties of spray-dried β -galactosidase," *J Pharm Pharmacol* **46**, 458-467 (1994).
 - 46) Labrude, P., Rasolomanana, M., Vigneron, C., Thirion, C. and Chaillot, B. "Protective effect of sucrose on spray drying of oxyhemoglobin," *J Pharm Sci* **78**, 223-229 (1989).
 - 47) Tahl, K., Claesson, M., Lilliehorn, P., Linden, H. and Backstrom, K. "The effect of process variables on the degradation and physical properties of spray dried insulin intended for inhalation," *Int J Pharmaceut* **233**, 227-237 (2002).
 - 48) Mumenthaler, M., Hsu, C. C. and Pearlman, R. "Feasibility study on spray-drying protein pharmaceuticals: Recombinant human growth hormone and tissue-type plasminogen activator," *Pharm Res* **11**, 12-20 (1994).
 - 49) Maa, Y. F., Nguyen, P. A. and Hsu, S. W. "Spray-drying of air-liquid interface sensitive recombinant human growth hormone," *J Pharm Sci* **87**, 152-157 (1998).
 - 50) Donsi, G. and Reverchon, E. "Micronization by means of supercritical fluids: possibility of application to pharmaceutical field," *Pharm Acta Helv* **66**, 170-173 (1991).
 - 51) Jung, J. and Perrut, M. "Particle design using supercritical fluids: Literature and patent survey," *J Supercritical Fluids* **20**, 179-219 (2001).
 - 52) Thiering, R., Dehghani, F., Dillow, A. and Foster, N. R. "The influence of operating conditions on the dense gas precipitation of model proteins," *J Chem Technol Biotechnol* **75**, 29-41 (2000).
 - 53) Steckel, H. and Muller, B. W. "Metered-dose inhaler formulation of fluticasone-17-propionate micronized with supercritical carbon dioxide using the alternative propellant HFA-227," *Int J Pharmaceut* **173**, 25-33 (1998).
 - 54) Steckel, H., Thies, J. and Muller, B. W. "Micronizing of steroids for pulmonary delivery by supercritical carbon dioxide," *Int J Pharmaceut* **152**, 99-110 (1997).
 - 55) Bodmeier, R., Wang, H., Dixon, D. J., Mawson, S. and Johnston, K. P. "Polymeric microspheres prepared by spraying into compressed carbon dioxide," *Pharm Res* **12**, 1211-1217 (1995).
 - 56) Falk, R., Randolph, T. W., Meyer, J. D., Kelly, R. M. and Manning, M. C. "Controlled release of ionic compounds from poly (L-lactide) microspheres produced by precipitation with a compressed antisolvent," *J Controlled Release* **44**, 77-85 (1997).
 - 57) Yeo, S. D., Lim, G. B., Debenedetti, P. G. and Bernstein, H. "Formation of microparticulate protein powders using a supercritical fluid antisolvent," *Biotechnol Bioeng* **41**, 341-346 (1993).
 - 58) Yeo, S. D., Debenedetti, P. G., Patro, S. Y. and Przybycien, T. M. "Secondary structure characterization of microparticulate insulin powders," *J Pharm Sci*

- 83**, 1651-1656 (1994).
- 59) Winters, M. A., Debenedetti, P. G., Carey, J., Sparks, H. G., Sane, S. U. and Przybycien, T. M. "Long-term and high-temperature storage of supercritically-processed microparticulate protein powders," *Pharm Res* **14**, 1370-1378 (1997).
- 60) Winters, M. A., Knutson, B. L., Debenedetti, P. G., Sparks, H. G., Przybycien, T. M., Stevenson, C. L. and Prestrelski, S. J. "Precipitation of proteins in supercritical carbon dioxide," *J Pharm Sci* **85**, 586-594 (1996).
- 61) Palakodaty, S., York, P. and Pritchard, J. "Supercritical fluid processing of materials from aqueous solutions: The application of SEDS to lactose as a model substance," *Pharm Res* **15**, 1835-1843 (1998).
- 62) Ghaderi, R., Artursson, P. and Carlfors, J. "Preparation of biodegradable microparticles using solution-enhanced dispersion by supercritical fluids (SEDS)," *Pharm Res* **16**, 676-681 (1999).
- 63) Maa, Y. F., Nguyen, P. A., Sweeney, T., Shire, S. J. and Hsu, C. C. "Protein inhalation powders: Spray drying vs spray freeze drying," *Pharm Res* **16**, 249-254 (1999).
- 64) Sellers, S. P., Clark, G. S., Sievers, R. E. and Carpenter, J. F. "Dry powders of stable protein formulations from aqueous solutions prepared using supercritical CO₂-assisted aerosolization," *J Pharm Sci* **90**, 785-797 (2001).
- 65) Lai, M. C. and Topp, E. M. "Solid-state chemical stability of proteins and peptides," *J Pharm Sci* **88**, 489-500 (1999).
- 66) Pikal, M. J. and Rigsbee, D. R. "The stability of insulin in crystalline and amorphous solids: observation of greater stability for the amorphous form," *Pharm Res* **14**, 1379-1387 (1997).
- 67) Maa, Y. F., Nguyen, P. A., Andya, J. D., Dasovich, N., Sweeney, T. D., Shire, S. J. and Hsu, C. C. "Effect of spray drying and subsequent processing conditions on residual moisture content and physical/biochemical stability of protein inhalation powders," *Pharm Res* **15**, 768-775 (1998).
- 68) Imamura, K., Iwai, M., Ogawa, T., Sakiyama, T. and Nakanishi, K. "Evaluation of hydration states of protein in freeze-dried amorphous sugar matrix," *J Pharm Sci* **90**, 1955-1963 (2001).
- 69) Forbes, R. T., Davis, K. G., Hindle, M., Clarke, J. G. and Maas, J. "Water vapor sorption studies on the physical stability of a series of spray-dried protein/sugar powders for inhalation," *J Pharm Sci* **87**, 1316-1321 (1998).
- 70) Bosquillon, C., Lombry, C., Preat, V. and Vanbever, R. "Comparison of particle sizing techniques in the case of inhalation dry powders," *J Pharm Sci* **90**, 2032-2041 (2001).
- 71) Bosquillon, C., Lombry, C., Preat, V. and Vanbever, R. "Influence of formulation excipients and physical characteristics of inhalation dry powders on their aerosolization performance," *J Controlled Release* **70**, 329-339 (2001).
- 72) Izutsu, K., Yoshioka, S. and Terao, T. "Effect of mannitol crystallinity on the stabilization of enzymes during freeze-drying," *Chem Pharm Bull (Tokyo)* **42**, 5-8 (1994).
- 73) Chan, H. K. and Gonda, I. "Solid state characterization of spray-dried powders of recombinant human deoxyribonuclease (RhDNase)," *J Pharm Sci* **87**, 647-654 (1998).
- 74) Kanig, J. L. "Pharmaceutical aerosols," *J Pharm Sci* **52**, 513-535 (1963).
- 75) Gonda, I. "A semi-empirical model of aerosol deposition in the human respiratory tract for mouth inhalation," *J Pharm Pharmacol* **33**, 692-696 (1981).
- 76) Crowder, T. M., Rosati, J. A., Schroeter, J. D., Hickey, A. J. and Martonen, T. B. "Fundamental effects of particle morphology on lung delivery: predictions of Stokes' law and the particular relevance to dry powder inhaler formulation and development," *Pharm Res* **19**, 239-245 (2002).
- 77) Hallworth, G. W. and Westmoreland, D. G. "The twin impinger: a simple device for assessing the delivery of drugs from metered dose pressurized aerosol inhalers," *J Pharm Pharmacol* **39**, 966-972 (1987).
- 78) Kawashima, Y., Serigano, T., Hino, T., Yamamoto, H. and Takeuchi, H. "Effect of surface morphology of carrier lactose on dry powder inhalation property of pranlukast hydrate," *Int J Pharmaceut* **172**, 179-188 (1998).
- 79) Chew, N. Y. K. and Chan, H. K. "Influence of particle size, air flow, and inhaler device on the dispersion of mannitol powders as aerosols," *Pharm Res* **16**, 1098-1103 (1999).
- 80) Edwards, D. A., Hanes, J., Caponetti, G., Hrkach, J., Ben-Jebria, A., Eskew, M. L., Mintzes, J., Deaver, D., Lotan, N. and Langer, R. "Large porous particles for pulmonary drug delivery," *Science* **276**, 1868-1871 (1997).
- 81) Snipes, M. B. and Clem, M. F. "Retention of microspheres in the rat lung after intratracheal instillation," *Environ Res* **24**, 33-41 (1981).
- 82) BenJebria, A., Chen, D. H., Eskew, M. L., Vanbever, R., Langer, R. and Edwards, D. A. "Large porous particles for sustained protection from carbachol-induced bronchoconstriction in guinea pigs," *Pharm Res* **16**, 555-561 (1999).
- 83) Dellamary, L. A., Tarara, T. E., Smith, D. J., Woelk, C. H., Adractus, A., Costello, M. L., Gill, H. and Weers, J. G. "Hollow porous particles in metered dose inhalers," *Pharm Res* **17**, 168-174 (2000).
- 84) Hirst, P. H., Pitcairn, G. R., Weers, J. G., Tarara, T. E., Clark, A. R., Dellamary, L. A., Hall, G., Shorr, J. and Newman, S. P. "In vivo lung deposition of hollow porous particles from a pressurized metered dose inhaler," *Pharm Res* **19**, 258-264 (2002).
- 85) Bustami, R. T., Chan, H. K., Dehghani, F. and Foster, N. R. "Generation of micro-particles of proteins for aerosol delivery using high pressure modified carbon dioxide," *Pharm Res* **17**, 1360-1366 (2000).

Author's short biography



Hirokazu Okamoto

Dr. Hirokazu Okamoto is an associate professor in the Faculty of Pharmacy, Meijo University. He received his Ph.D. from the Faculty of Pharmaceutical Sciences, Kyoto University in 1989. He worked at Upjohn Pharmaceuticals Limited, the Japanese branch of The Upjohn Co., as a research scientist in Pharmacy Research Group from 1989, and was transferred to Pharmacia & Upjohn as a Pharmacy Research Group leader in 1996 upon the merger of Pharmacia Co. and The Upjohn Co. He has occupied his present position since 1998. His research interests are in the development of drug delivery systems to improve bioavailability. His recent main research theme is the development of dry powder proteins and dry powder genes for inhalation.



Hiroaki Todo

Hiroaki Todo is a graduate student in the Faculty of Pharmacy, Meijo University. He received his B.S. from the same university in 1999. His research theme is improving the bioavailability of dry powder insulin prepared by spray-drying and SCF techniques.



Kotaro Iida

Dr. Kotaro Iida is a lecturer in the Faculty of Pharmacy, Meijo University. He received his Ph.D. from Meijo in 1992. He was a post doctoral fellow in the School of Pharmacy, University of Basel from 1997 to 1999. His research interests are the design of dry powders for inhalation with carrier particles. His recent main research theme is the characterization of powder systems for pulmonary application.



Kazumi Danjo

Dr. Kazumi Danjo is a professor in the Faculty of Pharmacy, Meijo University. He received his Ph.D. from the same institute in 1981. He was a post doctoral fellow in the School of Pharmacy, University of Wisconsin in 1986. His research interests are in the development of composite particles using the spray-drying technique. One of his recent research projects is a study on the dissolution of drugs with poor water solubility from porous particles.

Synthesis and Fabrication of Inorganic Porous Materials: From Nanometer to Millimeter Sizes[†]

Minoru Takahashi and Masayoshi Fuji

Ceramics Research Laboratory, Nagoya Institute of
Technology*

Abstract

In recent years, the functions of porous ceramics such as light weight, thermal insulation, permeability, separation, adsorption, and sound absorption have been paid attention. They are applied to materials for environmental improvement, materials for energy system, biomechanical materials, spatial materials and so on. In conjunction with this, many synthesis and fabrication methods for not only porous ceramics in the usual macropore range, but also those in the mesopore and micropore ranges were reported. The functions and fabrication methods of porous materials are closely related to pore size and structure. In this paper we reviewed recent synthesis and fabrication methods for porous materials across a wide range from nanometer to millimeter pore sizes while also touching upon material functions.

Introduction

Porous materials are widely used in everyday life, whether one is aware of them or not. The silica gel as a dehumidifying agent and the activated carbon as a deodorant are traditional porous materials. Another example is traditional Japanese houses, which are made of wood, earth, and paper. Such architecture resulted from long years of innovation through insights that these materials would function to insulate and adjust humidity in Japanese climate, whose temperature and humidity vary over broad ranges. It is amazing how people unconsciously worked out the use of materials with various pore sizes. Tightly sealed modern housing holds in humidity, which has created problems such as molds and bacteria, and there are also concerns about the many illnesses that could result from these. This has focused attention on building materials that incorporate porous materials, and many such materials are being developed. [1, 2] As this shows, porous materials are closely integrated into our lives. Here we shall attempt to classify the porous materials reported to date while taking their function expression mechanisms, and then, based on that classification, describe the synthesis and fabrica-

tion methods for some representative porous materials.

Functions and Classification of Porous Materials

Typical porous ceramics and the range of their pore sizes are shown in **Fig. 1**, [3]. There are currently many porous materials with pore sizes from about 0.1 nm to 10 mm. When considering these function expression mechanisms of these materials, the level at which we see pores is important. The function expression of Angstrom-order pores is likely related to interaction with ions, atoms, and molecules, while those in micrometer and millimeter ranges are probably related to the adhesion of solid particles on filter. It is assumed that pores size in the middle of this range are related to molecular aggregates and condensed liquids.

In this session, the relationship between pore size and function expression mechanisms is reviewed. **Fig. 2** shows the mechanisms of porous materials in relation to gas permeation. [4] When pore size is 10 μm or larger, the mechanism can be regarded as the flow passing through an equivalent packed bed, and for that reason the relationship between a porous material and function can be forecast from the Darcy equation and other relational equations for flow velocity and pressure loss. Molecular diffusion controls the

* 10-6-29 Asahigaoka, Tajimi, Gifu 507-0071 Japan

[†] Accepted: June 27, 2002

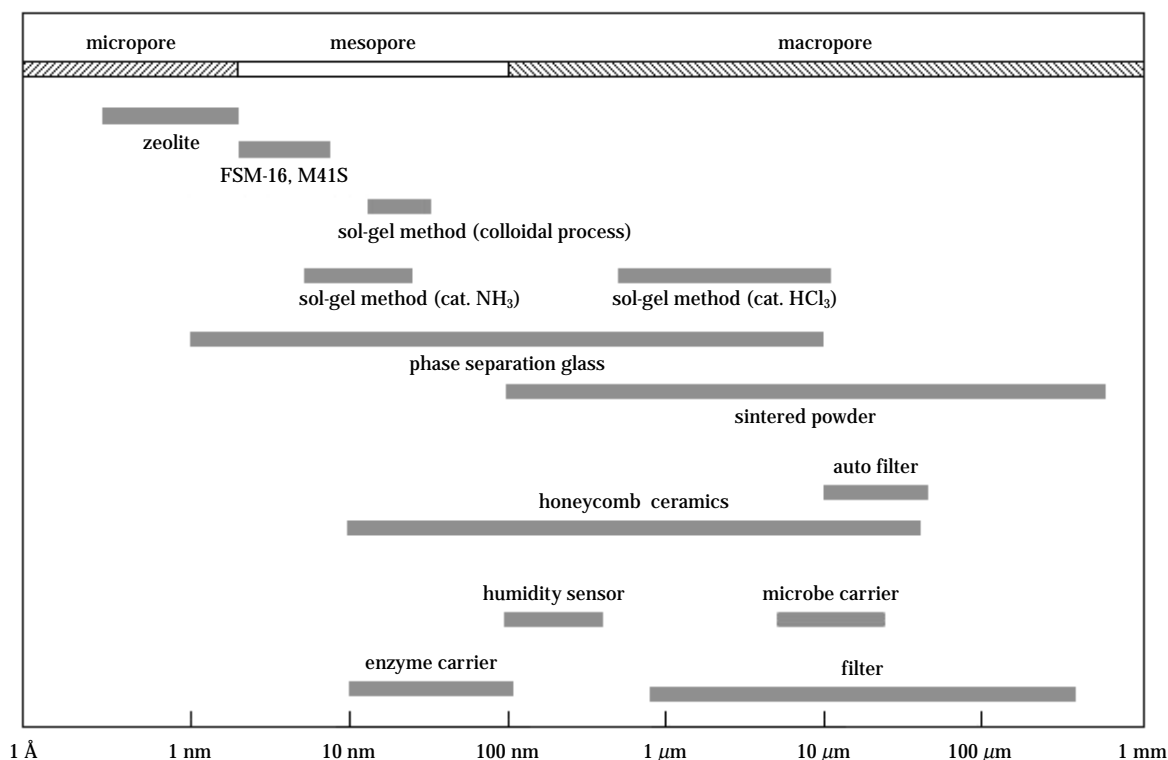


Fig. 1 Pore size of typical porous ceramics.

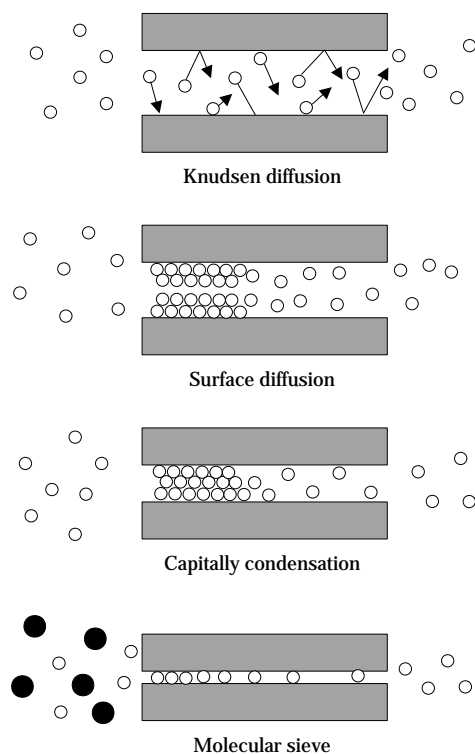


Fig. 2 Permeation model of gas in porous materials (modified from Matsukata [4]).

permeation mechanism of porous materials whose pore sizes are in the approximate range of 0.1 to 10 μm . When pore size and molecular mean free path fall below that range, they are governed by Knudsen diffusion. Permeation flow velocity then is proportional to molecular weight to the 0.5 power. At smaller pore sizes below several nm, an activation process caused by interaction between pore wall surfaces and molecules contributes to the permeation phenomenon, which is called “activation diffusion” or “surface flow.” This is a pore size range in which capillary condensation governs when the gas is a condensing gas such as water vapor. At still smaller pore sizes, permeation selectivity is expressed due to difference in molecule sizes, and one can expect the so-called “molecular sieve effect.” From these examples, the correspondence between pore size and function is apparent. It is in fact clear that properties including porosity, pore shape, interpore networks, pore opening, and pore closing contribute to various function expressions. **Table 1** presents the relationship between these pore properties and functions. [5] These are sufficient for considering rough design guidelines of porous materials, but owing to the complex connections between function expression and pore properties such as pore size, porosity, and pore

Table 1 Influence of porosity on properties (From Rice [5])

Porosity dependence		Examples of properties
No dependence on porosity		Lattice parameter, unit cell volume, thermal expansion, heat capacity per unit weight, density
Dependence only on the amount of porosity		Apparent density, dielectric constant, heat capacity per unit volume
Dependence both the amount and character of porosity	Flux or stress dominant in the solid phase	Mechanical properties, Electrical and thermal conductivity at low to moderate temperature and porosity
	All flux in the pore phase and filtration	Surface area and tortuosity, e.g., for catalysis
	Flux in both pore and solid phase	Thermal conductivity, with larger and more open pores at higher temperature

shape, or between function expression and material properties, a method of cataloging them more carefully is desirable from the standpoint of material design.

One method of classifying pores is the International Union of Pure and Applied Chemistry (IUPAC) method, which is internationally recognized. [6] It is based on the Russel classification, in which pores are classified mainly according to the results of nitrogen adsorption experiments. [7, 8] One should be well aware that classification is based on nitrogen adsorption, meaning that the relative sizes of nitrogen molecules and pores must be taken into account. With molecules larger than nitrogen, adsorption resembling micropore filling will occur in the mesopore range. Additionally, caution is needed when working with molecules smaller than nitrogen molecules, such as hydrogen and water. For example, even if materials are non-porous to nitrogen molecules, it is often the

case that they are not necessarily non-porous to these smaller molecules. Therefore we think that an index such as the relative pore sizes shown in **Table 2** is needed in pore classification. However nitrogen molecules are quadrupole interactive, generally in nitrogen adsorption they can be seen as often forming a multilayer structure as in BET theory, but comparable phenomena do not necessarily occur with other molecules. Thus at this time classification by the presence of molecules in pores is perhaps a practical method.

Based on the foregoing, and using the IUPAC classification as the standard, **Table 2** presents the classification based on the function expression discussed above and the phenomena occurring in pores, as well as the pore classification organized by considering the synthesis methods for existing porous materials, discussed below.

Table 2 Classification of porous materials

Category		Pore radius range	Origin of pore	State of atoms or molecules in pore	Characterization methods	Relative pore radius*
Atom and molecule pore	Micropore	<2 nm	Space among atoms or ions, Crystal lattice, Trace of solvent molecules after drying	Microporefilling, Atom, Ion, Molecule	Gas adsorption, TEM, XRD	<6
Aggregate Molecules pore	Mesopore I	2-10 nm	Micelle or liquid crystal templating	Intermediate state of microporefilling and condensation, Molecules interact with pore wall	Gas adsorption, TEM, XRD	6-30
Liquid phase pore	Mesopore II	2-50 nm	Phase separation, Space among particles	Capillary condensation, Liquid phase	Gas adsorption, SEM, TEM	30-141
Spatial pore	Macropore	50 nm<	Bubble, Cavity, Space among particles, Particle templating	The same on a flat surface, Pore is just a space	Porosimetry SEM	141<

* Pore radius divided by diameter of nitrogen molecule (0.354 nm)

Synthesizing Atom and Molecule Pore

Zeolite is a typical material in this pore range. It was in 1756 that the Swedish mineralogist A. F. Cronstedt was the first to observe that steam was emitted when a mineral called stilbite was heated. On account of this he coined the term “zeolite,” which is a combination of the Greek “*zeo*” for boil and “*lithos*” for stone. Since then about 40 kinds of such minerals have been discovered. Today zeolite is understood to be a hydrous crystallized aluminosilicate mineral. Many of these materials are tectoaluminosilicates which, as illustrated in **Fig. 3**, are MO_4 tetrahedra (M means the Si, Al, or other atom of a tetrahedron) that share their apex oxygen atoms with a neighboring tetrahedron. This means the atomic ratio O/M in the frame is 2.

Zeolite is characterized by its uniform pores, which are about the same size as its molecules. Because zeolite can be classified by the size of its molecules, it is also called a molecular sieve. [9] Many types of zeolite have been synthesized, as seen in the industrialization of ZSM-5 (MFI) as a catalyst. In addition to aluminosilicate, zeolite with many different compositions and structures have been synthesized. VPS-5, with pore sizes between 1.2 and 1.3 nm, is the first aluminophosphate zeolite with pore sizes over 1 nm. Its pore walls have an 18-ring structure comprising 18 MO_4 (M: Al, P) units. Gallium phosphate zeolite, which has a 20-ring structure have been synthesized recently. A characteristic is that although the pore entrance size is about the same as that of VPI-5, crys-

tal interiors have voids called supercages as large as 3 nm.

Generally zeolite is made by hydrothermal synthesis. Si and Al sources and crystallizing agents are put into an autoclave, where the materials are dissolved and recrystallized. Any number of different zeolite types may result depending on the ingredient ratios, crystallization temperature, and crystallization time. **Table 3** gives the conditions for synthesizing zeolite membranes, which are of particular interest. [10-16].

At the center of attention in recent years is zeolite that can change its pore size in accordance with external fields. Reported types of variable-pore-size zeolite that can adjust its pore size by temperature are aluminosilicate of RHO type, and a type of titanosilicate zeolite. In particular, the titanosilicate whose ETS-4 (Engelhard titanosilicate-4) counter cations have been replaced by strontium is stable under heat treatment and can reversibly and precisely adjust its pore size between 0.427 and 0.394 nm. [17] Further, recent environmental problems underlie frequent reports including those on the synthesis of zeolite from wastes, and there are expectations for increasing research advances in the field of zeolite synthesis.

In contrast with the three-dimensional spaces of zeolite, various attempts are underway to find ways to use the unique two-dimensional spaces of stratified substances, of which the clay minerals are representative. The water-caused swelling of montmorillonite, which has long been known, is a phenomenon that is closely connected to the plasticity of clay. While the distance between layers in dry montmorillonite is

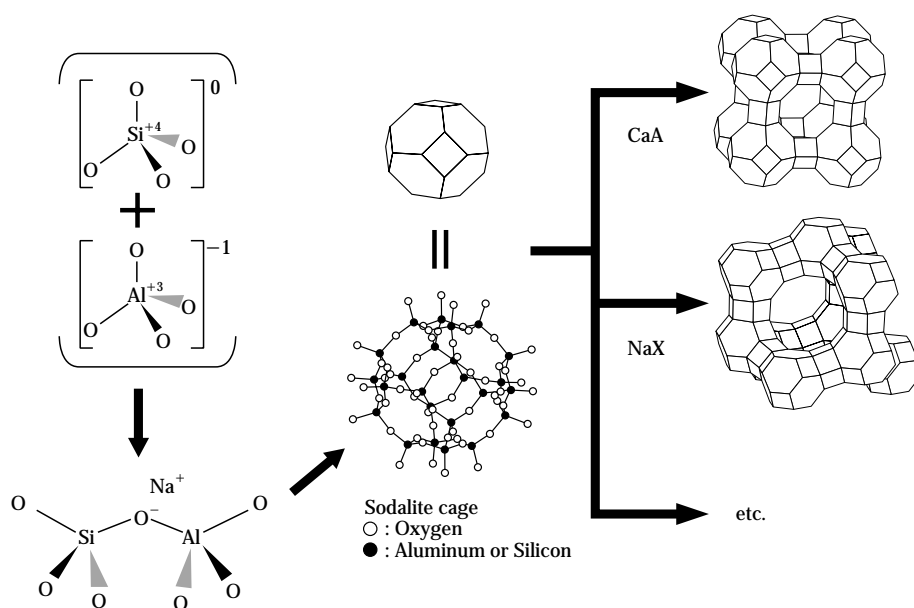


Fig. 3 Synthesis process and frame structure of zeolite.

Table 3 Hydrothermal conditions for Zeolite membrane Synthesis

Product	Si source	Al source	Crystallizing agent	Molar ratio				Crystallizing agent	Time (Day)	Temp. (K)	Ref.
				SiO ₂	Al ₂ O ₃	Na ₂ O	H ₂ O				
MFI	SiO ₂	Al(NO ₃) ₃	(C ₃ H ₇) ₃ HNBr	1	0.01	0.05	40-100	0.1	2-17	403-473	¹⁰⁾
MFI	SiO ₂	Al(NO ₃) ₃	(C ₃ H ₇) ₃ HNBr	1	0.01	0.05	80	0.1	0.25-1	443	¹¹⁾
SAPO-5	SiO ₂ H ₃ PO ₄ *	Al(OCH(CH ₃) ₂) γ-AlO(OH)	(C ₃ H ₇) ₃ HNBr	0.3	1.0	—	47	1.0	1-5.5	398-473	¹²⁾
MFI	SiO ₂	—	(C ₃ H ₇) ₃ HNBr	1	—	2.2	2832	5.22	9	453	¹³⁾
GME	SiO ₂ water glass	NaAlO ₂	Dab-4-Br**	1	0.067	0.6	26	0.16	4.17	368	¹⁴⁾
				1	0.033	0.6	44	0.24			
MFI	SiO ₂	Al(NO ₃) ₃	(C ₃ H ₇) ₃ HNBr	1	0-0.02	0.05	40-400	0.11	0.08-2	393-453	¹⁵⁾
FUA	SiO ₂	NaAlO ₂	—	1	0.09	0.7	30	0	1.25	353	¹⁶⁾

* As P source

** Polymer from 1,4-diazabicyclo[2.2.2]octane and 1,4-dibromobenzene

about 0.95 nm, it changes by steps from 0.95, 1.24, 1.54, and 1.90 nm as relative humidity rises. [18] These distances correspond to a compound in which water molecule layers each about 0.3 nm thick make their way between montmorillonite layers in numbers of 0, 1, 2, and 3 water layers, respectively. The inter-layer energy balance depends on: 1) inter-layer ions and silicate layer coulomb energy, 2) hydration energy of inter-layer cations, and 3) energy of water adsorption between layers in relation to humidity. [19] Hence, the behavior of change in inter-layer distance is controlled by the types of inter-layer cations and the nature of the silicate layers. [20] Montmorillonite with Na ions between its layers swells without limit under circumstances with much water, as in aqueous solutions, [18, 21] and there are reports that montmorillonite with Li ions between its layers undergoes similar unlimited swelling. [22] Additionally, various organic compounds become the guests of inter-layer substances. There have long been reports of attempts to obtain inter-layer compounds with guest organic polymers by polymerizing monomers between layers. Bentonite, montmorillonite, or other substances in which the inter-layer ions of layer substances have been replaced by ion exchange with cationic surfactant ions are used to put nonpolar organic molecules between layers. However, as illustrated in **Fig. 4**, limitless swelling is not observed at times like this because, in response to the size of the hydrophobic portion of surfactant ions, the material does not sorb

an amount of guest molecules larger than that which is held in the space formed between layers. [19]

In recent years there has been much research on the synthesis of intercalation compounds that are good at bringing various substances between layers, as happens in this swelling. In particular there is much research of great interest on providing various functions through surface modification between lay-

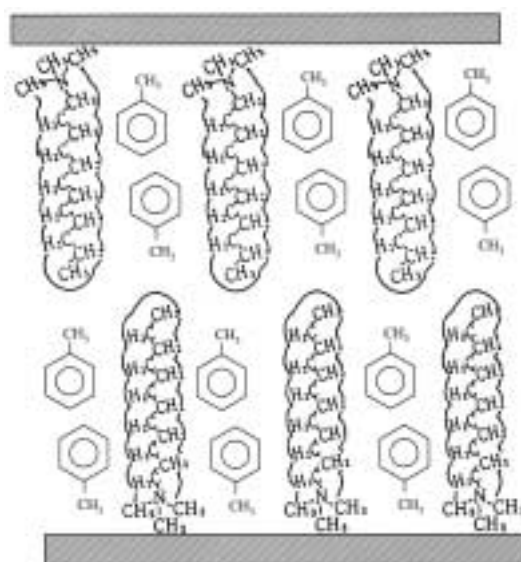


Fig. 4 Swelling model of toluene to montmorillonite intercalated by trimetyldodecylammonium cations. (modified from Fukushima [19]).

ers for the purpose of achieving molecular recognition and reactions that select certain substances. [23, 24] And in view of aim of this paper, our interest is in methods of synthesizing porous materials through inter-layer bridging, which have been researched for the purpose of molecular sieves. We have already noted that various organic and inorganic molecules are adsorbed between the layers of layered clay minerals, where they push the layers apart, but molecules adsorbed between layers are easily desorbed by washing or heating and exhausting. This makes it hard to use inter-layer adsorption compounds as stable molecular sieves. In that regard, ion-exchanging inter-layer compounds whose intercalated cations maintain a balance with the negative charge of layers will exist stably between the layers unless inter-layer ions undergo exchange or separation reactions with other ions. Shabtai et al. [25] and Mortland et al. [26] reported on inter-layer compounds that made possible a molecular sieve effect by making pillars of ethylenediammonium ions between montmorillonite layers (**Fig. 5**). This inter-layer compound, whose distance between layers is 0.53 nm, will not break down even if heated to 350°C in air. But in consideration of the usual catalytic reaction or catalyst preparation conditions, organic cation pillars are actually not stable enough as catalysts or carriers. For that reason creative efforts are being made to build sturdy pillars of metal oxides between layers by intercalating inorganic cations. Representative methods include inter-layer bridging by polynuclear inorganic ions, and by sol particles. Using the former method, dropping an alkali into an aqueous solution of a metallic salt will often result in the precipitation of a metal hydroxide. Under conditions in which hydrolysis is insufficient,

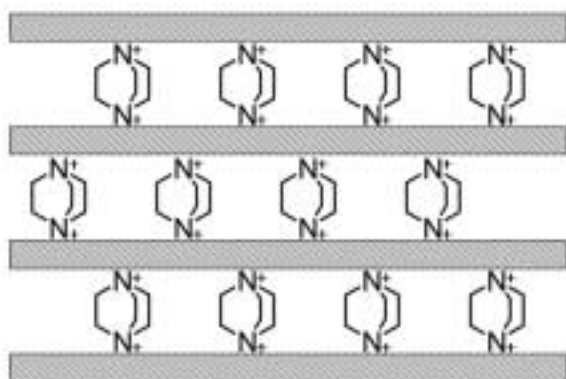


Fig. 5 Schematic model of montmorillonite pillared by ethylenediammonium ions (modified from Mortland [37]).

and just before a precipitate is formed, a number of metal ions gather by using OH group and are present in water as a polynuclear hydroxide ion. [27] Al^{3+} forms a variety of hydroxide ions, sometimes even bulky ions like $\text{Al}_{13}(\text{OH})_{32}^{7+}$. And when $\text{ZrOCl}_2 \cdot 8\text{H}_2\text{O}$ is dissolved in water, hydroxide ions of $\text{Zr}_4(\text{OH})_8^{8+}$ form. A method has been proposed to obtain bridges using metal oxide pillars by intercalating these large metal hydroxide ions between the layers of clay minerals using ion exchange, then firing the compounds between clay layers at high temperature. Brindley et al. [28] and Lahav et al. [29] used this method to prepare a montmorillonite bridge using alumina as pillars. The distance between layers is about 0.75 nm. The specific surface area of this pillared material is about 400 m^2/g , which is far larger than the 20 to 30 m^2/g of montmorillonite before pillaring. It is also reported that inter-layer distance is almost perfectly maintained even at 500°C, showing that thermal stability is also good. Yamanaka et al. [30] created zirconia pillars between montmorillonite layers and obtained an inter-layer compound with an inter-layer distance of 0.84 nm and a specific surface area of about 500 m^2/g . Also reported is a bridge formation method that selectively deposits metal hydroxides only between clay mineral layers, without using ion exchange. Yamanaka et al. [30] prepared nickel oxide pillars between layers and inter-layer distances of 0.52 nm by causing the deposition of nickel hydroxides between montmorillonite layers. Several methods have been devised to intercalate unstable metallic cations in water. For example, ions are introduced between layers in the form of complexes, or first organic materials are inserted between layers, and then the desired ions are introduced. [32]

Synthesis of Aggregate Molecules Pore

From physico-chemical point of view, gas adsorption has a boundary region in which the micropore filling phenomenon and the capillary condensation phenomenon occur. Attention has focused on the unique structure and synthesis method, making this one of the hottest research fields at present. The inter-layer compounds discussed above become pores in this boundary region, depending on the pillar synthesis method. Here we shall discuss a group of synthesis methods for what are known as mesoporous molecular sieves.

Pioneering mesoporous molecular sieves are FSM-16 [33-35] and MCM-41 (M41S) [36, 37], which were synthesized by an American group and a Japanese

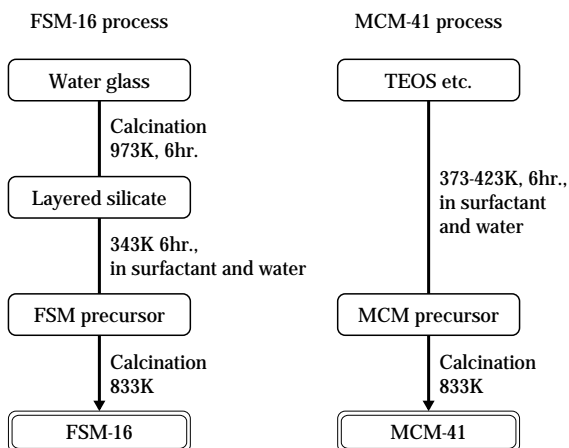


Fig. 6 Comparison of synthesis methods for mesoporous molecular sieve (modified from Beck [37] and Inagaki [38]).

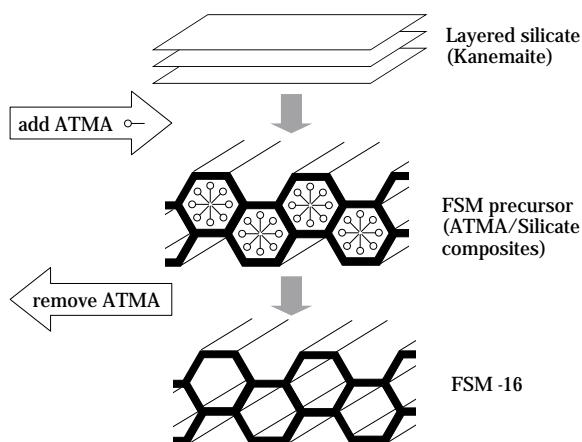


Fig. 7 Schematic model of FMS-16 synthesis (modified from Inagaki [38]).

group, respectively. It is very interesting that these new substances were independently synthesized at about the same time, and it would seem this is closely related to these factors: technical levels had matured to the point making synthesis possible, and there was a strong need for the synthesis of large-pore zeolite.

Fig. 6 is a block diagram illustrating the synthesis processes and conditions of these large-pore zeolite. Basically they are synthesized in a series of operations in which layered silicate, tetraethyl orthosilicate, silica, or other Si feedstocks are heated for several hours to several days at 70 to 150°C in a surfactant aqueous solution, after which the solid products are filtered out and fired at 550°C or higher. When making FSM-16 the process of synthesizing layered silicate comes in the first half. At first glance this appears to be a useless process, but its advantage is that one can obtain a highly crystalline product

with processing at lower temperature and shorter time than MCM-41. **Fig. 7** schematically models the synthesis mechanism of FSM-16. [38] Kanemite is a clay mineral consisting of single-layer silicate sheets having Na ions between layers. [39] Ion exchange introduces alkyltrimethylammonium (ATMA) between kanemite layers, whereupon the silicate sheets bend and form composites with ATMA. Next, dehydration and condensation of silanol radicals bridge the layers, resulting in a three-dimensional framework. This is a new inorganic synthesis method that demolishes the traditional concept of crystal synthesis methods by crystal growth. By contrast, the MCM-41 synthesis method is a process which, like the traditional method of synthesizing zeolite, basically puts the raw materials into a sealed reactor and heats them at a temperature and for a time that are appropriate. This method is illustrated in **Fig. 8**. [37] Varying the

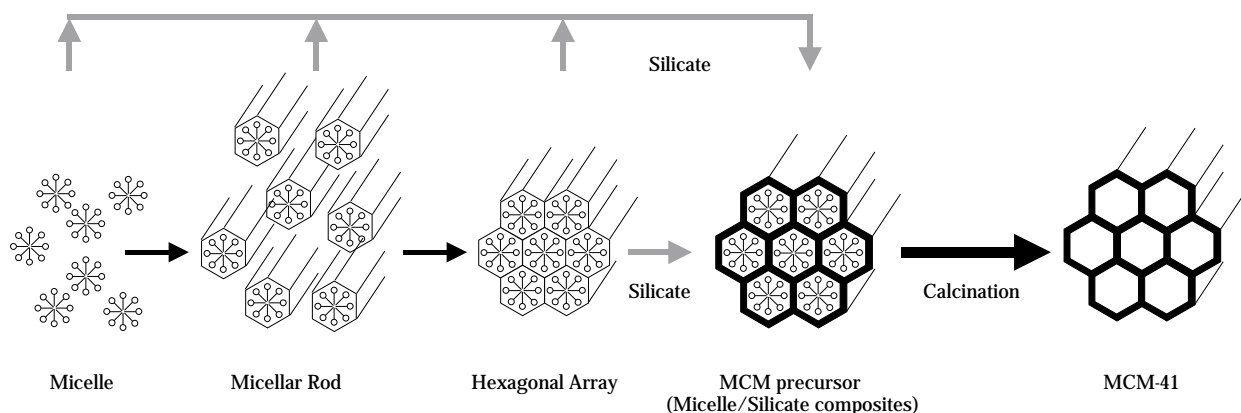


Fig. 8 Schematic model of MCM-41 synthesis (modified from Beck [37]).

ratios of ATMA, Si, and NaOH in the ingredients makes it possible to control the structure into hexagonal, cubic, sheet, and mesostructures. [40, 41] Micelles form when the surfactant exceeds the critical micelle concentration (CMC) in an aqueous solution. It is known that further raising the concentration over the CMC forms self-organizing molecular aggregates (liquid crystals) such as hexagonal, cubic, and sheet forms. [42] This is probably the reason that the mesopore family M41S synthesis mechanism, of which MCM-41 is representative, is known as the “liquid crystal templating (LCT)” mechanism, because the liquid crystal structure of surfactant become as a mold. [37] Like FSM-16, when synthesizing MCM-41 the pore size is controlled by changing the length of the ATMA alkyl chains. [37] And instead of using ATMA, the addition of mesitylene will further enlarge pore size to a maximum diameter of 10 nm. [37]

Little time has passed since these substances were first synthesized, but despite the many reports of applied research, they have yet to see practical use. We hope to see the industrial implementation of these unique structures.

Synthesis of Liquid Phase Pore

Pores discussed in this section are those of the size range in which capillary condensation occurs, and the molecules trapped inside the pores generally behave as liquid. Typical of the porous material manufacturing methods in this area are those which use the unique phenomenon called glass spinodal decomposition, developed by Dow Corning Corp. The typical synthesis process is as follows. [43] SiO_2 , H_3BO_3 , and NaCO_3 are used as the main ingredients to make $\text{Na}_2\text{O-B}_2\text{O}_3\text{-SiO}_2$ -based borosilicate glass, which is

made into forms such as tubes and plates. In these forms it is the borosilicate glass shown in **Fig. 9a**. To separate the phases, the product is then heat-treated at several hundred degrees, which yields a $\text{B}_2\text{O}_3\text{-Na}_2\text{O}$ -rich glass phase and a SiO_2 -rich glass phase whose sizes are on the order of several nm (**Fig. 9b**). The $\text{B}_2\text{O}_3\text{-Na}_2\text{O}$ phase is dissolved in an acid solution or hot water, where dissolution is performed to yield porous glass with a high SiO_2 content (**Fig. 9c**). The result is a porous material whose molded shape is retained and which has countless perforations.

There is also a method of making porous silica materials by inducing phase separation with a chemical trigger. Nakanishi et al. [43] report on a method that uses water-soluble polymers to induce phase separation in a sol-gel silica system. Water-soluble polymers can be classified into two groups. First, as is typical of polyacrylic acid, polymers having comparatively weak attractive interaction with silica are mainly partitioned into a different phase from silica when phase separation occurs, and the polymer-rich phase forms pores. Second, surfactants, and polymers that include polyoxyethylene units are partitioned into the same phase as silica owing to the formation of hydrogen bonds with silanol radicals. Therefore it is mainly the phase comprising the solvent phase that becomes pores. There are also reports that various pore sizes and structures can be obtained by adjusting hydrolysis conditions and solvent polarity. [45] **Fig. 10** shows the steps in the synthesis method. Silicon alkoxide (tetramethoxysilane, TMOS or tetraethoxysilane (TEOS)) is blended into a mixture of an acid catalyst and a solution in which an organic polymer is uniformly dissolved, and a hydrolysis reaction yields a product which is then gelled and matured under sealed conditions. After performing solvent

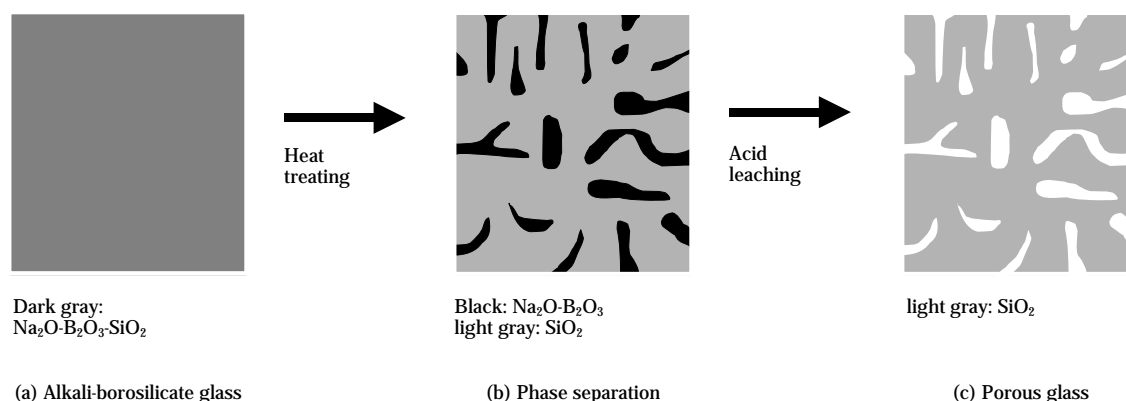


Fig. 9 Production process for porous glass (modified from Makishima [43]).

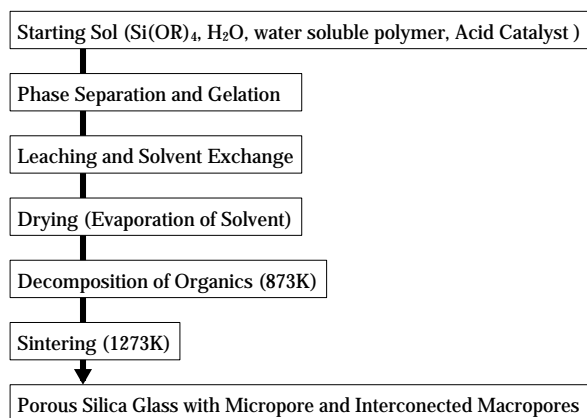


Fig. 10 Synthesis of porous glass by chemical phase separation (modified from Nakanishi [45]).

exchange if necessary, it is dried to obtain a porous material. The porous silica produced by this method finds increasing use as monolithic HPLC columns and in biology-related fields.

Synthesis of Spatial Pore

This is a group of porous materials with so called macropores, a range of pore sizes in which the capillary condensation phenomenon is no longer observed physico-chemically. For that reason pore characteristics are assessed mainly with the mercury porosimetry. Additionally, such materials have been made for a long time, and applied in many ways. There are many industrially important materials. Diatomaceous earth, which is the skeletons of diatoms, is well known as a natural mineral of this group having uniform pores of about 1 μm . The diatomaceous earth, after having been fired organic contents, is applied to filtering auxiliary for brewer's yeast, and moisture-adjusting building materials. [47] Various methods of making artificial macroporous materials include primitive methods that simply use the interstices between particles, methods that maintain the pores in a formed material by low-temperature sintering, and methods that impregnate organic objects having reticulate structures with ceramic slurry, then firing to eliminate the organic material and leave pores (replica method). [48] Another method entails embedding a ceramic or polymer matrix in the interstices of a packed particle structure, then removing the particles by either firing or using a solvent to dissolve them out. [49-51] With this method, pore size and structure are determined by the particle size and coordination number. When a structure is uniformly packed with

particles of a uniform size, uniform macropores will be formed. This method is spotlighted also as a method of making gas sensors and bioceramics. [52] A similar method is proposed that uses fibers in place of particles. Here we shall discuss methods using new and old forming agents, and the synthesis of porous materials using an in situ solidifying method, which is promising as a new porous material manufacturing process.

Autoclaved lightweight concrete (ALC) is one porous material made with blowing agents. ALC is a material derived from the sand-lime bricks that were long manufactured in Europe. It is made from about the same raw materials as the bricks, and is impregnated with bubbles for lightness. ALC was first made in 1929 by the Swede Ytong, and similar techniques then spread to other regions, primarily in Europe. In 1963 it came to Japan and its use widened. Common to these manufacturing methods is autoclave processing that uses siliceous and calciferous materials, but raw materials vary from one company to another.

We shall describe A manufacturing process. [53] The raw materials silica (50 to 70%), quicklime (5 to 20%), portland cement (10 to 40%), gypsum dihydrate (2 to 10%), and metallic aluminum (under 0.1%) are made into a slurry, which is put into molds after kneading well. The quicklime slurry is digested and becomes slaked lime, and the cement begins hydration. As this time, the metallic aluminum serving as the blowing agent evolves hydrogen gas, resulting in green body that are lightweight owing to the bubbles produced by forming. After demolding, the green body are cut to the prescribed thickness and treated for 5 to 10 h in an autoclave at about 180°C and under saturation vapor pressure, yielding finished ALC products. In terms of chemical reactions, at the green body formation stage the ALC manufacturing process involves mainly the hydration of cement that forms high-calcium-content calcium silicate hydrates and $\text{Ca}(\text{OH})_2$. High-calcium-content calcium silicate hydrates are also formed at the autoclaving stage. It is thought that hydrothermal reactions finish when the CaO supply is completely consumed, which means that some of the silicate in the SiO_2 supply is left unreacted. Usually the silica reaction rate is thought to be 40 to 60%. A major drawback of ALC is its water absorptivity. Its water retention has adverse effects such as freezing damage. Recently innovative steps are taken, such as making the product water-repellent.

Of particular interest in recent years as a forming metal manufacturing method is the slurry forming

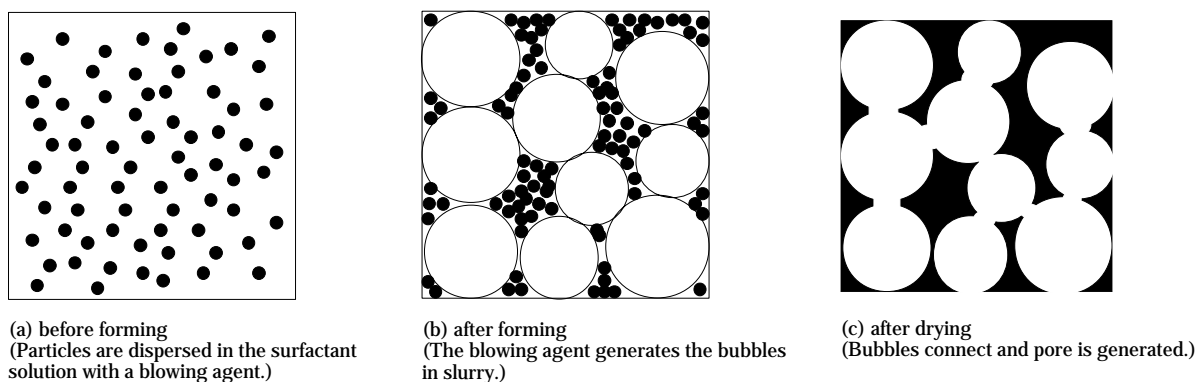


Fig. 11 Generation mechanism of pore by using blowing agent (modified from Wada [56]).

method. [53] In this method, a surfactant and an evaporating forming agent (a hydrophobic volatile organic solvent) are added to a water-based slurry containing metal powder. After formation, the forming agent is volatilized and its vapor pressure directly forms bubbles in the slurry. This is dried, degreased, and sintered to yield the final product. The pore size is controlled in the slurry forming process, whose mechanism is pictured in **Fig. 11**. A slurry is created with a water-based binder, and a surfactant and forming agent are added in amounts sufficient to form bubbles in the entire slurry. The surfactant makes the forming agent dissolve into the slurry, and the particles disperse (**Fig. 11a**). Raising the temperature causes the forming agent to gradually volatilize and form bubbles (**Fig. 11b**). The aqueous surfactant solution membrane makes the bubbles into isolated bubble aggregates, and the metal powder agglomerates in the spaces between bubbles. In the subsequent drying process the bubble aggregates arrange themselves in a three-dimensional reticulate configuration, and the solid components form a spongelike structure (**Fig. 11c**). Exercising strict control over slurry viscosity, surfactant types, forming agent amount, forming time, drying time, and other factors makes it possible to create various pore sizes and pore structures.

There is also a unique method known as solid-gas eutectic solidification that uses gas solubility to make metallic porous materials called gasars. This method takes advantage of the fact that when the solubility of gas atoms in a molten metal is high, but their solubility in the same solid metal is low, the gas atoms that could not completely dissolve when the metal solidified become bubbles. [55] Just as with the hydrogen gas solubility in Mg, Ni, Fe, Cu, Al, Co, W, Mn, Cr,

Be, and Ti, or alloys of these, metals which have large gas solubility differences between their solid and liquid phases readily form bubbles and yield porous products. It is also possible to control the orientation in which pores are formed by making a certain part of the mold cool, which cools the molten metal in a certain direction after it is put into the mold. **Fig. 12** schematically illustrates a mold constructed so that the bottom is partially cooled, and the product obtained with that mold. Making porous products with this method allows one to freely control pore orientation, pore size, and porosity by controlling a variety of parameters including melting temperature, cooling rate, pressure of ambient gas while being dissolved into metal, mixing volumetric ratio and pressure of inert gas, and gas pressure when solidifying. [56]

We shall now discuss methods of synthesizing porous materials by using *in-situ* solidification, developed as a gel casting method by Oak Ridge National Laboratory in the US. [57, 58] This method entails preparing a ceramic slurry into which monomers

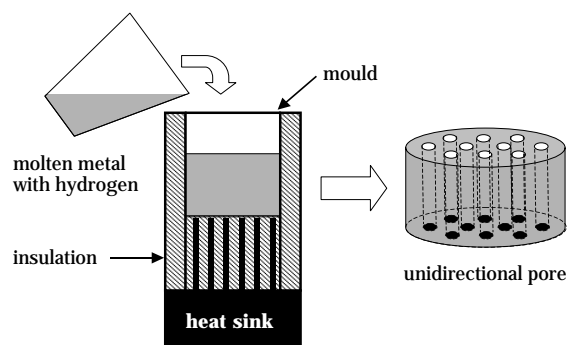


Fig. 12 Apparatus for solid-gas eutectic solidification and porous material (modified from Nakajima [56]).

have been dissolved, putting the slurry into non-porous molds, and then polymerizing the monomers, resulting in the formation of a polymer network in the dispersed medium, and yielding a molded wet product. This method offers the following advantages. [59] (1) Because slurry production is basically the same as casting, the method can be used if a high-concentration slurry is made; (2) molds of complex forms can be used, and near-net shaping is possible; (3) because the fluid and solidification processes can be kept separate, and because the ceramic particles are fixed in situ, unevenness and flaws occur in molded products only with difficulty; and (4) the small amount of organic binder in the molded product makes degreasing easy.

The in situ solidifying method makes it possible to obtain porous products because its series of processes introduces bubbles into the pre-polymerization slurry and then begins polymerization. [60] We explored the use of this method in creating porous ceramic materials which have high porosity and whose pore structure is controllable, and we succeeded in raising porosity to 80% or more even though it was limited to 50% with traditional methods.

We further reported that it is possible to control porosity, pore size, and other properties by taking into consideration the type of frother and the polymerization time. [61] In terms of strength as well, this method is superior to low-temperature firing and the replica method because in low-temperature firing the matrix does not completely assume a minute structure, and because with the replica method small cracks form in the matrix when the large amount of organic material decomposes. Innocentini et al. [62] report that porous materials made by gel casting have higher strength than those made by the replica method.

Fig. 13 shows the basic process of a porous material synthesis method that employs in situ solidification. First, a slurry of ceramic powder, distilled water, monomers, and other ingredients is prepared. A surfactant is added as a frother, and foaming is induced by mechanical stirring. A polymerization initiator and a catalyst are then added to the bubble-impregnated slurry, after which it is poured into molds. After hardening, the molded wet product is demolded, dried, degreased, and fired to yield a sintered porous product.

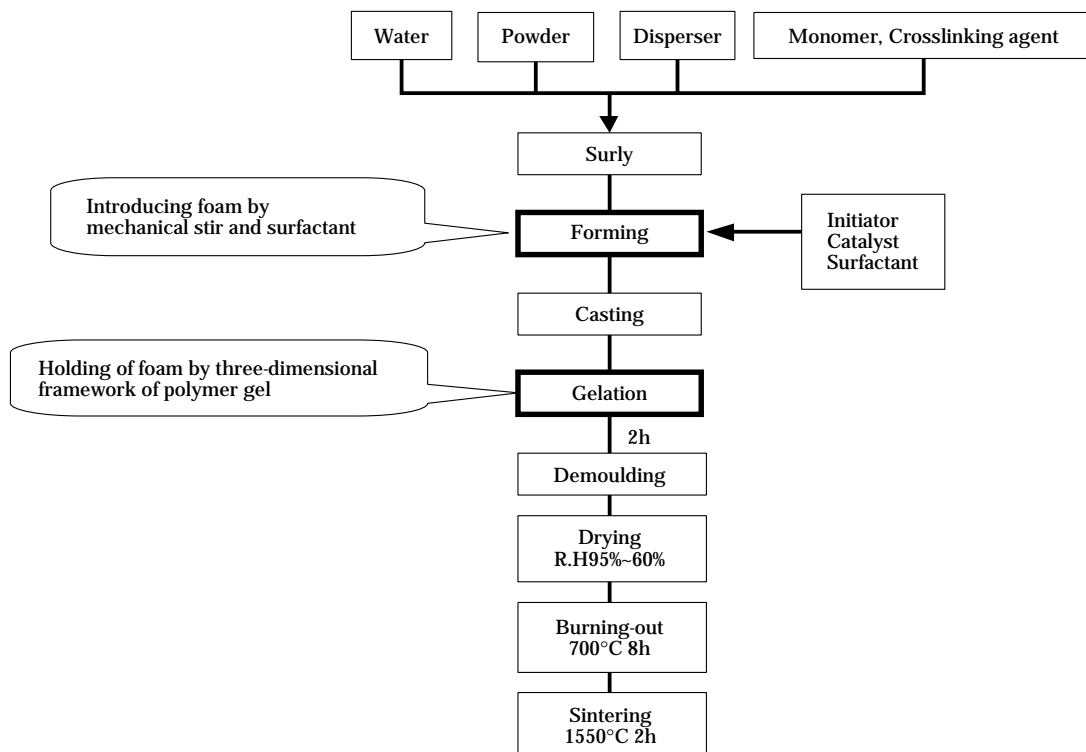


Fig. 13 Fabrication route of porous solid material by applying in situ solidifying method (modified from Sepulveda [60]).

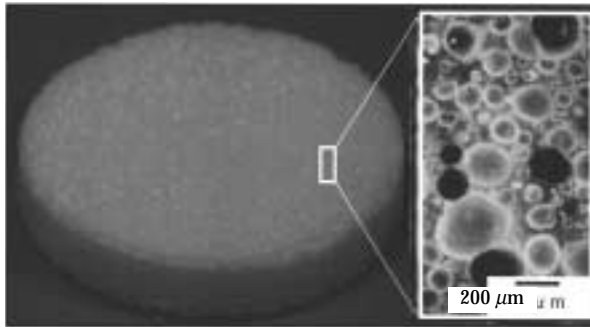


Fig. 14 Porous ceramics prepared by in situ solidification forming technique.

Fig. 14 shows a porous item made with this method. Research and development are underway for applications of these porous materials as high-temperature filters and various ultra-light building materials. It is also thought possible to create processes which take into consideration resource-cycling systems that include the productive use of wastes as raw materials, and reduced energy use. We hope that in the near future readers will find in their midst porous materials made with this method.

Conclusion

Porous materials can be conceived as composites whose first component is their solid portions, and whose second component is the air phase in their pores. Hence it is perhaps beneficial to incorporate composite characteristics and function expression mechanisms as guidelines for designing porous materials. While dispersed composites assume various structures depending on the properties, state, and form of their materials, two-phase composites are classified by the structural models in **Fig. 15**. [63] As this shows, the spatial connection state of each component, which can assume the zero, first, second, or third dimension, determines the type (m-n) of composite by the connection order of each component. Usually m is assigned to the functional component and n to the inactive component. For example, in a (0-3) type composite the functional component is isolated and dispersed, and the matrix component is connected in three dimensions. In other words, this porous material can be seen as having closed pores. Here we have shown only the structures, but readers can see that many other findings on composite materials can be turned to use as shared concepts for the development and manufacture of porous materials.

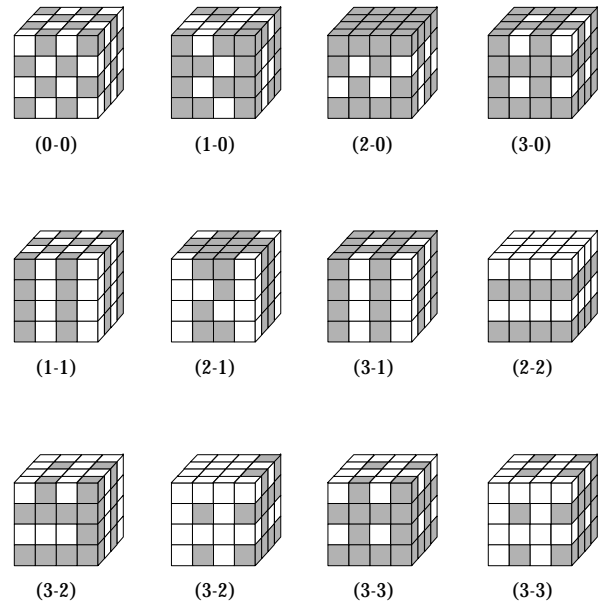


Fig. 15 Classification of two-phase composite. (From Newnham, Skinner and Cross [63])

The functions of porous materials are affected not only by pore size, but also by pore structure and other attributes. Incorporating methods of analyzing composites' physical properties should bring about progress in the assessment and analysis of porous materials. While our insufficient efforts are partly to blame for not being able to include these here, another reason is that often a number of factors underlie the function expression mechanisms of porous materials, and they have yet to be sufficiently analyzed. From another perspective this suggests the possibility of discovering many as yet unknown porous material properties.

This has been a review of porous materials that interest the authors. We hope this explanation will help people who are working on the design of new porous materials.

Acknowledgment

The study of super-light porous construction materials prepared by an in situ solidification forming technique was financed under a contract from the Ministry of Economy, Trade and Industry as a part of Industrial Science and Technology Research and Development.

References

- 1) Shibazaki, Y. *Ceramics*, **37**, 317 (2002).
- 2) Ishida, K. *Inorg. Mater.*, **4**, 507 (1997).
- 3) Toray Research Center, Japan. "New Development of Porous Ceramics," p. 5 (1998).
- 4) Matsukata, M. *Surface*, **15**, 385 (1996).
- 5) Rice, R. W. *Porosity of Ceramics*, Dekker, p. 44 (1998).
- 6) Sing, K. S. W., D. H. Everett, R. A. W. Haul, L. Moscou, and R. A. Pierotti. *Pure Appl. Chem.*, **57**, 603 (1985).
- 7) "Colloidal science I," *Chem. Soc. Jpn. Japan*, p. 275 (1995).
- 8) Kaneko, K. *J. Mem. Sci.*, **96**, 59 (1994).
- 9) McBain, J. W. *The Sorption of Gases and Vapors by Solids*, Rutledge, London (1932).
- 10) Sano, T., Y. Kiyozumi, M. Kawamura, F. Mizumaki, H. Haraya, T. Mouri, W. Inaoka, Y. Toida, M. Watanabe and K. Toyoda. *Zeolites*, **11**, 842 (1991).
- 11) Sano, T., F. Mizukami, H. Takaya, T. Mouri and M. Watanabe. *Bull. Chem. Soc. Jpn.*, **65**, 146 (1992).
- 12) Kiyozumi, Y., I. Mukoyoshi, Y. Sano, and F. Mizukami. *Bull. Chem. Soc. Jpn.*, **65**, 877 (1992).
- 13) Tsikoyiannis, J. G. and W. O. Haag. *Zeolites*, **12**, 126 (1992).
- 14) Anderson, M. W., K. S. Pachis, J. Shi, and S. W. Carr. *J. Mater. Chem.*, **2**, 255 (1992).
- 15) Kiyozumi, Y., K. Maeda and F. Mizukami. *Stud. Surf. Sci. Catal.*, **98**, 278 (1995).
- 16) Seike, T., M. Matsuda, and M. Miyake. *J. Mater. Chem.*, **2**, 366 (2002).
- 17) Kuznichi, C. T., et al. *Nature*, **412**, 720 (2001).
- 18) Norrish, K. *Disc. Faraday Soc.*, **18**, 120 (1954).
- 19) Fukushima, Y. *Surface*, **7**, 233 (1994).
- 20) Watanabe, T. and T. Sato. *Clay Sci.*, **7**, 129 (1988).
- 21) Fukushima Y. *Clays Clay Miner.*, **32**, 320 (1984).
- 22) Viani, B. E., P. F. Low and C. B. Roth. *J. Colloid Inter. Sci.*, **96**, 229 (1983).
- 23) Kijima, T. *Inorg. Mater.*, **3**, 147 (1996).
- 24) Segawa, K. and Y. Ban. *J. Surf. Sci. Soc. Jpn.*, **16**, 680 (1995).
- 25) Shabtai, J., N. Frydman, and R. Lazar. "Proc. 6th Intern. Congr. Catal.," Chem. Soc., London, p. 660 (1976).
- 26) Mortland, M. M. and V. Berkheiser. *Clays Clay Miner.*, **24**, 60 (1976).
- 27) Baes, C. F., Jr. and R. E. Mesmer. *The Hydrolysis of Cations*, John Wiley, New York, p. 419 (1976).
- 28) Brindly, G. W. and R. E. Semple. *Clay Miner.*, **12**, 229 (1977).
- 29) Lahav, N., U. Shani, and J. Shabtai. *Clays Clay Miner.*, **26**, 107 (1978).
- 30) Yamanaka, S. and G. W. Brindley. *Clays Clay Miner.*, **27**, 119 (1979).
- 31) Yamanaka, S. and G. W. Brindley. *Clays Clay Miner.*, **26**, 21 (1978).
- 32) Endo, T., M. M. Mortland and T. J. Pinnavaia. *Clays Clay Miner.*, **29**, 153 (1981).
- 33) Yanagisawa, T., et al. *Bull. Chem. Soc. Jpn.*, **63**, 988 (1990).
- 34) Inagaki, S., et al. *J. Chem. Soc., Chem. Commun.*, 680 (1993).
- 35) Inagaki, S. and Y. Fukushima. *J. Soc. Powder Technol., Jpn.*, **33**, 868 (1996).
- 36) Kresge, C. T., et al. *Nature*, 359, 710 (1992).
- 37) Beck, J. S., et al. *J. Am. Chem. Soc.*, **114**, 10834 (1992).
- 38) Inagaki, S., et al. *Bull. Chem. Soc. Jpn.*, **69**, 1449 (1996).
- 39) Beneke, K., et al. *Am. Mineral.*, **62**, 763 (1977).
- 40) Vartuli, J. C., et al. *Chem. Mater.*, **6**, 2317 (1994).
- 41) Firouzi, A., et al. *Science*, **267**, 1138 (1995).
- 42) Luzzati, V., et al. *Nature*, **215**, 701 (1967).
- 43) Makishima, A. *Surface*, **21**, 105-104 (1983).
- 44) Nakanishi, K. and N. Soda. *J. Am. Ceram. Soc.*, **74**, 2518 (1991).
- 45) Nakanishi, K. *Surface*, **8**, 671 (1992).
- 46) Nakanishi, K. and H. Mizuguchi. *Chem. Chem. Ind.* **55**, 653 (2002).
- 47) Kamigasa, S. "Diatomite and Its Applications in Industry," *J. Soc. Powder Tech., Jpn.*, **39**, 114 (2002).
- 48) Saggio-Woyansky, J., C. E. Scott, and W. P. Minnear. "Processing of Porous Ceramics," *Am. Ceram. Soc. Bull.*, **71**, 1674 (1992).
- 49) Holland, B. T., et al. *Chem. Mater.*, **11**, 795 (1999).
- 50) Carreon, M. A., et al. *Chem. Commun.*, 2001, 1438.
- 51) Soten, I., et al. *Adv. Funct. Mater.*, **13**, 1468 (2002).
- 52) Scott, R. W. J., et al. *Adv. Mater.*, **13**, 1468 (2001).
- 53) Soc. Inorg. Mater., Jpn., *Hand Book of Cement, Gypsum and Lime*, Gihodo, Japan.
- 54) Wasa, M. *Chem. Chem. Ind.*, **54**, 811 (2001).
- 55) Shapovalov, V. I. US Patent 5, 181, 549 (1993).
- 56) Nakajima, H. *Ferrum*, **6**, 33 (2001).
- 57) Omatete, O. O., M. A. Janney, and R. A. Strehlow. "Gelcasting – A New Ceramic Forming Process," *Ceram. Bull.*, **70**, 1641 (1991).
- 58) Young, A. C., O. O. Omatete, M. A. Janney, and P. A. Menchhofer. "Gelcasting of Alumina," *J. Am. Ceram. Soc.*, **74**, 612 (1991).
- 59) Jono, K., T. Hotta, H. Abe, M. Naito, and M. Takahashi. *Ceramic Processing Science VI*, **112**, 459 (2001).
- 60) Sepulveda, P. "Gelcasting Foams of Porous Ceramics," *Am. Ceram. Soc. Bull.*, **76**, 61 (1997).
- 61) Takahashi, M., M. Mizuno, Y. Shiroki, T. Yokoyama, H. Abe, and M. Naito. *Ceramic Processing Science VI*, **112**, 559 (2001).
- 62) Innocentini, M. D. M., P. Sepulveda, V. R. Salvini, V. C. Pandolfulli, and J. R. Coury. "Permeability and Structure of Cellular Ceramics: A Comparison Between Two Preparation Techniques," *J. Am. Ceram. Soc.*, **81**, 3349 (1998).
- 63) Newnham, R. E., D. P. Skinner and L. E. Cross. *Mater. Res. Bull.*, **13**, 525 (1978).

Author's short biography



Minoru Takahashi

Minoru Takahashi is Professor at the Ceramics Research Laboratory, Nagoya Institute of Technology, Gifu. A graduate of the University of Tokyo, he received his B.S. from the Dept. of Mineral Resources Development in 1973, his M.S. from the Faculty of Engineering in 1975, and his D. Eng. from the Faculty of Engineering in 1984. With the Nagoya Institute of Technology since 1975, he has been concerned with ceramic processing and powder technology.



Masayoshi Fuji

Masayoshi Fuji is Associate Professor of Ceramics Research Laboratory, Nagoya Institute of Technology, Gifu. A graduate of Tokyo Metropolitan University, he received his B.S. from the Dept. of Industrial Chemistry in 1989, his M.S. from the Faculty of Engineering in 1991, and his D. Eng. from the Faculty of Engineering in 1999. He joined the Department of Industrial Chemistry, Tokyo Metropolitan University, as a Research Associate in 1991. From 2000 to 2001 he was a Visiting Researcher at the University of Florida Engineering Research Center. He has been with the Nagoya Institute of Technology since 2002. His research interests are surface chemistry, ceramic processing, and powder technology.

The Feasibility of Ferro-alloy fines Recovery by using Centrifugal Separator Technology[†]

A. B. Nesbitt

*Cape Technikon**

S. Wanliss, and F. W. Petersen

*Mintek***

Abstract

The effect of an increase in gravitational force on the separation of a binary (different densities) mixture of particles in a centrifugal separator is investigated. An algorithm calculates the effect an increase in gravity has on improving separation using established particulated fluidised bed models. These results are compared to separation data generated by a continuous centrifugal separator.

Introduction

The development of a number of batch and continuous centrifugal separators over the past twenty years has resulted in the widespread use of these instruments in the gold mining industry [1]. Formerly, the industry was faced with the problem of removing free gold particles that entered the circuit of a typical gold plant, causing increased gold hold-up, spiking and a general drop-off in efficient recovery. There are many examples of gold plants that have solved this problem by the introduction of a centrifugal separator in a bleed stream of the mill product circuit, effectively scalping the free gold particles before they enter the leach train. Base metal plants that use flotation to recover copper, zinc and lead concentrate tend to lose trace amounts of gold that may enter the circuit if present in the mine ore body. The heavier gold particles tend to migrate to the tailings of the flotation cells and are lost, thus eliminating a potential source of revenue for the mining company. There are a number of examples where the use of centrifugal technology effectively improved gold recovery [2]. In one case, the improvement was so marked that the status of the plant changed from that of a base metal to that of a zinc/gold plant [3].

More recent publications have suggested that centrifugal technology could also be used in the recovery of less valuable synthesised minerals [4], i.e. ferro-

chrome from crushed slag dump material. The production of ferro-chrome by reduction in a smelter tends to generate a mixed stratum of matt and slag at the interface. The amount of ferro-chrome present in this stratum is sufficient to warrant processing and recovery. This challenge is common in the ferro-alloy industry and is topical at present. As comminution of this stratum results in total ferro-chrome particle liberation, the removal from the slag particles, which are approximately half the density, should be achievable by gravity/hindered settling techniques. Recent successes in this regard have shown that by gravity separation, most of the ferro-chrome particles larger than 200 microns are easily removed [5]. The same cannot be said for the fully liberated, sub-200-micron, ferro-chrome particles, which is where the bulk of the post-comminution ferro-chrome particles are found. **Figure 1** gives the mass percentage per size fraction of ferro-chrome in a typical 750-g grab sample taken from the tailings of a Titaco (slag dump material) processing plant. We observe that some 60% of the ferro-chrome particles are in the sub-200-micron range and have not been removed by conventional gravity separation, i.e. jigs. It is also apparent that approximately two percent of the entire sample is ferro-chrome. At an approximate market value of 1000 USD per tonne of ferro-chrome, this represents a calculable loss to the plant. It is reported that a similar loss occurs with other ferro-alloy producing plants.

In this paper it is assumed that the hindered settling zone found in a centrifugal separator is comparable to a fluidised bed approaching steady state. Our intention is to simulate the behaviour of such a bed

* P. O. Box 652, Cape Town 8000, South Africa

** Mintek, Private Bag X3015, Randburg, 2125, South Africa

[†] Accepted: June 5, 2002

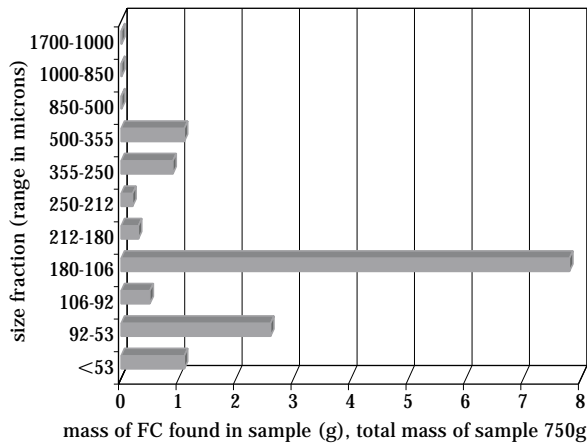


Fig. 1 Mass of Ferro-Chrome in the tailings of a Titaco processing plant

using typical fluidised bed mathematical models, accommodating the increase in gravity that would be the norm in a centrifugal separator. The density and general physical properties of chromium oxide (Cr_2O_3), with an RD of approximately 7.0, was deemed to be very similar to that of the majority of ferro-alloys and therefore, in the theoretical study and test work, this material was considered to be the valuable/recoverable material. Metal/silica oxides with RDs of approximately 3.0 were considered to be the gangue material. An algorithm was employed to simulate the fluidised mixed bed of these two species that demonstrably showed the presence of three zones: an upper zone, where only the lower density species is present (metal/silica oxides); a middle zone comprising a mixture of both species; and a lower zone containing only the higher density species (ferro-alloy). Having established this simulation in the form of a software package, the effect of an alteration in gravity could be observed. These results were then compared to those achieved by a centrifugal separator in chromium-oxide recovery duty.

Theory

The failure of gravity equipment to efficiently recover the sub-200-micron ferro-chrome particles by hindered settling can be attributed to two phenomena. The first is that the system is clearly in Stokes-laminar-settling regime. Calculation of the terminal velocity Reynolds numbers in water of the sub-200-micron ferro-chrome particles proves this. These can be estimated using a simple terminal velocity relationship proposed by Hartman *et al* [6], and are all less

than 14 for the sub-200-micron range. Classification under normal gravity will therefore be inefficient. The second challenge is the blinding effect of the free settling ratio of the ferro-chrome to slag particles. The presence of a skew distribution of particles results in the probability that the hydrodynamic characteristics of the sub-200-micron ferro-chrome particles are likely to be emulated by larger less dense slag particles. Assuming Stokes regime and that the ferro-chrome/slag particles are spherical, it may be calculated that a slag particle in the 16 to 320-micron range will emulate the terminal velocity of a ferro-chrome particle in the 10 to 200-micron range.

Common knowledge holds that by increasing the gravity forces (increasing terminal velocity of the particles) on a hindered settling system, the first challenge, i.e. the presence of Stokes settling regime, can be overcome. This can be achieved by a centrifugal-gravity separator. The blinding effect, as understood from the perspective of Stokes' or Newton's hindered settling equations, clearly shows that a sufficient increase in gravitational force will cause the hydrodynamics of a hindered settling system to change from the laminar settling regime to the turbulent, effectively altering the blinding ratio. It can be calculated that in the case of a switch from Stokes' to Newton's regime, the average ferro-chrome particle would now be blinded by a larger slag particle than was the case in the Stokes' regime. The removal of larger slag particles by means of screening after the application of conventional gravity separation (jigs) should lead to improved recoveries by subsequent treatment with high-gravity centrifugal separation. Examination of a centrifugal separator would indicate that the hindered settling zone is comparable to a fluidised bed approaching steady state, under severe gravity. **Figure 2** clearly shows how a mixture of particles of different

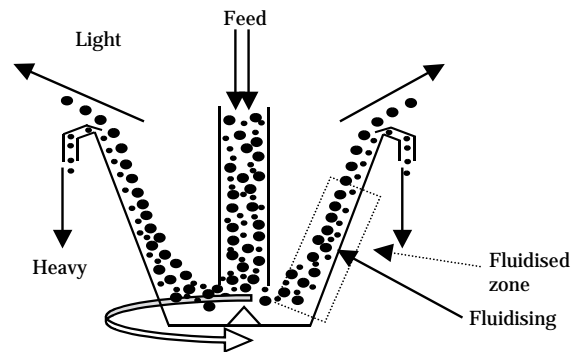


Fig. 2 Typical centrifugal separator mechanism

densities moves through a centrifugal separator, with the denser particles tending to move closer to the rotating wall while the less dense tend to migrate over the top of these particles under the influence of centrifugal forces. Fluidising water enters the separator through the rotating wall, effectively causing a fluidised bed at higher gravity.

Traditional fluidisation expansion models for particulate fluidisation correlate the voidage (e) of a system to the superficial fluid velocity (U) and the Galileo Number of the particles, which itself is closely related to terminal velocity (U_t).

These correlations are summed up in the Richardson and Zaki equation [7]:

$$U = U_t e^n \quad \text{Eq. 1}$$

where n is a function of the Galileo Numbers of the particles present.

The application of this model has traditionally been by means of the averaging [8], serial [9], or cell model [10] techniques. The model of Nesbitt and Petersen [11] has been shown to effectively predict the expansion of a fluidised bed of polysized spherical particles, and relies entirely on the serial model philosophy and an original technique for application.

The model of Nesbitt and Petersen [11]:

$$E_t = 1 + \int_{dp=s}^{dp=l} G(dp) \left(\frac{1 - e_{fws}}{1 - [U/F(dp)]^{1/n}} - 1 \right) d(dp) \quad \text{Eq. 2}$$

where $F(dp)$ is the terminal velocity function for the particle size range

$G(dp)$ is the function correlating particle size to bed mass fraction, and

s, l refer to the smallest and largest particle present, respectively (m).

In application, this model validates the assumption that a fluidised bed in an expanded state is a serial combination of the expansion of each particle size class. Each size class contributes to the overall extent of expansion to the same degree as it would demonstrate if isolated, with all other physical aspects remaining unchanged. The cell model was proposed by Patwardhan and Tien [10], where they show how each particle demands a certain volume around itself depending on its own physical properties and those of the fluid. This combination of the mass of particle and required void is said to act as a discrete finite element with a volume and density. An element located at the bottom will have the highest cell density of all elements in the bed. Cell density decreases with increased height in the bed, and the cell with the lowest density is found at the top. The stratification of

particles on the basis of size for a large particle size distribution was observed by Al-Dibouni and Garside [12]. No reference could be found in the literature effectively testing traditional fluidisation/bed expansion mathematical models in a gravity field other than that of $g=9.81 \text{ m.s}^{-2}$. However, for the purposes of this study, the simulation of a change in gravity force was deemed to be achievable by altering the g term in the Galileo Number, for the purpose of determining the n value in Eq. 1 and the terminal velocity of each particle present. Assuming the models of Nesbitt and Petersen [11] and of Patwardhan and Tien [10] to be effective, it now becomes possible to define the vertical position of a discrete cell relative to the total height of the bed on the basis of its density. It has already been stated that the discrete element density decreases with bed height, and assuming perfect stratification, which is reasonable for a large particle size distribution [12], the density of a discrete element is a function of particle size distribution and particle density, both of which are well defined.

An algorithm was produced in the form of a computer program that simulated the separation of the binary mixture of particles with each species possessing two distinct particle size distributions. A schematic diagram of the algorithm is given in **Figure 3**. To calculate the mass of particles that would be present in the mixed (central) zone, it is necessary to establish its vertical boundaries. The steady-state position of the largest of the less dense particles (dp_{1L}) would make up the lower boundary, while the smallest of the more dense particles (dp_{2S}) would form the upper boundary of this mixed zone. At a given flow rate the voidage for the largest particles of the less dense species (dp_{1L}) is calculated and consequently the bulk density of the associated discrete finite element is attained. The same calculation is achieved for the smallest particle of the denser species (dp_{2S}). The density of the discrete finite element in each case was thus judged to be the boundary density for the lower and upper boundaries, respectively. Once these boundaries were set, the bulk density of the discrete finite element associated with every particle class of both species present was calculated. If it fell between the boundary limits, the associated particle was judged to be part of the mixed zone. The particle size distribution of each species had to be defined and this was achieved by examining typical raw data. The particle size distributions of the two species were considered to be of a continuous nature and hence spline routines were used to represent each. The spline routines developed were impor-

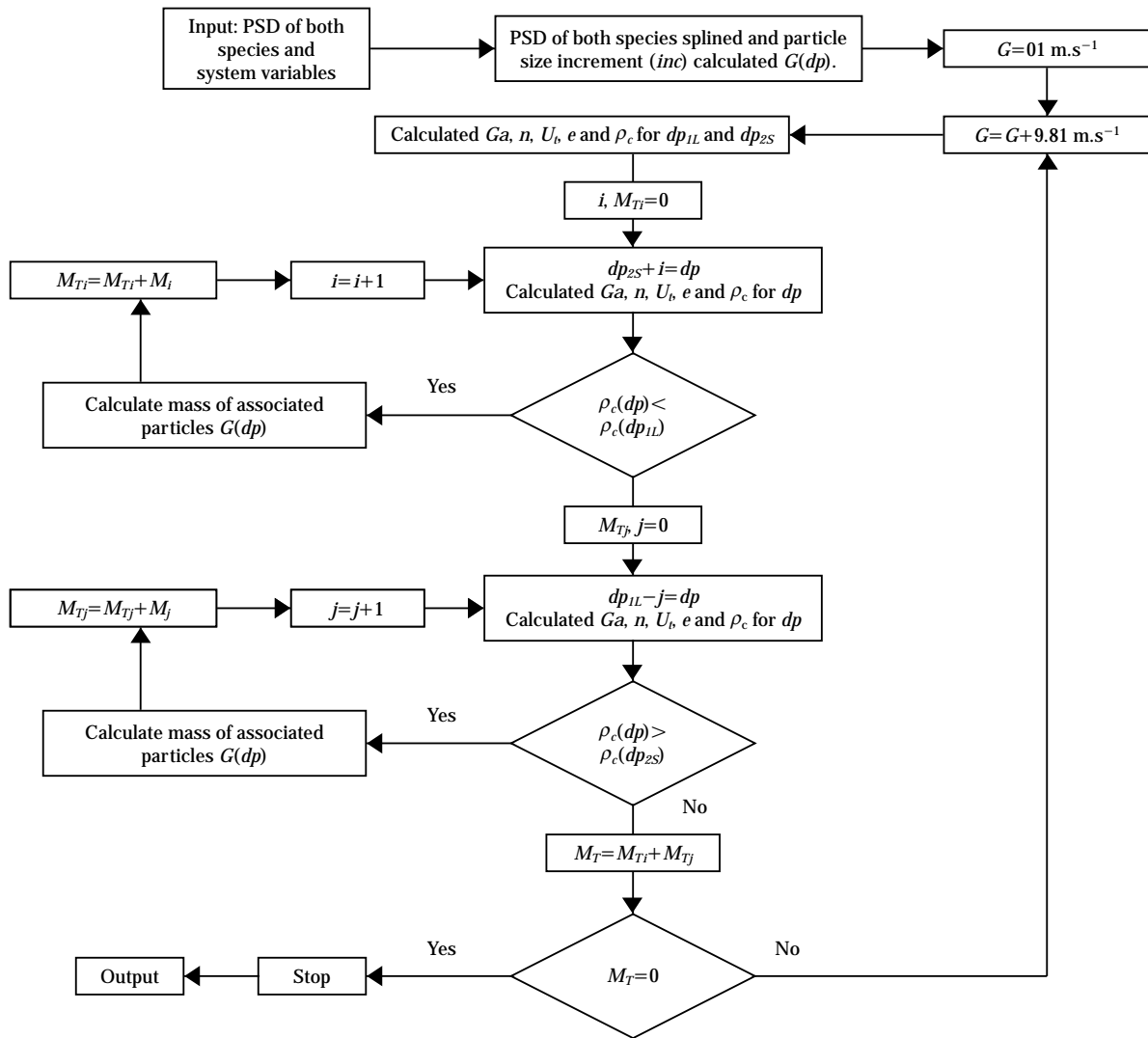


Fig. 3 The algorithm used to determine the mass of particles in the mixed (central) zone

tant for determining functions $F(dp)$ and $G(dp)$ for each species.

The calculation of the bulk density of each discrete finite element was achieved by using Eq. 3. Initially the voidage (e) is calculated by applying Eq. 1 discretely to every particle size class.

$$\rho_c = (1 - e)\rho_s + e\rho_f \quad \text{Eq. 3}$$

where ρ_c is the relative density of the discrete finite element

ρ_s is the intrinsic relative density of the solid particle

ρ_f is the relative density of the fluid.

Results and discussion

Figure 4a diagrammatically represents particles of both species on a mass basis that will migrate to the mixed zone – area between dotted lines – under a gravity force of one. The vertical component in the diagram refers to successive cell densities with the highest density cell being at the bottom and the lowest at the top. The simulation was then repeated at higher gravity forces, primarily to observe the influence this had on the mass of particles migrating to the mixed zone. **Figure 4b** shows the characteristic reduction in the mass of particles migrating to the mixed zone, observed for any increase in gravity. For all simulated gravity forces in excess of normal grav-

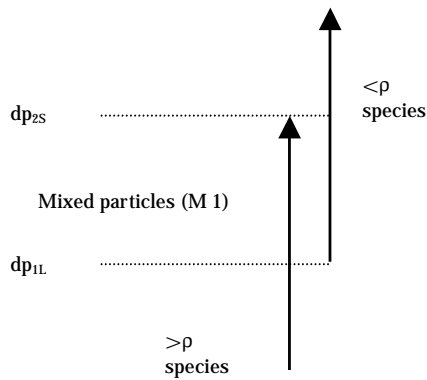


Fig. 4a shows the mixed bed under normal gravity

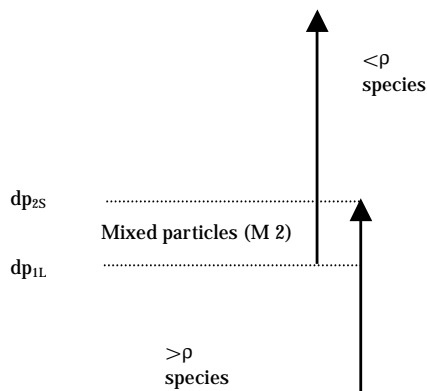


Fig. 4b is the identical system to **4a**, experiencing increased gravity.

ity, less mass migrated to the mixed zone. The fluidising medium used in the simulation was given the physical characteristics of water.

Certain parameters that would be present during centrifugal separation could not be brought into the simulation. An example is the mass pull of denser material that is an independent setting likely to have an influence on the efficiency of separation. An increase in this setting is likely to move the system away from steady-state fluidisation. The setting is normally presented as a “time duration” within a fixed time cycle for which the concentrate valve remains open, allowing denser material to leave the centrifugal separator. This oscillation effectively controls the changing ratio, at which the two species migrate through the centrifugal separator, relative to each other. In addition, the violent nature of the centrifugal phenomenon could well cause a greater degree of mixing than would be present in a steady-state fluidised bed experiencing a mild increase in gravity

force. **Figure 5** is a typical result developed by the simulator. It assumes the mass of particles present in the mixed zone at a gravity of one to be 100%, and effectively shows how a mixed fluidised bed experiencing an increase in gravitational forces results in a decrease in the mass of particles present in the mixed zone. It is notable that perfect separation is achieved relatively quickly at a gravitational force equivalent to an acceleration of 24.81 m.s^{-2} , and is an indication of the level of efficiency that could be achieved by a centrifugal separator.

From the results of test work carried out on a chromium oxide/silica oxide mix passed through a centrifugal separator, an improvement in separation with increase in gravity was clearly observed.

Table 1 gives the percentage of chromium oxide in the feed to migrate to the concentrate versus gravity. The gravity acceleration was calculated from the revolutions per minute of the centrifugal separator.

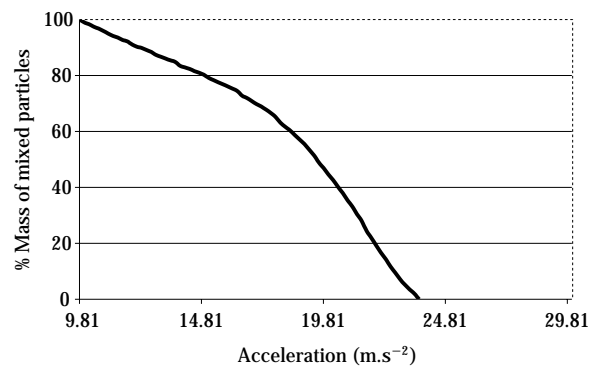


Fig. 5 % Mass of mixed particles

Table 1 Percentage chrome oxide fed to a Knelson concentrator (CVD) reporting to concentrate

Generated increased gravity as acceleration (m.s ⁻²)	Total chrome oxide in feed reporting to concentrate %
392.4	50.4
588.6	67.5
882.9	87.6

Conclusion

The simulation proves that existing fluidisation models can be used to show the improvement in separation under artificially increased gravity. However, the lack of direct experimentation proving the effec-

tiveness of fluidisation models under these circumstances is notable and can form part of a new study.

The test work categorically shows that an increase in gravity ultimately causes an improvement in classification efficiency for the process challenge presented in this paper. A process that consists of applying conventional-pulse fluidised bed separators (jigs) followed by a screening-off of the larger particles, almost all of which will be slag particles, and finally recovery of the sub-200-micron ferro-alloy in a centrifugal separator is suggested. Unlike gold particles, the low returns that are offered by ferro-alloys on the open market will mean that optimisation of such a process would be required. In addition, the task will be made more complicated by the reality that the mass pulls of the concentrate are much higher than in gold recovery service.

Nomenclature

dp	particle diameter	(m)
dp_{1L}	particle diameter of the largest particle of the less dense species	(m)
dp_{2L}	particle diameter of the largest particle of the more dense species	(m)
dp_{1S}	particle diameter of the smallest particle of the less dense species	(m)
dp_{2S}	particle diameter of the smallest particle of the more dense species	(m)
e	voidage	
e_{fws}	free wet-settled voidage	
E_t	total bed expansion factor	
$F(dp)$	is the terminal velocity function for the particle size range	
g	is gravitational constant	(9.81 m.s ⁻²)
G	increased particle acceleration due to centrifugal forces	(m.s ⁻²)
$G(dp)$	is the function correlating particle size to bed mass fraction	
i	particle size increment of one micron for the denser species	(m)
j	particle size increment of one micron for the less dense species	(m)
l	refers to the largest particle present	(m)
M_T	is the total mass in the mixed zone for a particular gravity	
M_{Ti}	is the mass fraction of the less dense	

	species in a mixed zone	
M_{Tj}	is the mass fraction of the more dense species in a mixed zone	
n	empirical parameter of the Richardson and Zaki equation	
s	refers to the smallest particle present	(m)
U	empty tube linear fluid velocity ($e=1$)	(m.s ⁻¹)
U_t	is the terminal velocity of the particle derived from $F(dp)$	(m.s ⁻¹)
ρ_f	is the relative density of the discrete fluid	
ρ_c	is the relative density of the discrete finite element	
ρ_s	is the relative density of the solid particle	

References

- 1) Knelson B.: The Knelson Concentrator: Metamorphosis from crude beginning to sophisticated world wide acceptance Byron Knelson, Minerals Engineering, Vancouver, Canada, 1992
- 2) Ounpuu M.: Gravity concentration of gold from Base Metal Flotation mills. 24th Annual Canadian Mineral Processor Conf., Ontario, Canada, 1992
- 3) Poulter S., Fitzmaurice C., Steward G.: The Knelson concentrator: Application and Operation at Rosebery. 5th Mill Operators Conf., Roxby Downs, Australia, 1994
- 4) Bogdanovich A., Baxilevsky A., Yermakov V., Pugachev V., Samosy A., Moshninov V.: Theoretical aspects of Fine Particle Separation. XXI IMPC, Rome, 2000
- 5) Vorster H.: Titaco/Mintek in ferro-alloys recovery project from slag dump material. Mining Mirror February, 1999
- 6) Hartman, M.; Trnka, O.; Svoboda, K.: Free Settling of Nonspherical Particles. Ind. Eng. Chem. Res., 33, 1994, pp. 1979-1983
- 7) Richardson, J. F.; Zaki W. N.: Sedimentation and fluidisation: Vol. 1. Trans. Instn chem. Engrs., 32, 1954, pp. 35-52
- 8) Wen C. Y., Yu Y. H.: Mechanics of fluidisation. Chem. Eng. Prog. Symp. Ser. Chem. 62, 1966, pp. 100
- 9) Lewis E. W., Bowerman E. W.: Fluidisation of solid particles in liquids. Chem. Eng Prog., 48, 1952, pp. 603
- 10) Patwardhan V. S., Chi Tien: Sedimentation and liquid fluidisation of solid particles of different sizes and densities. Chem. Eng. Science, 40, 1983, pp. 1051
- 11) Nesbitt, A. B., Petersen, F. W.: A model for the prediction of the expansion of a fluidised bed of poly-sized resin. Powder Technology, 98, 1998, pp. 258-264
- 12) Al-Dibouni, M. R., Garside J.: Particle mixing and classification in liquid fluidised beds. Trans IchemE., 1979, 57, pp. 94

Author's short biography



Allan Nesbitt

Allan Nesbitt is presently a lecturer at the Cape Technikon. He has formally held positions at the University of Stellenbosch, Mintek (South African National Institute of Metallurgy), Caltex South Africa and South African Breweries. He received a Masters Degree in Chemical Engineering from the Cape Technikon in 1996. Allan's research interests lie in the fields of mineral processing, the application of artificial-intelligence systems and the mathematical modelling of particulate fluidisation and ion-exchange systems. The latter has already earned him a South African patent. He has published in accredited journals and presented scientific papers, both internationally and locally. In 2001, he received the Cape Technikon award for Most Promising Researcher of the Year, and recently started with a project towards his Doctorate.



Francis Petersen

Francis Petersen is a former head of the Department of Chemical Engineering at the Cape Technikon from 1998 to 2001. Currently, he is a visiting-Professor in the Department. He holds a BEng (Chem), MEng (Chem) and a PhD (Eng) from the University of Stellenbosch. He has published widely in accredited journals. Other academic achievements include being recipient of the Ernest Oppenheimer Memorial Trust Award for research excellence, a study-visit to Singapore on technology transfer and Researcher of the Year at the Cape Technikon. He serves on the South African Government Commission, addressing the problem of toxic waste disposal. Although he presently holds the position of General Manager (Research and Development) at Mintek (South African National Institute of Metallurgy), he is still actively involved in the Chemical Engineering Department in research relating to hydrometallurgy, biotechnology, water treatment and mathematical modelling.



Stephen Wanliss

Stephen Wanliss is currently completing his Masters Degree in the department of Chemical Engineering at the Cape Technikon. He graduated with a bachelor's Degree in Chemical Engineering Technology in 1997. His thesis is on the mathematical modelling of the characteristics of particulate fluidised non-spherical particles in a liquid medium.

Stochastic Aspects of Granular Flow in Vibrated Beds[†]

R. Wildman and J. M. Huntley

Wolfson School of Mechanical and Manufacturing Engineering
Loughborough University*

Abstract

A stochastic approach has been taken to examine the flow behaviour of particles in a vibrated granular bed. The coordinates of a single grain were determined as a function of time using the technique of positron emission particle tracking. Following a particle for extended periods allowed a detailed representation of the displacement probability density to be built up. This showed that, initially, particles dispersed according to a Gaussian law, but that the variation in the solid fraction of grains, their granular temperature and the presence of walls meant that significant distortions were observed over longer timescales. The determination of the displacement probability density allowed the spatial distribution of the granular temperature and the diffusion coefficient to be measured in both mono- and bi-disperse granular systems.

1. Introduction

Interest in granular materials behaviour has steadily grown over the last few decades as the importance of powder technology has been increasingly realised. The challenges to understanding the underlying fundamental mechanisms of granular flow are considerable. Whether the granular materials have been fluidised or are being stored, one finds new phenomena that are not observable in the usual states of matter. For example, in vibro-fluidised granular beds, one finds that the kinetic theory approach is broadly applicable under a range of situations [1], but that important differences arise, principally due to the dissipation and friction during particle collisions [2]. In addition, it cannot be assumed *a priori* that a continuum approach will be appropriate [3]. Much progress has been made in predicting granular flow behaviour using the kinetic theory approach, but until recently however, there has been little experimental validation of these studies at the single particle level. Nevertheless, in the past few years significant research has been undertaken to investigate granular dynamics in two dimensions, and more recently in three dimensions.

Much of the progress in understanding granular flows has been through theoretical and numerical approaches (e.g. see Ref. [4]). Recently though, a number of experimental techniques have been developed to investigate two- and three-dimensional vibro-fluidised granular beds. In two dimensions, a series of experiments by Warr *et al* using high-speed digital photography, demonstrated that highly vibro-fluidised two-dimensional granular beds can operate near to equilibrium, e.g., the granular velocities broadly follow Maxwell distributions [5, 6], and the local structure of the granular bed is similar to that seen in a thermal fluid [7]. Later, a novel method of calculating granular temperature was developed [8] based upon the short-time behaviour of the mean squared displacement, which does not require detection of the collision events. This method was used to measure granular temperature concurrently with determination of the self-diffusion coefficient [1], and subsequently allowed simple kinetic theory approaches to granular beds to be validated [1].

The visualisation of the internal dynamics of three-dimensional granular flows is more challenging than viewing two-dimensional arrays of grains. A number of techniques have recently been developed to probe flows in three-dimensional geometries, including diffusive wave spectroscopy (DWS) [9], magnetic resonance imaging (MRI) [10, 11] and positron emission particle tracking (PEPT) [12]. The authors have recently demonstrated the suitability of PEPT for

* Loughborough, Leicestershire LE11 3TU, United Kingdom
E-mail: r.d.wildman@lboro.ac.uk

[†] Accepted: June 28, 2002

studies of highly fluidised granular beds [13]. In that article, it was shown that variables such as the mean squared displacement and self-diffusion coefficient could be measured, and that for very dilute systems (packing fractions ~ 0.05) the granular temperature could be measured.

In this paper, we demonstrate that stochastic approaches developed for near-equilibrium systems may be employed to develop an improved understanding of granular behaviour. We show that the displacement probability density is a useful measurand and leads naturally to the determination of variables such as packing fraction, granular temperature and the diffusion coefficient.

2. Stochastic Motion in Fluids

If we consider a gas of similar particles undergoing rapid motion and successive collisions, and within that gas we “tag” a small number of the particles, then if the concentration of the tagged particles is negligible, the motion of the tagged particles is equivalent to that of a single particle. In this case, the conditional displacement probability density $P(\mathbf{r}, t)$ and the current $\mathbf{j}(\mathbf{r}, t)$ satisfy the continuity equation [14]

$$\dot{P}(\mathbf{r}, t) + \nabla \cdot \mathbf{j}(\mathbf{r}, t) = 0 \quad (1)$$

and the Fickian constitutive relation

$$\mathbf{j}(\mathbf{r}, t) = -D \nabla P(\mathbf{r}, t) \quad (2)$$

where \mathbf{r} is the position vector of a tagged particle, D is the self-diffusion coefficient and t is the time. Solution of (1) and (2) in the low frequency limit, i.e. $t \gg \tau_E$, where τ_E is the mean time between collisions, leads to the result

$$P(\mathbf{r}, t) = \frac{1}{(4\pi Dt)^{3/2}} \exp\left(-\frac{\mathbf{r}^2}{4Dt}\right). \quad (3)$$

The mean squared displacement can be calculated from this probability density function in the usual way (see e.g. Ref. [14]) and leads to the well-known Einstein relation

$$D = \lim_{t \rightarrow \infty} \frac{1}{6t} \langle |\mathbf{r}(t) - \mathbf{r}(0)|^2 \rangle. \quad (4)$$

However, this analysis is only true for unbounded, homogeneous systems such as an unconstrained thermal gas or fluid. In a granular system, the presence of gravity, as well as causing acceleration between collisions, results in a varying packing fraction profile in the vertical (y) direction, and so D is actually a position-dependent quantity. In this situa-

tion, the constitutive relation (2) is modified to

$$\mathbf{j}(\mathbf{r}, t) = -D(\mathbf{r}) \nabla P(\mathbf{r}, t) - \mathbf{u}(\mathbf{r}) P(\mathbf{r}, t) \quad (5)$$

and the combination of (5) with (1) results in the Smoluchowski equation

$$\dot{P}(\mathbf{r}, t) = \nabla \cdot \{D(\mathbf{r}) \nabla P(\mathbf{r}, t) + \mathbf{u}(\mathbf{r}) P(\mathbf{r}, t)\} \quad (6)$$

where $\mathbf{u}(\mathbf{r})$ is the terminal velocity of a particle in a resisting medium, when an external potential field is applied.

In the case of a vibro-fluidised granular bed, $\mathbf{u}(\mathbf{r}) = u(y)$ only, as gravitational forces act only in the vertical direction. Similarly $D(\mathbf{r}) = D(y)$, since the granular temperature and packing fraction distributions on which D depends are only weak functions of x and z [15]. Knowledge of the displacement probability density $P(\mathbf{r}, t)$ can lead to determination of D from inverse analysis of (6), and as we shall see, a measure of the packing fraction and the granular temperature. A single particle tracking technique such as positron emission particle tracking is ideal for the determination of $P(\mathbf{r}, t)$, and developments in this area will be discussed in the following section.

3. Experimental Procedure

In this paper we present results using the recently upgraded Birmingham PEPT facility. Although PEPT tracks only a single particle, the automated facility allows experimental data to be logged for a considerable length of time (up to 6 hours), resulting in pseudo whole-field data for steady state systems. The technique has recently been used to investigate a number of experimental situations, e.g., rotating beds [12] and paste flow [16], and more recently it has been used to successfully analyse three-dimensional vibro-fluidised granular beds [17-21]. The technique uses a radionuclide that decays by positron emission, and relies on detecting the pairs of back-to-back gamma rays produced when positrons annihilate with electrons. These gamma rays are very penetrating and an accurate location can be determined from detection of a small number of back-to-back pairs. Coincident detection of two gamma rays in a pair of position-sensitive detectors defines a line passing close to the point of emission without the need for collimation. The University of Birmingham Positron Camera is a Forte dual-headed gamma camera (Adac Laboratories, Ca., USA). Each head contains a single crystal of NaI scintillator, 500×400 mm², 16 mm thick, optically coupled to an array of photo-multiplier tubes. The current maximum count rate of 4×10^4 s⁻¹

enables an ideal temporal resolution of 2 ms with a spatial accuracy of ~ 1 mm. In the following experiments, a tracer particle was created by irradiating a glass balltini sphere with a beam of ^3He , which leads to a bead that is physically indistinguishable from the remaining beads within the experimental cell. This radiolabelling process converts the available O nuclei to a radioisotope of F, which decays resulting in the emission of positrons. In a dense medium such as balltini, a positron quickly annihilates with an electron, producing two back-to-back 511-keV gamma rays. These are detected in the pair of diametrically placed camera heads (**Fig. 1**). Through triangulation of successive location events, the position of the tracer particle can be located in three dimensions.

A three-dimensional granular gas was generated using a Ling Dynamic Systems (LDS) vibration system. A sinusoidal signal was fed through a field power supply [LDS FPS 1] and power amplifier [LDS PA 1000] into a wide frequency band electro-dynamic transducer [LDS V651]. This system has a frequency range of 5–5000 Hz, a maximum acceleration of 100g and maximum amplitude of 12.5 mm. A cell of dimensions 145 mm in diameter and 300 mm in height was placed on the upper surface of the vibrating piston, itself placed between the photon detectors (**Fig. 1**). The cell was constructed of polymethyl methacrylate (PMMA) to limit the attenuation of the gamma rays as they travelled through the experimental apparatus, and the walls were coated with conducting copper tape to reduce electrostatic charging of the grains. The cell was vibrated at a frequency of 50 Hz. The

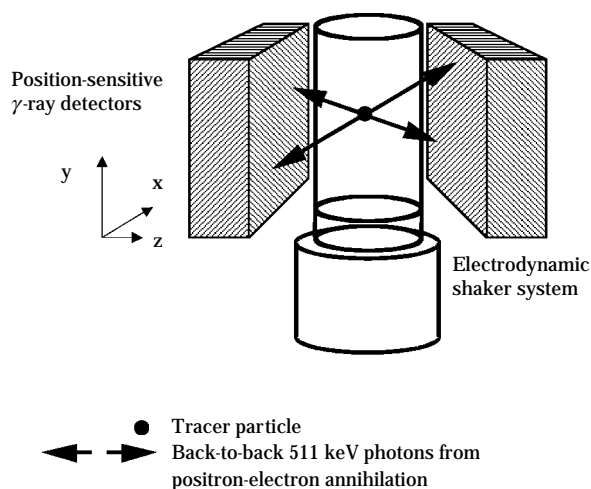


Fig. 1 A schematic of the positron emission particle tracking facility showing the placement of the vibration system between the gamma ray detectors.

amplitude of vibration A_0 was 1.74 mm. Initially, glass balltini balls of diameter $d=5.0\pm 0.2$ mm (with an inter-grain restitution coefficient, ϵ , measured using high-speed photography, of 0.91 and mass $m=1.875\times 10^{-4}$ kg) were used as the granular medium (the number of grains, $N=700$), though later 4 mm grains were also employed ($m=0.96\times 10^{-4}$ kg) in experiments on binary mixtures.

At grain speeds of about $\bar{c}=1$ m s $^{-1}$, the PEPT camera has an accuracy in the x-y plane of about ± 1 mm. However, the accuracy in the z direction is substantially worse as the grain needs to be located in a direction normal to the faces of the detectors. When calculating the granular temperature (Section 6), the average behaviour in the z direction was therefore assumed to be equivalent to that in the x direction, due to cylindrical symmetry. During each experiment, the motion of a grain was followed for about one hour, resulting in up to twenty million location events. Each location event was ascribed a coordinate in space and time (x,y,z,t).

4. Displacement Probability Density

One expects that granular particles placed into a highly agitated granular system will act very much like a Brownian particle; the buffeting of the grain by the external particles will result in a random walk, causing diffusion of the displacement probability density according to Eq. (6). The displacement probability density (DPD) is calculated experimentally by apportioning location events to discrete height intervals. The displacements of the grain at times after these location events are then binned to create the DPD. One then follows the development of the DPD as a function of time. **Figure 2** shows one example of the evolution of the density function $P(x,t)$ and $P(y,t)$ over 100 ms at steps of 10 ms, with the grain starting at 22.5 mm above the base. Initially, P is a delta function (not shown), as the particle is considered to have started at the same point every time it is located in that region, but as time progresses, the particles diffuse outward from this location. One can see this behaviour when examining the function at times $t>0$. At short times, the density function resembles the Gaussian function expected from Eq. (3), but in the y direction, as the particles move throughout the bed the influence of the variations in density and the base becomes apparent and distortions appear. The final positions of particles starting from different altitudes are shown overlaid onto **Figure 3**. This shows clearly that the long-time probability density of the grains is

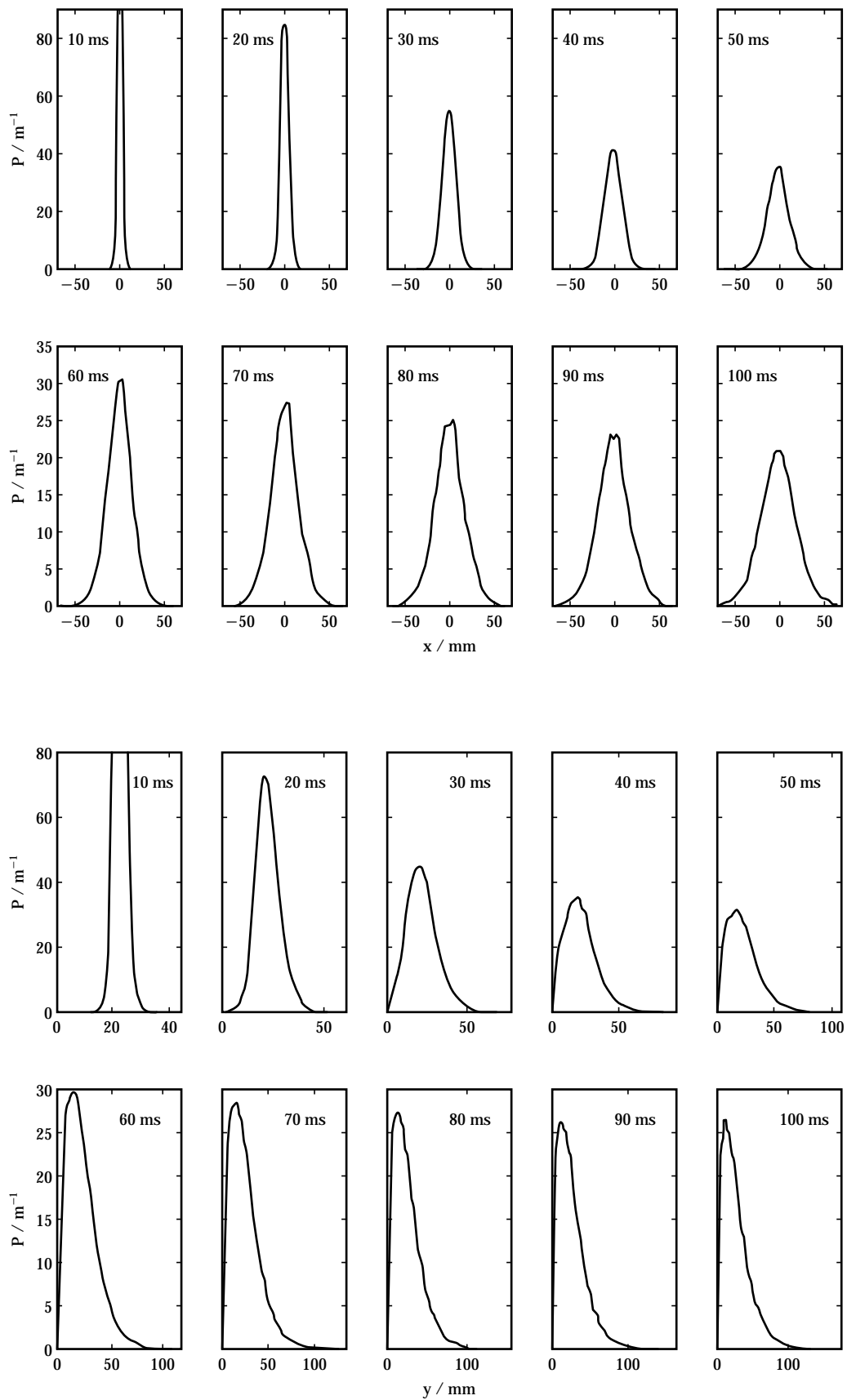


Fig. 2 Evolution of the displacement probability density as a function of time for the mono-disperse case, up to 100 ms. (upper figure) in the x direction and (lower figure) as a function of y.

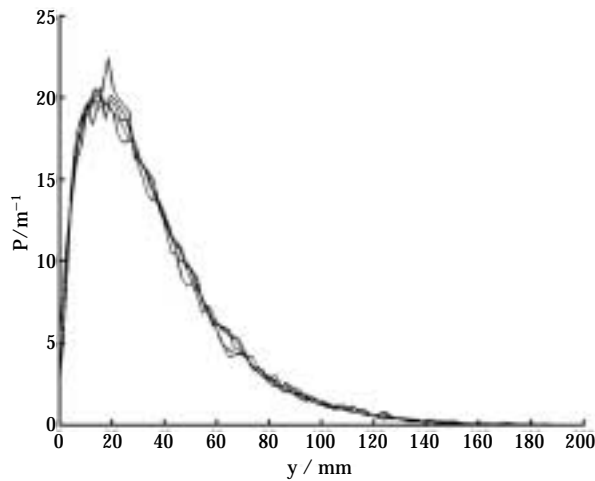


Fig. 3 A comparison of the long-time displacement probability curves for a range of grain start heights ($y=2.5, 7.5, 12.5, 17.5$ and 22.5 mm). This indicates that the long-time steady state behaviour of the system is broadly independent of the start location and suggests that an assumption of ergodicity is likely to be appropriate.

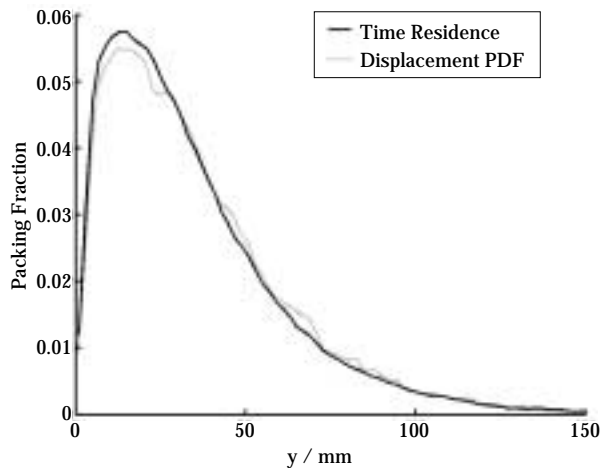


Fig. 4 Comparison of the packing fraction profile determined from the displacement probability density (start height = 22.5 mm) and one produced from the time residence distribution of the particles. The two curves should in principle be equivalent, though the time residence distribution gives a more accurate picture of the solids distribution.

the same regardless of their initial position, lending further credence to the assumption of ergodicity previously used [13]. Using such an assumption can lead to a more accurate measure of the packing fraction, η , and can be obtained by examining the residence time distribution of the grain. The assumed ergodicity means that a temporal average is equivalent to a spatial average leading to the following ex-

pression:

$$\eta = \frac{NF_i(y)\pi d^3}{6V_i} \quad (7)$$

where V_i is the volume of the i^{th} segment and $F_i(y)$ is the fraction of time spent by the particle in this volume element. The packing fraction distribution determined using this method is overlaid onto one obtained from the DPD (**Fig. 4**) because at extremely long times, the displacement density function is proportional to the packing fraction density. It shows the equivalence of the two methods but highlights the greater accuracy obtained by calculating the packing fraction from the residence time distribution.

5. Mean Squared Displacement

The mean squared displacement of the grains over time may be expressed as an integral equation in terms of $P(\mathbf{r}, t)$:

$$\langle |\mathbf{r}(t) - \mathbf{r}(0)|^2 \rangle = \int_{-\infty}^{\infty} (\mathbf{r}(t) - \mathbf{r}(0))^2 P(\mathbf{r}, t) d\mathbf{r} \quad (8)$$

or in the discretised form

$$\langle |\mathbf{r}(t) - \mathbf{r}(0)|^2 \rangle = \sum_{i=1}^{n_r} (\mathbf{r}_i(t) - \mathbf{r}(0))^2 P(\mathbf{r}_i, t) \Delta r. \quad (9)$$

where i is the i^{th} interval of displacement, n_r is the number of displacement bins and Δr is the DPD bin width. A typical result for the mean squared displacement is shown in **Figure 5**. Here we can observe a number of important features. The evolution of the mean squared displacement is clearly partitioned into a number of regions. At the shortest times ($\Delta t < 20$ ms), we can see the quadratic toe characteristic of ballistic motion [1, 8, 20]. At longer times, the system becomes diffusive and the mean squared displacement is linear with time. At the longest times, however, we see that the gradient of the mean squared displacement reduces. This is the effect of the caging of the particles in the cell. The walls confine the particles in the cell limiting the maximum mean squared displacement that is possible.

The behaviour of the grain in the x and y directions is somewhat similar. Nevertheless the density does not vary significantly in the radial direction, and the DPD in the x direction remains broadly Gaussian at short times. As the boundary regions are reached, clipping of the density function occurs, and this is reflected in the reduction of the gradient of the mean squared displacement. In the y direction, the presence of gravity has a profound effect, but nonetheless

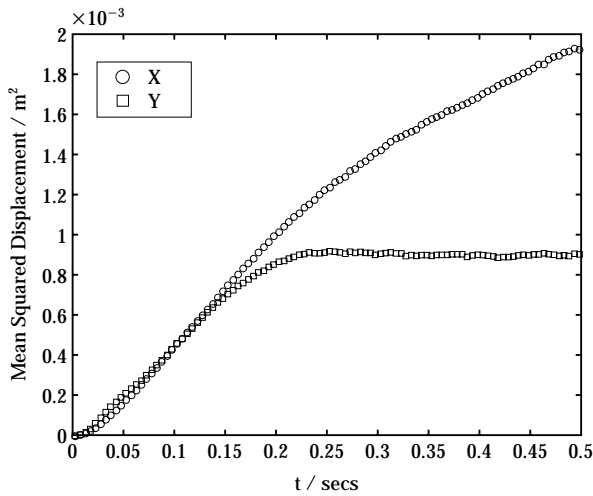


Fig. 5 A typical mean squared displacement plot for grains with a starting location of $y=22.5$ mm. This shows the three main regimes in which the grain exists: (1) short time, the grains are in free motion and the mean squared displacement is quadratic with time; (2) intermediate times, the grain undergoes random walk-type behaviour (at which point the grains obey the unbounded diffusion and Smoluchowski equations); and (3) long times, boundary effects become apparent.

the saturation effect is similar; once the base is reached or the particles reach the apex of their free trajectories at the top of the cell, the DPD and the mean squared displacement are constrained.

6. Granular Temperature

The granular temperature E_O , or mean kinetic fluctuation energy, is defined in the usual manner,

$$E_O = \frac{1}{3}(E_X + E_Y + E_Z) = \frac{1}{3}(m\overline{v_X^2} + m\overline{v_Y^2} + m\overline{v_Z^2}) \quad (10)$$

where m is the mass of the grain and v_X , v_Y and v_Z are the fluctuating particle velocity components about the mean, resolved in the x , y or z directions and E_X , E_Y , and E_Z are the granular temperatures for each of the respective directions. It is well known that due to dissipation, the granular temperature in a vibro-fluidised bed is anisotropic [1, 5, 8, 19, 20, 22], and that, unlike the case of elastic spheres, equipartition of energy does not hold. In most cases $E_Y > E_X = E_Z$ [20]. This is an important consideration when probing the spatial development of a system as it causes a corresponding anisotropy in the self-diffusion coefficients [1, 23]. For simplicity, however, we treat D as a scalar throughout this investigation.

We measure the granular temperature by analysing the short-time behaviour of the mean squared dis-

placement curves [24]. At times of the order of or less than the mean collision time, the random walk behaviour embodied in Eq. (4) no longer holds, and in the limit $t \rightarrow 0$, one can deduce from the equation of motion for a free particle that

$$\langle |\mathbf{r}(t) - \mathbf{r}(0)|^2 \rangle = \langle c^2 \rangle t^2. \quad (11)$$

By utilising the short-time mean squared displacement one can extract the mean squared speed, and thence the granular temperature. Bulk convection currents in the granular bed are small and are neglected in this procedure [21]. This method can be applied here for extracting the granular temperature from the particle DPDs. **Figure 6** shows an example of the granular temperature profile measured in this way as a function of altitude. This is quite typical; high kinetic energy is apparent at the base of the cell that is dissipated as grains collide with those positioned above them. Boundary effects are visible close to the bottom surface as the grain-base collisions lead to deviations from the expected form of the mean squared displacement versus time curve (Eq. (11)) [20].

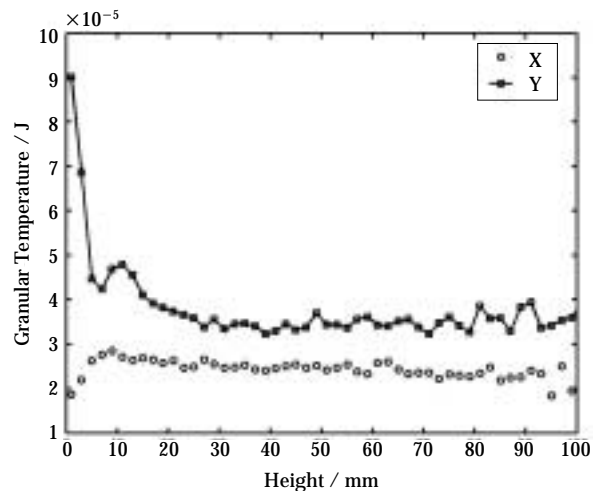


Fig. 6 Granular temperature profile for the system, showing the high fluctuation energy near to the base, which is dissipated at higher altitudes.

The relationships between D , E_O and packing fraction η have been investigated in two dimensions [1]. The Enskog kinetic theory equation in two dimensions was shown to be obeyed to within 10% for packing fractions up to about 0.6 and for the restitution

coefficient $\varepsilon=0.92$. In three dimensions, the corresponding Enskog relation reads [14]

$$D = \frac{3}{8nd^2g_o(d)} \left(\frac{E_o}{\pi m} \right)^{\frac{1}{2}} \quad (12)$$

where n is the number density and $g_o(d)$, the radial distribution function at contact is given by

$$g_o(d) = \frac{(2-\eta)}{2(1-\eta)^3} \quad (13)$$

At least two alternative expressions for D have been derived in which the Enskog theory is modified to take account of inelasticity [23, 25]. However, for the case of reasonably elastic collisions ($\varepsilon=0.91$ in the experiments described here), both modified expressions for D agree with Eq. (12) to within about 10%. The convective term in (6) can also be derived using kinetic theory and Brownian motion methods [14]:

$$u(y) = \frac{gd}{16\eta(y)g_o(d)} \left(\frac{E_o(y)}{\pi m} \right)^{-\frac{1}{2}} \quad (14)$$

where g is the acceleration due to gravity.

7. Self-diffusion

It can be seen from Eq. (6) that the dispersion of the grains in the system is effectively controlled by the diffusion coefficient. Provided with experimental values for the DPDs at given times, there are sufficient equations to calculate D as the system is overdetermined. This method will be presented in detail elsewhere, but will be briefly described here.

Equation (6) can be expanded into a form that is a polynomial in the operator $\partial/\partial y$. The coefficients of these terms are functions of D and u , each of which can be extracted by taking the experimental data and estimating the 1st and 2nd derivatives of the DPDs using a finite difference approach. There are as many DPDs as there are time steps, and as a result the random errors in using this method are reduced through the long timescale over which experiments are performed. This results in an overdetermined set of equations that then allows the coefficients, and thence D , to be extracted using non-linear regression methods.

Figure 7 shows the values of the self-diffusion coefficient extracted in this way. This compares reasonably with an estimate of D which can be obtained from the gradient of the mean squared displacement in **Figure 5** and predictions of D from Eq. (12), which suggests that $D \sim 0.005-0.01$ m²/s. However, this method tends to seriously underestimate D at high

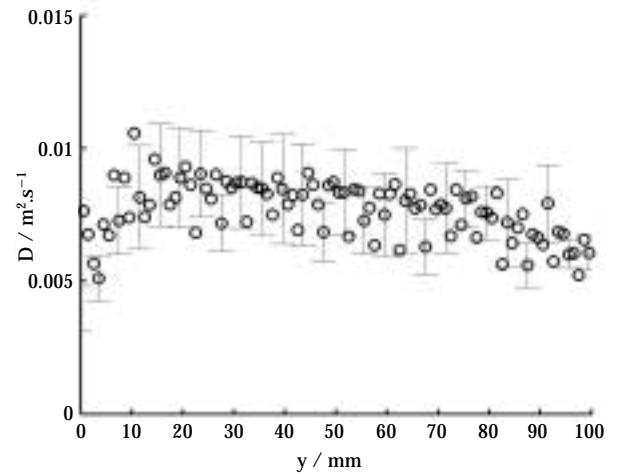


Fig. 7 Self-diffusion coefficient as a function of altitude, extracted from the displacement probability functions using equation (6). Error bars, representing the standard deviation of the mean, are shown for a sample of data points.

altitudes and Eq. (12) shows that D is expected to scale as $1/\eta$ which it clearly does not. This is most likely an artefact of the boundaries of applicability of the Smoluchowski equation. In rarefied systems, such as those near or in the Knudsen regime, the grains tend to move as if in free flight rather than as in a random walk. Therefore, at large heights, one sees a diffusion coefficient broadly independent of packing fraction and dominated by wall collisions rather than by grain-grain interactions.

One can attempt to quantify the conditions necessary to be able to extract the self-diffusion coefficient in this way as follows: Supposing that at least three grain-grain collisions must have occurred in the period it takes for a grain to return to its original height under the influence of gravity (i.e., if less than three occur then we assume that the grains are no longer in the random walk regime), then using simple kinetic theory predictions, one can estimate for a mean speed of ~ 0.43 m·s⁻¹ and particle diameter of 5 mm that a packing fraction of ~ 0.045 must exist for the extraction of D from Eq. (6) to be successful, indicating that the above method is only applicable at heights of less than about 30 mm.

8. Binary systems

In reality, most granular systems do not consist of mono-sized particles; but rather contain a distribution of particle sizes. Therefore, in order to understand true powder flow behaviour, one must go beyond monodispersity and study systems containing more

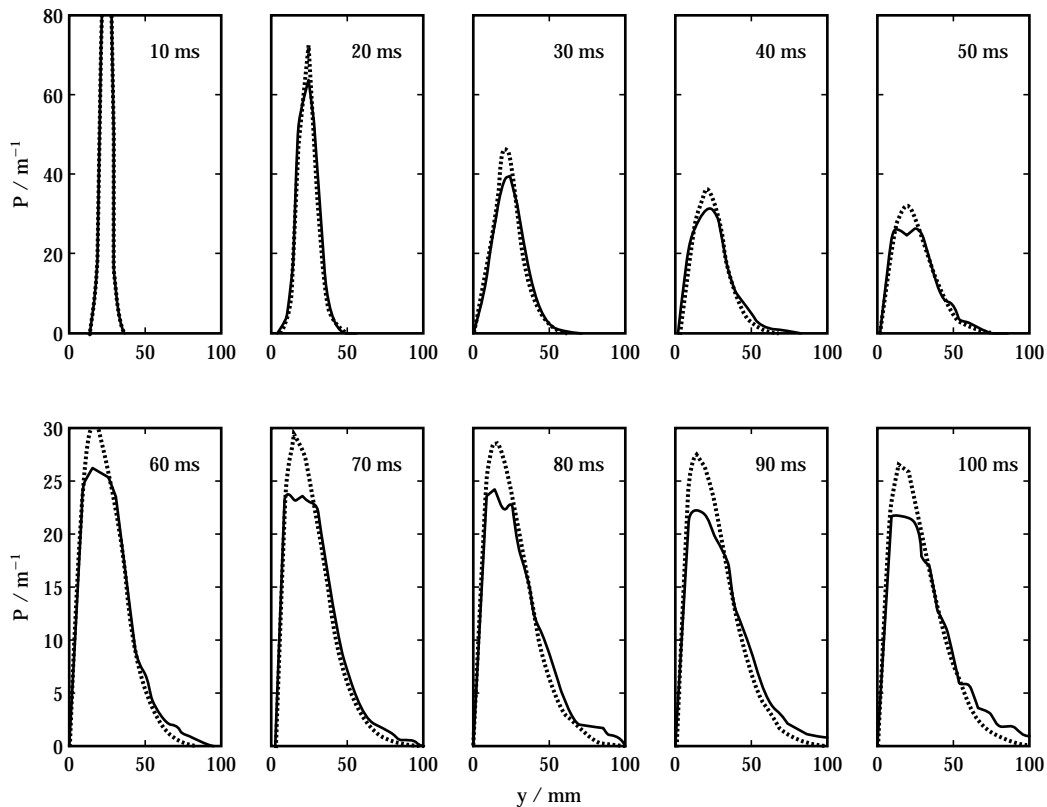


Fig. 8 Evolution of the displacement probability density as a function of time for the bi-disperse case, up to 100 ms, showing the behaviour of each phase as a function of y . Solid line is the 4 mm displacement probability density, dashed is that for the 5 mm grains.

than one particle size.

In the following experiments two grain sizes were used, 5 mm and 4 mm. The number of 5 mm particles N_1 was 525, and the number of 4 mm particles, N_2 was 270. The displacement probability density was measured for each phase by first using a 5 mm tracer particle, and then repeating the experiment using a 4 mm tracer. This allowed the particle coordinates for each phase in the shaker system to be determined independently. Subsequently, the methods described above for calculation of the granular temperature and the DPDs (**Fig. 8**) were used to determine these functions for each size phase. One can see systematic deviations in the development of the DPDs as the phases move towards their steady state distributions. The packing fraction profiles are shown in **Figure 9** and highlight the differences in the phase's steady state distributions of the two phases.

The granular temperature profiles for each phase are shown in **Figure 10**. As previously observed [17], the system does not normally relax towards a single temperature [26, 27]. The balance between energy introduced into the system by the vibrating

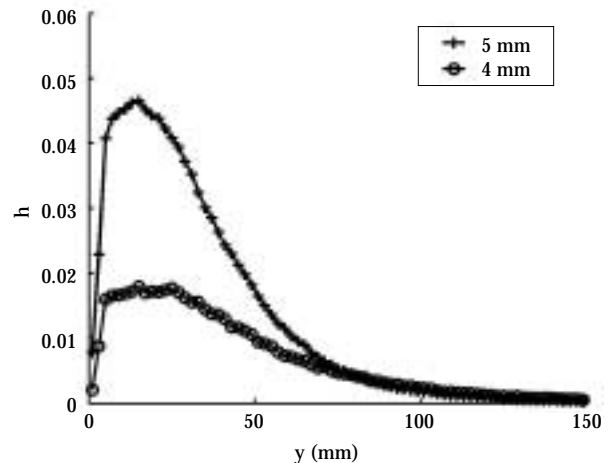


Fig. 9 Packing fraction profiles of the two phases in the binary-size vibrated granular bed.

base and that lost during inter-particle collisions and wall-particle collisions determines the granular temperature in a vibrated system. Because of differences in the mass and size of the particles, there are dif-

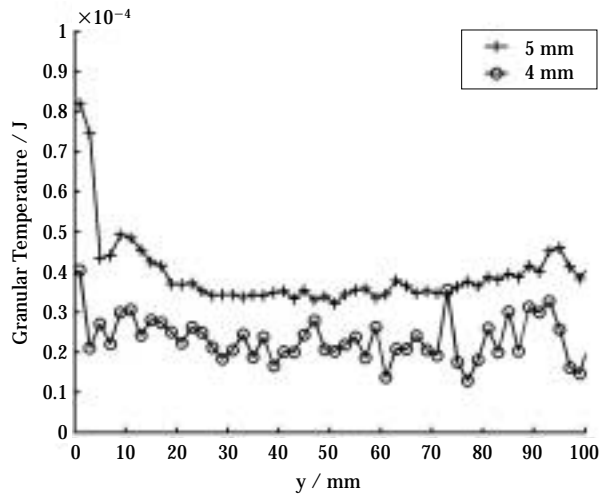


Fig. 10 Granular temperature profiles of each of the phases in the binary system.

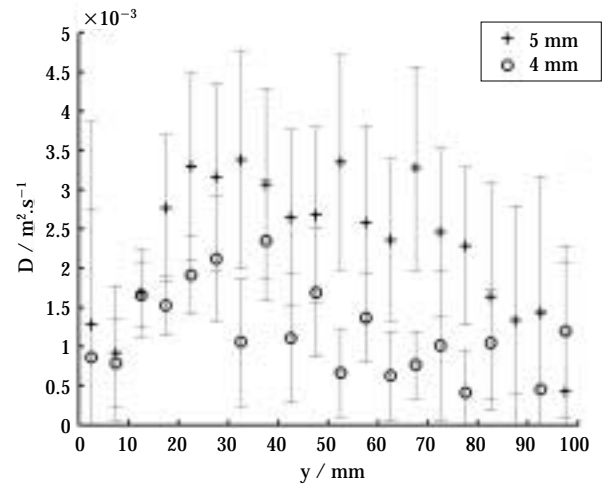


Fig. 11 Self-diffusion coefficient as a function of altitude, extracted from the displacement probability functions using equation (6), for the bi-disperse case. Errors bars are shown representing the standard deviation of the mean.

ferent solids distribution profiles for each phase, resulting in significantly different collision rates and dissipation rates. This has the effect that the particles relax towards different granular temperatures, which are coupled through the inter-phase particle collisions. The differences in the granular temperature and packing fraction propagate in turn due to differences in the diffusion coefficients.

The diffusion coefficients for each phase calculated by the method described in Section 7 are shown in **Figure 11**. Though the diffusion coefficient of a particle through particles of a different phase is usually referred to as the mutual diffusion coefficient, in this case it is a composite of both the mutual and self-diffusion coefficients, since the particle collides with other particles of both phases. The fact that the fraction of each phase varies as a function of height means that the relative dominance of the self-diffusion and mutual diffusion components also varies. As expected, the fact that each phase has its own packing fraction and granular temperature profile results in differing diffusion coefficients for the two phases.

Knowledge of the granular temperature and the packing fraction, as well as enabling the determination of the self-diffusion coefficient, is vital for investigating granular flow behaviour at the single particle level, and provides a powerful route to validating kinetic theory methods. The measurement of the particle displacement probability density provides both a qualitative insight into the behaviour of grains in the system, and a means by which the above variables

may be extracted, providing much required data for the understanding of granular flow mechanisms.

Conclusions

Particles in a granular gas are often observed to follow a random walk path. By investigating the motion of a single tracer particle in a vibrated granular bed, it is possible to estimate the displacement probability density. This function provides us with information on the system, both in a dynamic way, with the evolution of the displacement density, and on the steady state variables such as granular temperature and packing fraction and on the self-diffusion coefficient when the density is sufficiently high for the stochastic approach to be appropriate. Similar investigations on binary systems were used to quantitatively compare the diffusion coefficient for particles of different diameters.

References

- 1) Wildman, R.D., Huntley, J.M. and Hansen, J.P.: Phys. Rev. E, 60 7066 (1999)
- 2) Jaeger, H.M., Nagel, S.R. and Behringer, R.P.: Phys. Today, 49 32 (1996)
- 3) Kadanoff, L.P.: Rev. Mod. Phys., 71 435 (1999)
- 4) Campbell, C.S.: Annu. Rev. Fluid Mech., 22 57 (1990)
- 5) Warr, S., Huntley, J.M. and Jacques, G.T.H.: Phys. Rev. E, 52 5583 (1995)
- 6) Warr, S., Jacques, G.T.H. and Huntley, J.M.: Powder

- Technol., 81 41 (1994)
- 7) Warr, S. and Hansen, J.P.: Europhys. Lett., 36 589 (1996)
 - 8) Wildman, R.D. and Huntley, J.M.: Powder Technol., 113 14 (2000)
 - 9) Menon, N. and Durian, D.J.: Science, 275 1920 (1997)
 - 10) Ehrichs, E.E., Jaeger, H.M., Karczmar, G.S., Knight, J.B., Kuperman, V.Y. and Nagel, S.R.: Science, 267 1632 (1995)
 - 11) Knight, J.B., Jaeger, H.M. and Nagel, S.R.: Phys. Rev. Lett., 70 3728 (1993)
 - 12) Parker, D.J., Dijkstra, A.E., Martin, T.W. and Seville, J.P.K.: Chem. Eng. Sci., 52 2011 (1997)
 - 13) Wildman, R.D., Huntley, J.M., Hansen, J.P., Parker, D.J. and Allen, D.A.: Phys. Rev. E, 62 3826 (2000)
 - 14) Hansen, J.-P. and McDonald, I.: "Theory of Simple Liquids", 2nd Edition, Academic Press, London (1986)
 - 15) Campbell, C.S.: J. Fluid Mech., 348 85 (1997)
 - 16) Wildman, R.D., Blackburn, S., Benton, D.M., McNeil, P.A. and Parker, D.J.: Powder Technol., 103 220 (1999)
 - 17) Wildman, R.D. and Parker, D.J.: Physical Review Letters, 88 064301 (2002)
 - 18) Wildman, R.D., Hansen, J.P. and Parker, D.J.: Physics of Fluids, 14 232 (2002)
 - 19) Wildman, R.D., Huntley, J.M., Hansen, J.P. and Parker, D.J.: Phys. Rev. E, 64 051304 (2001)
 - 20) Wildman, R.D., Huntley, J.M. and Parker, D.J.: Phys. Rev. E, 63 061311 (2001)
 - 21) Wildman, R.D., Huntley, J.M. and Parker, D.J.: Phys. Rev. Lett., 86 3304 (2001)
 - 22) Lan, Y.D. and Rosato, A.D.: Physics of Fluids, 7 1818 (1995)
 - 23) Brey, J.J., Ruiz-Montero, M.J., Cubero, D. and Garcia-Rojo, R.: Phys. Fluids, 12 876 (2000)
 - 24) Chandrasekhar, S.: "Noise and Stochastic Processes", ed. Wax, N., Dover Publishing, New York (1954)
 - 25) Savage, S.B. and Dai, R.: Mech. Mater., 16 225 (1993)
 - 26) Jenkins, J.T. and Mancini, E.: Physics of Fluids A-Fluid Dynamics, 1 2050 (1989)
 - 27) Lu, H.L., Liu, W.T., Bie, R.S., Yang, L.D. and Gidaspow, D.: Physica A, 284 265 (2000)

Author's short biography



R. D. Wildman

Ricky Wildman graduated in Physics from the University of Manchester in 1992 subsequently completing a PhD in Chemical Engineering at the University of Birmingham in 1997. Since this time he has been involved in a range of fundamental studies of granular flows, with interests in shear flows, chute flows, vibrated and fluidised granular beds and stress propagation in granular packs. He has been a lecturer in the School of Mechanical and Manufacturing Engineering since August 2000, and was awarded an EPSRC Advanced Research Fellowship in 2002.



J. M. Huntley

Jonathan Huntley received his BA and PhD degrees in Physics from the University of Cambridge in 1983 and 1987, respectively. He was a research fellow at the Cavendish Laboratory, Cambridge, from 1987 until 1994, was appointed to a Readership at Loughborough University in 1994, became Professor of Applied Mechanics in July 1999 and is currently a Gatsby Fellow. His research interests include dynamic speckle pattern interferometry, shape measurement techniques and granular flow mechanics.

Low-Frequency Vibration Effects on Coarse Particle Filtration[†]

R.J. Wakeman and P. Wu

Advanced Separation Technologies Group,
Department of Chemical Engineering
Loughborough University*

Abstract

Results from an experimental investigation of the development of cake resistance during filtration assisted by vibration are presented and the vibration conditions that lead to improved filtration rates are identified. It is shown that vibration is a possible technique to increase the rate of filtration. However, a critical acceleration that is dependent on the vibration frequency and solids mass in the cake must be exceeded for filtration to be enhanced, otherwise the rate of filtration is slowed. Changes in the visual structure of the “cake” with vibration acceleration are described and related to changes in the “cake” resistance.

INTRODUCTION

In filtration, vibration has been considered to be a method to increase the rate of filtration. Ronningen-Petter Div.¹ introduced vibration as a means to produce slurry agitation to cut premature blinding of the filter medium, and Russel Finex² use vibration in their sieves and filters to prevent blinding of the separator medium. Sawyer³ suggested the use of vibration to break up the cake deposited on the filter medium, and Snowball⁴ has more recently patented a vibratory filtration technique. Notwithstanding these applications, there has been very little published work that set out to investigate how vibration affects the filtration process. The motion of particles settling towards a vibrating filter medium has been analysed by Wakeman *et al*⁵. It was shown that the vibration of the filter medium directly affects the motion of the particles in the suspension as they approach the medium, and that critical vibration conditions exist when the particle makes infrequent contact with the medium, leaving a liquid layer above the medium and hence a higher liquid flow rate through it.

In order to investigate the effect of vibration on the filtration velocity, Bakker *et al*⁶ studied the influence of vibrations on the resistance of a polystyrene filter cake. They found that vibrations caused an increase of the cake resistance, which seems contradictory

with the known practical applications in filtration. This suggests that if vibration is not applied properly it may reduce the filtration rate rather than improve it. Podkovyrin *et al*⁷ found that the use of vibration of the filter medium improves the filtration rate with an increase of the vibration amplitude, and Mellowes⁸ developed a filtration model for candle-type filters. Further work on applications of vibration to separation problems has been reported by Metodiev *et al*⁹.

To start to understand the effects of vibration on filtration rates, vibration filtration and permeation experiments were carried out under different vibration conditions. The experimental data were processed and analysed to determine the effects of vibration on the filtration of coarse particles. This paper reports the results from these experiments.

EXPERIMENTAL TECHNIQUES

The apparatus used for the measurements is shown in **Figure 1**. The suspension to be filtered was prepared and stored in vessel A. The suspension was pumped into the filter B. The overflow on filter vessel B ensured that the height of the suspension (and hence also the static pressure) remained constant during an experiment. The filter consisted of a filter medium (with an area of 0.002 m²) attached to a rigid support. The vibration was applied to the rigid support by a vibration generator (Model V406) driven by a vibration control system (Model DVC 48) and a power amplifier (Model PA500L), all supplied by Ling

* Loughborough, LE11 3TU, UK.

[†] Accepted: June 13, 2002

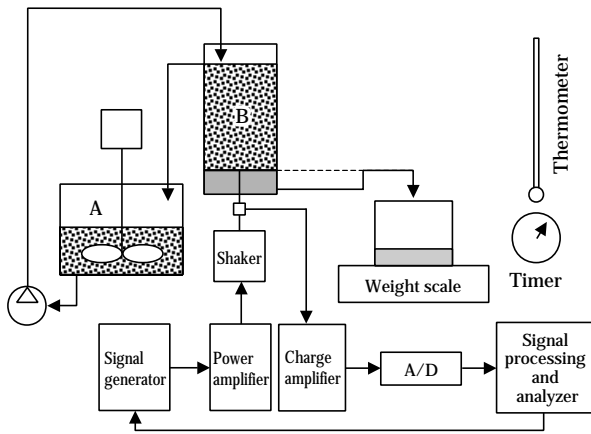


Fig. 1 Vibration filtration experimental system.

Dynamic Systems. The accelerometer (Endevco Model 7201-560) located between the filter medium and the shaker measured the vibration acceleration of the filter medium and provided the control signal to ensure that the shaker outputted a constant acceleration during vibration. The weighing scales and the timer measured the cumulative mass of filtrate and the filtration time.

In order to investigate the effect of vibration on filtration, three groups of experiments were carried out. The first was to investigate the effect of vibration on the flow rate of liquid through the filter medium. The second set of experiments investigated the effect of vibration on the cake formation process and on the resistance of the cake during its development. The third set of experiments investigated the effects of vibration on permeation after a cake had been formed, to elucidate the relationship between cake resistance and the dynamic characteristics of the filtration system. In each experiment, vibration with a fixed frequency and acceleration was exerted on the filter medium.

A primary purpose of this initial investigation was to establish that a vibratory force could assist filtration, before further investigations were carried out to establish the mechanisms and interacting parameters between feed properties and operating parameters. In order to do this, PVC particles with the same size distribution were used in both filtration and permeation experiments. The average diameter of the particles was 126 μm and the size range (measured using a Malvern MasterSizer) was 108 to 153 μm (105 to 125 μm by sieving).

EXPERIMENTAL RESULTS

To measure the resistance of the filter medium, clean liquid was pumped into the filter vessel. After the vessel began to overflow, the cumulative mass of permeate and the time were measured to give the liquid flow rate. This procedure was repeated using different vibration characteristics. Some typical results are shown in **Figure 2**. These show the linearity between the permeate volume collected and the collection time (the offset is a result of some liquid being in the permeate receiver at the start of the test). Changes in the gradients of the lines through the data points are very small, indicating correspondingly small variations in the medium resistance at different vibration frequencies.

In the cake filtration experiments, vibration was applied to the filter medium throughout. The PVC suspension, with a concentration of 6.1 kg m^{-3} , was fed into the filter. When the suspension began to overflow the filter vessel, the cumulative mass of filtrate and the corresponding filtration time were measured. The experiment was repeated under different conditions of vibration frequency and acceleration to give a series of filtration curves. **Figure 3** shows a typical set of filtration curves measured at different vibration accelerations when the vibration frequency was 500 Hz. The best achievable filtration rate is given by the line measured when there is no vibration and no particles in the feed, that is, water is permeating through the filter medium. Adding particles into the feed reduces the filtration rate, and low accelerations further reduce the filtration rate. Increasing the acceleration leads to higher filtration rates, and at an acceleration of 294 m s^{-2} , the filtration rate is almost

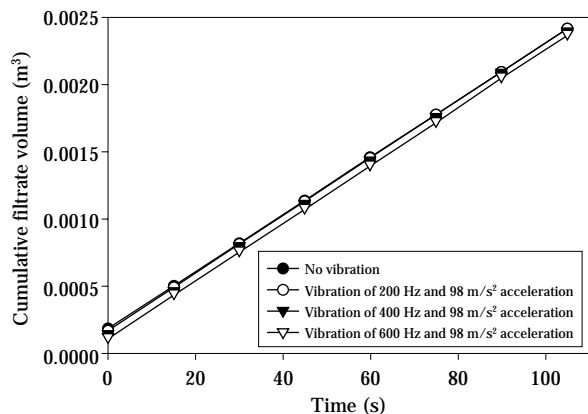


Fig. 2 The filtrate volume collected when passing a clean liquid through the filter medium.

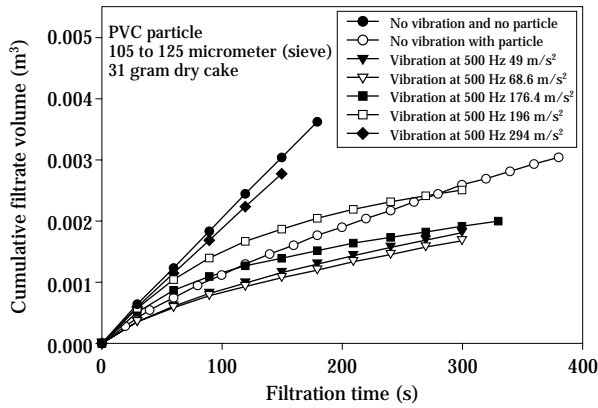


Fig. 3 The filtrate volume collected with 500 Hz vibration applied to the filter medium during cake filtration experiments.

as great as when only water was permeating through the filter medium, which is a substantial increase over the rate of filtration when no vibration is used.

In the cake permeation experiments, clean liquid was passed through the filter cake after it had formed. After the filter vessel started to overflow, the permeation flow rate was measured. Then vibration was applied to the filter medium. After about 30 minutes vibration, the flow of particles in the filter vessel approached a quasi-steady state and the permeation flow rate was measured. **Figure 4** shows a typical permeation flow rate curve under different conditions of vibration acceleration. From this it is seen that acceleration had little effect on the permeate flow rate until a threshold value was reached, when the flow rate was increased substantially. There is an accelera-

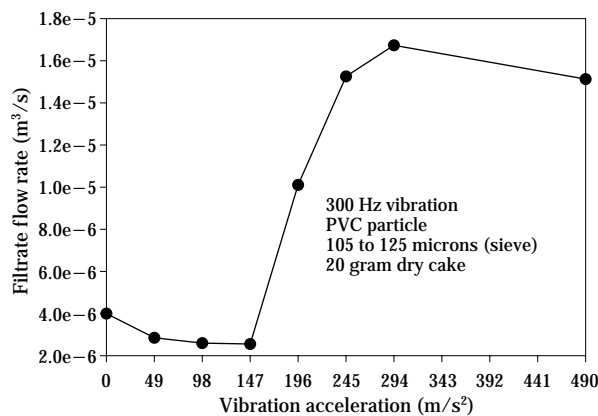


Fig. 4 Filtrate permeation rate under conditions of different vibration acceleration during cake filtration experiments.

tion at which a peak flow rate is reached, and beyond that the flow decreases gradually.

DISCUSSION

A method to analyse the data and enable comparisons to be drawn is outlined below, based on the form of Darcy's law that is usually used in filtration analysis. Observations made during the experiments are then described and the data is discussed with reference to these observations and the analysis of the data.

Vibration filtration theory

In the analysis of constant pressure cake filtration, the data is conventionally plotted as t/V versus V and the straight line relation is used to estimate the average specific resistance of the cake and the medium resistance, in which t is the filtration time and V is the cumulative filtrate volume (Wakeman and Tarleton¹⁰). The filtration experiments using vibration show that it is very different from cake filtration. At a fixed vibration frequency, when the acceleration is below a particular value, the straight line relation between t/V and V exists. Otherwise, the relation breaks down as shown in **Figure 5**. This means that the cake filtration theory cannot be used directly for the analysis of vibration filtration data.

During the vibration filtration process, the vibration affects the movement of particles above the filter medium and may change the flowing state of the liquid as it passes through the filter medium, when compared with filtration without vibration. This suggests

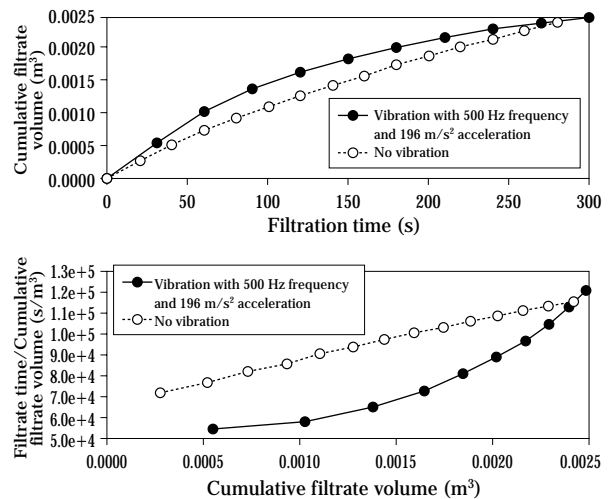


Fig. 5 Filtrate volume collected and the corresponding filtration curve obtained during a vibration filtration experiment.

that there needs to be an additional resistance term in the conventional filtration equation. As a preliminary approach, it is assumed that the resistance can be broken down into the following terms:

Resistance to liquid flow caused by the medium:	R_m (constant)
Resistance to unidirectional liquid flow through the cake:	R_c
Resistance to liquid flow arising from vibration of the medium and cake:	R_v

According to Darcy's law, the relation between the filtrate flow rate Q and the resistances can be written as:

$$Q = \frac{dV}{dt} = \frac{A\Delta p}{\mu(R_m + R_c + R_v)} \quad (1)$$

where μ is the viscosity of the filtrate, A is the area of the filter medium, Δp is the filtration pressure, V is the cumulative volume of filtrate and t is the filtration time.

The resistance R_v can be separated into two parts. One part, R_{vf} is caused by the change of the flowing state of liquid passing through the filter medium due to the vibration. The other part, R_{vp} is caused by the change of particle movement in the filter vessel immediately above the filter medium, which is defined as the vibrating particle movement resistance. When no particles are in the liquid, $R_{vp} = R_c = 0$. Under these circumstances, the resistance $R = R_m + R_{vf}$ is defined as the vibrating medium resistance. When the vibration is zero, $R_v = 0$, and the equation represents normal cake filtration.

It is difficult to estimate the R_c and R_v individually. Here it is investigated how the vibration affects $R_{cv} = R_c + R_v$, defined as the combined cake resistance. R_{cv} can be obtained from equation (1) as:

$$R_{cv} = \frac{A\Delta p}{\mu Q} - R_m = \left(\frac{A\Delta p}{\mu} \right) \left(\frac{dV}{dt} \right)^{-1} - R_m \quad (2)$$

R_m can be estimated from the experimental permeation data obtained without vibration and when only liquid was being fed to the filter. If the filtrate flow rate Q at time t is known, the relationship of R_{cv} with filtration time t can be obtained if the pressure difference Δp across the filter is assumed to be constant during the vibration filtration process.

For the normal cake filtration, the resistance of the cake is directly proportional to the mass of dry solids deposited per unit area of filter w , and the proportionality constant α is defined as the specific cake resis-

tance (Wakeman and Tarleton¹⁰). For the vibration filtration, like normal cake filtration, the combined cake resistance is related to the mass of dry solids deposited per unit area of filter w . But the ratio between the combined cake resistance and the mass of dry solids deposited per unit area of filter is not a constant during the vibration filtration process, which changes with the filtration time. It is defined as the vibrating specific cake resistance $\alpha_v(t)$. During vibration-assisted filtration, suppose that the concentration, c , of the feed suspension is a constant and ignore the liquid in the cake. The combined cake resistance has the relation with the vibrating specific cake resistance and the cumulative filtrate as in equation (3) (Wakeman and Tarleton⁶):

$$R_{cv} = \frac{cV}{A} \alpha_v(t) \quad (3)$$

Therefore, the average vibrating specific cake resistance, α_{avv} , can be obtained during the filtration time T as in equation (4):

$$\alpha_{avv} = \frac{A}{Tc} \int_0^T \frac{R_{cv}}{V} dt \quad (4)$$

where R_{cv} and V were related to the vibration frequency and acceleration and the filtration time. Therefore, α_{avv} is a function of the vibration characteristic (intensity) and the filtration time. When no vibration is exerted on the filter medium, α_{avv} is equal to the average specific cake resistance in conventional cake filtration.

Vibration effects on medium resistance

The vibrating medium resistance was estimated using the experimental data obtained from the medium resistance measurements, using equation (1). Some results are shown in **Figures 6** and **7**. When no vibration exists, $R_{vf} = 0$ and the medium resistance is equal to that found for a normal filtration process.

Figures 6 and **7** show that vibration changes to only a small extent the flowing state of liquid passing through the filter medium, indicated by the vibrating medium resistance being different from the medium resistance (the medium resistance is the value at zero frequency and zero vibration acceleration). The change ($R - R_m$) is very small compared with R_m . In further analyses of the data, R_{vf} is neglected and considered to be zero in vibration filtration.

Vibration effects on cake formation

The cake formation process (slurry thickening above the filter medium is included in this context)

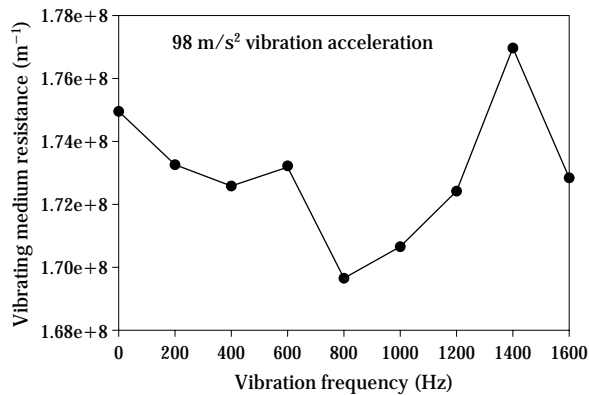


Fig. 6 The variation of the medium resistance with vibration frequency with clean liquid flowing through the medium (no filtration).

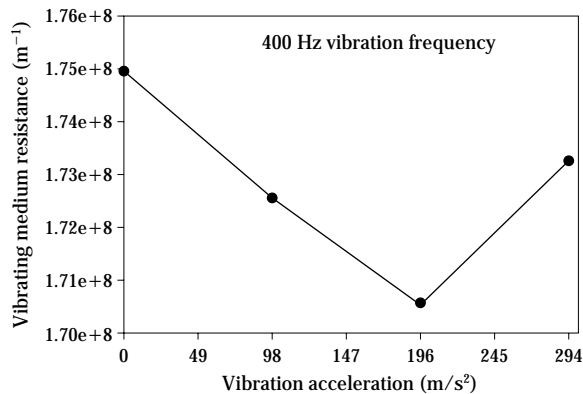


Fig. 7 The variation of the medium resistance with vibration acceleration with clean liquid flowing through the medium (no filtration).

depends on the vibration characteristics. Different vibration accelerations lead to different cake formation processes. The qualitative state of the cake or suspension in the filter chamber was observed visually through the perspex walls of the filter. When the vibration acceleration was low at a particular frequency, for example 49 m s^{-2} at 200 Hz, the cake formation process was similar to that without vibration; the particles progressed in a uniform direction through the filter vessel in an orderly manner to form the cake, as shown in **Figure 8(b)**. The cake formation process changed with an increase of the vibration acceleration. At the beginning of filtration, the state of the particles was as shown in **Figure 8(a)**, that is, the particles were uniformly distributed above the filter medium. Once the filtration had started, cake formed on the filter medium but the morphology of the cake was dependent on the vibration acceleration. For

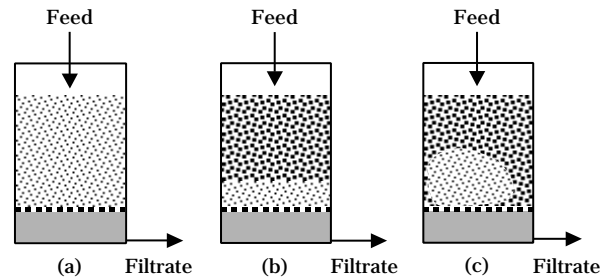


Fig. 8 State of the cake and particles during vibration-assisted filtration: the effect of increasing acceleration.

lower vibration accelerations, the shape of cake was as shown in **Figure 8(b)**, whilst at higher vibration accelerations, the form of the cake was as shown in **Figure 8(c)**. The “cake” in **Figure 8(c)** does not cover the filter medium, but exists as a dense “cloud” of particles lying just above the medium. There are zones around the “cloud” through which liquid is able to flow freely and which appear to have particle concentrations similar to the feed suspension. At 500 Hz, for example, the formation characteristics of the cake changed from that depicted in **Figure 8(b)** at 196 m s^{-2} to that shown in **Figure 8(c)** at 294 m s^{-2} .

Combined cake resistance (R_{cv}) during filtration

After filtration a typical thickness of cake was 27 mm. The pressure exerted on the cake was about 1638 Pa for a suspension with a depth of 196 mm in the filter vessel, and the pressure change on the cake from the beginning to the end of the filtration was about 262 Pa. Therefore, the pressure difference exerted on the cake was assumed to be constant in the following analysis, and a value of 1800 Pa was used.

The combined cake resistance was estimated using the data obtained in the filtration experiments, and is shown in **Figures 9, 10 and 11**. These figures show that the vibration characteristics strongly affect the filtration velocity because the combined cake resistance approaches zero when the vibration acceleration exceeds a particular value, which we define as the *critical vibration acceleration (CVA)*. The CVA depends on the vibration frequency. For example, at 200 Hz, an acceleration greater than 98 m s^{-2} caused the combined cake resistance to reduce to zero (**Figure 9**), whereas an acceleration of 294 m s^{-2} at 300 and 500 Hz was required to produce a similar effect (**Figures 10 and 11**, respectively).

The rate of increase of the combined cake resistance depends on the vibration acceleration exerted on the filter medium during the filtration process.

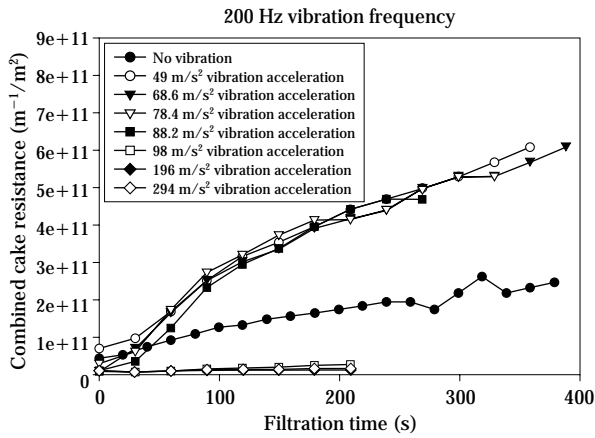


Fig. 9 Variation of the combined cake resistance with time during the vibration-assisted filtration process with the medium vibrating at 200 Hz.

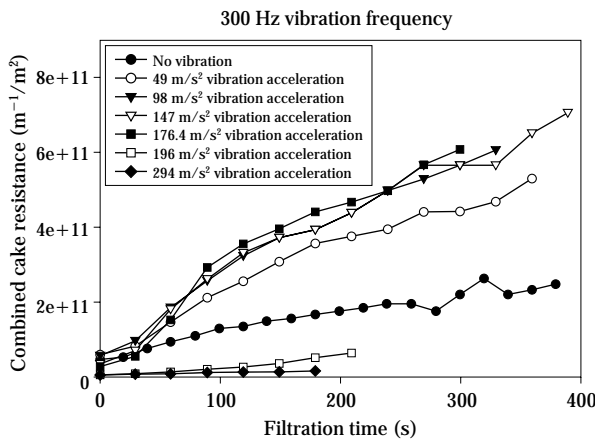


Fig. 10 Variation of the combined cake resistance with time during the vibration-assisted filtration process with the medium vibrating at 300 Hz.

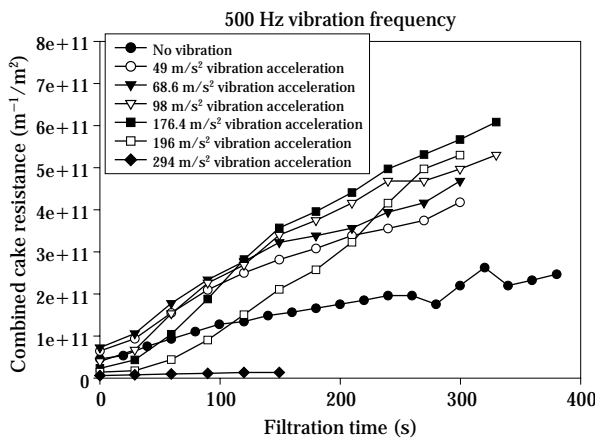


Fig. 11 Variation of the combined cake resistance with time during the vibration-assisted filtration process with the medium vibrating at 500 Hz.

Figures 9, 10, and 11 show that from the start of the filtration a weak vibration acceleration, for example, 49 m s^{-2} at 200 Hz and 98 m s^{-2} at 300 Hz, increases the combined cake resistance as compared with filtration without vibration. A stronger vibration acceleration decreases the resistance at the beginning of filtration, but as the filtration proceeds, all vibrations below the CVA allow the combined cake resistance to increase quickly compared with the filtration without vibration. For example, use of 88.2 m s^{-2} at 200 Hz or 196 m s^{-2} at 500 Hz leads to a resistance during the earlier stages of filtration that is lower than is the case without vibration, but the resistance later increases sharply to become greater. Higher accelerations delay the time before the resistance starts to increase quickly, as is shown in **Figure 11** by comparison of the curves for accelerations of 176.4 and 196 m s^{-2} at 500 Hz. When the vibration acceleration is greater than the CVA, the resistance remains lower than is the case in a normal filtration. There is some evidence that the CVA may depend on the weight of cake deposited on the filter medium; for example, the 196 m s^{-2} at 300 Hz curve lies below that measured for a normal filtration but after some time starts to rise towards it.

Average vibration specific cake resistance (α_{av}) during filtration

The average vibrating specific cake resistance changes with the vibration characteristic. The average vibrating specific cake resistance was estimated for vibration-assisted filtration at a filtration time of 150 seconds, using the experimental data and equation (4). The results are shown in **Figure 12**. The resistance increases at low vibration accelerations and reaches a peak value at a specific vibration acceleration dependent on the vibration frequency. The peak values are reached at 49, 98 and 68.6 m s^{-2} at 200, 300 and 500 Hz respectively. After the peak, the average vibrating specific cake resistance reduces with the increase of the vibration acceleration. The magnitude of these peak values are expected to depend on the size and density of the particles, a factor that will be investigated in later experiments.

Beyond the acceleration corresponding to the peak resistance values, the cake resistance falls sharply at 200 Hz and slowly at 500 Hz compared with that at 300 Hz. When the vibration acceleration at different vibration frequency exceeds a certain value, the average vibrating specific cake resistance approaches zero and remains fairly constant. In this region, the vibration-assisted filtration behaves similarly to the

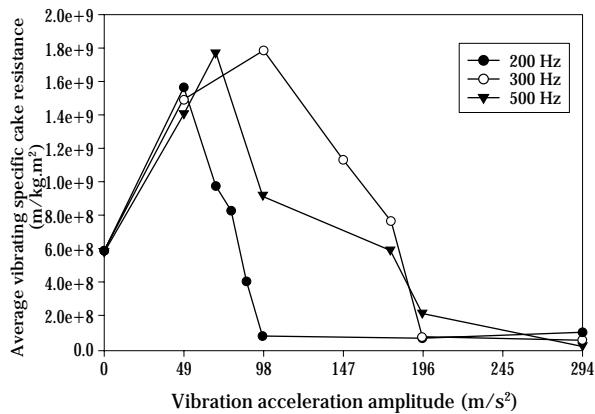


Fig. 12 Average vibrating specific cake resistance under different vibration characteristics.

permeation of a clean liquid (that is, filtration rates are similar to permeation rates through the filter medium). The filtration efficiency is then at a maximum, in the sense that a maximum filtrate flow rate is being reached even though filtration is still being achieved. The value of this vibration acceleration corresponds with the CVA.

Vibration effects on permeation

After a cake has formed, the vibration characteristics strongly affect the state of the cake. Whereas weak vibration compacted the cake, intense vibration loosened or broke up the cake and dispersed the par-

ticles in the liquid. When the vibration acceleration was low at a particular frequency, for example 98 m s^{-2} at 600 Hz, the cake compacted as shown in **Figure 13(b)** compared with filtration without vibration shown in **Figure 13(a)**. There was a tendency, also, for more intense vibration to densify the cake to a greater extent. For example, the thickness of the cake after vibration at 98 m s^{-2} and 300 Hz was 15 mm, while at 49 m s^{-2} and 300 Hz it was 16.5 mm.

With a small increase in acceleration, the thickness of “cake” in the centre zone of the filter just above the medium increased and the thickness around the boundaries of the cake reduced, as shown in **Figure 13(c)** (such a result was obtained at, for example, 147 m s^{-2} at 300 Hz). When the vibration acceleration was further increased, for example to between 196 and 274 m s^{-2} at 300 Hz, a channelling phenomenon occurred and some particles in the “cake” started to flow as shown in **Figure 13(d)**. The change from the compaction to the channelling phenomena was gradual, caused by the increasing vibration acceleration. Increasing the vibration acceleration still further caused the particles to disperse further into the liquid just above the filter medium, as shown in **Figure 13(e)**. At higher accelerations, for example using 490 m s^{-2} at 300 Hz, the “cake” broke up completely and the particles dispersed into the liquid as shown in **Figure 13(f)**. The acceleration at which each of the phenomena was prevalent depended on the mass of solids in the cake (in the above, the

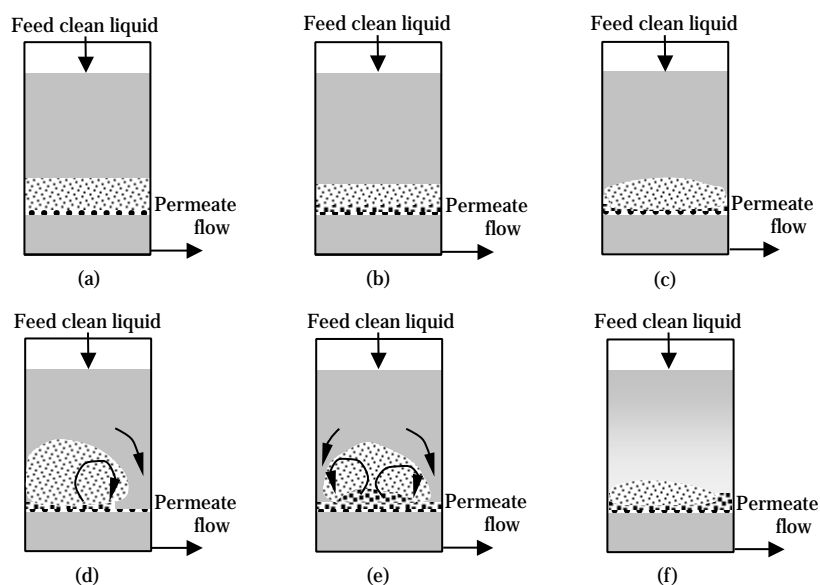


Fig. 13 State of the cake and particles during vibration permeation through a formed cake: the effect of increasing acceleration.

mass of dry solids in the cake was 20 grams).

Combined cake resistance during permeation

The critical vibration acceleration during permeation (CVAP) depended not only on the vibration frequency but also on the mass of cake, as shown in **Figure 14** obtained from the permeation experimental data. When the vibration frequency was 600 Hz, the combined cake resistance increased with the vibration acceleration applied to a 56.77-gram dry cake. In comparison, a frequency of 200 Hz caused the resistance to increase with acceleration until 98 m s⁻² was reached, beyond which the cake resistance fell to almost zero at 196 m s⁻².

When the cake contained 20 grams of dry solids, vibration with 200 Hz and 147 m s⁻² showed a similar effect (that is, the combined cake resistance approached zero). Compared with the result for the cake of 20 grams, resistances of cakes with masses of 30.06 and 56.77 grams increased to greater extents. Beyond the CVAP, the cake resistance rose again with the vibration acceleration for the 30.06- and 56.77-gram cakes. The greater the mass of the cake, the bigger the increase of resistance caused by the vibration.

The combined cake resistance was related to the dynamic characteristics of the filtration system, as shown in **Figure 15** from the permeation experimental data. For a vibration with a fixed acceleration, a higher frequency was associated with a lower vibration energy. Therefore, if the vibration acceleration was unable to break up the cake, the resistance should reduce with the increase of the vibration frequency. **Figure 15** further shows that the resistance

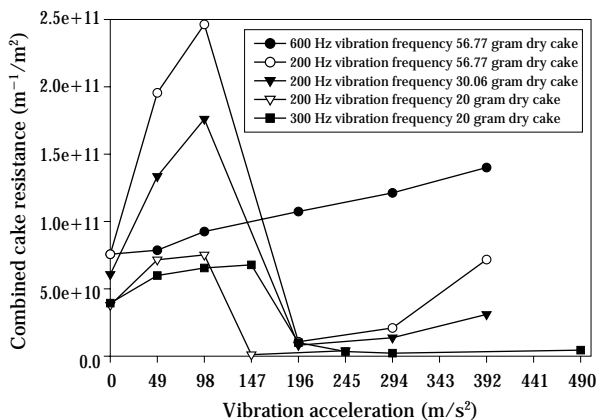


Fig. 14 Combined cake resistance for various masses of cakes under different vibration acceleration and frequency conditions during permeation experiments.

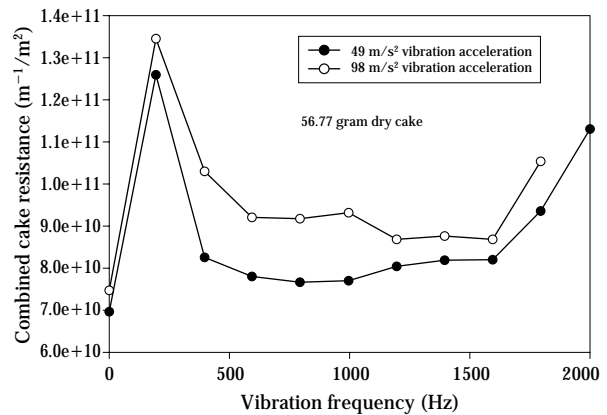


Fig. 15 Combined cake resistance under different vibration frequency and acceleration conditions during permeation experiments.

increases with an increase of the vibration frequency at frequencies above 1600 Hz.

Comparing the filtration and permeation experimental results, the conclusion can be obtained that critical vibration accelerations for filtration and permeation are different. The critical vibration acceleration during permeation is larger than that during filtration (CVA < CVAP). For example, when a 200-Hz vibration was applied, CVAP for a 20-gram cake was 147 m s⁻² as shown in **Figure 14**, while CVA for a 31-gram cake was 98 m s⁻² as shown in **Figure 9**.

CONCLUSIONS

Vibration of the filter medium caused only a small change to the resistance experienced by filtrate passing through it, which itself was small compared with the resistances of the cakes formed. However, the resistance of the cake could be reduced substantially under the correct conditions of vibration.

Vibration can increase the rate of filtration, but its intensity has to be greater than the critical vibration acceleration. In turn, the critical vibration acceleration is related to the vibration frequency, the weight of dry solids in the cake and the dynamic characteristics of the filtration system. Also, the critical vibration acceleration obtained during filtration is different from that obtained during fluid permeation through an already formed cake. If the vibration acceleration is smaller than the critical vibration acceleration, the vibration cannot improve the rate of filtration but will in fact slow it.

NOMENCLATURE

A	Filter area	(m^2)
p	Pressure	(Pa)
Q	Filtrate flow rate	$(\text{m}^3 \text{s}^{-1})$
R_c	Resistance of the filter cake	(m^{-1})
R_m	Resistance of the filter medium	(m^{-1})
R_v	Resistance arising from the applied vibrations	(m^{-1})
R_{vf}	Resistance of the vibrating filter medium	(m^{-1})
R_{vp}	Vibration particle movement resistance	(m^{-1})
T	Total filtration time	(s)
V	Filtrate volume	(m^3)
c	Concentration of suspension	(kg m^{-3})
t	Time	(s)
w	Mass of dry solid unit area deposited on the filter	(kg m^{-2})
$\alpha_v(t)$	Vibration specific cake resistance	(m kg^{-1})
α_{avv}	Average vibration specific cake resistance	(m kg^{-1})
μ	Filtrate viscosity	(Pa s)

ACKNOWLEDGEMENT

The authors wish to record their gratitude for receipt of an Engineering and Physical Sciences Research Council grant in support of this work.

REFERENCES

- 1) Ronning-Petter Div., Dover Corp.: *Chemical Engineering*, **80**(6), March 19, 1973.
- 2) Russell Finex, Company Brochures.
- 3) Sawyer, J.: Dynamic self-cleaning filter for liquids, US patent No. 4158629, June 19, 1979.
- 4) Snowball, M.R.: Fluid treatment by filtration and vibration, European patent No. EP1094036, April, 2001.
- 5) Wakeman R.J., Wu P. and Koenders M.A.K.: Simulation of the motion of particles settling towards a vibrating filter medium, *Transactions of The Filtration Society*, **2**(1), 2001, 13-19.
- 6) Bakker P.J., Heertjes, P.M. and Hibou, J.L.: The influence of the initial filtration velocity and of vibrations on the resistance of a polystyrene filter cake, *Chemical Engineering Science*, **10**, 1950, 130-140.
- 7) Podkovyrin A.I., Korol'kov V.V. and Isakov A.P.: Filtering a fibrous suspension through a vibrating grid, *Khimicheskoe I Neftyanoe Mashinostroenie*, **1**, 1973, 13-14.
- 8) Mellowes, W.A.: A vibratory filtration model for candle-type filters, *Powder Technology*, **43**, 1985, 203-212.
- 9) Metodiev M., Stoev S. and Hall S.T.: Vibration spiral filtration, Mining and Geology, Sofia, Bulgaria, No. 5, 1996, 28-31 (in Bulragian).
- 10) Wakeman R.J. and Tarleton E.S.: *Filtration: Equipment selection modelling and process simulation*, Elsevier, 1999.

Author's short biography



Richard J. Wakeman

Richard Wakeman is Professor and Head of the Department of Chemical Engineering at Loughborough University. He has worked extensively on most aspects of solid/liquid separation, including pre- and post-treatment processes, membrane filtration and the development of filter media. These works now also include field assisted separation techniques – the concentration and filtration of particulates using electrical, ultrasonic or vibrating force fields. He has been the recipient of Moulton Medals from the Institution of Chemical Engineers in 1978, 1991 and 1995 and the Gold Medal of The Filtration Society in 1993. He was elected a Fellow of The Royal Academy of Engineering in 1996.



Pihong Wu

Pihong Wu was born in China in 1964. He received his Bachelor degree in Taiyuan Heavy Machine Institute in 1984, Master degree in Shanxi Mining Institute in 1987, and PhD in Southampton Institute in 2001.

He worked as a Scientist in Mining Science and Technology Research Institute during 1987 to 1997. Currently he is a postdoctoral research associate at Loughborough University. His research interests include multivariate data analysis, neural networks, fuzzy logic, digital signal processing, system modelling and simulation, and vibration analysis and control.

Effects of Wall Inclinations and Wall Imperfections on Pressures during Granular Flow in Silos[†]

J. Tejchman

*Civil Engineering Department,
Gdansk University of Technology**

Abstract

The effects of wall inclinations and wall imperfections at the onset of granular flow in a silo are numerically studied. The calculations were carried out for the onset of quasi-static mass flow in a silo with a controlled outlet velocity along the entire bottom. In the analysis, a finite element method and a polar hypoplastic constitutive law were used. A polar hypoplastic law describes the salient properties of granular bodies. FE calculations were performed with a plane strain silo with parallel walls, slightly convergent walls, slightly divergent walls, and parallel and convergent walls. The influence of a wall imperfection directed inwards and a wall imperfection directed outwards in a silo with parallel walls was also analysed. The FE results showed a large sensitivity of stresses in bulk solids due to the change of the direction of shear deformation along the silo wall.

1. Introduction

Experiments with bulk solids during silo flow show a large effect of the wall inclination and wall imperfections on wall stresses [1]-[7]. In general, wall stresses increase when silo walls become convergent, and they decrease when silo walls are divergent. A significant growth of wall stresses is usually observed at the transition between bin and hopper (the so-called "switch"). A wall imperfection directed to the inside of the bulk solid causes an increase of wall stresses. In turn, a wall imperfection directed to the outside of the bulk solid diminishes wall stresses.

The wall inclinations and wall imperfections influence wall stresses due to the fact that bulk solids are very sensitive to every change in the direction of shear deformation [8]-[11]. Thus, a realistic calculation of wall pressures due to the change of the wall inclination and the occurrence of imperfections in a silo is possible using a constitutive law taking into account this important granular property.

The intention of the paper is to analyse numerically the effect of the wall inclination and wall imperfections on the evolution of wall stresses in granular materials at the beginning of confined granular flow in a plane strain model silo with very rough walls. The calculations were carried out for quasi-static

mass flow in a silo with a constant outlet velocity along the entire bottom (inertial forces were neglected). In a theoretical study, a finite element method on the basis of a polar hypoplastic constitutive law was used. The constitutive law can describe the salient properties of granular bodies during deformation with allowances made for shear localisation [12]-[15]. The effect of density, pressure, deformation direction, mean particle diameter and particle roughness is also captured. The FE calculations were carried out within a silo research study aimed at determining an optimal shape and roughness of silo walls to reduce an increase of wall stresses after outlet opening. In the paper, compressive stresses were considered negative (as in soil mechanics).

2. Constitutive law for granular bodies

A polar hypoplastic law [12]-[15] is an alternative to a polar elasto-plastic formulation [16]-[17] for continuum modelling of granular materials. It was formulated within a polar (Cosserat) continuum [18]. A polar (Cosserat) continuum differs from a non-polar one by additional rotations. For plane strain or axial symmetry, each material point has three degrees of freedom: two translations u_1 and u_2 , and one rotation ω^c . The polar rotation ω^c is related with the micro-rotation and is not determined by displacements as in a non-polar continuum

$$\omega_{ij} = 0.5(u_{i,j} - u_{j,i}). \quad (1)$$

* 80-952 Gdańsk-Wrzeszcz, Narutowicza 11/12, Poland

[†] Accepted: June 17, 2002

The gradients of the polar rotation are connected with curvatures which are associated with couple stresses. The deformation and stress tensor become non-symmetric. As a consequence of the presence of rotations and couple stresses, the constitutive equation is endowed with a characteristic length corresponding to the mean particle diameter. Thus, numerical results are independent of the spatial discretisation, and boundary value problems remain mathematically well posed. Due to the presence of a characteristic length, a polar approach can model the thickness of shear zones (which are inherent characteristics of granular flow in silos) and related particle size effects. The polar hypoplastic law can reproduce essential features of granular bodies. It takes into account such important properties as: dependence on pressure level, on density, and on the direction of deformation rate, dilatancy and contractancy during shearing with constant pressure, and increase and release of pressure during shearing with constant volume. The constitutive law is characterised by simplicity and a wide range of applications. The material constants can be found by means of standard element tests and simple index tests. They are simply correlated with particle properties. Thus, they can be estimated from granulometric properties (encompassing particle size distribution curve, shape, angularity and hardness of particles) [11], [19]-[21]. The capability of this law has been already demonstrated in solving boundary value problems involving localisation such as biaxial tests, monotonous and cyclic shearing of a narrow granular layer, trap door, silo filling, silo flow, furnace flow, footings, retaining walls and sand anchors. A close agreement between calculations and experiments was achieved. The FE calculations showed also that the thickness of shear zones did not depend upon the mesh discretisation if the size of finite elements in the shear zone was not more than five times the mean particle diameter when using triangular finite elements with linear shape functions for displacements and a Cosserat rotation [22].

Stress changes and couple stress changes during the plane strain deformation of granular bodies are expressed by

$$\overset{\circ}{\sigma}_{ij} = F(e, d_{50}, \sigma_{kl}, m_k, d_{kl}^c, k_k), \quad (2)$$

$$\overset{\circ}{m}_i = f(e, d_{50}, \sigma_{kl}, m_k, d_{kl}^c, k_k), \quad (3)$$

wherein σ_{ij} and m_i are the Cauchy stress tensor and the Cauchy couple stress vector, respectively, e denotes the void ratio, the Jaumann stress rate tensor, and the Jaumann couple stress rate vector, d_{kl}^c the

polar rate of deformation, k_k the rate-of-curvatures vector and d_{50} the mean particle diameter. The following representations of the general constitutive equations (Eqs. 2 and 3) are used:

$$\overset{\circ}{\sigma}_{ij} = f_s [L_{ij}(\hat{\sigma}_{kl}, \hat{m}_k, d_{kl}^c, k_k d_{50}) + f_d N_{ij}(\hat{\sigma}_{ij}) \sqrt{d_{kl}^c d_{kl}^c + k_k k_k d_{50}^2}], \quad (4)$$

$$\overset{\circ}{m}_i / d_{50} = f_s [L_i(\hat{\sigma}_{kl}, \hat{m}_k, d_{kl}^c, k_k d_{50}) + f_d N_i(\hat{m}_i) \sqrt{d_{kl}^c d_{kl}^c + k_k k_k d_{50}^2}], \quad (5)$$

wherein the normalised stress tensor $\hat{\sigma}_{ij}$ and the normalised couple stress vector \hat{m}_i are defined by

$$\hat{\sigma}_{ij} = \frac{\sigma_{ij}}{\sigma_{kk}}, \quad \hat{m}_i = \frac{m_i}{\sigma_{kk} d_{50}}. \quad (6)$$

The scalar factors $f_s = f_s(e, \sigma_{kk})$ and $f_d = f_d(e, \sigma_{kk})$ take into account the influence of the density and pressure level on the stress and the couple stress rates. The stiffness factor f_s is proportional to the granulate hardness h_s and depends on the mean stress and void ratio:

$$f_s = \frac{h_s}{nh_i} \left(\frac{1+e_i}{e} \right) \left(-\frac{\sigma_{kk}}{h_s} \right)^{1-n}, \quad (7)$$

with

$$h_i = \frac{1}{c_1^2} + \frac{1}{3} - \left(\frac{e_{i0} - e_{d0}}{e_{c0} - e_{d0}} \right)^\alpha \frac{1}{c_1 \sqrt{3}}. \quad (8)$$

The constant c_1 is defined by Eq. 16. The granulate hardness h_s represents a density-independent reference pressure and is related to the entire skeleton. It should not be confused with the particle hardness which refers to single particles. The density factor f_d , a kind of a pressure-dependent relative density index, is represented by

$$f_d = \left(\frac{e - e_d}{e_c - e_d} \right)^\alpha. \quad (9)$$

Here e is the current void ratio, e_c is the critical void ratio, e_d denotes the void ratio at maximum densification due to cyclic shearing, e_i is the maximum void ratio, and α and n are constants. The void ratio e is thus bounded by e_i and e_d . The values of e_i , e_d and e_c are assumed to decrease with pressure $-\sigma_{kk}$ according to the equations [21]:

$$e_i = e_{i0} \exp[-(-\sigma_{kk}/h_s)^n], \quad (10)$$

$$e_d = e_{d0} \exp[-(-\sigma_{kk}/h_s)^n], \quad (11)$$

$$e_c = e_{c0} \exp[-(-\sigma_{kk}/h_s)^n], \quad (12)$$

wherein e_{i0} , e_{d0} and e_{c0} are the values of e_i , e_d and e_c for $\sigma_{kk}=0$, respectively. For the tensor and vector

functions L_{ij} , L_i^c , N_{ij} and N_i^c , the following representations are used

$$\begin{aligned} L_{ij} &= a_1^2 d_{ij}^c + \hat{\sigma}_{ij} (\hat{\sigma}_{kl} d_{kl}^c + \hat{m}_i k_k d_{50}), \\ L_i^c &= a_1^2 k_i d_{50} + a_1^2 \hat{m}_i (\hat{\sigma}_{kl} d_{kl}^c + \hat{m}_i k_k d_{50}), \end{aligned} \quad (13)$$

$$N_{ij} = a_1 (\hat{\sigma}_{ij} + \hat{\sigma}_{ij}^*), \quad N_i^c = a_1^2 a_c \hat{m}_i, \quad (14)$$

where

$$\begin{aligned} a_1^{-1} &= c_1 + c_2 \sqrt{\hat{\sigma}_{kl}^* \hat{\sigma}_{lk}^*} [1 + \cos(3\theta)], \\ \cos(3\theta) &= - \frac{\sqrt{6}}{[\hat{\sigma}_{kl}^* \hat{\sigma}_{lk}^*]^{1.5}} (\hat{\sigma}_{kl}^* \hat{\sigma}_{lm}^* \hat{\sigma}_{mk}^*), \end{aligned} \quad (15)$$

$$c_1 = \sqrt{\frac{3}{8}} \frac{(3 - \sin\phi_c)}{\sin\phi_c}, \quad c_2 = \frac{3}{8} \frac{(3 + \sin\phi_c)}{\sin\phi_c}. \quad (16)$$

ϕ_c is the critical (residual) angle of internal friction, θ denotes the Lode angle, i.e. the angle on the deviatoric plane $\sigma_1 + \sigma_2 + \sigma_3 = 0$ between the stress vector and the axis σ_3 (σ_i is a principal stress component). The coefficient a_1^{-1} determining the shape of the stationary stress surface lies empirically in the range 3 to 4.5. The dimensionless polar constant a_c controls the influence of the Cosserat quantities on the material behaviour. It lies in the range of 1.0-5.0 and is correlated with the particle roughness; the higher the constant a_c , the smaller are the polar effects. $\hat{\sigma}_{ij}^*$ denotes the deviatoric part of $\hat{\sigma}_{ij}$. For an isotropic stress state with $\hat{\sigma}_{ij}^* = 0$, the expressions in Eq. 15 become $\cos(3\theta) = 0$ and $a_1^{-1} = c_1$. The first terms are linear and the second terms in Eqs. 4 and 5 are non-linear in d_{kl}^c and $k d_{50}$, respectively. The second terms in Eqs. 4 and 5 describe the modulus of the deformation. Thus, a polar hypoplastic law depends on the direction of deformation.

The FE analyses of silo flow for the case of plane strain were carried out with the following nine material constants (for so-called cohesionless Karlsruhe sand [21]): $e_{i0} = 1.3$, $e_{d0} = 0.51$, $e_{c0} = 0.82$, $\phi_c = 30^\circ$, $h_s = 190$ MPa, $\alpha = 0.3$, $n = 0.5$, $d_{50} = 0.5$ mm and $a_c = a_1^{-1}$. The parameters h_s and n are determined from a single oedometric compression test with an initially loose specimen, h_s reflects the slope of the curve in a semi-logarithmic representation, and n its curvature. The constant α is found from a triaxial test with a dense specimen. It reflects the height and position of the peak value of the stress-strain curve. The angle ϕ_c is estimated from the angle of repose or measured in a triaxial test with a loose specimen. The values of e_{i0} , e_{d0} , e_{c0} and d_{50} can be obtained with index tests ($e_{c0} \approx e_{\max}$, $e_{d0} \approx e_{\min}$, $e_{i0} \approx (1.1-1.5)e_{\max}$).

3. Finite element data

The plane strain calculations of granular flow were performed with a bin with a height of $h = 0.50$ m and a width of $b = 0.20$ m ($h/b = 2.5$, $b/d_{50} = 400$) [23]. The FE mesh with quadrilateral finite elements composed of four diagonally crossed triangles was applied to avoid volumetric locking and spurious element behaviour. A total of 3000 triangular elements with linear shape functions for the displacements and the Cosserat rotation were used. Symmetry with respect to the centre line was taken into account. In order to realistically describe the interface behaviour along the wall, the FE mesh was strongly refined at the wall. The width of three quadrilateral elements close to the wall was equal to 0.5 mm, 1.5 mm, 3 mm and the width of the next five elements was 5 mm, respectively. The height of all quadrilateral elements was 10 mm. Quasi-static flow (without inertial forces) was initiated through constant vertical displacement increments prescribed to all nodes along a smooth bottom. Thus, mass flow was obtained in the silo.

The FE calculations were carried out mainly with an initially dense solid (low initial void ratio) between very rough walls ($r_w \geq d_{50}$). In this case, the largest stress increments occur during silo flow after bottom displacement [22]-[24]. The wall roughness r_w is depicted as a relative height between the highest and the lowest point along the surface at a length of $(2-3) \times d_{50}$ [22]. For modelling of very rough walls in silos, full shearing of the material along a wall was assumed [22]:

$$u_1 = 0, \quad u_2 = 0, \quad \omega^c = 0. \quad (17)$$

As a result of the assumed polar boundary conditions along the wall (Eq. 17), the wall friction angle can be derived and no special interface elements are needed [22]. The remaining boundary conditions in the silo fill were along the top traction and moment-free, and in the symmetry axis: $u_1 = 0$, $\omega^c = 0$ and $\sigma_{21} = 0$ (σ_{21} – vertical shear stress).

To investigate the influence of the wall inclination and wall imperfection, the analyses were carried out with the same initial stress state, namely with the so-called K_0 state (frequently used in soil mechanics): $\sigma_{22} = \gamma x_2$, $\sigma_{11} = \sigma_{33} = K_0 \gamma x_2$, $\sigma_{12} = \sigma_{21} = m_1 = m_2 = 0$ (σ_{11} – horizontal normal stress, σ_{22} – vertical normal stress, σ_{33} – normal stress perpendicular to the plane of deformation, σ_{12} – horizontal shear stress, σ_{21} – vertical shear stress, m_1 – horizontal couple stress, m_2 – vertical couple stress, γ – initial unit weight of sand, x_2 – vertical coordinate measured from the top of the

solid, $K_0=0.40$ – pressure coefficient at rest). To study the effect of the initial stress state on wall stresses, a comparative calculation was also performed with initial stresses after filling according to a slice method by Janssen [6]:

$$\sigma_{22} = \frac{\gamma b}{2\bar{K}\tan\varphi_w} \left[1 - \exp\left(\frac{-2\bar{K}\tan\varphi_w x_2}{b}\right) \right], \quad (18)$$

$$\sigma_{11} = \bar{K}\sigma_{22}, \quad (19)$$

$$\sigma_{12} = \sigma_{21} = \sigma_{11}\tan\varphi_w(1 - 2x_1/b), \quad (20)$$

$$\sigma_{33} = \sigma_{11}, \quad (21)$$

where \bar{K} is the mean pressure coefficient, φ_w denotes the mean wall friction angle, x_1 is the horizontal coordinate measured from the wall, b denotes the silo width, and σ_{33} is the normal stress perpendicular to the plane of deformation. Both model experiments [22] and numerical calculations [12] show that stresses in silos during filling can be approximated with a slice method provided that \bar{K} and φ_w are empirically estimated. The choice was made on the basis of model tests [22]: $\bar{K}=0.29$ and $\varphi_w=43^\circ$ (initially dense sand between parallel and very rough walls).

Four different wall inclinations in a silo were assumed: parallel walls (**Fig. 1a**), slightly convergent walls with a wall inclination from the bottom equal to

$\alpha=88^\circ$ (**Fig. 1b**), slightly divergent walls with a wall inclination from the bottom equal to $\alpha=88^\circ$ (**Fig. 1c**), and parallel walls ($h=0.25$ m) and slightly convergent walls ($h=0.25$ m) with a wall inclination from the bottom equal to $\alpha=88^\circ$ (**Fig. 1d**).

Two different wall imperfections at the mid-height of the wall ($h=0.25$ m) were taken into account: a small imperfection directed to the inside of the bulk solid (**Fig. 1e**) and a small imperfection directed to the outside of the bulk solid (**Fig. 1f**). The height of both imperfections was $h_1=40$ mm ($h_1/b=0.2$) and the width $b_1=2.5$ mm ($b_1/b=0.0125$).

The calculations were carried out with large deformations and curvatures. In this case, an Updated Lagrangian formulation was applied using both the Jaumann stress rate and the Jaumann couple stress rate [22]. At the same time, the changes of the element configuration and the element volume were taken into account.

The integration was performed in 3 sample points placed in the middle of each triangular element side. The density of the silo fill was kept constant. For the solution of the non-linear equation system, a modified Newton-Raphson scheme with line search was applied using an initial global stiffness matrix calculated with only two first terms of the constitutive equations (Eqs. 4 and 5). To accelerate the calculations in the

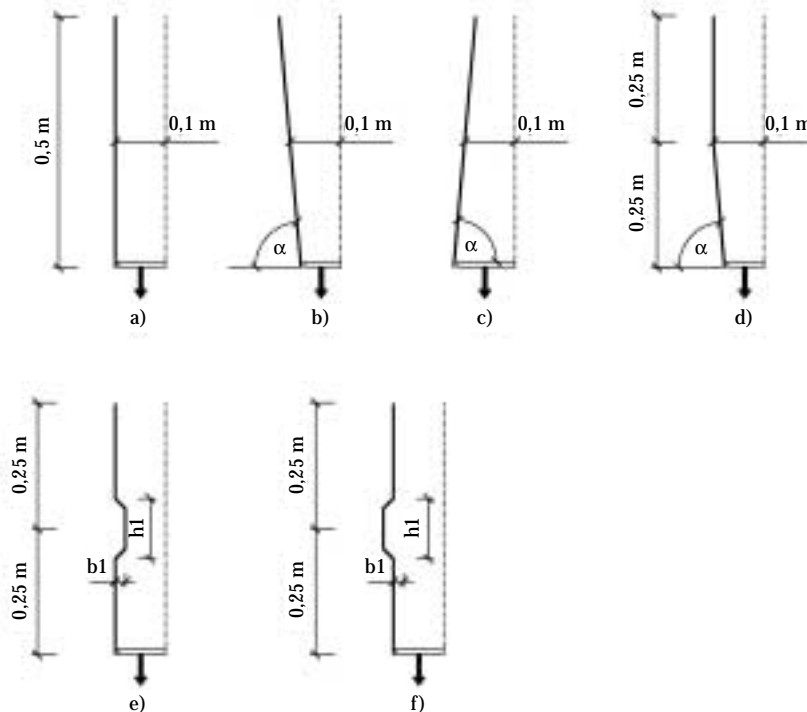


Fig. 1 Different wall inclinations and wall imperfections assumed for FE calculations

softening regime, the initial increments of displacements and the Cosserat rotation in each calculation step were assumed to be equal to the converged increments from the previous step. In addition, to prevent possible inadmissible stress states (in particular in the corner of the wall at the bottom), a sub-stepping algorithm was used (deformation and curvature increments were divided into smaller parts within each step). The iteration steps were performed using translational and rotational convergence criteria (found by means of preliminary FE calculations). For the time integration of stresses and couple stresses in finite elements, a one-step Euler forward scheme was applied.

4. Numerical results

Influence of initial void ratio and initial stress state

Figure 2 shows the evolution of normalised hori-

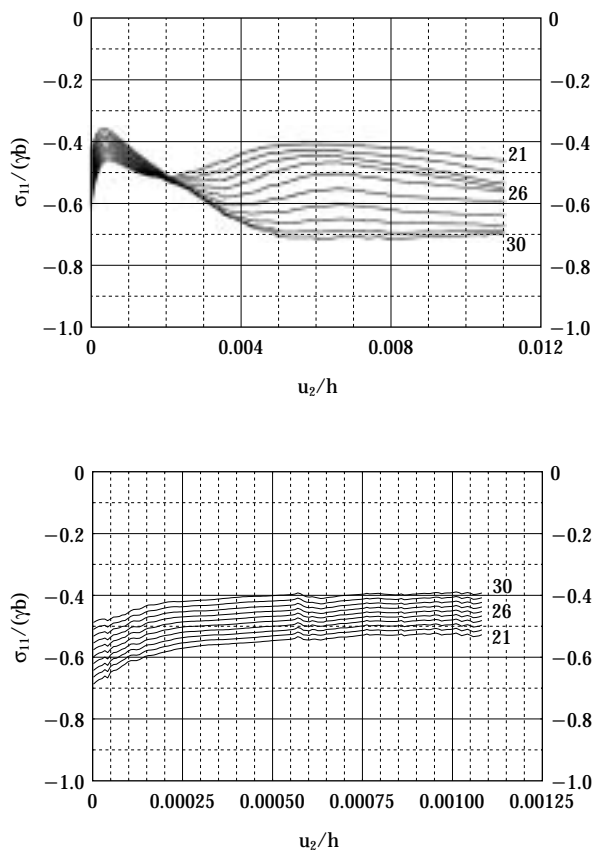


Fig. 2 Evolution of normalised horizontal normal stresses $\sigma_{11}/(\gamma b)$ during normalised vertical bottom displacement u_2/h along the wall at height $h=0.20-0.30$ m in a silo with parallel walls:
a) dense sand ($e_0=0.60$), b) loose sand ($e_0=0.90$)

zontal normal stresses $\sigma_{11}/(\gamma b)$ at the mid-height of the wall ($h=0.20-0.30$ m) during the normalised vertical bottom displacement u_2/h in a model silo with parallel walls of **Figure 1a** at the onset of quasi-static granular flow. The onset of silo flow is crucial with regard to maximum wall stresses [22]-[24]. Later, wall stresses have a tendency to oscillate with wandering small peaks due to the appearance of shear zones along a wall and inside of the flowing material [22]-[24]. The presented range of u_2/h for dense sand ($e_0=0.60$) and loose sand ($e_0=0.90$) in **Figure 2** is different.

The shear stresses were not taken into account during filling (K_0 – initial stress state), thus wall stresses decreased at the beginning of flow (**Fig. 2**). The wall element ‘21’ is located at a height of 0.20 m and the wall element ‘30’ at a height of 0.30 m above the bottom (**Fig. 2**). Other wall elements are located between ‘21’ and ‘30’ at a distance of 10 mm. The wall stresses in dense sand decrease first, then they increase and reach an asymptote or they reach an asymptote. The wall stresses in loose sand decrease and very quickly reach a residual state ($u_2/h=0.0005$). The maximum normalised horizontal stresses $|\sigma_{11}/(\gamma b)|$ in the middle of the wall are about 0.70 (dense sand) and 0.55 (loose sand). The stresses in loose sand increase with increasing depth. However, the stresses in dense sand are not distributed proportionally with a silo depth due to interior shear zones inside the flowing solid [22]-[24]. The maximum horizontal wall stresses for dense sand are higher by about 30% than those calculated by the German Silo Code (plane strain, dense sand, very rough walls): $|\sigma_{11}/(\gamma b)|=0.55$ kPa (with $\gamma=17.0$ kN/m³, $\bar{K}=0.70$, $\tan\phi_w=0.60$, $b=0.20$ m, $h=0.25$ m). In large silos, the normalised wall stresses become smaller due to a decrease of d_{50}/b and an increase of pressure (reduction of the internal friction angle, dilatancy angle and stiffness) [23], [24].

The effect of the initial stress state on the evolution of stresses $\sigma_{11}/(\gamma b)$ in a silo of **Figure 1a** is demonstrated in **Figure 3**. The calculations were performed with dense sand and initial stresses according to a slice method by Janssen (Eqs. 18-21). The results show that the initial stress state influences the horizontal wall stresses only up to $u_2/h=0.0005$. Later, the evolution of stresses is the same, independent of the initial stress state. The maximum normalised stress increment after outlet opening is about $|\Delta\sigma_{11}/(\gamma b)|=0.40$ (dense sand). The stresses during flow increase more than twice when compared to silo filling.

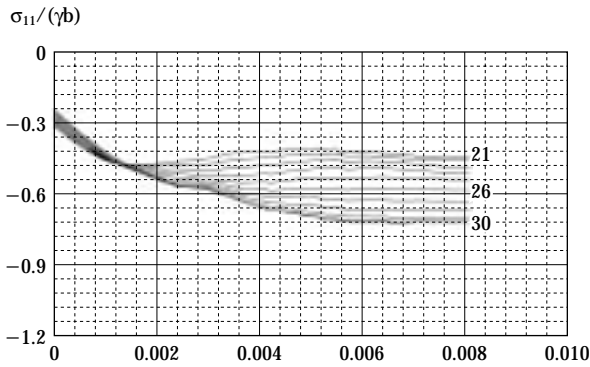


Fig. 3 Evolution of normalised horizontal normal stresses $\sigma_{11}/(\gamma b)$ during normalised vertical bottom displacement u_2/h along the wall at height $h=0.20-0.30$ m in a silo with parallel walls (dense sand, $e_o=0.60$, initial stress state by Janssen)

Influence of wall inclination

The effect of the wall inclination on horizontal wall stresses during flow (at different scales of u_2/h) is shown in **Figures 4** and **5** (K_o – initial stress state). Even a small change of the wall inclination influences the stresses. The maximum normalised horizontal normal stresses on the wall $|\sigma_{11}/(\gamma b)|$ (**Fig. 4**) in the middle region are 8% higher in a silo with slightly convergent walls of **Figure 1b**, and by 2% lower in a silo with slightly divergent walls of **Figure 1c** compared to the silo with parallel walls (**Fig. 2a**). The increase of horizontal normal stresses (**Fig. 5**) below the transition between a parallel and convergent part of the silo of **Figure 1d** is similar to that in the silo with convergent walls at mid-height (**Fig. 4a**).

Influence of wall imperfections

The evolution of normalised horizontal normal stresses $\sigma_{11}/(\gamma b)$ during vertical bottom displacement in the middle region of the wall in a model silo with parallel imperfect walls (dense sand with $e_o=0.60$, K_o – initial stress state) is depicted in **Figure 6**.

The FE results demonstrate that a small imperfection in the wall increases (by about 40%) or decreases (by about 30-50%) the maximum horizontal wall stresses compared to a perfect wall (**Fig. 2a**). The stresses increase significantly on the convergent part of the imperfection ($\alpha=75^\circ$) and decrease significantly on the divergent part of the imperfection ($\alpha=75^\circ$). They also increase directly above the divergent part. Other stresses at imperfections are approximately in the range of stresses for a silo with perfect walls.

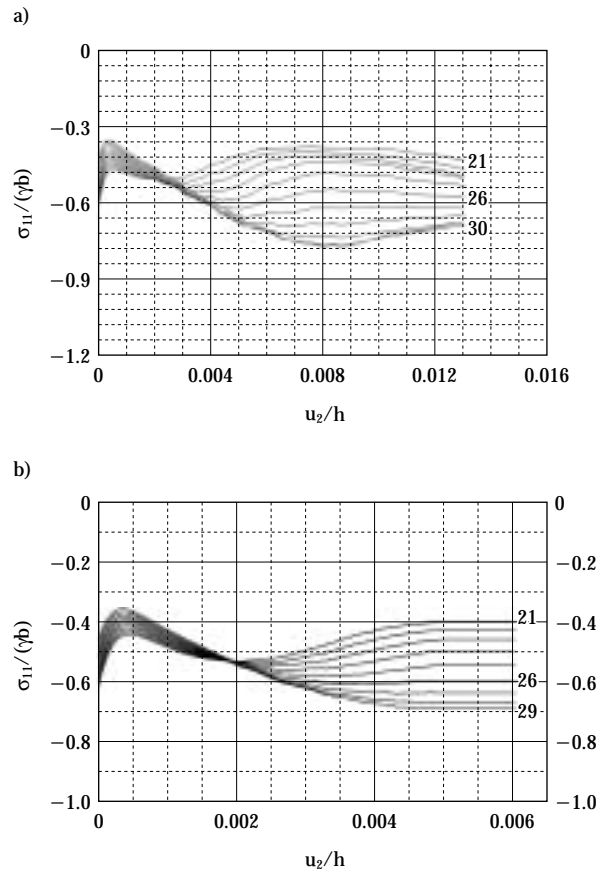


Fig. 4 Evolution of normalised horizontal normal stresses $\sigma_{11}/(\gamma b)$ in dense sand ($e_o=0.60$) during normalised vertical bottom displacement u_2/h along the wall at height $h=0.20-0.30$ m:
a) silo with slightly convergent walls, b) silo with slightly divergent walls

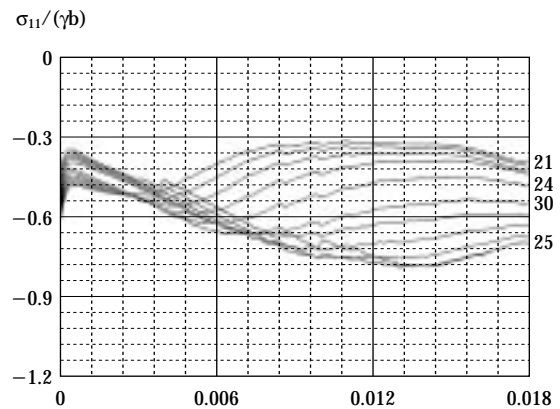


Fig. 5 Evolution of normalised horizontal normal stresses $\sigma_{11}/(\gamma b)$ in dense sand ($e_o=0.60$) during normalised vertical bottom displacement u_2/h along the wall at height $h=0.20-0.30$ m (silo with parallel and slightly convergent walls of **Fig. 1d**)

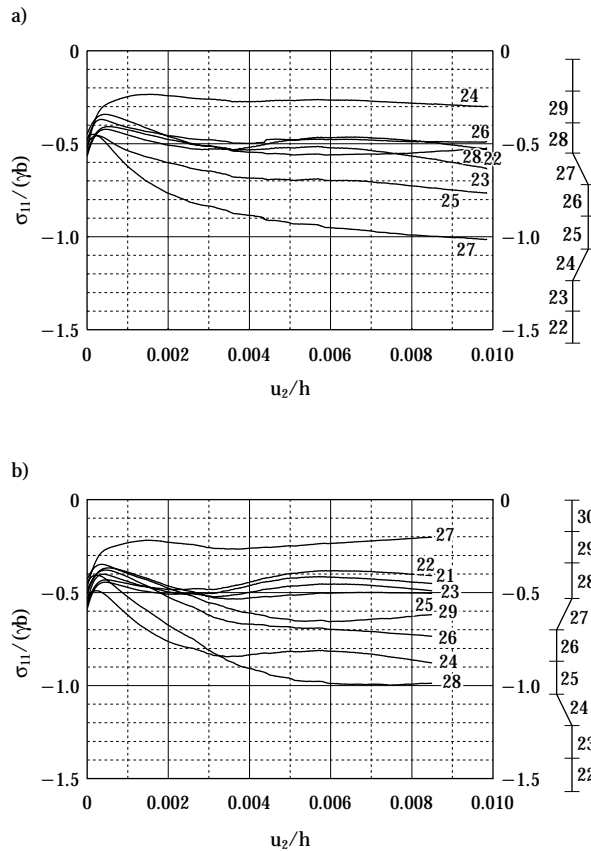


Fig. 6 Evolution of normalised horizontal normal stresses $\sigma_{11}/(\gamma b)$ in dense sand ($e_0=0.60$) during normalised vertical bottom displacement u_2/h along the wall ($h=0.25$ m) in a silo with:
a) inward wall imperfection, b) outward wall imperfection

5. Conclusions

The following conclusions can be drawn from FE calculations at the onset of granular flow in a silo with very rough walls using a polar hypoplastic law:

Bulk solids during silo flow are sensitive to every change in the direction of shear deformation.

The effect of the initial void ratio has a large influence on horizontal normal stresses on the wall. The wall stresses in a dense solid are larger during flow than in a loose one.

The initial stress state has an insignificant effect on maximum wall stresses.

Horizontal wall stresses decrease along divergent walls and increase along convergent ones.

Even small imperfections in a silo wall can cause a significant increase of local horizontal stresses.

The wall stresses during flow of dense solids in silos with very rough walls can be larger during flow than standard values.

The FE calculations will be continued. The influence of the wall roughness, the initial void ratio in the solid, and the magnitude and shape of wall imperfections will be analysed. To realistically describe the localisation of shear zones inside a flowing solid, the calculations will be performed for the entire silo. The initial void ratio will be stochastically distributed in the solid with a random generator.

Literature

- [1] Schwedes, J.: Fließverhalten von Schüttgütern in Bunkern, Verlag Chemie, Weinheim, 1968.
- [2] Jenike, A. W., Johanson, J. R., Carson, J. W.: Bin loads – part 2, 3 and 4, Journal of Engineering for Industry, ASME, pp. 1-6, 1973.
- [3] van Zanten, D. C., Mooij, A.: Bunker Design, part 2: Wall pressures in mass flow, Journal of Engineering for Industry, ASME, pp. 814-818, 1977.
- [4] Stashevskii, S. B.: Stresses in the neighbourhoods of defects in bunker walls, Fiziko-Tekhnicheskie Problemy Razrabotki Poleznykh Iskopaemykh, 5, pp. 29-37, 1982.
- [5] Stashevskii, S. B.: Neue Silo-Konzepte, Lecture at the Institute for Soil Mechanics, University Karlsruhe, 1992.
- [6] Schwedes, J., Schulze, D., Kwade, R.: Lagern und Fliessen von Schüttgütern, Script of the Institut für Mechanische Verfahrenstechnik, Technische Universität Braunschweig, 1999.
- [7] Tejchman, J., Ummenhofer, T.: Bedding effects in bulk solids in silos – experiments and a polar hypoplastic approach, Thin-Walled Structures, 37, 4, pp. 333-361, 2000.
- [8] Lo, S. C. R., Lee, I. K.: Response of granular soil along constant stress ratio path, ASCE Eng. Mech., SM6, pp. 117-141, 1990.
- [9] Wu, W.: Hypoplastizität als mathematisches Modell zum mechanischen Verhalten granularer Stoffe, Publication Series of the Institute of Soil and Rock Mechanics, University Karlsruhe, 129, 1992.
- [10] Tatsuoka, F., Siddiquee, M. S. A., Yoshida, T.: Testing methods and results of element tests and testing conditions of plane strain model bearing capacity tests using air-dried dense Silver Leighton Buzzard Sand, Internal Report, University of Tokyo, 1994, pp. 1-120, 1994.
- [11] Herle, I.: Hypoplastizität und Granulometrie einfacher Korngerüste, Publication Series of the Institute of Soil and Rock Mechanics, University Karlsruhe, 142, 1997.
- [12] Tejchman, J.: Numerical simulation of filling in silos with a polar hypoplastic constitutive law, Powder Technology, 96, pp. 227-239, 1998.
- [13] Tejchman, J., Herle, I., Wehr: FE-studies on the influence of initial void ratio, pressure level and mean grain diameter on shear localisation, Int. J. Num. Anal. Meth. Geomech., 23, pp. 2045-2074, 1999.

- [14] Tejchman, J., Gudehus, G.: Shearing of a narrow granular strip with polar quantities. *J. Num. and Anal. Methods in Geomechanics*, 25, pp. 1-28, 2001.
- [15] Tejchman, J.: Patterns of shear zones in granular materials within a polar hypoplastic continuum, *Acta Mechanica*, 155, 71-94, 2002.
- [16] Gudehus, G., Tejchman, J.: Silo music and silo quake – experiments and a numerical Cosserat approach, *Powder Technology*, 76, pp. 201-212, 1993.
- [17] Tejchman, J.: Silo-quake – measurements, a numerical polar approach and a way for its suppression, *Thin-Walled Structures*, 31/1-3, pp. 137-158, 1998.
- [18] Schäfer, H.: Versuch einer Elastizitätstheorie des zweidimensionalen ebenen Cosserat-Kontinuums, *Miszellaneen der Angewandten Mechanik*, Festschrift Tolmien, W., Berlin, Akademie-Verlag, 1962.
- [19] Gudehus, G.: A comprehensive constitutive equation for granular materials, *Soils and Foundations*, 36, 1, pp. 1-12, 1996.
- [20] Herle, I., Gudehus, G.: Determination of parameters of a hypoplastic constitutive model from properties of grain assemblies. *Mechanics of Cohesive-Frictional Materials*, 4, 5, pp. 461-486, 1999.
- [21] Bauer, E.: Conditions of embedding Casagrande's critical states into hypoplasticity, *Mechanics of Cohesive-Frictional Materials*, 5, pp. 125-148, 2000.
- [22] Tejchman, J.: Shear localisation and autogeneous dynamic effects in granular bodies, *Publication Series of the Institute for Rock and Soil Mechanics, Karlsruhe University*, 140, 1997.
- [23] Tejchman, J.: Scale effects in bulk solids during silo flow. *The International Journal of Storing, Handling and Processing Powder (Powder Handling and Processing)*, Vol.13, No.2, pp. 165-173, 2001.
- [24] Tejchman, J., Gudehus, G.: Verspannung, Scherfugenbildung und Selbsterregung bei der Siloentleerung. "Silobauwerke und ihre spezifischen Beanspruchungen", eds.: J. Eibl and G. Gudehus, *Deutsche Forschungsgemeinschaft, Wiley-VCH*, pp. 245-284, 2000.

Author's short biography



Jacek Tejchman

Prof. Dr.-Ing. habil. Jacek Tejchman was born in Poland. He received his MSc degree from the Civil Engineering Department at the Gdansk University of Technology (speciality: reinforced concrete structures). He received his PhD degree from the Technical University of Karlsruhe in Germany in 1989 (Institute of Rock and Soil Mechanics) with a thesis on scale and dilatancy effects during granular flow. Afterwards, he made his habilitation thesis in 1996 again at the Technical University of Karlsruhe (Institute of Rock and Soil Mechanics) on shear localisation and autogeneous dynamic effects in granular bodies. He has worked at the Technical University of Karlsruhe for 10 years (1986-1996). He became professor in 1998 and head of the Institute for Building and Material Engineering at the Gdansk University of Technology in Poland (Faculty of Civil Engineering). His main research interests concern numerical modelling of the behaviour of granular materials, concrete and reinforced concrete elements and structures taking into account the localisation of deformations (shear zones and cracks). He is a member of the Deutsche Gesellschaft für Erd- und Grundbau and the International Working Party on the Mechanics of Particulate Solids.

X-Ray Analysis of Fluidized Beds and Other Multiphase Systems[†]

J.G. Yates, D.J. Cheesman and P. Lettieri
*University College London**
D. Newton
*BP Chemicals***

Abstract

The attenuation of a beam of X-rays as it passes through a body has been used for over 100 years in diagnostic medicine. A more recent application of the technique has been in the study of industrial-type units such as gas-solid fluidized beds, and this paper reviews this application in the analysis of the hydrodynamic features of bubbling and circulating fluidized beds. The measurement of jet penetration into bubbling beds and the study of bubble slurry columns are also considered. The equipment used and its methods of operation are described and the salient results of the more revealing investigations are summarised both from a qualitative and a quantitative viewpoint.

1. Introduction

Non-invasive experimental techniques are invaluable for providing a detailed insight into the flow patterns and general hydrodynamic characteristics of multiphase systems. One such technique involves the use of X-rays and is based on the same principles as are used in diagnostic medicine to record the structures of body parts that are opaque to visible light. The first recorded use of X-rays to study gas-solid fluidized beds dates from the mid-1950s, and over the subsequent fifty or so years, the technique has been applied to a wide range of two- and three-phase fluidized systems. The technique has enabled gas and solids flow patterns to be observed and quantified and has led to the improved design of internal structures such as gas distributors and heat transfer surfaces in industrial units.

2. Bubbling fluidized beds

Grohse [1] first reported the use of X-rays to determine the instantaneous and time-averaged bulk density of a finely divided powder fluidized at a range of gas velocities and with three different designs of gas distributor, namely a perforated plate, a mesh screen and a porous plate. The X-ray source consisted of

standard components of an X-ray diffraction unit with a tungsten target X-ray tube. The detection equipment consisted of a modification of the rate meter in a standard X-ray detector fed by a scintillation probe. The rate meter response was logarithmic over most of its range of sensitivity and in accordance with Eq. (1) below, the reading varied approximately linearly with the local bed density being measured. The fluidized bed material was silicon powder with a mean particle size of about 50 μm and was contained in a cylindrical borosilicate glass column of diameter 8.5 cm. The results were analysed in terms of the Beer-Lambert law which for the attenuation of essentially parallel, monochromatic X-rays may be written:

$$I = I_0 \exp(-\mu_m \rho l) \quad (1)$$

where μ_m is the mass attenuation coefficient of the bed material, ρ is its density and l is the bed thickness. In practice, polychromatic radiation is normally employed but Eq. (1) is generally considered an adequate approximation. The term $\mu_m \rho l$ is called the *optical density* of the absorbing material and for two different materials A and B producing identical X-ray attenuation, the two optical densities are equal:

$$\mu_m^A \rho_A l_A = \mu_m^B \rho_B l_B \quad (2)$$

then the bulk density of A may be written:

$$\rho_A = K l_B \quad (3)$$

Grohse [1] determined the value of K , which has units of $\text{kg m}^{-3} \text{m}^{-1}$, by expanding the fluidized bed of

* Torrington Place, London WC1E 7JE, UK

** Chertsey Toad, Sunbury-on-Thames, Middlesex TW16 7LL, UK

[†] Accepted: June 17, 2002

powder at gas velocities between zero and the minimum bubbling point and accurately measuring the expanded bed height; then under knowledge of the mass of powder in the bed, an average bed density could be found for each gas velocity. The value of I_B was the thickness of pure aluminium that gave the same beam attenuation as a bed of solids of density ρ_A . The work clearly demonstrated the two-phase nature of fluidized beds but gave little in the way of detailed structure. It did, however, make the first mention of the “bed collapse” technique which has been applied more recently to investigate the effect of operating parameters on dense-phase voidage (see below).

Romero and Smith [2] used flash X-ray radiography to study the internal structure of fluidized beds and obtained data not only on bed density distribution but also on the shape, size and velocity of gas bubbles in an air-fluidized bed of sand. Their unit consisted of two flash tubes, one operating at 300 kV and the other at 600 kV, each producing a square pulse of energy at 1,000 amps for a duration of about 0.2 μ s. The tubes were mounted on opposite walls of a lead-lined room which housed a 7.6-cm square plexiglass column containing a fluidized bed of sand. After passing through the bed, the X-ray beam was recorded on 20 \times 25-cm sheets of film, the 300-kV tube illuminating the lower part of the bed and the 600-kV tube the upper part. To measure bubble velocity, the two units were fired in sequence a few tenths of a second apart.

To determine bed density, Romero and Smith measured the darkness of their films using an optical densitometer, but in order to compensate for variations in X-ray operating voltages and variations in the quality and processing of the films, each photograph was compared with a standard consisting of sand-filled wedges made from plexiglass. These were mounted on the side of the fluidization column so that an X-ray photograph of them was obtained each time the X-ray was fired. The wedge gave a film darkness gradation that could be related to sand thickness, and by comparing film darkness in the wedge with darkness in the bed, the local bed density could be obtained.

Rowe and Everett [3,4,5] described the design and operation of a fluidized bed X-ray system in which the attenuated beam on passing through the bed was registered on a 0.22-m diameter Mullard image intensifier. The X-ray tube used was a Machlett Super Dynamax 125 with a rotating anode and a fine or broad focal spot of 1 mm or 2 mm diameter. It had a rating of 200 mA at 120 kV_p for 10⁻² s on fine focus or 500 mA at the same voltage and duration on broad

focus. The image intensifier augmented the beam intensity by a factor of 3×10^3 and was filmed by a 70-mm cine camera at a rate of 6 or 8 frames/s, the X-ray beam being synchronised with the camera and pulsed for 2.5 ms. A series of rectangular section fluidized beds were studied with thicknesses from 1.4 cm to 29.5 cm. Bubble sizes, their number and velocity were measured at various heights up to 70 cm in beds of alumina, carbon, quartz, glass ballotini and crushed glass powder fluidized by ambient air; **Fig. 1** shows a typical image. **Fig. 2** shows a sketch of the X-ray imaging technique.

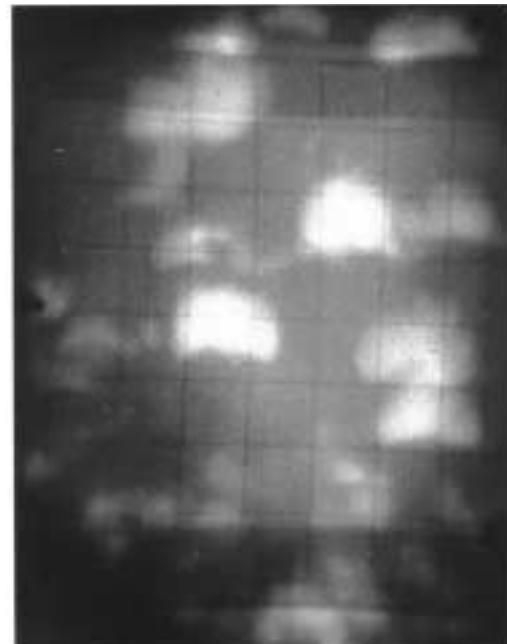


Fig. 1 X-ray image of a freely bubbling fluidized bed [3]

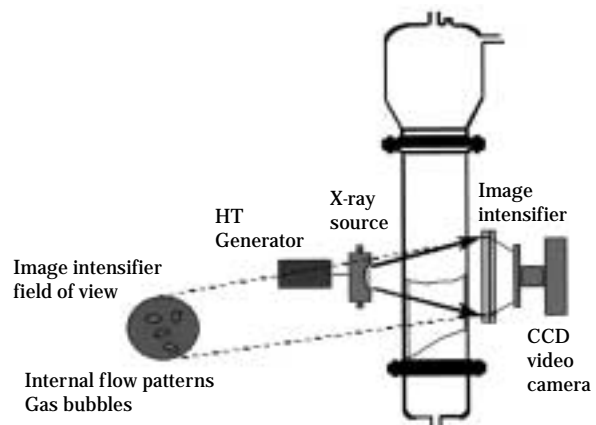


Fig. 2 X-ray imaging technique

One result to come from these three seminal papers related to the effect of the bed thickness on the minimum fluidization velocity, U_{mf} . It was found that U_{mf} remained constant for beds thicker than 15 cm but decreased by up to 50% as the bed size decreased to the smallest dimension of 1.4 cm.

A similar system to that of Rowe and Everett [3,4,5] was used by Rowe et al. [6] to make detailed measurements of the emulsion-phase voidage in fluidized beds and its variation with the particle size distribution of the bed material. In this study the cine camera was operated at 50 frames/s. As described above for Romero and Smith [4], a calibrating wedge filled with bed material was used to quantify the observations. By comparing the optical density of a region on the film with that at a given level of the wedge of known dimensions, the powder voidage in that region could be determined from:

$$\varepsilon_e = 1 - (1 - \varepsilon_w) (\Delta W / \Delta B) \quad (4)$$

where ε_e and ε_w are the powder voidages in the emulsion phase and the wedge, respectively, ΔW is the wedge thickness with the same optical density as the bed, and ΔB is the bed thickness. An example of such a measurement is shown in Fig. 3.

A series of powders with different contents of "fines" was studied, fines being defined as the weight percentage of particles with sieve sizes less than 45 μm . The experimental results are summarised in Figs. 4 and 5 and consisted of measurements of the dense-phase voidage in bubble-free regions of the bed and measurements of the bed height. No variation

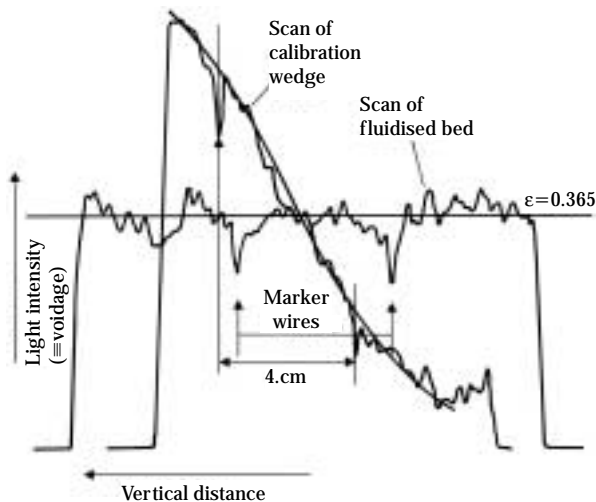


Fig. 3 Microdensitometer scan of an X-ray film and a calibrating wedge [6]

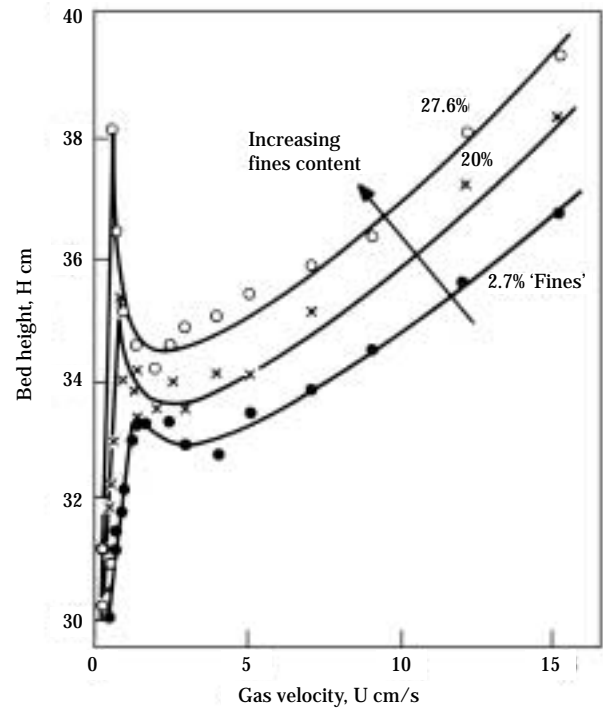


Fig. 4 Variation of fluidized bed height with superficial gas velocity [6]

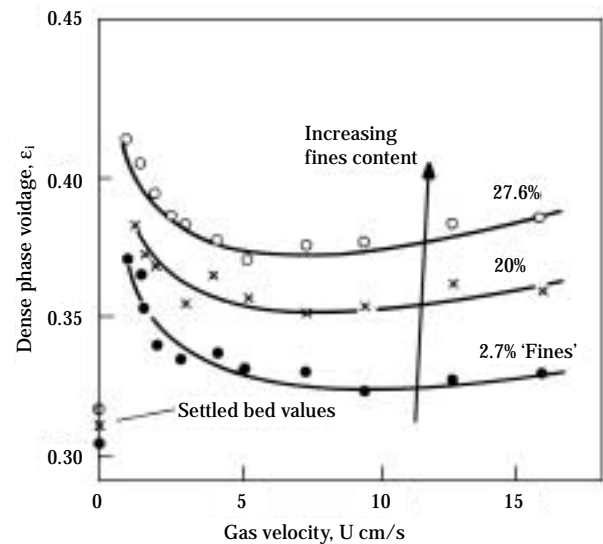


Fig. 5 Variation of emulsion-phase voidage with superficial gas velocity [6]

with height of the dense-phase voidage was observed. Settled-bed voidages refer to the tapped, unfluidized bed.

Theoretical considerations by Rowe et al. [6] led to the following expression for the emulsion-phase gas

flow rate:

$$Q_e/A = U_{ge}(3 - 4f_b)\epsilon_e/3 \quad (5)$$

where all the quantities on the right-hand side of the equation could be calculated from the experimental results. **Figure 6** shows the results of plotting Eq. (5), and it is clear that the emulsion gas flow rate is very much greater than the flow corresponding to that at minimum fluidization of the powder containing 27.6% fines, 0.207 cm/s, and that it increases with overall gas velocity and fines content.

This is favourable from the point of view of fluidized bed reactor operation, a conclusion that was verified in a subsequent study by Yates and Newton [7].

The X-ray technique was used by Hoffmann and Yates [8] to study the effect of pressure on fluidized beds of powders in Groups A and B of the Geldart [9] classification. They found in the case of Group A powders that while the minimum fluidization velocity, U_{mf} , was unaffected, the region of bubble-free expansion between U_{mf} and U_{mb} , the minimum bubbling velocity, increased with increasing pressure. This observation is in accordance with the theory of fluid-bed stability developed by Foscolo and Gibilaro and recently reviewed by Gibilaro [10]. For Group B powders, Hoffmann and Yates found that mean bubble diameters increased slightly up to 16 bar and decreased thereafter up to 60 bar pressure. In addition,

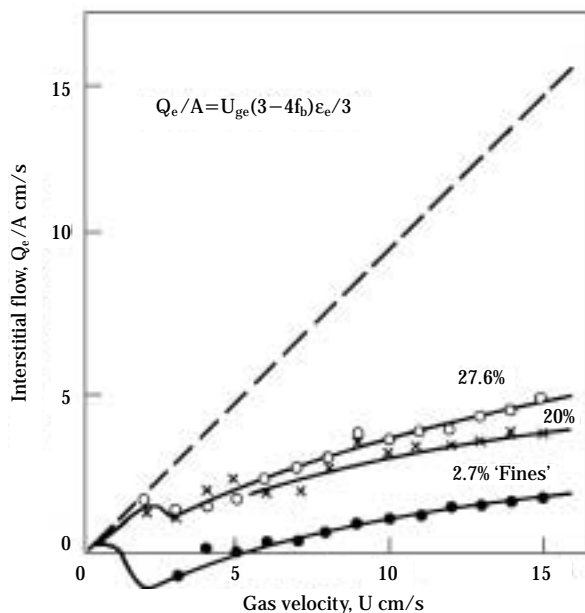


Fig. 6 Variation of emulsion-phase gas flow with superficial gas velocity [6]

the bubble velocity coefficient κ in:

$$u_b = \kappa (gd_b/2)^{1/2} \quad (6)$$

was found to decrease up to 20 bar pressure but then to increase quite markedly above 20 bar up to the highest pressures at which observations were made. This latter increase coupled with the observed decrease in bubble size meant that although bubbles were becoming smaller, their rise velocities were increasing, the reverse of the tendency observed at ambient pressure. These results were subsequently corroborated by Olowson and Almstedt [11] using a combined capacitance and pressure probe to measure bubble characteristics in a bed of Group B powder.

Other X-ray studies of the effects of system pressure on fluidization were reported by Rowe et al. [12] and Barreto et al. [13].

X-ray images of fluidized beds may be enhanced so as to investigate solids volume fractions in the regions close to the boundaries of bubbles. In one such study [14], the X-ray source was pulsed for a period of 1 ms and the pulses synchronised with a video recorder at an equivalent speed of 25 frames/s. Both the radiation source and the detector could be moved vertically relative to the fluidized bed, thus allowing different positions to be examined. The recorded images were transferred off-line for processing and analysis using a PC. The video signal was relayed to a framestore board (Imaging Technology VP 1100) via a timebase corrector, and the images processed using Bioscan Optimas software operating in Windows 3.0.

As discussed above, when X-rays pass through a solid material they are attenuated by processes of absorption, reflection and scattering, and the extent of the attenuation is a function of the chemical nature of the solid and of the quantity of material in the path of the beam. The Beer-Lambert law (Eq. 1) may be written:

$$I = I_0 - I_0(\mu_m \rho l) + \dots \quad (7)$$

In many cases, the second order and higher terms in the exponential may be neglected and Eq. (7) may be used to an acceptable degree of accuracy.

The attenuation of X-rays by ambient air is negligible and so for an air-fluidized bed we can express the bulk density ρ in terms of the solids fraction of the bed through which the beam passes:

$$I = I_0 - I_0(\mu_m \rho_s)(1 - \epsilon)l \quad (8)$$

where ρ_s is the solids density and ϵ is the voidage of the bed material.

In order to relate the measured intensity of the

transmitted beam to the voidage of the material through which it passes, it is necessary to calibrate the system according to Eq. (8) and this may be done as before using a wedge filled with the powder to be studied. The wedge is set up vertically in the X-ray beam and the transmitted intensity measured on a range of grey scales from 0 to 225 as a function of the wedge thickness l_w . The calibration for the Group B alumina powder used in this study [14] gave an explicit relationship between bed voidage, transmitted intensity and path length l of:

$$\varepsilon = 1 - (655.2 - I) / (55.47 I) \quad (9)$$

The recorded X-ray images of single bubbles were computer-enhanced to show coloured zones of varying voidage; such an image is shown in Fig. 7, where the regions of expanded voidage surrounding the bubble, the so-called “shell” region, are clearly visible. The black area is the emulsion phase with an average voidage of 0.445, the green with 0.495, the blue with 0.526, the cyan with 0.627 and the red area is the bubble itself with a voidage of 1.0.

Two points must be emphasised about this image. Firstly, the computer is programmed to calculate average values of voidage between any predetermined range of intensity values and to colour-code that range; there is in fact a continuous gradation in voidage between one zone and the next. Secondly, the image is a representation in two dimensions of a truly three-dimensional object, in other words a silhouette. This means that the voidage indicated is an average value across a chord of the more or less spherical region of the bed around the bubble. The deconvolu-

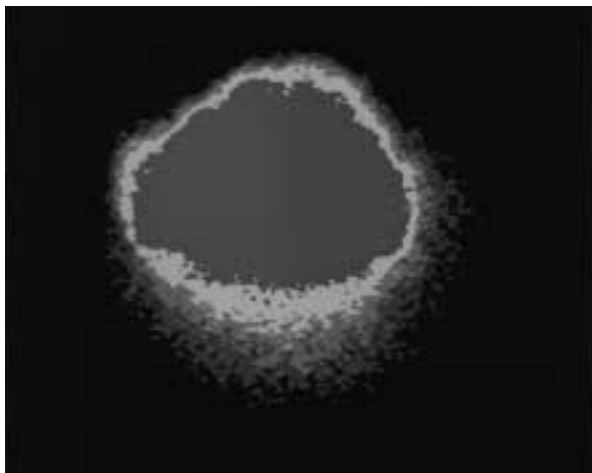


Fig. 7 X-ray image of a bubble in a fluidized bed of a Group B powder [14]

tion of these averages to give point values of porosity will now be considered.

The X-ray intensity measured in the x-direction across a section of such a sphere may be expressed as:

$$I(x) = b \int_{-\infty}^{+\infty} [\varepsilon(x, z) - \varepsilon_{mf}] dz \quad (10)$$

where b is a calibration factor, $\varepsilon(x, z)$ is the space-averaged voidage across a chord within the shell, and ε_{mf} is the voidage of the background emulsion phase.

$$\text{Now:} \quad z = (r^2 - x^2)^{1/2} \quad (11)$$

$$\text{and hence:} \quad dz = \frac{r dr}{(r^2 - x^2)^{1/2}} \quad (12)$$

$I(x)$ may be expressed in terms of the variation of voidage in the radial direction, $\varepsilon(r)$:

$$I(x) = 2b \int_x^{+\infty} \frac{[\varepsilon(r) - \varepsilon_{mf}] r dr}{(r^2 - x^2)^{1/2}} \quad (13)$$

This is the Abel transform of $[\varepsilon(r) - \varepsilon_{mf}]$ [15], and a solution for the inverse transform of the function $I(x)$ will enable the radial variation in voidage to be found. The Abel transform is useful for converting three-dimensional images into two dimensions and vice versa, and is based on the assumption that the three-dimensional object being considered is axially symmetrical, e.g., a perfect sphere. Clearly, bubbles in fluidized beds are not perfect spheres but they can be considered as having to a first approximation a sufficient degree of axial symmetry for the transform to be applicable, i.e. it can be assumed that the voidage around a bubble is a function of the radius of the sphere centred on the bubble. The transform may be reduced to a convolution integral and solved numerically to obtain $\varepsilon(r)$ [15]. The method was applied to a single bubble in the Group B powder observed 30 cm above the distributor with the results as shown in Fig. 8, and it is clear that no very sharply defined boundary exists between the shell and the emulsion phase.

Lettieri et al. [16] used the X-ray technique to study changes in the behaviour of the dense phase of fluidized beds with increasing temperature. The bed container was constructed from Inconel with a wall thickness of 3 mm, and was capable of being heated to 650°C. Fluidized beds of a range of materials were subjected to the “bed collapse test” in which the fluidizing gas supply was abruptly cut off and the resulting collapse of the bed surface observed using X-rays. Two solenoid valves were fitted to the equipment, one to cut the gas supply to the bed, the other to vent the

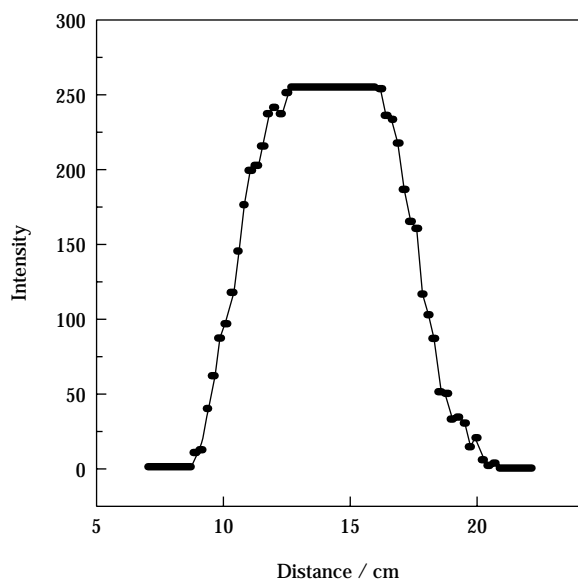


Fig. 8 Scan of X-ray intensity across a horizontal plane through the equator of a single bubble in a Group B powder [14]

gas trapped in the windbox below the gas distributor. From these observations, a number of quantities may be derived for Group A powders, including the emulsion-phase voidage, ε_e , and the “standardised collapse time” (SCT s/m) which gives a measure of the aeration capacity of the powder [17]. The SCT is defined as follows:

$$\text{SCT} = (t_c - t_0) / H_s \quad (14)$$

where t_0 and t_c are the initial cut-off time and the time for the bed to reach total collapse, respectively, and H_s is the settled bed height. The longer the SCT, the higher the aeration capacity of the powder and hence the larger the void fraction of the emulsion phase. Lettieri et al. [16] showed that for powders such as fluidized cracking catalyst (FCC) that are free from inter-particle forces, the SCT and hence the emulsion-phase voidage increase markedly with increasing temperature, whereas powders that were coated so as to induce inter-particle adhesion showed the opposite effect. **Table 1** summarises these results for three FCC powders and one silica powder coated with 10 wt % of potassium acetate.

Bed collapse experiments using X-rays to follow the process were also described by Chen and Weinstein [18]. The X-ray image of the bed was projected onto a 0.23-m diameter image intensifier screen, the visible light from which was focused onto another screen equipped with 48 phototransistors. These were positioned such that three rows of 16 transistors scanned

Table 1 Experimental SCT for FCC powders and a silica powder coated with KOAc

T(°C)	SCT (s/m)			
	FCC 1	FCC 2	FCC 3	Silica powder (10%wt KOAc)
18	27.3	38.2	32.6	16.7
100	36.1	44.4	39.6	24.7
200	42.9	54.4	43.3	16.0
300	47.4	59.8	48.1	
400	50.1	66.0	52.2	
500	51.7	67.5	55.1	
640	52.7	72.8	57.5	

the projected image of the bed across three elevations at 1 cm intervals. The system is described in detail by Feindt [19]. In this work, which also employed cracking catalyst, a single solenoid valve was used to shut off the gas supply to the bed. The bed collapse data were used to calculate the solids stress modulus and the drag coefficient for the catalyst powder in the solid fraction range between minimum fluidization and loose packing. The sedimentation wave velocity for the bed material was 0.027 m/s, a figure in good agreement with the SCT measurements of Lettieri et al. [16].

3. Jet penetration

When gas first enters a fluidized bed from a submerged orifice, it does so either in the form of discrete bubbles or as a flame-like jet which decays at some point above the grid into a bubble stream. Whether one or the other form seems to depend on the properties of the bed material and the size of the inlet nozzle. Rowe et al. [20] observed the point of entry of gas into a bed of a Group B powder using X-rays and saw only bubbles forming with a well-defined frequency.

Chen and Weinstein [21] carried out an X-ray study of a horizontal jet into a 15×38-cm cross-section fluidized bed of cracking catalyst. Instantaneous solids volume fractions averaged along 15-cm chords were measured for two jet diameters and three initial jet velocities, and it was shown that there are three discernible regions in the area of the bed influenced by the jet: a coherent void; bubble trains; and a surrounding compaction zone. The jet penetration length was found to agree well with the correlations developed by a number of earlier workers. Weinstein et al. [22] have more recently studied the sudden injection of a horizontal gas jet into a bed at just above the min-

imum fluidization conditions, but no quantitative correlation from the observations was given.

Yates and Cheesman [23] and Yates [24] measured jet penetrations, L_{\max} , in three-dimensional beds of two Group B powders at pressures of up to 20 bar at ambient temperature, and at temperatures of up to 800°C at ambient pressure. The results were correlated with:

$$\frac{L_{\max}}{d_o} = 9.77 \left[\left(\frac{1}{R_{cf}} \right) \left(\frac{\rho_f}{\rho_p - \rho_f} \right) \left(\frac{U_o^2}{gd_o} \right) \right]^{0.38} \quad (15)$$

$$R_{cf} = \frac{(U_{cf})_{\text{pressure / temperature}}}{(U_{cf})_{\text{ambient}}} \quad (16)$$

U_{cf} being the velocity of complete fluidization of the powder.

Newton et al. [25] reported results from an X-ray study of upshot, downshot, horizontal and 30°-angled upshot jet penetration lengths from multiple orifice grid plates and nozzle spargers. Bed materials were Geldart Group A. The study concluded that none of the correlations for predicting vertical and horizontal jet penetrations adequately accounted for the measured values, but that the correlation of Zenz [26] was well suited for downshot jet penetrations over the range of conditions studied.

4. Circulating fluidized beds

Fluidized beds undergo a number of state transitions as the superficial gas flow rate increases. Thus a bubbling bed exists at gas velocities somewhat in excess of the minimum fluidization flow rate but at higher flow rates, bubbles become unstable and the bed passes into the “turbulent” regime. At sufficiently high flow rates, the bed particles become entrained and carried out of the containing vessel, and in order to maintain a constant solids inventory, the entrained material must be captured in a cyclone and returned to the bed normally at a point near its base. Such a system is called a “circulating” fluidized bed, and industrial interest in this type of system goes back to the earliest days of fluidization when they were employed in the catalytic cracking process [27]. Serious scientific study of the area dates from the work of the group at City College, New York, in the mid-1970s [28], although Kehoe and Davidson [29] had identified the transition from bubbling to turbulent fluidization somewhat earlier. One of the earliest reports of the application of the X-ray technique to study gas and solids flow in the riser section (the so-called “fast” bed) of a circulating bed was that of Weinstein et al.

[30]. Their X-ray tubehead and the image recording devices (plate film and TV camera) were mounted on opposite sides of a carriage which could be moved up and down a 3-m long centre section of the fluidized bed. Data were obtained on the radial distribution of void fraction in the lower dense-phase region of the fast bed and demonstrated its dilute core-dense annulus structure. Variations in radial voidage were studied in response to three types of flow variation, (i) increasing superficial gas velocity from 1.1 m/s (a turbulent bed) to 5 m/s with varying solids circulation flux, (ii) increasing gas velocity with a constant solids flux, and (iii) holding the gas velocity constant at 3.1 m/s and varying the solids flux between 50 and 121 kgm⁻²s⁻¹. The results are shown in **Figs. 9-11**, from which it was concluded that (a) at a constant gas velocity changes in solids flux have a small effect on radial voidage, (b) decreasing solids flux moves the point of inflection between the lower fast bed and the upper dilute-flow region in a downward direction until at a sufficiently low value of the flux, the dense-phase region disappears.

Subsequent X-ray studies by the City College group have investigated internal scales of turbulence in high-velocity beds [31], the effect of gas nozzle configuration on the acceleration of solids and the distribution of solids and gases in a riser [32-34], and the flow characteristics of downflowing high-velocity fluidized beds [35,36].

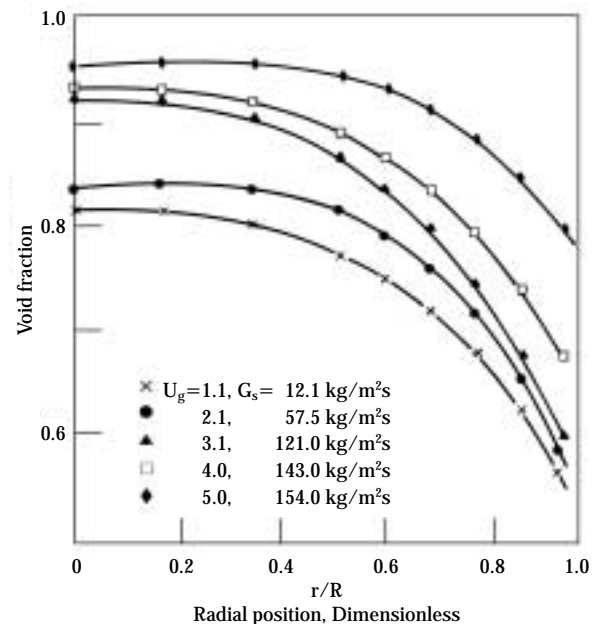


Fig. 9 Radial variation of void fraction at different velocities, open valve [30]

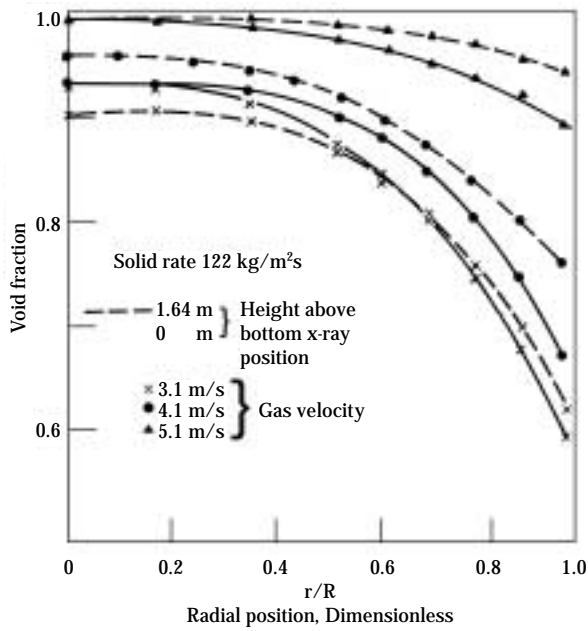


Fig. 10 Radial variation of void fraction, constant solids rate [30]

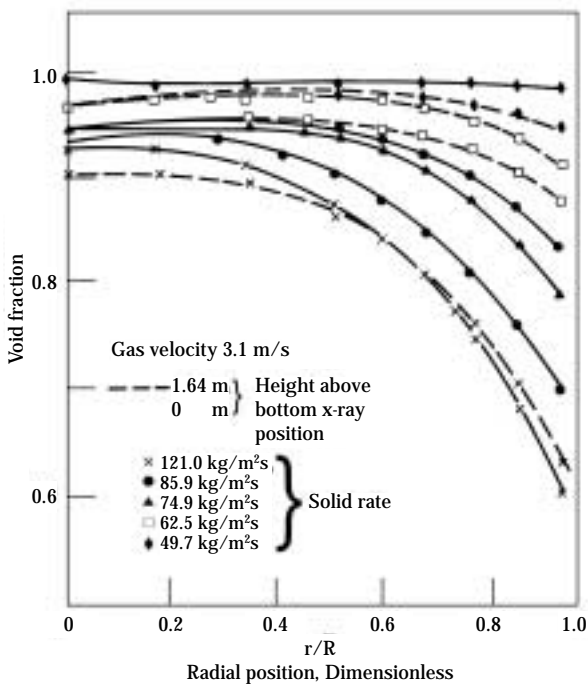


Fig. 11 Radial variation of void fraction, constant gas velocity [30]

5. Slurry bubble columns

By virtue of their excellent heat transfer characteristics, three-phase reactors – in which a gas is sparged into a solid-liquid slurry – are favoured for processes involving highly exothermic reactions such

as the Fischer-Tropsch process [37,38]. Smith et al. [39] used an X-ray system to study the hydrodynamics of a system in which an inert gas (nitrogen or helium) was passed into a slurry of zirconia particles in water. The solids loading was varied in the range 10-30%, and three 2-m long “reactors” with diameters of 50, 127 and 178 mm were used, each being fitted with a grade C sintered brass distributor plate. For comparison, a holed plate distributor was designed for the 127-mm column and consisted of 37×3-mm diameter holes arranged on a triangular pitch. System pressures were up to 8 bar and gas velocities up to 0.09 m/s. Gas bubbles were generally small, of the order of a few mm in diameter, and since the gases used were insoluble, the mean bubble diameter could be estimated from the extent of expansion of the slurry column:

$$V_{gs} - V_s = (\pi/6)d_b^3 n_b \quad (13)$$

where n_b is the number of bubbles of mean diameter d_b , n_b being obtained by direct counting from the video image. Figure 12 shows the effect of gas velocity on mean bubble size, and it is clear that system pressure has a significant effect. Increasing the solids loading was found to increase both the hold-up and the mean size of bubbles, the latter increasing from 8 mm to 12.5 mm on increasing the loading from 10% to

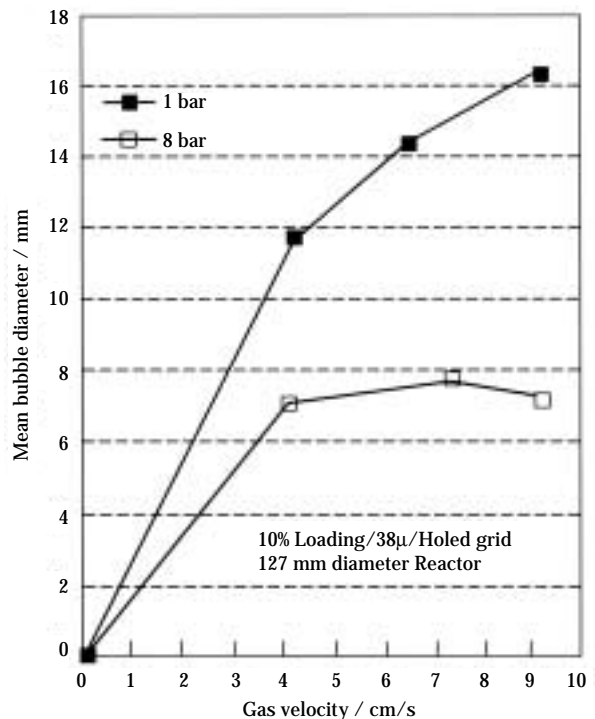


Fig. 12 Effect of gas velocity on bubble size [39]

20% in the 127-mm column at 8 bar and 0.04 m/s gas velocity.

6. Conclusions

The X-ray technique is one of an increasing number of non-invasive methods currently being employed to study multiphase systems of industrial interest [40]. The above examples demonstrate the versatility of the technique for real-time observation and analysis of the many hydrodynamic features of fluidized beds, and it will continue to be used for this purpose. An important application which is currently at an early stage is as a tool to validate theoretical models of fluidized systems based on computational fluid dynamic codes such as Fluent and CFX [41]. The high degree of discrimination possible with X-rays makes it ideal for this validation process, and much progress in this direction can be expected in the near future.

Nomenclature

A	area	m^2
b	calibration factor in Eq. (10)	—
d	diameter	m
f_b	bubble fraction	—
g	acceleration due to gravity	ms^{-2}
G_s	solids circulation flux	$kgm^{-2}s^{-1}$
H_s	settled bed height	m
$I, I(x)$	transmitted intensity	—
I_0	incident intensity	—
K	coefficient in Eq. (3)	$kgm^{-3}m^{-1}$
l	length	m
L_{max}	maximum jet penetration length	m
n	number	—
Q_e	volumetric flow rate	m^3s^{-1}
r	radial distance	m
R	riser diameter	m
R_{cf}	defined in Eq. (16)	—
STC	standardised bed collapse time	sm^{-1}
t_c	total collapse time	s
t_0	time at gas cut-off	s
u	velocity	ms^{-1}
u_g	gas velocity	ms^{-1}
U	superficial velocity	ms^{-1}
V	volume	m^3
x, z	Cartesian coordinates	m
Δ	thickness	m
ε	voidage	—
κ	coefficient in Eq. (6)	—
μ_m	mass attenuation coefficient	m^{-1}
ρ	density	kgm^{-3}

Subscripts

b	bubble
B	bed
cf	complete fluidization
e	emulsion phase
ge	emulsion gas
gls	gas-liquid-solid
ls	liquid-solid
mb	minimum bubbling
mf	minimum fluidization
o	orifice
s	solids
w	wedge

References

- [1] Grohse, E.W., 1955, Analysis of gas fluidized solid systems by X-ray absorption, *AICHEJ*, **1**, 358-365
- [2] Romero, J.B. and Smith, D.W., 1965, Flash X-ray analysis of fluidized beds, *AICHEJ*, **11**, 595-600
- [3] Rowe, P.N. and Everett, D.J., 1972, Fluidized bed bubbles viewed by X-rays, *Trans IChemE*, **50**, 42-48
- [4] Rowe, P.N. and Everett, D.J., 1972, *ibid* 49-54
- [5] Rowe, P.N. and Everett, D.J., 1972, *ibid* 55-60
- [6] Rowe, P.N., Santoro, L. and Yates, J.G., 1978, The division of gas between bubble and interstitial phases in fluidized beds of fine powders, *Chem Eng Science*, **33**, 133-140
- [7] Yates, J.G. and Newton, D., 1986, Fine particle effects in fluidized bed reactors, *Chem Eng Science*, **41**, 801-806
- [8] Hoffmann, A.C. and Yates, J.G., 1986, Experimental observations of fluidized beds at elevated pressures, *Chem Eng Commun*, **41**, 133-149
- [9] Geldart, D., 1973, Types of gas fluidization, *Powder Technol.*, **7**, 285-292
- [10] Gibilaro, L.G., 2001, *Fluidization Dynamics*, Butterworth Heinemann, Oxford
- [11] Olowson, P.A. and Almstedt, A.E., 1990, Influence of pressure and fluidization velocity on the bubble behaviour and gas flow distribution in a fluidized bed, *Chem Eng Science*, **45**, 1733-1741
- [12] Rowe, P.N., Foscolo, P.U., Hoffmann, A.C. and Yates, J.G., 1982, Fine powders fluidized at low velocity at pressures up to 20 bar with gases of different viscosity, *Chem Eng Science*, **37**, 167-174
- [13] Barreto, G.F., Yates, J.G. and Rowe, P.N., 1983, The effect of pressure on the flow of gas in fluidized beds of fine particles, *Chem Eng Science*, **38**, 1935-1945
- [14] Yates, J.G., Cheesman, D.J. and Sergeev, Y.A., 1994, Experimental observations of voidage distribution around bubbles in a fluidized bed, *Chem Eng Science*, **49**, 1885-1895
- [15] Bracewell, R.N., 1986, *The Fourier Transform and its Applications*, McGraw-Hill, Singapore
- [16] Lettieri, P., Newton, D. and Yates, J.G., 2001, high tem-

- perature effects on the dense phase properties of gas fluidized beds, *Powder Technology*, **120**, 34-40
- [17] Geldart, D. and Wong, A.C.Y., 1985, Fluidization of powders showing degrees of cohesiveness – II Experiments on rates of de-aeration, *Chem Eng Science*, **40**, 653-661
- [18] Chen, L. and Weinstein, H., 1994, Measurement of normal stress and hindrance factor in a collapsing fluidized bed, *Chem Eng Science*, **49**, 811-819
- [19] Feindt, H.J., 1990, Radial and axial density fluctuations in a high velocity fluidized bed. PhD Thesis, The City University of New York, New York
- [20] Rowe, P.N., MacGillivray, H.J. and Cheesman, D.J., 1979, Gas discharge from an orifice into a gas fluidized bed, *Trans IChemE*, **57**, 194-199
- [21] Chen, L. and Weinstein, H., 1993, Shape and extent of the void formed by a horizontal jet in a fluidized bed, *AIChE Journal*, **39**, 1901-1909
- [22] Weinstein, H., Cao, C., Mangado, K.B., Mohraz, A., Graff, R.A. and Koelle, P., 2001, Time resolution of a transient event in a gas fluidized bed, "Fluidization X", Kwauk, M., Li, J. and Yang, W-C. (Eds), United Engineering foundation, New York, 293-300
- [23] Yates, J.G. and Cheesman, D.J. 1987, Unpublished results
- [24] Yates, J.G., 1996, Effects of temperature and pressure on gas-solid fluidization, *Chem Eng Science*, **51**, 167-205
- [25] Newton, D., Smith, G.B. and Gamblin, B., 1997, Jet penetrations and gas entry effects from large scale multiple orifices into fluidized beds of fine powders, Proceedings 2nd European Conference on Fluidization, Bilbao, Spain, 83-90
- [26] Zenz, F.A., 1968, Bubble formation and grid design, IChemE Symposium Series, **30**, 136-139
- [27] Yerushalmi, J. and Avidan, A., 1985, Chapter 7 "High Velocity Fluidization" in "Fluidization", Davidson, J.F., Clift, R. and Harrison, D. (Eds), Academic Press, London
- [28] Yerushalmi, J., Turner, D.H. and Squires, A.M., 1976, The fast fluidized bed, *I&EC Proc Des Dev*, **15**, 47-52
- [29] Kehoe, P.W.K. and Davidson, J.F., 1971, Continuously slugging fluidized beds, IChemE Symposium Series, **33**, 97-101
- [30] Weinstein, H. Shao, M., Schnitzlein, M. and Graff, R.A., 1986, Radial variation in void fraction in a fast fluidized bed, "Fluidization V", Østergaard, K. and Sørensen, A. (Eds), Engineering Foundation, New York, 329-336
- [31] Weinstein, H., Feindt, H.J., Chen, L. and Graff, R.A., 1989, the measurement of turbulence quantities in a high velocity fluidized bed, "Fluidization VII", Potter, O.E. and Nicklin, D.J. (Eds), Engineering Foundation, New York, 305-309
- [32] Weinstein, H., Feindt, H.J., Chen, L. and Graff, R.A., 1995, Riser gas feed nozzle configuration effects on the acceleration and distribution of solids, "Fluidization VIII", Large, J-F and Laguerie, C. (Eds), Engineering Foundation, New York, 263-270
- [33] Kostazos, A.E., Weinstein, H. and Graff, R.A., 1998, The effect of the location of gas injection on the distribution of gas and catalyst in a riser, "Fluidization IX", Fan, L-S. and Knowlton, T.M. (Eds), Engineering Foundation, New York, 221-228
- [34] Kostazos, A.E. and Weinstein, H. 1997, A detailed experimental description of the flow in the entrance section of a fluidized catalytic cracking unit, *AIChE Symposium Series*, **93**(317), 36-39
- [35] Cao, C. and Weinstein, H., 2000, Characterization of downflowing high velocity fluidized beds, *AIChE Journal*, **46**, 515-522
- [36] Cao, C. and Weinstein, H., 2000, Gas dispersion in downflowing high velocity fluidized beds, *ibid* 523-528
- [37] Fan, L-S., 1989, "Gas-Liquid-Solid Fluidization Engineering", Butterworths, London
- [38] Deckwer, W-D., Louisi, Y., Zaidi, A. and Ralek, M., 1980, Hydrodynamic properties of the Fischer-Tropsch slurry process, *I&EC Proc Des Dev*, **19**, 699-708
- [39] Smith, G.B., Gamblin, B.R. and Newton, D., 1995, X-ray imaging of slurry bubble column reactors, *Trans IChemE*, **73(A)**, 632-636
- [40] Yates, J.G. and Simons, S.J.R., 1994, Experimental methods in fluidization research, *Int J Multiphase Flow*, **20**(Suppl), 297-330
- [41] Lettieri, P., Micale, G.D.M., Cammerata, L. and Coleman, D., 2002, Computational Fluid dynamics simulations of gas-fluidized beds; a preliminary investigation of different modelling approaches, Proc 10th Workshop on Two-Phase Flow Predictions, Sommerfeld, M. (Ed), Mersberg, Germany, April 9-12, 300-309

Author's short biography



John Yates

John Yates is Ramsay Memorial Professor and Head of the Department of Chemical Engineering at University College London. He trained as a chemist and received a BSc as an external student of London University in 1959. He then did research in the Department of Chemical Engineering at Imperial College and was awarded the PhD in 1963. Two years at BP research centre at Sunbury-on-Thames were followed by a move to UCL in 1964 as a Lecturer. He became a Senior Lecturer in 1976, a Reader in 1984 and a Professor in 1990. His research area is "fluidization" in which he has published a monograph and over 120 papers. He is a Fellow of the Institution of Chemical Engineers and of the Royal Society of Chemistry. He became a Fellow of the Royal Academy of Engineering in 1999.



David Cheesman

David Cheesman is an Experimental Officer in the Department of Chemical Engineering at University College London. He has been involved in fluidization research for almost 30 years with a special interest in the X-ray analysis of fluidized bed systems. He is co-author of over 35 publications in the area.



Paola Lettieri

Paola Lettieri is a Research Fellow of the Royal Academy of Engineering, the first woman Engineer to win one of The Academy's Research Fellowships. She joined the Department of Chemical Engineering at UCL in January 2001, after 5 years employment at BP Chemicals, Sunbury-on-Thames. She originally qualified in Mechanical Engineering from the University of Rome, and then obtained a PhD in Chemical Engineering at UCL. Her research activities to date have covered a variety of fluidization aspects including experimentation, theoretical modelling and computational fluid-dynamics (CFD) simulations, with emphasis on the effect of process conditions on the operation of gas fluidized beds.



David Newton

David Newton is a Research Associate in Fluidization with BP Chemicals. He has been involved since its inception in developing and applying X-ray imaging techniques to large-scale fluidized beds for both oil and chemicals applications. He has published over fifty papers on X-ray imaging of fluidized beds, fluid catalytic cracking (FCC) and other processes. The principle areas of research have included the study of commercial scale fluidized bed processes such as FCC, Gas-phase Polyethylene, Acrylonitrile, Polymer Cracking, Vinyl Acetate and Gas-to-Liquids Technology. He has been with BP for eighteen years. He is the current Chairman of the PICNAC Group.

Combination of SHS and Mechanochemical Synthesis for Nanopowder Technologies[†]

T. Grigorieva, M. Korchagin and N. Lyakhov
*Institute of Solid State Chemistry**

Abstract

The combination of mechanochemical activation and self-propagating high-temperature synthesis (SHS) have widened the possibilities for both methods. For metallic systems, the investigation showed that a short-term mechanochemical activation of heterophase SHS products leads to single-phase and ultrafine intermetallides obtained from the elements by mechanical alloying. It was demonstrated that metastable phases, usually obtained by mechanical alloying, can be obtained from the equilibrium intermetallic compounds synthesized by SHS. Besides this, the investigations showed that preliminary mechanical activation, during which layered composites are formed from the initial elements, allows one to extend the concentration limits of SHS processes up to a solid solution region.

The preliminary mechanical activation also allows production of single-phase ultrafine complex oxides.

Introduction

Mechanochemical synthesis and mechanical alloying are in wide use as experimental methods for the production of highly dispersed powders and nanocomposites. Using mechanical activation we have managed to prepare nanocomposites in immiscible systems such as Cu-Bi, Fe-Bi, Fe-In. It is possible to get supersaturated solid solutions in many other intermetallic systems (Cu-Ga, Cu-In, Cu-Sn, Ni-In, Ni-Bi, Ni-Sn, Ni-Ge, Ni-Al) [1, 2]. However, from a technological point of view, mechanical activation poses a lot of problems which cannot be easily solved. The biggest problem is the low productivity of the techniques currently available, as well as the contamination of the end products caused by abrasion of the grinding media. The energy consumption should also be taken into consideration in some large-scale processes.

One of the alternatives to mechanochemistry may be self-propagating high-temperature synthesis (SHS), which is energy-saving and can be applied to the large-scale production of many intermetallic compounds or complex oxides (nitrides, carbides) [3]. Nevertheless, this method includes a combustion stage which requires very high temperatures. As a

result, final products can be obtained only in the form of dense sintered or solidified products when SHS exceeds the melting point of reagents and/or products. To transform such products into commercially interesting powders, one needs to use milling as an unavoidable step. The grinding leads to further contamination and to additional energy consumption, which may be comparable with that required for the mechanochemical synthesis itself.

Another disadvantage of SHS is a relatively high temperature gradient near the combustion surface which leads to a non-uniform phase composition of the obtained products.

The shortcomings of these two methods can be overcome, and their advantages can be extended. This allows one to obtain the final products of required phase composition and disperse state, thus enabling the development of a new energy-saving and waste-free technology.

Experimental

The materials used in the investigation were: carbonyl nickel and iron, powdered aluminum, silicon, germanium, tungsten, molybdenum, titanium, and zirconium, pure gallium, barium peroxide, tungsten and molybdenum oxides.

A ball planetary mill AGO-2 [4] was used for the investigations. The volume of the mill drums was

* 18. Kytateladec Str., 630128 Novosibirsk, Russia

[†] Accepted: June 28, 2002

250 cm³, the ball diameter was 5 mm, the ball load was 200 g and the weighed portion of powder treated was 10 g. In order to avoid oxidation of the metals, all the experiments on mechanical alloying were carried out in an argon atmosphere. The X-ray phase analysis was performed with a DRON-3M diffractometer with CuK_α radiation.

IR absorption spectra were recorded with a SPECORD 75 IR spectrometer.

Electron microscopic studies were carried out using the JSM-T20 electron microscope and the high-resolution electron microscopes JEM-2010 and JEM-400.

The extent of aluminum recovery from intermetallic compounds was calculated as the ratio of the amount of hydrogen evolved in the reaction of samples with a 20% KOH solution to the amount of hydrogen that should be evolved in case of complete dissolution of the aluminum present in the sample. The amount of the evolved hydrogen was recorded automatically with a DAGV-70-2M volumeter.

1. Mechanochemical activation of SHS products in metal systems

1.1 Homogenizing effect of MA

Ultrafine single-phase intermetallic compounds are widely used in powder metallurgy for making heat-resistant materials, materials with a high corrosion stability and special magnetic properties. Single-phase intermetallic compounds are usually obtained by fusing or sintering followed by homogenizing and annealing for a long time [5]. The major disadvantages of these processes are deviations in the composition of the mixture in the case of high melting points of the initial components because of evaporation of the lower melting point ingredients. As a result, a long time interval is necessary for the process, and high energy consumption at the stage of homogenizing and annealing. Besides this, most of the powder intermetallics are obtained by grinding for a rather long time, which usually leads to substantial contamination caused by abrasion of the grinding media. In such cases, additional purification is required.

For metal systems with high enthalpies of the intermetallic formation, the SHS method can be applied; heterophase SHS products can be homogenized during mechanochemical activation at a simultaneous substantial decrease of the particle size, which should finally lead to finely dispersed material with a high structural defect content. This material is similar in its properties to that obtained by mechanical alloying

of the elements; however, the time for mechanical treatment in the former case is several decades shorter.

Phase formation and morphological changes were investigated for the mechanochemical synthesis of intermetallics from elements and for the mechanochemical activation of heterophase products of the SHS process. For comparison purposes, systems were considered for which it is known that the SHS process can be performed, but the products of this synthesis are substantially different in phase composition:

- Ni-Al within the concentration region of NiAl phase existence. It is known that this phase can be obtained by SHS [3];
- Ni-Si, in which the SHS process is possible [6], but it is difficult to achieve single-phase composition during SHS synthesis;
- Ni-Ge in the NiGe intermetallic homogeneity region. Due to the rather high melting point of Ni (1455°C) and the rather low temperature of NiGe intermetallic decomposition (850°C), the homogeneity region is very narrow for this compound.

The X-ray investigation of the mechanical alloying of an NiAl intermetallic from a mixture of metal powders of the composition Ni 32 wt.% Al demonstrated that the synthesis started after mechanical activation for about 2.5–3 minutes. First, the Ni₂Al₃ intermetallic forms. Some amounts of unreacted nickel and aluminum still remain (**Fig. 1a**). After activation for 5–7 min., the amount of the formed Ni₂Al₃ phase starts to decrease and the reflections of the NiAl intermetallic increase (**Fig. 1b**). Then, the Ni₂Al₃ intermetallic disappears, the nickel and aluminum contents decrease gradually and the intensities of NiAl reflections increase. After mechanochemical

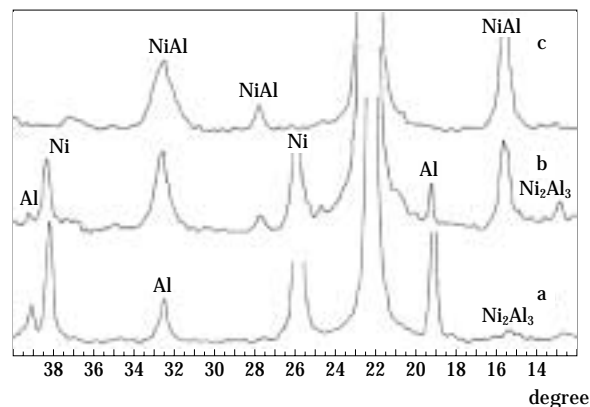


Fig. 1 X-ray patterns of Ni 32 wt.% Al mixture after mechanical activation during 3 (a), 7 (b), 25 min. (c).

activation for 25–30 min., very broad reflections only of the NiAl phase are present in the X-ray diffraction patterns (Fig. 1c). The coherent scattering domains for this product are 8–10 nm.

The electron microscopic investigation of the products of the mechanical alloying of NiAl-based solid solutions in a ball mill demonstrated that after activation for 30 s, the initial nickel and aluminum particles could not be detected in the sample. The products consist of agglomerates of various shapes and sizes. An increase of the activation time to 1 min. leads to an increase of the fraction of coarse agglomerates which attain a plate-like shape as their density increases. **Figure 2a** shows a microphotograph of the cross section of the agglomerate, clearly exhibiting its layered structure. A further increase to the time of mechanical alloying causes a drastic change to the morphology of the product particles. The destruction of large layered agglomerates starts after mechanical alloying for 3 min.; whereas they disappear completely after 5

min. of alloying. The major part of the samples by this time is composed of rather dense agglomerates of irregular shape with a size of $2 \div 10 \mu\text{m}$. Larger particles (up to $50 \mu\text{m}$) are also present. These agglomerates are composed of the layered particles $1 \text{--} 5 \mu\text{m}$ in size. It should be noted that according to XRD data, it is the mechanical alloying for 3 min. that causes the appearance of the Ni_2Al_3 intermetallide in the products, which is likely to be the reason of the significant change of the particle morphology. An increase in the time of mechanical alloying brings insignificant changes to the morphology of the formed products. The fine fraction ($1 \text{--} 5 \mu\text{m}$) content increases, the density of the formed particles increases (Fig. 2b).

The SHS of a metal powder mixture comprising Ni 32 wt.% Al results in the NiAl intermetallide with admixture of the Ni_2Al_3 phase; judging from the width of diffraction peaks, the formed products are well crystallized. Electron microscopic studies showed that the intermetallides were most likely crystallized

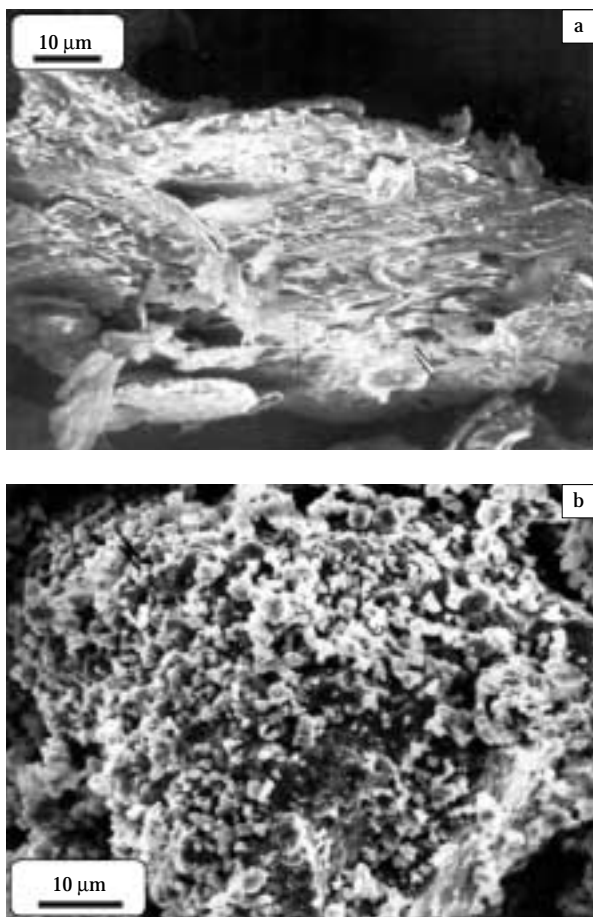


Fig. 2 Microphotograph of a cross section cleavage of the layered composite of the system of Ni 32 wt.% Al after mechanical activation for 30 s (a), 25 min. (b).

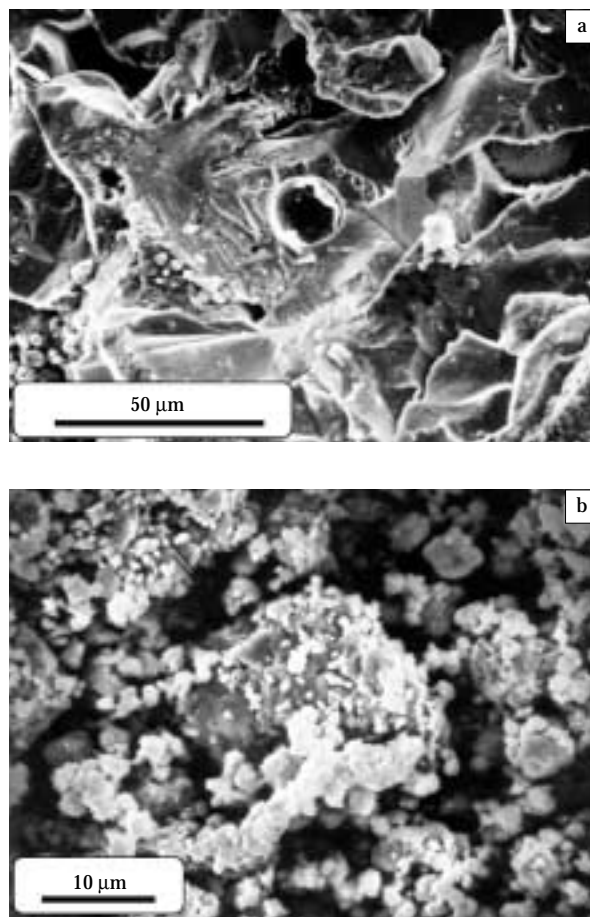


Fig. 3 Microphotograph of the SHS product in the system Ni 32 wt.% Al (a), the same product after mechanical activation for 1.5 min. (b).

from the melt (**Fig. 3a**).

Mechanochemical activation of SHS products for 1.5 min. results in a material similar in morphology, particle size and coherent scattering domain to the material obtained by the mechanical alloying of nickel and aluminum powders for 25 min. This means that a short-time mechanochemical activation of a mixture of phases obtained by the SHS process in this system allows preparation of an ultra-fine single-phase intermetallic product (**Fig. 3b**). Similar products were observed for the Ni-Si system (**Fig. 4**).

X-ray analysis showed that a significant amount of the Ni_3Si_2 phase can be found in the products of the mechanical alloying of an Ni+Si mixture corresponding to an Ni_5Si_2 intermetallic compound.

The X-ray diffraction investigation of the mechanical alloying of nickel and germanium at the ratio of Ni 55 wt.% Ge demonstrated that formation of the NiGe intermetallide starts within the first minute (**Fig. 5a**); a drastic increase in the intensity of the reflections from this phase starts after mechanical activation for 6–7 minutes (**Fig. 5b**); the maximum is achieved after 25 minutes of mechanical treatment (**Fig. 5c**). However, an admixture of the second phase (Ni_5Ge_2) appears during mechanochemical synthesis of the NiGe intermetallide; at first, the content of the second phase increases, then decreases and disappears completely after 12–13 minutes of mechanical alloying. By the end of the process (25–30 minutes) there is only one phase, which is the NiGe intermetallide, with a coherent scattering domain of 5–8 nm.

According to the data of the electron microscopic investigation, mechanical alloying in the mixture of a stoichiometric composition NiGe for 40 s results in the formation of rounded three-dimensional agglomerates with a maximal size of up to 400 μm , originating from particles of 0.2–1 μm in diameter. Besides this, separate particles of 0.2–1 μm in diameter are present; their number is rather large. An increase of the mechanical alloying time for this system to 5–7 minutes leads to the formation of very dense agglomerates; traces of a strong plastic deformation are sometimes observed on their surface. However, in this case the amount of separate fine particles is also rather large. A further increase of the mechanical alloying time to 30 min. has practically no effect on the morphology and size of the resulting particles; it is only the fraction of coarse agglomerates which increases. The final product of mechanochemical synthesis NiGe is composed of rather dense particles with a size of 0.5–2 μm ; they sometimes form larger

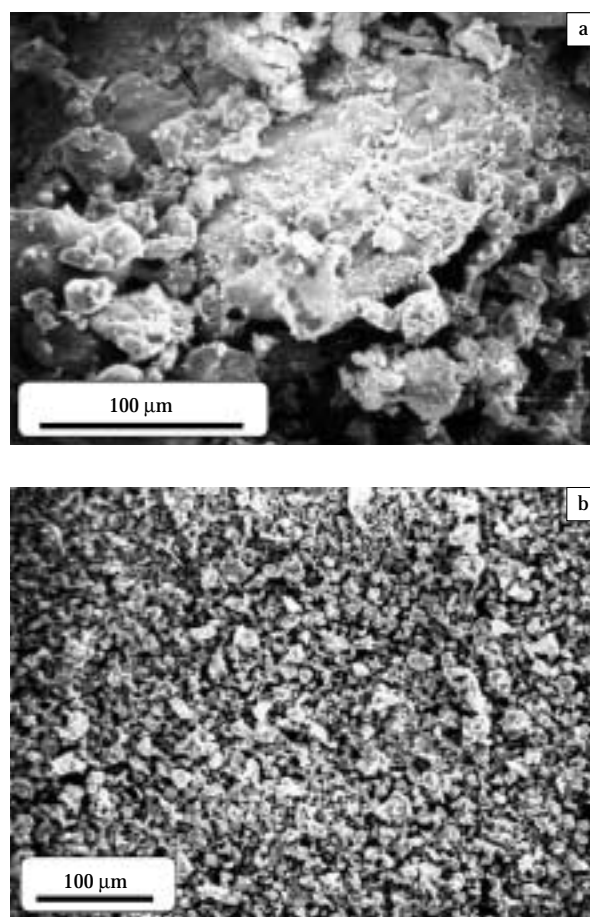


Fig. 4 Microphotograph of the SHS product in the system of Ni 16 wt.% Si (a), the product of mechanical alloying in this system for 10 min. (b).

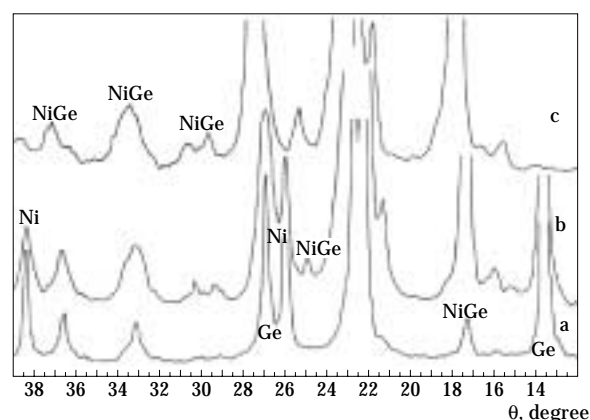


Fig. 5 X-ray patterns of Ni 55 wt.% Ge mixture after mechanical activation during 1 (a), 7 (b), 25 min. (c).

agglomerates.

An SHS process was carried out in a mixture of this composition. According to XRD data, it is mainly the

equilibrium well-crystallized NiGe which forms, with an admixture of a second intermetallide (Ni_5Ge_2) (**Fig. 6a**). One can see from microphotographs that the final products are formed from the melt (**Fig. 7a**), which means that the SHS proceeds via the liquid phase.

The X-ray diffraction investigations of the mechanochemical treatment of the SHS products demonstrate that a broadening of the diffraction patterns starts after mechanical activation for 30 s. Phase homogenization of the system (NiGe) is achieved after 1.5–2 minutes (**Fig. 6b**). After mechanical activation for 3 min., the material exhibits a coherent scattering domain of 8–10 nm. Further mechanical activation leads to some narrowing of the peaks. According to the electron microscopic data, after mechanical activation of the SHS products for 30 s, the major part of the sample is composed of fine particles of irregular shapes, their size being 0.2–3 μm (**Fig. 7b**). Larger particles are still present, though they rarely occur in this case. A sintered agglomerate of fine particles starts to form. An increase of the treatment time causes an intensive formation of such agglomerates. Their density increases gradually. Traces of substantial plastic deformation are observed on the surface of some of these agglomerates. After mechanical activation for 3 min., the sample consists of agglomerates of different density and shape, their size being 1 to 400 μm .

Similar results were obtained for the Ni-Si system (**Fig. 4a, 4b**).

The investigation of the metallic systems showed that a short-term mechanochemical activation of heterophase SHS products leads to single-phase and ultrafine intermetallides obtained from the elements by mechanical alloying.

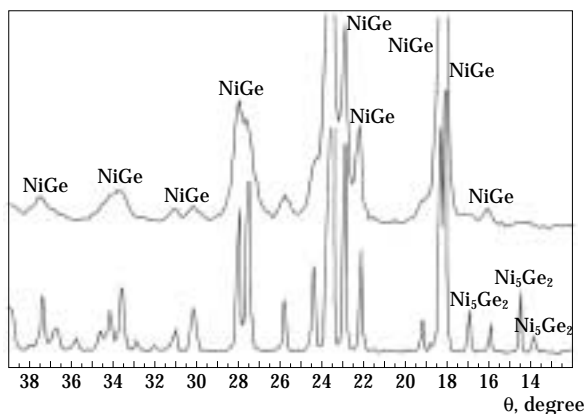


Fig. 6 X-ray patterns of the SHS product in the system Ni 55 wt.% Ge (a), the same product after mechanical activation for 2 min.

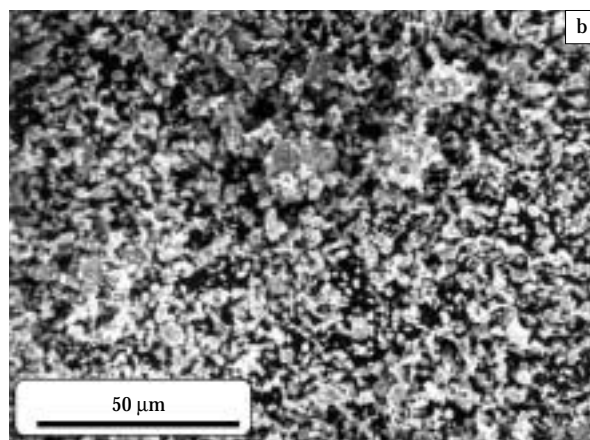
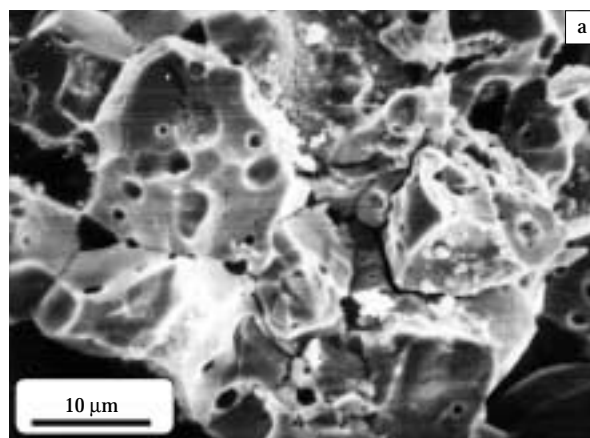


Fig. 7 Microphotograph of the SHS product in the system Ni 55 wt.% Ge (a), the same product after mechanical activation for 2 min.

1.2 Formation of non-equilibrium phases by activation of SHS products

It is known that it is practically impossible to obtain non-equilibrium intermetallic compounds by SHS; however, highly reactive intermetallic compounds (which is exactly what metastable phases usually are) are used in hydrogen energetics, in preparation of Raney catalysts, metal cements, diffusion-hardening solder, metal dental materials, etc. Mechanochemical synthesis and mechanical activation are among the most efficient methods to obtain metastable phases in metal systems; it is known that a series of equilibrium intermetallic compounds can be transferred into non-equilibrium concentration regions by means of mechanical activation.

A comparative investigation of phase and microstructural transformations during the mechanochemical synthesis of non-equilibrium solid solutions from the elements and during mechanical activation of

equilibrium intermetallic compounds obtained by SHS was carried out.

The Ni-Al system was selected for investigation, because it is known that the SHS process in the Ni-Al system can be carried out within a broad concentration range [3]. The limit solubility of aluminum in nickel ranges from 3.85 wt.% at 500°C to 10.3 wt.% at 1385°C. The structural similarity of the Ni₃Al intermetallide (cubic lattice of the Cu₃Au type) and β-nickel makes it possible to mechanochemically pass from the intermetallide to the non-equilibrium solid solution [7]. The structure of the Ni₂Al₃ intermetallide (40.8 wt.% Al) is close to that of NiAl. Aluminum atoms form distorted cubes in the rhombohedral lattice of Ni₂Al₃. Two-thirds of the positions in the centres of cubes are occupied by nickel atoms, the other positions are vacant. Disordering of these vacancies should lead to the formation of a supersaturated solid solution with a non-equilibrium concentration of vacancies.

The X-ray and electron microscopic studies of the mechanical alloying in a mixture of nickel and aluminum powders at a ratio of Ni 40.8 wt.% Al (calculated for the formation of the Ni₂Al₃ intermetallide) showed that the process is largely similar to the mechanical alloying of the Ni 32 wt.% Al mixture. At first, the Ni₂Al₃ intermetallide is formed; during further activation it is transformed into the supersaturated solid solution with a non-equilibrium concentration of vacancies based on the intermetallic compound NiAl. After mechanical activation for 30 minutes, the size of its coherent scattering domains is around 8 to 10 nm.

The X-ray diffraction patterns of the product of the SHS process in the Ni 40.8 wt.% Al mixture exhibit the formation of a well-crystallized Ni₂Al₃ intermetallide (**Fig. 8a**). Mechanochemical activation of this product for ~2 min., under the same conditions as those under which mechanical alloying was carried out, gives the diffraction patterns corresponding to the material obtained by mechanical alloying after 25–30 minutes (**Fig. 8b**), which has been mentioned above to be a supersaturated solid solution with a non-equilibrium concentration of vacancies based on the NiAl intermetallide. Further mechanical activation does not bring any substantial changes.

Electron microscopic investigations showed that the formed porous fused SHS product (**Fig. 9a**) can be transformed mechanochemically within 2 min. into a product which is morphologically very similar to that formed at the final stage of mechanical alloying (**Fig. 9b**).

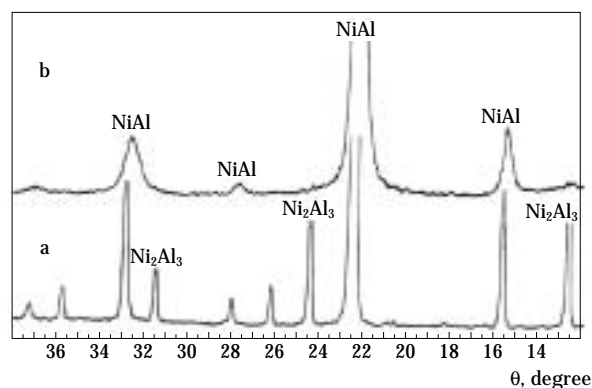


Fig. 8 X-ray patterns of the SHS product in the system Ni 40.8 wt.% Al (a), the same product after mechanical activation for 3 min.

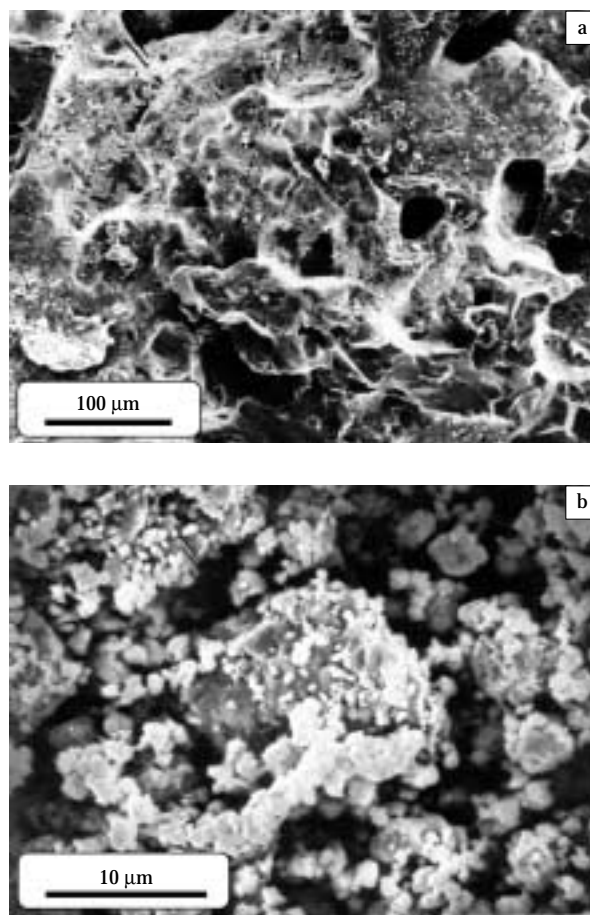


Fig. 9 Microphotograph of the SHS product in the system Ni 40.8 wt.% Al (a), the product of mechanical alloying in this system for 25 min. (b).

Metastable phases obtained by mechanical alloying and by mechanical activation of the SHS products have approximately equal reactivity.

For the example of a well-studied aluminum leach-

ing reaction, it was stated that non-equilibrium solid solutions based on NiAl, which were synthesized by mechanical alloying from metal powders within the concentration range of the Ni_2Al_3 intermetallide and activated for 1 min., exhibit a very high reactivity (**Fig. 10**). These samples exhibit similar dynamics to hydrogen evolution in leaching. This is one more confirmation of the fact that the formed metastable phases are identical. This means that the non-equilibrium solid solutions based on the NiAl intermetallide, with largely similar structure, particle morphology, coherent scattering domains, and reactivity can be obtained both by the mechanical alloying of the initial powders of the composition Ni 40.8 wt.% Al, and also by short-time mechanical activation of the Ni_2Al_3 intermetallide obtained by SHS. An important fact!

The X-ray diffraction studies of the mechanical alloying of the Ni 13.5 wt.% Al composition (the concentration region of equilibrium Ni_3Al intermetallide) showed that a broadening and a slight decrease of the intensity of diffraction peaks related to metals occur within the first two minutes of activation. Diffraction reflections of the Ni_2Al_3 intermetallide appear after 2.5 minutes of mechanical treatment. The intensity of aluminum peaks decreases drastically while the intensity of Ni reflections decreases slowly. The Ni lattice parameter remains unchanged. Only after mechanical activation for 5 min. do the diffraction patterns of aluminum disappear completely. The diffraction reflections of nickel broaden substantially (which is especially noticeable in the large-angle region). Its lattice parameter increases (**Fig. 11a**), which is evidence of the incipient formation of a nickel-based

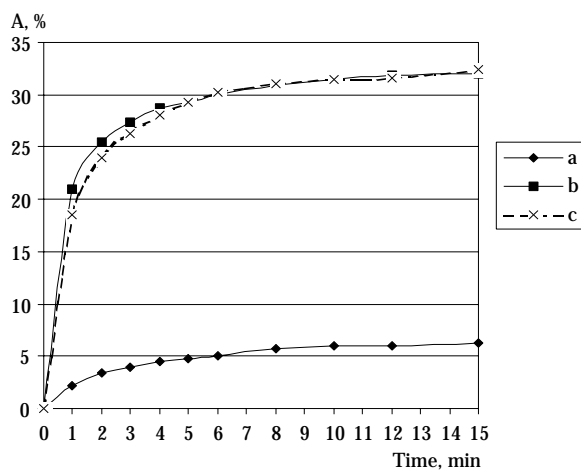


Fig. 10 Curves of leaching of the SHS product in the system Ni 40.8 wt.% Al (a), of the product of mechanical alloying in this system for 25 min. (b), of the SHS product after 1 min. activation (c).

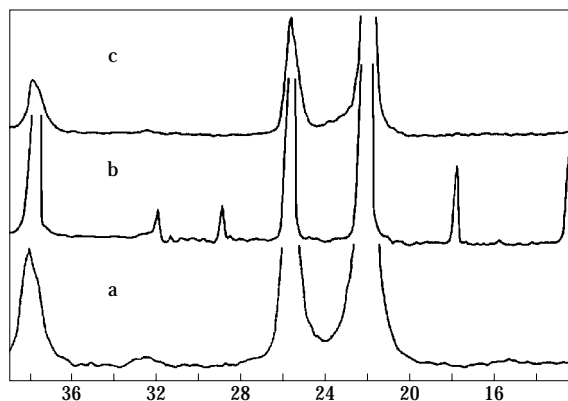


Fig. 11 X-ray patterns of Ni 13 wt.% Al samples: obtained from a metal powder mixture by mechanical alloying for 15 min. (a), obtained by SHS (b), the SHS product after mechanical activation during 1 min. (c).

solid solution. After 15 minutes of activation, the lattice parameter of the solid solution reaches its maximum $a=0.3590$ nm. The coherent scattering domain of the resulting solid solution is 8–10 nm. Further mechanical activation causes a narrowing of the diffraction peaks. The formation of the Ni_3Al phase, which is characteristic in this concentration range, was not detected at any stage of activation.

Electron microscopic investigations of the products of mechanical alloying in the mixture Ni 13.5 wt.% Al showed that the dynamics of particle morphology changes at the initial stages of the process is very similar to that observed for the composition Ni 32 wt.% Al. The formation of layered composites was observed, too. However, in this case they start to form as early as after only 30 s of mechanical alloying, which is much earlier than for the Ni 32 wt.% Al composition. The particles of the initial components are no longer detected at this moment. A substantial part of the resulting agglomerates look like plate-shaped particles with traces of strong plastic deformation on their surface. Relatively sintered and round-shaped agglomerates are also present. The maximal size of the plate-like agglomerates is 1–2 mm, while the rounded ones are between 1–2 and 40–50 μm in size. An increase of the mechanical treatment time to 15 min. leads to a decrease of the fraction of the smallest and the largest particles; they become more dense and uniform in size, almost monolithic.

A product of SHS in the mixture Ni 13.5 wt.% Al is an Ni_3Al intermetallide. Diffraction patterns are evidence of a high order in the structure of the formed phase (**Fig. 11b**). Mechanical activation of the SHS product for only 30 s results in a significant decrease

of the intensity of diffraction peaks and to their substantial broadening. After 1.5 min., a non-equilibrium solid solution of aluminum in nickel is formed. Its lattice parameters are identical to those of the product formed in a mixture of initial powders mechanically alloyed for 15 min. (Fig. 11c). Further activation of this SHS product causes no change in diffraction patterns.

It was stated in electron microscopic studies that the particle size decreases sharply at the very first stages of the mechanical treatment of SHS products. After mechanical activation for 1.5 min., the product particles are practically identical in size and morphology to the products obtained from the initial Ni and Al powders after mechanical alloying for 15 min.

The investigation demonstrated that metastable phases, usually produced by mechanical alloying, can be obtained from the equilibrium intermetallic compounds synthesized by SHS.

Short-term activation following the SHS process therefore allows one to homogenize intermetallic phases and to obtain metastable structures. The final products are formed in the ultrafine state with minimal contamination caused by abrasion of milling tools.

This approach can also be used in the SHS synthesis of complex oxides, nitrides, borides, and carbides, etc. However, for this method of preparing ultrafine powders, the range of compounds is limited by the possibilities of the SHS method, i.e. involved are systems with very high temperatures of the final product formation.

2. The effect of preliminary activation on SHS process

2.1 Metal systems

A high exothermal effect of reaction and a strong Arrhenius-type temperature dependence of the reaction rate are of decisive importance for the feasibility of SHS processes. For diffusion-controlled processes, to which SHS processes also belong, another important parameter is the disperse state of the initial components, including the uniformity of their mixing and the surface area of contacts between the components. Mechanical alloying is known as a process which leads to the formation of layered mechanocomposites formed at the initial stage of the mechanical activation of metal mixtures (see Fig. 2a). Most metals exhibit good plasticity; under mechanical action in ball planetary mills where shock and shock-with-shear occur [8], the metal undergoes plastic deformation resulting

in a change to the shape of the metal particles. They flatten, adsorption films on their surface are destroyed; components come into contact with each other by atomic-pure planes [9]. «Point» contacts of initial particles transform into flat ones, while the contact area increases considerably [10]. As a result, a short-term preliminary activation can extend the possibilities of reaction in a self-propagating regime even for systems where the SHS process cannot be carried out without preliminary heating.

In order to establish the lower limit of the conditions for the SHS process to occur with mechanical activation involved, we investigated the Ni-Al, Ni-Si, Ni-Ge systems, which are SHS systems and for which the lower concentration limits for silicon and aluminum in SHS without preliminary mechanical activation are known [11]. In the Ni-Al system, the limiting solid-phase solubility of aluminum in nickel is 10.3 wt.% at 1385°C and decreases to 3.85 wt.% at 500°C, but SHS cannot be performed in this concentration range. The minimal aluminum concentration at which SHS can be performed by the traditional method is 13 wt.% Al [3].

Preliminary mechanical activation in the Ni-Al system allows one to decrease the minimal content of Al in the initial mixture for the SHS process. This minimal Al content is 7 wt.%. We succeeded in performing SHS in the sample compacted from the powder after mechanochemical treatment. The Ni_3Al , Ni_2Al_3 intermetallics and unreacted nickel were detected in the synthesis products. Subsequent mechanochemical activation homogenizes the product and leads to the formation of a solid solution only.

In the Ni-Si system, similarly to the Ni-Al system, the concentration range of the solid solution is strongly dependent on temperature; at room temperature, the solubility of silicon in nickel is ~5 wt.%, while at 1150°C it is ~9.3 wt.% [12, 13]. It is not possible to realize an SHS process in the solid solution range without preliminary mechanical activation in this system.

Our investigations showed that in the solid solution range, the layered composites of nickel and silicon could be formed under activation within 1 min., though they do not look so dense as in the Ni-Al system. The SHS process was also performed in these mixtures containing 9 wt.% Si, the products being a mixture of the Ni_2Si , Ni_5Si_2 intermetallics and unreacted nickel. Similarly to the case of the Ni-Al system, subsequent mechanical activation results in a single-phase product which is a supersaturated solid solution.

In the Ni-Ge system, in which the limiting solubility of germanium in nickel is 13.8 wt.% [5, 14], we investigated the possibility of performing SHS also in the solid solution concentration range. Composites are formed in a Ni 13 wt.% Ge mixture after mechanical activation for 1.5 min. The Ni_5Ge_2 and NiGe intermetallics and unreacted nickel are the products of SHS. The formation of a single-phase solid solution is achieved by a subsequent short-term activation.

The investigations therefore showed that preliminary mechanical activation, during which layered composites are formed from the initial elements, allows one to broaden the concentration limits of SHS processes up to the solid solution region, perhaps due to reagent dispersion and an increase of contact area. The products of this synthesis are mixtures of intermetallics, the doping elements being completely consumed for their formation, and an excess of solvent metal. The conservation of the layered structure in SHS products allows us to assume that intermetallic compounds are formed locally inside the layered structure, its framework being built of solvent metal.

Using the discovered effect of preliminary mechanical activation on the possibility of performing SHS even in the concentration range of solid solutions, we tested it in the systems in which SHS cannot be performed without preliminary heating of the reaction mixture even in the range of intermetallic existence [3]. As an example, **Figure 12** shows the combustion rate and the maximum combustion temperature plotted versus time of the preliminary mechanical activation for the Ni 45 wt.% Ti composition. The samples start burning at room temperature after 2.5 min. of mechanical activation. Similarly to all the systems considered above, an increase of the burning rate is connected to the formation of dense layered composites. A photograph of the sample after mechanical activation for 2.5 min. is shown in **Figure 13**. Increasing the time of mechanical activation also leads to a further increase of the density of the composites, a decrease of the grain size to $<0.1 \mu\text{m}$, and to the appearance of particles with traces of strong plastic deformation on the surface. The decrease of the combustion rate is connected to the start of destruction of the largest composites. Only NiTi (the main phase) and Ti_2Ni lines are observed in the diffraction patterns of the SHS products at any time of mechanical activation. No titanium or nickel lines are observed! The relative content of these phases in the products remains practically independent of the time of mechanical activation.

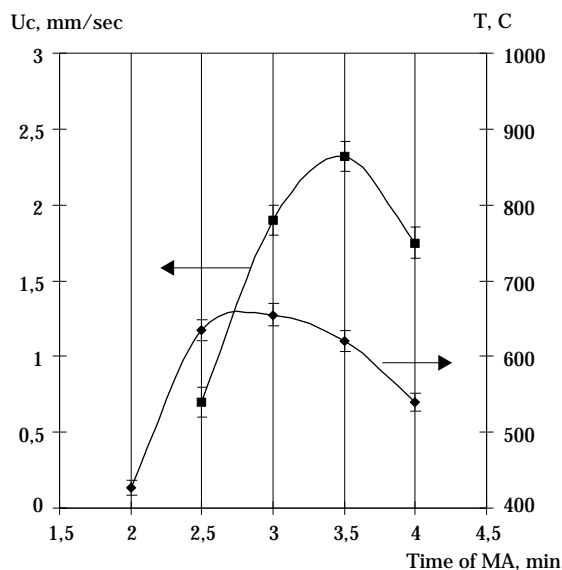


Fig. 12 Dependence of the combustion rate (U_c) and combustion temperature of the Ni 45 wt.% Ti mixture on the time of preliminary mechanical activation.

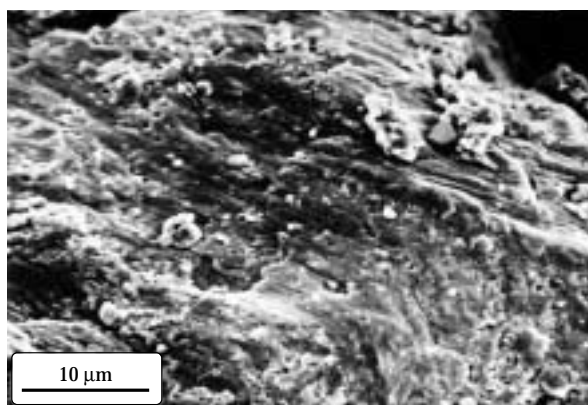


Fig. 13 Microphotograph of a Ni 45 wt.% Ti sample after mechanical activation for 2.5 min.

2.2 Oxide systems

The synthesis of nanocrystalline mixed oxides is among the major problems of advanced ceramic technology. Conventional processes for manufacturing multi component mixed-oxide ceramics involve high-temperature reactions between metal oxides or between metal oxides and carbonates. These diffusion-controlled processes require the application of high temperatures and the use of highly dispersed precursor powders; mixed oxides are formed in particles of 1 to $5 \mu\text{m}$ in size. Mechanochemical alloying partly removes the diffusion control. The consider-

able heat of the chemical reaction provides the high rate of the mechanochemical reaction. For example, for most reactions of mechanochemically assisted metal oxidation in a gaseous phase, the oxidation rate correlates with variations in Gibbs' free energy [15]. For the exothermal reactions, the mechanochemical reaction rate of solid solution formation is a function of the enthalpy of formation of intermetallic compounds in equilibrium [16]. Therefore, if reactions with small decreases in Gibbs' free energy are used in thermodynamically controlled mechanochemical synthesis, a large power supply and a long mechanical activation time would be necessary, by analogy with mechanochemical synthesis of mixed oxides from binary oxides, either alone or mixed with carbonates [17]. Efficient mechanochemical synthesis is not feasible unless in energy-intensive activators (steel drums and steel balls), and contamination of the product is inevitable. Therefore, mechanochemistry is almost useless for commercial ceramic processes with their extremely high purity requirements. The mechanochemical approach becomes practicable only with high rates of promoted reactions, i.e., those that are not only thermodynamically allowed, but that also give an energy gain. High rates of mechanochemical processes result in final products which are highly dispersed, and this can significantly influence the properties of the resultant ceramics.

The change of Gibbs' energy in the synthesis of complex oxides from simple ones shows that all these reactions are thermodynamically allowed, while the majority of reactions with the participation of carbonates are available only at high temperatures (**Table 1**).

Some of these reactions were performed mechanochemically when a sufficient amount of energy was applied [17]. All the values obtained for the systems under consideration are approximately of the same

order of magnitude, so the conditions for these reactions to proceed should be rather similar.

The use of peroxide compounds and oxides as the initial components of mixtures, as proposed by some authors [17], does not bring substantial changes to the ΔG of the reaction of complex oxide synthesis.

Among the methods to obtain oxides, the energetically most profitable ones are the direct oxidation of metals (or metal mixtures) by oxygen (**Table 2**). However, in reality one can hardly perform this type of synthesis mechanochemically due to the high plasticity of metals.

The most promising way seems to be the oxidation of metals by peroxide compounds, especially if we take into account that there is a rather large class of stable metal peroxides that can provide a couple for a proper metal to synthesize a complex oxide. In such cases, one should keep in mind that the mechanochemical interaction of metal peroxide with metals can follow two routes: either with the formation of complex oxides or with the formation of a mixture of

Table 1 Changes of Gibbs' energy in the reactions of the mixtures of metal oxides and the metal oxides with metal carbonates resulting in the formation of complex oxides.

No.	Reaction product Me'O+Me''CO ₃	ΔG°_{298}	ΔG°_{1273}
		kcal/mol	
1	BaTiO ₃	16.3	-17.7
2	BaZrO ₃	24.2	-10.0
3	BaHfO ₃	21.9	-13.2
4	BaMoO ₄	2.5	-30.5
5	BaWO ₄	-4.2	-42.6
6	BaAl ₂ O ₄	26.5	-16.3
7	CaMoO ₄	-9.3	-44.7
8	SrMoO ₄	-6.6	-41.7
9	PbMoO ₄	-1.6	-35.6

Table 2 Changes of Gibbs' energy in the oxidation of metals or metal mixtures by oxygen or barium peroxide resulting in the formation of oxides and complex oxides.

No.	Product of reaction Me+O ₂	ΔG°_{298} kcal/mol	Product of reaction Me'+Me''+O ₂	ΔG°_{298} kcal/mol	Product of Me+ BaO ₂ interaction	ΔG°_{298} kcal/mol
1	BaO	-251.1			Ba ₂ TiO ₄	-231
2	TiO ₂	-212.1	BaTiO ₃	-373.9	BaTiO ₃	-235
3	ZrO ₂	-248.5	BaZrO ₃	-402.0	BaZrO ₃	-263
5	MoO ₃	-159.7	BaMoO ₄	-334.9	BaMoO ₄	-196
6	WO ₃	-182.6	BaWO ₄	-364.5	BaWO ₄	-225
7	Al ₂ O ₃	-378.0	BaAl ₂ O ₄	-556.3	BaAl ₂ O ₄	-390

simple ones, because both reactions are profitable from the thermodynamic viewpoint, and the change of Gibbs' energy is much higher than that for the synthesis from oxides and carbonates. The calculation of ΔG_{298}° for the BaO_2 interaction with metals demonstrated that the decrease of Gibbs' energy was larger by 30–40 kcal/mol than when the products of the same reaction would be a sum of simple oxides. One can assume that synthesis will proceed to the formation of complex oxides.

According to X-ray diffraction data, the mechanochemical interaction of barium peroxide with titanium for 5 min. results in the formation of a mixture of barium titanates. The reflections corresponding to BaO_2 and Ti disappear and reflections corresponding to Ba_2TiO_4 , BaTiO_3 [18], etc. appear. No diffraction reflections from simple oxides of barium and titanium are observed.

The complex oxides were obtained for the system $\text{BaO}_2 + \text{Me}$ (Me=Zr, Al).

For the BaO_2 -Ti mixture, an antisymmetric absorption band peaking at 700 cm^{-1} and a very weak peak at 775 cm^{-1} appear after 1 min. of activation. After 5 min. of activation, a shoulder of the 700 cm^{-1} band appears at 550 cm^{-1} (**Fig. 14b**). This band is assignable [21-23] to ν (Ti-O) stretches in $[\text{TiO}_4]$ tetrahedra of barium titanates [23]. The positions of the peaks and the band shape do not correspond to ν (Ti-O) vibrations in various TiO_2 polymorphs [22, 24].

The BaO_2 -Zr mixture mechanically activated for 5 min. exhibits an absorption band with a peak at 550 cm^{-1} (**Fig. 14c**). This band can be assigned to barium zirconate [21, 23].

A broad asymmetric band with a maximum at 530 cm^{-1} appears as a result of activation of a mixture of BaO_2 with aluminum (**Fig. 14d**). Magnesium aluminate exhibits a similar IR spectrum in this region [21, 26, 27], and the formation of barium aluminate can be assumed in the BaO_2 -Al system under mechanical activation [28].

The electron microscopic investigation of the product of mechanochemical synthesis in a mixture of BaO_2 with Zr shows that activation for 1 min. results in the formation of particles of $0.3\text{--}1 \mu\text{m}$ in size. They are composed of small blocks of $6\text{--}12 \text{ nm}$ in size (**Fig. 15**). The microdiffraction picture obtained from a separate particle also points to a developed microblock structure. The diffraction spots are shaped as rings, which is characteristic of polydisperse materials, while microdiffraction from a separate block gives a point, which is evidence of the single crystal state of the substance. Diffraction reflections in both electron

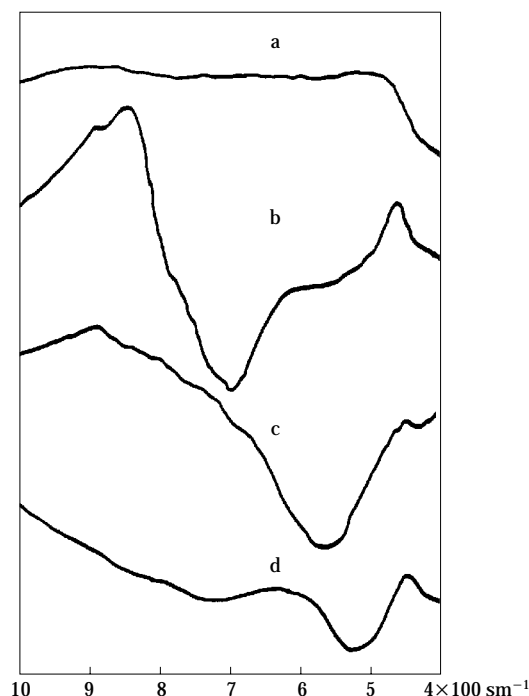


Fig. 14 IR spectra of (a) an initial mixture of barium peroxide with metals and after 1 min. mechanical activation: (b) - Ti, (c) - Zr, (d) - Al.



Fig. 15 Microphotograph of a BaZrO_3 particle obtained by mechanochemical synthesis during 1 minute.

diffraction patterns, though somewhat broadened, are point reflections, which is evidence of a rather high degree of crystallinity of the substance formed in mechanochemical synthesis. A similar picture was also observed for other complex oxides, with only a small difference in microblock size.

The investigations therefore demonstrate that the mechanochemical interaction of barium peroxide with

metals, which proceeds with a substantial decrease of Gibbs' free energy, as it follows from thermodynamic calculations, allows one to synthesize complex oxides with nanocrystalline particles in a relatively short time.

The mechanochemical oxidation of metals by peroxide compounds allows the preparation of single-phase particles of complex oxides with nanometer-sized microblocks [29-32]. However, in the case of some metals such as tungsten, molybdenum, and tantalum, mechanochemical synthesis does not proceed to completion, whatever reagent ratio is taken, even after prolonged mechanical activation. Some part of the metal always remains unreacted. At the reagents molar ratio of $\text{BaO}_2:\text{W}=1:1$, the products are BaWO_4 and Ba_2WO_5 ; unreacted W remains. At an increased barium peroxide content (up to 2:1), part of W also remains unreacted. A mixture of tungstates BaWO_4 , Ba_2WO_5 and Ba_3WO_6 is formed. At the reagents ratio of 3:1, only the content of complex oxide Ba_3WO_6 increases. Mechanochemical activation of the mixtures of BaO_2 with Mo, the molybdates BaMoO_4 , Ba_2Mo_5 and Ba_3MoO_6 are formed. Similarly to the case of tungsten, a part of molybdenum remains unreacted.

The SHS process in these mixtures also results in the formation of a mixture of complex oxide phases; unreacted metal remains. The preliminary mechanical activation of the mixture has practically no effect on the phase composition of the SHS products although it does increase the process rate.

For $\text{BaO}_2\text{-Me}$ ($\text{Me}=\text{W}, \text{Mo}, \text{Ta}$) systems, it was not possible to synthesize single-phase complex oxides, neither by mechanical activation nor by SHS.

IR spectroscopic investigations of the mechanochemical interaction of BaO_2 with WO_2 showed that the formation of a complex oxide starts within the first seconds of activation. The IR spectra of the initial mixture BaO_2+WO_2 contain one broad band at $850\text{--}550\text{ cm}^{-1}$, without clearly exhibited maximums. It is assigned to the stretching vibrations $\nu(\text{W-O})$ (Fig. 16a) [21]. The $\nu(\text{Ba-O})$ band is below 400 cm^{-1} . After activation for 10 s, a clear band with a maximum at 810 cm^{-1} is observed instead of the above-mentioned broad band; the intensity of this new band increases with increasing activation time (Fig. 16b, c). The similarity of the IR spectra of activated mixtures to the spectra of stolzite [21] allows us to assume that the activation of the BaO_2+WO_2 mixture results in the formation of BaWO_4 with a spinel structure. However, according to the IR spectroscopic data, the mechanochemical reaction of $\text{BaO}_2+\text{WO}_2 \rightarrow$

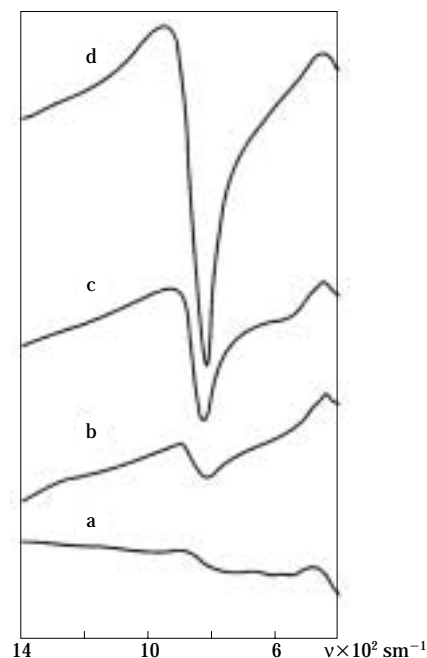


Fig. 16 IR spectra of an initial mixture of barium peroxide with WO_2 (a), after its mechanical activation for 10 s (b) and 2 min. (c), of the SHS product in this mixture (d).

BaWO_4 does not proceed to completion, which is evidenced by the presence of noticeable absorption in the region $800\text{--}500\text{ cm}^{-1}$ as a shoulder of the band with a maximum at 810 cm^{-1} related to $\nu(\text{W-O})$ of the lower tungsten oxide.

According to the XRD data, a growth of the reflections from the BaWO_4 phase starts at the second minute of activation and reaches its maximum by 5 minutes (Fig. 17 a, b). But, with increasing activation time, the intensity of the diffraction peaks of the complex oxide does not increase, and the intensities of the peaks related to the initial tungsten oxide do not decrease. This means that the result of mechanochemical interaction between BaO_2+WO_2 is a mixture of phases.

For the interaction of BaO_2 with MoO_2 , the IR spectra and XRD also reveal a mixture of phases.

The relatively high temperatures of formation of the complex oxides in the system involving the oxidation of the lowest tungsten oxide with barium peroxide allows one to perform these reactions by means of SHS. However, pretreatment of the barium peroxide and sometimes heating of the initial mixture are necessary [33]. This is due to the fact that BaO_2 particles entrained in air become coated with a layer of barium carbonate and hydroxide. This layer prevents an SHS reaction. One can assume that a short-term prelimi-

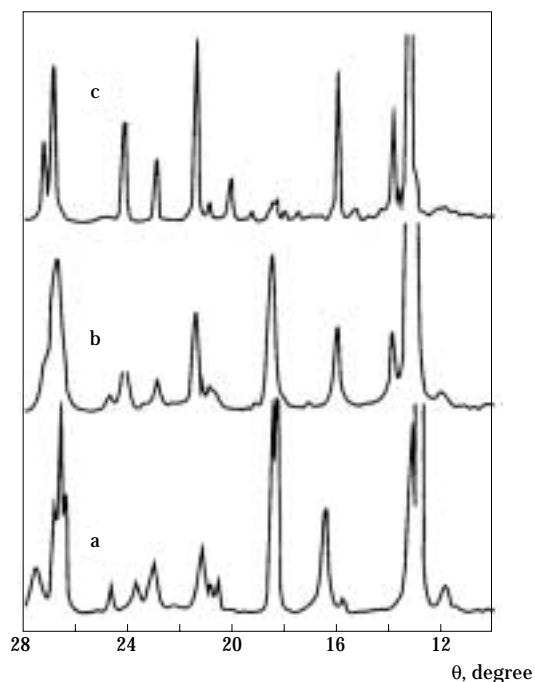


Fig. 17 X-ray patterns of an initial mixture of barium peroxide with WO_2 (a), after its mechanical activation for 5 s (b) and of the SHS product in this mixture (c).

nary mechanochemical activation of the initial mixture leads to the destruction of these barrier layers and provides a substantial increase of the area of contact between the oxides and the barium peroxide.

An investigation of the effect of the preliminary mechanochemical activation of commercially available BaO_2 with WO_2 showed that the maximal temperature and rate of SHS process are achieved after activation for 2 min., and the single-phase complex oxide BaWO_4 is formed (**Figs. 16d** and **17c**). A disadvantage of the resulting substance was the large particle size (300–500 nm) and in some places even partial agglomeration (**Fig. 18a**). Electron microscopic studies show that subsequent mechanical treatment of the product for 2 minutes in a high-energy activator of planetary type produces a material with a particle size of 20–30 nm (**Fig. 18b**) without changes of phase composition (!).

Similar results were also obtained for the $\text{BaO}_2 + \text{MoO}_2$ system, in which the maximal rate of the SHS process with the formation of the complex oxide BaMoO_4 is achieved after preliminary mechanical activation for 30 s.

The structural similarity of the higher oxide WO_3 and barium tungstate BaWO_4 and rather high temperature of the reaction $\text{BaO}_2 + \text{WO}_3 \rightarrow \text{BaWO}_4 + 1/2 \text{O}_2$ (–128 kJ/mol) allow us to assume that this reaction

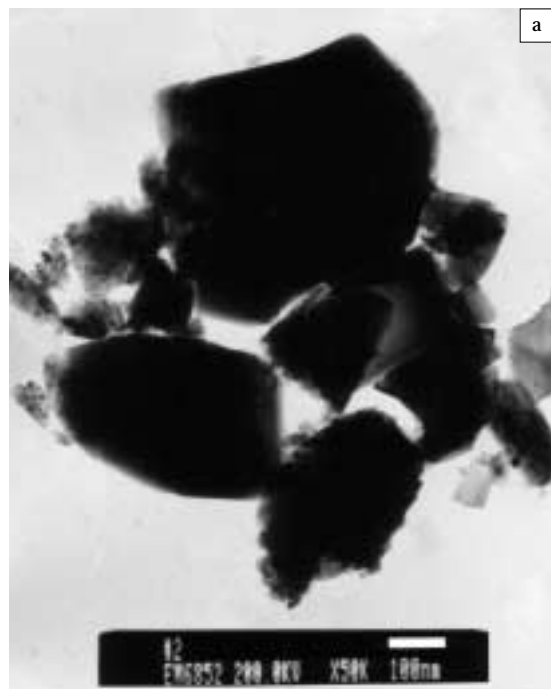


Fig. 18 Microphotograph of the SHS product of a $\text{BaO}_2 + \text{WO}_2$ mixture (a), the same product after mechanical activation for 2 min. (b).

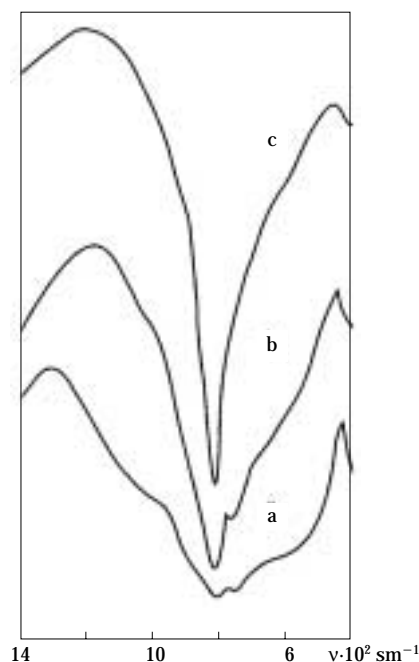


Fig. 19 IR spectra of an initial mixture of barium peroxide with WO_3 (a), after its mechanical activation for 10 s (b) and 1 min. (c).

can be conducted mechanochemically. It follows from the analysis of the IR spectra (**Fig. 19**). Similarly to the case of the lower oxide, the reaction starts during the first seconds of activation. The shape of the ν (W-O) band of WO_3 ($1000\text{--}500\text{ cm}^{-1}$) and the ratio of intensities of their maximums are changed. After activation of the mixture for 1 min., the IR spectrum of the sample contains only one intensive band with a maximum at 810 cm^{-1} . This band relates to ν_3 vibrations of WO_4 tetrahedrons of the reaction product BaWO_4 .

X-ray phase analysis showed that the growth of the intensity of the BaWO_4 phase reflections was accompanied by the decrease of the WO_3 reflections intensities till their complete disappearance after activation for 5 min. (**Fig. 20**). Microphotographs suggest that the initial stage of the process involves intensive dispersion of the particles; their aggregation starts at the second minute of the process. After activation for 5 min., complex oxide particles are formed; the size of their blocks is $20\text{--}30\text{ nm}$ (**Fig. 21**).

The mechanochemical activation of BaO_2 with MoO_3 results in the formation of the complex oxide BaMoO_4 . The complex oxide with the same composition (BaMoO_4) can be obtained via SHS between barium peroxide and the higher molybdenum oxide, both reagents being activated preliminarily for 30 s.

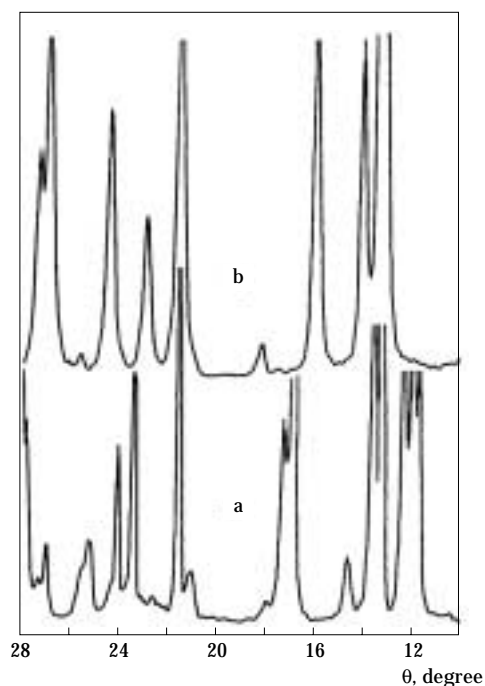


Fig. 20 X-ray patterns of an initial mixture of barium peroxide with WO_3 (a), after its mechanical activation for 5 min. (b).



Fig. 21 Microphotograph of the product of mechanochemical interaction of $\text{BaO}_2 + \text{WO}_3$ (time of MA 5 min.).

Conclusion

Our investigations show that a combination of the SHS process with the mechanical activation both of reagents and products could be rather attractive for

technological applications. The preliminary activation facilitates combustion, making it possible even in the concentration region where conventional SHS is never observed. In other cases, the *very short* mechanical activation of SHS products allows us to prepare uniform single-phase products.

For complex oxides, the picture is very similar if we can only provide the energetic conditions for SHS. There is usually quite a wide variety of precursors available for ceramic synthesis, which makes it possible to find an energetically efficient root.

The complex oxides can be obtained by mechanochemical synthesis, by SHS, and by a combination of mechanical activation and SHS.

The combination of mechanical activation and SHS brings advantages to both methods. As a result, the short-term mechanochemical activation of SHS products becomes an extremely convenient method for manufacturing nanopowders.

References

- 1) Grigorieva T.F., Korchagin M.A., Barinova A.P., Ivanov E.Yu., Boldyrev V.V. *Inorg. Materials. Engl. Tr.* 36(12), 1467 (2000).
- 2) Grigorieva T.F., Barinova A.P., Lyakhov N.Z. *Russian Chem. Reviews*, 70(1), 45 (2001).
- 3) Avvakumov E.G., Potkin A.R., Samarin O.I. A.C. USSR № 975068. BI, 1982, № 43 (in Russian).
- 4) Samsonov G.V., Bondarev V.N. *Germanides. Moscow, Metallurgia*, (1968). (in Russian).
- 5) Itin V.I., Naiborodenko Yu.S. *High-temperature synthesis of intermetallic compounds. Tomsk State University Publishing House, Tomsk*, (1989) (in Russian).
- 6) Munir Z.A., Anselmi-Tamburini U. *Materials Science Reports*, 3, No 7-8, 277 (1989).
- 7) Grigorieva T.F., Barinova A.P., Boldyrev V.V., Ivanov E.Yu. *Solid State Ionics*, 101-103, 17 (1997).
- 8) Avvakumov E.G., *Mechanical methods of the activation of chemical processes. Nauka, Novosibirsk* (1986) (in Russian).
- 9) Gilman P.S., Benjamin J.S. *Ann. Rev. Mater. Sci.*, 13, 270 (1983).
- 10) Charlot F., Gaffet E., Zeghmati B., Bernard F., Niepce J.C., *Mater. Sci. Eng.*, A262, 279 (1999).
- 11) Grigorieva T.F., Korchagin M.A., Barinova A.P., Lyakhov N.Z. *Doklady Akademii nauk (Reports of the Russian Academy of Sciences)*. 369, № 3, 345 (1999) (in Russian).
- 12) Nash A., Nash P. *Bull. Alloy Phase Diagrams*, Jun. 1987, 8(3).
- 13) Samsonov G.V., Dvorina L.A., Rud' B.M. *Silicides. Moscow, Metallurgia* (1979) (in Russian).
- 14) Vol A.E. *Structure and properties of binary metal systems. V. 2. Moscow, Fizmatgiz* (1962) (in Russian).
- 15) Heinicke, R. Riedel, H. Harenz. *Z. Phys. Chem.*, 227, 62 (1964).
- 16) Grigorieva T.F., Barinova A.P., Boldyrev V.V., Ivanov E.Yu. *Materials Science Forum*, 235-238, 577 (1997).
- 17) Zyryanov V.V., in: «*Mechanochemical synthesis in inorganic chemistry*», ed. by E.G. Avvakumov, Novosibirsk, Nauka, 1991, p. 102-125 (in Russian).
- 18) *Powder Diffraction File. Swarthmore: Joint Committee on Powder Diffraction Standards. Card №№ 8-277, 8-368, 8-372, 5-626.*
- 19) *ibid. Card № 6-0399.*
- 20) *ibid. Card № 17-306.*
- 21) Plyusnina I.I. *Infrared spectra of minerals, Moscow, MSU Publishers*, 1977 (in Russian).
- 22) Lawson L., *Infrared absorption spectra of inorganic substances, Moscow, Mir* (1964).
- 23) Barker M., Wood D.I. *J. Chem. Soc. Dalton Trans.*, 22, 2448 (1972).
- 24) Boldyrev A.I. *Infrared spectra of minerals, Moscow, Nedra*, 1976 (in Russian).
- 25) Last J.T., *Phys. Rev.*, 105, № 6, 1740 (1957).
- 26) Landolt-Bornstein H. *Physikalisch-Chemische Tabellen*, 1951, Teil 2.
- 27) Henning O., Paselt G., *Z. Phys. Chem.*, 233, № 3-4, 170 (1933).
- 28) Audette R.J., Quail J.W. *Inorganic Chemistry*, 11, № 8, 1904 (1972).
- 29) Grigorieva T.F., Barinova A.P., Ivanov E.Yu., Boldyrev V.V. *Doklady Akademii nauk (Reports of the Russian Academy of Sciences)*. 354, № 4, 489 (1997) (in Russian).
- 30) Grigorieva T.F., Barinova A.P., Kryukova G.N., Boldyrev V.V. *Proceeding of EUROMAT'97. (5th European Conference on Advanced Materials, Processes and Applications, Maastricht, April, 1997)*. 2, 333 (1997).
- 31) Grigorieva T.F., Barinova A.P., Vorsina I.A., Kryukova G.N., Ivanov E.Yu., Boldyrev V.V. *Chemistry for Sustainable Development*. 6, 115 (1998).
- 32) Grigorieva T.F., Barinova A.P., Vorsina I.A., Kryukova G.N., Boldyrev V.V. *Zhurn. Neorg. Khimii*. 43, № 10, 1594 (1998).
- 33) Smirnov V.I., Aleksandrov V.V. *Inzhenerno-fizicheskiy zhurnal*. 65, № 5, 594 (1993) (in Russian).

Performance and Cost-Effectiveness of Ferric and Aluminum Hydroxide Metal Oxide Coating on Filter Media to Enhance Virus Removal†

T.M. Scott¹, R.C. Sabo², J. Lukasik¹,
C. Boice¹, K. Shaw³, L. Barroso-Giachetti³,
H. El-Shall⁴, S.R. Farrah¹, C. Park²,
B. Moudgil⁴ and B. Koopman^{3*}

¹ Department of Microbiology and Cell Science

² Department of Chemical Engineering

³ Department of Environmental Engineering Sciences

⁴ Department of Materials Science & Engineering**

Abstract

Coating sand and granular activated carbon with iron aluminum hydroxides changed the zeta potential of these filtration media from negative to positive at pH 6-9, while also significantly improving removal of viruses (MS2, PRD1, Polio1). A quaternary ammonium based coating on sand also increased zeta potential, but led to limited improvement in virus removal. The coated activated carbon was effective in both columns and faucet filters. Performance of faucet filters decreased slightly (e.g., 98% removal initially vs. 89% removal after 1 month) with time. The chemical costs of coating would add approximately 10% to the cost of water delivered by large-scale municipal systems, whereas coating chemical costs would add less than 1% to the cost of water treated by point-of-use faucet filters. The improvement in virus removal performance gained by use of coated filter media provides a significant benefit to the consumer in terms of increased microbiological quality at a modest-to-negligible increase in cost.

1. Introduction

Chemicals such as aluminum sulfate or ferric chloride are traditionally added to water to reverse the surface charge on microbes, promoting their coagulation and flocculation with other particulate matter in the water. An alternate approach is to modify the surface properties of the filter media, e.g., by coating with an electropositive material. The first investigators of this approach (Brown et al., 1974a, Brown et al., 1974b; Farrah et al., 1988; Farrah et al., 1991) found that iron aluminum hydroxide coating increased removal of viruses by diatomaceous earth from less than 30% to greater than 80%. Subsequently, Lukasik et al. (1996, 1999) tested removal of viruses by columns filled with fine sand (less than 0.3 mm) coated with iron aluminum hydroxide. They reported

that virus removal by uncoated sand was typically less than 30%, whereas coated sand gave removals of greater than 99%.

One objective of the present work was to extend the evaluation of the use of coated granular media for virus removal. We chose a media size range (0.6-0.7 mm) for sand that lies within that used in large-scale municipal and industrial water filters (J.M. Montgomery, Inc., 1985). We also evaluated granular activated carbon as a filtration medium, because it is a common component of point-of-use filtration systems, e.g., faucet filters. Such systems are becoming increasingly popular in households because of concern over microbiological quality of water delivered by municipal utilities.

A second objective was to evaluate a coating with antibacterial activity. This is desirable to limit bacterial growth in point-of-use water filters. The coating chosen for this purpose (AEM 5700; Aegis, Midland, MI) consists of a positively-charged quaternary ammonium linked to a carbon chain. It is widely used as a bactericidal agent in consumer products.

* Corresponding author

**University of Florida, Gainesville, Florida

† Accepted: May 22, 2002

The final objective of this work was to determine the costs of chemicals used in the coating process and compare them, expressed on a unit volume basis, to the typical costs of water from municipal supply systems and point-of-use systems.

2. Materials And Methods

2.1 Chemicals

Aluminum chloride ($\text{AlCl}_3 \cdot 6\text{H}_2\text{O}$), ferric chloride ($\text{FeCl}_3 \cdot 6\text{H}_2\text{O}$), and ammonium hydroxide (28-30% as NH_3) were obtained from Fisher Scientific. AEM 5700 antimicrobial agent, consisting of 42% 3-(trimethoxysilyl) propyldimethyl-octadecyl ammonium chloride, with the balance of the solution consisting of methanol and inerts, was obtained from Aegis Environmental Management (Midland, MI).

2.2 Viruses and Viral Assays

The following phages and their hosts were used: MS-2 (ATCC 15597-B1) was assayed using *Escherichia coli* C-3000 (ATCC 15597) as a host. Bacteriophage PRD-1 was assayed using *Salmonella typhimurium* (ATCC 19585) as a host. These phages are commonly used models of enteric viruses (Gerba, 1984). Phages were assayed as plaque-forming units (PFU) using agar overlay procedure (Snustead and Dean, 1971). Poliovirus was proliferated and assayed as PFU on Buffalo Green Monkey (BGM) cells using an agar overlay method (Smith and Gerba, 1982).

2.3 Coating Procedure

2.3.1 Modification of Filter Media by *In Situ* Precipitation of Metallic Hydroxides

Activated carbon (20×40 mesh) was obtained from Aldrich Chemical Company. Ottawa sand (25×30 mesh after sieving) was obtained from Fisher Scientific. The media were first rinsed with deionized water, then soaked to saturation in a solution of 0.25M ferric chloride and 0.5M aluminum chloride, and finally heated at 60°C until dry. The media was then mixed to saturation with 3N ammonium hydroxide and heated at 60°C until dry. A second precipitation with ammonium hydroxide was performed to precipitate any un-reacted chlorides.

2.3.2 Modification of Ottawa Sand with AEM5700

Ottawa sand (25×30 mesh) was washed three times in deionized water then soaked to saturation in a 1% aqueous solution of AEM 5700. The solution was agitated for ten minutes at room temperature. The media

was then filtered from the solution using Whatman paper, rinsed 5 times, and dried overnight.

2.3.3 Faucet Filter Modification

Faucet filters (Ameritech Co.) were cut open and the activated carbon removed. The carbon was then coated with iron aluminum hydroxide as described previously. The modified carbon was placed back into the shell and the shell was sealed with epoxy. Unmodified filters were also cut open and resealed to act as controls.

2.4 Characterization of Filter Media

The zeta potential of the filtration media was determined using an Anton Paar Electro Kinetic Analyzer (EKA, Anton Paar, Graz, Austria). The cylindrical flow cell had an I.D. of 2.0 cm and a packed length of 4.0 cm. The electrolyte was 1.0×10^{-3} M KCl. Zeta potential (ζ) was computed according to the Fairbrother and Mastin (1924) equation:

$$\zeta = \left(\frac{\Delta U}{\Delta P} \right) \frac{\eta k}{\epsilon} \quad (1)$$

where η is the viscosity of water and k is conductivity. The parameter ϵ in SI units is found from:

$$\epsilon = \epsilon_r \epsilon_0 \quad (2)$$

where $\epsilon_r = 78.54$ at 25°C and $\epsilon_0 = 8.85 \times 10^{-12}$ C²/(J m).

2.5 Experimental Protocols

2.5.1 Comparison of Coated and Uncoated Media in Columns

Four identical filtration columns, each 1.9 cm in diameter and 50 cm long, were filled with either Ottawa sand, AEM 5700 coated Ottawa sand, or metal hydroxide coated Ottawa sand. The filter media was added incrementally through the top of the columns, which were partially charged with water from the bottom. After the addition of sand, the column was thoroughly tapped to pack the media and to remove any trapped air bubbles. Wire mesh was placed at the ends of the column to prevent loss of media. Acrylic plastic caps were secured to the columns to hold the mesh and to provide connections for the PVC tubing (1/8 in. ID) used in the experiments. Once packed and assembled, water was passed through the columns to further rinse the media. The columns were operated in parallel using two multi-head peristaltic pumps, which were calibrated prior to the experiments.

Viral suspensions were passed top-to-bottom through the columns at a superficial velocity of about

1 mm/s, which is typical of industrial and other water treatment processes. The same suspension was fed to all four columns. Samples were taken for assay from the inlet and from the exit of each column periodically for about two hours or about 70 pore volumes, ensuring steady-state conditions.

2.5.2 Comparison of Coated and Uncoated Granular Activated Carbon in Columns

Activated carbon (Aldrich Chemical Co.) was freshly prepared and coated with iron aluminum hydroxide as previously described. Modified carbon was packed into one column while unmodified carbon was packed into another column (30 cm long, 5 cm diameter). Four liters of deionized water, containing bacteriophage MS2, were then pumped through each of the columns at a rate of 40 mL/sec. After initial passage of the water through the columns, the effluent was recirculated through the columns to assess second-pass removals. Triplicate samples of column influent and effluent were collected and assayed for virus removal.

2.5.3 Comparison of Point-of-Use Filters containing Coated and Uncoated Media

Faucet filters containing either coated or uncoated granular activated carbon were attached to a pressure vessel that contained dechlorinated tap water seeded with bacteriophage and poliovirus 1. The test solution was forced through the filters at a rate of 25 mL/s using nitrogen gas. Multiple influent and effluent samples were collected and assayed to determine percent removal of viruses. For long term coating stability and performance studies, the filters were rinsed daily with at least 8 L of tap water. Samples were collected and assayed weekly for a period of one month.

3. Results

3.1 Surface Characteristics of Filter Media

The coating of Ottawa sand with iron aluminum hydroxide increased the zeta potential from -40 ± 6.6 mV to $+45 \pm 9.8$ mV at pH 7.0. The zeta potential of the uncoated activated carbon used in the column experiments (Aldrich) was -2.6 ± 3.0 mV. After coating, the Aldrich carbon had a zeta potential of $+24.8 \pm 8.2$ mV. The activated carbon used in the faucet filter experiments had a measured zeta potential of -1.2 ± 5.1 mV before coating. After coating, the zeta potential measured $+27.2 \pm 10.2$ mV (**Table 1**). Coating sand with AEM5700 also resulted in a change in zeta potential from negative to positive (data not shown).

Table 1 Zeta potentials of sand and activated carbon with and without iron aluminum hydroxide coating

Filter media	Zeta potential (mV)*
Sand (uncoated)	-40.0 ± 6.6
Sand (coated)	$+45.0 \pm 9.8$
Faucet Filter carbon (uncoated)	-1.2 ± 5.1
Faucet Filter carbon (coated)	$+27.2 \pm 10.2$
Aldrich carbon (uncoated)	-2.6 ± 3.0
Aldrich carbon (coated)	$+24.8 \pm 8.2$

* Values represent the mean ± 1.0 S.D. (N=10)

3.2 Effect of Coating on Virus Removal by Sand in Columns

Filtration columns packed with Ottawa sand, iron and aluminum coated Ottawa sand, and AEM5700 coated Ottawa sand were charged with suspensions of MS-2 and PRD-1. Virus removals for each column and organism are reported in **Figure 1**. Metal hydroxide coated sand removed $52 \pm 7\%$ and $46 \pm 9\%$ of MS-2 and PRD-1, respectively, whereas viral reductions for unmodified sand were $16 \pm 9\%$ and $-3 \pm 4\%$, respectively. A two-factor analysis of variance revealed a significant difference ($\alpha=0.05$) in percent removals between different sand columns. Tukey's test was performed with $\alpha=0.05$ to directly compare the percent removals of pairs of columns. Metal hydroxide coated Ottawa sand removed more MS-2 and PRD-1 than uncoated Ottawa sand and more PRD-1 than AEM5700 coated Ottawa sand. AEM5700 coated sand removed significantly more MS-2 than unmodified sand but not significantly more PRD-1.

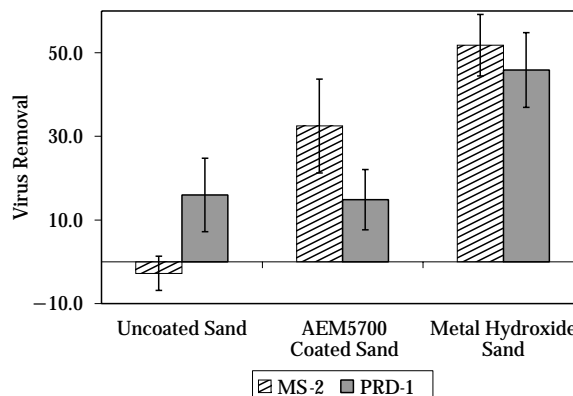


Fig. 1 Performance of coated and uncoated sand in columns [error bars give ± 1.0 S.D. (N=3)]

3.3 Effect of Coating on Virus Removal by Granular Activated Carbon in Columns

Columns containing modified activated carbon outperformed columns containing unmodified activated carbon in the removal of viruses from aqueous solutions. The first pass of water seeded with bacteriophage MS2 through the columns resulted in an average 92% reduction of MS2 by the coated carbon, compared to an average 32% reduction by unmodified carbon (**Table 2**). Passage of column effluents back through the respective columns resulted in a cumulative 99% reduction of bacteriophage MS2 by the coated carbon and a cumulative 54% reduction by the unmodified carbon.

Table 2 Effect of Coating on Performance of Activated Carbon in Columns*

Pass	% Cumulative removal	
	Coated	Uncoated
1	92±5**	32±4
2	99.6±0.5**	54±7

* Values are the means ±1.0 S.D. (N=3)

** Significantly greater than control (uncoated) at $\alpha=0.01$

3.4 Effect of Coating on Virus Removal by Activated Carbon in Faucet Filters

Faucet filters containing activated carbon coated with ferric and aluminum hydroxide removed more microorganisms from water than all unmodified filters. The modified filters removed >99% of MS2 and 84±8% of poliovirus 1 while the unmodified filters removed 34±11% of MS2 and 35±4% of poliovirus (**Table 3**). Long-term evaluation indicated that the coatings are stable and capable of maintaining their effectiveness for several weeks. Each filter tested removed greater than 85% of all organisms used to challenge the system after 30 days of use (**Fig. 2**).

Table 3 Effect of Coating on Granular Activated Carbon in Faucet Filters*

Virus	% Removal	
	Coated	Uncoated
MS2	99.7±0.4**	34±11
Polio 1	84±8**	35±5

* Values are the means ±1.0 S.D. (N=5)

** Significantly greater than control (uncoated) at $\alpha=0.01$

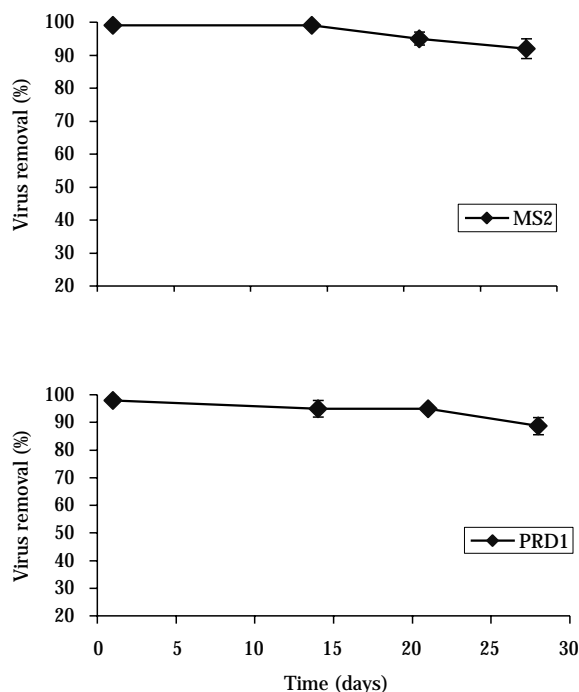


Fig. 2 Long-term performance of faucet filter containing coated activated carbon [error bars give ±1.0 S.D. (N=3)]

* Filters containing uncoated activated carbon removed less than 35% of viruses

3.5 Economic Comparison

The chemical costs of coating filter media with iron aluminum hydroxides were estimated based on observed chemical requirements for coating media in the laboratory, together with costs of chemicals in bulk quantities (**Table 4**). The total coating cost for sand was 7.0 cents per kg, whereas the coating cost for activated carbon was 55 cents per kg. These costs were used in determining the added price to the consumer of water treated by coated filter media.

The lower of the mean percent removals (46% achieved with PRD1) was chosen to be representative of virus removals obtained by coated sand. Given this level of performance in a 0.5 m deep column, a corresponding removal of 70% may be expected in a 1.0 m deep column based on first-order removal (Tien, 1989). The cost of coating filter media to achieve this removal can be based on a unit cross-sectional area of 1.0 m² (normal to the downward flow direction of the water being treated). The chemical cost to coat the media contained in this unit area would be \$120.57 (**Table 5**). The volume of water treated in 1 month by this unit area, based on a superficial velocity of 1.4 mm/s [2 gal/(ft² min)] and a 5% loss for backwashing, would be 3498 m³. The unit chemical cost for

Table 4 Chemical costs of coating sand and activated carbon

		$\text{FeCl}_3 \cdot 6\text{H}_2\text{O}$	$\text{AlCl}_3 \cdot 6\text{H}_2\text{O}$	NH_4OH^a	Total
Bulk chemical cost ^b		\$0.33/kg	\$1.76/kg	\$0.25/kg	–
Amount used to coat 1 kg media	Sand	16.9 g	30.2 g	45 g	–
	Activated carbon	135 g	231 g	346 g	–
Cost in cents per kg media	Sand	0.5	5.3	1.2	7.0
	Activated carbon	4.4	41	9.5	55

^a 28-30% as NH_3 with a specific gravity of approximately 0.9

^b Chemical Market Reporter (2001)

Table 5 Cost of using coated sand for municipal/industrial filtration

Filter coefficient	1.2 m^{-1}
Bed depth	1.0 m
Initial virus removal	70%
Porosity	0.35
Bed cross-sectional area	1.0 m^2
Bed depth	1.0 m
Bed volume	1.0 m^3
Media weight*	1722.5 kg
Unit coating cost	\$0.07/kg
Coating cost for 1.0 m^3 bed	\$120.57
Superficial velocity	1.4 mm/s
Volume treated in 1 month	3498 m^3
Unit cost	3.4 cents/ m^3
Typical U.S. delivered municipal water cost (conventional filter media)	40 cents/ m^3

* Specific gravity of sand=2.65

water treatment with coated media is thus computed to be 3.4 cents per cubic meter. This compares to a typical delivered water price in U.S. municipal systems of 40 cents per cubic meter.

The cost of water treatment by a conventional household faucet filter as compared to the chemical cost of coating the activated carbon in such a filter is determined in **Table 6**. Based on a retail cost of \$10 per filter, a lifetime of 1 month, and a daily throughput of 8 L, the unit cost of water treated by a faucet filter was estimated to be 4.1 cents per liter. Coating the activated carbon contained in one faucet filter would require 2.9 cents worth of chemicals, amounting to an additional cost of 0.01 cents per liter.

Table 6 Cost of using coated activated carbon in faucet filters

Media weight per filter	52 g
Initial virus removal	98%
Unit coating cost	\$0.55/kg
Coating cost for 1 filter	2.9 cents
Daily water consumption	8 L
Volume treated in 1 month	243.5 L
Typical retail cost of conventional faucet filter	\$10
Water cost for conventional faucet filter (assuming change-out after 1 month)	4.1 cents/L
Additional chemical cost for using coated media in faucet filter	0.01 cents/L

4. Discussion

Coating of sand and granular activated carbon with iron aluminum hydroxide made the zeta potential more electropositive, while also significantly improving virus removal. This effect on sand has been observed by several other investigators (Lukasik et al., 1999; Chen et al., 1998; Truesdail, 1999; Shaw et al., 2000), who attributed increased removals of viruses, bacteria and protozoa to the change in filter media potential from negative to near-zero or positive. A similar effect on zeta potential of sand was achieved by the AEM5700. Although AEM 5700 is a popular antimicrobial agent for consumer products, use of this material for coating water filter media is novel. However, the AEM 5700-coated sand showed a limited capacity to remove viruses.

Use of iron aluminum hydroxide coating to increase the zeta potential of granular activated carbon from negative to positive values was reported for the first time in this work. Uncoated granular activated carbon, which is a standard component in point-of-use fil-

ters, was a moderate to poor collector of viruses. After coating, the activated carbon achieved very high virus removals in both columns and faucet filters.

An important issue in the application of coated filter media is the lifetime of the coating. The performance of faucet filters decreased slightly (e.g., 98% removal of PRD1 initially vs. 89% removal after 1 month) with time. Previous studies using coated sand in columns indicated that little of the coating was lost over time. Chen et al. (1998), in a study of aluminum hydroxide coated sand for bacterial removal from wastewater, found that three-fourths of the aluminum originally coated on the sand was still present after 3 months of continuous flushing. Lukasik et al. (1999) reported that iron and aluminum concentrations in the effluents of filtration columns containing coated media were below the detection limit (0.1 ppm for Fe; 0.01 ppm for Al) of ICP.

The estimated chemical costs for coating sand and activated carbon, when expressed relative to the volume of water treated, are low relative to typical consumer costs for water. The chemical costs of coating would add approximately 10% to the cost of water delivered by municipal systems, whereas coating chemical costs would add less than 1% to the cost of water treated by faucet filters. Improvement in virus removal performance gained by use of coated filter media thus provides a significant benefit to the consumer in terms of increased microbiological quality at a negligible-to-modest increase in cost.

Acknowledgments

The authors gratefully acknowledge the financial support of the Engineering Research Center (ERC) for Particle Science & Technology at the University of Florida, the National Science Foundation (NSF) grant #EEC-94-02989, and the Industrial Partners of the ERC.

References

- 1) Brown, T.S., J.F. Malina, Jr., and B.D. Moore. Virus removal by Diatomaceous earth filtration, part 1. *J. Am. Water Works Assoc.* 66: 98-102 (1974a).

- 2) Brown, T.S., J.F. Malina, Jr., and B.D. Moore. Virus removal by diatomaceous earth filtration, part 2. *J. Am. Water Works Assoc.* 66: 735-738 (1974b).
- 3) Chemical Market Reporter. Inorganic chemicals. Vol. 257, No. 1, pp 18-25 (2001).
- 4) Chen, J., Truesdail, S., Lu, F., Zhan, G., Belvin, C., Koopman, B., Farrah, S., and Shah, D. Long-term evaluation of aluminum hydroxide-coated sand for removal of bacteria from wastewater. *Water Research* **32**, 2171-2179 (1998).
- 5) Farrah, S.R., M.A. Girard, G.A. Toranzos, and D.R. Preston. Adsorption of viruses to diatomaceous earth modified by in situ precipitation of metallic salts. *Z. Gesante Hyg.* 34, 520-521 (1988).
- 6) Fairbrother, F. and Mastin, H. Studies in Electro-endosmosis. Part I. *J. Chem. Soc.* 125, 2319-2330 (1924).
- 7) Farrah, S.R., D.R. Preston, G.A. Toranzos, M. Girard, G.A. Erdos, and V. Vasuhdivan. Use of Modified Diatomaceous Earth for Removal and Recovery of Viruses in Water. *Appl. Environ. Microbiol.* 57(9): 2502-2506 (1991).
- 8) Gerba, C.P. Applied and theoretical aspects of virus adsorption to surfaces. *Advances in Applied Microbiology.* 30: 133-167 (1984).
- 9) J.M. Montgomery, Inc. *Water Treatment Principles & Design.* John Wiley & Sons, New York (1985).
- 10) Lukasik, J., Y.F. Cheng, F. Lu, M. Tamplin, and S.R. Farrah. Removal of microorganisms from water by columns containing sand coated with ferric and aluminum hydroxide. *Wat. Res.* 33(3): 769-777 (1999).
- 11) Lukasik, J., S. Truesdail, D.O. Shah, and S.R. Farrah. Adsorption of microorganisms to sand and diatomaceous earth particles coated with metallic hydroxides. *Kona Particle and Powder.* 14: 87-91 (1996).
- 12) Shaw, K., Walker, S., and Koopman, B. Effect of Hydrous Iron Aluminum Oxide Coating on Sand in the Filtration of *Cryptosporidium* Oocysts. *Journal American Water Works Association.* **92**, 103-111 (2000).
- 13) Smith, E.M. and C.P. Gerba. Laboratory methods for the growth and detection of animal viruses. In C.P. Gerba and S.M. Goyal, ed. *Methods in environmental virology.* Marcel Dekker, Inc. New York (1982).
- 14) Snustad, S.A. and D.S. Dean. Genetic experiments with bacterial viruses. W.H. Freeman and Co., San Francisco (1971).
- 15) Tien, C. *Granular filtration of aerosols and hydrosols.* Butterworths, Boston (1989).
- 16) Truesdail, S. Fundamental forces important to the enhancement of biological colloid removal. Ph.D. Dissertation, University of Florida, Gainesville, FL USA (1999).

Author's short biography



T.M. Scott

Dr. T.M. Scott received his B.S., M.S., and Ph.D. degrees in Environmental and Molecular Microbiology from the University of Florida and was a graduate student member of the National Science Foundation Engineering Research Center for Particle Science and Technology at the University of Florida (ERC) when this research was carried out. He is currently a Visiting Scientist in the Environmental Microbiology Laboratory at the University of South Florida's College of Marine Science. His areas of research interest include the development of novel microbial source tracking methodologies as well as development and improvement of methods used for the concentration and detection of pathogenic viruses and protozoa in the environment.



R.C. Sabo

Dr. R.C. Sabo, Jr. graduated magna cum laude from Vanderbilt University with a Baccalaureate of Engineering in chemical engineering and mathematics in 1997. He then moved to Gainesville, Florida, where he obtained a Doctor of Philosophy in chemical engineering from the University of Florida. He was a graduate student member of the ERC at the time of this research and is currently an ERC post-doctoral fellow.

J. Lukasik

Dr. J. Lukasik was a post-doctoral fellow at the ERC when this research was carried out. He is currently Senior Research Scientist for Biological Consulting Services, Inc., Gainesville, Florida.



C. Boice

C. Boice received her B.S. (1998) and M.S. (2000) degrees in Microbiology and Cell Science from the University of Florida. She is currently pursuing a doctoral degree in Microbiology and Cell Science and is a graduate student member of the ERC. Her research interests include flotation, filtration, adsorption, and surface modification.



K. Shaw

Dr. K. Shaw was a graduate student member of the ERC when this research was carried out. She received her Ph.D. in Environmental Engineering Sciences from the University of Florida and is currently Project Manager for CH2M-Hill.

Author's short biography

L. Barroso-Giachetti

L. Barroso-Giachetti received his B.S. in environmental engineering sciences from the University of Florida and was an ERC undergraduate scholar when this research was carried out.



H. El-Shall

Dr. H. El-Shall is an Associate Professor of Materials Science and Engineering at the University of Florida and Associate Director of the ERC. His research interests are applied surface and colloid chemistry and mineral, chemical, and metallurgical engineering.



S.R. Farrah

Dr. S.R. Farrah is a Professor in the Department of Microbiology and Cell Science at the University of Florida. He received his B.A. in Science in 1965 and his Ph.D. in Microbiology in 1974 from the Pennsylvania State University. His research interests include detecting viruses in environmental samples and adsorption of microorganisms to solids.



C. Park

Dr. C. Park received his BS in Chemical Engineering from Seoul National University in Korea in 1980, and his MS and PhD in Chemical Engineering from Stanford University in 1982 and 1985, respectively. He worked for Union Carbide Corporation as a project scientist for 4 years since 1984. Subsequently he joined the faculty of Chemical Engineering at the University of Florida where he is currently a professor of Chemical Engineering. His research interest includes interfacial phenomena in multiphase flows, filtration of colloidal particles, and polymer rheology and processing.



B. Moudgil

Dr. B. Moudgil is a Professor of Materials Science and Engineering and Director of the ERC. His research interests are particulate processing, solid-solid/solid-liquid separations, fine particle packing, sol-gel processing, crystal modification, dispersion & aggregation of fine particles, polymer & surfactant adsorption, orientation of particles in slurries, and rheology of concentrated suspensions.

Author's short biography



B. Koopman

Dr. B. Koopman is a Professor of Environmental Engineering Sciences and Co-Leader of Goal I Advanced Separations in the ERC. His research interest is biological wastewater treatment.

Consolidation Behavior of Inhomogeneous Granular Beds of Ductile Particles using a Mixed Discrete-Continuum Approach[†]

S. Zheng and A. M. Cuitiño

Department of Mechanical and Aerospace Engineering
Rutgers University*

Abstract

In this paper we study the consolidation behavior of inhomogeneous granular beds of elasto-plastic particles by means of a discrete-continuum formulation, which systematically bridges the micro and meso scales. The methodology is particularly suitable for describing the post-rearrangement regime where consolidation proceeds mostly by elastic and inelastic deformation. This formulation is able to provide the quantitative estimates of the evolution of macroscopic variables, such as pressure and density, while following microlevel processes, such as local coordination number and loading paths. This methodology is used to simulate binary mixtures composed by particles with different nonlinear properties. The predictions are in general agreement with the experimental data during both loading and unloading cycle.

1. Introduction

Consolidation of granular materials is a complex process operated by several mechanisms including particle rearrangement, elastic and plastic deformation, fracture and pulverization [1]. The particle rearrangement is a void-filled-in process which is characterized by minute driving or applied forces and by large *non-affine* particle motion. In contrast, the post-rearrangement stage or compaction stage is identified by the inability of the particles to reduce the volume by relative motion, requiring larger driving forces to deform or fracture the particles for further consolidation [2, 3]. While for brittle particles fracture is the dominant mechanism of consolidation – after the initial and localized elastic deformation stage –, for ductile particles inelastic or plastic deformation provides a source for reducing the interparticle porosity, and consequently the total volume.

For systems dominated by frictional forces, rearrangement and compaction tend to operate simultaneously at different spatial locations of the specimen. In those cases, molecular dynamics methods [4] or discrete element methods (DEM) [5] provide a tool to simulate these conditions. However, due to the

intrinsic nature of these formulations, which trace each individual particle, only relatively small samples can be effectively simulated. Often the permissible sizes are too small to characterize the macroscopic properties of the material. In the present work, we restrict our attention to thoroughly lubricated systems where interparticle friction is weak. For this case, the compaction may be uncoupled from the particle rearrangement as a follow-up process. In this scenario, the rearrangement is simulated first, followed by the subsequent compaction. A description of the particle rearrangement methodology is briefly described in Section 2. This method is a modified DEM version (see for example [6, 7] for traditional DEM formulations) which can simulate large samples with keeping an excellent agreement with the experimental data. The compaction regime is simulated by the application of a mixed discrete-continuum or granular quasi-continuum (GQC) formulation. The main aspects of the model are presented in Section 3 and the details are available elsewhere [8].

The present GQC, which can simulate granular beds of nonlinear spherical (3D) or cylindrical (2D) particles with an arbitrary size distribution, is utilized to investigate the influence of the composition of granular structure and material properties on the macroscopic compaction behavior. To that effect, two groups of particles with a given size distribution are generated and later mixed with different ratios to conform the samples, as described in Section 4. A para-

* Piscataway, NJ 08854, USA

[†] Accepted: September 12, 2002

metric study of the effect of particle size, Young's modulus, yield stress and initial microstructure is then presented in Section 4 along with a detailed discussion.

2. Die Filling and Particle rearrangement

The initial particle bed structure is generated by a ballistic deposition technique, which simulates the die filling process. The algorithm proceeds by dropping individual particles from the container top until they reach a stable position. The condition of stability is dictated by the cohesivity of the powder. Cohesive powders result in open structures, as shown in **Fig. 1(a)** for a container of $50 \times 60 \text{ mm}^2$ filled with 0.4 mm-radius monosized particles. Due to the open structure of this powder bed, particle rearrangement operates in the early stages of densification. This process is simulated by forcing the particles residing at the top surface to move down at a specified rate. At each step, the punch is displaced 0.15 mm and the particles are allowed to accommodate until a new equilibrium configuration is attained. Due to the fact that the rearrangement is an evolution process of position change, an iterative scheme is required to establish the updated equilibrium configuration. **Fig. 1(b)** shows an intermediate stage during the rearrangement process, where the punch has been displaced by $\Delta = 5.1 \text{ mm}$. Three clear regions are observed: an unperturbed region near the bottom, a packed region near the punch, and a narrow gap in between or rearrangement front. Massive non-affine motion is only observed on rearrangement front in close agreement with the experiment record [9].

Fig. 1(c) depicts the final stages of rearrangement, where the front is reaching the bottom of the sample.

3. Compaction

Due to the inability of the particles to modified their current structure, further punch motion induces particle deformation as a mechanism of volume reduction. During this stage both relative roll and slip are drastically reduced and play a negligible role on the macroscopic response of the granular bed [2, 3]. Under these conditions a discrete/continuum approach can be effectively exploited to account explicitly for the interparticle interactions within a constrained kinematic field, as described succinctly in the next section and in [8].

3.1 Mixed Discrete/Continuum Approach

The central idea of this approach hinges on the ability of constraining particle motion by a coarse grid of dimensions commensurable with the sample size. In addition, the constrained displacement field can be realized by utilizing standard Finite Element techniques. Within this framework, a mesh is generated, in either 2D or 3D, and the motion of each particle is described by the element that contains the particle's center. Interaction with particles in the same and neighboring elements are allowed *via* an interparticle or local constitutive relation. It should be noted that this approach is equally applicable to both dynamic and quasi-static conditions, offering similar advantages. In the present case of analysis, we are interested in the evolution of the powder bed under relatively slow loading conditions – compared with

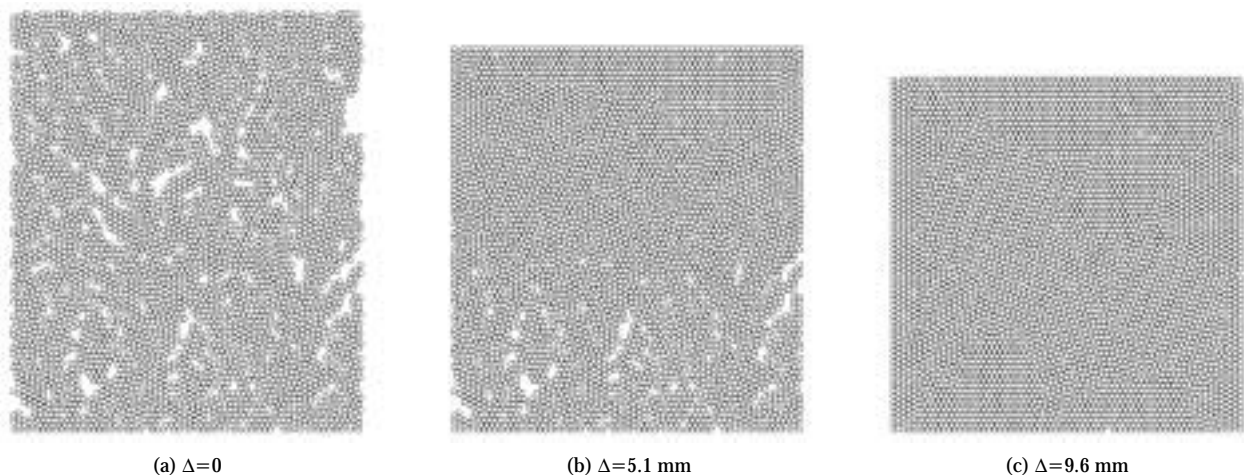


Fig. 1 Rearrangement processes of monosized particle bed. (a) Initial open structure; (b) intermediate structure; (c) closely packed structure.

characteristic wave speed in these materials –, and thus, we concentrate on a quasi-static formulation. Details of the formulation are presented in [8].

3.2 Local Constitutive Equations

The response between spherical particles can be divided into five regimes: *i*) tension, *ii*) local elastic contact, *iii*) local elastic-plastic contact, *iv*) fully plastic, and *v*) finite particle deformation. Although the present approach can be extended to describe the whole range, the present study is restricted to the first four. The tension regime (cohesion) is described by a potential law with Lennard Jones' functional dependence and a cut-off. The cohesivity is then modulated by the value of the only adjustable coefficient. While the elastic response is governed by a Hertzian law,

$$\frac{F}{\pi R^2} = \frac{4E}{3\pi} \left(\frac{\alpha}{R} \right)^{\frac{3}{2}}, \quad (1)$$

where F is the contact force, α is the relatively approaching displacement of the particle centers after contact, R and E are the equivalent radius and the equivalent modulus of the contact which are defined by

$$\frac{1}{R} = \frac{1}{R_1} + \frac{1}{R_2}, \quad \frac{1}{E} = \frac{1-\nu_1^2}{E_1} + \frac{1-\nu_2^2}{E_2}. \quad (2)$$

where E_1 , E_2 and ν_1 , ν_2 are Young's moduli and Poisson's ratios respectively of two particles in-contact with radius R_1 and R_2 . The elastic regime only dominates the initial stages of compaction where particle deformation is minimal, and the plastic deformation quickly eclipses the elastic part. If the elastic/plastic response of the solid materials of particles is described by assuming a linear elastic regime followed by a power-law plastic regime characterized by hardening exponent m (which is set equal to 3 in the present study)

$$\epsilon_i = \begin{cases} \frac{\sigma}{E_i} & \sigma \leq \sigma_{yi} \\ \left(\frac{\sigma}{\sigma_i} \right)^m & \sigma > \sigma_{yi} \end{cases}, \quad (3)$$

where the label $i=1, 2$ refers to the particles in contact, the interaction law for these particles is then given by the similarity solution [3]

$$\frac{F}{\pi R^2 \Gamma} = B(m) \left(2c^2(m) \right)^{1+\frac{1}{2m}} k(m) \cdot \left(\frac{\alpha}{R} \right)^{1+\frac{1}{2m}}, \quad (4)$$

and no interaction of the contacts need be considered due to the localized nature [3]. The reference yield

stress σ_i relates with yield stress σ_{yi} in

$$\sigma_i = \sigma_{yi}^{1-\frac{1}{m}} E_i^{\frac{1}{m}}, \quad (5)$$

and the equivalent reference stress Γ

$$\frac{1}{\Gamma^m} = \frac{1}{\sigma_1^m} + \frac{1}{\sigma_2^m}, \quad (6)$$

is given in terms of the yield stress σ_i of each particle i . The values of c , k and B for a given exponent are numerically estimated by [3] resulting in the following expressions

$$c^2(m) = 1.5 - \left(\frac{1}{m} \right)^{\frac{1}{2}}, \quad k(m) = 3.07 \times 0.16^{\frac{1}{m}},$$

$$B(m) = \begin{cases} 0.74 + 0.26^{\frac{1}{m}} & m < 3, \\ 0.64 + 0.57^{\frac{1}{m}} & m \geq 3. \end{cases} \quad (7)$$

The two limiting regimes of the local constitutive equation, elastic ($m=1$) and elastic/perfectly plastic ($m \rightarrow \infty$), agree well with experimental data. For $m=1$ the Hertzian regime is recovered for which exists ample experimental validation. For $m \rightarrow \infty$, a linear dependency is predicted by (4) which is in a good agreement with the recent experiments of [10] for nearly ideal plastic materials.

To account for the irreversibility of the plastic deformation, a Hertzian unloading branch is introduced, which allow us to trace elastic recovery during ejection as well as heterogeneous fields where loading and unloading are concurrent. The unloading regime is described by

$$\frac{F}{\pi R^2} = \frac{4E}{3\pi} \left(\frac{\alpha - \alpha_{res}}{R} \right)^{\frac{3}{2}} \quad (8)$$

where α_{res} is the residual indentation depth that left in the particle and might be obtained from both (4) and (1). Another indication of the irreversibility of the process is observed on the evolution of α_{res} , which satisfies $\dot{\alpha}_{res} \geq 0$.

4. Results and discussions

4.1 Sample Generation

In order to investigate the influence of particle size and material on the compaction behavior, different particle beds are generated by mixing two sets of particles, each one with a different size distribution and material properties. The Group I with a relatively small mean diameter and the Group II with a larger one. The size distribution follows a normal distribution characterized by an average radius \bar{r} and a vari-

ance σ which are listed in **Table 1** (units are mm). Lower and upper limits cut-off are introduced to simulate particle populations within two given thresholds. The details of the selection of the size distribution and material properties are provided in the following sections.

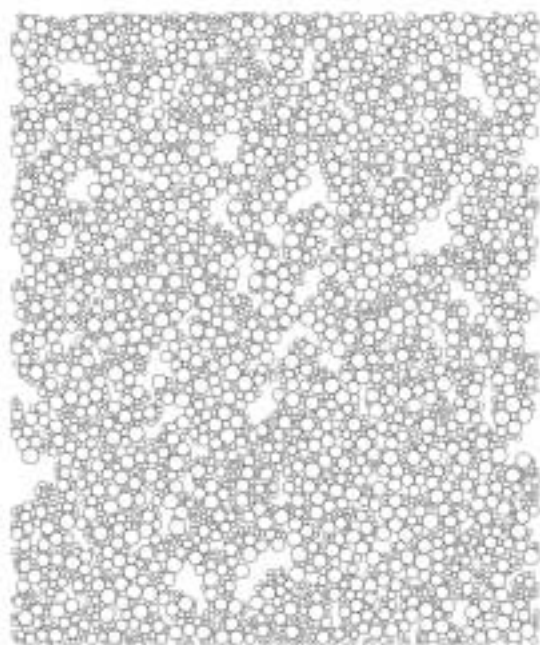
For the purpose of this analysis, two cohesive granular beds are generated by mixing Group I with Group II. The mixture A has 30% in volume of particles from Group I and 70% from Group II, conversely, mixture B has 70% of group I and 30% of group II. With these simulated mixtures we fill a frictionless container of $50 \times 60 \text{ mm}^2$ utilizing the ballistic deposition method described in Sec. 2. The resulting structures are shown in **Fig. 2**, which share common features, such as voids, with the monosized distribution shown in **Fig. 1(a)**.

The samples are then subjected to consolidation by rearrangement using the simulation approach described in Sec. 2, which provides the initial samples

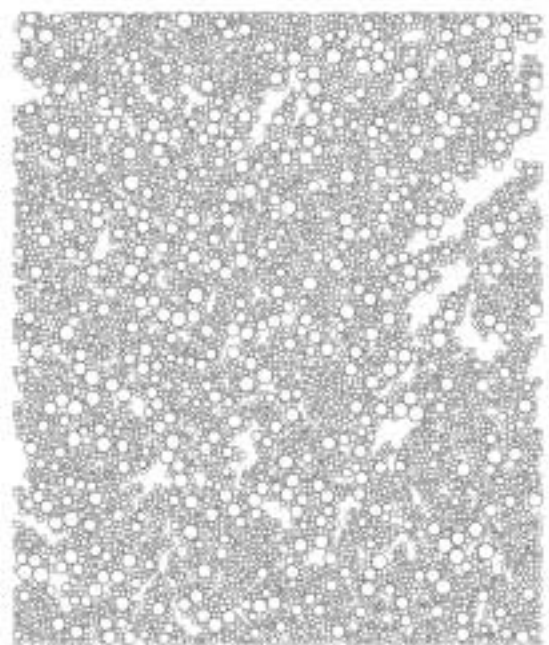
for consolidation by compaction. The post-rearrangement structures are shown in **Fig. 3**, where the overimposed mesh shows the resolution of the coarse grain simulation using our discrete-continuum approach. It is interesting to notice that the structures formed after the rearrangement of both inhomogeneous and monosized beds show some qualitative and quantitative differences, such as the appearance of grain-like structure, which is only observed in the monosized case. The inhomogeneous cases consistently exhibit a lower post-rearrangement average density, as indicated in **Table 2** (compare to the value of 0.867 for the monosized case), indicating a better packing for the monosized case. During the process of rearrangement both the average density, $\bar{\rho}$, and the average coordinate number, \bar{N}_c , increase as shown in **Table 2**. Also, there is a tendency to reduce the inhomogeneity on the initial or pre-rearrangement density distribution resulting from the die filling process. This effect is clearly indicated in **Fig. 3**. An interesting observation is that the post-rearrangement density of mixture B is not a direct function of the fraction of fines, in contrast, the average coordination number of the sample shows a direct correlation. This observation is in good agreement with the proposition that only when the size of the fine fraction is small enough to reside at the interparticle spaces of the coarse fraction (no perturbation of the packing),

Table 1 Characteristic distribution values of particle sets.

	Radius limits	Average radius	Specified/ actual variance
Group I	0.05~0.35	0.20	0.10/0.075
Group II	0.40~0.80	0.60	0.15/0.101

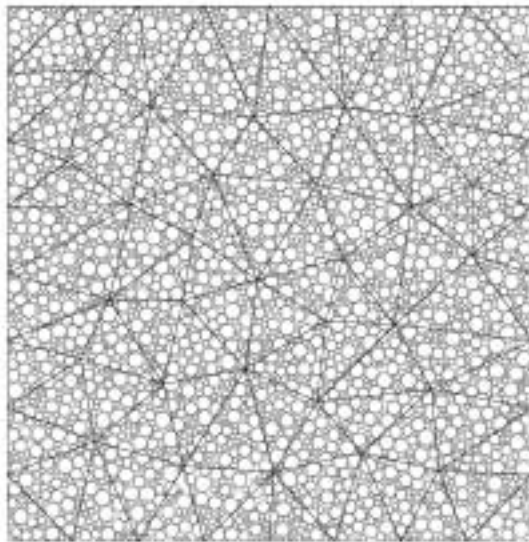


(a) Mixture A

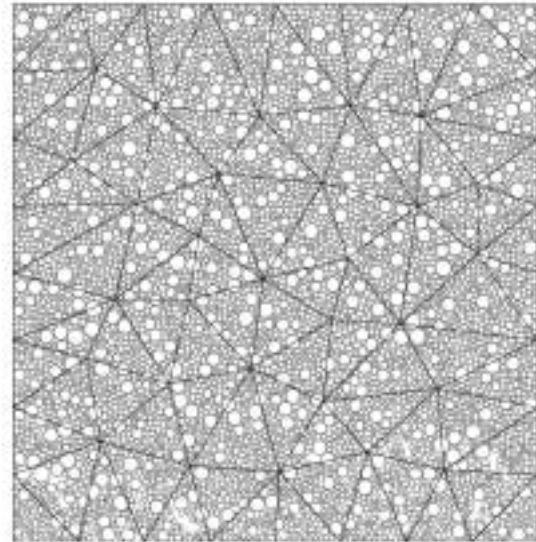


(b) Mixture B

Fig. 2 The initial open structure of polydispersed granular material of (a) mixture A; (b) mixture B.



(a) Mixture A



(b) Mixture B

Fig. 3 The closely packed structure of polydispersed granular material of (a) mixture A; (b) mixture B.

Table 2 Average density, coordinate number and particle bed region before and after particle rearrangement.

	Particles fine/coarse	Before rearrangement			After rearrangement		
		$\bar{\rho}$	\bar{N}_c	Bed region	$\bar{\rho}$	\bar{N}_c	Bed region
Mixture A	4609/1318	0.725	5.13	50×60	0.851	5.53	50×51.11
Mixture B	10643/549	0.716	5.19	50×60	0.845	5.65	50×50.86

the densification is improved [16]. Although $\bar{\rho}$ for the inhomogeneous samples are lower than the monosized ones, \bar{N}_c is higher. This is consistent with the observation that in monosized beds the low number of contacts along the disorder regions (grain boundaries) significantly reduces the average coordination number of the entire region (maximum coordination number is 6 for a perfect hexagonal arrangement). In contrast, in inhomogeneous beds large particles may be surrounded by more than 6 smaller particles, increasing the average coordination number.

4.2 Size Distribution

In order to focus on the effect of post-rearrangement structure, the Group I and II are assumed to have the same solid material behavior which is characterized by a Young's modulus of 10 GPa, a Poisson's ratio of 0.33 and yield stress of 100 MPa. The global pressure-deformation responses and unloading paths are plotted in **Fig. 4**, where the curve corresponding

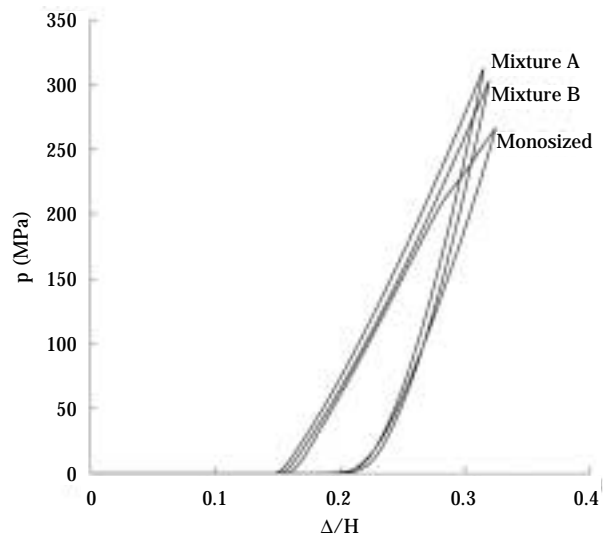


Fig. 4 The global pressure-deformation responses of mixture A, B and monosized particle bed.

to monosized bed is also included for comparison purposes. The pressure p is computed as the applied vertical force per unit of effective area. The effective area is estimated as the multiplication of the width of the container (50 mm) by the weighted average thickness of each particle in the bed, where the particle diameter is used as the weighting factor. The deformation is characterized by the ratio of the punch displacement over the initial height of particle bed (60 mm). An evident conclusion from the figure is that size distribution has small effects on the macroscopic response as indicated by the parallelism among the three curves. The only observed difference (horizontal shift) is due to the disparity of structures induced during the rearrangement process. This observation can be understood with the aid of (1) for the elastic regime and (4) for the plastic one. The average local or particle pressure may be equated to $F/\pi R^2$, which is a function (nonlinear) of the average particle deformation α/R . Thus, the average pressure vs. average deformation is then independent of the particle radius, in accordance with the simulation results. The present approach provides, in addition of the macroscopic pressure-deformation response, the local distribution of the average stresses and their temporal evolution. These distributions are of key importance in tracking regions with potential defects and imperfections. In Fig. 5 shows the spatial distribution of σ_{yy} (normal stress in the direction of the compaction) for mixtures A and B, and the monosized recorded for the same applied displacement of the punch. The samples show different distributions with more uniformity for the mixture B where a large number of fine particles present. The non-uniformity in the monosized particle bed agrees with the exis-

tence of the heterogeneous structure as grains and boundaries.

4.3 Elastic Behavior

The elastic properties affect not only the local stress distribution but also the global pressure-deformation response. In order to investigate the influence of Young's modulus on the compaction behavior, we conduct a parametric study by adopting $\eta_E = E_I/E_{II} = [0.1, 1, 10]$, where E_I and E_{II} are the modulus of the two groups. The global pressure-deformation curves are plotted in Fig. 6. The Young's modulus of the particle group with higher volume percentage controls the average responses, even in the plastic regime. In that regime, (4) shows that the interparticle pressure is proportional to the effective stress Γ which in turns relates to the Young's modulus by (5). In the elastic regime (initial loading or unloading), (1) and (8) provide a direct connection between pressure and Young's modulus.

The local stress distributions are highly dependent of the elastic properties as shown in Fig. 7, where the contour of σ_{yy} is plotted for both mixture A and B. The stress may have different limits due to the variety of Young's modulus, but the flood contours are drawn by setting the difference of the limits the same as it is done in Fig. 5, which is 50 MPa. At the same punch displacement as in Fig. 5, as expected, the stress distribution is more heterogeneous than the case of uniform material.

4.4 Plastic Behavior

To quantify the effect of the interparticle plastic behavior on compaction response, we vary, at constant Young's modulus, the parameter $\eta_{\sigma_y} = \sigma_{yI}/\sigma_{yII}$

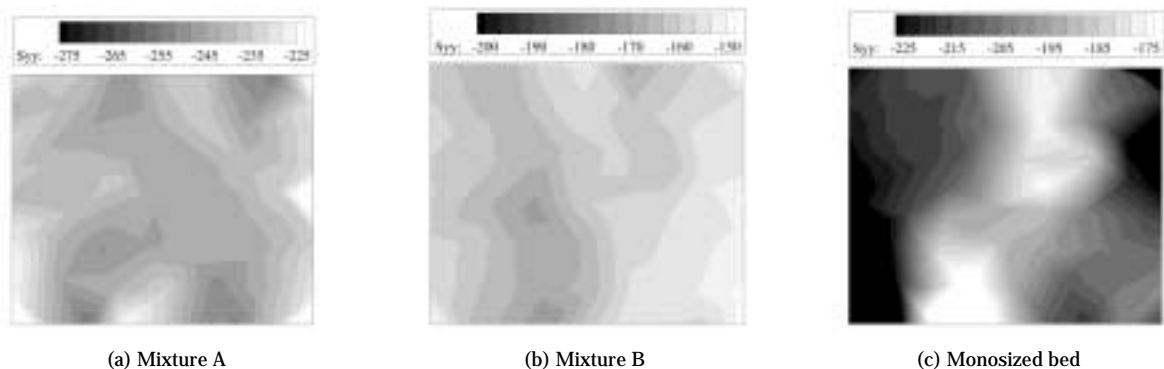


Fig. 5 The local stress contours of (a) mixture A; (b) mixture B; (c) monosized particle bed.

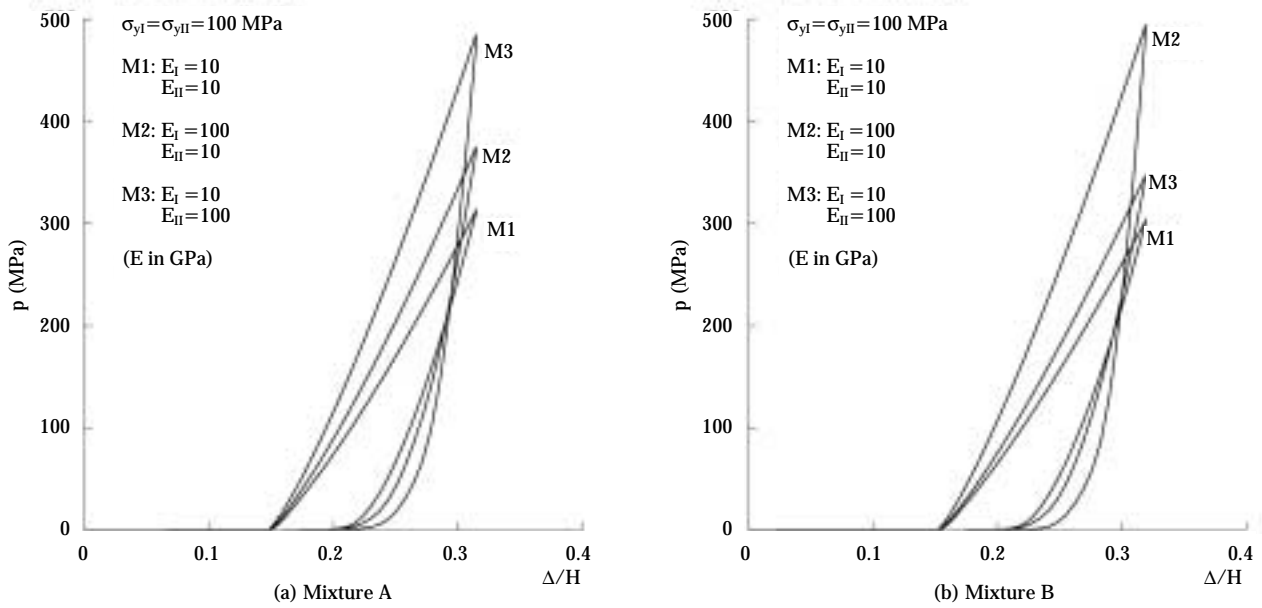


Fig. 6 The global pressure-deformation responses of both mixtures at a various of combinations of Young's moduli.

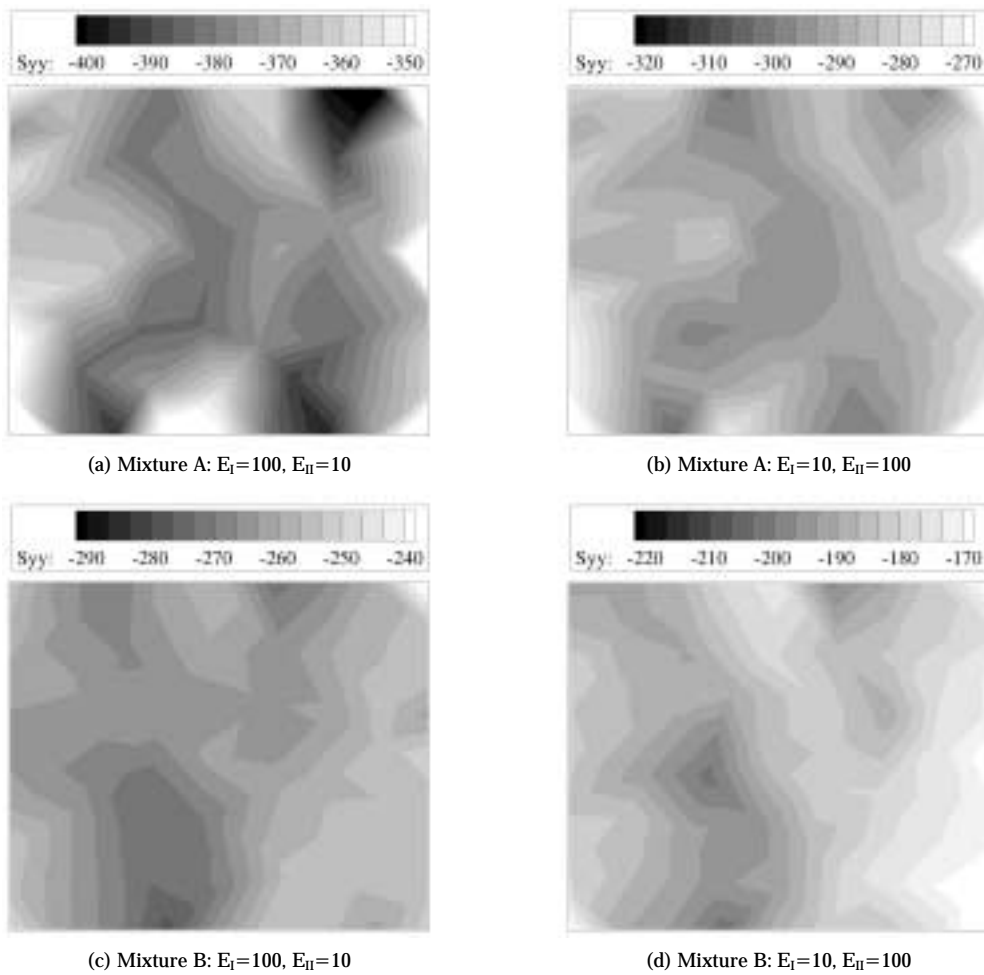


Fig. 7 The local stress contours of both mixtures at uniform yield stress but various combinations of Young's moduli.

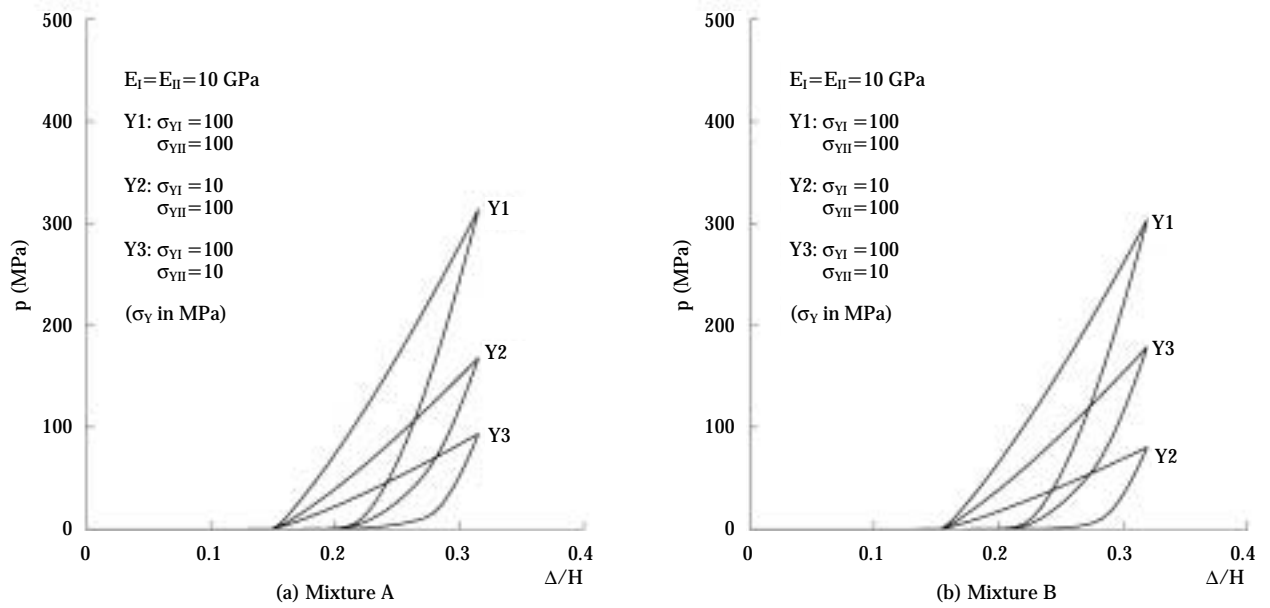


Fig. 8 The global pressure-deformation responses of both mixtures at a various of combinations of yield stresses.

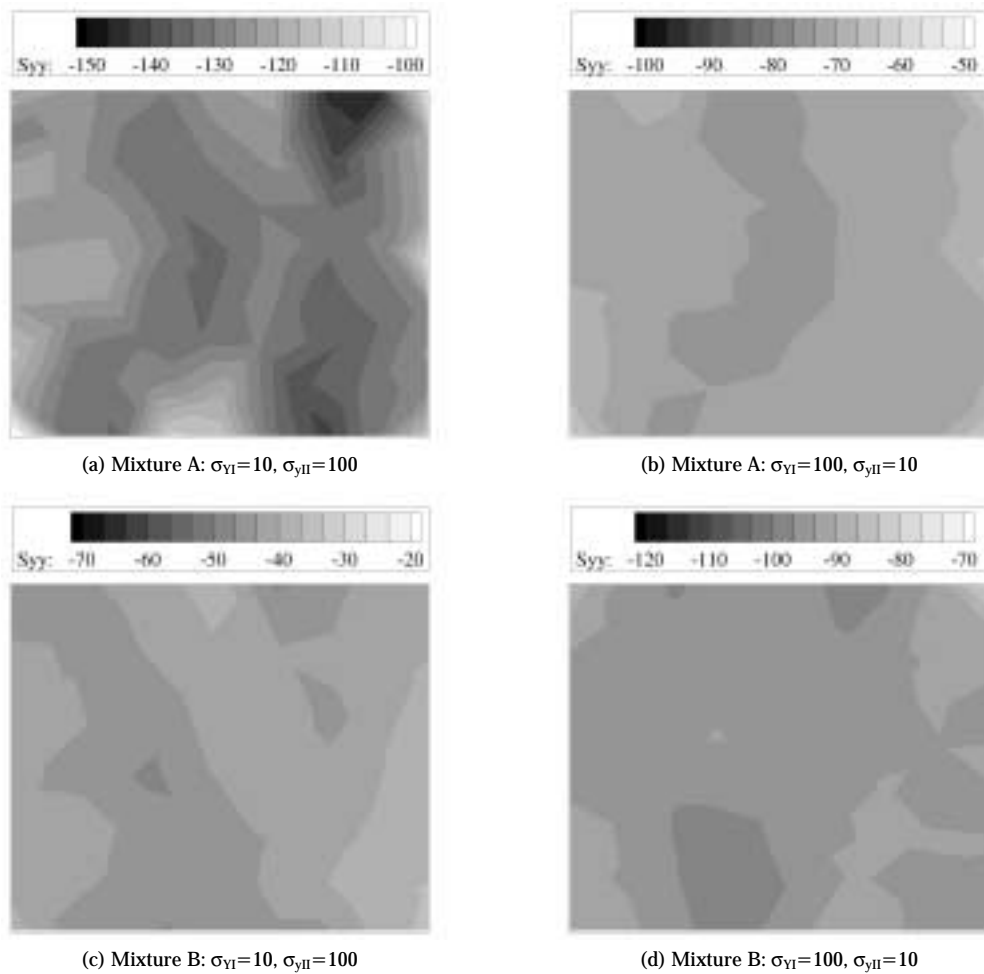


Fig. 9 The local stress contours of both mixtures at uniform Young's modulus but various combinations of yield stresses.

$= [0.1, 1, 10]$, where σ_{yI} and σ_{yII} are yield stress for each group. Changes in $\eta_{\sigma y}$ introduces not only quantitative effects but also qualitative ones, as observed in **Fig. 8**, where there is no crossing between the load and unload path on graphs of the load-displacement curves. The local stress distribution is also shown in **Fig. 9** for both mixtures and for $\eta_{\sigma y}=0.1$ and 10. Compared with **Fig. 5**, it may be found that decrease of yield stress in either of the particle groups will lead to more uniform of stress distribution.

5. Conclusions

The present mixed discrete-continuum approach provides a methodology to effectively link different length and time scales for nonlinear heterogeneous particle systems. This technique resolves the kinetics at interparticle level while constraining the kinematics by a grid with supraparticle resolution. This formulation is utilized to study the consolidation behavior of a series of *samples* after the pre-consolidation by means of particle rearrangement. The process of rearrangement, which consolidates the highly open structures resulting from simulation of die filling of cohesive powders, is simulated using a modified DEM approach. Model systems are studied to quantify the role of the size distribution as well as the elastic and plastic properties. In these studies, different composition of binary mixtures of two particle sets are consolidated to relatively high pressures. Each particle set is endowed with a particle size distribution (characterized by the mean and variance) and the particle's elastic module (E), yield stress (σ_y) and hardening exponent (m). The results clearly indicate the significant effect of each of these characteristics not only on the overall behavior of powder bed but also on the development of local stress states. It is interesting to notice that the post-rearrangement pre-consolidation structures are significantly affected by the disparity on the size distribution between the 2 particle sets. These structures prevail during the subsequent consolidation giving rise to dissimilar local states even when the overall applied force against punch displacement remains mostly unchanged. This observation shows some noteworthy features of the current methodology: 1) the ability to follow the history of the material before consolidation, which is indicated by the heterogeneity of the local fields and 2) the ability of computing consistent averages of these local states, which is indicated by the similar

force-displacement response. Finally, due to the introduction of non-elastic effects the different paths during loading and unloading can be readily traced in accordance with the experimental observations.

References

- [1] Huffine C.L., "A Study of the bonding and cohesion achieved in the compaction of particulate materials," Ph.D. Dissertation, Columbia University (NY) (1954).
- [2] N.A. Fleck, L.T. Kuhn and R.M. McMeeking, "Yielding of metal powder bonded by isolated contacts," *J. Mech. Phys. Solids*, **40** 1139-62 (1992).
- [3] B. Storakers, N.A. Fleck and R.M. McMeeking, "The viscoplastic compaction of composite powders," *J. Mech. Phys. Solids*, **47** 785-815 (1999).
- [4] R.L. Williamson, "Parametric studies of dynamic powder consolidation using a particle-level numerical model," *J. Appl. Phys.*, **68** 1287-96 (1990).
- [5] P.A. Cundall and O.D.L. Stack, "A discrete numerical model for granular assemblies," *Grotechnique*, **29** 47-65 (1979).
- [6] Chu-Wan Hong, "New concept for simulating particle packing in colloidal forming processes," *J. Am. Ceram. Soc.*, **80** 2517-24 (1997).
- [7] Y.F. Cheng, S.J. Guo and H.Y. Lai, "Dynamic simulation of random packing of spherical particles," *Powder Technol.* **107** 123-30 (2000).
- [8] A.M. Cuitiño, S.F. Zheng and G. Gioia, "A Quasi-continuum approach for particle systems," *to be submitted for publication*.
- [9] G. Gioia, A.M. Cuitiño, S. Zheng, and T. Uribe "Two-phase densification of cohesive granular aggregates," *Phys. Rev. Lett.* **88** 204302 (2002).
- [10] M. Naito, K. Nakahira, T. Hotta, A. Ito, T. Yokoyama and H. Kamiya, "Microscopic analysis on the consolidation process of granule beds," *Powder Technol.*, **95** 214-19 (2000).
- [11] J.L. Finney, "Fine structure in randomly packed, dense clusters of hard spheres," *Mater. Sci. Eng.*, **23** 199-205 (1976).
- [12] G.T. Nolan and P.E. Kavanagh, "Computer simulation of random packing of hard spheres," *Powder Technol.*, **72** 149-55 (1992).
- [13] G.T. Nolan and P.E. Kavanagh, "Computer simulation of random packings of spheres with log-normal distributions," *Powder Technol.*, **76** 309-16 (1993).
- [14] Yasuhiro Konakawa and Kozo Ishizaki, "The particle size distribution for the highest relative density in a compacted body," *Powder Technol.*, **63** 241-6 (1990).
- [15] S.Dj. Mesarovic, N.A. Fleck, "Frictionless indentation of dissimilar elastic-plastic spheres," *Int. J. Solids Struct.*, **37** 7071-91 (2000).
- [16] A.B. Yu and N. Standish, "Analytical-parametric theory of the random packing of Particles," *Powder Technol.*, **55** 171-86 (1988).

Author's short biography



Shanfu Zheng

Shanfu Zheng is a research associate at Rutgers, the State University of New Jersey. He received his Ph.D. degree in Mechanical & Aerospace Engineering at Rutgers University in 2000. He can be reached by email at szheng@jove.rutgers.edu



Alberto M. Cuitiño

Alberto M. Cuitiño is an associate professor in the Department of Mechanical and Aerospace Engineering at Rutgers University since 1993. Cuitiño received a Civil Engineering Diploma from the University of Buenos Aires, Argentina, in 1986, and a MS degree in Applied Mathematics and a Ph.D. degree in Solid Mechanics from Brown University in 1992 and 1994 respectively. His research interests include multi-scale modeling, dislocation mechanics, fracture in metal single crystals, granular materials, mechanical behavior of solid foams and folding patterns in thin films. Cuitiño is subject editor for Applied Mechanics of the Latin American Applied Research. He can be reached by email at cuitino@jove.rutgers.edu

Physical Properties of Supercritically-Processed and Micronised Powders for Respiratory Drug Delivery[†]

**Boris Y. Shekunov^{1,2}, Jane C. Feeley²,
Albert H. L. Chow³, Henry H. Y. Tong³
and Peter York^{1,2}**

¹ School of Pharmacy, University of Bradford

² Bradford Particle Design Ltd

³ School of Pharmacy, The Chinese University of Hong Kong

Abstract

Comparative analysis between salmeterol xinafoate (SX) powders was carried out to define quantitatively the solid-state and surface particle properties relevant to formulation of these materials into dry powder respiratory drug delivery systems. SX powders were prepared in supercritical CO₂ using a single-step crystallization process (Solution Enhanced Dispersion by Supercritical fluids, SEDSTM), the volume mean diameter and deagglomeration behaviour of pure drug compound were optimised for respiratory applications. This compound together with reference samples of starting granulated material and micronised powder were used in analytical studies which involved assessment of polymorphic purity and crystallinity (domain size and strain) using high-resolution X-ray powder diffraction, determination of powder surface energetics using inverse gas chromatography (IGC), electrostatic charge and adhesion measurements. The supercritically-processed powders showed low surface energy, low strain, higher crystallinity and higher polymorphic purity than both granulated and micronised powders and resulted in reduced agglomeration, electrostatic charge and adhesion of this powder.

1. Introduction

The traditional method for producing active drug particles within the respirable range involves solvent based crystallisation followed by filtering, drying and high energy micronisation. This processing sequence only provides limited opportunity for control over particle characteristics such as size, shape and morphology and introduces uncontrolled structural variations (decreased crystallinity, polymorphism) and surface modifications (increased surface free energy, adhesion, cohesiveness and charge). These uncontrolled variations have an adverse effect on dry-powder formulation and may even render the formulation ineffective. Salmeterol xinafoate (SX), selected as a model drug compound in this work, exhibits similar prob-

lems. SX is a long-acting β_2 adrenoreceptor agonist, widely used in the management of moderate and severe chronic asthma. This compound has been formulated for both metered-dose suspension (MDI) and dry powder inhalers (DPI). It is reported that SX materials are generated by a conventional crystallization process using dissolution in 2-propanol at elevated temperatures and natural cooling to induce supersaturation [1]. These products were highly cohesive and showed very poor powder flow properties making it unsuitable for fluid energy milling. A more advanced crystallization process therefore was developed in which a hot SX solution in 2-propanol is added to a chilled quench solvent inducing large (in the range between 100-250 μm) spherical aggregates. These granular SX powders have improved flow and handling properties and are used for micronisation [1].

Supercritical fluid (SCF) technology offers a more benign and commercially viable process capable of direct production of respirable drug particles. The advantages of this technology are related to the abil-

¹ Bradford BD7 1DP, United Kingdom

² 69 Listerhills Science Park, Campus Road, Bradford BD7 1HR, United Kingdom

³ Shatin, N.T., Hong Kong SAR, China

[†] Accepted: September 20, 2002

ity of supercritical solvents, the most important of which is supercritical carbon dioxide (scCO₂), to be efficiently separated, by decompression, from both organic co-solvents and solid powders, facilitating one-step, clean and recyclable process engineering. Particle formation using SCF is a crystallisation process [2], with sufficient flexibility to produce single crystal, uniform particles with low surface energy. The benefits of SCF-processed particles in both DPI and MDI formulations have been demonstrated. For example, particles of several steroid drugs were produced by direct spraying of drug solutions into the medium of scCO₂ [3] and an increase of fine particle fraction (*FPF*) for steroid formulations prepared with lecithin for an MDI was observed [3,4]. Protein powders were also prepared and tested using this method for DPI applications [5]. The SEDS™ method (Solution Enhanced Dispersion By Supercritical Fluids) [6] has an added advantage of very fast, homogeneous nozzle mixing between supercritical antisolvent and drug solution leading to consistent production of micron sized particulate products [7]. By changing the working conditions of pressure, temperature, solution concentration and flow rates, it is possible to control the size, shape, morphology and crystal form of the micron sized particles [2,7-9]. In studies with DPI formulations of salbutamol sulphate, increased *FPF* and targeted *in vitro* delivery have been demonstrated for SEDS-prepared powders when compared with micronised material [10,11]. For salmeterol xinafoate, aerosols of both polymorphs have been produced [12,13] and a detailed thermal analysis has shown a high degree of chemical and crystallographic purity of these compounds [13]. The present work represents a comparative study of the micronised and supercritically-processed powders with the aim to distinguish the solid-state properties important for successful formulation of dry-powder aerosols.

2. Materials and methods

2.1 Chemicals and reagents

Salmeterol xinafoate (SX) in the form of granulated material (G-SX) used for micronisation and micronised powder (M-SX) were generously supplied by GlaxoWellcome, Ware, UK. HPLC grade solvent for SEDS were purchased from BDH Chemicals, Leicester, UK. All analytical grade liquid probes used in IGC studies were purchased from Labscan, Dublin, Ireland. Industrial grade (>99.95% pure) CO₂ was supplied by Air Products (Manchester, UK).

2.2 Production of SX powders

The SEDS™ method was employed to prepare powders of SX, form I (S-SX). This technique (**Fig. 1**) is based on mixing between supercritical CO₂ antisolvent and a drug solution using a twin-fluid nozzle. Methanol, acetone and tetrahydrofuran were tested in this work, after which methanol was selected for further studies because of high yield (>95%) and suitable particle size distribution (PSD) ($x_{90} \cong 10 \mu\text{m}$) of the SX products. The particle formation vessel (500 ml volume) with the nozzle was placed in an air-heated oven. The temperature in the vessel was monitored by a thermocouple with accuracy $\pm 0.1^\circ\text{C}$ and was kept constant at 40°C. Pressure in the vessel was controlled by an air-actuated back-pressure regulator (26-1761 with ER3000 electronic controller, Tescom, Elk River, MN, USA) and kept constant at 250 ± 1 bar. The difference in the inlet and outlet pressure was typically within 1% of its absolute value. The CO₂ flow rate, supplied by a water-cooled diaphragm pump Milton Roy B (Dosapro Milton Roy, Pont-Saint-Pierre, France) was typically between 25 and 50 NL/min as monitored after expansion using a gas flow meter (SHO-Meter 1355, Brooks Instruments B.V., Veenendal, Holland) and also controlled before expansion using high-pressure liquid flow meter (DK34, Krohme Messtechnik GmbH, Duisburg, Germany). Solution concentration of SX varied between 1 and 10% w/v. Solution flow rate was provided by a metering pump PU-980 (Jasco Co, Tokyo, Japan) and varied from 0.5 to 10 ml/min.

Prior to crystallization experiments, an on-line dynamic solubility method [14] was used to determine the equilibrium solubility profile of SX in methanol/

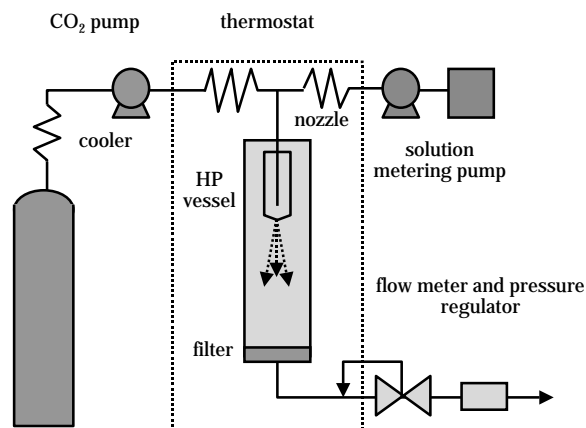


Fig. 1 Experimental system for particle formation using supercritical CO₂ as an antisolvent.

CO₂ mixtures at different mole fractions of methanol. On this basis, the solution flow rate and the solution concentration were optimised to achieve maximum supersaturation and maximum yield according to a developed method [15]. Several batches were prepared with batch quantities between 1 and 10 g. The obtained cumulative PSD for all batches had $x_{90} \cong 10$ μm and volume-moment mean particle diameter, $d_{4,3} \cong 5$ μm , as determined using the laser diffraction (LD) method. Further improvement in nozzle geometry (the diameter, length and volume of the mixing zone) allowed the mean particle diameter to decrease down to $d_{4,3} \cong 3.5$ μm with cumulative $x_{99} \cong 10$ μm .

2.3 High resolution X-ray powder diffraction

This technique was used to determine the characteristic diffraction peaks of SX forms I and II and to distinguish crystallographic changes (peak shift and peak broadening) of G-SX, M-SX and S-SX compounds. The experiments were carried out at the Synchrotron Radiation Source (SRS) Daresbury Laboratory, station 2.3 (Warrington, UK). The X-ray wavelength was $\lambda = 1.4016$ \AA . The diffractometer had a flat-plate/parallel foils Hart-Parrish geometry and was calibrated using the diffraction peaks of crystalline silicon with accuracy 10^{-4} degrees. The instrumental broadening (shape of diffraction peaks related to the instrument geometry) was obtained using lanthanum hexaboride standard (NIST, Denver, USA). All samples were placed in rotating plate holders and scanned between $2\theta = 1 - 40^\circ$ with resolution 0.01° (0.005° for the standard) and typical signal integration time 1 s.

The diffraction data of SX were corrected for the beam decay and indexed using program CHEKCELL [16] in order to find the crystal cell parameters. The exact position of a minimum of five characteristic diffraction peaks, 2θ , the Full Width at Half Maximum, *FWHM*, and the mixing parameter, η , of pseudo-Voigt function were determined using peak fitting option of program ORIGIN. The instrument broadening was assessed using program SHADOW [16]. The obtained parameters were then input into program BREATH [16] to analyse the physical diffraction line broadening caused by distribution of domain size and strain in particles [17]. Alternatively, the diffraction data were examined using program POWDER CELL [16] applying the whole profile Le Bail fitting option of this software. In this case, the instrument broadening *FWHM* was assumed to be 0.025° which is typical for an SRS diffractometer [18]. This procedure was less accurate than that using calibration line broad-

ening and therefore only relative trends on the size/strain were interpreted from these results.

2.4 Time-resolved small-angle X-ray powder diffraction

Dynamic analysis of polymorphic transition of SX was carried out at the SRS Daresbury Laboratory using temperature-controlled small-angle X-ray scattering (SAXS) arrangement at station 8.2. The experimental method [19] involved time-resolved detection of the SX polymorphic transition with characteristic peaks at diffraction angles $2\theta < 5^\circ$. Measurements were carried out at wavelength $\lambda = 1.54$ \AA . The quadrant SAXS detector was placed at a distance 1 m from the sample. Samples were placed in a modified aluminium DSC pan. The pan top and bottom were removed with a punch and replaced with thin mica discs. Sealed pans were placed in a spring-loaded holder in a modified Linkam TMH600 (Linkam Scientific Instruments, Tadworth, UK) hot stage mounted on the optical bench in the center of X-ray beam. Heating rates between $5^\circ\text{C}/\text{min}$ and $40^\circ\text{C}/\text{min}$ were used. Prior to X-ray measurements, the Linkam temperature range was calibrated using potassium nitrate (melting onset 128°C), indium (154°C) and tin (230°C). The diffraction pattern of silver behenate was used to calibrate the SAXS detector. Incident and transmitted beam intensity monitored by ionization detectors were used to correct for X-ray beam decay, detector sensitivity and background scattering. The signal integration time was 6 s.

2.5 Inverse gas chromatography (IGC)

IGC was performed on a Hewlett Packard Series II 5890 Gas Chromatograph (Hewlett Packard, Wilmington, DE, USA) equipped with an integrator and flame ionization detector. Injector and detector temperatures were maintained at 100 and 150°C respectively. Glass columns (60 cm long and 3.5 mm i.d.) were deactivated with 5% solution of dimethyldichlorosilane in toluene before being packed with SX powder. The columns were plugged with silanised glass wool at both ends and maintained at 40°C . Data were obtained for a known weight and surface area of the sample using a nitrogen gas (purity $> 99.995\%$) flow at 20.0 ml/min. The column was weighed before and after the experiment to ensure no loss of materials during the run. A trace amount of vapour from non-polar and polar probes was injected. The retention times and volumes of the injected probes were measured at infinite dilution and thus were independent of the quantity of probes injected. The non-polar

probes employed were pentane, hexane, heptane, octane and nonane; the polar probes were dichloromethane, chloroform, acetone, ethyl acetate, tetrahydrofuran and diethyl ether. Triplicate measurements in separate columns were made for G-SX, M-SX and S-SX powders. Differences in surface energetics were reflected in the calculated dispersive component of the surface free energy, γ_s^D ; specific component of surface free energies of adsorption, $-\Delta G_A^{sp}$; and the acid-base parameters, K_A and K_B . A more detailed theory of these measurements is discussed elsewhere [13,20-22].

Data on specific surface areas required for IGC studies were determined by BET nitrogen adsorption using a Surface Area Analyzer Coulter SA 3100 (Coulter Corp., Miami, FL, USA). Samples were placed in glass sample holders and out-gassed with helium (purity > 99.999%) at 40°C for 16 hours before analysis. Nitrogen (purity > 99.999%) was used as adsorbate and BET surface area was recorded as specific surface area of the samples. All measurements were performed in triplicate using the same batch of each material.

2.6 Electric charge and adhesion measurements

Triboelectrification was undertaken against a stainless steel contact surface using either a turbula mixer or a cyclone separator. Triboelectrification in a turbula mixer (Glen Creston, UK) was carried out by agitating a powder sample for 5 minutes at 30 rpm in a 100 ml stainless steel vessel at ambient temperature and relative humidity. A sample was poured in a reproducible manner into a Faraday well connected to an electrometer (Keithley 610, Keithley Instruments, Reading, UK). Charge and mass of sample was then recorded to give specific charge before and after triboelectrification. % w/w adhesion to the inner surface of the mixing vessel was calculated from the original mass of sample and the mass of sample poured into the Faraday well. During triboelectrification in a cyclone separator, a powder was fed from a steel vibratory table into a venturi funnel. Compressed air (velocity 8 m/s, relative humidity below 10%, ambient temperature) was used to convey the powder from the venturi along a horizontal pipe into the cyclone separator. The Faraday well and force compensation load cell was fitted at the base of the cyclone and used to collect charged particles. Final specific charge was recorded for non-adhered powder residing in the Faraday well and, where possible, powder adhering to the cyclone wall was dislodged by a stream of air and its charge and mass recorded. In

both cases, the results were obtained from triplicate measurements.

2.7 Particle size analysis

The instrument consisted of a laser diffraction sensor HELOS and dry-powder air-dispersion system RODOS (Sympatec GmbH, Germany) with WINDOX OS computer interface. The dispersion process was controlled by means of adjusting pressure of the compressed air flow between 0.5 and 5 bar. The pressure of 2 bar was found to be sufficient to disperse most of the agglomerates avoiding, at the same time, attrition of the primary particles. All measurements were performed in triplicate. The particle shape factor, f , was calculated as $f = S_v / S_v^*$ where S_v is the experimental specific surface area and S_v^* is the specific surface area determined using the LD instrument assuming the particle sphericity.

3. Results and discussion

3.1 Crystallinity

Analysis of diffraction patterns (**Fig. 2**) showed that peak-fitting, background determination and indexing were performed more consistently and with higher accuracy using the S-SX sample than with the M-SX and G-SX samples. This fact is related to the smaller diffraction line-broadening and higher signal-to-noise ratio for the S-SX sample (see **Fig. 2**). The strongest characteristic peaks of SX were identified as (001), (1 $\bar{1}$ 3) and ($\bar{1}$ 34). The crystal cell calculated from this diffraction pattern is of triclinic P-1 (or P1) form with parameters: $a=9.487$; $b=16.242$; $c=21.372$ Å; $\alpha=93.16$; $\beta=97.73$; $\gamma=90.94^\circ$, calculated cell volume $V=3257.3$ Å³ and theoretical crystal density $\rho=1.256$ g/cm³.

Physical broadening of diffraction peaks is a cumulative measure of crystal lattice imperfections. This is grouped into size effects (grains, small-angle boundaries, stacking faults) or as strain defects (point defects and dislocations). The basis for discrimination between these effects lies in the fundamental principle that the size term does not depend on the diffraction angle whereas the strain does [17]. Comparison of the diffraction peaks (**Fig. 2**) indicates that the peak broadening is much smaller for S-SX sample than for both G-SX and M-SX samples. Quantitatively, these differences can be expressed through the shift in the peak position, 2θ , the peak width, $FWHM$, and the integral breadth, β^* (all expressed in the degree units). The latter parameter is defined as the width of rectangle having the same area, A , and height, I , as

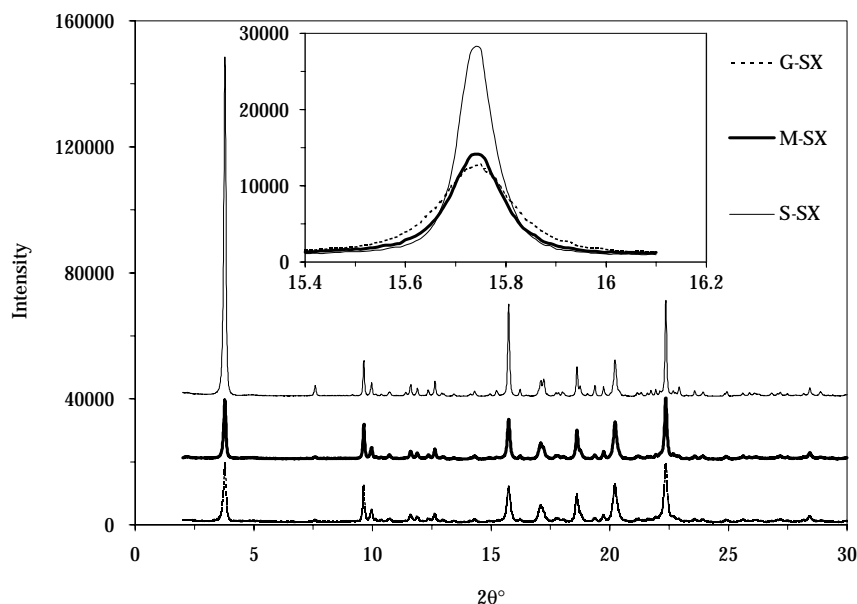


Fig. 2 X-ray diffraction patterns of salmeterol xinafoate samples: granulated (G-SX), micronised (M-SX) and SEDS-produced (S-SX) obtained at the wavelength 1.4 Å. The inserted diagram allows a comparison between characteristic (113) diffraction peaks for these samples.

the observed line profile:

$$\beta^* = A/I \quad (1)$$

Table I shows these parameters for two characteristic diffraction peaks. S-SX sample shows higher crystallinity (smaller *FWHM* and β^*) than the other two compounds. In addition, there is a small but significant shift of the diffraction peaks produced by M-SX and G-SX compounds towards smaller 2θ , relative to the same peaks of S-SX compound. Such shift is between 0.001-0.003° for different lines which corresponds to a relative increase of *d*-spacing, $\Delta d/d$ between $\cong 1$ and 2% and to correspondent increase of crystal volume, $\Delta V/V$ between $\cong 1$ to 2% for both M-SX and G-SX samples.

More fundamental analysis of line broadening con-

sists of the “double-Voigt” method [17] which approximates the physically broadened line profile as a convolution of Cauchy (C) and Gauss (G) integral breaths, containing size (S) and strain (distortion, D) contributions according to the equations:

$$\beta_C = \beta_{CS} + \beta_{CD} s^2 / s_0^2 \quad (2)$$

$$\beta_G^2 = \beta_{GS}^2 + \beta_{GD}^2 s^2 / s_0^2 \quad (3)$$

The integral breaths, β , are given in the units (\AA^{-1}) of the wave-vector, s :

$$s = 2\sin\theta/\lambda \quad (4)$$

$$\beta = \beta^* \cos\theta/\lambda \quad (5)$$

Here, β_{CD}/s_0^2 and β_{GD}/s_0^2 are constant for the whole pattern (taken at zero-value of the wave-vector, s_0 , of the first peak). The integral breaths found from the

Table I The position (2θ), width (*FWHM*) and integral breadth (β^*) of characteristic diffraction peaks of the salmeterol xinafoate samples.

		S-SX	M-SX	G-SX
(113)	2θ	15.7420±0.0003	15.7396±0.0003	15.7395±0.0003
	<i>FWHM</i>	0.084±0.001	0.122±0.001	0.171±0.001
	β^*	0.093±0.001	0.132±0.001	0.178±0.001
(134)	2θ	22.3613±0.0005	22.3595±0.0005	22.3605±0.0005
	<i>FWHM</i>	0.080±0.002	0.110±0.002	0.141±0.002
	β^*	0.088±0.002	0.119±0.002	0.150±0.002

experimental diffraction profiles allow calculation of the surface-weighted, D_S , and volume-weighted, D_V , domain size and a mean-square (Gaussian) strain, ε , which is the total strain averaged over infinite distance:

$$D_S = 1 / (2\beta_{CS}) \quad (6)$$

$$D_V = (EF) \exp(\beta_{CS}^2 / \beta_{GS}^2) / \beta_{GS}^2 \quad (7)$$

$$\varepsilon = \beta_{GD} / (s_0 \sqrt{2\pi}) \quad (8)$$

Here EF denotes a complementary error function related to the background determination [17].

The results of computation using eqs. [2-8] are given in **Table II**. Clearly, S-SX compound consists of larger crystalline domains (by about 20%) and smaller strain (by about 60%) than both M-SX and G-SX compounds. The granulated batch under investigation, G-SX, was shown to be the least crystalline material. **Table II** also presents the data obtained using the alternative computation method with Le Bail diffraction profile fitting. Both methods gave consistent results in terms of domain size and strain.

It should be emphasized that S-SX shows higher crystallinity compared to both M-SX and G-SX compounds. In the first instance, this fact seems to be contradictory. It is widely believed that micronisation procedure is the major factor responsible for the crystallinity decrease, and in general, for transition into a higher free energy solid state. The analytical results obtained in this work indicate that "aggressive" crystallisation procedures [1] may also lead to crystal disordering which is comparable to or greater than those defects induced by micronisation. It is unlikely that micronisation can improve the crystallinity. The fact that G-SX sample has a higher crystal strain and spe-

cific surface free energy is likely to indicate that M-SX compound was obtained from a different batch of granular SX than that available for the present study. Low consistency of batch solution crystallisation has been acknowledged in the pharmaceutical industry.

3.2 Polymorphic purity

SX has two polymorphs which are related enantiotropically [1,12,13]. The estimated transition temperature is between 90 and 110°C [13]. Although the X-ray analysis shows that there is no significant presence of form II in form I substances produced using both SEDS and micronisation, the polymorphic purity of these compounds was under question because they showed different melting-recrystallization behaviour according to differential scanning calorimetry (DSC). This problem was addressed in the present work using time-resolved X-ray diffraction combined with a thermal analysis.

The strongest characteristic diffraction peaks (001) of both SX polymorphs are located at low angles $2\theta = 4.13^\circ$ (form I) and $2\theta = 2.87^\circ$ (form II) at $\lambda = 1.54 \text{ \AA}$. These high intensity peaks enable presence of form II to be detected above $\cong 0.5\%$ w/w in samples prepared by mixing the two polymorphs. **Fig. 2** shows that, within this sensitivity, the S-SX, M-SX and G-SX are the form I compounds. However, the dynamic X-ray studies of melting behaviour (**Fig. 3**) indicated that at relatively fast heating rates equal or above $10^\circ/\text{min}$, a single diffraction profile of form I, without recrystallization into form II was obtained for S-SX samples. At the same heating rate, M-SX samples showed melting of form I and immediate recrystallization into form II. The characteristic (001) peak of form II appeared

Table II The integral breadths of Voigt-approximated diffraction profile, β , and calculated values of the surface-weighted, D_S , and volume-weighted, D_V , domain size and the Gaussian strain, ε . The corresponding size and strain parameters, D_V^* and ε^* , were calculated on the basis of the diffraction profile Le Bail fitting and the instrument broadening $FWHM = 0.025^\circ$.

	S-SX	M-SX	G-SX
$\beta_{CS}, \text{ \AA}^{-1}$	0.11×10^{-2}	0.13×10^{-2}	0.15×10^{-2}
$\beta_{CD}, \text{ \AA}^{-1}$	0.30×10^{-5}	0.13×10^{-4}	0.21×10^{-4}
$\beta_{GS}, \text{ \AA}^{-1}$	0.39×10^{-3}	0.40×10^{-3}	0.38×10^{-3}
$\beta_{GD}, \text{ \AA}^{-1}$	0.63×10^{-4}	0.97×10^{-4}	0.12×10^{-3}
$D_S, \text{ \AA}$	453 ± 44	382 ± 60	326 ± 50
$D_V, \text{ \AA}$	785 ± 60	682 ± 86	606 ± 74
ε	$(0.53 \pm 0.02) \times 10^{-3}$	$(0.83 \pm 0.03) \times 10^{-3}$	$(0.101 \pm 0.006) \times 10^{-2}$
$D_V^*, \text{ \AA}$	1320	670	640
ε^*	0.70×10^{-3}	0.17×10^{-2}	0.22×10^{-2}

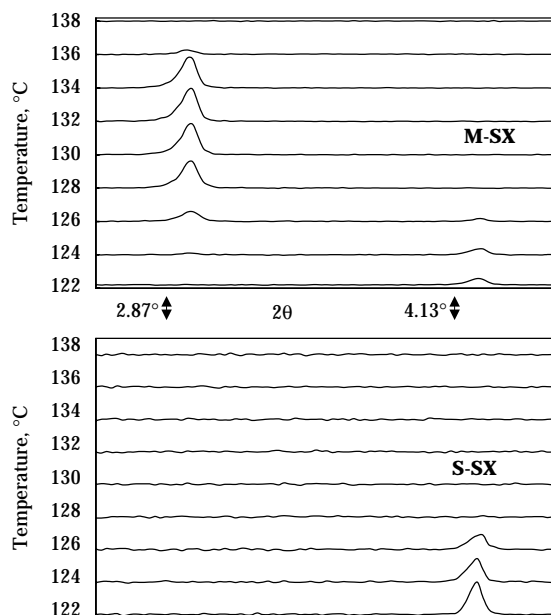


Fig. 3 Kinetics of melting and recrystallization of M-SX and S-SX compounds as shown by time-resolved small-angle X-ray diffraction. Heating rate is $10^\circ/\text{min}$. The characteristic diffraction peaks correspond to the (001) reflections with d -spacing: $d_{001}=21.348 \text{ \AA}$ (form I) and $d_{001}=30.708 \text{ \AA}$ (form II).

simultaneously with the corresponding (001) peak of form I and coincided with the exothermic DSC peak at this temperature. When the heating rates were decreased below $10^\circ/\text{min}$, both S-SX and M-SX materials showed recrystallization into form II at about 130°C . These data indicate that S-SX compound has a higher activation energy barrier to recrystallization into form II than M-SX compound. Assuming that S-SX consists of pure polymorph I, the characteristic time required for formation of polymorph II nuclei in the melt is estimated to be $\Delta T/10^\circ\text{C} \cong 90 \text{ s}$ where $\Delta T(^\circ\text{C})$ is the difference of melting temperatures of the polymorphs I and II. In the case of M-SX, this time is significantly smaller, possibly indicating a presence of seeds of the high-melting polymorph II in the micronised sample.

The crystallinity and polymorphic purity are directly related to the physical stability of SX powders. The present study demonstrates that while the M-SX material possesses the crystal structure of form I, it is more prone to polymorphic conversion than the S-SX compound, as evidenced by time-resolved diffraction analysis. It is likely that the micronization and solution crystallisation processes employed for production of these particles created nuclei of form II which accelerate the polymorphic transition at high temper-

ature. It is also possible that supercritical fluid processing removes some impurities (soluble in the supercritical phase) from the starting salmeterol compound also lowering the activation energy of nuclei formation.

3.3 Surface free energy and specific surface area

The fundamental quantity of inverse gas chromatography is the net retention volume, V_N , determined from the retention time of a given solvent [20]. Adsorption of the probe molecules on solid surfaces can be considered in terms of both dispersive and specific components of surface free energy, corresponding to non-polar and polar properties of the surface. By virtue of their chemical nature, non-polar probes of the alkane series only have dispersive component of surface free energy, which can be determined from the slope of the plot based on the following equation:

$$RT \ln V_N = 2a N_A (\gamma_S^D)^{1/2} (\gamma_L^D)^{1/2} + \text{const} \quad (9)$$

where R is the gas constant, T is the absolute temperature of the column, a is the probe's surface area, N_A is the Avogadro's number, γ_S^D is the dispersive component of surface free energy of a SX powder and γ_L^D is the dispersive component of surface free energy of the solvent probes.

Polar probes have both dispersive and specific components of surface free energy of adsorption. The specific component of surface free energy of adsorption (ΔG_A^{SP}) can be estimated from the vertical distance between the alkane reference line and the polar probes of interest. This free energy term can be related to the donor number (DN) and acceptor number (AN^*) of the polar solvent by the following equation:

$$\Delta G_A^{SP} = K_A DN + K_D AN^* \quad (10)$$

DN describes the basicity or electron donor ability of a probe whilst AN^* defines the acidity or electron acceptor ability. Here AN^* denotes a correction for the contribution of the dispersive component and the entropy contribution into the surface energy is assumed negligible [22]. Thus plotting $-\Delta G_A^{SP}/AN^*$ versus DN/AN^* yields a straight line where K_A and K_D correspond to the slope and intercept respectively. The IGC data for the various SX samples analysed by the above approach are summarized in **Tables III** and **IV**. Comparison between different materials shows that the magnitude of γ_S^D is 15% smaller for S-SX compounds than for both M-SX and G-SX com-

Table III The dispersive component of the surface free energy, γ_s^D , the acidic, K_A , and basic, K_D , surface parameters, surface area, S_V and calculated particle shape factor, f

	S-SX	M-SX	G-SX
$\gamma_s^D \pm$ (s.d.), mJ/m ²	32.476 (0.254)	38.285 (0.907)	36.972 (0.520)
K_A (s.d.)	0.110 (0.013)	0.172 (0.001)	0.233 (0.003)
K_D (s.d.)	0.356 (0.120)	0.298 (0.021)	0.157 (0.018)
$S_V \pm$ (s.d.), m ² /g	7.040 (0.029)	9.243 (0.002)	10.699 (0.016)
f	3.78	2.80	–

pounds. In addition, ΔG_A^{SP} for all polar probes used reduced by at least half for S-SX compound compared to the other two materials. Comparison between M-SX and G-SX materials indicates that, although the γ_s^D are almost equal within the experimental error, ΔG_A^{SP} for all the polar probes is larger for the granulated material.

The reduced magnitude of γ_s^D for S-SX compound implies that the surfaces of these particles are less energetic for non-polar, dispersive surface interactions than the other two compounds. The overall strength of the polar interactions (ΔG_A^{SP}) is also the smallest for S-SX compound. Comparison between the K_A and K_D values of the three samples indicate that the acidity constant has the following trend: $K_A(\text{S-SX}) < K_A(\text{M-SX}) < K_A(\text{G-SX})$. The basicity constants follows the reverse order with $K_D(\text{S-SX})$ being the largest. Thus S-SX sample which has the weakest acidic property exhibits the strongest basic interactions with respect to its exposed polar groups at the interface. This suggests that S-SX crystal surfaces have, in relative terms, more exposed basic groups but fewer exposed acidic groups than both G-SX and M-SX compounds. Particles of all three samples have a similar platelet shape with the dominant {001} crystal faces. However, S-SX particles have the largest shape factor, f (see **Table III**), which means that

platelets of G-SX and M-SX are thicker. The other materials have more energetic lateral crystal surfaces as a result of the solution crystallisation procedure (G-SX) and particle breakage on micronisation (M-SX). Therefore the observed differences in K_A and K_D , combined with the smallest value of ΔG_A^{SP} and γ_s^D for S-SX compound, suggest a combination of three different factors affecting the specific surface energy: (a) difference in the crystal habit, *i.e.* the {001} crystal faces have stronger basic and weaker acidic interactions than the lateral crystal faces, (b) smaller overall specific surface energy of the {001} crystal planes as compared to any other crystallographic planes and (c) disturbances of the crystal structure which also contribute to the higher surface energy of G-SX and M-SX compounds.

It is clear that solvent adsorption progresses more rapidly with the M-SX and G-SX samples than with S-SX material. This fact indicates that supercritical fluid process is capable of producing particles with lower surface activity (and greater surface stability) than powders produced by solution crystallisation and micronisation.

3.4 Electrostatic charge and adhesion

Table V presents results on the charge, Q , and fraction of adhered material, AD . S-SX particles exhibited significantly less (between one and two orders of magnitude) accumulated charge than the micronised powder before and after turbula mixing and also for the non-adhered drug in cyclone separator. Correspondingly, the fraction of adhered material is several times smaller for S-SX powder than for M-SX powder in both the turbula mixing and cyclone separator tests.

These results are consistent with the superior powder flow properties of S-SX material. Although the bulk powder density of S-SX material is very low (about 0.1 g/cm³ vs. 0.5 g/cm³ for M-SX) it flows well and does not adhere to the container walls.

Table IV The specific component of surface free energies of adsorption, $-\Delta G_A^{SP}$.

	$-\Delta G_A^{SP}$, kJ/mol					
	Dichloromethane	Chloroform	Acetone	Ethyl acetate	Diethyl ether	Tetrahydrofuran
S-SX	2.808 (0.147)	0.153 (0.080)	3.797 (1.173)	2.705 (0.613)	1.488 (0.390)	2.446 (0.279)
M-SX	–	0.810 (0.053)	4.560 (0.096)	3.995 (0.013)	2.774 (0.041)	3.609 (0.027)
G-SX	–	1.885 (0.047)	5.454 (0.154)	4.739 (0.015)	2.958 (0.038)	4.854 (0.069)

Table V Summary of the mean specific charge, Q , and mean adhesion fraction, AD , of supercritically-processed (S-SX) and micronised (M-SX) powders. The data represent the mean of three determinations with coefficient of variation (% CV).

	Turbula Mixer			Cyclone Separator		
	Q , nCg ⁻¹ (before mixing)	Q , nCg ⁻¹ (after mixing)	AD , % w/w	Q , nCg ⁻¹ (for non-adhered drug)	Q , nCg ⁻¹ (for adhered drug)	AD , % w/w
S-SX	-0.52 (51)	-0.17 (431)	1.5 (1.4)	+4.9 (6.8)	-34.6 (42)	5.5 (1.6)
M-SX	-12.1 (7.3)	-42.6 (53)	27 (58)	-48.4 (17.5)	-49.7 (14.8)	16.7 (9.7)

3.5 Particle size and powder dispersability

The difference in particle size distribution (PSD) of S-SX and M-SX powders is reflected in the magnitude of the mean particle sizes $d_{4,3}$ = 3.5 μm (S-SX) and 1.8 μm (M-SX) as measured using the LD technique. For both materials the cumulative PSD >98% is within respirable particle size range $0.5 < x < 10 \mu\text{m}$. However, a significant difference was observed between the dispersion behaviour of micronised and supercritically-processed powders. At high dispersing pressures above $\cong 2$ bar, $d_{4,3}$ is smaller for M-SX powder, as indicated by the primary PSD for this compound. This situation changes dramatically at dispersing pressures below 2 bar. At low pressures, S-SX powders consistently produce a large fraction of primary particles in the respiratory size range, whereas M-SX powders form stable agglomerates outside the 5 μm range which are not be dispersed at such pressures.

The enhanced dispersability of S-SX powders means a decrease of the inter-particulate contact area and/or reduction of the cohesive forces leading to better performance of S-SX compound in the inhalation devices as shown in our work [23]. Despite a larger geometric (and volume) diameter for S-SX particles, the Andersen cascade impactor measurements indicated a greater than two-fold increase (from 25.15 to 57.80%) of *FPF* for S-SX powder compared with *FPF* of M-SX powder.

4. Conclusion

The physical properties of micronised and supercritically-processed powders for respiratory drug delivery have been quantitatively defined in terms of specific surface energy, polymorphic purity, acquired charge and crystallinity. The enhanced physical properties for S-SX powders correlate well with the enhanced dispersion and flow behaviour of this powder. However, new analytical approaches are required to discriminate between the specific contributions such as aerodynamic forces and powder cohesiveness, nature and statistics of inter-particulate forces,

contact area and average distance between non-spherical particles. These problems will be addressed in our following study.

Acknowledgements

We would like to thank Prof. G. Rowley, Mr. A. Brennan and Dr. P. Carter (the University of Sunderland) for performing the electrostatic tests and Mr. S. Bristow and Ms. D. Huddleston for obtaining the solubility data of salmeterol xinafoate in modified supercritical CO₂. We gratefully acknowledge a continuous support from the SRS Daresbury Laboratory, in particular, Dr. L. Cranswick (CCP-14 computation), Dr. J. G. Grossmann (SAXS studies) and Dr. C. Tang (High Resolution Powder Diffraction). G-SX and M-SX compounds were generously supplied by GlaxoWellcome. This work was also supported by the UK Engineering and Physical Sciences Research Council (EPSRC).

References

- 1) S. Beach, D. Latham, C. Sidgwick, M. Hanna and P. York. Control of the physical form of salmeterol xinafoate. *Organic Process Research & Development*, **3**: 370-376 (1999).
- 2) B. Y. Shekunov, M. Hanna and P. York. Crystallization process in turbulent supercritical flows. *J. Crystal Growth*, **198/199**: 1345-1351 (1999).
- 3) H. Steckel, J. Thies and B. W. Müller. Micronizing of steroids for pulmonary delivery by supercritical carbon dioxide. *Int. J. Pharm.*, **152**: 99-110 (1997).
- 4) H. Steckel and B. W. Müller. Metered-dose inhaler formulation of fluticasone-17-propionate micronized with supercritical carbon dioxide using the alternative propellant HFA-227. *Int. J. Pharm.*, **173**: 25-33 (1998).
- 5) R. T. Bustami and H.-K. Chan and N. R. Foster. Aerosol delivery of protein powders processed by supercritical fluid technology. *Proceedings of the Conference on Respiratory Drug Delivery*, Palm Harbor, Florida, **VII**: 611-613 (2000).
- 6) P. York and M. Hanna. Particle engineering by supercritical fluid technologies for powder inhalation drug delivery. *Proceedings of the Conference on Respiratory*

- Drug Delivery*, Phoenix, Arizona, **V**: 231-239 (1996).
- 7) B. Y. Shekunov, J. Baldyga. and P. York. Particle formation by mixing with supercritical antisolvent at high Reynolds numbers. *Chem. Eng. Sci.* **56**: 1-13 (2001).
 - 8) R. Sloan, M. E. Hollowood, G. O. Humphreys, W. Ashaf and P. York. Supercritical fluid processing: preparation of stable protein particles. *Proceedings of the 5th Meeting on Supercritical Fluids*, Nice, France. **1**: 301-306 (1998).
 - 9) S. Moshashae, M. Bistrat, R. T. Forbes, H. Nyqvist, P. York. Supercritical fluid processing of proteins I: Lysozyme precipitation from organic solution. *Eur. J. Pharm. Sci.*, **11**: 239-245 (2000).
 - 10) P. York. Strategies for particle design using supercritical fluid technologies. *PSTT*, **2**: 430-440 (1999).
 - 11) J. C. Feeley, P. York, B. S. Sumby, H. Dicks and M. Hanna. In vitro assessment of salbutamol sulphate prepared by micronisation and a novel supercritical fluid technique. *Drug Delivery to the Lungs*, **IX**: 196-199 (1998).
 - 12) M. Hanna, P. York and B. Yu. Shekunov. Control of polymorphic forms of a drug substance by SEDS technique. *Proceedings of the 5th Meeting on Supercritical Fluids*, Nice, France. **1**: 325-330 (1998).
 - 13) H. H. Y. Tong, B. Y. Shekunov, P. York, A. H. L. Chow. Characterisation of two polymorphs of salmeterol xinafoate crystallized from supercritical fluids. *Pharm. Res.* **18**: 1-7 (2001).
 - 14) S. C. Bristow, B. Y. Shekunov and P. York. Solubility analysis of drug compounds in supercritical carbon dioxide using static and dynamic extraction systems. *Ind. Eng. Chem. Res.* **40**: 1732-1739 (2001).
 - 15) S. C. Bristow, T. Shekunov, B. Y. Shekunov and P. York. Analysis of the supersaturation and precipitation process with supercritical CO₂. To be published in the *J. Supercritical Fluids* (2001).
 - 16) J. J. Laugier and B. Bochu. "Chekcell"; G. Nolze and W. Kraus. "Powder Cell 2.3", S. A. Howard and R. L. Snyder. "Shadow"; D. Balzar and H. Ledbetter. "Breath". CCP14 Suite for Windows (www.ccp14.ac.uk);
 - 17) D. Balzar and H. Ledbetter. Software for comparative analysis of diffraction line broadening. *Advances in X-ray Analysis*, **39**: 457-464 (1997).
 - 18) J. I. Langford and D. Louër. Powder diffraction. *Rep. Prog. Phys.* **59**: 131-234 (1996).
 - 19) A. D. Edwards, B. Yu. Shekunov, R. T. Forbes, J. G. Grossmann and P. York. Polymorphic transition of carbamazepine studied using simultaneous small- and wide-angle x-ray scattering. In print. *J. Pharm. Sci.* (2001).
 - 20) J. Schultz and L. Lavielle. Interfacial properties of carbon fiber-epoxy matrix composites. In D. R. Lloyd, T. C. Ward, H. P. Schreiber and C. C. Pizana (eds.), *Inverse Gas Chromatography – Characterization of Polymers and Other Materials*, American Chemical Society, Washington, 185-202 (1989).
 - 21) M. D. Ticehurst, R. C. Rowe and P. York. Determination of surface properties of salbutamol sulphate by inverse gas chromatography. *Int. J. Pharm.* **111**: 241-249 (1994).
 - 22) J. C. Feeley, P. York, B. S. Sumby and H. Dicks. Determination of surface properties and flow characteristics of salbutamol sulphate, before and after micronisation. *Int. J. Pharm.* **172**: 89-96 (1998).
 - 23) B. Y. Shekunov, J. C. Feeley, A. H. L. Chow, H. H. Y. Tong, S. E. Walker and P. York. Aerosol performance of salmeterol xinafoate powders prepared by micronisation and by direct supercritical fluid crystallisation. *Proceedings of the AAPS Annual Conference, Denver, AAPS PharmSci.* **3**: 96 (2001).

Particle Shape Modification in Comminution[†]

E. Kaya

*Process Technology Center,
Phelps Dodge Mining Company**

R. Hogg

*Department of Energy and Geo-Environmental
Engineering, The Pennsylvania State University***

S. R. Kumar

*Seisint, Inc****

Abstract

The evolution of particle shape during the course of comminution processes has been investigated. Shape is characterized using a variety of quantitative shape descriptors determined from particle profiles obtained by image analysis. Descriptors related to particle elongation, roundness and angularity are emphasized. Distributions of the descriptors have been determined for a range of particle sizes, for different extents of grinding for various equipment types. For a given descriptor, the distributions of measured values generally follow a consistent pattern (often roughly log normal). Typically, the means and standard deviations show progressive changes as grinding time increases. For the most part, prolonged exposure to the grinding environment leads to rounding of the particles.

Introduction

The importance of particle shape has gained increasing recognition in recent years. It is clear that shape can play a significant role in the use of particles as abrasives and in applications involving packing in powder compacts, slurry rheology, etc. For particles produced by comminution, shape may be determined by material characteristics such as crystal cleavage and by the nature of the breakage process involved. While it is generally recognized that comminution can lead to changes in particle shape, relatively few attempts to quantify these effects have been reported. Furthermore, largely due to the lack of widely accepted measures of shape, there is some disagreement on the evolution of particle shape in grinding processes. For example, Bond [1] considered that the character of the material being broken has more influence on the shape of the product than the type of size reduction machine used. Similarly, Heywood [2] stated that the shape of particles produced on initial

fracture is dependent upon the characteristics of the material. On the other hand, Rose [3] suggested that the type of the mill has the major effect on the particle shape although the properties of the material are also a factor. Similarly, Charles [4] observed that the shape of glass particles produced by a single fracture depended on the rate of application of stress.

The particular mode of breakage is likely to affect the shape of product particles. Massive fracture can be expected to produce highly irregular particles with sharp edges formed by the intersection of propagating cracks. Attrition of particles, by surface erosion or chipping at edges or corners, is more likely to cause rounding of particles although the small fragments removed may be quite irregular in shape. It follows that grinding conditions that favor one breakage mode over another may be critical in determining product particle shape. For any system, the prevailing conditions will generally depend on the type of machine and the properties and size of the particles being broken. Since there are normally distributions of particle sizes and applied stresses, it is reasonable to expect a distribution of product shapes. Gaudin [5] observed that large particles were often subject primarily to attrition, tending to become more rounded in shape, while finer material typically underwent

* Safford, AZ

** University Park, PA

*** Boca Raton, FL

[†] Accepted: September 20, 2002

massive fracture leading to more angular product particles. Based on examination of crushed glass particles, Tsubaki and Jimbo [6] concluded that particle shape varies with size.

Holt [7] reviewed the effect of comminution devices on particle shape and concluded that single-pass devices such as roll crushers generally produce angular particles while retention systems such as ball mills produce more rounded particles. Dumm and Hogg [8] showed that the rounding effect in ball mills becomes more pronounced with increased grinding time. Durney and Meloy [9] investigated the shape of particles produced by jaw crushers using Fourier analysis to provide a quantitative description of the shape characteristics. In particular, they compared the results of crushing under single-particle and choke-feeding conditions. They observed that when the particles were fed into the mill one at a time the products were highly angular, while choke feeding produced more “blocky” or rounded particles. In each case, the finer particles had more angular and irregular shapes.

In the present paper, populations of crushed particles from different comminution devices were evaluated using a computerized image analysis technique to quantify particle shape in terms of physically recognizable shape descriptors.

Shape Analysis

Several different approaches to the analysis of particle shape have been described in the literature. Fourier analysis of the vector of polar coordinates that represent the particle profile yields a set of Fourier coefficients that, in principle, define the shape of the particle [10,11]. Meloy [12] observed simple correlations among the coefficients for a variety of different shapes and defined a two-parameter particle “signature” as an overall characteristic of the particle shape. Durney and Meloy [9] used statistical procedures to detect significant differences in the Fourier coefficients obtained from different populations. Fractal analysis [13,14] has been widely applied to particle shape characterization and is especially attractive for highly complex shapes such as those of agglomerates. The approach adopted in the present work is based on an attempt to define shape in terms of physically recognizable features such as elongation and angularity.

An image processing system was used to provide digitized particle profiles from optical microscopy (or from scanning electron micrographs) by means of a

procedure developed by Dumm and Hogg [8] and modified by Kumar [15] and Kaya [16]. A series of straight-line segments was fitted to the set of N points representing the complete profile as illustrated in **Figure 1**. The intersections of these linear segments define a reduced set of n perimeter points ($n \ll N$) and describe an n -sided polygon that represents the essential features of the original profile.

In order to minimize the errors associated with the use of the fitted polygon, the projected area and centroid of the image were first obtained from the original digitized profile. Designating the x - y coordinates of the original perimeter points as (x_i, y_i) , the cross-sectional area of the particle was determined from:

$$A = \frac{1}{2} \sum_{i=1}^N (x_{i+1} - x_i) (y_{i+1} + y_i) \quad (1)$$

where the point at (x_{N+1}, y_{N+1}) represents the return to the initial starting point ($i=1$). The coordinates \bar{x}, \bar{y} of the centroid of the image can be obtained from:

$$\bar{x} = \frac{\sum_{i=1}^N (x_{i+1}^2 - x_i^2) (y_{i+1} + y_i)}{2 \sum_{i=1}^N (x_{i+1} - x_i) (y_{i+1} + y_i)} \quad (2)$$

and

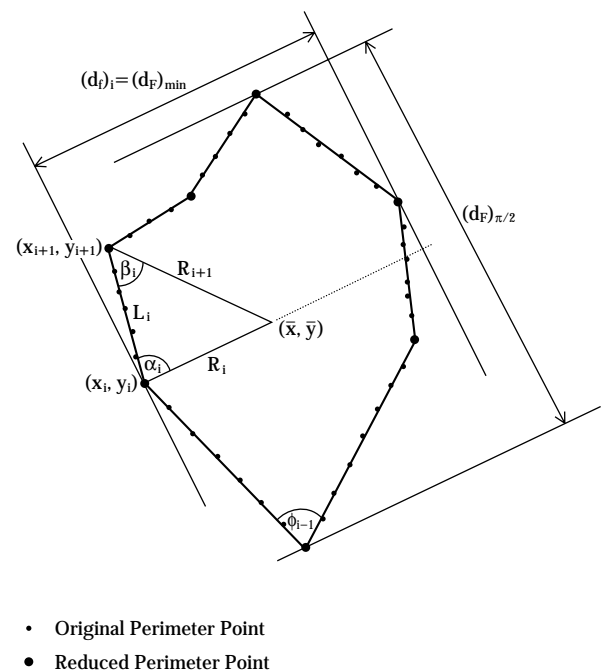


Fig. 1 Representation of a particle profile consisting of N perimeter points ($N=40$ in this example) by a fitted polygon defined by a set of n reduced perimeter points ($n=7$ in this case).

$$\bar{y} = \frac{\sum_{i=1}^N (y_{i+1}^2 - y_i^2) (x_{i+1} + x_i)}{2 \sum_{i=1}^N (y_{i+1} - y_i) (x_{i+1} + x_i)} \quad (3)$$

The equivalent-circle mean radius of the particle can be calculated using:

$$R_0 = \sqrt{A/\pi} \quad (4)$$

The radial vectors R_i from the centroid to each of the n perimeter points on the reduced profile are given by:

$$R_i = \sqrt{(x_i - \bar{x})^2 + (y_i - \bar{y})^2} \quad (5)$$

The angles ϕ_i between adjacent edges of the fitted polygon were evaluated by applying the cosine rule to the triangles defined by the edge and the adjacent radial vectors as shown in **Figure 1**. Thus, for the edges intersecting at the perimeter point (x_i, y_i) the angle α_i is given by:

$$\cos \alpha_i = \frac{R_{i+1}^2 + L_i^2 - R_i^2}{2R_i L_i} \quad (6)$$

where L_i is the length of the edge connecting points (x_i, y_i) and (x_{i+1}, y_{i+1}) (see **Figure 1**). Similarly, β_i can be obtained from:

$$\cos \beta_i = \frac{R_{i+1}^2 + L_i^2 - R_{i+1}^2}{2R_{i+1} L_i} \quad (7)$$

The angle ϕ_i is simply the sum: $\alpha_i + \beta_i$.

Feret's diameters are defined as the distance between two parallel lines tangent to opposite sides of a particle, in some particular orientation. For any perimeter point, the corresponding Feret's diameter, $(d_F)_i$ can be obtained by projecting the other perimeter points on to the vector R_i and determining the maximum distance from the original point (see **Figure 1**).

The following shape descriptors were defined to represent specific geometric features of the profile.

1) The elongation E was defined using the ratio of the minimum Feret's diameter to that at right angles to it. Thus,

$$E = [(d_F)_{\pi/2} / (d_F)_{\min}] - 1 \quad (8)$$

where $(d_F)_{\min}$ is the minimum of the set of measured Feret's diameters and $(d_F)_{\pi/2}$ is the Feret's diameter measured perpendicular to $(d_F)_{\min}$. As defined, the elongation is zero for a circular profile.

2) The angular variability V_ϕ was defined to represent the variation in the angles ϕ_i between adjacent

edges on the reduced profile. Specifically, for ϕ_i expressed in radians,

$$V_\phi = \sum_{i=1}^n \left(1 - \frac{\phi_i}{\pi} \right)^3 \quad (9)$$

The third power was used in order to emphasize the role of the smaller angles, which are considered to contribute the most to the "angularity" of a particle [15]. A many-sided polygon fitted to a circle gives a set of angles close to π with a corresponding angular variability close to zero.

3) The radial variability V_R was used to describe the departure of the profile from a circle. The particular definition used was

$$V_R = \sum_{i=1}^n \left| \frac{R_i}{R_0} - 1 \right| \quad (10)$$

where R_0 is the equivalent spherical diameter as defined by Equation 4 and the R_i are the lengths of the radial vectors from the centroid to each of the n perimeter points (Equation 5). Since each R_i would be equal to R_0 for a circle, the radial variability would be zero.

Calculated values of the various parameters are given in **Table 1** for the schematic profile shown in **Figure 1**.

Table 1 Relative dimensions and calculated shape descriptors for the schematic particle profile shown in **Figure 1**.

Reduced Perimeter Point, i (clockwise from top)	Relative Distance from Centroid, R_i/R_0	Angle between Adjacent Faces, ϕ_i	
		Radians	Degrees
1	1.409	1.479	84.7
2	1.070	2.336	133.8
3	0.885	2.549	146.0
4	1.454	1.227	70.3
5	0.878	2.656	152.2
6	1.111	1.855	106.3
7	0.915	3.607	206.7

Shape Parameters:

Elongation, E :	0.41
Radial Variability, V_R :	1.37
Angular Variability, V_ϕ :	0.47

Experimental Systems

Shape descriptors were measured for a range of particle sizes produced by crushing and grinding under a variety of conditions. Approximately 600 particles were analyzed from each population and the distribution of each descriptor was evaluated. The

materials used were a high-volatile bituminous coal from a continuous mining operation in the Pittsburgh Coal Seam (Green Country, PA) and quartz from North Carolina. The following crushing and grinding devices were used to produce particles in different size ranges:

- Jaw Crusher – used to reduce feed materials about 1 cm in size to less than about 5 mm
- Hammer Mill (Holmes pulverizer) – used to crush coal particles in the 5 mm to 1 cm size range to less than 1 mm
- Disk Mill (Quaker City) – used to pulverize 1 mm feed particles
- Ring and Puck Mill (Bleuler Pulverizer) – used for fine grinding of disk mill product to micron sizes
- Planetary Ball Mill (Retsch) – also used for fine grinding of disk mill product.

The jaw crusher, hammer mill and disk mill are essentially single-pass devices, although some, lim-

ited retention of broken material may occur. The ring-and-puck and planetary mills are retention devices that can subject particles to repeated breakage. In the case of the latter two devices, different grinding times were used to vary the exposure of particles to the grinding environment.

Experimental Results

Analysis of Shape for Different Materials

In order to evaluate particle shape effects for different materials, samples of the coal and quartz were prepared as 9.5×12.7 mm size fractions and fed to a jaw crusher with a gap setting of 6.4 mm. Products in different size classes (30×40, 50×70, 70×100, 140×200 and 200×270 US mesh) were analyzed using digitized images obtained by optical microscopy.

Examples of the distributions of angular variability for coal and quartz particles of different sizes are presented in **Figures 2** and **3**. In each case, the distribu-

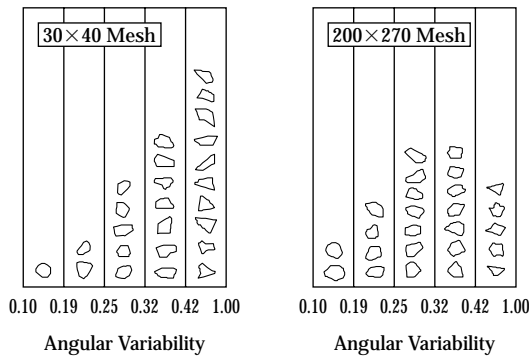
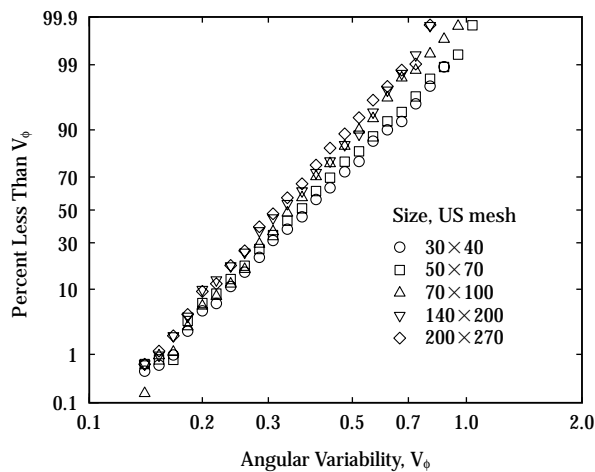


Fig. 2 Graphical and visual representations of the number distributions of angular variability for coal particles produced in a jaw crusher (feed size 9.5×12.7 mm; gap setting 6.4 mm).

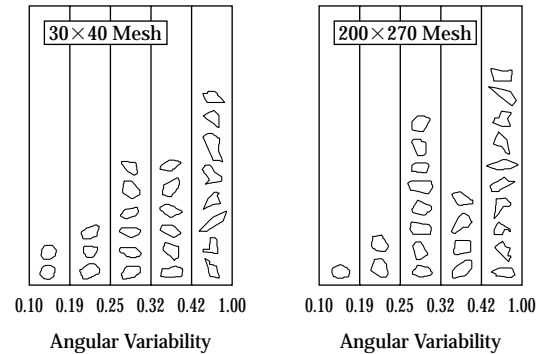
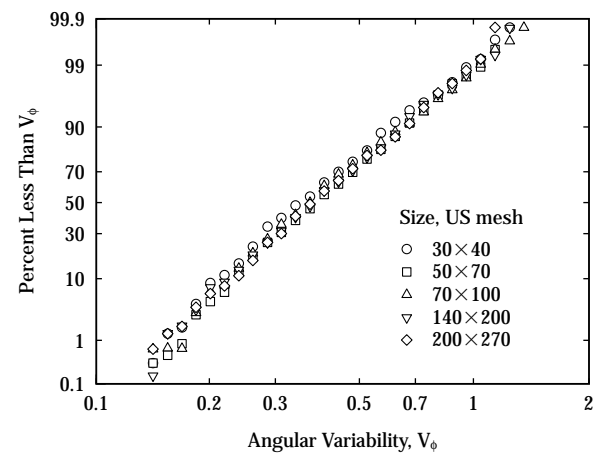


Fig. 3 Graphical and visual representations of the number distributions of angular variability for quartz particles produced in a jaw crusher (feed size 9.5×12.7 mm; gap setting 6.4 mm).

tions are shown graphically as cumulative plots and a visual representation to illustrate the significance of the variations is included. The particles in each column are typical of that range of angular variability while the number of particles in each column represents the number fraction in that range. The results indicate that, for coal particles, the distributions generally become somewhat narrower and shift to lower values as size decreases, implying a size dependency of the shape. On the other hand, the distributions of angular variability for the quartz particles show no clear systematic variation with size. Very similar trends were observed for the other shape descriptors: elongation and radial variability. It is interesting to note that the distributions appear to conform quite closely to the log-normal distribution.

Effect of Grinding Procedure

The particle shape is expected to be affected by the type of machine, by the specific breakage mechanism in a grinding device and by the time spent in the grinding environment. The effect of grinding device on shape was analyzed for coal particles using the Bleuler ring-and-puck pulverizer and the planetary ball mill. The grinding times were set so as to give a similar extent of grinding for each mill. The quantity of feed (-10 mesh) was 20 g for the Bleuler and 9.5 g for the planetary mill. The distributions of elongation are presented in **Figure 4**. The graph indicates that different grinding devices affect shape differently. Shape does not change substantially with grinding time in a high-energy mill (Bleuler). On the other hand, the shape distributions of the particles produced in the planetary mill shifted towards lower values, indicating that particles become more rounded with increased grinding time. Similar trends have been observed for particle sizes in the size range from 3 to 5 μm .

Examples of the distributions of angular variability for 70×100 US mesh coal obtained from a single pass through different crushing and grinding devices are shown in **Figure 5**. It appears that the jaw crusher, for which massive fracture is the dominant breakage mechanism, produces the most irregular particles. The Quaker City mill, for which most of the breakage is probably by massive fracture of coarse feed particles, also produces quite irregular particles. The Holmes pulverizer, which allows some retention of material and may include contributions from the attrition-type mechanisms, and the Bleuler mill (30 second grinding time), generally produce particles of more regular shape. Similar trends have been ob-

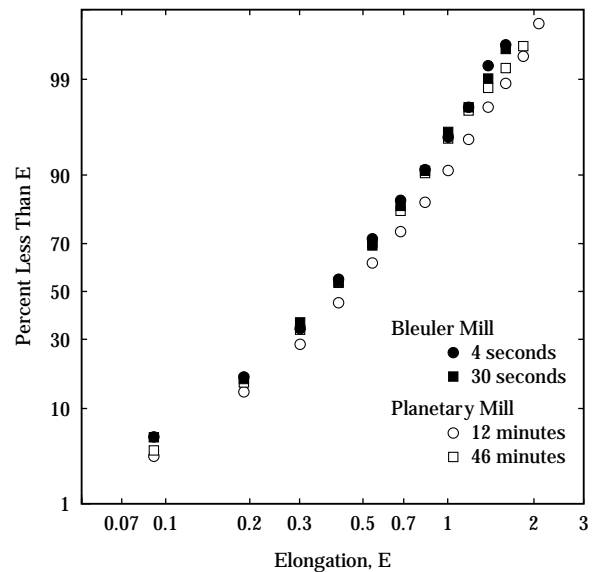


Fig. 4 Number distributions of elongation for coal particles (200×270 US mesh) produced in both the Bleuler and planetary mills using different grinding times.

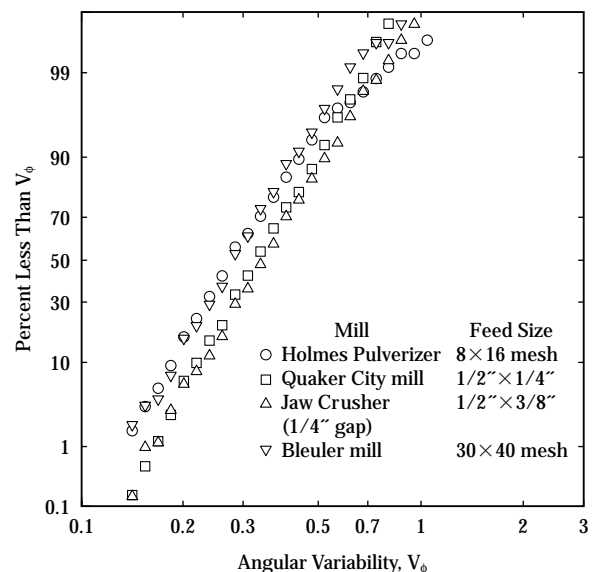


Fig. 5 Number distributions of angular variability for coal particles (70×100 US mesh) produced by different comminution devices.

served for 200×270 US mesh fractions. Changes in feed size to the devices did not lead to significant differences in product particle shape.

The effects of mill type on the average particle shape for different coal product sizes are illustrated in **Figure 6**. While the variations are generally small,

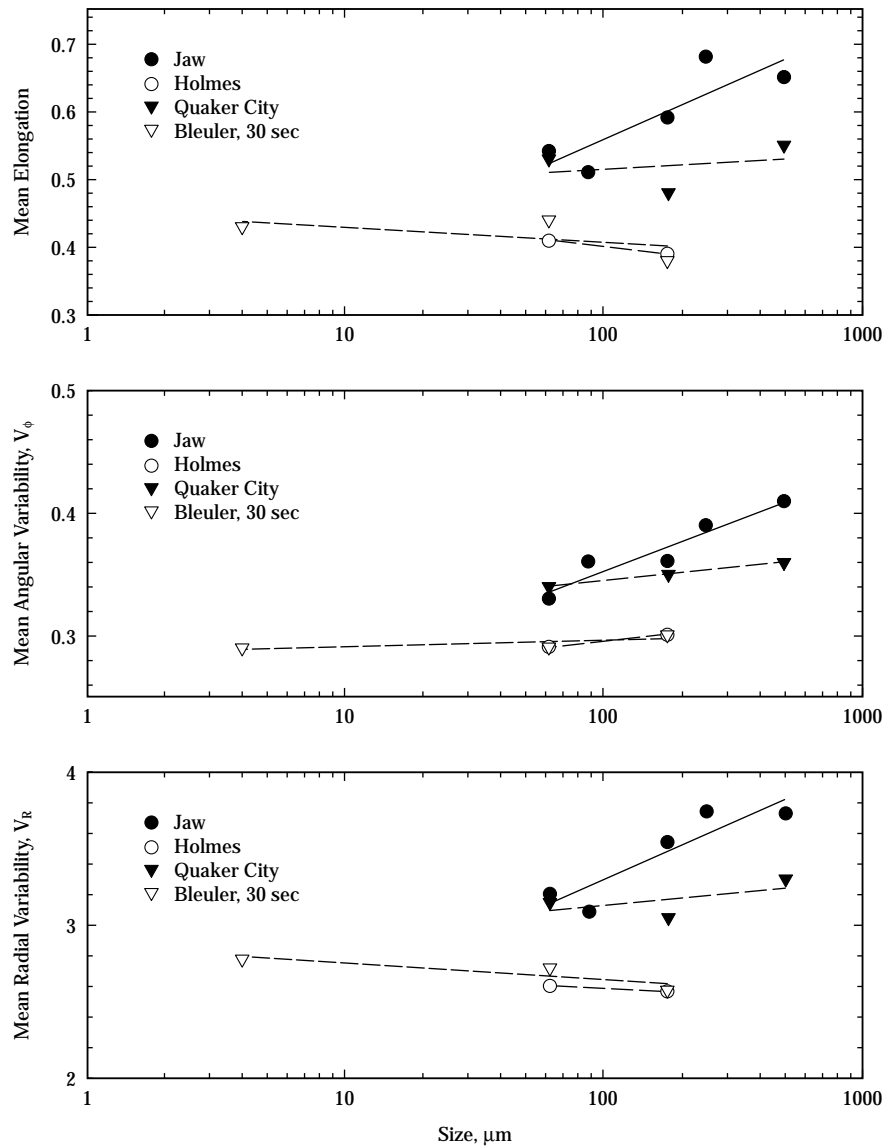


Fig. 6 Variation in shape with particle size for coal ground in different mill types.

the trends are consistent and similar for each of the three descriptors. Large particles produced by single breakage events tend to be quite irregular in shape while particles subject to repeated breakage or long exposure to the grinding environment are usually more rounded.

Conclusions

The results of this investigation indicate that, for the materials studied (quartz and coal), the shape of particles produced by size reduction is controlled by

- a) the nature of the material being reduced
- b) the type of comminution device used and the

predominant breakage mechanisms involved

- c) the time spent in the grinding environment.

In particular, it is concluded that the products of individual breakage events are typically angular and irregular in shape. Continued exposure to the grinding environment leads to rounding of the particles. For a given product size distribution, devices that employ high energy input yield products containing a high proportion of newly-created particles. Such devices, therefore, favor the production of irregular particles. Grinding machines for which the energy input is relatively low, on the other hand, rely on repeated breakage action for size reduction and tend to produce more rounded product particles.

The differences in the size dependence of product-particle shape for coal and quartz suggest that the existence of structural features such as cleats in coal or cleavage planes in crystals may lead to more angular and irregular products of comminution. Furthermore, since the effect appears to be more pronounced for low-energy devices, it may be possible to achieve some degree of control over shape through appropriate equipment selection. However, considerable additional work would be needed to establish the basis for such control.

Acknowledgements

The work described in this paper was supported in part under the Mineral Institutes Program by Grant Nos. G1105142, G1115142 and G1125142 from the Bureau of Mines, US Department of the Interior, as part of the Generic Mineral Technology Center for Respirable Dust.

Nomenclature

A	: Cross-sectional area	[m ²]
(d _f) _i	: Feret's diameter corresponding to perimeter point i	[m]
(d _f) _{min}	: Minimum Feret's diameter of a particle	[m]
(d _f) _{π/2}	: Feret's diameter perpendicular to (d _f) _{min}	[m]
E	: Elongation of a particle	[-]
L _i	: Edge-length on a particle profile	[m]
n	: Number of reduced perimeter points on a fitted particle profile	[-]
N	: Number of measured perimeter points on a particle profile	[-]
R ₀	: Equivalent-circle mean particle radius	[m]
R _i	: Length of radial vector from particle centroid to the i th perimeter point	[m]
V _R	: Radial variability	[-]
V _φ	: Angular variability	[-]
x _i , y _i	: Cartesian coordinates of the i th perimeter point	[m]
\bar{x} , \bar{y}	: Cartesian coordinates of a particle centroid	[m]
α _i	: Angle defined in Figure 1	[radians]
β _i	: Angle defined in Figure 1	[radians]
φ _i	: Angle between adjacent edges on a particle profile	[radians]

References

- 1) Bond, F. C., "Control Particle Shape and Size," *Chemical Engineering*, pp. 195-198 (Aug. 1954).
- 2) Heywood, H., "Powder Production by Fine Milling," in *Powders in Industry*, Society of Chemical Industry, pp. 25-26 (1962).
- 3) Rose, H. E., "Particle Shape, Size and Surface Area," in *Powders in Industry*, Soc. Chem. Ind., pp. 130-149 (1961).
- 4) Charles, R. J., "High Velocity Impact in Comminution," *Mining Engineering*, pp. 1028-1032 (1956).
- 5) Gaudin, A. M., "An Investigation of Crushing Phenomena," *Trans AIME*, 73. pp. 253-317 (1926).
- 6) Tsubaki, J. and Jimbo, G., "Identification of Particles Using Diagrams and Distributions of Shape Indices," *Powder Technology*, 22. pp. 171-178 (1979).
- 7) Holt, C. B., "The Shape of Particles Produced by Comminution – A Review," *Powder Technology*, 28. pp. 59-63 (1981).
- 8) Dumm, T. F. and Hogg, R., "Characterization of Particle Shape," *Proceedings of International Symposium on Respirable Dust in the Mineral Industries*, SME, Littleton, CO, pp. 283-288, (1990).
- 9) Durney, T. E. and Meloy, T. P., "Particle Shape Effects due to Crushing Method and Size," *Intl. J. Miner. Process*, 16. pp. 109-123 (1986).
- 10) Beddow, J. K. and Meloy, T. P., *Advanced Particulate Morphology*, CRC Press, Boca Raton FL (1977).
- 11) Meloy, T. P., "Particulate Characterization: Future Approaches," Chapter 3 in *Handbook of Powder Science and Technology*, M. E. Fayed and L. Otten, editors, van Nostrand Reinhold, New York, pp. 69-98 (1984).
- 12) Meloy, T. P., "Fast Fourier Transforms Applied to Shape Analysis of Particle Silhouettes to Obtain Morphological Data," *Powder Technology*, 17. pp. 27-35 (1977).
- 13) Mandelbrot, B. P., *Fractals: Form, Chance and Dimension*, W. H. Freeman, San Francisco (1977).
- 14) Kaye, B. H., "The description of Two-Dimensional Rugged boundaries in Fineparticle Science by Means of Fractal Dimensions," *Powder Technology*, 46. pp. 245-254 (1986).
- 15) Kumar, S. R., "Characterization of Particle Shape," M. S. Thesis, The Pennsylvania State University (1996).
- 16) Kaya, E., "Control of Particle Characteristics in the Production of Fine Powder By Grinding," Ph.D. Thesis, The Pennsylvania State University (1996).

Author's short biography



Erol Kaya

Erol Kaya is currently a Senior Research Engineer at the Process Technology Center, Phelps Dodge Mining Company. He received a B. Sc. degree in mining engineering from the Istanbul Technical University, the M.S. and Ph.D. degrees in mineral processing and M. Eng. in environmental pollution control from the Pennsylvania State University. His research interests include particulate technology, grinding and copper flotation.



Richard Hogg

Richard Hogg is Professor of Mineral Processing and GeoEnvironmental Engineering at the Pennsylvania State University. He received a B.Sc. from the University of Leeds and the M.S. and Ph.D. degrees from the University of California at Berkeley. Dr Hogg's research interests include fine particle processing, particle characterization, and colloid and surface chemistry.



Senthil Kumar

Senthil Kumar graduated from the Pennsylvania State University with an M.S. in Mineral Processing and an MEng. in Computer Science and Engineering. He received his BTech. in Metallurgical engineering from the Indian Institute of Technology, Bombay. He is presently a technical architect at Seisint Inc., a software company in Boca Raton, Florida.

Primary Segregation Shear Cell for Size-Segregation Analysis of Binary Mixtures[†]

S. P. Duffy and V. M. Puri

Department of Agricultural and Biological Engineering
The Pennsylvania State University*

Abstract

Segregation is important in many bulk handling industries due to its impact on product quality and mixing. Previous studies have focused on quantifying segregation as a coefficient for a particular process. Although this has provided insights into the effect of segregation during particular processes, it has not provided a rational approach to understanding the phenomena of segregation. Toward this end, a vertically oriented segregation shear cell was designed, fabricated and used to test the response of binary mixtures of spherical glass beads. Three size ratios of 10.9:1, 8.7:1, and 5.1:1 were used in this study. Variables such as strain, strain rate (i.e., cycle speed) and bed depth were used to quantify size-segregation characteristics under different input energies. Size ratio was the most dominant variable that affected the percolation rate of fines through a bed of coarse particles. Based on the differences in percolation between the smaller ratio of 5.1:1 and larger ratios of 8.7:1 and 10.9:1, there are indications of a critical size ratio that determines the mechanism of percolation. Two mechanisms were observed. First, the larger size ratios exhibited an initial free-fall discharge of fines at the beginning of the test. This initial discharge was followed by a diffusive behavior, i.e., monotonically increasing trend that approaches an asymptotic value. The smaller ratio did not exhibit the initial discharge and the responses were described adequately by the diffusive behavior. Strain also had an effect. Input energy, as related to strain, was found to be critical in the type of percolation exhibited, i.e., the presence or absence of an initial rapid discharge. For the size ratio of 10.9:1, the amount of input energy was critical because the size of the fine particles was near the size of the coarse bed pore space. When the input energy was below a critical limit, mechanical arching was occurring. Although, the input energy is a function of bed depth and strain rate, these parameters did not influence the results outside random behavior.

1. Introduction

The handling, storage, flow, and mixing of particulate materials are important processing steps in many industries. During all of these processing steps, product quality may be lowered by a phenomenon known as segregation. Segregation is defined as a demixing process in which components of a mixture separate as long as one component of the mixture is different than another. Size-segregation is the most common in which finer particles gather in the center and larger

particles tend towards the walls of storage container. However, other types of segregation caused by density, shape and composition have been observed. Segregation is a serious problem in the processing and manufacturing of particulate materials. Several studies have investigated segregation for a particular process and reported a segregation coefficient in order to quantify the severity of segregation. Some of the processes that have been studied include discharge from a hopper, vibrated channels, vibrated columns, heap formation, and die filling. Another approach in solving segregation problems was identifying fundamental segregation mechanisms for a given process and determining the dominant mechanism. By identifying the dominant mechanism of a particular process, segregation can be predicted

* 229 AG Engineering Building
University Park, PA 16802

[†] Accepted: October 17, 2002

based on previously observed and simplified experiments. For example, heap formation is the process in which a stream of powder is deposited onto a flat plate. The powder forms a conical heap as powder is continuously deposited onto itself. It has been shown during this process that fines tend to the center of the conical heap and coarse particles concentrate on the outer boundaries of the cone. The dominant mechanism for this example of size-segregation was identified to be a rolling mechanism. Coarse particles more easily roll down the conical plane formed during deposition. Therefore, fines concentrate at the center due to the inability to roll down the conical plane and coarse particles concentrate at the outer surfaces.

A particulate material will flow as long as the process induces enough internal shear to overcome the shear strength of the powder. This is the fundamental approach to hopper design using the Mohr-Coulomb theory and Jenike's Flow/No-Flow hypothesis. Previous observations have shown that segregation is occurring in a hopper during flow/discharge. Based on these observations, researchers developed a simple shear test apparatus to measure size-segregation during shear. When the shear mechanism was isolated, size-segregation was quantified by measuring the drainage of fine particles through a bed of coarse particles. This type of segregation is known as percolation. In this study, percolation was defined as a demixing process perpendicular to the shear deformation and parallel to gravity where the fines traveled through the bed of coarse particles during a shear disturbance. The size of the particles that were studied had mean diameters ranging from 2.4 mm to 37.2 mm. The mean sizes selected were limited by the construction of the simple shear cell and applicable fines to coarse ratios. The bed of coarse particles was fixed similar to a roller assembly so that pure shear could be obtained and the fines could easily escape at the bottom of the tester. Therefore, a primary shear apparatus that would overcome the mean diameter limitations of the previous work by measuring the discharge of fine particles through a bed of coarse particles will be an invaluable experimental device to quantify size-segregation induced by percolation. Therefore, a vertically oriented the primary segregation shear tester was designed, fabricated, and tested to evaluate its feasibility for quantifying percolation segregation.

2. Literature Review

Segregation, while important in every aspect of

powder technology, has limited understanding. Most researchers define a segregation coefficient and explore segregation for a particular process. The following subsections summarize the key segregation-related findings relevant to this study.

2.1 Mechanisms of Segregation

Ten unranked main mechanisms of segregation have been identified (Mosby et al., 1996): 1) Rolling, 2) Sieving, 3) Push-away, 4) Angle of repose, 5) Percolation, 6) Displacement, 7) Trajectory, 8) Air current, 9) Fluidization, and 10) Impact. *Rolling effects* are dominant in heap formation, because segregation in a heap has been described as a surface phenomenon where the heap surface remains constant. Rolling effects are also important, because friction varies as a function of size and stumbling effects, the ability of larger particles to roll over obstacles. *Sieving effects* occur in conjunction with rolling effects during heap formation. The larger particles rolling along the surface create a non-blinding screen. This type of segregation continues as long as the large particles are in motion. Sieving effects are also present in die filling. Different densities cause *push-away effects*. A top layer with a higher density will push the bottom layers with lower densities to the side. Therefore, the center core of the powder sample will have a higher density than the wall area of the sample. Johanson (1988) gave the first indication of *angle of repose effects* in a binary sample of mung beans and fine salt. A high percentage of salt prohibited sieving effects, however high contents of mung beans were near the wall. *Percolation* has been studied as a function of vibration and induced by gravity. Vibration can cause a small individual particle to travel downward through the powder mass. Bridgwater et al. (1978) developed a simple shear apparatus that induced percolation. Percolation is similar to sieving during shear, however a moving layer is absent.

Displacement segregation describes the phenomena in which a single large particle placed at the bottom of a pile of smaller particles travels to the top during vibration. A critical frequency of vibration was found. *Trajectory effects* encompass larger particles traveling further off a chute than do smaller particles. Studies have shown that a large amount of fines were found on the side of a heap closest to the chute. Particulate material filled centrally into a tall bin or hopper that contains a significant amount of fines (defined as $<50 \mu\text{m}$) creates an *air flow* channel. This air flow causes fines to travel to the sides of the silo or hopper and leaves the core filled with coarse particles. *Flu-*

idization effects are similar to air current effects. During the filling of a hopper, fines become fluidized, or aerated, which enables the coarse particles to fall through the aerated fines. The two mechanisms of *impact effects* are interparticle collisions and particle-boundary collisions. As a small particle collides with a larger particle, the small particle can either stop or increase in velocity. This results in a wider distribution among the fine particles. Impact effects are increased with an increase in flow rate.

2.2 Segregation Testers

This section has been divided into two major categories. First, testers that were specifically designed to measure segregation are reviewed. Second, test techniques used to measure segregation for existing handling equipment are examined.

2.2.1 Specific test designs

The following test designs were developed to quantify segregation during a specific operation. Flow out of a hopper, filling a hopper, and free-surface flow were operations that were targeted for this review because of their relevance to the present study.

Mosby et al. (1996) detailed two testers that were developed at Telemark. The first was a two-dimensional, rectangular box, tester that has an interior, inclined channel. The angle of the channel and nine sampling holes can be adjusted simultaneously so that the sampling holes are parallel to the channel. Various channel lengths were tested and it was found that a channel length of 630 mm gave reproducible results. Five types of tests were completed to show the different segregation mechanisms in a heap. Variables that were changed between the tests were mixing ratios, feed rates, and length of channel. The mixing ratio was not defined, but it appears to be the percent of fines (alumina). Sand and alumina were the two components of the mixture. It was concluded from this work that fluidization, rolling, and sieving are predominant mechanisms in heap segregation.

Bagster (1996) built a tester similar to that of Telemark. It consists of a Perspex box with three feeder guides and several sampling holes. The feed tube is adjusted during the test so that no impact velocity occurs at the feed point. This also minimizes the lateral velocity of the particles. Sand was used as the test material and several concentrations of fines were used. Segregation was measured by determining a non-dimensional parameter of coarse concentration. No correlation between the non-dimensional parameter and degree of segregation was found.

Harwood (1977) used radioactive tracer sand to measure segregation in a powder bed during vibration. The tracer technique did not disturb the powder bed and enabled time measurements of segregation. The following conclusions were made: 1) migration of larger particles tends to be upwards when the vibration is at the base of the powder sample; 2) in a binary system (similar density and size) of free-flowing particles, very slow migration takes place in both upward and downward directions; 3) in a binary system (one free flowing, one slightly cohesive), limited migration takes place; 4) there exists a level of vibrational energy that maximizes segregation; and 5) particle size is the main effect that controls segregation.

Williams and Shields (1967) introduced vibration to free flowing particles on an inclined channel. Equal weights of feed of coarse and fine fertilizer granules were fed onto a fixed plate. The particles continued down the chute into a vibrating channel. The test device was constructed so that the length of the bed, direction, and amplitude and frequency of the vibration could be varied. Segregation was defined as a coefficient. It was concluded from the study that most segregation took place in the first 15 cm of the bed and segregation was maximum when direction of incline was about 30° with a frequency of 1300 rpm and amplitude of 0.35 cm.

Hwang (1978) used a chute to create a two layer flow. The chute was 10.1 cm wide by 3.8 cm deep and the length could be varied by raising and lowering the chute. The angle of the chute could also be changed. The stainless steel chute surface was roughened by applying a thin layer of particles using contact paper. This roughness was used to enhance mixing during flow. The twin hoppers were used to produce a two layer flow stream. A sampling device was used at the end of the chute to collect particles at various locations in the flow stream. Using experimental data, Hwang developed a mathematical model for diffusion-type segregation.

Stephens and Bridgwater (1978a) selected an annular shear cell to study the mixture quality of cohesionless powders in the failure zone. The annular shear cell was selected so that powder behavior after initial failure could be maintained. This aspect is not available in the linear direct shear cell of Jenike (1964). Two particle sizes (1.91 and 4.00 mm) were used in the shear cell. Velocity distributions for the two sizes were similar in the failure zone. However, the depth of failure zone could not be characterized by either dimensional or dimensionless values. It was determined that increasing the normal load decreased the

failure zone depth. Stephens and Bridgwater (1978b) in a second part presented the significance of the annular shear cell in determining percolation velocities and diffusion coefficients. Using an annular shear cell, they found that for spherical particles large concentration gradients or zones of constant concentration can arise in failure zones. It was concluded that percolation, migration and diffusion are the controlling factors of segregation in concentration profile. The steady-state profile was influenced by the amount of material in the failure zone.

2.3 Tester Techniques

Sleppy and Puri (1996) examined size-segregation of granulated sugar discharging from mass flow and funnel flow bins. Two particle size ratios were used in each of the bins, 2:1 and 5.7:1, and mixed by equal weight. It was concluded that funnel flow leads to predominant fines in the first half of discharge and a predominant coarse flow in the second half of discharge. No specific segregation pattern was observed during mass flow. There was no difference in segregation between the two size ratios in mass flow, but segregation patterns in funnel flow had a minimal difference between the two size ratios. Segregation coefficient was defined as a fines to coarse ratio in this study. Markley and Puri (1998) continued the work of Sleppy and Puri by examining the effect of hopper size on segregation of granulated sugar. Two hopper sizes (small and large) were used for both funnel flow and mass flow conditions. The same trends were observed, i.e., during funnel flow a predominant fine mixture at the beginning and coarse mixture at the end. In addition, more segregation was found in the large bins for both mass and funnel flows.

Ahmad and Smalley (1973) investigated particle segregation of a coarse particle and fine mixture during vibration. At a given frequency, segregation increased with an increase in acceleration. However, an increasing frequency reduced segregation in a range of accelerations. Segregation was found to increase with an increase in the particle size of the large particle and lighter particles were found to segregate more quickly than heavier particles under the same operating conditions. Shape did not seem to have an effect on segregation.

Lawrence and Beddow (1968) examined segregation of lead (Pb) particles during deposition into a die. It was found that the fines filtered down through moving mass and resulted in a collection of fines at the bottom. This filtering of fines caused the larger particles to drift outwards toward the die wall. The size

ratio affected segregation by increasing segregation with an increase in size ratio. It was also found in this study that particle shape and density had little effect on segregation and increasing drop height minimized segregation.

Williams (1976) introduced a coefficient of segregation, which was later revised by Popplewell et al. (1989) based on their results. The difference between Williams' index and Popplewell et al.'s index is that Popplewell et al. consider the fines weight fraction at the very bottom of the cell. They found that this segregation index was much more sensitive and produced better results. A simple shear model was proposed by Bridgwater et al. (1978).

In summary, segregation has been measured using a coefficient, mechanism, and model. The coefficient technique is by far the most common. However, it only describes the degree of segregation taking place for a particular set of operating conditions. The mechanism technique provides insight for processes that exhibit a dominating segregation mechanism. However, the most encompassing method is to model a particular process. It is neither possible nor practical to model every mechanism for a given process. However, if a specific mechanism can be identified that explains the majority of segregation taking place, it would provide a powerful tool in understanding and minimizing segregation. Therefore, the objectives of this paper were: 1) to conduct tests to demonstrate the feasibility of the primary segregation shear tester using binary mixtures, and 2) to determine segregation characteristics of these mixtures.

3. Experimental Methodology

This section describes the selection of test materials, rationale for test technique, primary tester design, and test methodology.

3.1 Selection of Test Materials

For this study, three binary particulate material mixtures of glass beads were selected. Glass beads were used based on the availability of narrow cut sizes, sphericity, and non-hygroscopic properties under controlled ambient test conditions. All tests were conducted in an environment-controlled laboratory with average temperature of $21^{\circ}\text{C} \pm 3^{\circ}\text{C}$ and relative humidity less than 40% to minimize the effects of moisture on the test results. The glass spheres were considered dry (i.e., moisture content was equal to zero). A dehumidifier, placed near the shear apparatus, was used to reduce the ambient moisture in the

environment.

Two size ranges of fines (106-125 μm and 180-212 μm) and two size ranges of coarse particles (800-1200 μm and 1000-1500 μm) were used to obtain three size ratios, 5.1:1 (1000:196), 8.7:1 (1000:115), and 10.9:1 (1250:115), for size-segregation (**Table 1**). Size ratio of 6.4:1 (1250:196) was used to validate segregation constitutive models. These results will be reported in a subsequent publication. The particle density and bulk density of the glass spheres were 2500 kg/m^3 (Quantachrome Multipycnometer) and 1300 kg/m^3 , respectively.

Table 1 Summary of size ratios used for this study

Coarse Size, d_{50}	1000 μm	1250 μm	
Fine Size, d_{50}	115 μm	196 μm	
Size Ratios For Segregation Data	1250:115 (10.9:1)	1000:115 (8.7:1)	1000:196 (5.1:1)

Preliminary tests determined the applicable size ranges used in this study. Smaller ratios (3:1 to 5:1) were attempted with different size ranges. However, due to the design of the tester, significant blinding (i.e., clogging of the screen) of the exit screen and/or insignificant percolation occurred at the small size ratios. The sizes of the coarse and fine particles were changed until significant percolation was measured and blinding was eliminated.

3.2 Tester Design

Due to its advantages, a vertically oriented shear tester was designed (Duffy and Puri, 2000). The new tester – the Primary Segregation Shear Cell (PSSC) – is capable of applying strains from 5 to 25% by changing the cam (Figure 1). The cam is connected to a variable speed motor that can cycle the cam between 0.25 revolutions per second and 1.67 revolutions per second. A confining pressure between 0 kPa (no confining pressure) and 10 kPa can be applied using the air inlets and the flexible membrane. A mesh screen with an opening of 533 μm at the bottom of the tester prevents coarse particles from passing and allows fine particles to pass without blinding. The mesh screen is replaceable, based on the selected test particle size ratio.

The tester is mounted on a frame that also houses the load cell collection assembly and electric motor that drives the cam. Nylon walls were used as side-walls to contain the particulate system and minimize the friction between the moving walls and fixed walls. The load cell collection assembly is aligned below the

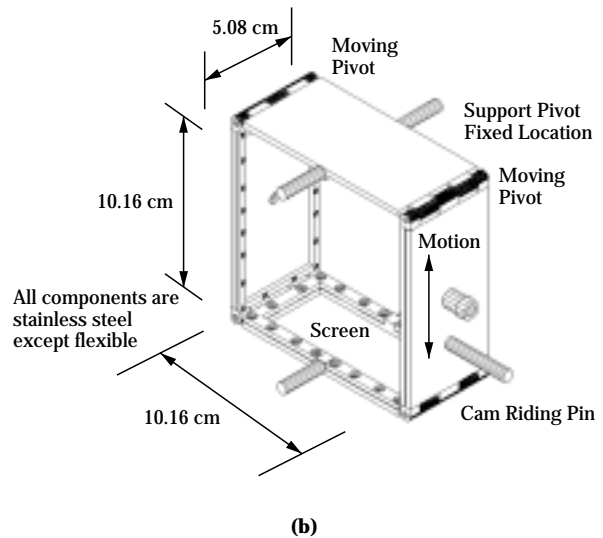
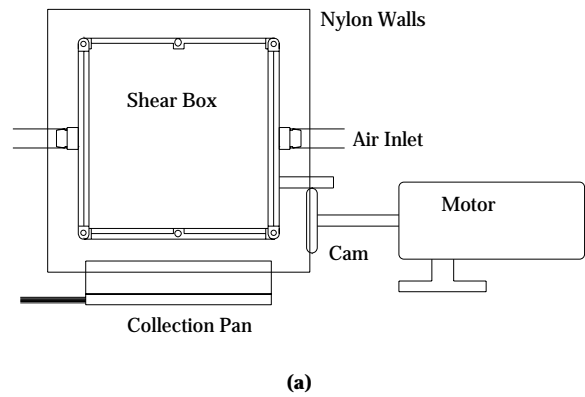


Fig. 1 Vertically oriented primary segregation shear cell (a) overall schematic, and (b) 3D schematic

mesh screen of the tester (**Figure 2**). There are 18 individual compartments in the collection assembly with six of the compartments containing load cells. All compartments were square with dimension 16.9 mm \times 16.9 mm including divider plates (2 mm thickness). Six load cells were selected to measure the percolation of fines and minimize the cost of the tester. Each load cell had a capacity of 50 g \pm 0.01% (0.005 g). This was the smallest load cell that could be used due to the handling involved with the collection assembly during emptying after each test while preserving significant precision and accuracy. Each load cell was preloaded with a 5 g plate to minimize drift and noise associated with an unloaded load cell. The data from the load cells was collected using a Hewlett Packard 3852A data acquisition system connected to a personal computer through the general purpose in-

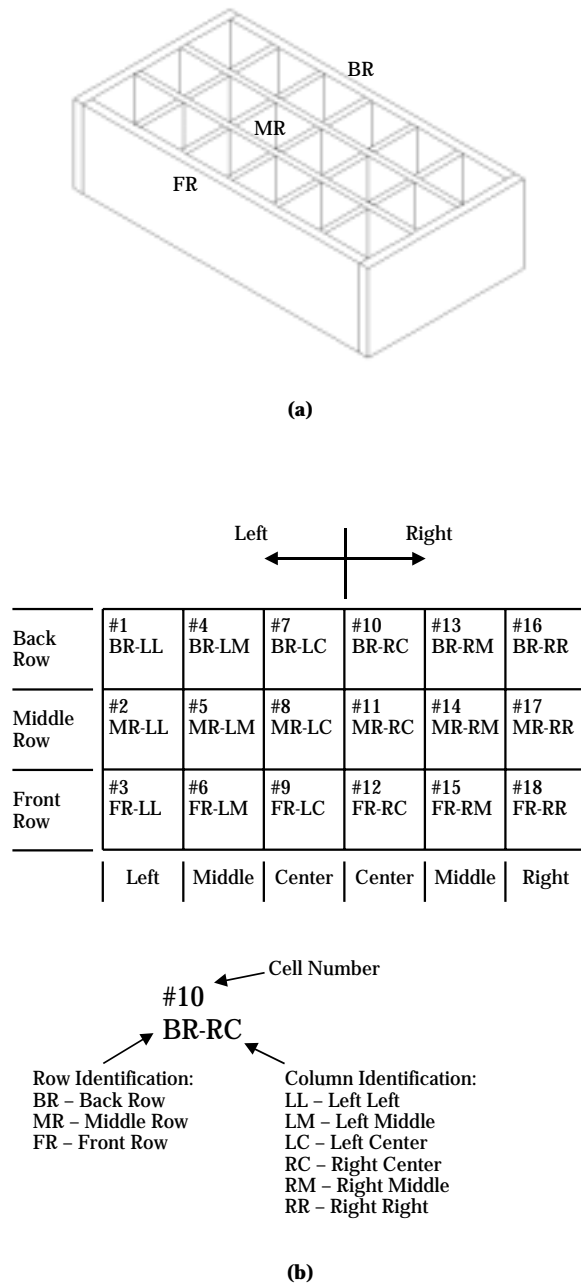


Fig. 2 Schematic of load cell collection assembly (a) isometric view, (b) top view

formation bus (GPB). LabVIEW software (National Instruments, Austin, TX) provided the translation from analog to digital so that the information could be processed using standard spreadsheets.

In order to facilitate the identification of cell location, a lettering system was developed. The three rows (left to right) were identified as Front Row (FR), Middle Row (MR), and Back Row (BR) as shown in **Figure 2 (a)**. The collection assembly was divided into two halves – Left (L) and Right (R) as shown in

Figure 2 (b). Furthermore, the left half was subdivided into Center (C), Middle (M), and Left (L), and the right half into Center (C), Middle (M) and Right (R). To identify a cell by the lettering system, the first two letters designate the row location, the subsequent two letters pinpoint the cell location. The first of the last two letters identifies the half (L or R) and the second letter identifies the cell location (L or M or C). As an example, cell #10 has letter identification of BR-RC. This refers to Back Row (BR) – Right (R) half and Center (C) cell as illustrated in **Figure 2**. The six load cells were placed in BR-LM (Cell #4), FR-LM (Cell #6), MR-LC (Cell #8), MR-RC (Cell #11), BR-RM (Cell #13), and FR-RM (Cell #15). Theoretically, two load cell locations (e.g., BR-LM and FR-RM) could be used to determine anisotropy. Therefore, the six selected locations can measure anisotropic behavior and give an average (or overall) degree of anisotropy.

3.3 Design of Experiment and Test Methodology

Based on preliminary experimentation, 25% and 20% strains provided excessive energy into the particulate assembly. At these strains, the fines flooded through the bed of coarse particles. Flooding is defined as a very rapid percolation rate that could not be consistently measured for meaningful comparisons by the load cell sensors. Strains of 25% and 20% are also extreme limits in shear cell testing (i.e., Jenike shear tests and conventional triaxial shear tests are completed under 20% strain). Therefore, the design of experiments included 5%, 10%, and 15% strains. In this study, strain is defined as 100 times the maximum vertical movement of the moving pivot (**Figure 1 (b)**) divided by the vertical wall dimension (10.16 cm). Two cycle speeds, 0.75 cycles/second and 1.33 cycles/second, were selected in the operating range of the electric motor. Rates below 0.75 cycles/second did not provide enough energy to percolate the fines through the bed of coarse particles in an efficient manner especially at the lower strains. Rates above 1.33 cycles/second caused flooding. Both of these strains produce linear velocities in the powder sample larger than standard shear testing techniques. The strain and cycle speeds selected for this study represent the upper and lower operating limits for meaningful comparisons. Three bed depths were also incorporated into the study to determine the effect of travel length on percolation velocity, i.e., determine if the dimensions of the cell influenced the results (**Table 2**).

Table 2 Testing schedule for size-segregation analysis of binary mixtures

Parameter	Number (Values)
Size Ratios	3 (10.9:1, 8.7:1, 5.1:1)
Strains	3 (5%, 10% 15%)
Cycle Speed	2 (0.75 cycles/s, 1.33 cycles/s)
Bed Depths	3 (2.54, 5.08, 7.68)
Replications	4 per combination
Total Number of Tests	216

3.3.1 Test methodology

For each test described above, the following procedure was used:

1. The nylon walls were screwed tightly towards each other to secure the tester for deposition.
2. Moving pivot at top of tester was removed and top plate swung open.
3. Flexible membranes were inflated to 2 kPa using nitrogen gas.
4. Collection pan assembly was aligned with the mesh screen at the bottom of the tester using alignment guides and visual alignment marks.
5. The coarse particles were deposited into the tester using a spoon to a specific bed height.
6. Fines deposition mould was aligned on the top of the bed of coarse particles.
7. Data collection was started.
8. Fines were deposited into mould (~40 grams) and mould was removed.
9. Top plate was closed and moving pivot replaced.
10. The nylon walls were relaxed and the motor was set at specified strain rate.

4. Results and Discussion

This section includes the statistical, qualitative, and quantitative comparisons of the mass versus time relationships for the different treatments. The comparisons have been grouped based on the treatment of size ratio, which was found to be the dominating treatment. However, the effect of strain, cycle speed, and bed depth are included to highlight trends of these treatments.

4.2 Statistical Analysis

The statistical analysis is divided into two subsections. The first subsection includes statistical comparisons between mass versus time relationships at

different load cell locations for the same treatment to determine the degree of anisotropy. All treatments were analyzed. However, due to the large number of treatments, typical data are presented to give an overview. The second subsection compares (significance level, $\alpha=0.05$) the same load cell location for two different treatments. Again, typical data are presented to give an overview of the statistical analysis.

4.2.1 Statistical analysis at different locations and same treatment

Seven statistical comparisons were calculated for each treatment to determine any anisotropic behavior of percolation. The comparisons include Cells BR-RM vs. FR-RM, Cells BR-LM vs. FR-LM, Cells MR-LC vs. MR-RC, Cells BR-LM vs. BR-RM, Cells FR-LM vs. FR-RM, Cells BR-LM vs. FR-RM, and Cells BR-LM vs. FR-RM (**Figure 2**). Comparisons for Cells BR-RM vs. FR-LM and the 95% confidence interval are shown in **Figure 3**. Other comparisons being similar are not included. The comparison between Cell BR-RM and Cell FR-RM had a small time zone of significant difference ($p<0.05$). This only occurred between 18 s and 36 s with the final masses being statistically similar ($p>0.05$). The remaining comparisons were not significantly different ($p>0.05$) during the entire duration of the test. Therefore, it was concluded that the percolation of fines through the bed of coarse particles was isotropic, i.e., directionally independent or cell location independent. The size of the 95% confidence intervals for the individual load cells is larger than normal ($COV>10\%$). However, the 95% confidence intervals decrease considerably when computed in the effective percolation direction. This is

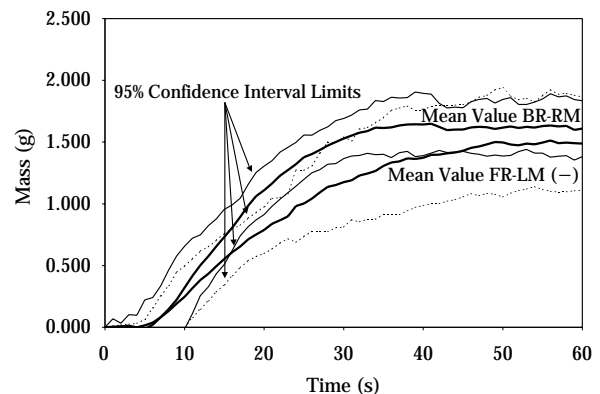


Fig. 3 Mean measured mass versus time relationships for Cell BR-RM and Cell FR-LM and the 95% confidence intervals

due to the fact that the fines percolate through the bed of coarse particles along a preferred direction, which may lead to high deviations when looking at one particular cell location. The size of the 95% confidence intervals in the effective percolation direction supports the foundation of four replications in the design of experiment. An average coefficient of variation for all treatments was 9.7%, which is within standard error of other powder testing techniques (Kamath et al., 1993, Puri et al., 1995, Duffy and Puri, 1999).

4.2.2 Statistical analysis at same location and different treatments

Mass versus time relationships at specific load cell locations were statistically compared ($\alpha=0.05$) to determine any significant differences between treatments. All treatment trends being similar, the graphical statistical comparison at measurement location FR-LM is given in **Figure 4**. In most treatment comparisons, only one or two of the cell locations were significantly different. This was due to relatively large 95% confidence intervals at certain locations. Most of the variation was attributed to the paths that the fines traveled. In other words, the mean path length varied from test to test. It is hard to determine the overall effect by looking at the individual load cells separately. Therefore, a normalized mass versus time along an effective percolation direction was created to better describe the percolation process utilizing the data from all load cells. Normalized mass values were calculated for each measurement location by dividing with the maximum mass accumulated at that location upon completion of the test.

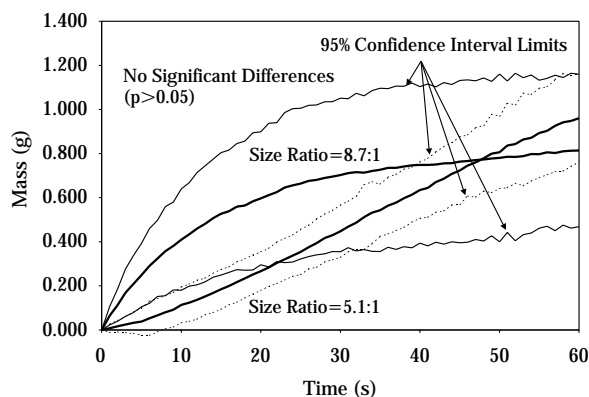


Fig. 4 Mean measured mass versus time relationships at FR-LM and 95% confidence intervals

4.3 Qualitative Analysis

Normalized mass versus time relationships were used to qualitatively assess percolation data from the primary segregation shear cell (PSSC). Extensive analysis of data clearly showed that size ratio was the most dominant treatment. Therefore, the qualitative analysis focuses on the effect of size ratio on the mass versus time relationships. A similar effect has been observed and reported by Bridgwater et al. (1978). For a given strain and cycle speed, there are three comparisons based on bed depths of 2.54 cm, 5.08 cm, and 7.62 cm. The analysis groups the comparisons based on strain and cycle speed and summarizes the results for the three bed depths. The 95% confidence intervals are also given and represented by labeled symbols.

4.3.1 Comparisons of 15% strain and 0.75 cps

A typical normalized mass versus time relationship for bed depth of 2.54 cm is given in **Figure 5**. Typical results were collected at 15% strain and 0.75 cps cycle speed. At any given time, the normalized mass for the size ratios of 10.9:1 and 8.7:1 were significantly ($p < 0.05$) greater than the normalized mass for the size ratio of 5.1:1. In addition, the normalized mass relationships for 10.9:1 and 8.7:1 were statistically similar ($p > 0.05$). At the bed depth of 7.62 cm, the normalized relationship of 8.7:1 approached the normalized relationship of 10.9:1. For deeper coarse beds, the mean path lengths for fines about a certain size ratio (such as 10.9:1 and 8.7:1) approach each other. This hypothesis explains the similar normalized mass profiles. The similarity of profiles for 10.9:1 and 8.7:1 was observed for other treatments.

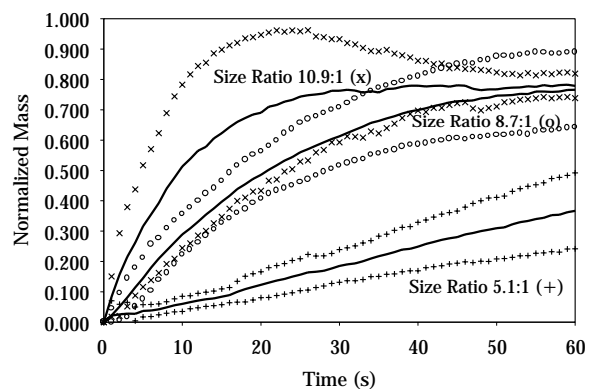


Fig. 5 Mean (solid lines) and 95% CI (symbols) for normalized mass as a function of time – Strain=15%, Cycle Speed=0.75 cycles/second and Bed Depth=2.54 cm

4.3.2 Comparisons of 15% strain and 1.33 cps

The normalized mass versus time relationships for bed depth of 5.08 cm is given in **Figure 6**. The increase in cycle speed resulted in the normalized relationships of 10.9:1 and 8.7:1 to have similar responses while maintaining a significantly ($p < 0.05$) faster percolation through the coarse bed than the 5.1:1 size ratio. Generally, the increase in cycle speed provided enough energy for the fines of the 8.7:1 treatment to percolate through the bed of coarse particles with minimal resistance, i.e., simulating the 10.9:1 treatment. The relationships for the 10.9:1 treatment and 8.7:1 treatment at a bed depth of 5.08 cm are reversed. This trend, which is more pronounced at lower energy inputs, may be attributed to the minimum pore size of the 10.9:1 ratio (1250 μm : 115 μm). The pore size is large enough for two fine particles to mechanically arch. However, the minimum pore size of the 8.7:1 ratio (1000 μm : 115 μm) prevents two fine particles from arching and allows fine particles to freely travel through the bed of coarse particles. For the filling method used, the coarse particle structure is expected to be between that of cubic and orthorhombic arrangements. It is known that the cubic arrangement is unstable; whereas, orthorhombic is stable but does require tapping or vibration to attain the theoretical porosity. The minimum pore sizes for the two arrangements are given in **Table 3**. The mean pore size was calculated by assuming that the orthorhombic arrangement is the dominant arrangement, i.e., 2/3 weight factor was assigned to this arrangement, compared with the cubic arrangement which contributes only 1/3. The mean pore sizes for 1250 μm and 1000 μm

Table 3 Minimum pore sizes for cubic and orthorhombic arrangements

Coarse Particle Size	Minimum Pore Size (μm)		Weighted Mean (μm)
	Cubic	Orthorhombic	
1250 μm	520	150	270
1000 μm	415	120	215

assemblies were estimated to be 270 μm and 215 μm , respectively. For both size ratios, the size of fines was 115 μm . The calculated pore sizes of 270 μm and 215 μm lend credence to the mechanical arching hypothesis.

4.3.3 Comparisons of 10% strain and 0.75 cps

The same trend as for 15% strain continues for strain of 10% and cycle speed of 0.75 cps. For a bed depth of 2.54 cm, the normalized mass versus time relationship for the 8.7:1 treatment has a faster percolation rate than the 10.9:1 treatment as shown in **Figure 7**. At bed depths of 5.08 cm and 7.62 cm, the percolation rates of 8.7:1 and 10.9:1 are very similar. For all three bed depths, the percolation was statistically similar ($p > 0.05$) between 10.9:1 and 8.7:1. Again, the reversal observed for 2.54 cm bed depth was attributed to the pore size of coarse particles and the ability of the fines in the 10.9:1 ratio to form a mechanical arch in the pore spaces. In the preceding section's comparison the reversal occurred for bed depth of 5.08 cm, which had a higher strain (15%) and cycle speed (1.33 cps) compared with this case. Higher energy inputs impact deeper beds, thus a criti-

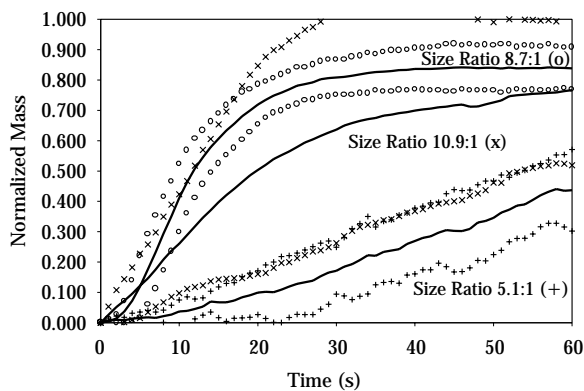


Fig. 6 Mean (solid lines) and 95% CI (symbols) for normalized mass as a function of time – Strain=15%, Cycle Speed=1.33 cycles/second and Bed Depth=5.08 cm

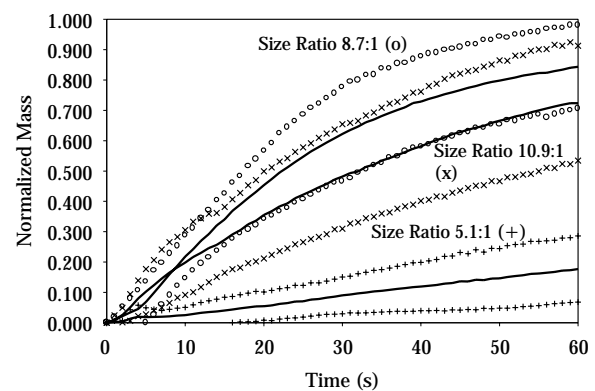


Fig. 7 Mean (solid lines) and 95% CI (symbols) for normalized mass as a function of time – Strain=10%, Cycle Speed=0.75 cycles/second and Bed Depth=2.54 cm

cal energy exists that selectively influences the reversal, i.e., can not dislodge the mechanical arches. As was the case with the previous comparisons, the percolation for 5.1:1 size ratio is significantly ($p < 0.05$) less than the other treatments. It was hypothesized that the fines in the 5.1:1 ratio are actually changing the pore structure of the coarse bed. In other words, the size of the fine particle is nearer the size of the pore space of the coarse particles and does not freely flow through the bed of coarse particles. Rearrangement of the coarse bed may be taking place. Generally, the fines in the other treatments are flowing freely through the pore spaces of the coarse bed and may alter the pore structure, but not to the extent to impede the rapid flow of fines.

4.3.4 Comparison at 10% strain and 1.33 cps

A change in cycle speed from 0.75 cycles/second to 1.33 cycles/second at a strain of 10% did not change the relationships found for 0.75 cycles/second. At the smaller bed depths of 2.54 cm and 5.08 cm, it appears a strain of 10% and cycle speed of 1.33 cycles/second provides enough energy to dislodge the fine particles for the 10.9:1 treatment because the percolation was greater than or equivalent to the 8.7:1 treatment (**Figure 8**). However, when the bed depth was 7.62 cm, it appears there was mechanical arching at the 10.9:1 treatment due to the lower percolation rate. However, for all three bed depths, the responses for 10.9:1 and 8.7:1 are statistically similar ($p > 0.05$). From these observations, it appears that the energy combination of a strain of 10% and a cycle speed of 1.33 cycles/second is large enough to dislodge mechanical arches in the 10.9:1 treatment at small bed depths. However,

this energy input is near its limiting value, because at the largest bed depth, arching is occurring.

4.3.5 Comparison at 5% strain

Several changes occur when the energy input is decreased to a strain of 5%. For all cases at strain of 5%, the percolation is greater for the 8.7:1 treatment than the 10.9:1 treatment and significantly greater ($p < 0.05$) at a cycle speed of 0.75 cycles/second. In fact at low input energy level corresponding to 0.75 cycles/second, the 10.9:1 treatment behaves statistically similar ($p > 0.05$) to the 5.1:1 treatment. An increase in energy input, i.e., increase in cycle speed from 0.75 cycles/second to 1.33 cycles/second, affects the relative percolation of the 10.9:1 ratio. The 10.9:1 percolation approaches the 8.7:1 percolation. This supports the hypothesis of mechanical arches forming in the pore spaces of the coarse particles. The relationships at strain of 5% also show the effect of strain on the percolation. The normalized mass accumulated after 60 seconds at a strain of 5% is appreciably lower than the mass accumulated at higher strains.

4.4 Other Treatment Variables and Their Effect on Percolation

The previous analyses qualitatively assessed the effect of size ratio on the percolation. However, the effects of three other parameters (strain, cycle speed, and bed depth) were also quantified. Strain, as discussed above, has a significant ($p < 0.05$) effect on the percolation rate. Higher strains resulted in a faster percolation (**Figure 9**). In most cases, cycle speed had minimal effect on the percolation rate (**Figure 10**).

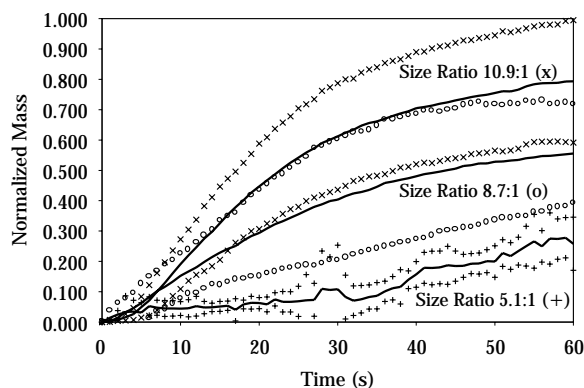


Fig. 8 Mean (solid lines) and 95% CI (symbols) for normalized mass as a function of time – Strain=10%, Cycle Speed=1.33 cycles/second and Bed Depth=2.54 cm

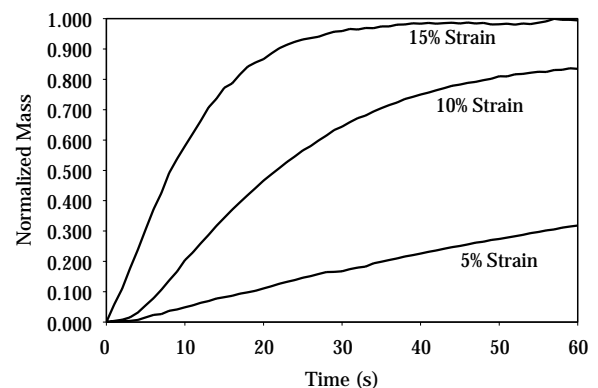


Fig. 9 Typical mass versus time relationships as a function of strain – Size Ratio=10.9:1, Cycle Speed=0.75 cycles/second, Bed Depth=5.08 cm

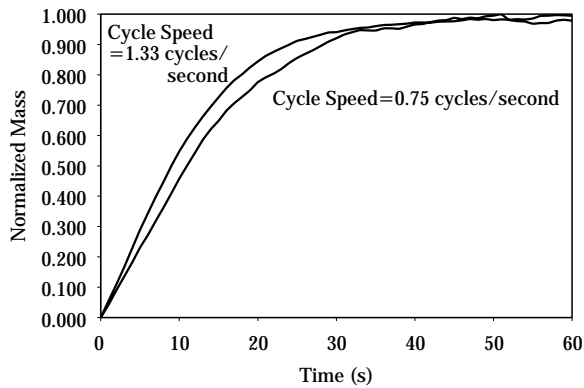


Fig. 10 Typical mass versus time relationships as a function of cycle speed – Size Ratio=10.9:1, Strain=15%, Bed Depth =7.62 cm

For 5.1:1 ratio, the bed depth also did not influence the percolation as expected. In some cases bed depth of 2.54 cm had a lower percolation rate than bed depth of 7.62 cm. However, these differences are not significant ($p > 0.05$).

5. Conclusions

A primary segregation shear cell (PSSC) has been designed and fabricated to measure the size-segregation response of fines traveling through a bed of coarse particles. The effects of size ratio, strain, cycle speed, and bed depth on the percolation of fine particles in binary mixtures of glass spheres were evaluated. Based on the test results, the following conclusions were made.

1. Size ratio was the most dominant variable that affected the percolation rate of fines through a bed of coarse particles. Based on the differences in percolation between the smaller size ratio of 6.4:1 and larger ratios of 8.7:1 and 10.9:1, there exists a critical size ratio which determines the mechanism of percolation. Two mechanisms were observed. First, the larger size ratios exhibited an initial free-fall, i.e., convective, discharge of fines at the beginning of the test. This initial discharge was followed by a diffusive behavior. The smaller ratios did not exhibit the initial discharge and their response was observed to be diffusive behavior.
2. Strain also had an effect. Input energy, as related to strain, was found to be critical in the type of percolation exhibited, i.e., the presence or absence of an initial rapid discharge. For the size ratio of

10.9:1, the amount of input energy was critical because the size of the fine particles was near the size of the coarse bed pore space. When the input energy was below a critical limit, mechanical arching was occurring. Although the input energy is a function of bed depth and cycle speed, these parameters did not influence the results outside random behavior.

3. The percolation of fines through a bed of coarse particles was isotropic. There was no observed bias in the collection pan at the end of the tests.
4. Significant differences ($p < 0.05$) were measured between individual load cells under different treatments in one out of six treatments. Many treatments were not significantly different ($p > 0.05$). However, when statistical comparisons were made in the effective percolation direction, differences ($p < 0.05$) were significant when comparing the size ratios of 10.9:1 and 8.7:1 to the size ratio of 5.1:1.

6. Acknowledgements

This study was partially funded by the U.S. Department of Agriculture and Pennsylvania Agricultural Experiment Station.

7. References

- 1) Ahmad, K. and I. J. Smalley. 1973. Observation of particle segregation in vibrated granular system. *Powder Tech.* 8:69-75.
- 2) Bagster, D. F. 1996. Studies on the effect of moisture content and coarse and fine particle concentration on segregation in bins. *KONA* 14:138-143.
- 3) Bridgwater, J., M. H. Cooke, and A. M. Scott. 1978. Inter-particle percolation: equipment development and mean percolation velocities. *Trans IChemE*, 56: 157-167.
- 4) Duffy, S. P. and V. M. Puri. 2000. Measurement of percolation velocity during shear. ASAE Paper No. 00-4008. ASAE, St. Joseph, MI.
- 5) Duffy, S. P. and V. M. Puri. 1999. Evaluation of the computer controlled dynamic yield locus tester. *Powder Tech.* 101:257-265.
- 6) Harwood, C. F. 1977. Powder segregation due to vibration. *Powder Tech.* 16:51-57.
- 7) Hwang, C. 1978. Mixing and segregation in flowing powders. Doctor of Philosophy Thesis. The Pennsylvania State University, University Park, PA.
- 8) Jenike, A. W. 1964. Bulletin No. 123 – Storage and flow of solids. Utah Engineering Experiment Station. Salt Lake City, Utah.
- 9) Johanson, J. R. 1988. Solids segregation – causes and solutions. *Powder and Bulk Eng.* 13-19.
- 10) Kamath, S., V. M. Puri, H. B. Manbeck, and R. Hogg.

1993. Flow properties of powders using four testers – measurement, comparison, and assessment. *Powder Tech.* 76:277-289.
- 11) Lawrence, L. R. and J. K. Beddow. 1968. Powder segregation during die filling. *Powder Tech.* 2:253-259.
 - 12) Markley, C. and V. M. Puri. 1998. Scale-up effect on size-segregation of sugar during flow. *Transactions of the ASAE*, Vol. 41(5): 1469-1476.
 - 13) Mosby, J., S. R. de Silva, and G. G. Enstad. 1996. Segregation of particulate materials – mechanisms and testers. *KONA* 14:31-42.
 - 14) Popplewell, L. M., O. H. Campanella, V. Sapru, and M. Peleg. 1989. Theoretical comparison of two segregation indices for binary powder mixtures. *Powder Tech.* 58:55-61.
 - 15) Puri, V. M., M. A. Tripodi, G. L. Messing, and H. B. Manbeck. 1995. Constitutive model for dry cohesive powders with application to powder compaction. *KONA* 13:135-150.
 - 16) Sleppy, J. A. and V. M. Puri. 1996. Size-segregation of granulated sugar during flow. *Trans. of the ASAE* 39(4): 1433-1439.
 - 17) Stephens, D. J. and J. Bridgwater. 1978a. The mixing and segregation of cohesionless particulate materials – Part I. Failure zone formation. *Powder Tech.* 21:17-28.
 - 18) Stephens, D. J. and J. Bridgwater. 1978b. The mixing and segregation of cohesionless particulate materials – Part II. Microscopic mechanisms for particles differing in size. *Powder Tech.* 21:29-44.
 - 19) Williams, J. C. and G. Shields. 1967. The segregation of granules in a vibrated bed. *Powder Tech.* 1:134-142.
 - 20) Williams, J. C. 1976. The segregation of particulate materials – a review. *Powder Tech.* 15:245-251.

Author's short biography



Shawn P. Duffy

Dr. Shawn P. Duffy was a Graduate Research Fellow in the Department of Agricultural and Biological Engineering at the Pennsylvania State University. He received his BS, MS and PhD from Penn State specializing in Powder Mechanics. Dr. Duffy received numerous recognitions including US Department of Agriculture National Needs Fellowship and Particulate Materials Center's Research Fellowship. He served on American Society of Agricultural Engineers Bulks Solids Storage and Properties of Cohesive Materials Committees. The work reported in this paper is based on his PhD research. Currently, Dr. Duffy is employed by PPG Industries, Inc, as a Research Engineer.



Virendra M. Puri

Dr. Virendra M. Puri is Professor in the Department of Agricultural and Biological Engineering at the Pennsylvania State University. Professor Puri also served as the Acting Director of the Particulate Materials Center, a National Science Foundation's Industry/University Cooperative Research Center. He is also the research thrust leader of *Powder Mechanics* group of the Particulate Materials Center. Dr. Puri received his B.S. from Indian Institute of Technology and M.S. and Ph.D. from the University of Delaware in Mechanical Engineering. Professor Puri's research interests include: measurement of fundamental engineering properties of powders, development and validation of constitutive models, and use of numerical methods to model flow, segregation, and compaction behavior of powders. He has served as the chairperson of the Bulk Solids Storage Systems Committee of the American Society of Agricultural Engineers. Professor Puri is a Co-Editor-in-Chief of the *Particulate Science and Technology, An International Journal*. Dr. Puri regularly offers a postgraduate course in the area of powder mechanics and several hands-on industrial short courses. Professor Puri has received several teaching and research awards.

A Load-Interactive Model for Predicting the Performance of Autogenous and Semi-Autogenous Mills[†]

Homero Delboni Jr.

*Dept. of Mining and Petroleum Engineering
University of São Paulo**

Steve Morrell

*Julius Kruttschnitt Mineral Research Centre
University of Queensland***

Abstract

The Julius Kruttschnitt Mineral Research Centre (JKMRC) has been involved in the study and modelling of industrial autogenous (AG) and semi-autogenous (SAG) mills for over 25 years. Recent research at the JKMRC has developed a new AG/SAG mill model which is based on charge dynamics. The model relates charge motion and composition to power draw and size reduction. Size reduction is described by considering impact and attrition/abrasion as separate processes. These are linked to energy available in the mill, the charge size distribution and the relative motion of the grinding media. Ore specific energy-breakage are described using laboratory data which are obtained from breakage tests over a wide range of energies and particle sizes. Slurry transport is described using the JKMRC's latest model which incorporates the effect of grate design. This paper describes the overall structure of the model together with its main sub-processes.

1. Introduction

The word autogenous is derived from the Greek autogenes which means self (auto) generated, born or produced (genes). In mineral processing however, autogenous grinding designates generically the action of rocks grinding upon themselves, as occurring in tumbling mills. For reasons that will be further addressed in this work, grinding in autogenous (AG) mills is frequently assisted by steel balls, in which case it is called semi-autogenous (SAG) grinding.

Conceptually, any AG/SAG mill consists of a rotary cylindrical metallic chamber in which the feed is continuously introduced through the hollow feed trunnion at one end and discharged to another. The discharge mode does vary substantially between hollow discharge trunnions to screen plates (grates) that can be either placed at the periphery of the cylinder or radially to the trunnion. The mill shell is internally protected by means of steel liners.

Today's extensive use of AG/SAG mills is credited to the combination of relative high throughput and

high reduction ratios allied with compactness of their physical installations. There is, consequently, an increasing demand for techniques, which enable the prediction of the performance of such equipment, under a wide range of conditions. Mathematical modelling and simulation have proven to be a reliable technique to assist the development of comminution circuits in conceptual design, scale-up from pilot plant test work and the optimisation of industrial operations. Over the last 30 years JKMRC has been continuously developing mathematical models of AG/SAG mill performance. The current model is incorporated in a computer program for process simulation – JKSimMet, which has been used successfully to simulate a number of closed and open circuit situations. It is arguably the most popular and widely used model in the world. There are, however, a number of areas where the model is still limited in its ability to predict the effect of changes in operational variables. In particular its limited inherent ability to relate the performance with charge composition and motion is seen as a major drawback. This has prompted the use of empirical “corrections” to the model (Mutambo, 1992; Morrell and Morrison, 1996), which resulted in the formulation of equations that have been only partially successful. Significant progress has been recently achieved towards the modelling of mill charge

* Av. Prof. Mello Moraes, 2373 – São Paulo, SP 05508-900 Brazil

** Isles Rd. Indooroopilly QLD 4075 Australia

[†] Accepted: October 28, 2002

dynamics, particularly those related to the effect of lifter bar design and the estimation of mill power draw. These progresses have been based on physically sound descriptions of the charge motion and the principal variables, which affect it. This scenario of increasing demand for a comprehensive model and the development of better knowledge of charge dynamics, lead to the initiation of a new AG/SAG mill mathematical model.

2. Objective

The main objective of this work is to describe the influence of the charge composition and motion on breakage performance such that it can predict the performance of the mill under all normally encountered operational conditions. The derived model should then incorporate a number of operating conditions as they influence the charge dynamics and therefore the breakage mechanisms involved in AG/SAG grinding as opposed to a rate process approach.

3. Review of AG/SAG Grinding Process Models

Researchers involved with power prediction were motivated by the possibility of reducing the large amounts of energy consumed in comminution plants. Accordingly, the energy-size relationships, or "laws of comminution" were extensively used in attempts to predict the power draw by crushers and ball/rod mills, based on one characteristic of the broken material. However, the energy approach proved to be inadequate for meaningful process simulation, specially in AG/SAG mills where the mill charge weight varied substantially.

The difficulty in maintaining the operation of AG mills in steady state motivated research groups to develop models to predict and control their dynamic behaviour. Such models were based on statistical correlations thus representing an intermediate stage towards more comprehensive approaches (Kelly, 1970). Three lines of models were since then pursued to model AG/SAG mills i.e., matrix models, kinetic models and perfect mixing models. However, following the evolution of computers, kinetic and perfect mixing models received much more attention from research programmes, to the detriment of matrix models, which were eventually abandoned.

The majority of the models developed were essentially case-specific and strongly dependent on site conditions. Moreover, they were not designed to take

into account the mechanisms involved in the process.

Wickham (1972) first incorporated the perfect mixing equation (Whiten, 1974) to AG/SAG modelling. A simplified matrix form was used, in which a condensed term adapted the model structure to ignore both load and discharge rate. Two distinct functions for rock breakage were considered i.e. impact and abrasion, but were non-ore specific.

Stanley (1974) published the first successful effort to model AG/SAG mills according to a mechanistic approach, as a result of a series of survey campaigns on both pilot plant and industrial mills. The underlying mechanism assumed was that AG/SAG mills are mixers in which both transport and breakage occurs. Furthermore, when rock fragments collide inside the mill, they generate broken particles, which will be distributed in other size fractions. Although the concepts used by Stanley were essentially mechanistic, the model created can be better classified as a phenomenological, because the mechanisms involved were treated as rate processes rather than genuine physical interactions, which could be predicted from simple generic laws.

Austin et al (1977) developed an AG/SAG model structure based on the kinetic model. The mean residence time of the particles within the load was used to correlate the batch grinding conducted in the laboratory, to the performance of pilot plant and industrial mills.

Leung (1987) used the perfect mixing model equation in its full form as well as a mass transfer empirical relationship. Leung developed a combined ore-dependent impact and abrasion function for describing breakage. Although average values were established, breakage rates were mill/ore dependent thus had to be fitted.

Morrell and Stephenson (1996) incorporated a phenomenological mass transfer relationship to Leung's model, based on an extensive work carried out on industrial mills.

3.1 The Perfect Mixing Model

The basic concepts of the perfect mixing model were developed by Whiten (1974) in which the rate of change of mill contents, due to breakage and flow, can be described by the following equation:

$$p_i = d_i s_i = f_i + \sum_{j=1}^i a_{ij} r_j s_j - r_i s_i$$

where

f_i mass flow rate of size fraction i in the mill feed

p_i mass flow rate of size fraction i in the mill discharge

- s_i mass of size fraction i in the mill load
- r_i breakage rate of size fraction i
- a_{ij} appearance function (fraction of broken particles from size fraction j which appears in size fraction i)
- d_i discharge rate of size fraction i

The perfect mixing model equation represents the mass balance of each individual size fraction of the mill charge. Accordingly, the entering particles (mill feed plus broken particles coming from coarser fractions of the charge) balance with the leaving particles (mill product plus the broken particles going to finer fractions of the charge).

3.2 Breakage Mechanisms

Much work has been conducted on the determination of breakage mechanisms prevailing in tumbling mills. The results obtained in the analysis of rod and ball mill operation, which dominated the literature, are not adequate for AG/SAG mill load analysis as the particle size range is more ample.

The majority of the authors dedicated to investigate the subject (Wickham, 1972; Stanley, 1974; Austin et al, 1977; Manlapig et al, 1979; Goldman et al, 1988, Kelly et al, 1990, Loveday et al, 1997) have selected a number of breakage mechanisms. Although a lot of controversy still persists in the literature, mainly derived from different nomenclatures for similar phenomena, the following mechanisms are considered to be predominant in AG/SAG mills: impact, abrasion, chipping and attrition.

It is important to emphasise that much of the confusion in the literature originates from the indistinct differentiation between cause and effect. The former is here defined as a combination of intensity and mode to impart energy to a fragment, while the latter is the resulted size distribution of broken fragments.

Schönerer (1993) affirmed that only the amount of energy imparted to a particle in any comminution machine should be considered to characterise the breakage event. The form of interaction is therefore irrelevant. However, both the breakage energy and mode are related to the motion of the charge. Hence, by relating the mode of breakage to charge dynamics, the energy associated with each mode can be determined.

A number of different tests to characterise the physical properties of material subjected to comminution are reported on the literature. They can be divided into those which are designed to reproduce the whole size reduction process within a mill (Bond, 1952; Kjos, 1985; MacPherson, 1987; Mörsky et al,

1994), and the ones created to assess an individual fragmentation mechanism, specific of the AG/SAG mill process (Narayanan, 1985; King et al, 1993).

The characterisation tests relevant to the present work are those which correlate specific energy imparted to a rock fragment and its correspondent degree of breakage.

Based on the above discussions, this work considers three main modes to impart energy to any particle in AG/SAG mills, which are showed schematically in **Figure 1** and described below.

- Impact, here referred as the action of a falling charge element, including balls or rocks, onto the particles lying on the exposed part of the charge.
- Abrasion, which includes the rubbing action of rock particles against each other, against balls or mill liners.
- Attrition, including the mechanism of particles being nipped between steel balls and larger ore particles rolling and sliding against each other.

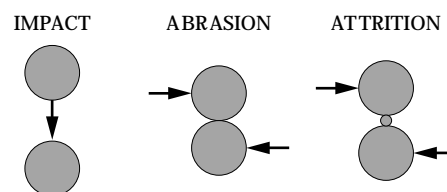


Fig. 1 Fragmentation Mechanisms and the Resultant Size Distributions.

3.3 Breakage Rates

Breakage rates are associated with the frequency breakage events. Leung (1987) assumed that the breakage rates were fixed and calculated average values for AG and SAG mills separately. The breakage rate distribution was not described by back-calculated relationships, but in terms of five values, at 128, 44.8, 16.0, 4.0 and 0.25 mm. The intermediate values for other sizes are calculated by interpolation which results in a smooth breakage rate curve as shown in **Figure 2**.

The robustness of Leung's model contrasts with the fact that breakage rates are affected by a number of operating conditions instead of depending only upon the equipment. Morrell et al (1994) also showed that the influence of variables such as ball charge, ball size, feed size distribution determines the perfor-

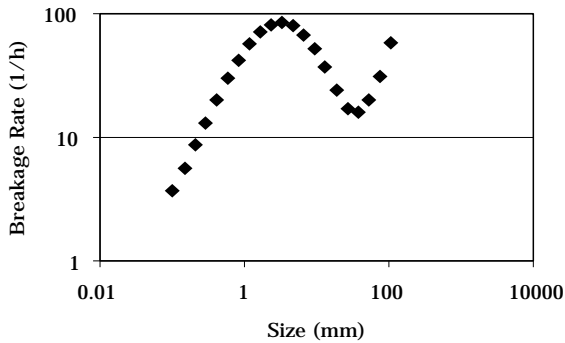


Fig. 2 Breakage Rate Distribution as Obtained by Leung.

mance of the process, thus directly affecting the breakage rate values.

As operating conditions determine breakage rates, difficulties were frequently experienced in predicting the performance of the mill under conditions much different from those used to fit the model parameters. In addition, design of full scale mills where no pilot data were available was limited to matching to the design of existing mills for which data were available.

The subject was investigated in detail by Mutambo (1992) in an attempt to empirically correlate breakage rate values with the operating conditions and design characteristics of a range of mills in the JKMRRC database.

4. The New Model

4.1 Description

In grinding mills the kinetic energy that the rotation of the mill shell imparts to the grinding media is subsequently transferred to ore particles with which they are in contact, so causing breakage. The kinetic energy of these breakage events is related to both the size and velocity of the grinding media whilst the frequency of these events is associated with the number of grinding media and the rate at which they circulate within the mill. The process has a discrete nature, as it comprises many individual collisions or breakage 'events'. The product of these breakage events may leave the mill via the discharge grate due to entrainment by slurry, or remain within the charge to undergo further breakage.

It follows from these arguments that for modelling purposes it is necessary to have a description of at least the following:

- Energy associated with each breakage event and its relationship to the charge.

- Frequency of breakage events for each size fraction and its relationship to the charge.
- Size distribution of the products from each breakage event.
- Classification performance of the grate.
- Relationship between slurry hold-up in the mill and its flow rate out of the mill.

The assessment and modelling of each individual element listed above are summarised in the following sections.

The modelling approach adopted in this work is based on the interaction between mill charge motion and size reduction mechanisms, which is believed to resemble a real mill operation. Although the individual assessment of mill charge dynamics and size reduction mechanisms have progressed substantially, none of the published AG/SAG models are directly based on the interactions between them.

The charge is assumed to be comprised of two different fractions i.e. the one which causes breakage, described as grinding media or 'contactors', and the one which receive the contacts, or 'contactees'. The motion of the contactors will therefore determine both the frequency and the intensity of the size reduction mechanisms. The two mechanisms selected to represent the size reduction mechanisms in AG and SAG mills were impact and attrition, which therefore have to be described according to the approach adopted in the charge motion model.

Modelling of the charge motion was based on the approach adopted by Morrell (Morrell, 1993) for predicting the power draw of tumbling mills. The model assumes the mill charge to be comprised of concentric shells. The slip between the shells causes a shearing motion and creates the conditions necessary for attrition breakage where relatively small particles are nipped between grinding media as they slide against one another. Impact breakage occurs predominantly in the vicinity of the toe of the charge where the grinding media impact after falling from the shoulder of the charge.

The Morrell model differentiates between the power associated with each of these mechanisms individually and provides separate estimates of impact and attrition power.

The grinding media are viewed as "contactors" in the model and are used to determine the input energy for breakage in each of these modes. The model using the rate at which the charge rotates as well as the rate at which the shells slide against one another also provided an estimate of the total frequency of breakage events in each mode.

The relationship between contactors and contactees is assumed to follow a pattern according to each mode of breakage. Underlying each of these relationships is the assertion that the surface area of the grinding media dictates the breakage frequency, whilst the probability that a contactee will be involved in a collision with a contactor is related to the surface area of the contactee.

The model operates in an interactive manner, which is believed to resemble a real mill operation. Therefore, after each iteration of the charge motion the grinding media is re-calculated according to the size reduction relationship. Accordingly, an arbitrary value of grinding charge volume is initially used as means to start the calculation of the charge size distribution. The grinding charge is considered to reach steady state after the constraint of fixed charge volume is eliminated and the grinding charge loop runs for a fixed number of iterations.

After each interaction the model calculates the slurry volume, which will fill the interstices of the grinding charge and may eventually raise above the grinding charge surface, thus giving rise to the formation of the slurry pool. If a slurry pool is formed, the next interaction will take into account its effect on the falling grinding media. The net result is a reduction of the impact velocity due to the buoyancy effect of the slurry pool.

The slurry volume is dictated by the discharge function and the mill throughput, together with the attrition mode of breakage, which is assumed to be prevalent on finer size fractions of the charge.

The mill charge motion is considered to be comprised of a number of shells, which slide against one another. Attrition breakage therefore occurs in the interstices between contiguous shells as well as in the voids of the grinding charge. It follows that for a breakage charge volume and mill charge motion there is a limited "volume associated to attrition sites" to be filled with particles. For situations where the charge slurry volume is smaller than the volume of attrition sites, no correction is necessary as any solid particle in the slurry will be within the breakage charge. However, as the slurry pool starts to build up in the mill chamber, the reverse occurs i.e. there will be more particles than breakage sites which decreases the attrition breakage performance of the mill. The model therefore incorporates a correction factor to take into account the slurry pool effect on attrition breakage.

After the stabilisation of the grinding charge loop, the model iterates until the entire charge size distrib-

ution, charge volume and product size distribution stabilises.

One of the most prominent characteristics of the model resides on its structure and consequently on the mode in which it iterates. Instead of utilising the information to iterate backwards as most models do, the new model generates the necessary information based solely on the mill design characteristics, operating conditions and ore characterisation results, as input data. Therefore, the new model is not based on variables that are inherently operation dependent or necessitate scale-up procedures.

The fact that current AG/SAG mill models are not based on mill charge dynamics determines a number of limitations with them. Although a number of operating variables and mill design characteristics have been carefully assessed, they were incorporated in current models by simplistic parameterisation that limited their application.

The load-interactive approach adopted in the model incorporates a comprehensive description of the charge motion. Initially designed by Morrell (1993) to predict the power draw, the Morrell model was based on the location of the charge toe and shoulder for each shell, as the bulk of the charge was divided. The Morrell model was modified to incorporate Powell's (1991) equations for describing the trajectory of particles in contact with the lifter bars, including the effect of the angle of the lifter bar on the trajectory to be determined. Apart from the shell structure of the charge no assumptions are made about the shape that the charge takes up.

The net result is a model which predicts the motion of the grinding charge as well as the power draw under a wide range of operational and design conditions, and includes the effects of such factors as particle size, lifter bar geometry, mill filling and mill speed. The effects of the grate design is also directly included in the model as the discharge model is determined by grate open area and geometry. These factors are therefore incorporated into the size reduction part of the model.

The model also includes the prediction of the ball consumption of the simulated mill, together with the ball size distribution in the mill charge. The first is a characteristic not found in the current AG/SAG mill models even though it is valuable information in a mill design scenario. The estimation of the ball size distribution in the mill charge represents a significant decrease in the amount of input data to the model, which is also convenient for the user as this information is rarely available.

4.2 Model Structure

The model structure involves a number of sub processes according to different levels in a rather complex scheme. **Figure 3** summarises the main structure of the model showing the input data, calculation loops and output data. Following the input of mill design characteristics, operating conditions and feed, the model begins execution by assigning an initial estimate of the mill charge volume.

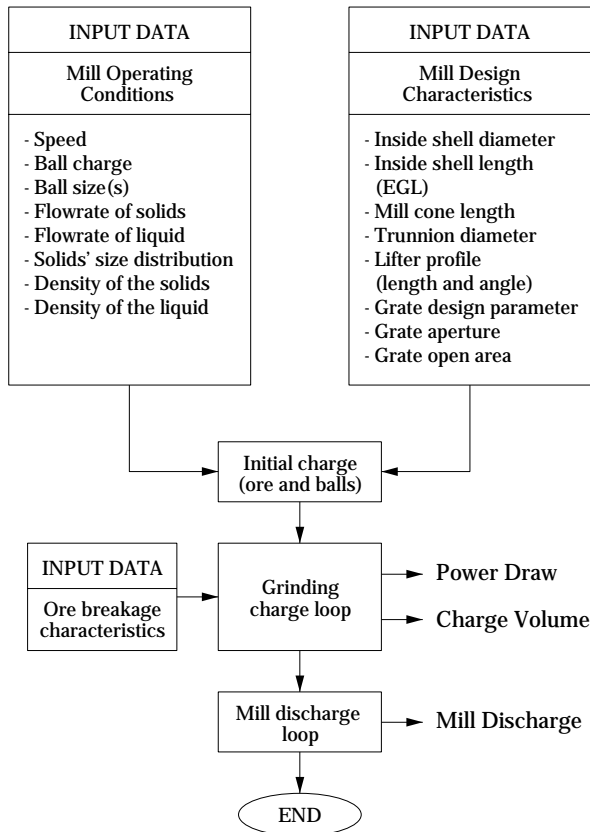


Fig. 3 Schematic Flow Sheet of the AG/SAG Mill Model.

The initial charge has the same size distribution as the mill feed, therefore resembling the start of the mill operation. The initial charge enters the grinding charge loop following an iterative process that provides the charge volume and mill power draw based on the mill charge motion and ore breakage characteristics. As the grinding charge loop reaches the stabilisation criterion, the model proceeds to the calculation of the mill discharge size distribution and thus finishing the cycle. Both grinding charge loop and mill discharge loop are further discussed in the following sections.

4.3 Grinding Charge Loop

Figure 4 shows in detail the schematic flow sheet of the grinding charge loop. Initially, the charge motion model provides the first estimation of the initial charge breakage energy and frequency based on the calculated characteristic media size. The total breakage energy and frequency are divided according to each of the breakage mechanism i.e. impact and attrition. The energy is then distributed to each size fraction which results in the estimation of individual values of impact and attrition specific breakage energies for all particle sizes.

The breakage of each size fraction according to both impact and attrition are calculated considering the individual values of breakage energy together with the ore breakage characteristics.

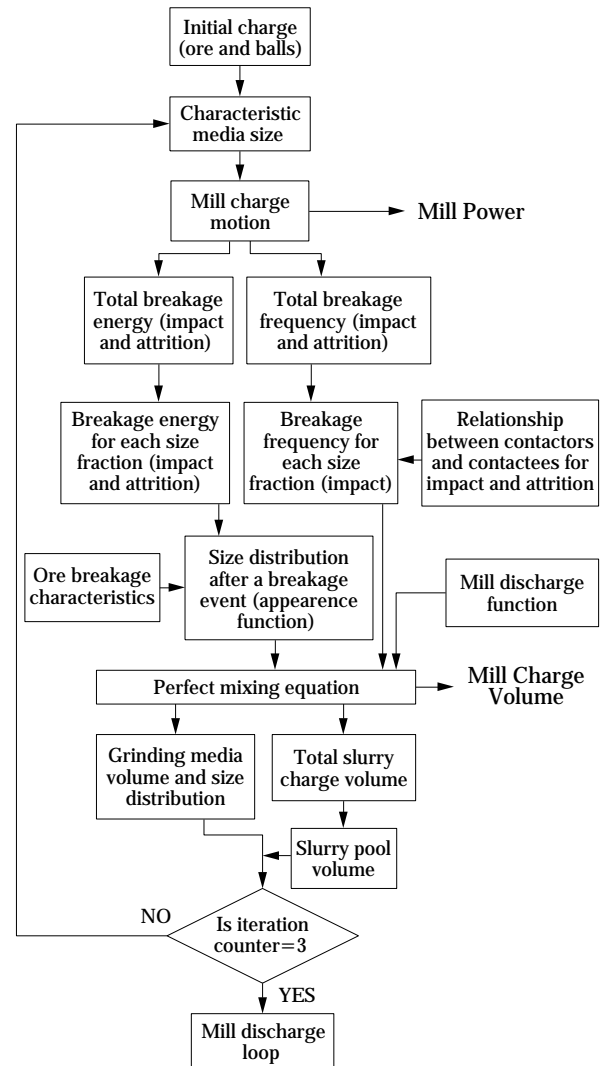


Fig. 4 Grinding Charge Loop.

The frequency of contacts follow the same procedure as the total amount of contacts is distributed to each size fraction according to a relationship between contactors and contactees. The resulting breakage of each individual size fraction is then calculated on the basis of breakage energy and frequency.

A discharge rate is associated with each size fraction using a hold-up – flow rate model. Mathematically the various sub processes are brought together according with an extended version of the perfect mixing model equation, as follows:

$$f_i - d_i s_i + \sum_j^{i-1} s_j (a_{ij}^{imp} r_j^{imp} + a_{ij}^{att} r_j^{att}) - s_i [r_i^{imp} (1 - a_{ii}^{imp}) + r_i^{att} (1 - a_{ii}^{att})] = 0$$

where

- r_i^{imp} impact breakage rate of size fraction i
- r_i^{att} attrition breakage rate of size fraction i
- a_{ij}^{imp} impact appearance function
- a_{ij}^{att} attrition appearance function

Therefore, after each interaction the model estimates the total volume, which is discharged out of the mill through the grate. The discharge rate is calculated using a hold-up flow rate model (Morrell and Stephenson, 1996) in combination with the classification function, resulting in the following equation:

$$d_i = C_i Q^{0.5} A^{0.5} \gamma^{1.25} \phi^{-0.67} D^{0.25} V_m^{-1}$$

where

- C_i classification function at size i
- Q flowrate through the grate
- A grate open area
- γ mean relative position of the grate apertures
- ϕ fraction of mill critical speed
- D mill diameter
- V_m volume of the mill charge

The net result after the discharged volume calculation is a new grinding charge volume and new grinding charge size distribution, which serves as the starting values for subsequent interactions. At this stage the model estimates the total slurry volume in the mill charge comprising the finer fractions of ore together with the water held-up in the mill.

As the model assumes that only part of the charge will determine the frequency and intensity of the breakage events, the structure was configured in a way to first establish a stable grinding charge. Therefore, after each iteration of the charge motion the grinding media is re-calculated according to the size reduction relationship. The grinding charge is considered to reach steady state after the constraint of fixed charge volume is eliminated and the grinding charge

loop runs for a fixed number of iterations.

After each interaction the model calculates the slurry volume, which will fill the interstices of the grinding charge and may eventually raise above the grinding charge surface, thus giving rise to the formation of the slurry pool. If a slurry pool is formed, the next interaction will take into account its effect on the falling grinding media. The net result is a reduction of the impact velocity due to the buoyancy effect of the slurry pool.

4.4 Charge Motion

The motion of the mill charge is caused primarily by the transfer of momentum from the mill shell to contiguous particles according to a succession of contacts. As there is a slip between particles, part of the imparted energy is dissipated, resulting in a loss of rotational rate among adjacent layers from the mill shell to the inner surface of the charge.

Morrell (1993) established an experimental campaign in a laboratory glass ended mill from which he was able to calculate a series of velocity profiles of mill charge according to variations in mill rotational speed, mill charge volume, particle size, among others. He derived a series of expressions, which allowed the charge angular velocity gradient to be calculated. He also derived expressions to calculate the position of toe and shoulder angles as a function of selected operating variables.

The subject is in fact one of paramount importance for mill operation, as it drives both the mill power draw and the comminution process performance. Accordingly, depending upon the amount of slip in the mill charge, the energy imparted to the charge will be split into attrition, abrasion or dissipated through heat as a by-product of friction.

However, it was assumed in the Morrell model that no slip occurs at the shell wall. Such a simplification is a valid first approximation in the case of AG/SAG mills, as it does not significantly influence the power draw by this equipment, which in fact was the main purpose of the Morrell model. Nevertheless, as a wide variety of lifter bar profiles are currently found in industrial units the comminution performance of the mill can be altered depending upon the specific application. Moreover, there is an increasing interest of industry towards a means of predicting the trajectory of the outer shells' particles as a function of the lifter bar profile. Most of that interest is motivated by the consequences of inadequately designed lifter bars, which have reportedly caused severe damage to mill shells (Johnson et al, 1994).

It is important therefore to separate the behaviour of shells whose trajectories are directly influenced by the lifter bars and those which are not. The former are physically elevated by the action of the lifter bar surface thus showing no slippage with mill shell, whereas the latter are mostly influenced by the coefficient of friction between neighbouring shells.

Two distinct treatments were therefore adopted to predict both the shoulder and toe angles of individual shells. A theoretical one comprising the motion of those shells directly influenced by the lifter bars and an empirical one for the inner shells.

The theoretical approach was based on the work initiated by Vermeulen (1985) and further enhanced by Powell (1991), whilst the empirical one was based on Morrell (1993).

Once the trajectories of the shells influenced by the lifter bar are established, the remaining shell trajectories are determined based on Morrell's expressions to calculate the loss of rotational rate between contiguous shells, together with the empirical expressions for the shoulder and toe positions.

The net result of the above scheme was a model which predicts the motion of the grinding charge as well as the power draw under a wide range of operational and design conditions, and includes the effect of such factors as particle size, lifter bar geometry, mill filling and mill speed.

Apart from the shell structure of the charge no further assumptions were made about the shape that the charge takes up. However a lifelike prediction of the charge motion is provided by the model and is typified by the example shown below.



Fig. 5 Simulation of Charge Motion Profile.

4.5 Breakage Energy

The new AG/SAG model differentiates the breakage processes occurring in AG/SAG mills into two main mechanisms. Accordingly, the slip between the shells causes a shearing motion and creates the conditions necessary for attrition breakage where rela-

tively small particles are nipped between grinding media as they slide against one another. Impact breakage occurs predominantly in the vicinity of the toe of the charge where the grinding media impact after falling from the shoulder of the charge.

The Morrell model estimation of the bulk power associated with each of these mechanisms was the basis to establish the relationships, which associates the mill charge motion with specific comminution energy for all size fractions of the mill charge. The grinding media are viewed as contactors in the model and are used to determine the input energy for breakage in each of these modes.

The separation of impact from attrition was a departure from the way most models treat breakage. Until now it has been usual to describe breakage in terms of a single specific energy imparted to the particles, resulting from a combination from various size reduction mechanisms.

The motion of the charge was therefore described in terms of the breakage frequency and energy associated to each size reduction mechanism. Accordingly, the bulk power associated to the grinding charge according to impact and attrition was distributed to the entire charge of the mill. The interpretation of the physical mechanisms involved in the charge motion was therefore the basis to model the selected size reduction mechanisms independently.

To fully describe the model, it was necessary to have functions, which describe the way the total breakage frequency and energy is distributed amongst the size fractions of the contactees.

The total power associated with impact was directly derived from the mill charge motion model. The power attributed to impact was thus calculated from the power consumed by each shell to elevate the media elements and the frequency of contacts attributed to the media elements. The power consumed by individual shells was provided by the Morrell model.

The charge motion model adopted a shell description of the charge according to which all grinding media elements follow a circular trajectory up to the point where they enter a free fall trajectory. The cycle is completed as the grinding element re-enters the circular path at the toe of the charge.

To determine the rate at which breakage energy is imparted to the contactees, or the total number of impacts as shown in **Figure 6**, a simple approach was adopted by assuming that impact is directly related to the motion of the charge. These two assumptions were used to calculate the average energy associated with each impact event. From the shell description

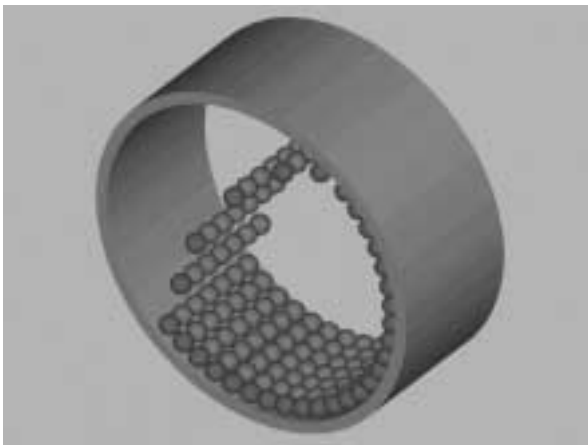


Fig. 6 Three-Dimensional Representation of a Shell Cycle.

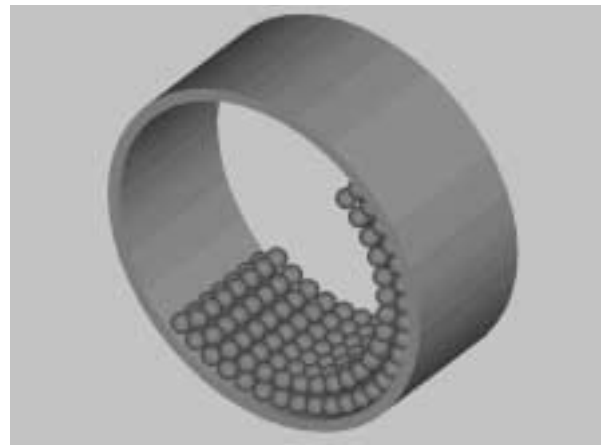


Fig. 8 Three-Dimensional Representation of the Surface Formed Between Contiguous Shells.

used by the model the mean energy associated with each impact was then estimated.

Attrition breakage was considered to occur due to nipping in between media as they slide and roll over one another. It was further assumed that attrition has an upper limit which is equal to the charge lower limit size i.e. attrition mode of breakage is restricted to particles smaller than those which form the grinding media.

The approach adopted to describe attrition energy was equivalent to the one described for impact. Accordingly, the energy attributed to attrition was calculated from the power consumed as a result of slip amongst contiguous shells and the frequency of contacts attributed to the media elements. The attrition power consumed by individual shells was provided by the Morrell model whereas the frequency of attrition events was determined from the relative velocity of contiguous shells and their surface area, as schematically described in **Figures 7 and 8**.

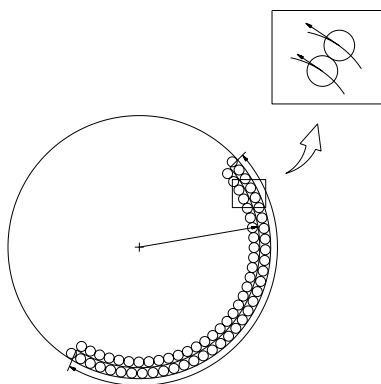


Fig. 7 Surface Formed Between Contiguous Shells with Different Rotational Speeds.

4.6 Breakage Frequency

The frequency at which impact and attrition breakage occur was considered to be the amount of impacts per particle per unit of time, according to the definition established by Morrell (1989). The definition of what constitutes a breakage event and its subsequent parameterisation was then necessary to describe the frequency at which the size reduction mechanisms occur in the mill.

The approach adopted in this work was based on the mechanistic description of the interactions between contactors and contactees. A more detailed interpretation was however necessary in order to establish a procedure to predict the breakage frequency associated with impact and attrition according to each mill charge size fraction.

The equations developed to represent both impact and attrition breakage frequency were based on the same approach i.e. the total number of breakage events associated with the contactors was distributed amongst the mill charge particles according to a partition term. These partition terms were established on the basis of the mechanisms derived from the charge motion and according to each specific size reduction mode used.

The impact events generated by the motion of the grinding media (impactors) are distributed amongst the impactees according to a mechanism based on surface area of the particles. Therefore, the estimation of impact breakage frequency involves two main terms i.e. a specific impact generation rate as well as a partition term, which divides such a rate of events amongst each individual size fraction. A secondary term was introduced as recourse to calibrate the relationship.

The impact breakage rate was therefore estimated as follows:

$$r_i^{imp} = \Gamma^{imp} P_i^{imp} K_i^{imp}$$

where

- r_i^{imp} impact breakage frequency of size fraction i
- Γ^{imp} specific impact generation rate
- P_i^{imp} impact partition term
- K_i^{imp} constant

The average number of impact contacts per particle comprises the ratio between the total number of impact contacts generated and the total number of particles which forms the grinding charge.

The total number of impact contacts was derived from the Morrell model, which was based on the grinding charge comprising solely of mono-sized particles. This number was subsequently normalised according to the number of grinding media particles. Numerically this relationship was expressed as follows:

$$\Gamma^{imp} = \left\{ \frac{\sum_1^n N_s^{imp}}{\varepsilon} \right\}$$

where

- N_s^{imp} number of impact contacts per unit time given by shell s
- n number of shells
- ε total number of grinding charge particles with an equivalent size equal to C , given by:

$$\varepsilon = \left[\frac{\sum_1^m (s_i + s_i^b)}{\left[\frac{C^3 \pi}{6} \right]} \right]$$

where

- s_i volume of all ore particles contained in size fraction i
- s_i^b volume of all steel balls contained in size fraction i
- m size fraction which contains media size lower limit value
- C characteristic media size

The specific impact generation rate is the average frequency with which a grinding media element impacts the toe region.

The impact partition term represents the distribution of the impact breakage events provided by the grinding media elements to the impactees. Accordingly, this term incorporates the mechanism attributed to the interactions between impactors and

impactees, according to which the surface area dictates the interactions.

The impacts generated by the entire ball charge were considered to act indistinctly on all impactees regardless of the particle size. It was assumed that below the toe of charge steel balls re-transmit any impact they received. This energy was therefore considered to be absorbed by the rock charge. Hence balls were not considered impactees.

As for impact, the attrition events generated by the motion of the grinding media (attritors) are distributed amongst the attritees according to a characteristic mechanism based on surface area of the particles. However, the effective attrition contacts i.e. those which cause attrition breakage, were considered to represent a size relationship between attritors and attritees. Accordingly, the model assumes that only a certain size of particle provides adequate sites to capture and subsequently break other particles by attrition.

4.7 Ore Characterization

The size distribution resulting from a breakage event, or appearance function, comprises the combination of the energy associated to the breakage event together with the results of the energy-breakage relationship calibrated for the ore investigated. Although two modes of imparting breakage energy to the particles were presented and further parameterised, the particle's response in terms of breakage is considered solely on the basis of the corresponding fragmentation, which results from the amount of energy imparted, regardless the mode of breakage. This is equivalent to assuming that even though the mode of applying energy to a particle in a AG/SAG mill may vary substantially, the resulting breakage will depend only on the particle characteristics and the total amount of energy received by the particle.

The ore breakage characterisation data resulted from two particular laboratory tests, which were developed at JKMRRC i.e. the drop-weight impactor and the tumbling test (Napier-Munn et al, 1996).

The drop-weight impactor is able to accommodate particles in the size range 10-100 mm thus covering the range of sizes typically found in the grinding media of AG and SAG mills. It is used to generate energy-breakage data comprising usually a 0.25 to 2.5 kWh/tonne range of specific energies applied to particles. The test reproduces breakage events carried out on individual particles, even though in a typical programme a number of particles are tested as to minimise the effects of ore heterogeneity as well as

experimental errors. **Figure 9** shows a schematic of the JKMRC drop weight testing device.

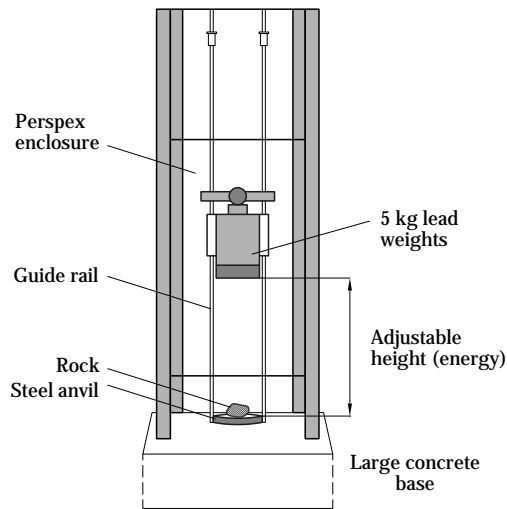


Fig. 9 The JKMRC Drop-Weight Testing Device.

The autogenous tumbling test was designed to create an environment where the breakage energy imparted to each particle is very small thus resulting in size reduction typical of abrasion and chipping. The data generated from this test were re-interpreted not as a secondary parameter to the model but instead, in terms of a energy-breakage relationship.

The experimental data obtained from drop-weight and tumbling tests were treated separately according to the procedures described in previous sections. The information derived from such treatment were combined into a single system which constitutes the ore breakage characterisation, further used by the model to calculate the appearance function.

The breakage characterisation system adopted by the AG/SAG model consists of two complementary groups of information. The first group involves the relationship between specific energy associated to a breakage event and a breakage parameter representing a single point of the size distribution of corresponding broken particles. Accordingly, the specific energy (kWh/tonne) values derived from the drop-weight test impacts were associated with a breakage parameter obtained from the sizing of broken fragments, in this case t_{10} or the percent passing at one-tenth of the original fragment size. The specific energy (E_{cs}) and breakage parameter (t_{10}) relationship was described in terms of a matrix, as shown in the first two columns of **Table 1**. The information

obtained from the tumbling test was directly incorporated to this matrix as noted in the first line. The combination of results from both drop-weight device and tumbling tests provided a comprehensive assessment to the energy/breakage relationship.

The second group of information related the breakage parameter t_{10} to the entire size distribution of broken fragments. The t_{10} was therefore associated with t_2 , t_4 , t_{100} or the other t_n 's which characterise the corresponding size distribution. The full size distribution is predicted by successive interpolations conducted over the regressed t_n values. The tumbling test results were also included into the drop-weight t_{10}/t_n matrix as an extra line, as shown in **Table 1**.

Table 1 Relationship Between E_{cs} and t_n .

E_{cs} (kWh/tonne)	t_{10} (%)	Parameter t (%)	
		t_2	t_{100}
6.0×10^{-4}	1.77×10^{-2}	1.87×10^{-2}	1.38×10^{-2}
0.50	20	63.1	7.5
1.25	30	84.2	11.4
2.50	50	99.9	20.2

5. Validation

The model validation exercise represents a critical step in the analysis of the model's ability to reproduce a real mill operation and, by extension, establishes the limits of the model's application as well. Accordingly, the new AG/SAG mill model was evaluated on its predictive capacity to resemble the interactions between the load and mill operating conditions. The simulations thus aimed to assess the load composition as influenced by different conditions on the resulting breakage and power draw. The analysis included the load interaction with the following variables:

- Mill Throughput
- Slurry Pooling
- Grate Design and Open Area
- Lifter Bar Design
- Mill Speed
- Ore Breakage Characteristics

Industrial AG/SAG mills have a characteristic relationship between the load and the mill throughput, which tends to be more prominent as the ball charge decreases. Accordingly, the load of an industrial AG mill increases with throughput up to a point where the increments will decrease progressively. This is equivalent to say that there is a non-linear relationship

between them.

In terms of mathematical simulation of AG/SAG mills the relationship between load and throughput determines the ability of the model to reproduce overload conditions, which in industrial mills, often coincides with the filling of 35%.

To assess this relationship, the data obtained from a selected industrial mill was chosen as they represent the operation of a large mill (9.5 m in diameter) in conditions of high load level. The simulation results obtained with new and Leung's model are shown in **Figure 10**.

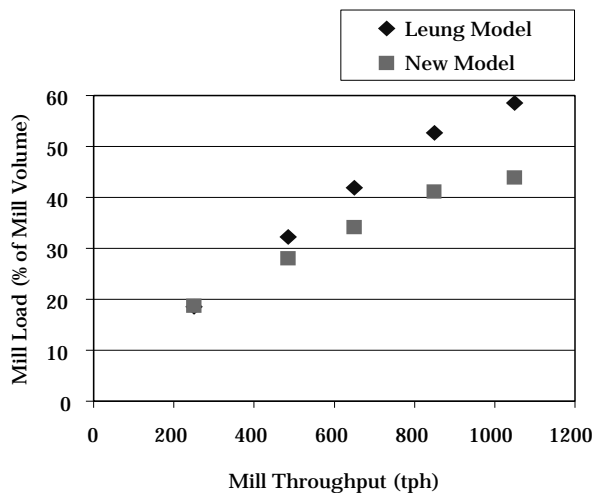


Fig. 10 Relationship Between Mill Load and Throughput.

It is clear from **Figure 10** that the simulations using Leung's model resulted in tendency of a linear relationship between the mill throughput and mill load whereas the new model showed a non-linear response. Accordingly, both Leung's and new model load level predictions coincides at the throughput of 250 tonne/h which in this case was equivalent to 19% of mill volume. However, from this point onwards Leung's model predicts mill loads up to more than 55% as the throughput increases whilst the new model shows a tendency to flat out at 40% of the mill volume.

Even though the survey campaign carried out on the selected mill operation did not include a step change procedure to validate the above simulated results, the new model clearly resembles the industrial mill operation as opposed to the results obtained with Leung's model.

Although the new AG/SAG mill model was designed to incorporate a number of mill operating con-

ditions and design characteristics not included in existing models, its predictive capacity was compared with Leung's AG/SAG model. The comparisons were conducted in terms of the most significant variables of the mill performance i.e. power draw and discharge size distribution.

Each of the models was then applied to an industrial mill database and the relative error of their predictions calculated. The comparisons were based on the predictions relative to the mill power draw and mill discharge P_{80} . **Table 2** summarises the individual values obtained according to each data set and model used. The mean relative error and standard deviation were calculated for each set of model predictions.

The fact that the new AG/SAG model predicted steady mill charges for all the 17 data sets as opposed to the other model tested indicated its superior capacity to reproduce the database. However, as Leung imposed no limits for the mill charge, it was decided to conduct the comparisons using the charge volumes as predicted by the models.

The results showed in **Table 2** indicated generally very high values of the standard deviation associated with the mean relative error. Accordingly, although the mill power draw predictions showed relatively

Table 2 Predictions of Mill Power Draw and Product Size Distribution.

Operation/ Survey	Mill Power Draw (MW)			Mill Discharge P80 (mm)		
	Exper.	Leung	New	Exper.	Leung	New
Mill # 1						
1	7.13	7.77	7.12	0.97	2.22	1.42
2	6.85	7.53	7.04	1.13	4.97	1.31
3	7.13	7.43	7.04	0.96	8.19	1.90
4	6.77	7.33	6.55	1.13	5.72	1.75
Mill # 2						
1	5.76	3.85	3.91	0.24	0.27	0.42
2	2.34	3.72	2.60	0.82	0.34	0.32
3	3.28	5.15	4.60	1.02	0.33	0.55
4	3.93	5.76	4.89	0.86	0.32	1.50
5	6.07	5.02	5.79	0.69	0.34	0.60
6	5.72	4.55	4.80	0.58	0.28	0.50
7	6.07	6.24	4.82	1.08	0.33	0.47
8	5.68	4.40	4.98	0.26	0.28	0.28
9	5.95	5.41	4.37	1.43	0.32	1.73
Mill # 3						
1	2.50	2.88	2.80	0.44	0.62	0.44
2	2.60	2.00	1.95	0.20	0.45	0.42
3	2.45	2.30	2.24	0.40	0.50	0.33
4	2.63	2.89	2.85	0.89	0.67	0.43
Relative Error	Mean	-7.1	1.7		-78.2	-8.4
	Std. Dev.	27.3	18.6		230.6	50.3

lower mean values the standard deviations varied in the range of 18.6 to 27.3%. The new AG/SAG model is better than Leung's as determined by the respective relative error means and standard deviations. Accordingly, the new model over predicted the power draw by 1.7% whilst the other model under predicted by 7.1%.

The predicted mill discharge size distributions represented by the P_{80} parameter showed a totally different picture as the new model resulted much superior than the other model. The new model provided the lowest standard deviation of the relative error (50.3%) whereas the other model resulted in a corresponding value of 231%.

Overall the new model provided the lowest mean relative error and standard deviation for both mill power draw and mill discharge size distributions.

Additional Model Features

The slurry accumulation within the mill load was investigated in terms of its effects on mill performance for all 17 data sets. A series of comparisons between different circuit configurations showed that the effects caused by slurry pooling at both impact and attrition terms of the new model resulted in correct tendencies of both mill power draw and mill discharge size distribution.

The simulations designed to assess the mill performance caused by grate design and total open area predicted variations of slurry hold up in the mill charge according to the expected behaviour of a full scale mill. The results should therefore be coupled with effects of slurry pooling on the mill power draw and discharge size distribution.

The new model incorporated the effects of the lifter bar design on the mill performance. The simulated mill performance reflected accordingly the changes in the charge motion. Supplementary information was obtained as the simulations indicated whether the points of impact associated with the outer shells were onto the charge or the mill liner. This is a potential feature for optimisation of the lifter bar profile. **Figure 11** shows the representation of a simulated charge profile.

The effects of mill speed on the charge motion were evaluated. The results indicated consistent variations of charge volume and corresponding mill power draw. The mill discharge size distribution reflected accordingly the relative variations of impact and attrition breakage mechanisms with mill speed.

On the basis of 17 AG/SAG mill data sets the new



Fig. 11 Simulated Charge Profile Corresponding to a Lifter Bar of 120 mm and Angle of 90° for a 9.6 m diameter SAG mill.

model was found to provide consistent estimations of both mill power draw and product size distribution. In both cases the differences between the standard deviation of the relative error associated with the estimations were very close to the data measurement standard error.

Even though the differences obtained for the mill power draw and product size distribution were relatively small, it should be emphasised that the high magnitude of the data relative error which may not be tolerable in greenfield estimations.

6. Conclusions

A model was developed to describe the influence of the charge composition and motion on breakage performance such that it can predict the performance of AG/SAG mills under all normally encountered operational conditions. The parameters derived from the mechanistic description of the charge dynamics were incorporated into distributions of both impact and attrition breakage frequency and intensity. The validation exercise indicated that the new model predictions were better than an existing model as well as incorporates a number of additional features related to the mill design and operating conditions.

7. Notation

A	grate open area	(m^2)
a_{ij}	appearance function (fraction of broken particles from size fraction j which appears in size fraction i)	
a_{ij}^{att}	attrition appearance function	
a_{ij}^{imp}	impact appearance function	
C	characteristic media size	(m)
C_i	classification function at size i	

D	mill diameter	(m ²)
D _i	discharge rate of size fraction i	(h ⁻¹)
f _i	mass flowrate of size fraction i in the mill feed	(t/h)
K _i ^{imp}	constant	
n	number of shells	
m	size fraction which contains media size lower limit value	
N _s ^{imp}	number of impact contacts per unit time given	
P _i ^{imp}	impact partition term	
p _i	mass flow rate of size fraction i in the mill discharge	(t/h)
Q	flow rate through the grate	(m ³ /h)
r _i	breakage rate of size fraction i	(h ⁻¹)
r _i ^{imp}	impact breakage rate of size fraction i	(h ⁻¹)
r _i ^{att}	attrition breakage rate of size fraction i	(h ⁻¹)
s _i	mass of size fraction i in the mill load	(t)
s _i ^b	volume of all steel balls contained in size fraction i	(m ³)
V _m	volume of the mill charge	(m ³)
ε	total number of grinding charge particles	
φ	fraction of mill critical speed	
γ	mean relative position of the grate apertures	
Γ ^{imp}	specific impact generation rate by shell s	(h ⁻¹)

8. Glossary

angle of the lifter – angle formed between the lifter face and its base

appearance function – size distribution of broken fragments

breakage rates – frequency of breakage

comminution – process of size reduction

discharge function – description of the probability of a size fraction to be discharged from the mill chamber

grate – perforated steel plate installed in the mill discharge end designed to classify the mill charge

greenfield estimation – estimation not based on operating mill or pilot plant campaign

grinding media or contactors – coarse rocks and steel balls contained in the mill charge

JKMRC – Julius Kruttschnitt Mineral Research Centre, University of Queensland, Australia

JKSimMet – commercial software for mass balancing, modelling and simulation of comminution

lifter bar – steel bar installed in the mill internal wall to assist the charge lifting

matrix models – mathematical models where all variables are structured in matrices

mechanistic approach – representing a phenomenon by its mechanisms

P₈₀ – size at which 80% of the mass passes of a given size distribution

rate process approach – mathematical description of comminution based on rates of change

reduction ratio – ratio between the characteristic sizes of the mill feed and discharge solids

shoulder of the charge – uppermost point reached by grinding media

slurry hold-up – pulp retention in the mill chamber

slurry pool – accumulation of pulp above the charge in the mill chamber

specific energy – energy per mass (kWh/tonne) imparted to a fragment

toe of the charge – outermost point where the grinding media impact after a falling trajectory

trunnion – steel cylindrical projection forming the mill feed and discharge ends

tumbling test – test in which 3 kg of –55+38 mm fragments are tumbled in a laboratory mill for 10 minutes

References

- 1) AUSTIN L.G., WEYMONT, N.P., PRISBREY, K.A., HOOVER, M., Preliminary results on modelling of autogenous grinding. Proc. 14th Int. Symp. APCOM, 1977, p.207-26.
- 2) BOND, F.C., The third theory of comminution. Trans. AIMME, 1952, 193, p.484-94.
- 3) GOLDMAN, M. and BARBERY, G., Wear and chipping of coarse particles in autogenous grinding: Experimental investigation and modelling. Minerals Engineering, 1988, 1 (1), p.67-76.
- 4) JOHNSON, G., HUNTER, I., HOLLE, H., Quantifying and improving the power efficiency of sag milling circuits. Minerals Engineering, 1994, 7 (2/3), p.141-152.
- 5) KELLY, F.J., An empirical study of comminution in open circuit ball mill. Trans. CIM, 1970, 73, p.119-127.
- 6) KELLY, E.G. and SPOTTISWOOD, D.J., The breakage function; what is it really?. Minerals Engineering, 1990, 3 (5), p.405-414.
- 7) KING, R.P. and BOURGEOIS, F., Measurement of fracture energy during single-particle fracture. Minerals Engineering, 1993, 6 (4), p.353-367.
- 8) KJOS, D.M., 1985. Wet autogenous mills. In: SME Mineral Processing Handbook. WEISS, N.L., ed., SME-AIME, 1985, Sec. 3C, chap.4, p.3C-60/3C-70.
- 9) LEUNG, K., An energy based ore specific model for autogenous and semi-autogenous grinding. Ph.D. Thesis, University of Queensland, Australia, 1987.
- 10) LOVEDAY, B.K. and NAIDOO, D., Rock abrasion in autogenous milling. Minerals Engineering. 1997, 10 (6), p.603-612.
- 11) MANLAPIG, E.M., SEITZ, R.A., SPOTTISWOOD, D.J., Analysis of the breakage mechanisms in autogenous

- grinding. In: Autogenous Grinding Seminar, 1979, Trondheim. p.A3/1-14.
- 12) MACPHERSON, A.R., Autogenous grinding 1987 – update. CIM Bulletin, 1987, 82 (921), p.75-82.
 - 13) MORRELL, S., Simulation of bauxite grinding in semi-autogenous mill and DSM screen circuit. M. Eng. Sc. Thesis, University of Queensland, Australia, 1989.
 - 14) MORRELL, S., The prediction of power draw in wet tumbling mills. Ph.D. Thesis, University of Queensland, Australia, 1993.
 - 15) MORRELL S., FINCH, W.M., KOJOVIC, T., DELBONI JR., H., Modelling and simulation of large diameter autogenous and semi-autogenous mills. Proc. Eur. Symp. Comm., Vol. 8, Stockholm, 1994.
 - 16) MORRELL, S. and MORRISON, R.D., Ag and Sag mill circuit selection and design by simulation. Proc. Advances in Autogenous and Semiautogenous Grinding Technology. Sag 96, Vancouver, 1996.
 - 17) MORRELL S. and STEPHENSON I., Slurry discharge capacity of autogenous and semi-autogenous mills and the effect of grate design. Int. J. Min. Proc. 1996, 112, p.53-72.
 - 18) MÖRSKY, P., KLEMETTI, M., KNUUTINEN, T., KALAPUDAS, R., KOIVISTOINEN, P., The development of laboratory testing for autogenous grinding. Proc. Eur. Symp. Comm. Vol. 8, Stockholm, 1994, p.308-317.
 - 19) MUTAMBO, J.P.C., Further development of an autogenous and semi-autogenous mill model. M. Eng. Sc. Thesis, University of Queensland, Australia, 1992.
 - 20) NAPIER-MUNN, T.J., MORRELL, S., MORRISON, R.D., KOJOVIC, T., Rock testing – determining the material-specific breakage function. In: Mineral comminution circuits – their operation and optimisation. Napier-Munn, T.J., ed., Chap.4, JKMRc, Brisbane, 1996, p.49-94.
 - 21) NARAYANAN, S.S., Development of a laboratory single particle breakage technique and its application to ball mill modelling and scale up. Ph.D. Thesis, University of Queensland, Australia, 1985.
 - 22) POWELL, M.S., The effect of liner design on the motion of the outer grinding elements in a rotary mill. Int. J. Min. Proc., 1991, 31, p.163-93.
 - 23) SCHOENERT, K., 1993. Personal communications.
 - 24) STANLEY, G.G., The autogenous mill: a mathematical model derived from pilot and industrial-scale experiment. Ph.D. Thesis, University of Queensland, Australia, 1974.
 - 25) VERMEULEN, L.A. 1985. The lifting action of lifter bars in rotary mills. Journal SAIMM, 85 (2), 1985, p.41-49.
 - 26) WHITEN, W.J., A matrix theory of comminution machines. Chemical Eng. Sc., 1974, 29, p.589-599.
 - 27) WICKHAM, P. 1972. Comminution of pebbles and fine ore. M. Eng. Sc. Thesis, University of Queensland, Australia, 1974.

Author's short biography



Homero Delboni, Jr.

Dr. Homero Delboni, Jr. graduated in Mining Engineering from the University of São Paulo, Brazil. In 1989 he obtained a M. Eng. degree in Minerals Engineering at the same university. He joined the Julius Kruttschnitt Mineral Research Centre in the University of Queensland, Australia, where he obtained his Ph.D. degree in 1999. He is currently a lecturer in the Department on Mining and Petroleum Engineering at the University of São Paulo, where he is involved in both teaching and research in mineral processing, particularly in comminution.



Steve Morrell

Dr. Steve Morrell graduated with Honours in Metallurgical Engineering from the Royal School of Mines. He joined the Julius Kruttschnitt Mineral Research Centre – JKMRc in the University of Queensland, Australia, where he obtained his M.Sc. degree in 1989 and Ph.D. in 1993. He is currently a researcher in the JKMRc, where he is involved in research in comminution.

Development of an Apparatus for Measuring Adhesive Force between Fine Particles[†]

Yasuhiro SHIMADA^a, Yorinobu YONEZAWA^a,
Hisakazu SUNADA^a, Ryusei NONAKA^b,
Kenzou KATOU^b and Hiroshi MORISHITA^c

^a Faculty of Pharmacy, Meijo University

^b OKADA SEIKO Co., Ltd.

^c HMI Inc.

Abstract

We developed an apparatus that uses the direct separation method to measure adhesive force between fine particles, and between a fine particle and a flat-surface substrate. This apparatus was able to measure adhesive force with high resolution (approximately 2 nN) and monitor the behavior of each particle with a microscope and image analyzer when separating particles from each other, and to calculate the adhesive force of the particles. Of the organic particles tested (corn starch, potato starch, and lactose), potato starch had the highest adhesive force, while lactose had the lowest adhesive force toward flat-surface substrates. The diameter and size distribution of fine particles clearly affected their adhesive force.

Key words: Adhesive force, fine particle, organic particle, HPMC capsule, gelatin capsule

1. Introduction

Various methods have been used to quantify the adhesive force between particles. Indirect methods include those which measure adhesive force by determining properties of powder beds such as angle of repose, shearing stress, fluidization threshold force, and degree of volume reduction. Direct methods that investigate many individual particles include adhesive force measurement methods that use image processing or statistical processing, such as the centrifugal method [1, 2, 3] and the impact separation method. [1, 4] One method that works with a single particle uses a spring scale or other instrument to measure the force needed to directly separate a particle from a

flat surface or another particle, [5] but this method is usable only with particles that are at least 200 μm large, and it is meant for inorganic powders. The fine particle adhesive force measuring apparatus (PAF-300, Okada Seiko Co. Ltd., Tokyo) used in this study is capable of directly measuring, during visual observation, the adhesive force between a flat surface and a fine particle, or between two fine particles, even down to particle sizes of about 10 μm . In other words, this apparatus can focus on a single particle, tear it away from a substrate or from an aggregate of fine particles to which it is attached, and gauge the tiny force needed to dislodge it. Because the PAF-300 can use a microscope or CCD camera to select the desired particle and measure its adhesive force, it can determine the relationship between the adhesive force and how it is attached or how it is released. This paper reports also on adhesive force measurement with the centrifugal method, and compares the results with those obtained with this measuring apparatus.

2. Sample Materials

Our sample powders were corn starch (Cornstarch W, Nippon Syokuhin Kakou, Co. Ltd., Okayama), lac-

^a 150 Yagotoyama, Tempaku-ku, Nagoya, Aichi Pref., 468-8503, Japan. TEL 052-832-1781 (Ext. 272)

^b 4-27-8 Minami-karasuyama, Setagaya-ku, 157-0062, Tokyo, Japan. TEL 03-3308-1217

^c Matsudo Palace 1002, 35-2 Koyama Matsudo-shi, 271-0093, Japan. TEL 03-3308-1217

[†] This report was originally printed in J. Soc. Powder Technology, Japan. **37**, 658-664 (2000) in Japanese, before being translated into English by KONA Editorial Committee with the permission of the editorial committee of the Soc. Powder Technology, Japan.

tose (Pharmatose 200M, DMV International), and potato starch (refined starch, Hokuren Agricultural Cooperative, Hokkaido). In experiments measuring adhesive force between a fine particle and flat surface, the materials used as the substrate for making particles adhere were slide glass (Micro Slide Glass, Matsunami Glass Ind., Ltd., Osaka), tablets formed by compressing a powder of the same material as the sample particles made to adhere to the flat surface, and gelatin capsule "0" (CLEAR Y, Shionogi Qualicaps Co. Ltd., Nara), which is widely used in the pharmaceutical field. We used the same gelatin capsule "0" for centrifugal method measurements in comparison experiments. We used gelatin capsule "3" and HPMC capsule "3" (CLEAR 1, Shionogi Qualicaps Co. Ltd., Nara) as the substrates when measuring adhesive force between fine particles.

3. Apparatus and Method

3.1 Measuring Basic Physical Characteristics of Powders

Powder particle size was measured with a laser diffraction and scattering particle size analyzer (LMS-30, Seishin Kigyo Co. Ltd., Tokyo). Shape index was measured with a high-speed image analyzer (LUZEX-FS, Nireko Co. Ltd., Tokyo). When performing these measurements, Eqs. 1 and 2 were used in measuring two indexes: the index showing unevenness (ψ_1), and that showing roundness (ψ_2).

$$\psi_1 = 4\pi A / PM^2 \quad (1)$$

$$\psi_2 = 4A / \pi ML^2 \quad (2)$$

Where:

A is the particle's actual projected area,

PM is the circumference of the particle's projected image, and

ML is the maximum length of the projected particle image.

We used a differential scanning thermal scale (TG-DTA2000, Mac Science Co. Ltd., Kanagawa) to measure the moisture content of powders.

3.2 Overview and Operation of the Fine Particle Adhesive Force Measuring Apparatus (PAF-300)

The apparatus used to measure adhesive force (Fig. 1) comprises a sensor unit (6) that measures adhesive force, the computer (1-b) that controls the sensor unit, an image analyzer (1-a), a stereoscope (8) for monitoring the adhesive force measuring unit, and

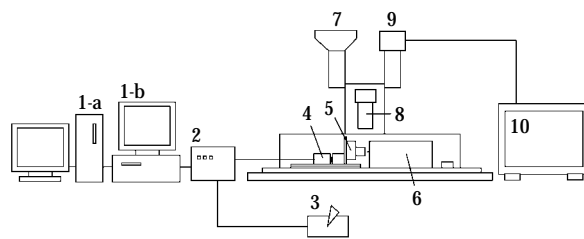


Fig. 1 Apparatus for Measuring Adhesive Force

- | | |
|---------------------------------------|---------------------------|
| 1-a: Image analyzer | 5: Triaxial movable stage |
| 1-b: Sensor unit computer | 6: Sensor unit |
| 2: Triaxial movable stage control box | 7: Optical microscope |
| 3: Triaxial movable stage joystick | 8: Stereoscope |
| 4: Driving motor | 9: CCD video camera |
| | 10: Video monitor |

a CCD video camera (9). A detailed view of the sensor unit (Fig. 2) shows it is composed of a contact needle (6-b) that comes into contact with the sample and dislodges particles, two plate springs (6-a) connected to the needle, and a laser displacement gauge (6-c) behind the springs. When the stage (5-a) moves slightly in the direction of the large arrow, the contact needle is pulled toward the sample substrate by the particle adhering to the needle, stress is caused on the plate springs, the needle moves to the left, and the laser displacement gauge measures its change in position. When the stage is moved slightly more to the left, the stress on the plate springs exceeds the adhesive force between the particle and sample substrate, and the particle comes loose, which releases the stress on the springs. At that moment needle displacement is maximum, and computer processing converts the displacement into adhesive force. Powders were caused to adhere to the surface by passing each power through a screen with 75 μm openings from about 20 cm above the surface, and allowing particles to fall freely. The experiment was performed in

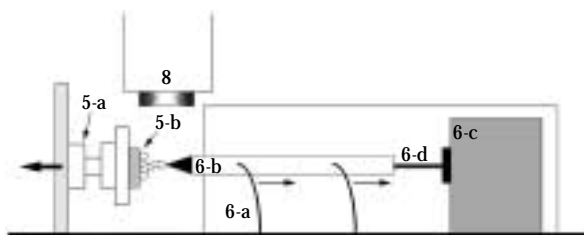


Fig. 2 Sensor Unit

- | | |
|-----------------------------|-----------------|
| 5-a: Triaxial movable stage | 6-c: Laser unit |
| 5-b: Sample | 6-d: Laser beam |
| 6-a: Plate springs | 8: Stereoscope |
| 6-b: Contact needle | |

a laboratory where temperature was maintained at 20 to 23°C and humidity at 50 to 55%. Adhesive force between a flat surface and fine particle was measured in the following manner (**Fig. 3-A**): A particle was attached to the surface and the contact needle was attached to the particle, then the computer automatically dislodged the fine particle from the surface. Adhesive force between two fine particles was measured in the same manner (**Fig. 3-B**). As an example of this latter type of measurement (**Fig. 4**), a particle was attached to the contact needle, and then the stage was moved under computer control to the left at a rate of about $0.6 \mu\text{m s}^{-1}$, at which time adhesive force was automatically measured. In the data plot obtained in this operation (**Fig. 5**) the distance the stage moved is on the horizontal axis, and the calculated force acting on the plate springs is on the vertical axis. That force corresponds to the particle's adhesive force. At the moment the contact needle dislodged the particle from the surface to which it had adhered, the maximum value at point 4 was attained, after which the value instantly dropped. We determined adhesive force to be the difference between the center line and the maximum amplitude of the springs' free vibration, which steadily weakens. Because the force acting on the two plate springs is given by the product of the spring constant k and displacement L in Eq. 3, finding k makes it possible to calculate adhesive force F . Because spring constant k is given by Eq. 4, [6] the constant can be obtained by plotting Eq. 4 (**Fig. 6**).

$$F = kL \quad (3)$$

$$k = 4\pi^2(\text{add.w. } c) / (T_1^2 - T_0^2) \quad (4)$$

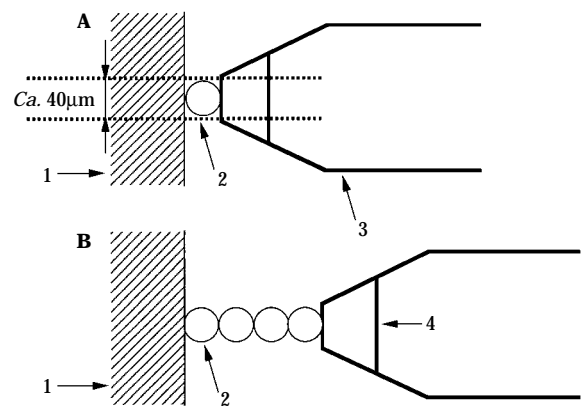


Fig. 3 Adhesion Force Measurement
 A: Between particle and substrate
 B: Between particles
 1: Substrate 3: Contact needle
 2: Particle 4: Diamond head

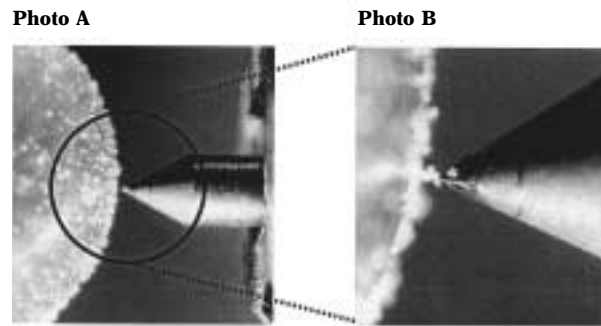


Fig. 4 Contact Needle, Particles, and Capsule
 Photo A: Particles adhering to a capsule surface
 Photo B: An enlargement, showing particles just before separation

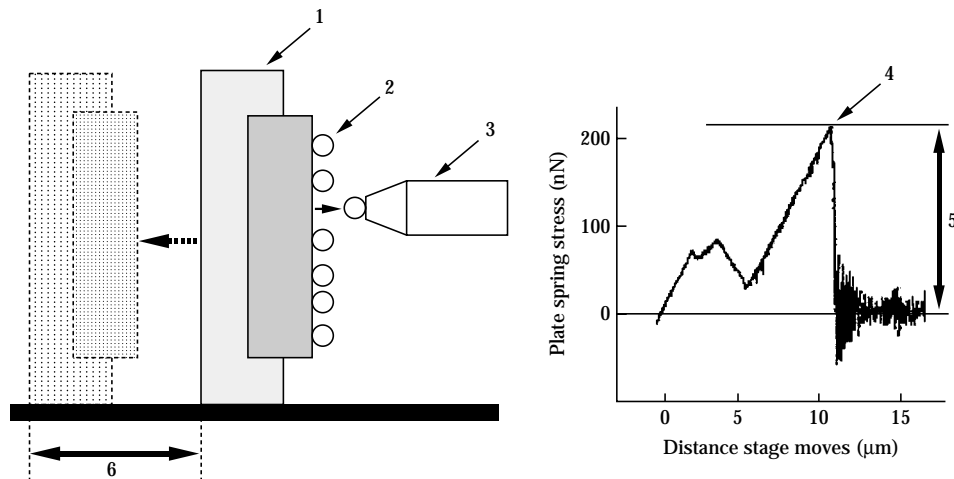


Fig. 5 Separation and Adhesive Force
 1: Stage 2: Particle 3: Contact needle 4: Adhesive force peak 5: Net adhesive force 6: Distance stage moves

Where:

add. w is the additional weight attached to the springs,

T_i is the characteristic frequency of the springs measured when the additional weight was attached,

T_0 is the initial characteristic frequency of the plate springs, and

c is the y-axis intercept.

From **Fig. 6** we calculated the value of the sensor unit spring constant k as 0.18. Further, because this apparatus pulls particles horizontally, we used Eq. 5 to find the influence of a powder's own weight on measurement, and considered the effect of the force acting vertically.

$$F_g = 4\pi(d/2)^3\rho \alpha/3 \quad (5)$$

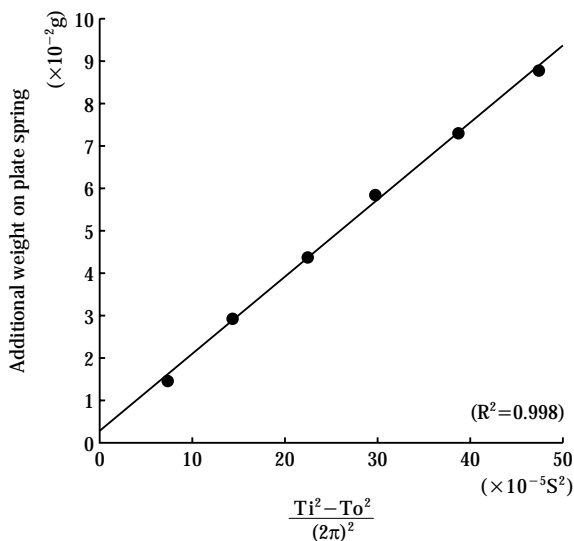


Fig. 6 Sensor Unit Calibration

$$F = kL$$

F is adhesive force, L is distance contact needle moves, T_0 is initial characteristic frequency of plate springs, and T_i is characteristic frequency of plate springs when additional weight is attached.

3.3 Adhesion between Contact Needle and Measured Particle

When the adhesive force between a particle and the contact needle is weaker than that between the flat surface and particle, it is necessary to somehow attach the particle to the needle. In our measurements of the adhesive force between potato starch and gelatin capsules, the adhesive force between the starch and gelatin was greater than that between the starch and needle, making measurements impossible

without using an adhesive. We therefore attached individual particles to the needle with an adhesive, which was a 40% aqueous solution of the macromolecular polymer hydroxypropyl cellulose (HPC-L, Nippon Soda Co., Ltd., Tokyo). However, we used no adhesive when the adhesive force between the needle and particle was greater than that between the flat surface and particle.

3.4 Comparison of Centrifugal Measurement and PAF-300 Measurement of Adhesive Force between a Flat Surface and Fine Particle

We used the centrifugal method to measure the mean adhesive force F_{50} of potato starch to a gelatin capsule, and we used the PAF-300 to measure the adhesive force of a fine particle to a flat surface, i.e., that of potato starch to a gelatin capsule. A comparison can be made because both methods were used to measure the adhesive force between a flat surface and an individual particle. The centrifugal method determines mean adhesive force F_{50} by applying a constant centrifugal force on a group of particles, finding the particle size at which half the particles break away, and then calculating the adhesive force. Thus it is possible to find the particle size that corresponds to mean adhesive force F_{50} . With the PAF-300 one can freely select the particle size one wants to measure, and our results in this study were those for comparatively large particles of about 60 μm , a size that allows stable results. Both experiments were conducted at a temperature of 20 to 23°C and humidity of 55 to 55%, conditions that make the effects of liquid bridging comparatively small. [7] Therefore we took into account only van der Waals force, and used Eq. 6 to calculate the Hamaker constant H of the potato starch from the adhesive force determined. The H of hydrocarbons is reported [7] to be generally between 4.0 and 10.0 $\times 10^{-20}$ (J), and the constant calculated from the adhesive force obtained was examined to see if it conformed to the usual range. Adhesion distance a corresponds to the distance at which van der Waals force is the maximum, and we used the value of 0.4 nm found in the literature. [8]

$$F_{vdw} = Hd/24a^2 \quad (6)$$

4. Results and Discussion

4.1 Measuring Adhesive Force between a Flat Surface and a Fine Particle [1, 9-11]

Table 1 presents the measurement results for aver-

age particle size, 10% diameter in cumulative distribution, 90% diameter in cumulative distribution, shape index, and moisture content of the powders used in this study. **Table 2** gives the results obtained from measuring the adhesive force of these three powders using slide glass as the substrate. Adhesive force increased in the order from lactose, corn starch, and potato starch, and the adhesive force of potato starch was over four times greater than that of lactose. The adhesive force of potato starch was larger than that of corn starch by the same extent. **Table 2** also includes the adhesive forces of the three powders when the flat surface used for each powder was a tablet formed by compressing the same powder. Just as with slide glass, adhesive force increased in order from lactose, corn starch, and potato starch, although the differences between them were not as great as when slide glass was the flat surface. As seen in **Table 1**, the particle size [1, 10, 11] and particle shape [9, 11, 12] would seem to be the biggest reasons. It would seem that the more spherical a particle is, and the more its surface is smooth and lacks roughness, the greater its effective contact area, thereby reducing the mean distance between the particle and flat surface, in turn increasing van der Waals force. [11] A powder's moisture content is another conceivable influence, which will be larger especially for adhesive force between different substances. The adhesive force of lactose, whose moisture content of about 5% is lower than the other two powders, was smaller than the adhesive force of the other powders, and moisture content was

Table 1 Physical Properties of the Samples

Sample	Adhesive force (nN)					
	D ₁₀ (μm)	D ₅₀ (μm)	D ₉₀ (μm)	ψ ₁	ψ ₂	Water content (%)
Corn starch	10.1	18.0	33.6	0.854	0.701	12.4
Potato starch	18.2	34.2	60.3	0.898	0.722	14.1
Lactose	5.7	28.8	80.6	0.557	0.511	5.2

Table 2 Adhesive Force between Particle and Glass Plate, and Tablet Surface of Same Substance

	Adhesive force (nN)		
	Corn starch	Potato starch	Lactose
Glass plate ^a	66.9±26.1	188.8±60.7	37.8±6.3
Tablet surface ^b	144.4±28.0	161.3±29.0	67.3±26.3

^a Each value represents the mean ±S.D. (n=5).

^b Each value represents the mean ±S.D. (n=8).

thought to be one reason. The influence of a powder's own weight when using this apparatus was provisionally calculated with Eq. 5 to be 0.49 nN vertically for potato starch (particle size 40 μm, true density 1.48 g cm⁻³). Because this is about 1/1,000th the measured adhesive force and hardly affects the results, we treated it as part of measurement error.

4.2 Measuring Adhesive Force between Fine Particles

Table 3 presents the results of measuring, as shown in **Fig. 3-B**, the inter-particle adhesive force of corn starch, lactose, and potato starch on a gelatin capsule surface. When the particle type changed we discerned a clear difference, just as with the measurement of adhesive force between flat surfaces and particles in **Table 2**. Adhesive force in order of low to high went from lactose to corn starch to potato starch. As shown in **Table 3**, we likewise measured the inter-particle adhesive force of corn starch, lactose, and potato starch on the surface of an HPMC capsule. Results were about the same as with the gelatin capsule, and we previously reported slight differences, [12] but we believe this is attributable to the difference in the particle-attracting electrostatic adhesive force [13] due to differences between the gelatin and HPMC capsules with respect to material, capsule moisture content, and electrification amount.

Table 3 Adhesive Force between Particles on the Gelatin Capsule and HPMC Capsule

	Adhesive force (nN)		
	Corn starch	Potato starch	Lactose
Gelatin capsule	145.0±30.4	270.8±49.9	78.1±11.5
HPMC capsule	127.1±27.6	222.6±57.5	79.5±24.9

Each value represents the mean ±S.D. (n=8).

4.3 Comparison of Centrifugal Method and Our Method in Measuring Adhesive Force between a Flat Surface and Fine Particle

Table 4 shows the results obtained when using the centrifugal method to measure the mean adhesive force F_{50} between potato starch and a gelatin capsule, and the results from using the PAF-300 to measure the adhesive force between a flat surface and fine particle, i.e., gelatin capsule and potato starch. Also given in the table is the Hamaker constant, which was calculated with Eq. 6 using these results. **Table 4** shows that measurement results obtained with the well-

Table 4 Comparison of Centrifugal Separation Method and PAF-300 Method

	Particle diameter (μm)	Adhesive force ^{a,b} (nN)	H (J)
Centrifugal separation method	34.2	230.7 \pm 92.3	1.5–3.6 $\times 10^{-20}$
PAF-300 method	62.3	610.0 \pm 175.8	2.6–4.8 $\times 10^{-20}$

^a Each value represents the mean \pm S.D. (n=3).

^b Adhesive force of the potato starch to gelatin capsule.

established centrifugal method closely agree with the results yielded by the PAF-300, and suggests that the PAF-300 can perform measurements of more or less the same accuracy as the centrifugal method. Further, both methods yielded values for the Hamaker constant that are within or close to the range of 4.0 to 10.0 $\times 10^{-20}$ (J) for hydrocarbons found in the literature. [7]

5. Conclusion

In this study we used an apparatus that, by directly dislodging adhering particles, can measure adhesive force between two particles or between a particle and a flat surface, and we measured the adhesive forces of three organic powders. The apparatus was able to measure clear differences in adhesive force. When dislodging particles with the apparatus, particle behavior was monitored with a microscope and an image analyzer, and recorded as an animated image, making it possible to calculate the adhesive force of a single particle. Of the three organic powders used, potato starch had the highest adhesive force, followed by corn starch, and finally lactose. We found that lactose had an especially weak adhesiveness to slide glass in comparison to the other powders. It is likely that particle size, shape, and moisture content had the most to do with the difference in adhesiveness, but it is conceivable that powder electrification also had some effect. By making comparisons with the measured values yielded by this apparatus, we believe it will be possible to further explore adhesive force changes in the same powders under different temperature and humidity conditions, and to study the adhesive force equations that have been under investigation for some time.

Nomenclature

a	distance between two particles	(m)
A	actual projected area of a particle	(m ²)

add.w	additional weight attached to spring	(kg)
c	y-axis intercept	
d	mean Heywood diameter of particle measured	(m)
D ₁₀	10% diameter in cumulative distribution	(μm)
D ₅₀	50% diameter in cumulative distribution	(μm)
D ₉₀	90% diameter in cumulative distribution	(μm)
F	adhesive force	(N)
F ₅₀	mean adhesive force in centrifugal separation	(N)
F _g	force of gravity	(N)
F _{vdw}	van der Waals force	(N)
H	Hamaker constant	(J)
k	spring constant	(N m ⁻¹)
L	distance that contact needle moves	(m)
ML	maximum length of projected particle image	(m)
n	number of samples	
PM	diameter of circle having a circumference equivalent to the perimeter of the projected particle image	(m)
T _i	characteristic frequency of plate springs when additional weight is attached	(s)
T ₀	initial characteristic frequency of plate springs	(s)
α	acceleration of gravity	(m s ⁻²)
ρ	density of particle	(kg m ⁻³)
ψ_1	shape index based on PM	
ψ_2	shape index based on ML	

References

- Mizuno, M., H. Sunada, K. Iida, A. Otsuka, H. Sakashita, H. Tada and H. Kimura. "Measurement of the Adhesive Force of Fine Particles on the Tablet Surfaces and Its Removal Method," *J. Pharm. Sci. Technol., Jpn.*, **57**, 181-189 (1997).
- Okada, J., Y. Matsuda and Y. Fukumori. "Measurement of the Adhesive Force of Pharmaceutical Powders by Centrifugal Method, I," *Yakugaku Zasshi*, **89**, 1539-1544 (1969).
- Iida, K., A. Otsuka, K. Danjo and H. Sunada. "Measurement of the Adhesive Force between Particles and Polymer Films," *Chem. Pharm. Bull.*, **40**, 189-192 (1992).
- Otsuka, A., K. Iida, K. Danjo and H. Sunada. "Measurement of the Adhesive Force between Particles of Powdered Organic Substances and a Glass Substrate by Means of the Impact Separation Method, I, Effect of Temperature," *Chem. Pharm. Bull.*, **31**, 4483-4488 (1983).
- Arakawa, M. and S. Yasuda. "The Measurement of Interaction Force on Microparticles," *J. Soc. Mat. Sci., Japan*, **26**, 858-862 (1977).
- Matsumura, S., N. Kanda, T. Tomaru, H. Ishizuka and

- K. Kuroda. "A Measurement of the Frequency Dependence of the Spring Constant," *Phys. Lett. A*, **244**, 4-8 (1998).
- 7) Okuyama, K., H. Masuda, K. Higashitani, M. Chikazawa and T. Kanazawa. "Ni ryuushikan sougosayou," *J. Soc. Powder Technol., Japan*, **22 (7)**, 451-475 (1985).
- 8) Massimilla, L. and G. Donsi. "Cohesive Forces Between Particles of Fluid-Bed Catalysts," *Powder Technology*, **15**, 253-260 (1976).
- 9) Otsuka, A., K. Iida, K. Danjo and H. Sunada. "Measurement of the Adhesive Force between Particles of Powdered Materials and a Glass Substrate by Means of the Impact Separation Method, III, Effect of Particle Shape and Surface Asperity," *Chem. Pharm. Bull.*, **36**, 741-749 (1988).
- 10) Shimada, Y., M. Sunada, M. Mizuno, Y. Yonezawa, H. Sunada, K. Takebayasi, M. Yokosuka and H. Kimura. "Measurement of the Adhesive Force of Fine Particles on Tablet Surfaces and Method of Their Removal," *Drug Dev. Ind. Pharm.*, **26**, 149-158 (2000).
- 11) Otsuka, A. "Adhesive Properties and Related Phenomena for Powdered Pharmaceuticals," *Yakugaku Zasshi*, **118 (4)**, 127-142 (1998).
- 12) Shimada, Y., T. Ito, Y. Yonezawa, H. Sunada, M. Yokosuka and K. Takebayasi. "Measurement of the Adhesive Force of Contaminative Particles on the Capsule Surface and Method of Their Removal," *J. Pharm. Sci. Technol.*, **60 (1)**, 35-42 (2000).
- 13) Kulvanich, P. and Peter J. Stewart. "An Evaluation of the Air Stream Faraday Cages in the Electrostatic Charge Measurement of Interactive Drug Systems," *Int. J. Pharm.*, **36**, 243-252 (1987).

Author's short biography



Yasuhiro Shimada

March, 1998 Graduated from Faculty of Pharmacy, Meijo University
 April, 1998 Research Associate at Faculty of Pharmacy, Meijo University
 April, 1999 Entered Master Course of Faculty of Pharmacy, Meijo University
 March, 2001 Graduated from Master Course of Faculty of Pharmacy, Meijo University
 April, 2001 Entered Doctor Course of Faculty of Pharmacy, Meijo University
 Research Work Analysis of Powder Adhesive Force and Removal Process



Yorinobu Yonezawa

March, 1967 Graduated from Faculty of Pharmacy, Kyoto University
 April, 1967 Research Associate at Faculty of Pharmacy, Meijo University
 July, 1983 Ph.D. degree (Pharm. Sci., Kyoto Univ.)
 April, 1989 Assist Professor at Same University
 April, 1989 Associate Professor at Same University
 August, 1983-August, 1985 Research Worker at University of Wisconsin-Madison (USA)
 Research Work Analysis of Dissolution Process of Solid Dosage Forms

Author's short biography



Hisakazu Sunada

March, 1960 Graduated from Department of Pharmacy, Faculty of Medicine, Kyoto University
 April, 1960 Entered Research Student, Kyoto University
 April, 1962 Entered Master Course of Pharmaceutical Science, Kyoto University
 July, 1963 Research Associate at Faculty of Pharmaceutical Science, Kyoto University
 April, 1967 Associate Professor at Faculty of Pharmacy, Meijo University
 Sept., 1967 Ph.D. degree (Pharm. Sci., Kyoto Univ.)
 April, 1983 Professor (full) at Same University
 1992 KONA AWRD (Hosokawa Powder Technology Foundation)
 Research Work Powder Technology, Solid Dosage Form, Suspension
 Chairman of Standard Formulation Research Association



Ryusei Nonaka

March, 1997 Graduated from Faculty of Pharmacy, Tokyo University of Pharmacy and Life Science
 April, 1997 Entered Master Course of Faculty of Pharmacy, Tokyo University of Pharmacy and Life Science
 March, 1999 Graduated from Master Course of Faculty of Pharmacy, Tokyo University of Pharmacy and Life Science
 April, 1999 Employed as a Staff of Technical Division in the Okadaseiko Co., Ltd. in Tokyo Japan. He is now senior staff of technical division.
 Research Work Tableting, Measurement of Compression Force, Compression Energy Analysis



Kenzou Katou

March, 1986 Graduated from Faculty of Commercial Science, Aichi Gakuin University.
 April, 1993 Employed as a Staff of Account Service Division in the Okada-seiko Co., Ltd. Chubu Branch, Nagoya Japan. He is now director of account service division.
 He contributed to development of GRANO (particle hardness tester), PAF300 (particle adhesive-force analyzer) and many other machines.



Hiroshi Morishita

President, HMI Corporation, specializes in ultra-micro manipulation technology for MEMS (Microelectro-Mechanical Systems). He founded HMI Corporation in 1991 to commercialize his ultra-micro manipulator system. He extended his interest and business to the field of sensor-actuator systems for human-robot symbiosis environments. He graduated from the University of Tokyo (B.A., M.A., mechanical engineering), and is in the final stage of preparing his doctoral thesis. He was a visiting researcher in Mechanical Engineering Department in 1992 and 1993, and at RCAST (Research Center for Advanced Science and Technology) of the University of Tokyo in 1994 and 1995.

Continuous Synthesis of Monodispersed Alumina Particles by the Hydrolysis of Metal Alkoxide Using a Taylor Vortex[†]

Takashi OGIHARA and Mamoru NOMURA
 Department of Materials Science and Engineering,
 Fukui University*

Abstract

A continuous reactor was developed for industrial production of monodispersed alumina particles from metal alkoxide. Taylor vortex flows were used for solution mixing. Each of the Taylor vortices functioned as a batch reaction vessel. Monodispersed spherical alumina particles were prepared by hydrolyzing aluminum alkoxide in a mixture of octanol and acetonitrile. The particles were continuously produced for 5 h by using this reactor. Particle size and distribution were comparable to those obtained by batch processing. We investigated the effects of Taylor number (Ta) and residence time on the particle size, particle size distribution, yield, and particle number density of monodispersed alumina particles, which were obtained at Ta numbers from 50 to 150.

1. Introduction

Until now the usual way of synthesizing monodispersed oxide particles on an industrial scale has been to use reactors that hydrolyze metal alkoxide (the alkoxide route).^{1,3} As in the reactor developed by Ring^{4,5} and Fisher et al.,⁶ the principle of the system is as follows: when a hydrolyzed solution is put into a pipe under ideal plug-flow conditions, nucleation and growth occur continuously and form monodispersed particles. Consequently, it is difficult to maintain an ideal plug flow in a large pipe for a long time. We noted that using a Couette-Taylor vortex to prepare monodispersed particles keeps a large quantity of solution at the ideal plug flow for a long time. This vortex is generated by filling the space between the walls of two coaxial cylinders with a liquid, and generating a Couette flow with the viscous frictional force induced by rotating the inner cylinder. Increasing rotation speed causes a transition from a Couette flow to a doughnut-type Couette-Taylor vortex (C-T vortex) while spinning the inner cylinder (Fig. 1). The diameter of the C-T vortex is equal to the space between the inner and outer cylinders, and each vortex is independent.^{7,8} Each Taylor vortex generated

functions as a batch reaction vessel and brings about homogeneous mixing in the vortex. It is possible to improve non-homogeneous mixing in a large reaction vessel. C-T vortices have already been used for continuous seed emulsion polymerization in the preparation of monodispersed Latex particles.⁹ We created a trial version of a reaction apparatus which uses vortex flow, and used it to prepare monodispersed silica colloids.¹¹ We found that monodispersed silica colloids could be continuously prepared, while the hydrolysis and polymerization reaction of ethyl silicate (Stöber method¹⁰) was controlled, and the particle size distri-

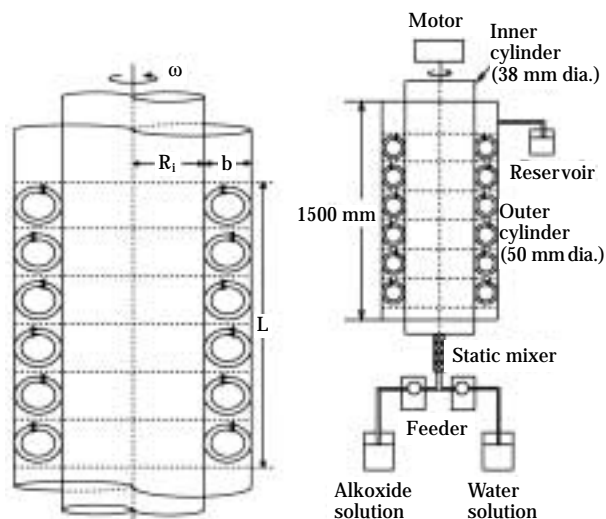


Fig. 1 Schematic diagrams of Couette-Taylor vortex flow and reactor

* 9-1, Bunkyo 3, Fukui-shi, Fukui-ken, 910-8507 Japan.

[†] This report was originally printed in J. Soc. Powder Technology, Japan. **37**, 722-727 (2000) in Japanese, before being translated into English by KONA Editorial Committee with the permission of the editorial committee of the Soc. Powder Technology, Japan.

bution of silica colloids obtained was the same as that yielded in batch processing.¹¹ This paper describes the continuous preparation of monodispersed alumina particles by applying this vortex flow to the hydrolysis of aluminum alkoxide, and relates our investigation on the effect of reaction conditions on particle formation. Especially in the synthesis of monodispersed particles^{12,13} from aluminum alkoxide, it is necessary to prepare the emulsion in a different kind of solvent mixture. Taking continuous reaction into account, it appears that using a C-T vortex is very effective because the size and size distribution of the emulsion are influenced by mixing uniformity and strength.

2. Materials and Methods

2.1 Starting solution

Al (sec-OC₄H₉)₃ (ASBD, Takefu Fine Chemical Co., Ltd.) was used as the starting material, which was prepared as described below. Water (Nacalai Inc.) was double distilled and deionized. Octanol (Nacalai Inc.) and acetonitrile (Nacalai Inc.) were used to prepare an emulsion as an organic solvent. Organic solvents were dehydrated using a molecular sieve (3A, 1/16) for 24 h. Hydroxy-propyl-cellulose (HPC, Wako Chemical Co., Ltd., MW 100,000) was used as the dispersant. For the preparation of monodispersed alumina particles, the starting solution was prepared according to concentration conditions for batch processing^{13,14} and the use of a continuous tube-type reactor.¹⁵ The concentration of HPC, which was dissolved in the octanol at R. T., was 0.2 g/cm³. ASBD was dissolved in the octanol at 50°C for 2 h under reflux, after which hydroxy-propyl-cellulose (0.2 g/dm³) was added to prepare a 0.05 mol/dm³ ASBD solution. Meanwhile, water was used to prepare a 0.05 mol/dm³ solution in octanol (60 vol %) and acetonitrile (40 vol %).

2.2 Preparation of alumina particles

The apparatus (Fig. 1) consisted of a starting solution tank, a feeder for supply to the mixer, a T-type mixer, a C-T vortex flow reactor, and collector.¹⁵ The reaction vessel consisted of a glass outer cylinder (50 mm diameter, 1500 mm length) and a stainless steel inner cylinder (38 mm diameter, 1500 mm length) with a common axis. The sum of the vortices developed in this reactor vessel was determined by dividing height (L) by inter-cylinder space width (b), which yielded a value of 125. The ASBD solution and aqueous solution were fed into the T-type mixer by

the feeder at the same rate (3×10^{-4} dm³/s). After mixing, they were put into the reaction vessel where the emulsion formed. Solution residence was controlled by pushing the mixture upward, and residence time is the interval starting when the mixed solutions enter the reactor vessel, and ending when the mixture exits. We set residence time to a maximum of 1 h in these experiments. For the sake of convenience, reaction temperature was 25°C because the experiments were carried out in a room kept at 25°C. The Taylor (Ta) number was defined as the determining flow condition factor in the C-T vortex, and it was determined by Equation (1).

$$Ta = \frac{\omega R_i b}{\nu} \cdot \left(\frac{b}{R_i} \right)^{0.5} \quad (1)$$

Where:

Ta is the Ta number,

ω is the angular speed of the inner cylinder (1/s),

R_i is the inner cylinder radius (mm),

b is the annular gap width (mm), and

ν is the fluid viscosity (m²/s).

The Ta number was controlled by the motor's rotational speed, and ranged between 30 and 200. Upon leaving the reaction vessel, the solution containing alumina particles was collected in a beaker, and the alumina particles were separated from the mother liquid using a centrifugal separator. After washing the alumina particles ultrasonically with ethanol for 10 min, an agglomerated chalk-like powder was obtained by drying at 100°C for 24 h.

2.3 Characterization of as-prepared particles

We used a scanning electron microscope (Hitachi Co., Ltd., S-800) to determine the as-prepared particles' average size, geometrical standard deviation, morphology, and state of agglomeration. SEM photomicrographs were analyzed to assess average size and geometrical standard deviation, and 200 particles were measured for each sample. Particle number density was calculated with Equation (2).

$$N = \frac{Y}{dV} \quad (2)$$

Where:

N is the particle number density ($\times 10^{26}$ /dm³),

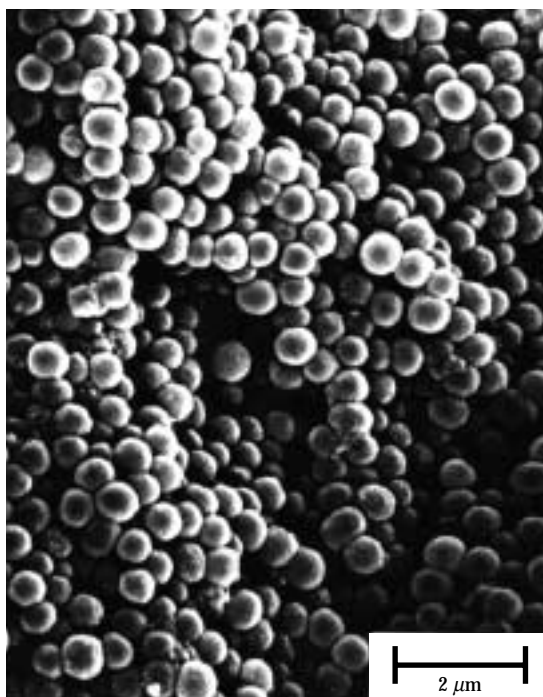
Y is the yield (%),

d is the particle density (g/cm³), and

V is particle volume (cm³)

Particle volume was determined from average size,

C-T flow reactor



Batch reactor

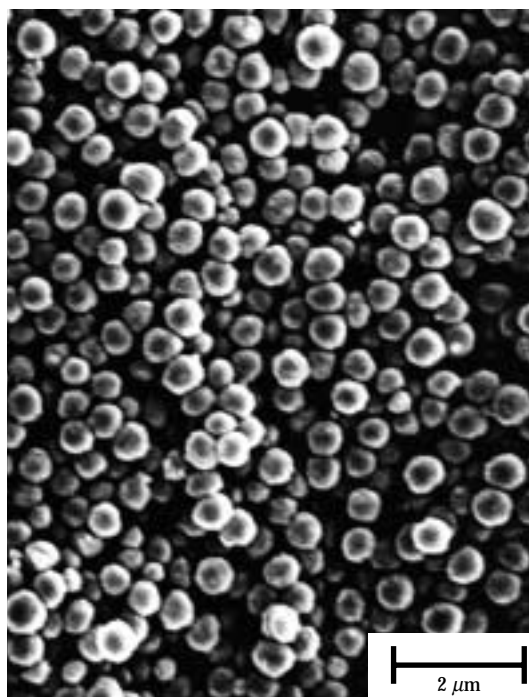


Fig. 2 SEM photomicrographs of monodispersed alumina particles prepared with a C-T flow reactor and a batch reactor

assuming the particles are solid true spheres. The density of α -alumina (3.98 g/cm^3)¹⁶ was used as particle density. Hence, these values are not accurate, but they give us an idea of the relative tendency. Crystal phase was determined by powder X-ray diffraction (Macscience Co., Ltd., MXR-3V). Water and organic species contents of the particles were measured by a thermogravimetric and differential thermal analysis (Rigaku Co., Ltd., PTC-10).

3. Results and Discussion

3.1 Comparison of C-T vortex reactor and batch processing

Typical alumina particles shown in the SEM photomicrograph (**Fig. 2**) were made with a C-T vortex reactor. Their Ta number is 92 and residence time was 30 min. An SEM photograph of alumina particles obtained by batch processing¹⁷ is also shown in **Fig. 2** for comparison with monodispersed alumina particles obtained from the C-T vortex reactor. As-prepared alumina particles are spherical and unagglomerated. XRD showed that the crystal phase of as-prepared powders was amorphous. DTA-TG showed that the content of water, octanol, and unreacted ASBD was about 40 wt% (**Fig. 3**). The particle

size distributions of alumina particles prepared by the C-T vortex reactor and batch processing are shown in **Fig. 4 (a)** and **(b)**, respectively. The average size and geometrical standard deviation of alumina particles obtained from the C-T vortex reactor were $0.2 \mu\text{m}$ and 1.15, respectively. On the other hand, those of alumina particles obtained with batch processing were $0.17 \mu\text{m}$ and 1.16, respectively, showing that the size of alumina particles obtained by the C-T vortex reac-

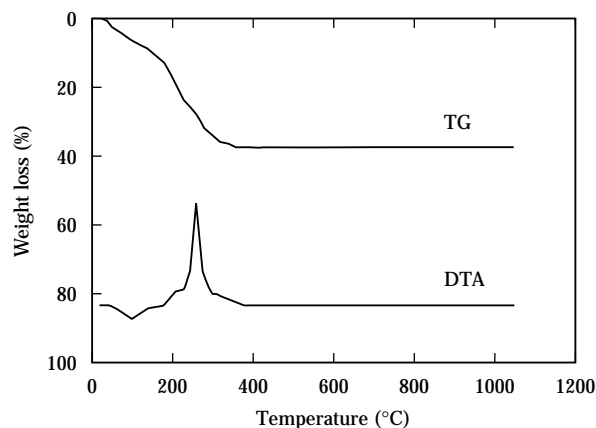


Fig. 3 DTA-TG curves of monodispersed alumina powders

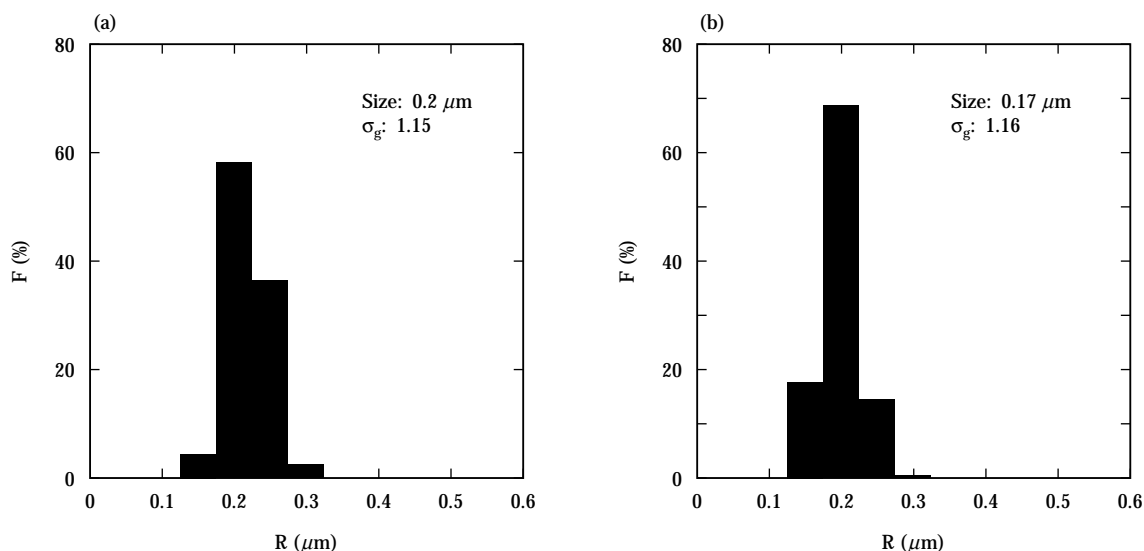


Fig. 4 Particle size distribution of monodispersed alumina particles prepared with a C-T flow reactor (a) and a batch reactor (b)

tor was comparable to that of particles made by batch processing.

3.2 Continuous preparation

It is apparent that this system is capable of preparing monodispersed alumina particles. We performed continuous production with this reactor for 5 h, during which time we collected 0.1 dm³ of solution at 30-min intervals and examined the change in average size (R), geometrical standard deviation (σ_g), yield (Y), and particle number density (N) of the monodispersed alumina particles obtained after centrifugal separation (**Fig. 5**). The Ta number was 92 and residence time was 30 min. There were no changes in the average size, geometrical standard deviation, yield, and particle number density of alumina particles during any one of the five hours. It was therefore evident that the ASBD hydrolysis reaction was controlled by this apparatus, which was able to maintain continuous production of alumina particles having uniform quality. One can presume that there is little ASBD diffusion from one vortex to another because if ASBD readily diffused among vortices, ASBD concentration differences among vortices might cause non-uniformity in both the droplet size distribution and emulsion number density. As a result, the average size, geometrical standard deviation, and particle number density of alumina particles obtained in each vortex would differ widely. However, as the variance in these values for alumina particles was slight in this experiment, the diffusion of ASBD is controlled among the vortices to an extent at which the particle size and

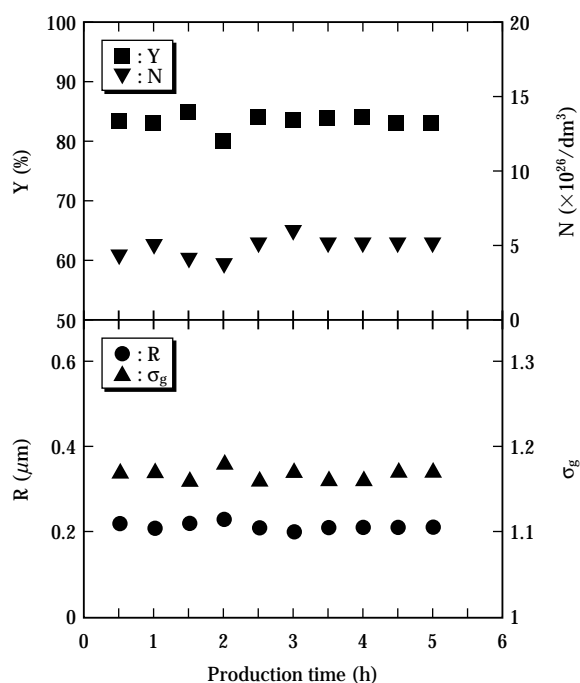


Fig. 5 Dependence of particle size, σ_g , yield, and particle number density on production time

yield of alumina particles are not influenced.

3.3 Effect of Ta number

We investigated the effect of Ta number on particle size, geometrical standard deviation, yield, and particle number density (**Fig. 6**). Residence time was 30 min. When the Ta number was less than 50, the apparatus produced polydispersed alumina particles with a

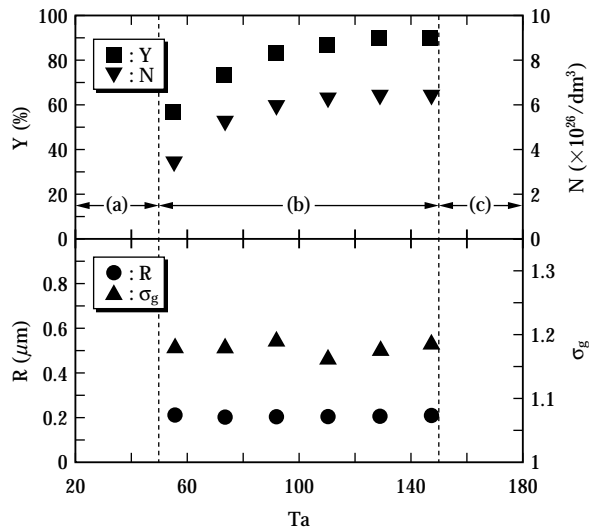


Fig. 6 Dependence of particle size, σ_g , yield and particle number density on Ta number. (a) Polydispersed region, (b) monodispersed region, (c) agglomerate region.

geometrical standard deviation of more than 1.2 and a broad particle size distribution. As a result, both the separation between vortices and the mixing in each vortex were incomplete because each vortex exists in

the boundary where the transition from a Couette flow to a Couette-Taylor vortex flow occurs. Monodispersed particles were obtained when the Ta number was more than 50. The particle size and geometrical standard deviation of alumina particles were constant in the Ta number range where monodispersed particles were formed.

On the other hand, the alumina particle yield increased as the Ta number increased, with 85% yield obtained at 150. Particle number density also increased as the Ta number increased. This is probably because the ASBD hydrolysis reaction was promoted by uniform mixing in the vortex when the Ta number grew larger. When the Ta number was greater than 150, the yield and particle number density further increased. However, unlike the alumina particles obtained at Ta 92, those formed at Ta 160 were agglomerated (**Fig. 7**), which indicated that the particles were agglomerated by the high collision frequency that occurred during particle formation by vigorous mixing. This showed that when preparing monodispersed particles using this apparatus, particle agglomeration occurs even in the range in which a Couette-Taylor vortex with plug flow is formed. Consequently, monodispersed alumina particles were produced in the range from 50 to 150.

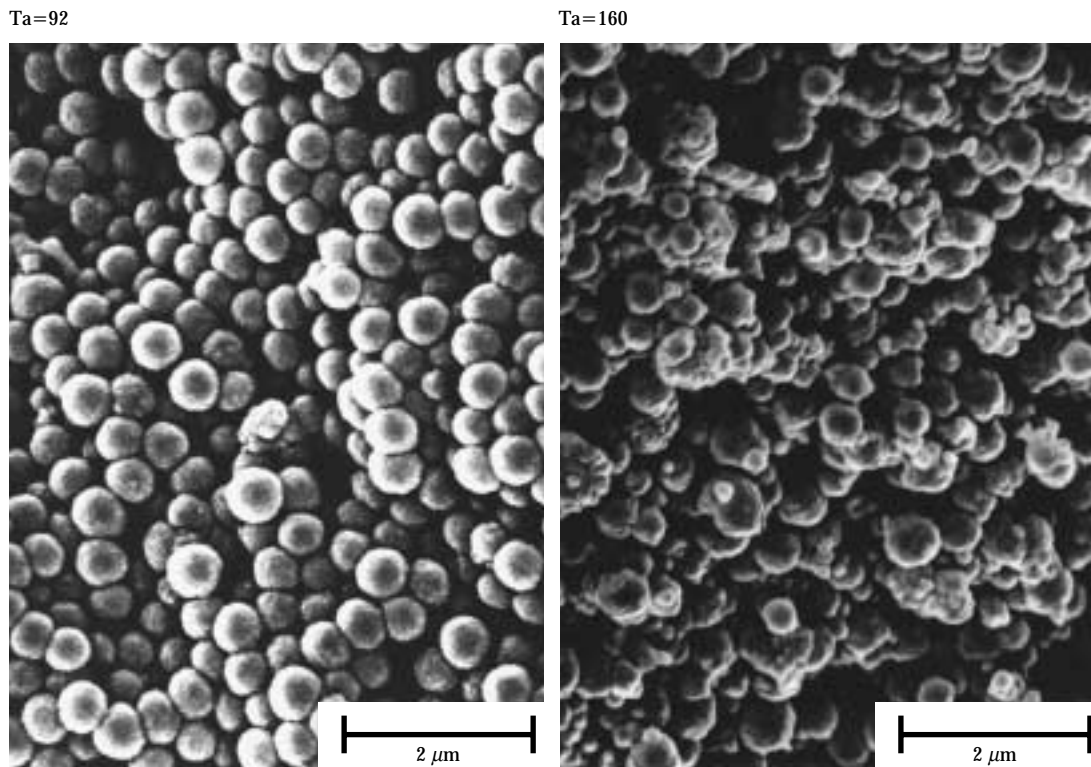


Fig. 7 Effect of Ta number on the agglomeration of alumina particles

3.4 Effect of residence time

We investigated the relation among residence time, average size, geometrical standard deviation, yield, and particle number density (Fig. 8). The Ta number was 92. Residence time was controlled by allowing the feeder supply rate to change from 1.5×10^{-4} to 9×10^{-4} m³/s. Because the average size and geometrical standard deviation of alumina particles were always the same at a certain residence time, it was evident that these values were independent on residence time. On the other hand, yield rose to 86% at 1 h, and the particle number density also increased. Fig. 8 indicates that because the size of alumina particles did not change until the 1 h mark, the yield increase is not due to the growth of alumina particles, but to the increase in particle number density.

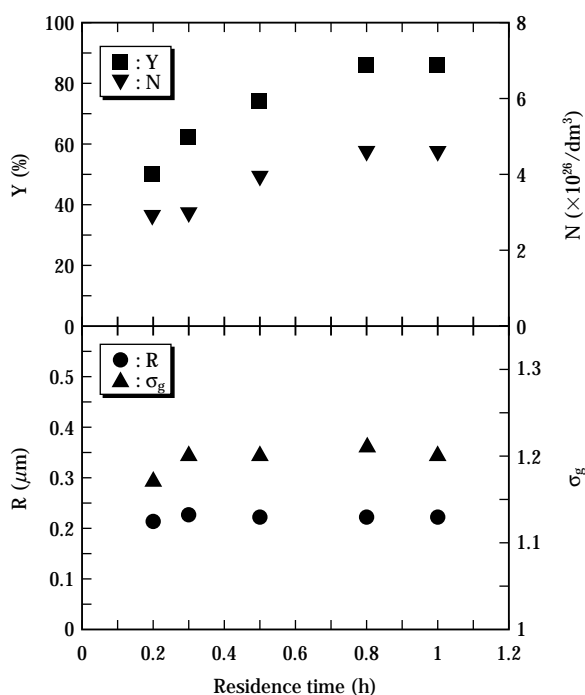


Fig. 8 Dependence of particle size, σ_g , yield, and particle number density on residence time

4. Conclusion

Monodispersed alumina particles were continuously prepared by the hydrolysis of aluminum alkoxide using a C-T vortex flow reactor. We reached the following conclusions:

(1) Monodispersed alumina particles were amorphous, and the particle size and particle size distribution were comparable to those obtained by batch processing.

- (2) The average size, geometrical standard deviation, yield, and particle number density of monodispersed alumina particles were constant during continuous preparation, and reproducibility is possible.
- (3) The Ta number range in which monodispersed alumina particles were formed was from 50 to 150. Particle size and geometrical standard deviation were independent on the Ta number in this range, but the yield and particle number density increased as the Ta number increased. Alumina particles were also agglomerated when the Ta number was greater than 150.
- (4) The particle size and geometrical standard deviation of monodispersed alumina particles were independent on residence time, but yield increased with residence time. Yield increase is not due to the growth of alumina particles, but to the increase in particle number density.

Nomenclature

b	Annulus width	(mm)
d	Particle density	(g/cm ³)
F	Frequency	(%)
L	Length of cylinder	(mm)
N	Particle number density	($\times 10^{26} \cdot \text{dm}^{-3}$)
R	Average particle size	(μm)
R _i	Radius of inner cylinder	(mm)
Ta	Taylor number	
V	Particle volume	(cm ³)
Y	Yield	(%)
σ_g	Geometrical standard deviation of average size	
ν	Kinematic viscosity	(m ² /s)
ω	Angular velocity	

References

- Ogihara, T., M. Ikeda, M. Kato and N. Mizutani. "Continuous Processing of Monodispersed TiO₂ Powders," *J. Am. Ceram. Soc.*, **72**, 1598-1601 (1989).
- Ogihara, T., M. Iizuka, T. Yanagawa, N. Ogata and K. Yoshida. "Continuous Reactor System of Monosized Colloidal Particles," *J. Mater. Sci.*, **27**, 55-62 (1992).
- Ogihara, T., M. Yabuuchi, T. Yanagawa, N. Ogata, K. Yoshida, N. Nagata, K. Ogawa and U. Maeda. "Preparation of Monodispersed, Spherical Ferric Oxide Particles by Hydrolysis of Metal Alkoxides Using a Continuous Tube-Type Reactor," *Advanced Powder Technol.*, **8**, 73-84 (1997).
- Ring, T. A. "Continuous Precipitation of Monosized Particles with a Packed Bed Crystallizer," *Chem. Engng. Sci.*, **39**, 1731-34 (1984).
- Jean, J. H., D. M. Goy and T. A. Ring. "Continuous Pro-

- duction of Narrow-Sized and Unagglomerated TiO₂ Powders," *Am. Ceram. Soc. Bull.*, **66**, 1517-20 (1987).
- 6) Kallay, N. and I. Fischer. "A Method for Continuous Preparation of Uniform Colloidal Hematite Particles," *Colloids & Surf.*, **13**, 145-9 (1985).
 - 7) Kataoka, K. and T. Takigawa. "Intermixing over Cell Boundary between Taylor Vortices," *A. I. Ch. E. J.*, **27**, 504-8 (1981).
 - 8) Mizushima, A., R. Itoh, K. Kataoka, Y. Nakajima and A. Fukuda. "Velocity Distribution of Taylor Vortex Flow in an Annulus between Rotating Coaxial Cylinders," *Kagaku Kougaku*, **35**, 1116-21 (1971).
 - 9) Imamura, T., K. Saito, S. Ishikura and M. Nomura. "A New Approach to Continuous Emulsion Polymerization," *Int. Symp. Poly. Microsphere*, Preprints, p. 151 (1991).
 - 10) Stöber, W., A. Fink and E. Bohn. "Controlled Growth of Monodispersed Silica Spheres in the Micron Size Range," *J. Colloid Interface Sci.*, **26**, 62-69 (1968).
 - 11) Ogihara, T., G. Matsuda, T. Yanagawa, N. Ogata, K. Fujita and M. Nomura. "Continuous Synthesis of Monodispersed Silica Particles by Using Couette-Taylor Vortex Flow," *J. Ceram. Soc. Jpn.*, **103**, 151-154 (1995).
 - 12) Lee, S. K., K. Shinozaki and N. Mizutani. "Influence of Mixed Solvent on the Formation of Monodispersed Al₂O₃ Powders by Hydrolysis of Aluminum sec-Butoxide," *J. Ceram. Soc. Jpn.*, **101**, 470-474 (1993).
 - 13) Ogihara, T., T. Yanagawa, N. Ogata and K. Yoshida. "Formation of Monodispersed Oxide Particles by Hydrolysis of Metal Alkoxide in Octanol/Acetonitrile Solutions," *J. Ceram. Soc. Jpn.*, **101**, 315-320 (1993).
 - 14) Mizutani, N., M. Ikeda, S. K. Lee, K. Shinozaki and M. Kato. "Preparation of Monodispersed Hydrous Aluminum Oxide Powders," *J. Ceram. Soc. Jpn.*, **99**, 183-186 (1991).
 - 15) Ogihara, T. and N. Mizutani. "Synthesis of Monodispersed Ceramic Particles from Emulsion Route," *Inorg. Mater.*, **3**, 177-187 (1996).
 - 16) JCPDS Card 10-173.
 - 17) Ogihara, T., H. Nakajima, T. Yanagawa, N. Ogata, K. Yoshida and N. Matsushita. "Preparation of Monodispersed, Spherical Alumina Powders from Alkoxides," *J. Am. Ceram. Soc.*, **74**, 2263-2269 (1991).

Author's short biography



Takashi Ogihara

Takashi Ogihara has been an associate professor of material science and engineering at Fukui University since 1994. He received his B.S. degree from the Department of Synthesis Chemistry, Chiba University in 1983 and his M.S. and Dr. of Engineering degrees from the Department of Inorganic Materials, Tokyo Institute of Technology in 1986 and 1989, respectively. His research interests are the synthesis and sintering of functional ceramic fine powders derived from liquid phase processes such as the sol-gel route, spray pyrolysis, and hydrothermal treatment. Recently, he has been studying the development of high-performance Li battery materials and TiO₂ photocatalytic materials by nanotechnology.



Mamoru Nomura

Mamoru Nomura is a professor of chemical engineering in the Materials Science and Engineering Department, Fukui University. He graduated from Kyoto University in 1964 and received his M.S. in 1966 and Ph.D. in 1976 from Kyoto University. His research interests are the kinetics and mechanisms, simulation, and reactor design of heterophase radical polymerization such as emulsions and microemulsion polymerizations. He has delivered several invitation and keynote lectures at international conferences such as those organized by the Gordon Research Foundation and the American Chemical Society. He started "The 1st Polymeric Microspheres Symposium" in 1980 in Fukui, which is domestically organized every two years, and celebrated its 20th anniversary in 2000. He also organized "The 1st International Symposium on Polymeric Microspheres" in 1991 in Fukui.

Production of Silica Particles by Electrostatic Atomization[†]

Yasushige MORI and Yuusuke FUKUMOTO

Department of Chemical Engineering and Materials
Science, Doshisha University*

Abstract

Electrostatic atomization is a method typically used to produce fine liquid droplets with diameters between ten and several hundred micrometers and a relatively narrow size distribution. This method is simple but its mechanism is not yet fully understood.

Our research involved producing fine silica particles by forming droplets of water glass no. 3 using electrostatic atomization, then dehydrating them and removing their sodium ions. The atomization state was classified into three modes according to applied voltage: dripping, uniform cone-jet, and discharge modes. Uniformly sized droplets were produced only with the uniform cone-jet mode at a positive high voltage. The mean volume diameter of silica particles could be estimated as a function of flow rate and applied voltage, as well as the surface tension, viscosity, and conductivity of the water glass solution.

Key words: Electrostatic atomization, silica particles, sodium silicate solution, uniformly sized particles, high voltage field

1. Introduction

One way of obtaining fine particles from liquid is to first make the liquid into fine droplets, then remove the solvent by drying or other procedures to obtain solid particles. Typical methods of atomizing liquids include those using pressure energy such as binary nozzles and nebulizers, and methods that apply mechanical vibration energy, such as ultrasonic spraying and vibrating orifices. By contrast, electrostatic atomization [1, 7] applies electrical energy to liquid at the nozzle tip, thereby breaking the liquid column at the nozzle into fine droplets. Although it is possible to vary the size of the produced droplets from the sub-micrometer level to several millimeters, and to obtain droplets of a comparative monodispersion, there is currently little promise of increasing its processing capacity. The influence of a liquid's surface tension and its electrophysical characteristics on the electro-

static atomization is very large. For example, there are few reports to use solutions with high conductivity or high viscosity [12].

There are an interfacial reaction [3] and a membrane emulsion as the method to produce spherical particles from solutions [4]. For the interfacial reaction, silica particles are produced by mixing water glass (a sodium silicate solution) into benzene, and then solidifying at the droplet interface. As droplet fusion and dispersion occur at both the droplet formation stage and the solidification stage, it yields particles with a broad size distribution. Membrane emulsion yields a monodispersion of spherical silica by passing water glass through an inorganic membrane treated hydrophobic, and making droplets of a uniform size. However, it is a complicated procedure that has difficulty delivering particles bigger than 10 μm . There are reports by Sato *et al.* [8, 9] on making silica particles by electrostatic atomization, but they offer little discussion on the effects of physical properties of liquid.

We therefore used water glass with high conductivity and high viscosity to explore the influence of their physical properties, supply flow rate, and applied voltage on electrostatic atomization, and examined the conditions for making spherical silica particles of uniform size in the several hundred μm range.

* 1-3 Tatara Miyakodani, Kyotanabe, Kyoto 610-0321 Japan.
TEL: 0774-65-6626 FAX: 0774-65-6847
E-mail: ymori@mail.doshisha.ac.jp

[†] This report was originally printed in J. Soc. Powder Technology, Japan. **38**, 90-96 (2001) in Japanese, before being translated into English by KONA Editorial Committee with the permission of the editorial committee of the Soc. Powder Technology, Japan.

2. Materials and Methods

An aqueous solution of sodium silicate, known as water glass (water glass no. 3, made by Fuji Chemical Co., Ltd.) was used. Water glass no. 3 contains 29% silicon in the form of SiO_2 , and its $\text{SiO}_2/\text{Na}_2\text{O}$ molar ratio is 3.2. Pure water was added to the water glass to change the physical characteristic values of the aqueous solution. The surface tension of the solution was measured with a Wilhelmy tensiometer (CBVP-A3, Kyowa Science Co., Ltd.), viscosity coefficient with a cone and plate type viscometer (ED, TOKIMEC INC.), and conductivity with a conductivity meter (ES-12, Horiba, Ltd.). **Table 1** shows that adding more pure water brings a linear decrease in surface tension, and an exponential decrease in the viscosity coefficient, while conductivity maximized at the condition added 40 vol.% pure water. This can be explained by the declining concentration of sodium silicate (water glass) and the attendant change in dissociation.

Droplets were formed by the nozzle (N) in the schematic diagram of the experimental apparatus as shown in **Fig. 1**. It was a stainless steel pipe with an outside diameter of 0.7 mm and an inside diameter of 0.4 mm. Its tip was polished and finished to a 90° angle. Facing the nozzle was the earth electrode (E), a brass disk 60 mm in diameter and 2 mm thick. In its center was a 10 mm hole that allowed atomized droplets to pass through. The earth electrode was 6 mm away from the nozzle tip. A high-voltage power supply (HV; model HEOPS-10B2-PV made by Matsusada Precision) was used to apply a positive or negative DC voltage between the nozzle and the earth electrode. To prevent electricity leakage, we used a microfeeder (JP-S, Furue Science) to supply silicone oil (KF-96-100CS, Shin-Etsu Chemical Co., Ltd.) to

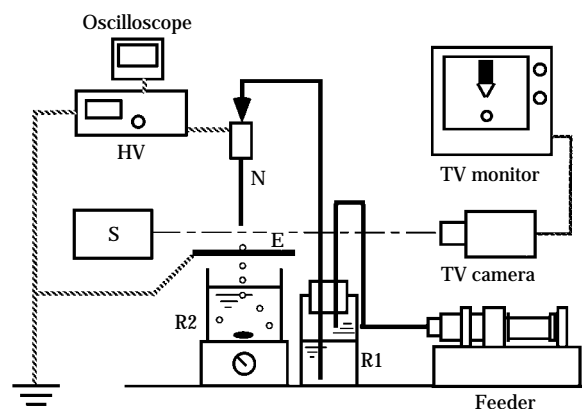


Fig. 1 Schematic Diagram of Experimental Apparatus
 HV: High voltage power supply, N: Nozzle, E: Earth electrode, S: Stroboscope, R1: Vessel with water glass and silicone oil, R2: Container of alcohol solution

the sealed container (R1), thereby supplying a certain quantity of the water glass solution from R1 to the nozzle. Droplets formed by electrostatic atomization were captured in a polyethylene container (R2) holding alcohol, where the droplets were instantaneously dehydrated and solidified. Atomization was observed with a video camera, video monitor, and a stroboscope (S).

To remove the sodium from the water glass particles solidified in the alcohol (solid particles of sodium silicate), they were separated from the alcohol and then immersed for 5 min in a 500 mol/m^3 aqueous solution of dilute sulfuric acid. We used an optical microscope to count out over 200 of the silica particles thus made, and determined their particle size distribution. To find the mean size we calculated the mean volume diameter on a number basis from counted data.

3. Results and Discussion

3.1 Solution to Capture Water Glass Droplets

Water glass becomes silica particles after reactions to remove water and sodium. Accordingly, we experimented with a method of removing water and sodium by dripping the atomized water glass droplets directly into a 500 mol/m^3 aqueous solution of dilute sulfuric acid. Water glass reacted rapidly with the dilute sulfuric acid and immediately solidified, but it flocculated instead of becoming spherical particles, probably because of the low interfacial tension between water glass and dilute sulfuric acid. We therefore decided to obtain spherical silica particles by forming an inter-

Table 1 Physical Properties of Sample Solutions Measured at 293 K

Sample No.	Volume ratio of water glass No.3 and water	Viscosity (mPa s)	Surface tension (mN m ⁻¹)	Conductivity (S m ⁻¹)
30	100 : 0	139.3	71.0	3.46
31	90 : 10	37.3	66.7	3.79
32	80 : 20	21.7	64.0	3.83
33	70 : 30	10.8	55.7	4.09
34	60 : 40	6.7	52.3	4.11
35	50 : 50	4.3	48.5	4.05

face with the water glass, removing water and solidifying with alcohol, which has a dehydration effect, and then immersing the particles in 500 mol/m³ aqueous solution of dilute sulfuric acid to remove sodium.

Methanol, ethanol, and 2-propanol were tested to select an alcohol suited to solidifying particles while keeping them spherical. Photomicrographs in **Fig. 2** were taken of the captured silica particles. We were unable to obtain spherical particles with 2-propanol (**Fig. 2a**) or ethanol (**Fig. 2b**). Using methanol yielded the most spherical particles (**Fig. 2c**). Sato *et al.* [9] used a 60 vol.% solution of ethanol when making silica particles from water glass no. 3. Particles dehydrated and solidified with methanol are almost concentric circles as in **Fig. 2c**. Dehydration and solidification begin at a droplet's surface, with interior water exiting later, which is likely what gives the particles their hollow centers, and therefore their concentric circle configuration. Particles made with 2-propanol appear to have solid centers in the photomicrograph. It would seem that when water exits slowly and solidification proceeds unhurriedly, particles without hollows are obtained even though droplet shape cannot be retained, but when solidification is rapid, one can obtain spherical, hollow silica particles. However, because hollow particles in the making are

sometimes destroyed when interior water exits, further study will be necessary for choosing an appropriate capture solution.

3.2 Effect of Applied Voltage

Silica particles were produced when a positive high voltage applied on the nozzle with grounding the opposed electrode. The relationship between the mean volume diameter and applied voltage shows **Fig. 3**. Zone A, where applied voltage ranged up to 4.6 kV, was an electrostatic drip zone where the size of the droplets gradually decreased as applied voltage rose. At 4.6 kV zone A suddenly became zone B, a uniform cone-jet zone where small droplets were produced. Electrostatic force caused by the electric charge accumulated on droplet surfaces, overcame surface tension, and allowed the formation of uniformly sized small droplets. We observed at this point that droplets emerging from the nozzle tip were stretched into cone shapes called Taylor cones [10]. This uniform cone-jet mode continued at about 5.0 kV at the flow rate of 0.13 ml/min, and at around 5.2 kV with a large flow rate of 0.32 ml/min. Further increasing the applied voltage, we noted a discharge atomization mode where the current amount suddenly increased (zone C). Average particle size was some-

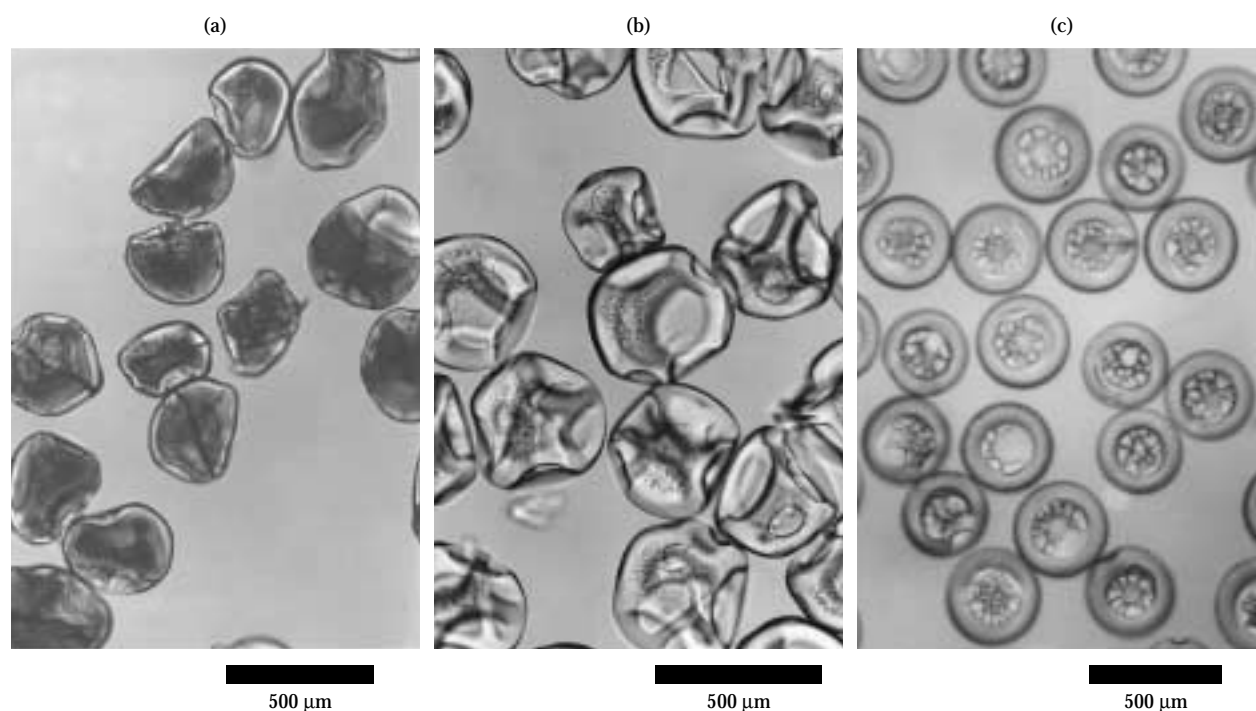


Fig. 2 Effects on Particle Shape of Various Alcohols Used as Collection Liquids
Experimental conditions were the same as the uniform cone-jet mode in Fig. 4.
(a) 2-propyl alcohol, (b) Ethyl alcohol, (c) Methyl alcohol

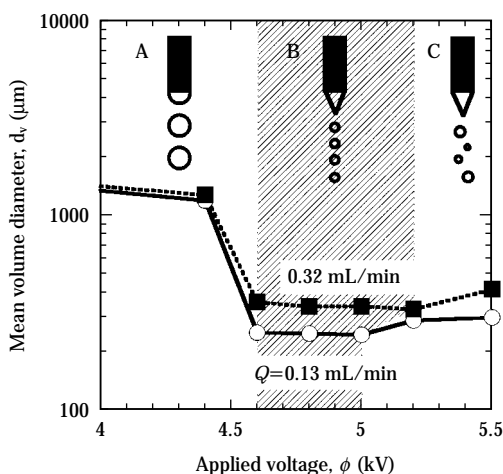


Fig. 3 Effect of Applied Voltage on Mean Volume Diameter
 A: Dripping mode B: Uniform cone-jet mode
 C: Discharge mode

what larger in this zone because under these conditions some of the droplets were large, but the wider particle size distribution produced a clear distinction between zones B and C. As can be seen from the particle size distributions of these two zones (Fig. 4) and the photomicrographs of zone B (Fig. 2c) and zone C (Fig. 5), there was a very narrow particle size distribution at 4.8 kV, at which the uniform cone-jet mode arose (zone B), while the distribution was very broad at 5.5 kV, where discharge atomization proceeded (zone C). Because the purpose of this research was to obtain silica particles of uniform size, we then turn-

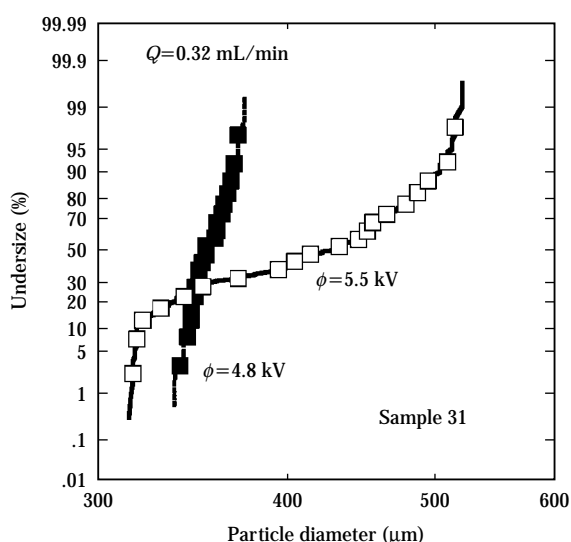


Fig. 4 Comparison of Particle Size Distribution in Uniform Cone-jet Mode (4.8 kV) with That in Discharge Mode (5.5 kV)

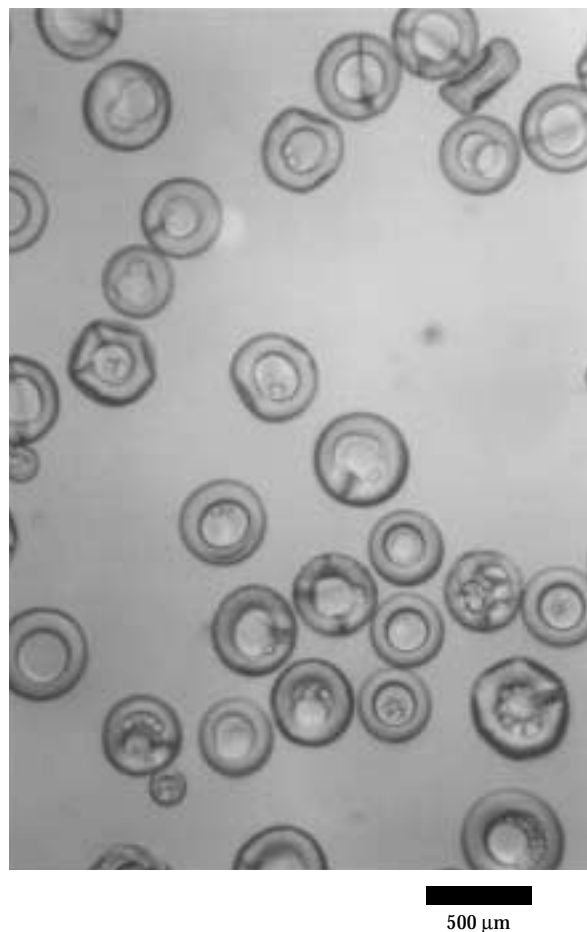


Fig. 5 Silica Particles Produced in Discharge Mode
 Experimental conditions were the same as those in Fig. 4.

ed our attention exclusively to the uniform cone-jet mode.

Next we investigated the effect of the polarity of the voltage applied to the nozzle. When a positive voltage was applied, uniform cone-jet atomization was observed across the range from 4.6 to 5.2 kV, but applying a negative voltage yielded different results. When applying 4.6 kV there was an immediate transition from zone A to zone C, and we observed no uniform cone-jet atomization. Mori *et al.* [2] and Sato *et al.* [8] reported that it is easier to achieve uniform cone-jet atomization when applying a positive voltage than when applying a negative voltage, which agrees with our results. We conjecture the reason is the difference between positive and negative discharge characteristics when a corona discharge arises between the nozzle tip and the earth electrode disk as electrostatic atomization proceeds. Specifically, when there is a positive electrode corona discharge, nitrogen and oxygen atoms are ionized and move toward the earth

electrode, but under a negative electrode corona discharge, highly mobile electrons themselves move, resulting in dielectric breakdown and difficulty in obtaining a stable corona discharge.

The following equation provides the strength of the electric field between the nozzle and disk [11].

$$E_0 = 4\phi / \{d_0 \ln(8L/d_0)\} \quad (1)$$

When 5 kV were applied under the electrode conditions in Fig. 3, the electric field strength at the nozzle's tip, E_0 , was calculated to be 6.7 MV m^{-1} , which was greater than the 3 MV m^{-1} dielectric breakdown strength of air. Thus electrostatic atomization is presumably difficult with negative high voltage. Results discussed below were obtained by applying positive high voltage.

As Fig. 6 shows the effects of applied voltage and volumetric flow rate on the mean volume diameter of silica particles, the high-viscosity Sample 31 yielded large silica particles whose sizes decreased only slightly when a high voltage was applied. But Sample 33, whose viscosity was one-fourth that of Sample 31, was heavily affected by applied voltage. In all samples, particle size was less affected by applied voltage at smaller flow rates.

3.3 Flow Rate

Fig. 6 also shows the influence of flow rate. The lower the flow rate, the smaller the silica particles that were formed. But we also found that as flow rate

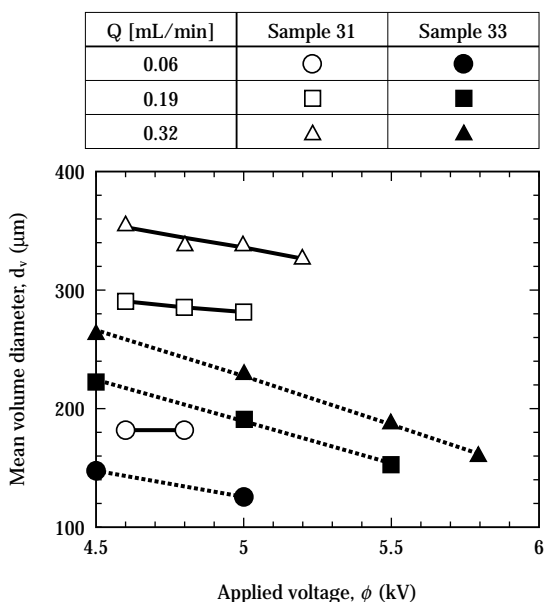


Fig. 6 Effects of Applied Voltage and Flow Rate on Mean Volume Diameter in Uniform Cone-jet Mode

decreased, the uniform cone-jet zone narrowed. When the flow rate was 0.06 ml/min, the lowest in our experiment, uniform cone-jet atomization occurred between 4.6 and 4.8 kV in Sample 31, and between 4.5 and 5.0 kV in Sample 33.

At a 5 kV applied voltage, the size distribution of silica particles narrowed as the flow rate increased as shown in Fig. 7. But when the flow rate was reduced, average particle size decreased while the distribution broadened. The reason appears to be that decreasing the flow rate makes it hard to control, and even a small variation in flow rate has a big effect on atomization.

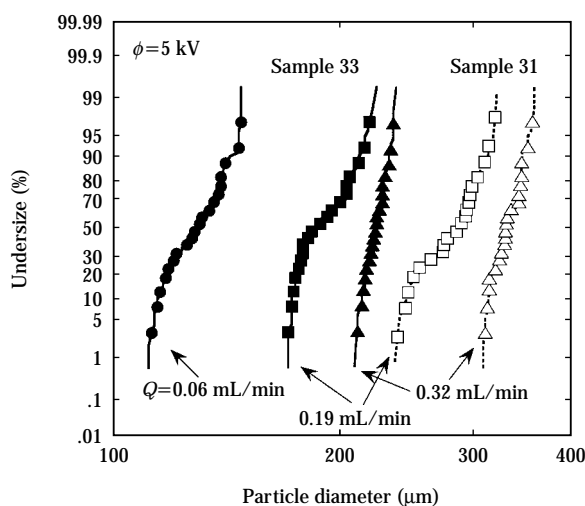


Fig. 7 Particle Size Distributions in Uniform Cone-jet Mode Applied Voltage was 5 kV.

3.4 Addition of Pure Water

We manufactured silica particles from an aqueous solution whose ratio of water glass to pure water was varied while maintaining a 5 kV applied voltage and a 0.13 ml/min flow rate. Fig. 8 shows that undiluted water glass (Sample 30) yields a two-peak distribution. As the amount of added water increased, mean particle diameter decreased and the distribution narrowed. One way to obtain small silica particles is to reduce the flow rate, but it is also effective to use water glass whose viscosity has been attenuated by adding water.

As water content increases, it is anticipated that droplets will contract more during dehydration. To investigate the contraction rate of droplets when turning into particles, we made a comparison by conducting an experiment in which atomized droplets were captured directly by silicone oil. When using a water

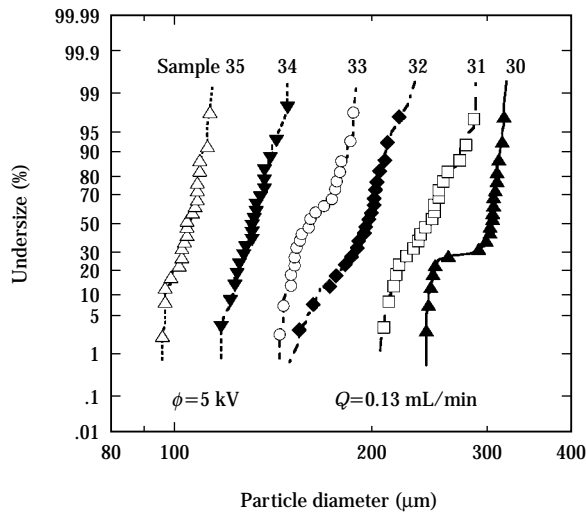


Fig. 8 Particle Size Distributions of Various Samples
Applied voltage was 5 kV and flow rate was 0.13 ml/min.

glass solution to which 10 vol.% pure water had been added (Sample 31), diameter contracted 5.8%, and with a water glass solution to which 30 vol.% pure water had been added (Sample 33), contraction was 7.8%. Far greater than this change was the change in average particle diameter, thereby demonstrating that physical properties of a solution are the larger influence.

3.5 Estimating the Diameter of Particles Formed

Substantial changes occurred in atomization by diluting water glass with pure water, but because some physical properties of the solution also change simultaneously, it is unknown which physical property has the largest influence. For that reason we performed a multiple regression analysis for flow rate, applied voltage, surface tension, viscosity coefficient, and conductivity using the data for the uniform cone-jet mode under conditions of a 0.06 to 0.32 ml/min flow rate, and a 4.5 to 5.8 kV applied voltage. The analysis yielded the following correlation equation.

$$d_v = 5.06 \times 10^4 \phi^{-1.56} Q^{0.383} \gamma^{0.861} \eta^{0.313} \kappa^{2.29} \quad (2)$$

Fig. 9 shows the relationship between the mean volume diameter calculated with this equation, $d_{v,calc}$, and the measured value, $d_{v,obs}$, has a high multiple correlation of 0.986, which is significant. Particle diameter was most affected by conductivity, while the influences of the flow rate and viscosity coefficient were low.

Mori *et al.* [2] reported a correlation equation using

distilled water, ethanol, and an aqueous glycerin solution. Ogata *et al.* [5, 6] derived a correlation equation using distilled water, ethanol, propanol, and an aqueous glycerin solution for a solution up to 130 mPa s. Further, Yamaguchi *et al.* [13] made atomized droplets using an aqueous solution of calcium chloride, an aqueous solution of glycerin, and a solution made by adding liquid paraffin and/or an antistatic agent to xylene, and described the relationship between droplet size and physical properties. Although they propose a dimensionless correlation equation, a direct comparison is difficult because the dimensionless quantity differs from one researcher to another. For that reason we made the following simplification to compare Eq. 2 with the dimensionless correlation equations proposed heretofore.

As our experiment used only one nozzle, the ratio of its inner and outer diameters was fixed. Although we did not measure permittivity, we made its contribution constant under the assumption that its value would not change very much due to the large amount of water. Using these assumptions, we summarized the dependency of physical properties in **Table 2** using dimensionless correlation equations in previous reports. There is no value for conductivity in the data from Mori *et al.* [2] because they did not include it. The dependence on physical property values exhibits considerable differences among ours and the previous four reports. Conductivity was especially large in our study: while it was under 0.2 S m^{-1} in the previous reports, it was in the high range of 3 to 4 S m^{-1} in our study. Also, we examined the correlation with the

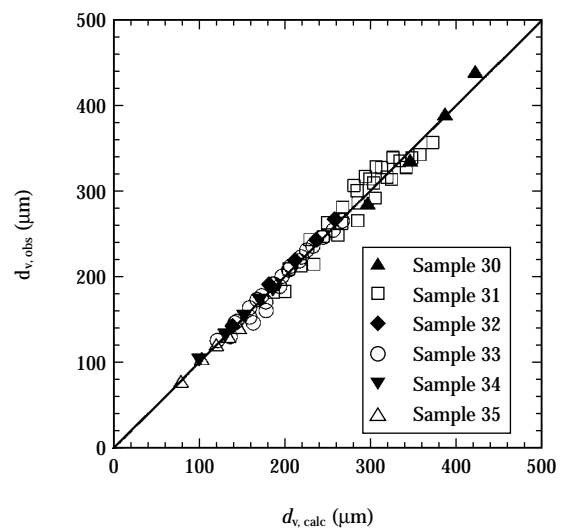


Fig. 9 Dimensionless Correlation of Mean Volume Diameter of Silica Particles Produced under the Conditions of This Study

Table 2 Values for Dependence on Physical Properties

	flow rate Q	applied voltage ϕ	surface tension γ	viscosity η	conductivity κ
this study	0.383	-1.599	0.861	0.313	2.291
Mori [2]	0.43	-0.51	-0.022	0.124	-
Ogata [5]	0.667	-1.111	0.111	0.444	-0.222
Ogata [6]	0.667	-1.111	0.208	0.25	-0.222
Yamaguchi [13]	0.47	-1.50	0.52	0.07	-0.08

Power indexes of physical properties of sample solution and of operating conditions for the empirical correlation to the size of particles produced by electrostatic atomization. Our results are compared with those of four previous studies.

size of particles formed. Specifically, particle diameter was 5 to 10% smaller than droplet diameter, and the shrinkage factor was dependent on the amount of water added. For this reason, it would seem there is a slight difference between the correlation with droplet diameter in previous reports and the correlation in our case.

Because Eq. 2 is an empirical equation, it is inappropriate for understanding the phenomenon, and we therefore derived a dimensionless correlation equation from Eq. 2. Assuming that a relative permittivity of the solution is constant, we found the following dimensionless correlation equation with the dimensionless quantity used by Yamaguchi *et al.* [13].

$$\frac{d_v}{d_0} = 3.83 \times 10^{-9} \left(\frac{\epsilon_0 E_0 d_0}{\gamma} \right)^{-0.917} \left(\frac{\rho u^2 d_0}{\gamma} \right)^{0.65} \left(\frac{\eta u}{\gamma} \right)^{0.382} \left(\frac{\epsilon_f \epsilon_0 u}{\kappa d_0} \right)^{-1.3} \quad (3)$$

The multiple correlation coefficient was slightly worse, at 0.977. Comparison with the dimensionless quantity range of Yamaguchi *et al.* [13] produces a considerably different conductivity range as discussed above, so the index of the fourth dimensionless quantity in Eq. 3 is different. Further, the index of the dimensionless quantity including u was also different to adjust the dependence of flow velocity u . Judging from this, obtaining a general equation to estimate the droplet diameter in electrostatic atomization would require the accumulation of further data on different physical properties.

4. Conclusion

We added various amounts of pure water to a solution of water glass with high conductivity and high viscosity to change the solution's physical properties and investigated electrostatic atomization, and arrived at the following conclusions.

1) As applied voltage was increased, the electrostatic drip mode, uniform cone-jet mode, and discharge mode were observed. It was in the uniform cone-jet mode that droplets of uniform size were obtained.

2) When the DC high voltage applied to the nozzle was positive, we observed uniform cone-jet atomization, but making it negative caused a direct shift from electrostatic drip mode to discharge mode, with no uniform cone-jet atomization observed.

3) When the applied voltage increased, the high electric field strength at the nozzle tip resulted in a higher frequency of droplet ejection and a smaller mean volume diameter, but the effect of the applied voltage on the particle size was small.

4) Decreasing the flow rate reduced mean volume diameter, but it was necessary to increase flow rate to obtain silica particles with a narrow size distribution.

5) Diluting the water glass with pure water resulted in silica particles having a small mean volume diameter and a narrow particle size distribution.

6) Based on the results of this study, we obtained the following empirical equation estimating to the mean volume diameter of the silica particles formed.

$$d_v = 5.06 \times 10^4 \phi^{-1.56} Q^{0.383} \gamma^{0.861} \eta^{0.313} \kappa^{-2.29}$$

Acknowledgments

This research benefited from the cooperation of Mr. Masaaki Mizuguchi at Suzuki Yushi Industrial Co., Ltd. for the supply of water glass. We received the advice from Professor Masayuki Sato of Department of Biological and Chemical Engineering in Gunma University, and from Chief Researcher Keiko Nakahara at the Research Institute of Innovative Technology for the Earth. Part of this research was supported by RCAST at Doshisha University. We express our appreciation to all these people and institutions.

Nomenclature

d_0	outer diameter of nozzle	(m)
d_v	mean volume diameter of silica particle	(m)
E_0	electric field strength of nozzle tip, defined in Eq. 1	(V m ⁻¹)
L	electrode gap	(m)
Q	volumetric flow rate of sample solution	(m ³ s ⁻¹)
u	linear velocity of sample solution through nozzle	(m s ⁻¹)
γ	surface tension of sample solution	(N m ⁻¹)
ϵ_0	permittivity of vacuum	(F m ⁻¹)
ϵ_f	dielectric constant of sample solution	(F m ⁻¹)
η	viscosity of sample solution	(Pa s)
κ	electrical conductivity of sample solution	(S m ⁻¹)
ρ	density of sample solution	(kg m ⁻³)
ϕ	applied voltage	(V)

References

- 1) Cloupeau, M. and B. Prunet-Foch. "Electrostatic Spraying of Liquids: Main Functioning Modes," *J. Electrostat.*, **25**, 165-184 (1990).
- 2) Mori, Y., K. Hijikata and T. Nagasaki. "Fundamental Study on Electrostatic Atomization," *Nippon Kikai Gakkai Ronbunshu, B-hen*, **47**, 1881-1890 (1981).
- 3) Nakahara, Y. and K. Miyata. "Preparation of Spherical Fine Particles by Interfacial Reaction," *Kagaku Kogaku*, **46**, 541-546 (1982).
- 4) Nakashima, T. and M. Shimizu. "Preparation of Monodispersed O/W Emulsion by Porous Glass Membrane," *Kagaku Kogaku Ronbunshu*, **19**, 984-990 (1993).
- 5) Ogata, S., T. Hatae, K. Shoguchi and H. Shinohara. "The Dimensionless Correlation of Mean Particle Diameter in Electrostatic Atomization," *Kagaku Kogaku Ronbunshu*, **3**, 132-136 (1977).
- 6) Ogata, S., K. Shoguchi, T. Hatae and H. Shinohara. "Average Sizes of Droplets Electrostatically Sprayed," *Kagaku Kogaku Ronbunshu*, **4**, 656-658 (1978).
- 7) Sato, M. "Production of Uniformly Sized Droplets by Means of Electrostatic Methods," *J. Soc. Powder Technol. Jpn.*, **29**, 376-383 (1992).
- 8) Sato, M., T. Hatori, T. Ikawa, M. Saito and T. Ohshima. "Production of Uniformly Sized Silica Particles with a Wide Controllable Diameter Range," *Proc. Inst. Electrostat. Jpn.*, **20**, 294-300 (1996).
- 9) Sato, M., H. Takahashi, M. Awazu and T. Ohshima. "Production of Ultra-uniformly-sized Silica Particles by Applying AC Superimposed on DC Voltage," *J. Electrostat.*, **46**, 171-176 (1999).
- 10) Taylor, G. "Disintegration of Water Drops in an Electric Field," *Proc. R. Soc. London*, **A280**, 383-97 (1964).
- 11) The Institute of Electrostatics ed. *Handbook of Electrostatics*, p. 172, Ohm Sha (1983).
- 12) Watanabe, H., T. Matsuyama and H. Yamamoto. "The Formation of an Immobilized Enzyme Particle by Electrostatic Atomization and Its Performance," *J. Soc. Powder Technol. Jpn.*, **34**, 679-683 (1997).
- 13) Yamaguchi, M., A. Matsui, H. Murakami and T. Katayama. "Formation of Uniformly Sized Droplets of Newtonian Liquids in a DC Electric Field," *Kagaku Kogaku Ronbunshu*, **21**, 357-364 (1995).

Author's short biography



Yasushige Mori

Yasushige Mori is a professor in Department of Chemical Engineering and Materials Science at Doshisha University. He graduated from Kyoto University, Department of Chemical Engineering in 1974, and received his doctorate in engineering from the same University in 1980. His research interests include the formation of nanoparticles of metals and/or semiconductors in liquid systems, measurements of interaction and adhesion forces between particles and plates, particle size analysis, and applications of mesoporous materials.



Yuusuke Fukumoto

Yuusuke Fukumoto is an engineer at Matsushita Battery Industrial Co., Ltd. He received his B.S. in 1996 and M.S. in 1998 from Department of Chemical Engineering and Materials Science at Doshisha University.

Flocculation Mechanism of Suspended Particles Using the Hydrophilic/Hydrophobic Transition of a Thermosensitive Polymer[†]

SHUJI SAKOHARA, TAKASHI KIMURA
and KAZUO NISHIKAWA

Department of Chemical Engineering, Hiroshima
University*

Abstract

We examined the flocculation of suspended particles using a thermosensitive polymer which undergoes a reversible hydrophilic/hydrophobic transition when heating or cooling its aqueous solution. As a thermosensitive polymer poly(*N*-isopropylacrylamide) (polyNIPAM), whose transition temperature is about 32°C, was used. Flocculation experiments were performed by the jar test using kaolin suspension. In the case of operating temperature lower than the transition temperature of polyNIPAM, there was an optimum polymer dosage, and by dosing excessively kaolin particles were dispersed stably in the same manner as conventional polymeric flocculants. However, floc formation was observed by heating the suspension above the transition temperature under the excess polymer dosage. Furthermore, by cooling the floc-containing suspension down to below the transition temperature again, the flocs were disorganized to the particles. These phenomena show that the floc formation caused by heating to above the transition temperature is due to the hydrophobic interaction of polyNIPAM molecules adsorbed on the particles.

Key words: Solid-liquid separation, flocculation, poly(*N*-isopropylacrylamide), thermosensitive polymer, hydrophobic interaction

Introduction

Polymeric flocculants, which are widely used in the flocculation and dehydration of suspensions, are generally hydrophilic polymers and therefore have the drawback that the flocs contain large amounts of water which cannot be easily removed. In our previous paper (Sakohara and Nishikawa, 2000) we proposed the use of thermosensitive polymers as a way to alleviate this problem.

Thermosensitive polymers in aqueous solutions become soluble (hydrophilic) at low temperatures, but are insoluble (hydrophobic) at high temperatures. This hydrophilic/hydrophobic transition is reversible and occurs at the transition temperature, which is determined by a primary structure of polymer (Ito, 1989). In our previous paper (Sakohara and

Nishikawa, 2000) by using the plunger test the compaction of a highly concentrated kaolin suspension with poly(*N*-isopropylacrylamide) (polyNIPAM), a representative thermosensitive polymer, was examined. The suspended particles were fully mixed with polyNIPAM, and the mixture was heated to above the transition temperature. Then by applying an appropriate external force, the compacted flocs was readily obtained.

We proposed the mechanism illustrated in **Fig. 1** for the formation of such compacted flocs employing thermosensitive polymers. First, the polymer molecules are fully adsorbed onto the suspended particles below the transition temperature (process 1, left). If the conventional hydrophilic polymer is used, the particles disperse stably under these conditions. But in case of thermosensitive polymer, by heating the suspension to above the transition temperature (process 2, center), the adsorbed polymer molecules change to hydrophobicity, in turn making the surfaces of the suspended particles hydrophobic, and resulting in the flocculation (floc formation) of the suspended particles due to the hydrophobic interaction. Applying an

* Higashi-Hiroshima 739-8527

[†] This report was originally printed in Kagaku Kogaku Ronbunshu, **26**, 734-736 (2000) in Japanese, before being translated into English by KONA Editorial Committee with the permission of the editorial committee of the Soc. Chemical Engineers, Japan.

appropriate external force at this point will cause the rearrangement of the particles, thereby forcing out the water and readily allowing compaction. On the other hand, since the hydrophilic/hydrophobic transition of thermosensitive polymers is reversible, by cooling the mixture down below the transition temperature (process 3, right) the flocs disorganize and return to stable suspended particles.

However, the plunger test in our previous paper was meant to obtain the compacted flocs and did not allow us to adequately investigate this flocculation mechanism. In this research, therefore, we performed the flocculation experiments and examined the validity of this model by using an agitator tank.

1. Materials and Methods

As a thermosensitive polymer we used poly(*N*-isopropylacrylamide) (polyNIPAM), which were synthesized by the same methods as in our previous paper (Sakohara and Nishikawa, 2000). The molecular weight is about 3.95×10^6 , and its transition temperature in water is about 32°C. As a sample suspension, kaolin (Katayama Chemicals, Inc.) suspension with a concentration of 20 kg/m³, containing 0.5 mM sodium hydroxide as a dispersant, was used. The transition temperature of polyNIPAM in the aqueous solution of 0.5 mM sodium hydroxide is about 34°C, slightly higher than that in water.

We performed the flocculation experiment with an acrylic resin agitation tank which had an inside diameter of 109 mm and a height of 135 mm, and which was fitted with six baffle plates. Into this tank we put 1 dm³ of the test suspension, and submerged it in a thermostatic bath at the prescribed temperature. The suspension was stirred at 300 rpm using a turbine blade (six flat blades, 50 mm in diameter) installed at half the liquid depth. After the temperature of suspen-

sion reached the prescribed temperature, the desired amount of polymer was added, and the mixture was stirred rapidly (300 rpm) and then slowly (150 rpm) under each of three experimental conditions described below. Although the slow stirring speed was faster than that generally used in the jar test, this speed was chosen to ensure good contact between the suspended particles and the polymer molecules, or among suspended particles. The flocculation performance was evaluated by settling for 30 minutes after stirring finished. The sample supernatant was taken from the depth of 50 mm below the surface, and the measurement of transmittance was performed at a wavelength of 600 nm using a spectrophotometer.

The flocculation experiment was conducted under each of the following three conditions to confirm the viability of the mechanism proposed in Fig. 1.

(1) Flocculation experiment below and above the transition temperature

The mechanism in Fig. 1 assumes that the hydrophilic polyNIPAM molecules adsorb onto suspended particles shown as in process 1 in the figure. To verify this we examined the flocculation performance at 30°C, below the transition temperature of polyNIPAM, and at 40°C, above the transition temperature. The desired amount of polyNIPAM was added to the suspension after the suspension had attained the prescribed temperature, and the stirring was performed at high speed for 30 min, and then at low speed for 20 min.

(2) Flocculation experiment by heating

We performed the following experiment to verify process 2 in Fig. 1, that is, the formation of flocs by heating the suspension. PolyNIPAM was added at 30°C, below the transition temperature, and the mixture was stirred at high speed for 10 min. The ther-

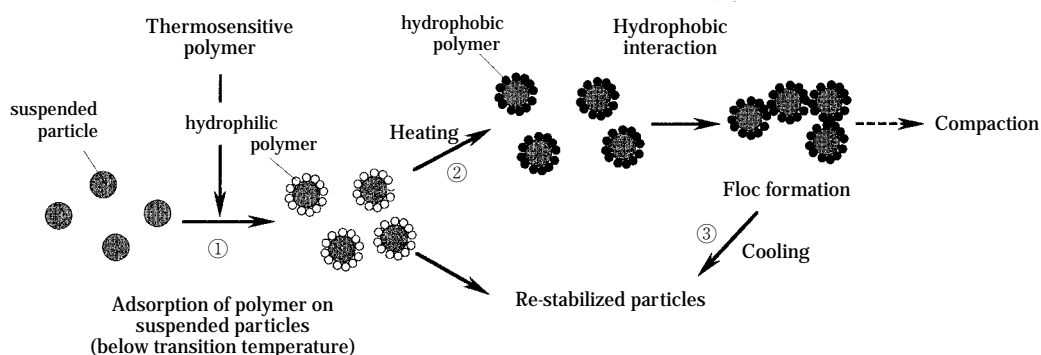


Fig. 1 Mechanism causing flocculation of suspended particles by using a thermosensitive polymer

mostatic bath water of 30°C was then quickly changed to water of 60°C, and the rapid stirring was continued for 20 min, followed by 20 min slow stirring. The change in suspension temperature is indicated by the open circles in **Fig. 2**. Measurements of temperature were carried out with a thermocouple near the agitator blades.

(3) Flocculation experiment by cooling suspension back below the transition temperature after heating

We performed the following experiment to verify process 3 in **Fig. 1**, in which flocs formed by heating will again disperse when the suspension is cooled below the transition temperature (reversibility). The suspension was stirred at low speed for 20 min under the heating conditions described above, and then the thermostatic bath water was quickly replaced with water of 25°C, and slow stirring was continued for another 50 min. The closed circles in **Fig. 2** show the suspension's temperature change.

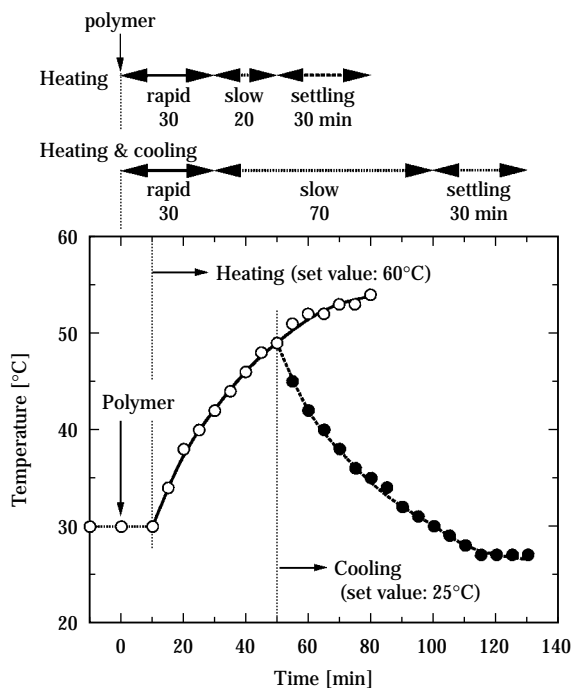


Fig. 2 Temperature change in the flocculation tank

2. Results and Discussion

2.1 Effect of Temperature on Floc Formation

Fig. 3 shows the flocculation performance at 30°C and 40°C. Since polyNIPAM is hydrophilic at 30°C, it acts like the conventional hydrophilic polymeric

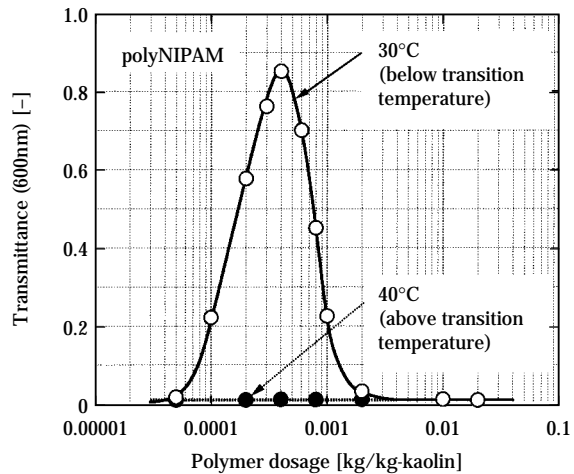


Fig. 3 Flocculation performance above and below the transition temperature (about 34°C)

flocculant: The transmittance of the supernatant increased with increasing the polymer dosage, and then decreased after peaking. This means there is an optimum polymer dosage. At and near that dosage, the bridging adsorption of polyNIPAM on the suspended kaolin particles encourages floc formation, and the transmittance of supernatant increases. But when too much polyNIPAM is added, the surfaces of the suspended kaolin particles are covered with polyNIPAM, and thereby disperse stably, which reduces transmittance (Sakohara et al., 1980). At 40°C, however, flocs were hardly formed no matter what the additive amount of polymer, and the supernatant transmittance remained low. It is considered due to the fact that the added polyNIPAM molecules immediately became hydrophobic and that they could not adsorb onto the kaolin. As a result, flocs did not form. Therefore, to make kaolin adsorb the polyNIPAM as in the **Fig. 1** model, the operation must be performed below the transition temperature.

We have seen no instances as in our experiment in which polyNIPAM was used as the flocculant, but there are some reports of the flocculation of inorganic particle suspensions by copolymers of NIPAM and cationic monomers (Guillet et al., 1985; Deng et al., 1996). When this kind of cationic polymer is used, floc formation has been observed even if the polymer is added to a suspension at the temperature higher than the transition temperature. In this kind of polymer, the portion of polyNIPAM that has become hydrophobic agglomerates through hydrophobic interaction, and forms polymer fine particles with cationic components on their surfaces. It appears that

these surface with cationic components function as flocculants. As a result, they cause flocculation even above the transition temperature.

2.2 Effect of Heating Suspension on Floc Formation

Fig. 4 compares the flocculation performance obtained by heating suspension to 60°C after poly-NIPAM adsorption at 30°C, and that obtained at 30°C. By heating from 30°C to 60°C, the transmittance increased and then decreased with increasing poly-NIPAM dosage. By adding more polyNIPAM the transmittance increased again, and then remained fairly steady (range A in the figure). In this range the supernatant had very low transmittance at 30°C, meaning that hardly any flocs were formed. This shows that flocs formed by heating the suspension after the surfaces of the suspended particles were covered enough with polyNIPAM. In fact, before the temperature of agitator tank was raised (when it was still 30°C), we did not discern floc formation, but when the tank was heated we clearly discerned floc formation with the unaided eye at the point the temperature of suspension exceeded the transition temperature. This seems to bear out the mechanism illustrated in **Fig. 1**: By heating a suspension of kaolin particles whose surfaces are covered enough with polyNIPAM, the polyNIPAM becomes hydrophobic, which in turn makes the particle surfaces hydrophobic, thereby making particles adhere to each other and form flocs due to the hydrophobic interaction.

Even when the suspension was heated, the transmittance increased with the same polymer dosage as

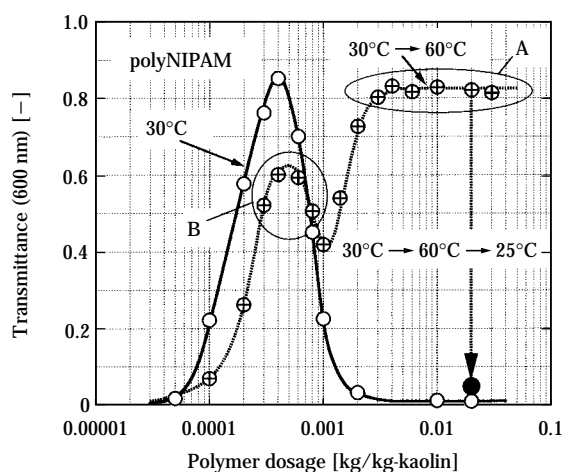


Fig. 4 Effects on flocculation performance of heating and cooling the suspension

the optimum dosage for 30°C (range B in the figure). The reason appears to be that floc formation during the 10 min of rapid stirring after adding polyNIPAM to an almost optimum amount increased supernatant transmittance. This fact suggests that even though polyNIPAM adsorbed onto the surfaces of suspended particles might become hydrophobic, they do not readily desorb from the suspended particle surfaces. As stated in our previous paper (Sakohara and Nishikawa, 2000), this is likely because polymer adsorption onto the suspended particles is multipoint adsorption by functional groups in the polymer molecules.

2.3 Reversibility of Floc Formation by Hydrophobic Interaction

The closed circle in **Fig. 4** shows one example of the flocculation performance by adding polyNIPAM, by raising the suspension temperature from 30°C to 60°C, then by cooling it down to below the transition temperature. The polymer dosage was 0.02 kg/kg-kaolin. As the figure shows, the suspension returned to a nearly completely dispersed state. We also observed clearly with the unaided eye that the floc quickly disappeared when the suspension temperature fell below the transition temperature. This shows that flocculation (floc formation) caused by the hydrophobic interaction occurs reversibly in response to the change in temperature.

Conclusion

We investigated the flocculation mechanism utilizing the hydrophilic/hydrophobic transition of poly-NIPAM, a representative thermosensitive polymer, by using an agitation tank to perform a flocculation experiment on a kaolin suspension. Since flocculation hardly occurred above the transition temperature (about 32°C), the adsorption operation of polyNIPAM onto suspended kaolin particles needs to be performed in a hydrophilic state below the transition temperature. When the kaolin particle surfaces are coated enough with polyNIPAM by increasing the polymer dosage, kaolin particles disperse stably below the transition temperature, but flocs form by heating the suspension. When the flocculated suspension is cooled back to below the transition temperature, particles disperse again. From these results, it can be concluded that the flocculation mechanism due to the hydrophobic interaction proposed in our previous paper (Sakohara and Nishikawa, 2000) is valid.

Acknowledgments

Kohjin Co., Ltd. supplied the *N*-isopropylacrylamide used in this research. Mr. Shuichi Nakano (currently at Taiheiyo Cement Co.) and Mr. Hideaki Ootake (currently at Mitsui Chemicals, Inc.) cooperated in synthesizing the polymer and performing the flocculation experiments. We wish to thank them for their help.

Literature Cited

Deng, Y., H. Xiao and R. Pelton. "Temperature-Sensitive Flocculants Based on Poly(*N*-isopropylacrylamide-co-

diallyldimethylammonium chloride)," *J. Colloid Interface Sci.*, **179**, 188-193 (1996).

Guillet, J., M. Heskins and D. G. Murray. "Polymeric Flocculant," U. S. Patent 4,536,294 (1985).

Ito, S.. "Phase Transition of Aqueous Solution of Poly(*N*-alkylacrylamide) Derivatives: Effects of Side Chain Structure," *Kobunshi Ronbunshu*, **46**, 437-443 (1989).

Sakohara, S., H. Unno and T. Akehata. "Turbidity Removal by Polymeric Flocculant: Analysis Through a Simple Bridging Model," *Kagaku Kogaku Ronbunshu*, **6**, 198-203 (1980).

Sakohara, S. and K. Nishikawa. "Flocculation and Compaction of Highly Concentrated Suspensions by Using Thermosensitive Polymers," *Kagaku Kogaku Ronbunshu*, **26**, 298-304 (2000).

Author's short biography



Shuji Sakohara

A professor in the Chemical Engineering Department at Hiroshima University since 1994. His major research interests are polymer technology, water treatment, and membrane separation. He received his B.S. and M.S. degrees from Hiroshima University in 1974 and 1976. In 1983 he received a Dr. of Engineering degree from Tokyo Institute of Technology on the flocculation of suspended solids with polymers.



Takashi Kimura

Now working as an engineer at Sumitomo Mitsui Polyolefin Co., Ltd.



Kazuo Nishikawa

Now working as an engineer at Tokushu Paper Co., Ltd. He received his B.S. and M.S. degrees from Hiroshima University in 1999 and 2002.

Development of Agglomerated Crystals of Ascorbic Acid by the Spherical Crystallization Technique for Direct Tableting, and Evaluation of Their Compactibilities[†]

Yoshiaki KAWASHIMA, Misato IMAI,
Hirofumi TAKEUCHI, Hiromitsu YAMAMOTO
and Kazunori KAMIYA
Gifu Pharmaceutical University*

Abstract

Spherically agglomerated crystals of ascorbic acid for direct tableting were successfully prepared by the spherical crystallization technique. This agglomeration dramatically improved the micromeritic and compaction properties of the original ascorbic acid crystals. The dominating mechanisms that improved compaction properties of the spherically agglomerated crystals depended on their fragmentation and plastic deformation during compaction. Support for this mechanism existed because the compacted agglomerated crystals had higher stress relaxation and lower elastic recovery than the original crystals. Spherically agglomerated crystals were tableted directly without capping by using a single-punch tableting machine under dynamic compaction, although the tensile strength of tablets with spherically agglomerated crystals decreased when the compression speed increased.

1. Introduction

Tablets are the most frequently used form of pharmaceuticals. The main tableting method in Japan used to involve first making granules, and then compressing them into tablets by way of indirect (granule) tableting, but the need in recent years for process validation, GMP, and automation of production processes has focused renewal attention on the direct tableting method, which involves few steps.

Because direct tableting necessitates an active ingredient powder that excels in flowability, bindability, mechanical strength, and other qualities more than the materials for indirect tableting, there are currently limited pharmaceutical tablets on commercial production that can be made by direct tableting. For that reason development of the design method of active ingredient crystals that can be directly tableted has been waited. As the model drug in our research ascorbic acid, which is difficult to tablet directly, was

used to develop directly compactable crystals without a binder for direct tableting. The compactibility of resultant crystals were evaluated.

Our design method involved using a process called spherical crystallization developed originally by us [1], which allowed us to manufacture agglomerated crystals with two different internal structures that were suited to our purpose. After assessing the crystals' flowability and packability to ascertain their adequacy as the powder for direct tableting, we conducted static and dynamic compression tests. We analyzed the static compression process and determined the factors related to improving the granulated crystals' compactibility. Further, anticipating the commercial production of tablets, we determined the effect of compression speed on compactibility.

2. Materials and Methods

2.1 Materials

Ascorbic acid was chosen as a model drug because of its brittleness and its strong cohesive properties. As a control for assessing powder physical properties such as flowability and packability fine crystals (100 mesh product, average particle diameter of 18.8 μm , made by Takeda Chemical Industries, Ltd.) was used, and for assessing compactibility it was coarse crystals with excellent flowability (FG product, average parti-

* 5-6-1 Mitahorahigashi, Gifu, 502-8585 Japan
TEL: +81-58-237-3931 (ext. 244) FAX: +81-58-237-6524

[†] This report was originally printed in J. Soc. Powder Technology, Japan. **38**, 160-168 (2001) in Japanese, before being translated into English by KONA Editorial Committee with the permission of the editorial committee of the Soc. Powder Technology, Japan.

cle diameter of 425 μm , made by Takeda Chemical Industries, Ltd.). A control for both assessments was commercially available granulated ascorbic acid for direct tableting (hereinafter, "C97 granules," average particle diameter of 422 μm , made by Takeda Chemical Industries, Ltd.). C97 granules are produced in a fluidized bed with 3% starch added as a binder. As the model drug for plastic deformability we used potassium chloride (Japanese Pharmacopoeia, hereinafter written "KCl," average particle diameter of 650 μm , produced by Yamazen Corporation).

2.2 Preparation of Ascorbic Acid Agglomerated Crystals for Direct Tableting

Ascorbic acid was dissolved in 50°C purified water (a good solvent) to prepare a 0.4 g/ml saturated solution. A pipette was used to quickly drop a prescribed amount of the solution into a 500 ml cylindrical agitator tank containing 300 ml of ethyl acetate (a poor solvent, maintained at 5°C) while stirring with a four-bladed propeller-type agitator at either 300 or 800 rpm. By choosing a water-to-ethyl acetate volumetric ratio of either 1:100 or 4:150, we prepared spherical agglomerated crystals of ascorbic acid by two different crystal agglomeration mechanisms: spherical agglomeration (SA), and emulsion solvent diffusion (ESD). We inserted baffles in the agitator tank to promote granulation with SA, but with ESD we let granulation occur without using baffles so as to prevent the breakdown of emulsion droplets. After stirring for 20 min the crystal agglomerates obtained were suction filtered, washed with a small amount of methanol, and dried under reduced pressure for at least 24 h. We used the agglomerate fraction in the 125 to 500 μm range, obtained by classifying with a screen to bring them into line with the C97 granule particle size range. This fraction's yield was good at 70 to 80%.

2.3 Measuring Physical Properties of Agglomerated Crystals

A scanning electron microscope (JTM-T330A, JEOL., Ltd.) was used to observe the particle form of the original crystals (100 mesh product), coarse crystals (FG product), and C97 granules, and the surface property and cross sections of the two types of spherically agglomerated crystals (SA and ESD products).

Sample flowability was measured and assessed by using the pouring method to make them pile, then measuring their angle of repose.

Sample packability was assessed by analysis of the tapping process with the Kawakita [2] (Eq. 1) and Kuno [3] (Eq. 2) methods, and using the parameters

a, b, and k in the equations.

$$(n/C) = (1/ab) + (n/a), C = (V_0 - V_n)/V_0 \quad (1)$$

$$\rho_f - \rho_n = (\rho_f - \rho_0) \exp(-kn) \quad (2)$$

Where:

a is the degree of volume reduction when the tap number is infinity,

b and k are constants for the apparent packing rate, V_0 and V_n are the volume in the initial loosely packed and the n^{th} tapped state, and

ρ_0 , ρ_n , and ρ_f are the apparent density in the initial state, the n^{th} tapped state, and the most densely packed state.

2.4 Tablet Preparation

A screen was used to classify the test samples into a 125 to 500 μm fraction. We placed 150 mg of each sample into a die with diameter of 8 mm, and used an AUTOGRAPH (Instron type press) (AG5000D, Shimadzu Corporation) to tablet the samples at a constant rate of 10 mm min^{-1} and at various compression pressures between 50 and 300 MPa $\pm 5\%$. Assuming commercial production, we mixed 1% magnesium stearate into each sample and used the universal tensile compression tester and a single-punch tableting machine (TabA11, Okada Seiko Co., Ltd.) to produce tablets under a constant compression pressure of 200 MPa $\pm 5\%$ and at various compression speeds. The compression speed of single-punch tableting machine was calculated from the displacement rate of upper punch when compressing.

2.5 Compression Behavior Analysis

2.5.1 Heckel Analysis [4, 5]

We used Heckel's equation (Eq. 3) to analyze the compression process of agglomerated crystals, and assessed their compactibility.

$$\ln [1/(1-D)] = KP + A \quad (3)$$

Where:

D is the relative density of the tablets under compression pressure P (MPa; the ratio of tablet density to the powder's true density),

K is the slope of the straight portion of the Heckel plot, and

the reciprocal of K is the mean yield pressure (P_y).

Eq. 4 gives the intercept obtained by extrapolating the straight portion of the plots.

$$A = \ln [1/(1-D_0)] + B \quad (4)$$

Where:

D_0 is the relative density of the powder bed when $P=0$.

Eqs. 5 and 6 give the relative densities corresponding to A and B.

$$D_A = 1 - e^{-A} \quad (5)$$

$$D_B = D_A - D_0 \quad (6)$$

2.5.2 Stress Relaxation Test

We put 150 mg of each sample in a die with 8 mm diameter the surface of which was coated with magnesium stearate in advance, then used the universal tensile compression tester to compress the samples at a constant speed of 10 mm min^{-1} . After the pressure attained 200 MPa, the upper punch was held in the same position for 20 min, during which time we measured the reduction amount of the stress applied on the upper punch. [6] The result was corrected by subtracting from this measurement the relaxation measured without powder in the die under the same conditions. We used Eq. 8 to find the relationship between relaxation ratio $Y(t)$ and time t , calculated the parameters A_s and B_s , and assessed relaxation behavior. [7, 8]

$$Y(t) = (P_0 - P_t) / P_0 \quad (7)$$

Where:

P_0 is the maximum compression pressure, and P_t is the pressure at time t .

$$t / Y(t) = 1 / A_s B_s + t / A_s \quad (8)$$

2.5.3 Tablet Elastic Recovery Test

We placed 150 mg of each sample in a die with 8 mm diameter and used the universal tensile compression tester to compress them up to 200 MPa at the constant speed of 10 mm min^{-1} . We measured the thickness of each tablet under maximum pressure (H_c) and at about 24 h after tablet ejection (H_e). Eq. 9 was used to calculate the elastic recovery ratio (ER). [9]

$$ER = [(H_e - H_c) / H_c] \times 100 \quad (9)$$

About 24 h after the tablet was ejected, its weight, diameter, and thickness was measured, and its apparent density (ρ_a) calculated. Eq. 10 was used to calculate internal tablet porosity (ε) from true density (ρ_t), which was measured with an air comparison pycnometer (Model 930, Beckman-Toshiba, Ltd.).

$$\varepsilon = 1 - \rho_a / \rho_t \quad (10)$$

2.6 Tablet Tensile Strength Test

Tablets were kept in a desiccator (silica gel) for about 24 h, and then a hardness tester (GRANO, Okada Seiko Co., Ltd.) was used to measure a load across the diameter of each tablet at a compression speed of $100 \text{ } \mu\text{m s}^{-1}$ to find the hardness F when crushing. Eq. 11 was then used to calculate the tensile strength T . [10]

$$T = 2F / \pi dL \quad (11)$$

Where:

d and L are a tablet's diameter (m) and thickness (m).

We crushed the tablets made by compressing the two types of spherically agglomerated crystals, and observed the fracture planes with a scanning electron microscope.

3. Results and Discussion

3.1 Spherical Crystallization Mechanism and Physical Properties of Agglomerated Crystals

It was found that crystal agglomeration was possible with two different types of mechanisms depended on the amount of drug solution added to the system (poor solvent). When both solvents were mixed at a small water-to-ethyl acetate volumetric ratio (1:100), a W/O emulsion formed at first. Then as the emulsion drops cooled and the water and ethyl acetate counter-diffused, solubility in the emulsion drops decreased, and crystals precipitated on the surfaces of drops. Spherical agglomerates were obtained when crystallization completed. This agglomeration mechanism is called emulsion solvent diffusion, or ESD. On the other hand, when the water-to-ethyl acetate volumetric ratio was large (4:150) and the solvents did not mix, crystals precipitated in the same way after an emulsion formed. At this system a small amount of water that was liberated from the ethyl acetate phase acted as a liquid bridging agent (forming a liquid bridge), which caused particles to randomly agglomerate, and then become spherical under the shearing force of stirring, after first passing through funicular and capillary forms. This agglomeration mechanism is called spherical agglomeration, or SA. **Fig. 1** illustrates the SA and ESD mechanisms, and **Fig. 2** presents electron photomicrographs of the surfaces and cross sections of the two types of ascorbic acid agglomerated crystals. Both types of agglomerated crystals were spherical.

As one can see from the agglomeration mechanism

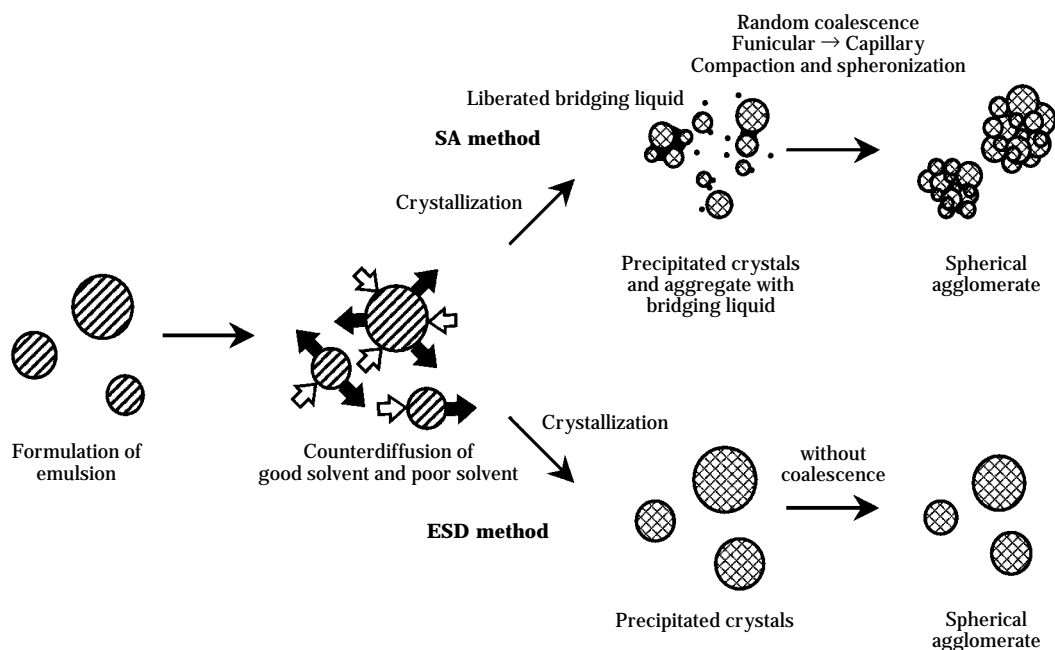


Fig. 1 Mechanism of spherical crystallization

in Fig. 1, while in the SA method the primary crystals randomly agglomerated, crystals in the ESD method grow toward the center. Owing to this difference in the agglomeration mechanism, the two methods yield two types of agglomerated crystals with different internal structures.

The physical properties of the agglomerated crystals are shown in Table 1.

The angle of repose of agglomerated crystals was clearly lower than that of the original crystals, and about the same as that of commercially available C97 granules. We used the equations of Kawakita and Kuno to analyze the tapping process. The value a in Kawakita's equation was lower than that of the original crystals, while b in Kawakita's equation and k in

Kuno's equation were both higher. Both of the agglomerated crystals obtained had excellent flowability and packability, and in terms of handling properties such as feeding into die, the agglomerated crystals were useful for direct tableting.

3.2 Compression Behavior Analysis

To determine the compression characteristics of the agglomerated crystals, Heckel's equation [4, 5] was used to analyze the compression behavior of agglomerated crystals (Fig. 3).

Except for KCl, none of the agglomerated crystal types exhibited a linear relationship at low compression pressures, while they did at high pressures. This shows that at low compression pressures the rearrangement and crushing of agglomerated crystals proceeds simultaneously, and that at high pressures crystal particles are cohered and bonded with one another while undergoing plastic deformation. The initial portions of Heckel plot curves are a general indication of the tendency for particle fracturing. Doelker used the values for D_A , D_0 , and D_B calculated from Heckel plots respectively, as an indicator of compaction by the densest packing of rearranged and fractured particles into a die; an indicator of compaction by initial packing; and an indicator of fracturing characteristics (compaction of a powder bed by the rearrangement of primary particles and fractured particles). The higher the value of D_0 , the better the

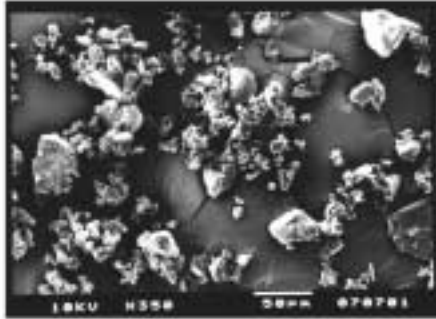
Table 1 Flowing and packing properties

Sample	Angle of repose (°)	$a^{1)}$	$b^{1)}$	$k^{2)}$
Original	56.1±2.3	0.508	0.066	0.021
C97	33.7±1.0	0.079	0.151	0.045
SA	33.8±2.6	0.224	0.176	0.065
ESD	33.0±1.6	0.133	0.155	0.063

1) Parameters in Kawakita's equation: $(n/C) = (1/ab) + (n/a)$ and $C = (V_0 - V_n)/V_0$, where n is the tap number and V_0 and V_n are the powder volumes at the initial and n^{th} tapped state, respectively.

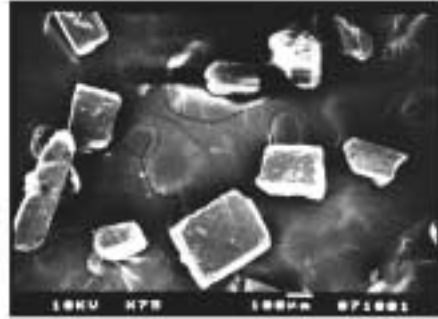
2) Parameter in Kuno's equation: $\rho_t - \rho_n = (\rho_t - \rho_0) \exp(-kn)$, where ρ_t , ρ_n , and ρ_0 are the apparent densities at equilibrium, the n^{th} tapped, and initial state, respectively.

a) Original crystals



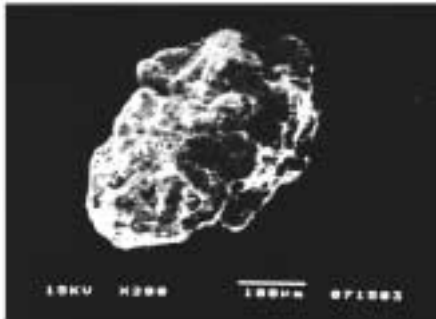
50 μm

b) Original coarse crystals



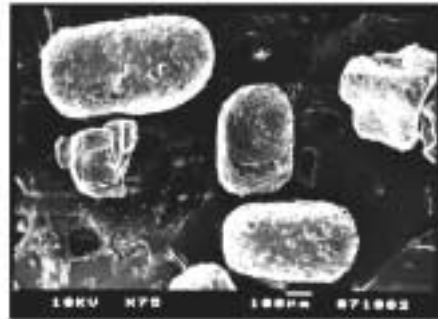
100 μm

c) C97 granule



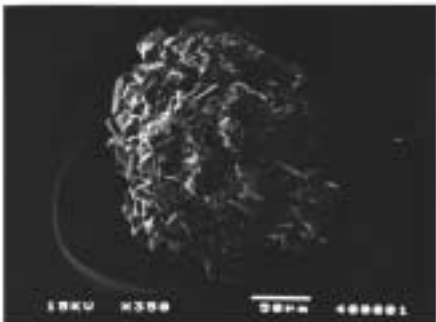
100 μm

d) Potassium chloride crystals

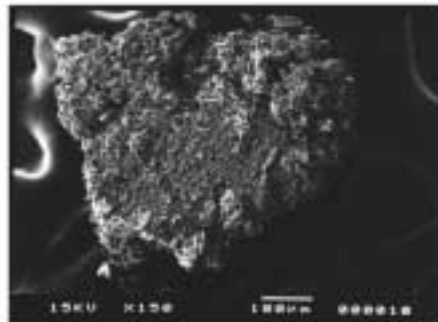


100 μm

e) SA agglomerated crystal

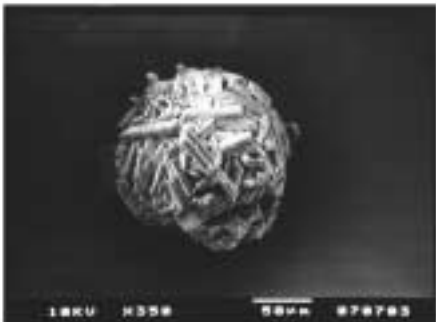


50 μm

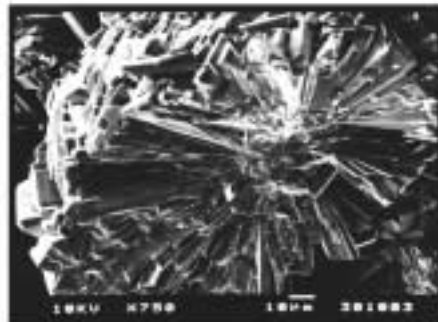


100 μm
Cross section

f) ESD agglomerated crystal



50 μm



10 μm
Cross section

Fig. 2 Scanning electron photomicrographs of external appearance and cross-section of original ascorbic acid crystals, a C97 granule, potassium chloride crystals, and SA and ESD agglomerated crystals of ascorbic acid

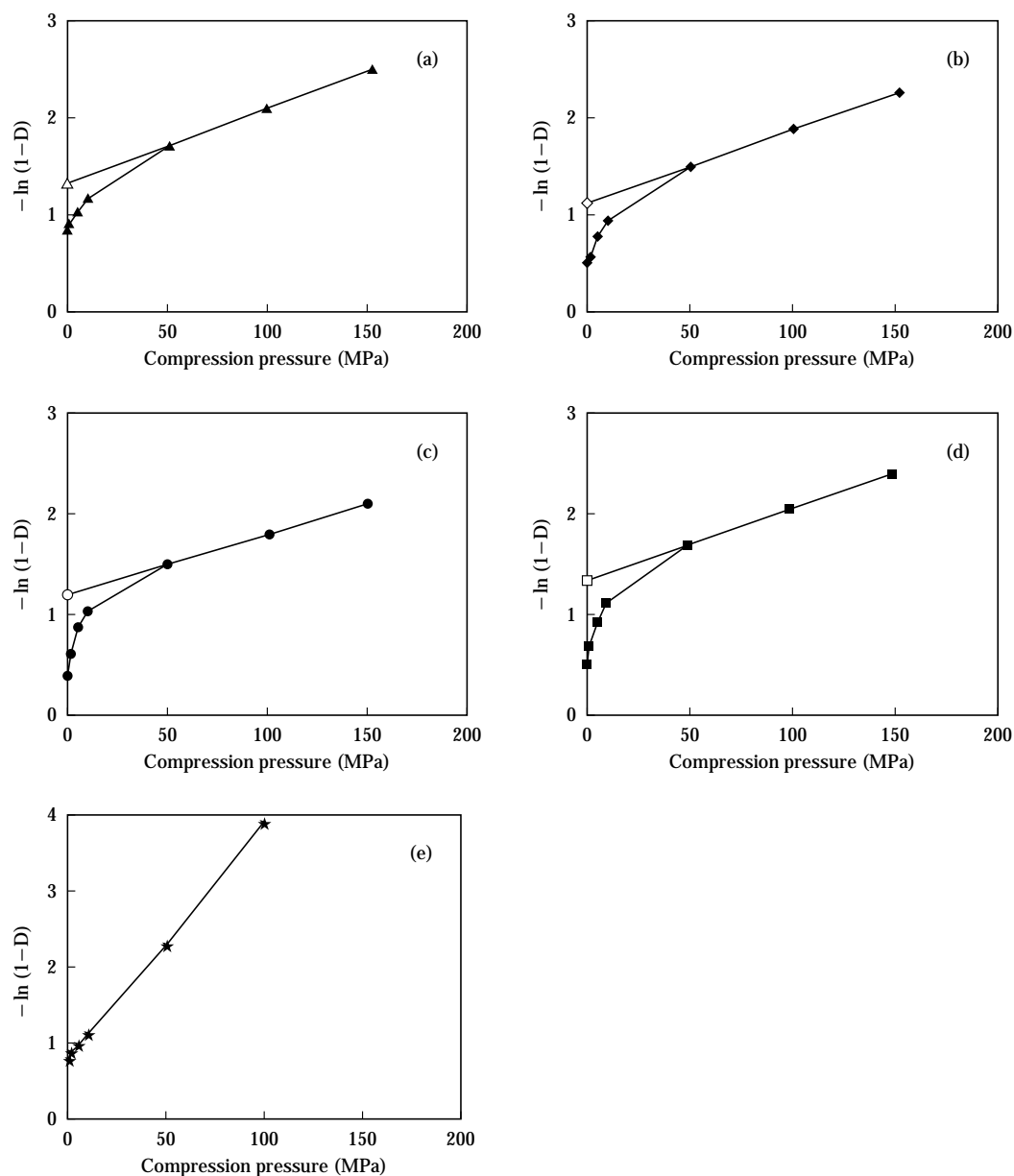


Fig. 3 Heckel's plot for ascorbic acid and potassium chloride crystals at a compression speed of 10 mm min^{-1} . Straight lines were obtained by a linear regression analysis of data between 50 and 150 MPa. (a) Original coarse crystals, (b) C97 granules, (c) SA agglomerated crystals, (d) ESD agglomerated crystals, and (e) KCl crystals

initial packability in a die, while the higher the value of D_B , the greater the fracturing tendency exhibited by a powder. [11] Analysis results indicated that the original coarse crystals and KCl had high D_0 values, which is probably because the surfaces of these crystals were comparatively smooth (**Fig. 2**), which made them easy to pack into a die. Because SA agglomerated crystals had the highest D_B value, it was evident that considerable fracture occurred during compression (**Table 2**).

Plastic flow of the particles during compression

occurred mainly after rearrangement and fracture. Plastic deformability is generally evaluated according to mean yield pressure (P_y), which was calculated from the slope of the linear portion of plots. P_y values in descending order were SA crystals, ESD crystals, C97 granules, and the original coarse crystals (**Table 2**). All these values are higher than that of KCl, a substance that tends to undergo plastic deformation, and they are about the same with regard to plastic deformability. They had lower elastic recovery values than the original coarse crystals.

Table 2 Analysis of compaction behavior

Sample	Heckel analysis				Relaxation pressure (MPa)	Elastic recovery (%)
	P_y (MPa)	D_A	D_0	D_B		
Original	127.4±2.9	0.741±0.001	0.561±0.013	0.180±0.013	7.0±0.2	9.3±0.5
C97	134.8±4.0*	0.682±0.001***	0.400±0.005***	0.282±0.006***	28.4±0.4***	5.1±0.4***
SA	168.8±3.5***	0.702±0.002***	0.330±0.011***	0.372±0.010***	146.1±0.4***	5.0±0.5***
ESD	142.9±2.9***	0.747±0.001***	0.409±0.010***	0.338±0.011***	124.9±0.5***	4.7±0.2***
KCl	35.4±1.6***	0.551±0.005***	0.523±0.017*	0.028±0.012	13.5±1.1**	8.9±1.1

The results are expressed as mean ±S.D. of four runs. There was a significant difference with the value for original coarse crystals at $p < 0.001$ (***), $p < 0.01$ (**) and $p < 0.5$ (*).

To investigate compactibility in more detail, we measured stress relaxation, which is an indicator of plastic deformability (Table 2). Fig. 4 shows the results obtained by interpreting the relaxation process with Eq. 8. Good linear correlations were obtained with all samples, and constants A_S and B_S were determined from their slopes (Table 3).

A_S indicates the relaxation ratio at infinity time; the higher the value, the greater the stress relaxation. $1/B_S$ indicates the time until the relaxation ratio attains $A_S/2$, and means that the larger the B_S value, the faster the relaxation rate. Spherically agglomerated crystals had larger stress relaxation than other crystals, with that of SA crystals larger than that of ESD crystals. And because the A_S and B_S values were large, Table 3 shows that stress relaxation under static pressure was large, and that the relaxation rate was rapid. Stress relaxation occurred because of particle fracturing and rearrangement caused by packing, and because of the plastic deformation of the particles themselves. [12] It is thought that because spherically agglomerated crystals were easily fractured during compression, their particle sizes became smaller, and their stress relaxation increased due to rearrangement. By contrast, the original coarse crystals

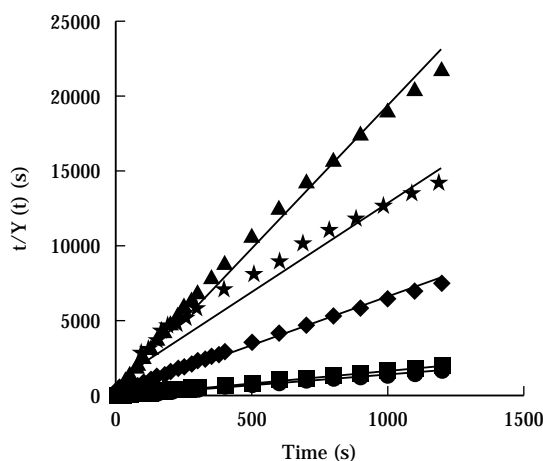


Fig. 4 Relationship between $t/Y(t)$ and t
 (○) Original coarse crystals, (□) C97 granules, (△) SA agglomerated crystals, (◇) ESD agglomerated crystals, and (◻) KCl crystals

and C97 granules had small relaxation values. This is likely because, as one can estimate from the values for D_0 and D_B calculated from the Heckel plots, the initial packing rate in the die was high, and little rearrangement was caused by fracturing during compression. KCl had small stress relaxation. The small A_S value shows that stress relaxation under static pressure decreased owing to the adequate stress relaxation afforded by the strong plastic flow during compression (Fig. 3). Further, the low B_S value means that the relaxation rate under static pressure was extremely slow.

3.3 Improving the Compactibility of Spherically Agglomerated Crystals

We assessed the compactibility of agglomerated crystals samples according to the tensile strength of tablets (Fig. 5). [10]

Table 3 Parameters of stress relaxation process

Sample	A_S	B_S
Original	0.058±0.001	0.012±0.001
C97	0.168±0.002***	0.013±0.000
SA	0.778±0.004***	0.021±0.001***
ESD	0.658±0.006***	0.029±0.001***
KCl	0.103±0.005***	0.004±0.000***

The results are expressed as the mean ±S.D. of four runs. There was a significant difference with the value for original coarse crystals at $p < 0.001$ (***).

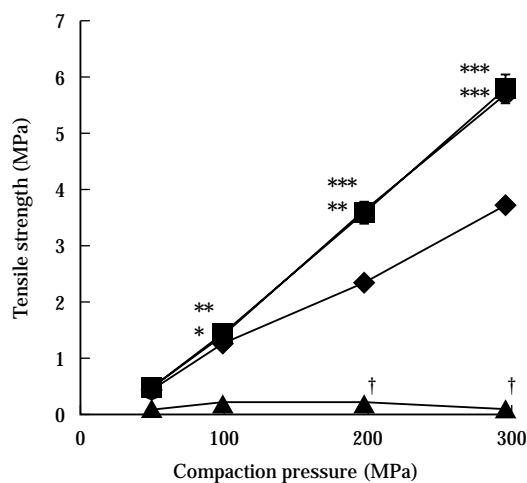


Fig. 5 Relationship between tensile strength of ascorbic acid tablets and compaction pressure
 Sample: 150 mg
 Compression speed: 10 mm min⁻¹
 (○) Original coarse crystals, (△) C97 granules, (□) SA agglomerated crystals, and (◇) ESD agglomerated crystals
 †: Some tablets are capped during compaction. The results are expressed as the mean ±S.D. of four runs. There was a significant difference with the value for C97 granules at p<0.001 (***), p<0.01 (**) and p<0.5 (*).

Capping of the original coarse crystals occurred at compaction pressures of 200 MPa and above. Owing to the small D_B value of the original crystals, there was less fracturing than agglomerated crystals and elastic recovery was high (Table 2), thereby allowing capping. When ascorbic acid was made into crystal agglomerates by crystal agglomeration, tableting was possible without the occurrence of capping. What is more, the tensile strength of the resulting tablets improved dramatically; it was significantly better even than C97 granules, and displayed superior compactibility. The reasons for this are likely that as the D_B value of spherically agglomerated crystals was significantly high (Table 2), making the crystals fracture easily under compression, this increased the points of contact among particles; the large stress relaxation (Table 2) facilitated plastic flow, thereby increasing the contact area; and new high-energy surfaces appeared because of fracturing, which strongly bonded the particles. [13]

3.4 Effect of Compression Speed on the Compactibility of Spherically Agglomerated Crystals

It was found that spherically agglomerated crystals exhibited an excellent capacity for compactibility

under static compression. Nevertheless, powder beds are compressed rapidly in the commercial production of tablets. For that reason we mixed a lubricant (magnesium stearate) into the samples, and used a single-punch tableting machine as well as universal tensile compression tester to investigate the effect of compression speed on tensile strength. Fig. 6 shows the relationship between compression speed and tensile strength.

When the universal tensile compression tester was used to compress the original coarse crystals, the tablets exhibited low tensile strength, but there was a tendency for tensile strength to increase somewhat as the compression speed increased. Although the commercially available C97 granules had a value higher than that of the original coarse crystals, the tendency was the same. KCl, which tends to undergo plastic deformation, had a tendency for tensile strength to decrease as the compression speed increased. While spherically agglomerated crystals displayed the same tendency as KCl, under compression with the compression tester its tensile strength increased at a compression speed of 300 mm min⁻¹. But when compressing with the single-punch tableting machine, all samples had about the same tensile strength, no matter what the compression speed. When compression was performed with both the universal tensile com-

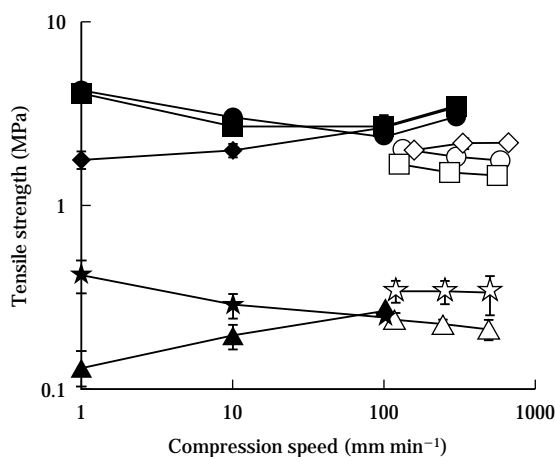


Fig. 6 Relationship between tensile strength of ascorbic acid tablets and compression speed
 Sample: 150 mg
 Compaction pressure: 200 MPa
 (○, △) Original coarse crystals, (□, ◇) C97 granules, (□, ◇) SA agglomerated crystals, (△, ▽) ESD agglomerated crystals, and (○, △) KCl crystals
 Tablets were prepared using an Instron-type hydraulic press (closed symbols) or single-punch tableting machine (open symbols) at a 200 MPa compaction pressure. The results are expressed as the mean ±S.D. of four runs.

pression tester and the tableting machine at the same compression speed, tablets made with the compression tester had the higher tensile strength. We assume this is due to a characteristic of the compression imposed by the tester, which is static compression at a constant speed that places uniform stress on the powder. By contrast, compression applied by the tableting machine initially has a high speed, then gradually slows. It is therefore characterized as dynamic compression in which changes in the powder bed's internal stress are non-equilibrium. Thus, it is likely that tablet tensile strength was low because the compression energy was not effectively applied for powder compaction and formation.

Fig. 7 shows the relationship between tablet porosity and compression speed.

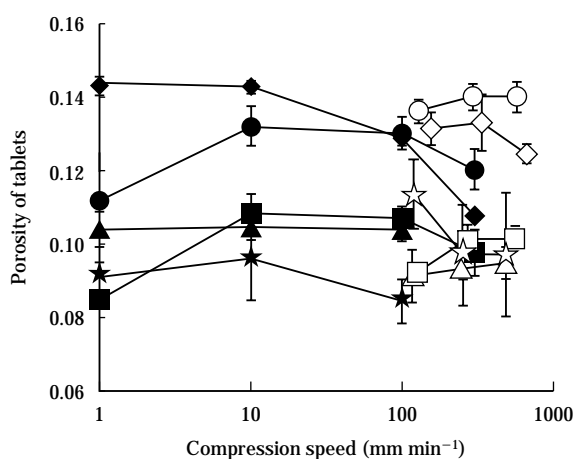


Fig. 7 Relationship between porosity of ascorbic acid tablets and compression speed

Sample: 150 mg

Compaction pressure: 200 MPa

(○, □) Original coarse crystals, (△, ◇) C97 granules, (▽, ◆) SA agglomerated crystals, (◇, ◆) ESD agglomerated crystals, and (○, □) KCl crystals

Tablets were prepared using an Instron-type hydraulic press (closed symbols) or single-punch tableting machine (open symbols) at a 200 MPa compaction pressure. The results are expressed as the mean \pm S.D. of four runs.

Tablets made from the original coarse crystals with the single-punch tableting machine had lower porosity than those made with the universal tensile compression tester. This is probably because when the compression speed was high, the powder was subjected to a bigger impact, and brittle original crystals were fragmented, rearranged, and compacted by compression. With respect to spherically agglomerated crystals, although no clear difference in ESD crystals

was found, when making SA crystals at the same compression speed with the universal tensile compression tester and the single-punch tableting machine, the tablets made with the compression tester had lower porosity. This correlates to the above-noted fact that tablets made with the compression tester have a higher tensile strength. To investigate the packed state of crystals in tablets made with the compression tester we used a scanning electron microscope to examine tablet cross sections (**Fig. 8**).

At a low compression speed, solid bridges formed between crystals in both types of agglomerated crystals, but when the compression speed was high there was no fusion between crystals, and the cross sections were very similar to those of agglomerated crystals prior to compression. We assume this is because when compression time is long, crystals undergo considerable plastic deformation. [6] In our examination of tablets obtained from SA agglomerated crystals we observed only the primary crystals that made up the agglomerated crystals, suggesting that compression fractured the agglomerated crystals back down to their primary crystals, which is the reason for the large D_B value. On the other hand, examination of tablets obtained from ESD agglomerated crystals revealed that the internal structure of agglomerated crystals in the tablets was partially retained, suggesting that compression fractured only the outside surface of the agglomerated crystals. Because the internal structures of agglomerated crystals differed according to the mechanism by which spherically agglomerated crystals were made, the agglomerates also differed with respect to the extent of fracturing during compression and the arrangement of crystals in tablets, which is likely the reason for their different plastic deformability (**Table 2**).

4. Conclusion

By applying spherical crystallization methods to ascorbic acid with strong cohesive and brittle properties, we were able to make agglomerated crystals with excellent flowability and packability, and with better compactibility than commercially available granulated particles for direct tableting, thereby determining that these agglomerated crystals are useful as particles for direct tableting. In consideration of the drying conditions for this method, it is believed that the ethyl acetate remaining in the agglomerated crystals is under the 5,000 ppm standard of the residual solvent guideline. [14] We found that major reasons for the superior compactibility of spherically

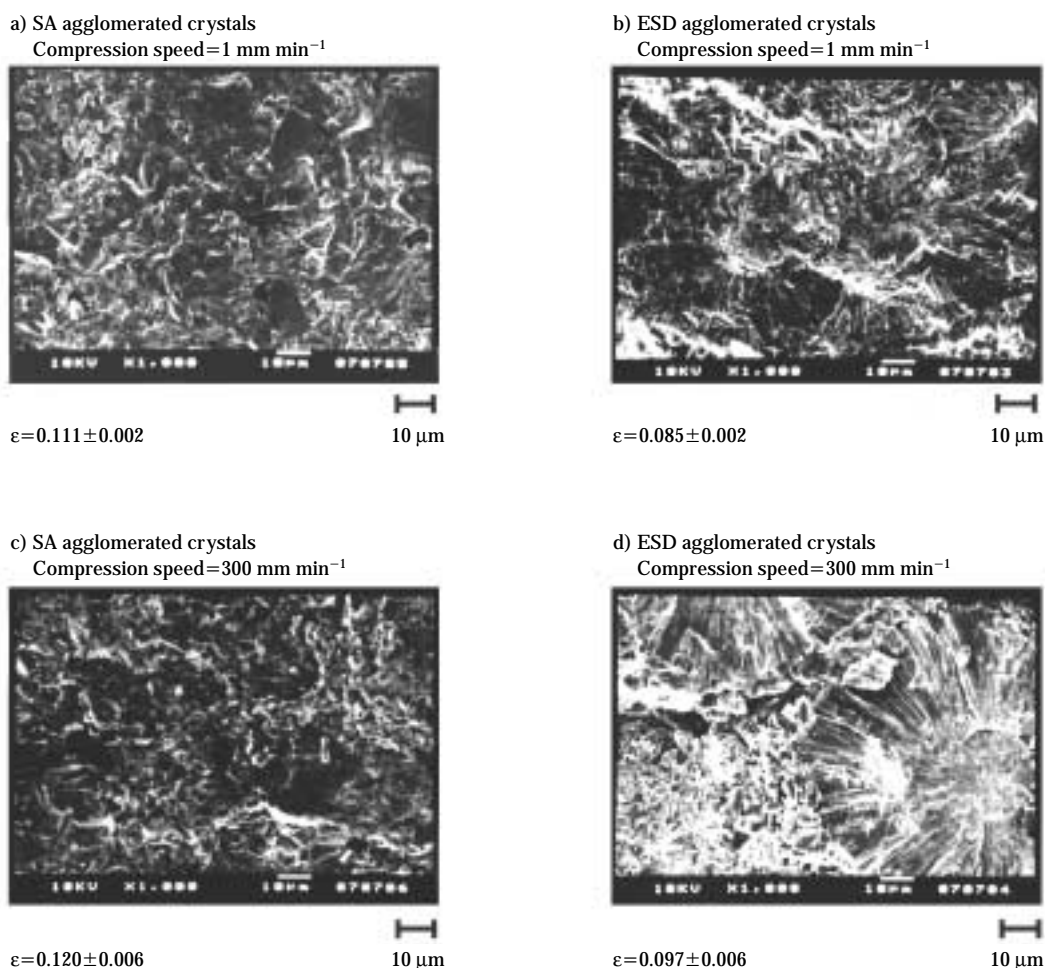


Fig. 8 Scanning electron photomicrographs of cross section of ascorbic acid tablets prepared by static compression

agglomerated crystals are the increased fragmentation of granulated crystals and plastic deformability (flowability) of fractured particles under compression, and the low elastic recovery. An increase in the speed of compression on spherically agglomerated crystals reduces the tensile strength of tablets, but our study showed that even direct tableting can be done at high speed. Spherical crystallization can be used for any drug as long as an appropriate solvent is chosen. This is a useful granulating technology that can solve the problems of poor powder physical properties and compactibility that make other drugs hard to tablet, and that can make them into powder that is responsive to direct tableting.

Acknowledgements

We wish to thank Takeda Chemical Industries, Ltd. for supplying the samples used in this research.

Nomenclature

A	total densification of powder bed due to die filling and particle rearrangement	
A_S	constant	
a	constant	
B	densification of powder bed due to particle fragmentation	
B_S	constant	
b	constant	
C	constant	
D	relative density of powder at applied pressure P	
D_0	relative density of powder when pressure is 0	
d	tablet diameter	(m)
ER	elastic recovery ratio	(%)
F	crushing hardness	(N)
H_c	tablet thickness at maximum pressure	(m)
H_e	tablet thickness at 24 h after ejection	(m)
K	slope of straight line by Heckel plot	(1/Pa)

k	constant	
L	tablet thickness	(m)
n	tap number	
P	applied pressure	(Pa)
P_0	maximum pressure (at time $t=0$)	(Pa)
P_t	pressure after time t	(Pa)
T	tensile strength	(N/m^2)
V_0	volume at initial state	(m^3)
V_n	volume at n^{th} tapped state	(m^3)
Y(t)	pressure relaxation ratio	
ϵ	tablet porosity	
ρ_0	apparent density at initial state	($kg\ m^{-3}$)
ρ_a	apparent density	($kg\ m^{-3}$)
ρ_f	apparent density at equilibrium state	($kg\ m^{-3}$)
ρ_n	apparent density at n^{th} tapped state	($kg\ m^{-3}$)
ρ_t	true density	($kg\ m^{-3}$)

References

- 1) Kawashima, Y. "New Processes – Application of Spherical Crystallization to Particulate Design of Pharmaceuticals for Direct Tableting and Coating, and New Drug Delivery Systems," *Powder Technology and Pharmaceutical Process*, edited by D. Chulia et al., 493-512, Elsevier (1994).
- 2) Kawakita, K. "Compression of Powder," *Kagaku*, **26**, 149 (1956).
- 3) Kuno, H. *Funtai (Powder Theory and Application)*, ed. by G. Jimbo et al., Maruzen, Tokyo, p. 342 (1979).
- 4) Heckel, R. W. "Density-pressure Relationships in Powder Compaction," *Trans. Met. Soc. AIME*, **221**, 671 (1961).
- 5) Heckel, R. W. "An Analysis of Powder Compaction Phenomena," *Trans. Met. Soc. AIME*, **221**, 1001 (1961).
- 6) Kawashima, Y., F. Cui, H. Takeuchi, T. Niwa, T. Hino and K. Kiuchi. "Improved Static Compression Behaviors and Tablettabilities of Spherically Agglomerated Crystals Produced by the Spherical Crystallization Technique with a Two-solvent System," *Pharm. Res.*, **12** (7), 1040-1044 (1995).
- 7) Peleg, M. and R. Moreyra. "Effect of Moisture on the Stress Relaxation Pattern of Compacted Powders," *Powder Technol.*, **23**, 277 (1979).
- 8) Danjyo, K., A. Hiramatsu and A. Otsuka. "Effect of Punch Velocity on the Compressibility and Stress Relaxation of Particles and Granules," *J. Soc. Powder Technol. Japan*, **35**, 662-670 (1998).
- 9) Armstrong, N. A. and R. F. Haines-Nutt. "Elastic Recovery and Surface Area Changes in Compacted Powder Systems," *Powder Technol.*, **9**, 287-290 (1974).
- 10) Fell, J. T. and J. M. Newton. "Determination of Tablet Strength by the Diametral-compression Test," *J. Pharm. Sci.* **5**, 688-691 (1970).
- 11) Doelker, E. "Assessment of Powder Compaction," *Powder Technology and Pharmaceutical Process*, edited by D. Chulia et al., 403-512, Elsevier (1994).
- 12) Cutt, T., J. T. Fell, P. J. Rue and M. S. Spring. "Granulation and Compaction of a Model System, II Stress Relaxation," *Int. J. Pharm.*, **39**, 157-161 (1987).
- 13) Kawashima, Y., F. Cui, H. Takeuchi, T. Niwa, T. Hino and K. Kiuchi. "Improvements in Flowability and Compressibility of Pharmaceutical Crystals for Direct Tableting by Spherical Crystallization with a Two-solvent System," *Powder Technol.*, **78**, 151-157 (1994).
- 14) Kojima, S. "ICH Guideline for Residual Solvents in Drugs," *PHARM TECH JAPAN*, **16** (5), 7-24 (2000).

Author's short biography



Yoshiaki Kawashima

Dr. Yoshiaki Kawashima is Professor of Laboratory of Pharmaceutical Engineering at Gifu Pharmaceutical University. He received B.S. (1964) degree from Nagoya City University and M.S. (1966) and Ph.D. degree (1969) from Kyoto University. He joined Gifu Pharmaceutical University as a faculty member in 1969. Since 1991, he becomes a visiting professor of Shen-Yang Pharmaceutical University. He received FIP Colocon award and AAPS fellow ship in 1995 and 1996. He is chairman of the society of Powder Technology, Japan since 1999. He developed spherical crystallization techniques and his research interests are in the development and application of spherical crystallization for drug delivery system with nanoparticulate carriers.

Author's short biography



Misato Imai

Misato Imai was born in 1975. She graduated from Gifu Pharmaceutical University in 1998 and received B.S. in Pharmaceutical Chemistry in Gifu Pharmaceutical University. She worked in Gifu Pharmaceutical University from 1998 to 2002. Now, she is working in Pharmacy.



Hirofumi Takeuchi

Dr. Hirofumi Takeuchi is Associate Professor of Pharmaceutical Technology at Gifu Pharmaceutical University. He received his B.S. (1979), M.S. (1981) and Ph.D. (1984) in pharmaceutical sciences from Kyoto University. He joined Gifu Pharmaceutical University as a faculty member in 1984, and became Lecturer in 1988. He spent 1 year as a visiting scientist at University of Alberta in 1989-1990. He has been Associate Professor of Gifu Pharmaceutical University since 1991. His research interests are designing the novel solid dosage forms and dispersed systems for drug delivery.



Hiromitsu Yamamoto

Dr. Hiromitsu Yamamoto graduated from Gifu Pharmaceutical University in 1992 and obtained master degree in Pharmaceutical Engineering in 1994. He received a Ph.D. degree from Gifu Pharmaceutical University in 1999. Since 1995, he is working in laboratory of Pharmaceutical Engineering at Gifu Pharmaceutical University as assistant professor. His major research interests are development of drug delivery system with microparticulate drug carriers and dry powder inhalation system.



Kazunori Kamiya

Kazunori Kamiya is a pharmacist, who received B.S. and M.S. degrees from Gifu Pharmaceutical University in 1996 and 1998.

Dispersion and Flocculation Behavior of Fine Metal Oxide Particles in Various Solvents[†]

Junji SHIBATA, Katsuya FUJII,
Norihiko MURAYAMA and Hideki YAMAMOTO
Department of Chemical Engineering, Kansai University*

Abstract

The objective of this study is to investigate the relation between the flocculation and dispersion of Al_2O_3 , TiO_2 and Fe_2O_3 particles and the properties of solvents such as dielectric constant and solubility parameters. The median diameter of these metal oxide particles was measured in many organic solvents. The effect of the kind of solvent on the flocculation/dispersion behavior of metal oxide particles was evaluated from these results.

Hansen's solubility parameters with three dimensions were applied to the evaluation of the flocculation/dispersion behavior for fine metal oxide particles in organic solvents. The numeral balance among the Hansen's solubility parameters of various solvents was plotted in a triangular chart, and then the points of solvents with similar median diameter of the particle were linked. In the triangular chart, these linked lines were not intersected each other and there was the specific point at which the best dispersibility of the particles was obtained.

1. Introduction

The dispersibility of fine particles in various solvents affects the quality of the products in the manufacturing process treating suspensions. It is important to control the dispersion/flocculation behavior of fine particles in various solvents in the field of paint, printer ink, magnetic material, electronic parts, etc. [1]. The DLVO theory, as is well known, explains the dispersion/flocculation behavior of fine particles in aqueous solution. However, this theory cannot be applied to the particles in organic solvents, because the factors on dispersibility in organic solvents are very complicated.

The dielectric constant of a substance is closely concerned with the dipole moment, and also the polarity of a substance with high dielectric constant is considered to be large. Generally, the affinity becomes higher between the solvent with large polarity and the metal oxide particle with large polarity. Therefore, dispersibility of fine particles in a solvent

may be concerned with the dielectric constant of the solvent. On the other hand, Hildebrand [2] proposed the concept of regular solution theory and gave the experimental solubility parameter δ in order to expand it to real solutions. However, this concept is applicable only to nonionic solution with no dipole interaction. In order to extend this theory toward polymer solutions, the Hildebrand's solubility parameter δ was divided into London dispersion effect δ_d , polar effect δ_p and hydrogen bonding effect δ_h by Hansen, and then the applicability of these solubility parameters was investigated for the solubility of pigments and polymers [3, 4, 5, 6].

In this study, the relationship between dispersibility of fine particles and various properties of the solvent, such as dielectric constant and solubility parameters, was investigated in various solvents [7, 8]. The median diameters of fine particles of Al_2O_3 , TiO_2 and Fe_2O_3 were measured in various solvents to evaluate the dispersibility of particles, and also Hansen's solubility parameters were used for the evaluation of dispersibility of fine particles in various solvents.

2. Hildebrand's solubility parameter and Hansen's solubility parameter

As the concept of ideal solution is not well applicable to real solutions, many useful approximations

* 3-3-35, Yamate-cho, Suita-shi, Osaka, 564-8680, Japan
Tel: +81-6-6368-0856, Fax: +81-6-6388-8869,
E-mail: shibata@kansai-u.ac.jp

[†] This report was originally printed in Kagaku Kougaku Ronbunshu, **27**, 497-501 (2001) in Japanese, before being translated into English by KONA Editorial Committee with the permission of the editorial committee of the Soc. Chemical Engineers, Japan.

have been made to real solutions. Hildebrand proposed the concept of regular solution theory and he gave the following equation to evaluate the solubility of various materials [2],

$$\delta = \{(\Delta H - RT) / V\}^{1/2} \quad (1)$$

where R , T , ΔH and V are gas constant, temperature, enthalpy of vaporization and molar volume, respectively. The solubility parameter δ can be calculated by the following equation [2],

$$\delta = 3.75 (\gamma / V^{1/3})^{1/2} \quad (2)$$

where γ is surface tension of the solvent.

On the other hand, the concept of regular solution is applicable only to nonionic solutions in which association and dipole interaction do not take place between solvent and solute. However, hydrogen bonding and dipole interactive force should not be ignored in many solvents. It is important to extend the regular solution theory to real solutions. Hansen divided Hildebrand's solubility parameter δ into three terms as follows [3],

$$\delta^2 = \delta_d^2 + \delta_p^2 + \delta_h^2 \quad (3)$$

where δ_d , δ_p and δ_h are corresponding to London dispersion effect, polar effect and hydrogen bonding effect, respectively. In estimating the value of δ_h , Hansen noticed the fact that the hydrogen bonding energy of -OH group was about 5kcal and then he proposed the next equation taking account of the contribution of -OH group to aggregation [5],

$$\delta_h = \sqrt{5000 n / V} \quad (4)$$

where n is the number of -OH group in a unit molecule.

The value of δ_p is calculated by the following equation derived by Bottcher [9],

$$\delta_p^2 = 12.108 / V^2 \cdot (\epsilon - 1) / (2\epsilon + n_D^2) \cdot (n_D^2 + 2) \mu^2 \quad (5)$$

where ϵ is dielectric constant, n_D is refractive index for Na-D ray and μ is dipole moment. The value of δ_d is estimated from the vaporization energy of the material in which the -OH and -CO groups do not exist.

As the dispersion phenomenon, similar to dissolution, is related to the diffusion phenomenon, it is possible to express the dispersion/flocculation behavior of fine particles using Hansen's solubility parameters. The fine particles of α -Al₂O₃, α -Fe₂O₃ and anatase type-TiO₂ were used as a model particle, and the median diameters of these particles in various solvents were measured. The dispersibility of the fine particles was considered from the obtained results.

3. Experimental

Fine particles of α -Al₂O₃ (Sumitomo Chemical Corp., 0.5 μ m median diameter), α -Fe₂O₃ (Toda Kogyo Corp., 0.7 μ m median diameter) and anatase type-TiO₂ (Ishihara Sangyo Kaisya Ltd., 0.2 μ m median diameter) were used as a model particle. These particles were dried in oven at 423K for 24hrs. Twenty seven types of solvents were selected as dispersion media. **Table 1** shows the list of used solvents with some physical properties. These solvents were dehydrated with molecular sieves for 24hrs before preparing suspensions. Each value of f_d , f_p and f_h shown in **Table 1** indicates the numerical balance among the Hansen's three solubility parameters, and these values are calculated by the following equations, respectively.

$$f_d = \delta_d / (\delta_d + \delta_p + \delta_h) \times 100 \quad (6)$$

$$f_p = \delta_p / (\delta_d + \delta_p + \delta_h) \times 100 \quad (7)$$

$$f_h = \delta_h / (\delta_d + \delta_p + \delta_h) \times 100 \quad (8)$$

The particles and solvents were mixed at 10g/dm³ of slurry concentration, and then shaken at 300spm for 24hrs. The particle size distribution in each suspension was measured by using a laser scattering particle size analyzer (LA-910, Horiba Ltd.). The degree of dispersion and flocculation was evaluated from the value of the median diameter in each solvent.

4. Results and discussion

The median diameters of particles in various solvents are shown in **Fig. 1** as a function of dielectric

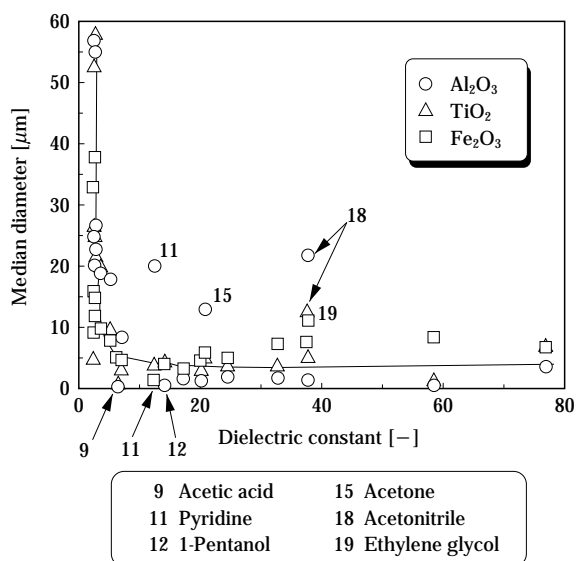


Fig. 1 Relationship between median diameter and dielectric constant of various solvents

constant of the solvent. Each number in **Fig. 1** means the kind of solvent listed in **Table 1**. The median diameter decreases with an increase in dielectric constant. In the range of dielectric constant over 5, the values of median diameter are under $10\mu\text{m}$ for many particle-solvent systems and good dispersion can be obtained under this condition. However, some particle-solvent systems are confirmed to be against this tendency. For example, the values of median diameter are more than $10\mu\text{m}$ in case of Al_2O_3 -pyridine ($\epsilon_r=12.3$), Al_2O_3 -acetone ($\epsilon_r=20.7$), Al_2O_3 -acetonitrile ($\epsilon_r=37.5$), Fe_2O_3 -ethylene glycol ($\epsilon_r=37.7$) and TiO_2 -acetonitrile ($\epsilon_r=37.5$) systems. The particles in these

suspensions indicate strong flocculation in spite of high dielectric constant of these solvents. On the other hand, the median diameter for Al_2O_3 -acetic acid ($\epsilon_r=6.15$), Al_2O_3 -pentanol ($\epsilon_r=13.9$) systems is less than $0.6\mu\text{m}$, and good dispersion is confirmed in these systems though these solvents have low dielectric constant. In case of pyridine, Al_2O_3 particles have strong flocculation (median diameter $>20\mu\text{m}$), while Fe_2O_3 particles indicate good dispersion (median diameter $<2\mu\text{m}$). For almost all of metal oxide particles the dispersibility of particles tend to be related to the polarity of solvent, but there are some systems for which the dispersibility of particles does not obey the

Table 1 Physical properties of solvents used in this study

No.	Solvent	ϵ	δ	δ_d	δ_p	δ_h	f_d	f_p	f_h
1	Hexane	1.89	7.24	7.24	0.1	0.2	94	2	4
2	Cyclohexane	2.20	8.18	8.18	0.2	0.2	96	2	2
3	1,4-Dioxane	2.21	10.01	9.30	0.9	3.6	67	7	26
4	Benzene	2.28	9.02	8.95	0.5	1.0	85	5	10
5	Xylene	2.37	8.79	8.65	0.5	1.5	81	5	14
6	Toluene	2.38	8.90	8.82	0.7	1.0	84	7	9
7	Trichloroethylene	3.40	9.28	8.78	1.5	2.6	68	12	20
8	Chloroform	4.81	9.21	8.65	1.5	2.8	67	11	22
9	Acetic acid	6.15	10.45	7.10	3.9	6.6	40	22	38
10	Aniline	6.89	11.05	9.53	2.5	5.0	56	15	29
11	Pyridine	12.3	10.60	9.25	4.3	2.9	56	26	18
12	n-Pentanol	13.9	10.59	7.81	2.2	6.8	46	13	41
13	1-Butyl alcohol	17.1	11.32	7.81	2.8	7.7	42	16	42
14	1-Propyl alcohol	20.1	11.97	7.75	3.3	8.5	40	17	43
15	Acetone	20.7	9.75	7.58	5.1	3.4	47	32	21
16	Ethyl alcohol	24.3	12.98	7.73	4.3	9.5	36	20	44
17	Methyl alcohol	32.6	14.49	7.42	6.0	10.9	30	25	45
18	Acetonitrile	37.5	11.95	7.50	8.8	3.0	39	46	15
19	Ethylene glycol	37.7	16.07	8.23	5.4	12.7	31	21	48
20	Formic acid	58.5	12.18	7.00	5.8	8.1	33	28	39
21	Water	78.3	23.43	6.00	15.3	16.7	16	40	44
22	Methyl isobutyl ketone	—	8.31	7.49	3.0	2.0	60	24	16
23	2-(2-butoxy ethoxy) ethanol	—	9.97	7.80	3.4	5.2	47	21	32
24	Diacetone alcohol	—	10.13	7.65	4.0	5.3	45	24	31
25	2-Ethoxy ethanol	—	11.44	7.85	4.5	7.0	41	23	36
26	Diethylene glycol	—	14.56	7.86	7.5	9.7	31	30	39
27	Ethanolamine	—	15.35	8.35	7.6	10.4	32	29	39

ϵ : Dielectric constant, δ : Hildebrand's solubility parameter, $\delta_d, \delta_p, \delta_h$: Hansen's solubility parameter

above tendency. Furthermore, it is very interesting that water is not the best dispersion medium for metal oxide particles.

When the particles can be regarded as a complete spherical body with radius a , the van der Waals attractive energy V_A is expressed as follows,

$$V_A = -\frac{A_{131}}{12} \left[\frac{1}{x(x+2)} + \frac{1}{(x+1)^2} + 2 \ln \frac{x(x+2)}{(x+1)^2} \right] \quad (9)$$

where x is the distance between particles (L) divided by the radius of particle (a), and A_{131} is Hamaker constant of particles in the solvent. Therefore, it is recognized from Eq.(9) that the van der Waals attractive energy between particles increases with an increase in the value of A_{131} . When A_{11} and A_{33} are individual Hamaker constants of particles and solvent, respectively, the Hamaker constant of the particles in the solvent A_{131} can be approximated by the following equation,

$$A_{131} = (\sqrt{A_{11}} - \sqrt{A_{33}})^2 \quad (10)$$

The relationship between the van der Waals attractive energy and the dispersibility of the particles was investigated. The relationship between Hamaker constant of particle A_{131} and dielectric constant of solvent is shown in **Fig. 2**. In case of Al_2O_3 and TiO_2 systems, some values of A_{131} are as high as 10×10^{-20} J in the range of dielectric constant around 5. Because the van der Waals attractive energy of them becomes large, the particles tend to flocculate under the condition. In case of Fe_2O_3 system, A_{131} values is less than 10×10^{-20} J through all range of dielectric constant. The results indicate that the van der Waals attractive

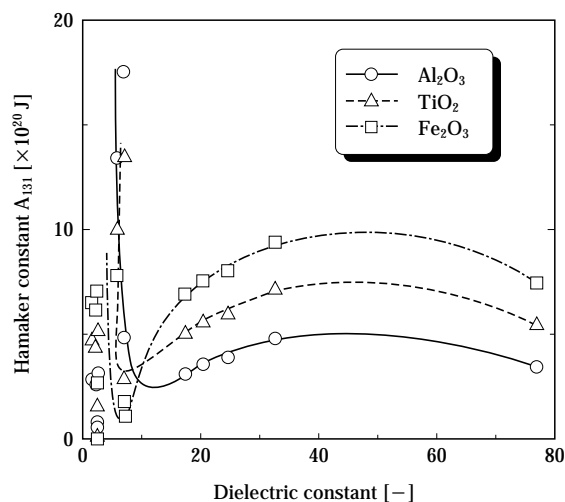


Fig. 2 Relationship between Hamaker constant and dielectric constant of various solvents

energy of Fe_2O_3 is small in the solvents used in this study and the particles have a tendency to disperse. Though high Hamaker constants are calculated in the range of dielectric constant more than 20, the electrostatic repulsive energy by charged particles affects strongly dispersion and flocculation. From the above results, it is difficult to evaluate the dispersibility of particles in a solvent by using only the Hamaker constant.

The Hansen's solubility parameters were used to investigate the dispersibility of particles without using dielectric constant and Hamaker constant. The numeral balance of Hansen's solubility parameters for each solvent was calculated from Eqs. (6)–(8), and then the value was plotted in the triangular chart. The points of solvents with a similar median diameter were linked to make the isometric particle lines.

Figure 3 shows the isometric particle lines for Al_2O_3 . The intersected point of three broken lines in **Fig. 3** indicates the values of f_d , f_p and f_h of the hypothetical solvent in which the best dispersibility is obtained. The point is defined as the optimal dispersible point. The same examinations were carried out by using TiO_2 and Fe_2O_3 particles to evaluate the applicability of Hansen's solubility parameters to the dispersibility of several particles. In **Fig. 3**, the optimal dispersible point can be determined to be the center point of the largest inscribed circle for the closed isometric particle line comprising the solvents with the particle size of $1.0-4.0 \mu m$. The values of the optimal dispersible point for Al_2O_3 are $f_d=44\%$, $f_p=19\%$ and $f_h=37\%$, respectively. As f_d , f_p and f_h values of a solvent approach to the optimal dispersible point, the dispersibility of the particles becomes better. The solvents causing high dispersion to Al_2O_3 particles are acetic acid, formic acid, 2-(2-butoxy ethoxy) ethanol, 2-ethoxy ethanol, diethylene glycol, ethanolamine and 1-pentanol, respectively.

The isometric particle lines of TiO_2 and Fe_2O_3 are shown in **Figs. 4** and **5**, respectively. The optimal dispersible point of TiO_2 system locates at $f_d=49\%$, $f_p=18\%$ and $f_h=33\%$, and the good solvents for TiO_2 are acetic acid, formic acid, 2-(2-butoxy ethoxy) ethanol and 2-ethoxy ethanol. In the case of Fe_2O_3 system, the optimal dispersible point exists at $f_d=55\%$, $f_p=22\%$ and $f_h=23\%$, and the good solvent for Fe_2O_3 is pyridine. From these results, the specific optimal dispersible point exists for each metal oxide particle.

Generally, the affinity between the two materials is considered to be high when the chemical and physical properties of two materials resemble each other. For example, nonpolar materials can be easily dis-

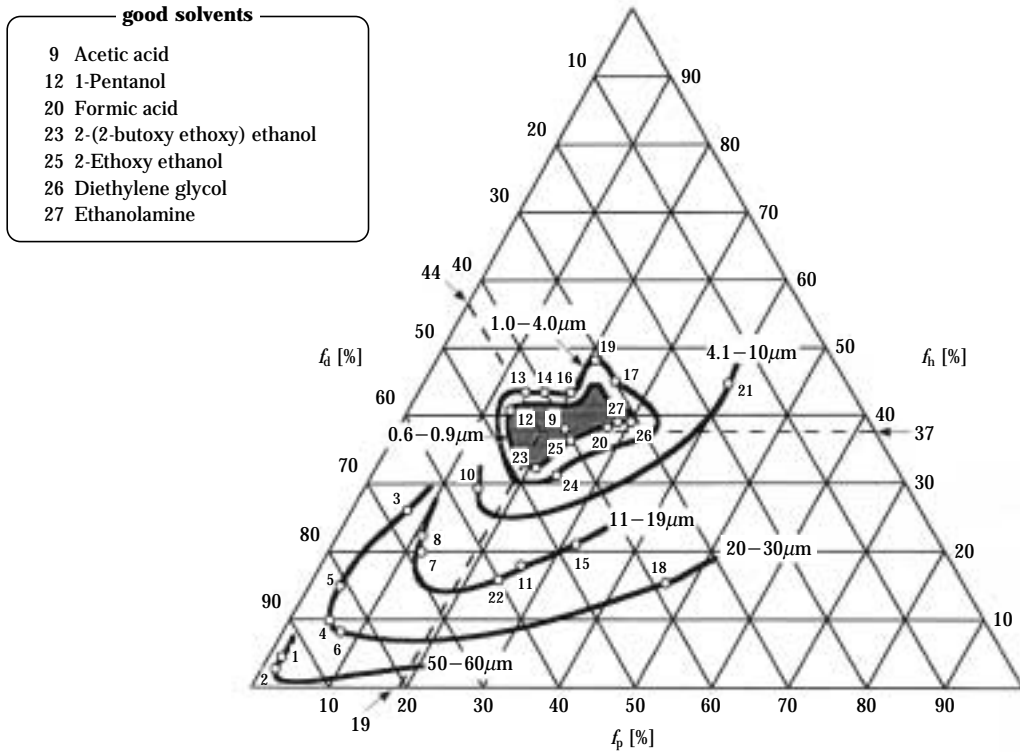


Fig. 3 Isometric particle lines on triangular chart for Al_2O_3 (Each number means a solvent listed in **Table 1**)

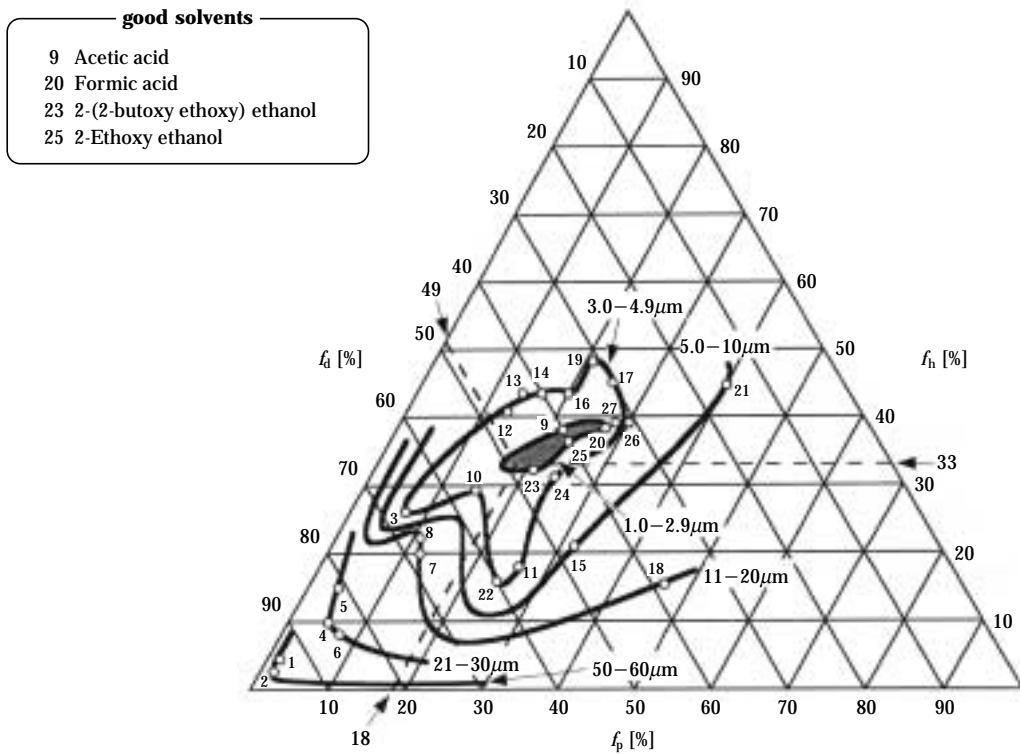


Fig. 4 Isometric particle lines on triangular chart for TiO_2 (Each number means a solvent listed in **Table 1**)

good solvent
11 Pyridine

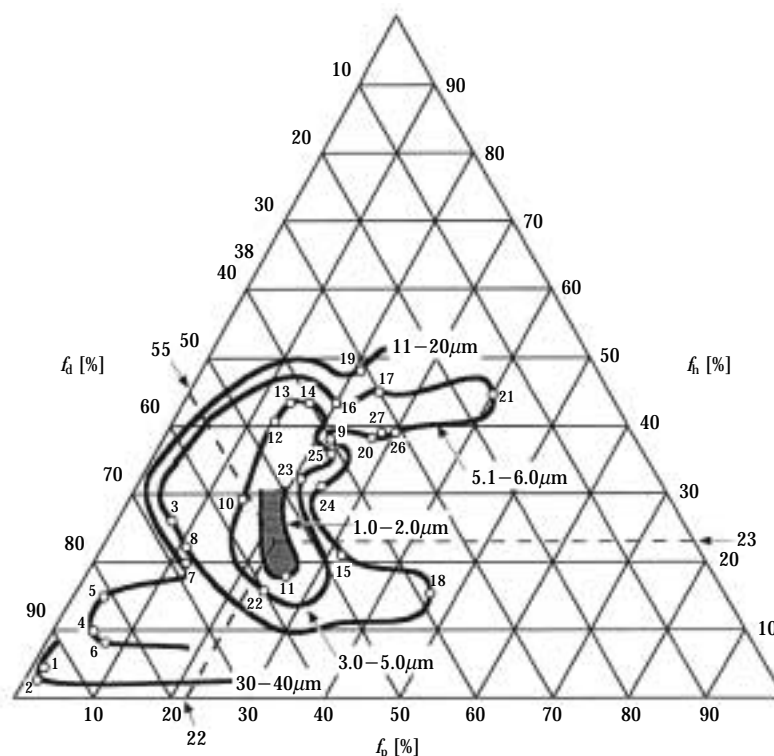


Fig. 5 Isometric particle lines on triangular chart for Fe_2O_3 (Each number means a solvent listed in Table 1)

solved in nonpolar solvents, but hardly dissolved in polar solvent. On the other hand, polar materials are easily dissolved in polar solvents, but hardly dissolved in nonpolar solvents. It can be also said that the dispersibility of fine particles is related with the affinity between a particle and a solvent. Therefore, the values of f_d , f_p and f_h of a hypothetical solvent for which the optimal dispersible point is obtained may correspond to the values of f_d , f_p and f_h of each particle itself. When the values of f_d , f_p and f_h of a solvent approach to the optimal dispersible point, the particle is well dispersed in the solvent.

5. Conclusion

In order to clarify the relationship between the flocculation/dispersion of fine metal oxide particles and the properties of solvents, the dispersibility of TiO_2 , Al_2O_3 and Fe_2O_3 particles in various solvents was investigated in this study.

High polar solvents tend to disperse metal oxide particles. The Hamaker constant of particles becomes large in the solvent with low dielectric constant, and then the particles have tendency to flocculate. However, some particle-solvent systems do not obey this tendency. It is difficult, therefore, to evaluate the flocculation/dispersion behavior by using only polarity of solvent or the Hamaker constant of particle.

The dispersibility of particles in various solvents can be evaluated by using the numeral balance, f_d , f_p and f_h of Hansen's three solubility parameters. The values of f_d , f_p and f_h of the hypothetical solvent giving the optimal dispersion exist for each particle. As the values of f_d , f_p and f_h approach to the optimal dispersible point, the fine particles are well dispersed in a solvent. The f_d , f_p and f_h values for an optimal dispersible point seem to be the values of f_d , f_p and f_h of the particles themselves.

Nomenclature

A	= Hamaker constant	[J]
a	= Particle diameter	[m]
f_d, f_p, f_h	= Numeral balance of $\delta_d, \delta_p, \delta_h$	[%]
H	= Enthalpy	[J mol ⁻¹]
L	= Distance between particles	[m]
n	= Number of -OH group in a molecule	[-]
n_D	= Refractive index	[-]
R	= Gas constant	[J mol ⁻¹ K ⁻¹]
T	= Temperature	[K]
V	= Molar volume	[m ³ mol ⁻¹]
γ	= Surface tension	[N m ⁻¹]

δ = Hildebrand's solubility parameter [-]
 $\delta_f, \delta_p, \delta_h$ = Hansen's solubility parameters [-]
 ϵ = Dielectric constant [-]
 μ = Dipole moment [C m]

- 3) Hansen, C. M.: *The Three Dimensional Solubility Parameter and Solvent Diffusion Coefficients*, Danish Technical Press, Copenhagen (1967)
- 4) Hansen, C. M.: *J. Paint Technology*, **39**, 104-117 (1967)
- 5) Hansen, C. M.: *J. Paint Technology*, **39**, 505-510 (1967)
- 6) Hansen, C. M.: *J. Paint Technology*, **39**, 511-514 (1967)
- 7) Shibata, J., K. Fujii, K. Horai and H. Yamamoto: *Kagaku Kogaku Ronbunshu*, **27**, 497-501 (2001)
- 8) Shibata, J., K. Fujii and H. Yamamoto: *Kagaku Kogaku Ronbunshu*, **28**, 641-646 (2002)
- 9) Bottcher, C. F. J.: *Theory of Electric Polarization*, Elsevier, Amsterdam (1952)

References

- 1) Kitahara, F. and K. Furusawa: *Saishin koroido kagaku*, Koudansha Scientific, Tokyo (1990)
- 2) Hildebrand, J. H. and R. L. Scott: *The Solubility of Non-Electrolytes*, Interscience, New York (1950)

Author's short biography



Junji SHIBATA

Dr. Junji Shibata is a professor of Chemical Engineering at Kansai University. He has had a research interest centered in Applied Surface Chemistry including the particle dispersion, solvent extraction, flotation, mineral processing etc.



Katsuya FUJII

Katsuya Fujii received the degrees of BS and MSc in the Department of Chemical Engineering at Kansai University under the supervision of Prof. J. Shibata in 1999 and 2001, respectively. He is researching as a student of Doctor Course at Graduate School of Kansai University. His main research work is to clarify the mechanism of flocculation/dispersion behavior of metal oxide particles in various solvents.



Norihiro MURAYAMA

Dr. Norihiro Murayama is Research Assistant in the Department of Chemical Engineering at Kansai University, Japan. He received the degrees of BS and MSc in Chemical Engineering from Kansai University in 1994 and 1996, respectively, and got his Ph.D. degree from the same university in 2000. His research deals with the synthesis of inorganic materials by using various metallic wastes, such as coal ash, incineration ash, aluminum dross and so on, as a raw material.



Hideki YAMAMOTO

Dr. Hideki Yamamoto is Associate Professor in the Dept. of Chem. Eng. at Kansai University, Japan. He received the degrees of BS and MSc in Chemical Engineering from Kansai University in 1982 and 1984, respectively, and got his Ph.D. degree from the same university in 1991. He has experience as visiting professor of Dept. of Chem. Eng., Texas A&M University. His research deals with environmental protection engineering such as removal of toxic materials in water, harmless disposal of global warming gas from semiconductors manufacturing process.

Information Articles

The 36th Symposium on Powder Technology

The 36th Symposium on Powder Technology was held on August 30, 2002 at the Arcadia-Ichigaya in Tokyo under the sponsorship of the Hosokawa Powder Technology Foundation and with the support of Hosokawa Micron Corporation. The symposium in

this year was also very successful with the attendance of 208 with about 20 academic people. The main subject of this year was “Industrial Development of Nanoparticles”.

The 36th Symposium on Powder Technology
Subject: “Industrial Development of Nanoparticles”

Session 1 Chairperson: Prof. Hitoshi Emi (Kanazawa Univ.)

• Particle Electrification (KONA Award Commemorative Lecture)	Prof. Hideo Yamamoto (Soka Univ.)
• Problems and Application of Material and Bio- Nanotechnology	Prof. Yukio Yamaguchi (Tokyo Univ.)

Session 2 Chairperson: Prof. Kiyoshi Nogi (Osaka Univ.)

• Control of Powder and Nanoparticle properties — Key to Creation of New Industries	Prof. Makio Naito (Osaka Univ.)
• Manufacture and Application of the Fullerenes	Dr. Gohei Yoshida (Honjo Chemical Corporation)

Session 3 Chairperson: Prof. Jusuke Hidaka (Doshisha Univ.)

• Aerosol Deposition Method for Thick Film Coating on Electroceramic Material	Dr. Jun Akedo (National Institute of Advanced Industrial Science and Technology)
• Particle Engineering using Nano-sized Particles and Its Application to Drug Delivery System	Dr. Toyokazu. Yokoyama (Hosokawa Powder Technology Research Institute)



The 10th KONA Award

As the winner of the KONA Award, which is sponsored by Hosokawa Powder Technology Foundation and given to the scientists or groups who have achieved excellent researches in the field of particle science and technology, Professor Hideo Yamamoto of Soka University was selected.

Prof. Yamamoto has achieved remarkable results in the field of particle science and technology, which

include those on the mechanism of contact electrification of particles and preparation of functional particles.

On January 24, 2002, Mr. Masuo Hosokawa, President of the Foundation, handed the 10th KONA Award to Prof. Yamamoto at the ceremony of presentation held at the R&D Center of Hosokawa Micron Corporation in Hirakata, Japan.



Academic publication concerning powder technology in Japan (2001)

Journal of the Society of Powder Technology, Japan Vol.38 (2001)

Title	Author(s)	Page
<Research Papers>		
• Separation of Silicestone and Pyrophyllite by Gas-Solid Fluidized Bed Utilizing Slight Difference of Density	J. Oshitani, M. Kondo, H. Nishi and Z. Tanaka	4
• Analysis of Settling Interface Formation Process in Suspension	T. Sugimoto, H. Hirose, H. Mori and J. Tsubaki	11
• Effect of Bulk Density and Flowability of Powders on the Feed Rate of Screw Feeder	M. Kimata, H. Tsujikawa and K. Matsumoto	18
• Relationship between Water-holding Capacity of Powder and Physical Properties of Granules Prepared by Agitating Granulation	H. Ueda, J. Ueda and T. Sato	84
• Production of Silica Particles by Electrostatic Atomization	Y. Mori and Y. Fukumoto	90
• Evaluation of Particle Behavior in Gas-Solid Fluidized Bed Composed of Different Size Particles by Measurement of Apparent Buoyancy	J. Oshitani, B. Trisakti and Z. Tanaka	97
• Numerical Simulation of Particle Sedimentation in Liquid and Experimental Verification	T. Umekage, S. Yuu, K. Nakashima, T. Sugimoto and J. Tsubaki	140
• Compressive Flow Property of Powder in Roll-type Presses –Numerical Simulation by Discrete Element Method–	K. Odagi, T. Tanaka and Y. Tsuji	150
• Development of Agglomerated Crystals of Ascorbic Acid for Direct Tableting by Spherical Crystallization Technique and Evaluation of Their Compactibilities	M. Imai, K. Kamiya, T. Hino, H. Yamamoto, H. Takeuchi and Y. Kawashima	160
• Agitating Granulation and Compression Compact for Compacting Detergents	K. Terashita, C. Kyoufuji and K. Miyanami	169
• Microstructure and Surface Behavior of Silica Gel Prepared from Metal Alkoxide	H. Kamiya and M. Yoshida	230
• Transport Characteristics of Ultrahigh Bulk Density Granules by Shot Type Plug Flow Transporter	M. Konami, S. Tanaka, A. Iwai and K. Matsumoto	236
• Interaction Forces between Silica Surfaces in Wet Cyclohexane	Y. Kanda, T. Nishimura and K. Higashitani	316
• Release Process of Enzymes From Baker's Yeast by Disruption in Agitating Bead Mill	S. Morohashi, T. Tachibana, N. Takai and K. Hoshino	323
• Grinding Aluminum Hydroxide and its Effect on Properties of Hardened Cement Material Forming Calcium Aluminate	M. Miyazaki, M. Kitamura, M. Kamitani, J. Kano and F. Saito	331
• Crystallization and Densification of Cordierite Ceramics using Kaolinite as Raw Material	Y. Kobayashi	338
• Particle Morphology and Battery Property of Lithium Manganate Synthesized by Ultrasonic Spray Pyrolysis	T. Ogihara, H. Aikiyo, N. Ogata, K. Katayama, Y. Azuma, H. Okabe and T. Ookawa	396
• Kneading and Dispersion of Positive Electrode Materials in Lithium Ion Secondary Battery for High Density Film	K. Terashita and K. Miyanami	401
• Particle Composite Process by a New Vessel Type Mixer	T. Hotta, T. Fukui, H. Okawa, S. Ohara, M. Naito, S. Asahi, S. Endoh and K. Nogi	408
• Improvement of Property of Solid Oxide Fuel Cells Anode with Fine and Coarse Yttria Stabilized Zirconia Particles	H. Itoh	414
• Effect of Hydrophobic Surface Treatment of Quartz Particles on Packing and Flowability of Powder	M. Suzuki, M. Kobayashi, K. Iimura and M. Hirota	468
• Consideration on Dynamics of Decelerated Ascent Motion of Grains in Inclined Disc Pelletizer	T. Moriwaki	473
• Improved Dispersibility of Iron Oxide Particle Coated by Ether-modified Poly-Siloxane for Water-based paint	K. Hayashi, M. Ohsugi, H. Morii and K. Okuyama	482

Title	Author(s)	Page
● Material Separation from Automobile Shredder Dust by Pneumatic Separation Method	J. Oshitani, K. Kiyoshima and Z. Tanaka	487
● Effective Sulfur Dioxide Removal by Powder-Particle Fluidized Bed Using Fine Calcined Lime Powders Reformed by Inorganic modifiers	T. Tashimo, Y. Lin and K. Kato	536
● Oxidation Behavior of Spray Pyrolyzed Ag-Pb Alloy Particle	N. Iida, K. Nakayama, I.W. Lenggoro and K. Okuyama	542
● Evaluation of Compression-Permeability Characteristics based on Vacuum Filtration Test Using Nutsche Equipped with Floating Disk	E. Iritani, Y. Mukai and J.H. Cho	548
● Concentration and Desalination of Protein Solutions with Superabsorbent Hydrogels	E. Iritani, Y. Mukai and C. Ueki	555
● Effect of Surface-treatment Additive on Particle Characteristics and Catalytic Activity of Molybdenum Sulfide Prepared by Wet Comminution	K. Uchida, Y. Kuriki, K. Shimada, K. Kamiya, H. Hayakawa, A. Kawai, A. Gotoh and F. Ikazaki	600
● Improved Coal Pulverization Using Embrittlement due to Cracks Generated in Pores of Coal	T. Ono	607
● Dispersing Abilities of New Microbial Dispersants and Their Derivatives	T. Yoshiyasu, T. Kakiuchi, T. Yamashita and K. Furusawa	612
● Particle Discharge Characteristics from a Nozzle of Thin Tube Immersed in Liquid Subject to Ultrasonic Wave Force	K. Yamamoto, M. Shiokari, T. Miyajima, M. Kawamura and M. Sugimoto	617
● Particle Classification with Improved Hydro-cyclone Separator	H. Yoshida, S. Akiyama, K. Fukui and A. Kumagaya	626
● Development of Ceramic Shaping Device with Electrophoretic Deposition Method	E. Usuki, N. Asai, K. Oda and S. Suzuki	633
● Powder Characteristics of Filler for Molding Compound of Thermosetting Plastics	T. Kawaguchi, M. Suzuki and M. Hirota	688
● Impact Electrification of Particles with Metal Plate in Nitrogen Atmosphere	A. Ema, K. Tanoue, H. Maruyama and H. Masuda	695
● Material Separation from Automobile Shredder Dust by Gravity Method Using Gas-Solid Fluidized Bed	J. Oshitani, T. Kajiwara, K. Kiyoshima and Z. Tanaka	702
● Analysis of Filtration Process of Body-Feed Microfiltration Forming Compressible Filter Cake	E. Iritani, Y. Mukai and H. Hayashi	710
● Recovery of Valuable Materials from Wasted Printed Wiring Board by an Impact Mill	M. Furuuchi, C. Kanaoka and S. Hara	770
● Wet Agglomeration in a Suspension of Particles of Multiple Materials	H. Takase and A. Kojima	779
● Basic Study on the Resource Recovery of Metal Plating Sludge and Aluminum Dross Using Thermint Reaction	K. Terashita, S. Sugimoto, T. Ohnishi and K. Miyanami	788
● Coating of Pharmaceutical Particles by Spouted Bed with a Draft Tube – Control of Seed Particle Circulation Rate –	S. Ando, T. Maki, Y. Nakagawa, H. Emi and Y. Otani	795
● Preparation of Active Hydrated Alumina by Mechanical Activation and its Application to Rapid Cement Hardener	M. Kitamura, T. Sahara, M. Miyazaki, M. Kamitani and M. Senna	844
● Application of Core/Shell Type Granulation Process for Preparation of Compression Molding Granules Containing Fibrous Material and Powders	A. Hashimoto, M. Satoh, T. Iwasaki and M. Kawasaki	850
● Estimation of the Critical Outlet Size to prevent Arch Formation in a Miniature Silo under Centrifugal Force	H. Tsunakawa	857

Kagaku Kougaku Ronbunshu Vol.27 (2001)

Title	Author(s)	Page
● Improvement in Coercivity of Magnetic Iron Fine Particles Produced from α -FeOOH	E. Hilmawan, S. Mori, M. Kumita and Y. Takao	63
● Preparation of Spinel Lithium Manganese Oxide Fine Particles Using Ultrasonic Spray Pyrolysis Method	I. Taniguchi and L.C. Kuang	93
● Influence of Fiber Cross-sectional Shape on Filter Collection Performance	M. Inagaki, K. Sakai, N. Namiki, H. Emi and Y. Otani	113
● Effect of mechanochemical Treatment on Gasification of Carbon by Carbon Dioxide in Stirred Mill Reactor	T. Ido, M. Mori, G. Jin and S. Goto	121
● Effect of Rotor Shape on Particle Composite Process by a High-Speed Elliptical-Rotor-Type Mixer	T. Hotta, M. Naito, J. Szepvolgyi, S. Endoh and K. Nogi	141
● Correlation Equation of Nucleate Boiling Heat Transfer from Horizontal Cylinder to Liquid Containing Movable Particles	T. Tsuyuki, Y. Iida and K. Okuyama	275
● Preparation of Silica-Coated Co-Fe ₃ O ₄ Nanoparticles and their Magnetic Properties	T. Tago, T. Hatsuta, R. Nagase, M. Kishida and K. Wakabayashi	288
● Captive Particle Imaging during Combustion and Quantitative Evaluation	M. Yokota, T. Nishimura, Y. Kawasaki and M. Hayashi	243
● Preparation and Microscopic Structure Control of Fine Particle Materials by Using Emulsion Liquid Membrane System as a Microreactor	T. Hirai and I. Komasa	303
● Change in Particle Morphology During Production Process of Magnetic Iron Fine Particles and Its Effect on the Product Coercivity	E. Hilmawan, S. Mori, M. Kumita and Y. Takao	392
● Effect of Ambient Conditions on the Compressive Strength of Granules	K. Nakahira, H. Abe, M. Naito, N. Shinohara, N. Miyagawa, H. Kamiya and K. Uematsu	416
● Dispersion and Flocculation behavior of Metal Oxide Powders in Organic Solvent	J. Shibata, K. Fujii, K. Horai and H. Yamamoto	497
● Orientational Distributions of a Ferromagnetic Spherocylinder Particle in a Simple Shear Flow – Analysis for a Magnetic Field Parallel to the Angular Velocity Vector of a Shear Flow –	M. Aoshima, A. Satoh, G.N. Coverdale and R.W. Chantrell	528
● Decrease in Fluidization Quality by Mixing Two Types of Catalyst Particles	T. Kai, K. Makado, T. Takahashi, T. Tsutsui and K. Sato	524
● Direct Numerical Simulation of the Flow Fields in a Medium Reynolds Number Non-Baffled Stirred Tank (Re=4,500) and Experimental Verification	S. Yuu, Y. Nakano and T. Umekage	554
● Computation of Air and Particle Motion in Bubbling Fluidized Bed Using Distinct Element Method	S. Yuu, T. Umekage, S. Kawakami and Y. Johno	560
● Fine Control of Cut Size with Dry Cyclone	H. Yoshida, S. Akiyama, K. Fukui, S. Taniguchi and A. Miyatake	574
● A Statistical Estimation of Precision in Sampling of Aerosol Particles by the Monte Carlo Method	M. Samata	610
● Preparation of Calcium Alginate Micro-Gel Beads Using a Rotating Nozzle	R. Nagata, K. Koga, S. Gondo, Y. Uemura and Y. Hatate	648
● Kinetics of Coagulation of Ultrafine Particles in Reverse Micellar and Homogeneous Solutions	H. Sato, K. Suzuki and I. Komasa	678
● Morphology of TiO ₂ Particles Dispersed in Zinc Electrodeposition	K. Kondo, K. Shimada and Z. Tanaka	696
● Control of Polymer Coating Thickness of Microcapsules Containing Inorganic Microparticles Using Cosolvency of Supercritical Carbon Dioxide	K. Mishima, K. Matsuyama, A. Furukawa, T. Fujii, J. Shida, N. Nojiri, H. Kubo and N. Katada	700
● Microencapsulation of Proteins with Polymer-Blend by Rapid Expansion of Supercritical Carbon Dioxide	K. Matsuyama, S. Yamauchi, T. Hirabaru, K. Hayashi, S. Hattori and K. Mishima	707

Title	Author(s)	Page
• Preparation of Gold Nanoparticles in Water-in-Oil Microemulsions	Y. Mori, S. Okamoto and T. Asahi	736
• Mechanism of Nanoparticle Formation in Hydrolysis and condensation of tetraethyl Orthosilicate	Y. Saito and M. Konno	749
• Orientational Distributions of a Ferromagnetic Spherocylinder Particle in a Simple Shear Flow – Analysis for A magnetic Field Parallel to A Shear Flow Direction –	M. Aoshima, A. Satoh, G.N. Coverdale and W. Chantrell	799
• Effect of Vibration on Particle Motion in Two Dimensional Fluidized Bed	Y. Takemoto, Y. Mawatari, M. Yamamoto and K. Noda	824

Hosokawa Powder Technology Research Institute has been founded for the new powder business of Hosokawa Group in the future

Hosokawa Micron Corporation recently announced that it will enter the nanotechnology-based/nanostructured material industry in order to expand its range of business opportunities through exploiting its abundant knowledge and experiences in the powder processing technology and microengineering. In line of this new strategy, Hosokawa Powder Technology Research Institute (HPTRI) was established in October 2002 to further promote R&D activities, in view of the major importance and infinite potentialities of nanotechnology and its application.

HPTRI consists of three divisions: R&D Division, Test Centers and Powder Contract Processing Division. Within the R&D Division, Nanoparticle Technology Center (NPTC) was newly established in order to carry out research in producing and processing nanoparticles. Various methods to produce nanoparticles are now being examined, and some of them are ready for commercialization/ready for the market. One of them is Joule Quench Method, a chemical-synthetic method using plasma technology which was recently introduced from NanoProducts Inc. Colorado, USA. In a pilot plant at NPTC in Hirakata, Osaka, sample nanoparticles have been already produced and distributed for customers' use and evaluation.

Another new and original technology of Hosokawa Micron is Mechano-Chemical Bonding (MCB), a method of creating new/nanostructured materials through activation of nanoparticles. The MCB processing systems are available for tests at HPTRI in Hirakata and its branch laboratory at Hosokawa Bepex Division, Minneapolis, USA.

HPTRI has two test centers, one in Hirakata, Osaka

Pref., and another in Tsukuba, Ibaraki Pref. (near Tokyo). Most kinds of test machines are available to meet the requirements of customers.

Also incorporated into HPTRI is Hosokawa Micrometrics Laboratory (HMLab). Originally founded in 1958, its main function is to carry out contract R&D projects for particle design and particle engineering as well as for the development of new advanced machines and systems for powder processing.

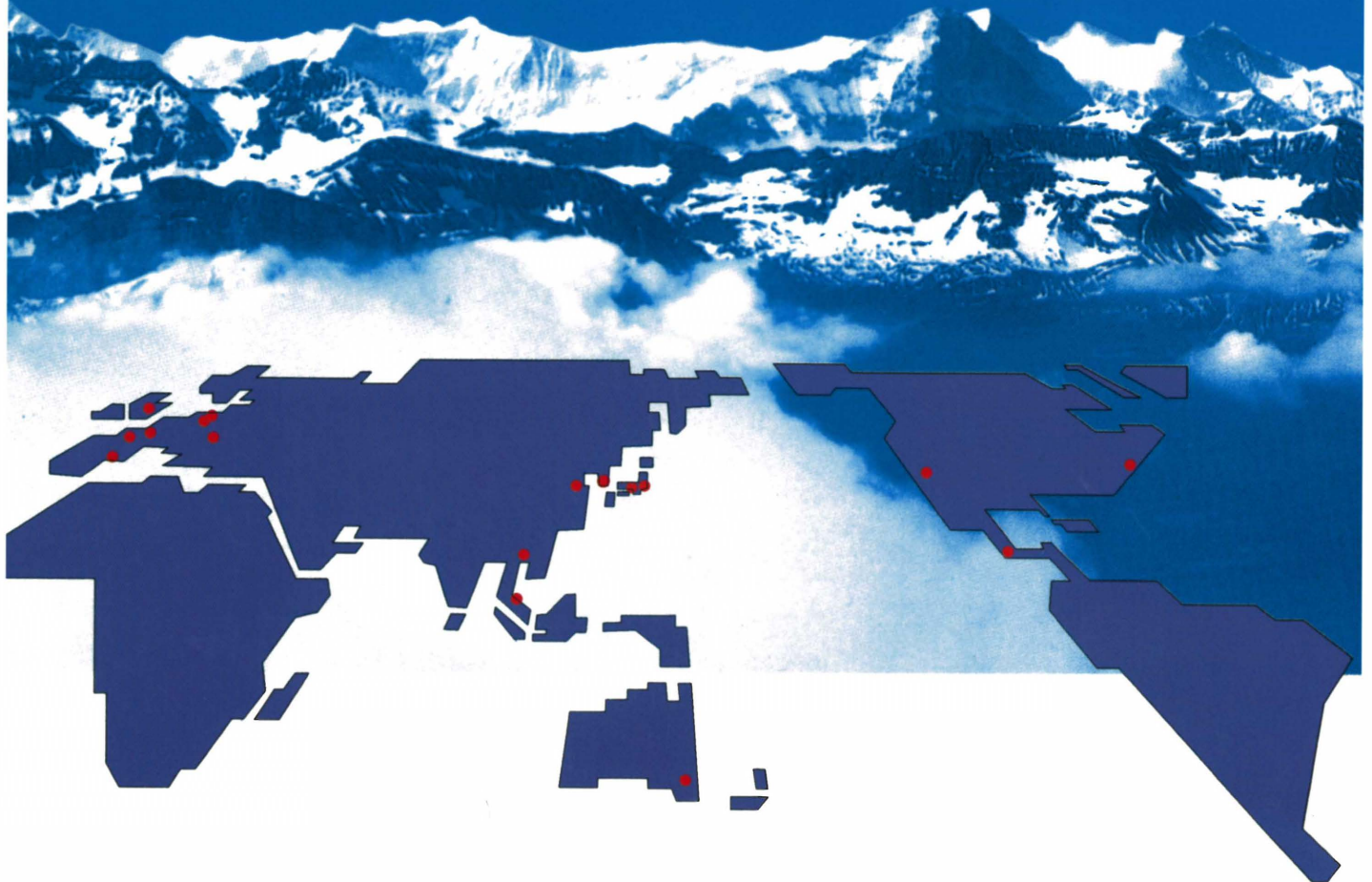
The Contract Powder Processing Division is also an important part of HPTRI, with the growing needs for the contract powder processing, which minimizes investment risks by cutting construction cost of production facilities, or enabling the customer to examine products in small portions.

With these comprehensive R&D systems and centers, the new research institute HPTRI is sure not only to support but also pioneer the business opportunities and possibilities of the present and the future.



HOSOKAWA MICRON

Hosokawa Micron Ltd. is a member of the Hosokawa Micron Group, responding to global needs through an emphasis on materials science and engineering. The Group is an international provider of equipment and Technology for powder and particle processing, product recovery, plastics processing and confectionery products. The Group maintains facilities for research, engineering, manufacturing, and service in each of the world's major industrial markets.



Process Technologies for Tomorrow



HOSOKAWA MICRON

Headquarter Locations;

HOSOKAWA MICRON CORPORATION

5-14, 2-chome, Kawaramachi, Chuo-ku,

Osaka 541-0048, Japan

Tel: 81-6-6233-3968

Fax: 81-6-6229-9267

<http://www.hosokawamicron.com/japan>